Impact of natural scenes on the reliability and correlations of cortical dynamics across layers in cat primary visual cortex

Yannick Passarelli

▶ **To cite this version:**

Yannick Passarelli. Impact of natural scenes on the reliability and correlations of cortical dynamics across layers in cat primary visual cortex. Neurons and Cognition [q-bio.NC]. Sorbonne Université, 2019. English. NNT : 2019SORUS291 . tel-03140353

HAL Id: tel-03140353
https://theses.hal.science/tel-03140353

Submitted on 12 Feb 2021

HAL is a multi-disciplinary open access archive for the deposit and dissemination of scientific research documents, whether they are published or not. The documents may come from teaching and research institutions in France or abroad, or from public or private research centers.

L'archive ouverte pluridisciplinaire **HAL**, est destinée au dépôt et à la diffusion de documents scientifiques de niveau recherche, publiés ou non, émanant des établissements d'enseignement et de recherche français ou étrangers, des laboratoires publics ou privés.

Sorbonne Université

Ecole doctorale Cerveau, Cognition et Comportement

Impact of Natural Scenes on the Reliability and Correlations of Cortical Dynamics across Layers in Cat Primary Visual Cortex

Par Yannick Passarelli

Thèse de doctorat de Neurosciences Cognitives

Dirigée par Cyril Monier et Yves Frégnac

Présentée et soutenue publiquement le : mercredi 11 décembre 2019

Devant un jury composé de :

Pr. Stéphane Molotchnikoff	Rapporteur
Dr. Lionel Nowak	Rapporteur
Dr. Sulian Ben Hamed	Examinatrice
Dr. Timo Van Kerkoerle	Examinateur
Pr. Régis Lambert	Examinateur
Dr. Yves Frégnac	Directeur de thèse
Dr. Cyril Monier	Co-directeur de thèse

Remerciements

J'aimerais tout d'abord remercier les membres de mon jury. Je tiens particulièrement à remercier Stéphane Molotchnikoff qui m'a accueilli en stage lors de mon séjour à Montréal et qui m'a permis de rentrer dans le monde des neurosciences visuelles. Merci de m'avoir guidé à l'époque, de m'avoir permis de rejoindre l'UNIC en me recommandant auprès de Yves, et de toujours me guider maintenant en évaluant mon travail de thèse.
Merci à Lionel Nowak qui aura suivi mon travail de son début, à travers les nombreux comités de mi thèse, jusqu'à sa fin en acceptant d'être rapporteur de celle-ci.
Merci à Régis Lambert, qui en plus d'évaluer ce travail, m'aura permis de patcher le seul et unique neurone de ma vie lors du cours de neurophysiologie du master BIP.
Thanks to Timo Van Kerkoerle for accepting to participate to this jury. Your suggestions on the analysis of the frequency bands of the unlocked LFP allowed the exploration of very nice aspects of V1.
Merci à Suliann Ben Hamed d'avoir accepté de faire partie de ce jury. Je suis heureux que les neurosciences lyonnaises soient représentées lors de ma soutenance.

Je tiens à remercier Yves Frégnac de m'avoir donné l'opportunité de travailler au sein de son équipe et de m'avoir fourni l'apport scientifique nécessaire à la réalisation de cette thèse.

Cyril, merci de m'avoir toujours laissé l'indépendance nécessaire pour apprendre les choses par moi-même mais d'avoir été là pour me guider lorsque cela était nécessaire. Ces derniers mois où nos discussions ont été les plus riches et les plus nombreuses ont été les moments les plus agréables de ma thèse. J'attends avec impatience la suite, pour la rédaction des papiers !

Margot en plus d'avoir égayé la vie du bureau en chantonnant de façon spontanée et involontaire pendant toutes ces années, je n'aurais jamais pu faire toutes ces manip sans toi.
Benoît, je suis très heureux que nous ayons fait nos thèses (à peu près) en même temps, heureusement que tu étais là pour qu'on partage nos galères V1 dépendantes (et pour défendre la Bretagne comme si ta vie en dépendait).
Marc et Christophe, merci d'avoir toujours été là pour me guider sur mes diverses questions à propos de la neurophysiologie et de la physiologie du chat.
Domenico, merci pour toutes nos discussions plus ou moins sérieuses sur le trajet du RER !
Jonathan, que Dieu bénisse toi, tes Motion Cloud et ton support permanent pendant toutes ces années.

Gérard, merci pour ton aide constante avec Elphy (et ta gentillesse). Tu n'as jamais craqué face à mes demandes répétées plus ou moins intelligentes.

Aurélie, un grand merci à toi. Pour l'apprentissage des techniques de chirurgie, pour avoir répondu à mes questions débiles liées à ces dites chirurgies, pour ta bonne humeur constante (et pour les pokémons !!!!)

Merci à Guillaume, en plus de couper les cerveaux comme personne, tu m'as appris qu'il faut toujours arriver tôt à la cantine (un enseignement fondamental dans la vie de quelqu'un).

Evan, merci d'avoir été un ami formidable et de m'avoir toujours aidé scientifiquement et moralement pendant ces 4 dernières années. Si j'ai pu finir cette thèse c'est en partie grâce à toi. J'espère que tu verras Arsenal regagner quelque chose de ton vivant, car tu mérites un tel bonheur…

Matias, merci à toi aussi d'avoir été un ami incroyable et de m'avoir aidé tout au long de cette thèse, à laquelle tu as contribué grandement ! Tu me donnes presque envie de voir l'Argentine gagner une coupe du monde… (Presque !)

Un grand merci à toute l'équipe moustache d'avoir fait de moi un membre honoraire de votre équipe (j'ai dit deux fois équipe). Merci à Dan d'avoir toujours été à l'écoute de mes problèmes. Valérie et Isabelle, merci de m'avoir soutenu et d'avoir supporté mes jérémiades tout au long de mon séjour à l'UNIC ! Vous m'avez rassuré plus d'une fois sur l'avenir incertain qu'est celui d'un étudiant en thèse…
Luc, merci de m'avoir fait rire avec tes petites blagues sur ma vie et avec tes imitations d'accent jamais réussies.
Dorian, merci d'avoir tu as été d'un soutien indéfectible pendant toutes ces années (mais pas merci de ne jamais avoir fait tomber ton plateau à la cantine).
Ah Titi…les épis de blé…Russell Crowe…
Aamir, je suis très heureux d'avoir rencontré quelqu'un d'aussi nul à Catane que toi ! Sophie, grâce à toi mon budget resto japonais a doublé, mon ventre te dit merci. Henri, merci pour tes explications détaillées sur la viande utilisée dans un bœuf bourguignon je suis prêt pour Top Chef et pour affronter la vie.
Pauline, merci de m'avoir montré qu'un être humain peut parler pendant 20 minutes de suite sans respirer.

Un énorme merci à Aline et Justine qui ne m'ont jamais envoyé bouler malgré mes demandes plus ou moins (surtout plus) pénibles. Vous méritez tous les pains surprises du monde.

Merci à tous les autres étudiants (en particulier les copains du bas Anthony et Seb), post-doc et permanents que j'ai plus ou moins harcelé lors de ces dernières années.

Merci à mes amis « parisiens », Nico « le Matuidi blanc » Sch, Martin « mon Ami… » Dupraz, Hugo, Loïc (on a vu Federer gagner !!!!!), Gabriel, Rym, Louise, Franfran, Baptiste, Pierre, Ghez, Raphael, Philippe, Maxime D, Maxime B, Vadim, Romain et Marie Lods (et Garonne) : Vos sourires m'ont toujours réchauffé le cœur…

A mes amis lyonnais, Marion, Claire, Garance, Bob, Raoul, Clément, Chloé, Edouard : vous êtes des petits anges de lumière.

Jules et Léonard, Léonard et Jules, comme un grand sage l'a dit : L'amitié est comme un melon. Il faut en essayer plusieurs avant d'en trouver un bon. Je peux affirmer que j'ai trouvé les meilleurs melons du marché…

Guigui, petit ange de lumière, un chef. Merci pour l'aide technique pendant cette thèse, la table des matières de ce manuscrit t'es dédiée. Je ne te remercie pas de m'avoir ramené à ma médiocrité car je ne sais pas jouer aux jeux vidéo. Rappelle-toi qu'on oublie jamais rien, on vit avec.

Merci à mes beaux-parents, Dominique et Vincent, pour les matchs à Roland Garros, les délicieux repas et de m'avoir toujours accueilli chez eux avec la même gentillesse, que ce soit pour un week-end ou un mois.

Un grand merci à la famille Monvignier-Monnet qui m'a toujours soutenu lors de ces différentes années de thèse !
Merci à Jo et Françoise, mes grands-parents, qui ont toujours été passionnés par mes recherches. Votre intérêt m'a toujours beaucoup touché et motivé !

Obrigadão a toda a família Passarelli que sempre se interessou pelas minhas pesquisas. Obrigado por ter vindo me ver aqui na França. Agora eu vou poder vim ver vocês!!!!
Obrigado a minha avó Eletice, pelos tatu-bolas, as feijoadas e pelo todo o carinho que você me deu.

Rafa, petit pignouf, que ça soit au Brésil, à Lyon, Québec ou à Paris tu as toujours été un petit frère formidable. Que ce soit formidablement nul à Fifa ou formidablement chouette.

Merci à mes parents, Véronique et Fernando. Vous avez toujours cru et investi en moi. Sans votre soutien inconditionnel je ne pense pas que j'aurai eu l'envie, ni le courage de commencer un doctorat. Pour cela (et bien d'autres choses), je vous serai toujours reconnaissant.

Marine, sans toi cette thèse n'aurait jamais commencé et ne se serait jamais terminée. Ton courage, ton intelligence et ta motivation sans faille m'ont inspiré et m'inspireront toujours. Ceci est un aperçu de ce que tu m'as apporté car est impossible de quantifier à quel point tu as été essentielle à ma vie pendant ces années.

Résumé

Selon le principe de codage efficace introduit par Horace Barlow en 1961, le traitement visuel de l'information par les systèmes sensoriels primaires devrait être optimisé et adapté aux propriétés statistiques de l'environnement sensoriel. Ce principe affirme que (i) l'exposition à des statistiques naturelles devrait réduire la redondance de populations de neurones individuels présente dans les suites de potentiels d'action, qui sera associée à (ii) une diminution de la variabilité des réponses liées aux stimuli et (iii) une parcimonie de l'activité de la population globale. Cependant, la plupart des études du cortex visuel primaire (V1) se sont limitées à des fonctions visuelles artificielles telles que des points, des barres, des grilles et du bruit épars, qui sont utiles dans les systèmes linéaires d'identification mais rarement rencontrées dans l'environnement naturel. Dans les cas de telles simulations artificielles, les réponses des neurones de V1 montrent une variabilité très importante pour des présentations répétées du même stimulus. Cette variabilité a généralement été expliquée par différents facteurs tels que l'état général du réseau cortical, les propriétés stochastiques des neurones V1 ou le recrutement de neurones inhibiteurs responsables de la réalisation d'une opération appelée « divisive normalization » (Heeger, 1990).

Pour répondre aux questions relatives au paradigme de codage efficace, une étude réalisée sur le chat anesthésié et paralysé (Baudot et al., 2013) a comparé les réponses intracellulaires de neurones V1 à des stimuli de différentes complexités (réseaux dérivants (DG), réseaux dérivants animés à l'aide de mouvement des yeux artificiels (GEM), des images naturelles animées à l'aide de mouvement des yeux artificiels (NI) et du bruit dense (DN). Ils ont observé que les images naturelles induisaient des réponses neuronales reproductibles, précises et éparses alors même que les stimuli artificiels causaient des réponses denses, imprécises et peu reproductibles. Par ailleurs, une étude deux photons dans V1 de la souris (Rikhye & Sur, 2015) a montré que la reproductibilité des réponses corticales à des scènes naturelles varie d'une part en fonction des basses fréquences contenues dans une image naturelle, d'autre part en fonction de la puissance de ses corrélations spatiales. Ces observations restent cependant à confirmer chez les mammifères supérieurs. L'étude mentionnée précédemment était centrée sur les statistiques spatiales de scènes naturelles. En effet ; les stimuli naturels sont généralement composés d'un spectre fréquentiel de $1/f^{\alpha}$ à la fois dans les domaines spatiaux et temporels. Si les effets des statistiques spatiales ont été étudiés, il n'existe que peu de données quant au rôle des statistiques temporelles.

Les études susmentionnées étudiaient les différents aspects de la théorie du codage efficace, d'une part dans un échantillon de cellules restreint mais également au sein d'une couche corticale. Lors de ce travail de thèse nous avons enregistré l'activité neuronale dans toutes les couches de V1, chez le chat anesthésié et paralysé, à l'aide une électrode linéaire dense à 64 canaux. Nous avons enregistré la réponse de l'activité unitaire (SUA), multi-unitaire (MUA) ainsi que le potentiel de champ local (LFP) en réponse à DG, GEM, NI et DN — stimuli qui furent précédemment utilisés par Baudot et al (2013). Nous avons cependant enrichi ces stimuli à l'aide de différents contrôles. En effet, nous avons développé des images naturelles où nous avons manipulé les statistiques des trajectoires du mouvement oculaire (*i.e.* les statistiques temporelles) et les statistiques spatiales. Les stimuli ont tous été présenté sur le centre du champ récepteur (condition « centre seul »), uniquement sur le pourtour du champ récepteur (condition « pourtour seul » ou bien sur le centre et le pourtour simultanément (condition « plein champ »)

L'enregistrement de l'activité neuronale à l'aide d'une électrode linéaire dense à nombreux canaux, couplé aux méthodes de tri automatique des potentiels d'action, nous a permis d'enregistrer, de distinguer et de caractériser les sous-classes d'un grand nombre de neurones (« regular » ou « fast spiking » neurones (neurones RS et FS)) à travers toutes les couches corticales. En procédant ainsi, nous avons cherché à comparer la reproductibilité des signaux mésoscopiques (LFP et MUA) et microscopiques (neurones SUA, RS et FS) en fonction des différentes conditions de stimulation ainsi qu'à explorer la dépendance laminaire de la réponse. Nos résultats montrent que des images naturelles animées par le mouvement des yeux évoquent

des réponses plus reproductibles que les autres stimuli, quelle que soit la couche ou l'échelle d'enregistrement. Parmi la population de neurones isolés, les neurones FS ont induit des réponses plus reproductibles que les neurones RS. De façon générale, le LFP a présenté les plus hauts niveaux de reproductibilité alors que le SUA a présenté les plus bas niveaux. Si les réponses à des images naturelles présentaient un haut niveau de fiabilité à travers toutes les couches, elles l'étaient le plus dans les couches recevant des entrées thalamiques, c'est-à-dire les couches 4 et 5/6.

La baisse de variabilité des réponses observées dans le cas des images naturelles est fortement modulée par les interactions centre-pourtour. En effet, la stimulation du centre seul résulte en une reproductibilité plus faible que celle du centre-pourtour, dans toutes les couches et à toutes les échelles d'enregistrement. La stimulation du pourtour seul à l'aide de scènes naturelles évoque également un LFP reproductible dans toutes les couches. De plus, le pourtour seul évoque une réponse LFP plus reproductible que le centre seul dans les couches où les connexions horizontales sont présentes (2/3 et 5/6), ce qui met en évidence le rôle crucial des propriétés anatomiques de V1 dans le traitement de scènes naturelles.

En manipulant les statistiques temporelles et spatiales de la stimulation naturelle au niveau LFP, nous avons démontré que les statistiques temporelles ayant un spectre de $1/f^{\alpha}$ sont cruciales dans la génération de réponses reproductibles. Nos résultats montrent que le pourtour est essentiel dans le traitement de ces données temporelles, et ce à toutes les échelles neuronales.

Nous nous sommes particulièrement intéressés au rôle des corrélations entre les neurones en étudiant la corrélation de la réponse et la corrélation de la variabilité de la réponse de neurones situés dans une même couche ou dans des couches différentes. Nous avons observé que les images naturelles suscitent systématiquement une corrélation plus forte que des stimuli artificiels alors même qu'aucune différence n'était observée dans le cas de la corrélation de la variabilité de la réponse. Par ailleurs, la présentation de scènes naturelles dans les conditions centre-pourtour a provoqué une décorrélation de la corrélation de la variabilité par rapport aux conditions du centre uniquement. Enfin, nous avons montré que les corrélations sont plus importantes au sein des couches qu'entre elles.

Nous n'avons pas observé de forte décorrélation au niveau du neurone individuel, mais plutôt à l'échelle d'un groupe de neurones ; les plus proches étant plus corrélés et les plus éloignés l'étant moins. Cela va dans le sens d'un regroupement des neurones en une « masse neurale » cohérente. Ces groupes de neurones pourraient encoder des morceaux d'une scène visuelle contenant des informations significatives (comme suggéré par Rikhye & Sur, 2015). Ainsi, ces résultats appuient fortement la nécessité d'une version modifiée de la théorie du codage efficace où la décorrélation de l'activité neuronale n'agirait pas au niveau du neurone individuel mais plutôt à celui d'un groupe de neurones spatialement proches.

Mots Clés : Électrophysiologie ; Cortex Visuel Primaire ; Reproductibilité ; Corrélations ; Interactions Centre-Pourtour ; Enregistrements Laminaires

Abstract

The principle of efficient coding introduced by Horace Barlow in 1961 suggests that visual processing in early sensory systems should be optimized and adapted to the statistical properties of the sensory environment. It asserts that (i) exposure to natural-like statistics should reduce the redundancy present in the spike trains of populations of individual neurons, which will be associated with (ii) a decrease in stimulus-locked response variability at the single neuron level and (iii) an increase in the sparseness of the global population activity. However, most studies on the primary visual cortex (V1) have been restricted to artificial visual features such as spots, bars, gratings and sparse noise, which are useful in linear systems identification but not often encountered alone in the natural environment. For such artificial stimulation types, the responses of single neurons in V1 show a considerable amount of variability for repeated presentations of the same stimulus. This variability has typically been explained by several factors such as the global state of the cortical network (ongoing activity), the stochastic properties of V1 neurons, or the recruitment of a diffuse inhibitory intracortical pool of neurons responsible for carrying out a computation called divisive normalization (Heeger, 1990).

In order to address these questions in the efficient coding framework, one study performed on the anesthetized and paralyzed cat (Baudot *et al.*, 2013) compared intracellular responses of V1 neurons to full field stimuli of different complexity (Drifting Gratings (DG), Gratings animated with eye movements (GEM), Dense Noise (DN) and Natural images animated with eye movements (NI)). They observed that natural images trigger sparse, precise and reliable membrane potential dynamics and spiking activity, whereas artificial stimuli induce dense, imprecise and unreliable responses. Additionally, a two-photon study in mouse V1 (Rikhye & Sur, 2015) found that the reliability of cortical responses to natural scenes depends on the low frequency content of the natural image, and on the strength of its spatial correlations. However, these observations remain to be confirmed in higher mammals. The study mentioned above focused on the spatial statistics of natural scenes. Indeed, natural stimuli are generally comprised of power law frequency spectra ($1/f^{\alpha}$) in both spatial and temporal domains. While the impact of spatial statistics has been investigated, very limited data about the role of temporal ones is available.

The aforementioned studies investigated the different aspects of efficient coding theory either on a small sample of cells or within one cortical layer. In this PhD project, we recorded across all layers in V1 in the anesthetized and paralyzed cat with a 64-channel high-density linear silicon probe. Single unit and multi-unit activity (SUA, MUA), as well as local field potential (LFP) were examined in response to DG, GEM, DN and NI. These stimuli were previously used in the intracellular study of Baudot *et al* (2013). Yet, we enriched their stimulus set with additional controls. We incorporated natural images where we manipulated the statistics of the eye movement trajectories (*i.e.* the temporal statistics) and the spatial statistics. All stimuli were presented either on the center of the receptive field only (center condition), in the surround only (surround condition), or on both simultaneously (full field condition).

Choosing a high-channel count silicon probe coupled with automated spike sorting methods allowed us to record, discriminate and label the subclasses of a large number of neurons (regular or fast spiking cells) across all cortical layers. In this way, we aimed to compare the reliability of the mesoscopic signal (LFP and MUA) across the different stimulus conditions with the microscopic signal (SUA, RS and FS neurons) and to explore its laminar dependency. Our results show that natural images animated with eye movements evoked more reliable responses, across all layers and at all scales, than the other stimuli. Among the single units, FS neurons evoked more reliable responses than RS. In general, the LFP displayed the highest levels of reliability while the lowest was observed for the SUA. Although responses to natural images were highly reliable across all layers, they were the highest in the layers receiving thalamic inputs, *i.e.* layers 4 and 5/6.
We observed that the decrease in the variability of the responses observed for natural images is strongly mediated by center surround interactions. Indeed, the stimulation of the center alone results in a lower reliability, in all layers and at all recording scales, than the center surround condition. The stimulation of the surround alone with natural scenes also evoked a reliable LFP across all layers. In addition, the surround alone

condition evoked a more reliable LFP response than the center condition in the layers where horizontal connections are present (2/3 and 5/6), which highlights a crucial role of the anatomical properties of V1 in the processing of natural scenes.

We were able to identify which statistical features are important to drive reliable responses. By manipulating the spatial and the temporal statistics of the natural stimulation, we demonstrate that, at the LFP level, temporal statistics following a power law of $1/f^{\alpha}$ are crucial in the generation of a reliable response. Our results also highlight the fact that, at all scales, the surround is essential in the processing of these temporal features.

We specifically addressed the role of the correlations between neurons (within and between layers) by measuring the amount of shared variability and signal (*i.e.* the noise and signal correlations, respectively) of the neuronal population in response to artificial and natural stimuli. We observed that natural images always evoked a higher signal correlation than artificial stimuli while almost no difference was observed for noise correlations. In addition, the presentation of natural scenes in the center surround condition decreased the noise correlations compared to the center alone condition. Finally, we show that the correlations are higher within layers than between layers.

We did not observe a strong decorrelation at the single cell level but instead at the scale of groups of neurons, with those that are close together being more correlated and farther apart less correlated. This argues for a functional clustering of the neurons into a coherent “neural mass”. These clusters could encode for a piecewise decomposition of the visual scene into meaningful features (as suggested by Rikhye & Sur, 2015). Thus, these findings strongly argue for a modified version of the efficient coding theory where the decorrelation of neuronal activity does not happen at the single cell scale but instead at the scale of spatially local neuronal clusters.

Keywords : Electrophysiology; Primary Visual Cortex; Reliability; Correlations, Center-Surround Interactions; Laminar Recordings

CONTENT

I. INTRODUCTION 1

1. STRUCTURAL ORGANIZATION OF CAT EARLY VISUAL SYSTEM 1

1.1. ORGANIZATION OF CAT PRIMARY VISUAL CORTEX 2

1.2. THE EARLY VISUAL SYSTEM 6

1.2.1 The Retina 6

1.2.2 The Lateral Geniculate Nucleus 7

1.3. STRUCTURAL AND FUNCTIONAL ORGANIZATION OF CAT PRIMARY VISUAL CORTEX 8

1.3.1 Cortical neuronal diversity 8

2. ELECTROPHYSIOLOGICAL RECORDINGS OF CORTICAL ACTIVITY 13

2.1. DIVERSITY OF DISCHARGE TYPES AMONG CORTICAL NEURONS 13

2.1.1 Intracellular Classification 13

2.1.2 Extracellular Classification 17

3. FUNCTIONAL MICROCIRCUITS OF CAT PRIMARY VISUAL CORTEX 20

3.1. VISUAL PROCESSING INTRINSIC TO V1 20

3.1.1 Thalamic inputs 20

3.1.2 Intra V1 inputs 20

3.2. FEEDFORWARD AND FEEDBACK CONNECTIVITY 22

3.3. LAMINAR PROCESSING WITHIN THE CORTICAL COLUMN 23

4. VISUAL STIMULATION 26

4.1. ARTIFICIAL STIMULI 27

4.2. NATURAL STIMULI 29

4.2.1 Luminance and contrast 29

4.2.2 Spatial Statistics 30

4.2.3 Temporal Statistics 32

5. FUNCTIONAL ORGANIZATION OF CAT PRIMARY VISUAL CORTEX 37

5.1. RECEPTIVE FIELDS 37

5.1.1 Simple receptive fields 37

5.1.2 Complex Receptive Fields 41

5.1.3 Mesoscopic receptive fields 41

5.2. LAMINAR DISTRIBUTION OF RECEPTIVE FIELDS 42
5.3. RECEPTIVE FIELD SURROUND 44
5.4. NEURONAL FUNCTIONAL SELECTIVITY 44
5.4.1 Spatial Frequency Selectivity 44
5.4.2 Temporal Frequency Selectivity 47
5.4.3 Orientation Selectivity 48
5.4.4 Direction Selectivity 50
5.5. CORTICAL MAPS IN CAT PRIMARY VISUAL CORTEX 51
5.5.1 Retinotopy 51
5.5.2 Ocular Dominance 52
5.5.3 Light-Dark polarity 52
5.5.4 Orientation Map 53
5.5.5 Direction Map 55
5.5.6 Spatial Frequency Map 55
6. STIMULUS DEPENDENCE OF THE FUNCTIONAL RESPONSE 57
6.1. ARTIFICIAL STIMULI AND FUNCTIONAL RESPONSES 58
6.1.1 Surround Modulation 58
6.1.2 Linear nonlinear models 60
6.1.3 Stimulus dependence of Simple and Complex cells. 63
6.2. NATURAL STIMULI AND FUNCTIONAL RESPONSES 64
7. CORTICAL VARIABILITY DYNAMICS 70
7.1. STIMULUS-INDEPENDENT SOURCES OF NEURONAL VARIABILITY 71
7.2. STIMULUS-DEPENDENT SOURCES OF VARIABILITY 73
7.2.1 Correlations 73
7.2.2 Sparseness 80
7.2.3 Reliability 82

II. METHODS **87**

1. ANIMAL PREPARATION **87**

2. EXTRACELLULAR RECORDINGS **88**

3. VISUAL STIMULATION **88**

4. HISTOLOGY **93**

5. SPIKE SORTING **94**

6. NEURONAL CLASSIFICATION **94**

7. SIGNAL ANALYSIS **96**

7.1. CURRENT SOURCE DENSITY 96

7.2. TRIAL-TO-TRIAL CROSS CORRELATION 96

7.3. CORRELATIONS 96

7.4. POWER SPECTRAL DENSITY 97

7.5. COHERENCE 97

7.6. SPARSENESS 97

7.7. FANO FACTOR 98

7.8. STIMULUS-LOCKED TIME-FREQUENCY ANALYSIS 98

7.9. RESULTS REPRESENTATION 99

III. RESULTS **100**

1. CHARACTERIZING THE NEURONAL ACTIVITY **100**

1.1. RECEPTIVE FIELD MAPPING 100

1.2. CHARACTERIZING THE RECEPTIVE FIELD FUNCTIONAL PROPERTIES 103

1.3. NEURONAL CLASSIFICATION 106

2. QUANTIFICATION OF THE VISUAL RESPONSE. **108**

2.1. IMPACT OF THE FULL FIELD RESPONSE ON THE NEURONAL ACTIVITY 108

2.1.1 Quantification of the spiking response 108

2.1.2 Quantification of the local field potential 124

2.2. IMPACT OF THE CENTER SURROUND INTERACTIONS ON THE NEURONAL ACTIVITY 132

2.2.1 Quantification of the spiking activity 133

2.2.2 Quantification of the local field potential 141

3. SPARSENESS AND RELIABILITY OF THE NEURONAL RESPONSE 147
3.1. IMPACT OF THE FULL FIELD STIMULATION 147
3.1.1 Sparseness of the spiking activity 147
3.1.2 Fano Factor 155
3.1.3 Reliability of the spiking activity 163
3.1.4 Reliability of the local field potential 171
3.2. IMPACT OF THE CENTER SURROUND INTERACTIONS 177
3.2.1 Sparseness of the Spiking Activity 177
3.2.2 Fano Factor 185
3.2.3 Reliability of the Spiking Activity 189
3.2.4 Reliability of the Local Field Potential 196
4. TIME FREQUENCY ANALYSIS OF THE VISUAL RESPONSE 203
4.1. IMPACT OF THE FULL FIELD STIMULATION 205
4.1.1 Time Frequency Analysis of the Spiking Activity 205
4.1.2 Time Frequency Analysis of the Local Field Potential 230
4.1.3 Power Spectral Density and Reliability of the Local Field Potential 243
4.1.4 Spectral Analysis of the Unlocked Local Field Potential 252
4.2. IMPACT OF THE CENTER SURROUND INTERACTIONS 258
4.2.1 Time Frequency Analysis of the Spiking Activity 258
4.2.2 Time Frequency Analysis of the Local Field Potential 277
4.2.3 Power Spectral Density and Reliability of the Local Field Potential 288
4.2.4 Spectral Analysis of the Unlocked LFP 302
5. CORRELATION OF THE NEURONAL ACTIVITY 310
5.3. IMPACT OF THE FULL FIELD STIMULATION 311
5.3.1 Correlation of the Spiking Activity 311
5.4. IMPACT OF THE CENTER SURROUND INTERACTIONS 338
5.4.1 Correlation of the Spiking Activity 338

IV. DISCUSSION **360**

V. ANNEX **379**

1. INTRACELLULAR RECORDINGS **379**

2. EXTRACELLULAR RECORDINGS **380**

2.1. SINGLE UNIT ACTIVITY 380

2.2. MULTI-UNIT ACTIVITY 382

2.3. LOCAL FIELD POTENTIAL 382

VI. BIBLIOGRAPHY **384**

I. INTRODUCTION

1. STRUCTURAL ORGANIZATION OF CAT EARLY VISUAL SYSTEM

Brain is one of the most complex structures known to exist. Over many millions of years, it evolved to form a highly complex connected network composed of many distinct regions, forming an elaborate mosaic of specialized areas at the cortical level (Felleman and Van Essen, 1991). This elaborated cortical organization allows the extraction of useful multimodal sensory information from our environment. One of the most important brain areas in carnivores and primates is the area linked to visual processing.

Visual processing is a phenomenon that requires network interactions. The fact that neocortex is organized according to unique cortical layers and that each laminar compartment receives different connections coming from different areas (Scannell et al., 1995), raises the possibility that visual information could be processed differently in distinct layers (*i.e.* different networks). In the visual system, information is initially transmitted from the retina, to the lateral geniculate nucleus, this latter sending inputs to primary visual cortex (V1). Thalamic inputs project to layers 4 and 6, once visual information reaches V1, this latter projects feedback inputs, originating from layers 5 and 6 to thalamus while feedforward inputs (projecting to other cortical regions) originate from layers 2 and 3, arguing for a laminar processing of the visual information. The actual knowledge about the laminar organization of primary visual cortex mainly relies on anatomical and functional studies. However, the understanding about the functional properties of each layer is far from complete.

Despite the incomplete knowledge about V1 laminar functional properties, primary visual cortex has been extensively investigated. The first pioneering studies, performed in the primary visual cortex of cats (Hubel and Wiesel, 1959, 1962) demonstrated that, within V1, neurons could be referred to as simple cells and complex cells. Both types responded to black or white bars, presented at different orientations. However, complex cells had a greater latitude in position of the bar and gave little response to spots of light. They argued that the properties of complex cells could more logically result from combining input from similarly oriented simple cells. Along the years, other functional properties of primary visual cortex have been discovered, such as the laminar properties of the receptive fields

An extracellular study, performed in the awake primate, showed that as a function of the presented stimulus, the receptive fields of neurons in layer 2/3 were different. This was not observed in layer 4 where the receptive fields were not stimulus dependent (Yeh et al., 2009).

Another striking functional property observed in V1 is the surround modulation. The center of the RF is considered as the region that is going to elicit a response while stimulated. The region around the RF center is called the surround and is by definition the region where a stimulus presentation is not going to elicit any neuronal response. Different studies observed a suppressive or a facilitatory modulation when different stimuli are presented both in the center and in the surround of the receptive field (Angelucci et al., 2017).

The diversity of functional properties observed in V1 has been investigated with artificial stimuli (*i.e.* mathematically well-characterized stimulus, in opposition to natural stimuli which are representations of our environment, poorly characterized). Based on the knowledge gathered with artificial stimuli,

many models reproducing the V1 responses to these stimuli were developed. However, these models poorly predicted the visual response to natural stimuli.

Indeed, in the past twenty years, several studies demonstrated that primary visual cortex responds to natural scenes in a very different way than what was observed with artificial stimuli. The principle of *efficient coding* introduced by Horace Barlow in 1961 suggests that visual processing in early sensory systems should be optimized and adapted to the statistical properties of the sensory environment. It asserts that exposure to natural-like statistics should reduce the redundancy present in the spike trains of populations of individual neurons through a decrease in stimulus-locked response variability at the single neuron level, and an increase in the sparseness of the global population activity.

A few groups started to investigate how primary visual cortex respond to natural images, Vinje & Gallant (2000), were among the first ones to do so. They observed extracellularly, in the awake primate, that the stimulation of both the center and the surround of the receptive fields with natural images increased the sparseness and decorrelated the activity of V1 neurons in comparison to a center only stimulation. Their findings support Barlow's theory. Others, such as Frégnac, demonstrated that visual processing seems optimized for natural statistics. By recording intracellularly, in the anesthetized and paralyzed cat, they observed that natural scenes evoke, at the subthreshold (membrane potential) and at the spiking level, a sparser and more reliable response than artificial stimuli (Baudot et al., 2013). Unfortunately, these two studies only investigated the response to natural scenes in a restricted number of neurons (less than 40 for both studies), which limits the conclusions that can be drawn about how V1, is modulated by natural statistics at the population level. Moreover, these studies did not investigate the laminar dependency of the response to natural scenes.

Therefore, in this PhD we decided to investigate how cat primary visual cortex (area 17) encodes, at the population level, these natural stimuli. Moreover, we looked into how these stimuli, which are a combination of spatial and temporal statistics, affect the correlations, the sparseness and the reliability. Recent technological advances now allow us to record simultaneously a great number of neurons across all layers. We are also able to extract more mesoscopic signals, such as the multi-unit activity and the local field potential. Finally, we explored the laminar dependency of the response to natural scenes.

1.1. Organization of cat primary visual cortex

Visual processing is one of the most complex and important tasks humans can achieve. Because of the importance of vision, this sensory modality has been extensively studied but our understanding about it remains incomplete. In humans, one fourth of the cortical surface is allocated to vision. Visual processing is performed through a highly complex connected network composed of many brain regions, forming an elaborate mosaic of specialized areas at the cortical level (Angelucci et al., 2017).
Nevertheless, primitive species having smaller brains and less specialized visual centers are capable of detecting simple visual cues and extracting useful information from these cues. In very primitive species such as Drosophila, that are only able to discriminate between black and white bars but fail at complex visual tasks (Paulk et al., 2013), much of the elaborate processing takes place at the level of the retina and optic lobes. Structures responsible for the processing of visual information

have evolved into more and more complex information-handling units. For example, retinal ganglion cells in the frog respond to small moving objects, and this feature is referred to as “bug detector” (Barlow, 1953). If we look a few steps higher on the evolutionary ladder, turtles have a three-layered visual cortex that is sensitive to complex visual stimuli (Fournier et al., 2018; Hall et al., 1977; Mulligan and Ulinski, 1990). However, they do not analyze visual scenes as higher mammals do, *i.e.* through elaborate retinotopic maps (Mulligan and Ulinsky, 1990; Fournier et al., 2018). As we progress through the evolutionary tree, cortex takes over a major role in vision and the number of dedicated functional areas increases in non-human primates all the way to 35 in humans. Of note, not all mammals share the same organization of the visual pathway. For example rodents present a visual pathway dedicated to visuomotor integration that has not been observed in higher mammals such as primates or cats (Beul et al., 2015).
Therefore, deep understanding of the specific visual organization of the studied species and the consideration of previous results in this framework is critical.

The work presented in this thesis was performed on cats, a higher mammal that possesses an extremely developed visual system. Indeed, cats are carnivorous predators and display a visual system very close to primates (Van Hooser, 2007). The similarities of their visual system are observed both at the anatomical level and at the functional level. As shown in table 1.1.1, like primates, cats have their eyes positioned in a frontal position and possess a large binocular field. Despite differences in the lamination of the lateral geniculate nucleus (LGN) between cats and monkeys, similar functional properties are observed in these subcortical structures (Usrey and Alitto, 2015). Finally, cats and primates show an important cortical surface allocated to visual processing and share crucial functional properties such as orientation maps and ocular dominance (Table 1.1.1). Importantly, these anatomical and functional properties are not observed in prey such as rodents or three shews. Therefore, the use of higher mammals, such as cats (*i.e.* the model of this thesis work), as a model for investigating visual processing is justified. An open question is if rodents are adapted for the study of vision (Table 1.1.1).

Table 1. Major Features of Primary Visual Cortex in Selected Mammals

Animal	Rat	Gray Squirrel	Tree Shrew	Cat	Owl Monkey	Macaque
Order	Rodentia	Rodentia	Scandentia	Carnivora	Primates	Primates
Adult weight (kg)	0.35	0.6	0.15	3	0.8	7
Retinal photorecptor ratio (rod %/cone %)	98.5/1.5	40/60	5/95	>95/5	98/2	0/100 (ctr) 95/5 (all)
Cone activation peak wavelengths (nm)	359, 512	444, 543	444, 556	440, 555	543	430, 535, 565
Life rhythm	Nocturnal	Diurnal	Diurnal	Crepuscular	Nocturnal	Diurnal
Eye position	Lateral	Lateral	Lateral	Frontal	Frontal	Frontal
Acuity (cycle/°)	1.2	2.8, 3.9	2.4	6.0	10	46.0
V1 single neuron properties:						
Orientation tuning width (°)	~30	28	24	19-25	27	24
Orientation selective (%)	84-93	75	75	95-99	90	69-95
Direction selective (%)	59	22	20.2	64	48	41
Optimal spatial frequency (cycles per degree)	0.1	0.21		0.9	0.7	1.5-4.2
Spatial frequency bandwidth (octaves)	2	2.3		1.49	2.1	1.5
V1 spatial organization:						
Area (mm^2)	7	~80		380	275	1325
Retinotopic map	Yes	Yes	Yes	Yes	Yes	Yes
Magnification^{-1} (°/mm)	~25	3.5-4	4-4.5	1.5	1.25	0.077
Orientation maps	No	No	Yes	Yes	Yes	Yes
Ocular dominance bands	No	No	No	Yes	Yes	Yes
Cytochrome oxydase blobs	No	No	No	Yes	Yes	Yes

Table 1.1.1. Major features of primary visual cortex in different mammals (reprinted from Van Hooser, 2007)

Regarding the connectivity, cats have 22 cortical areas involved in visual processing (see Fig 1.1.1, Scannell et al., 1995; see also Beul et al., 2015). This graph shows 224 connections, of which 168 are reciprocal, between the 22 cortical areas, highlighting the complexity of the intercortical connections dedicated to visual processing.

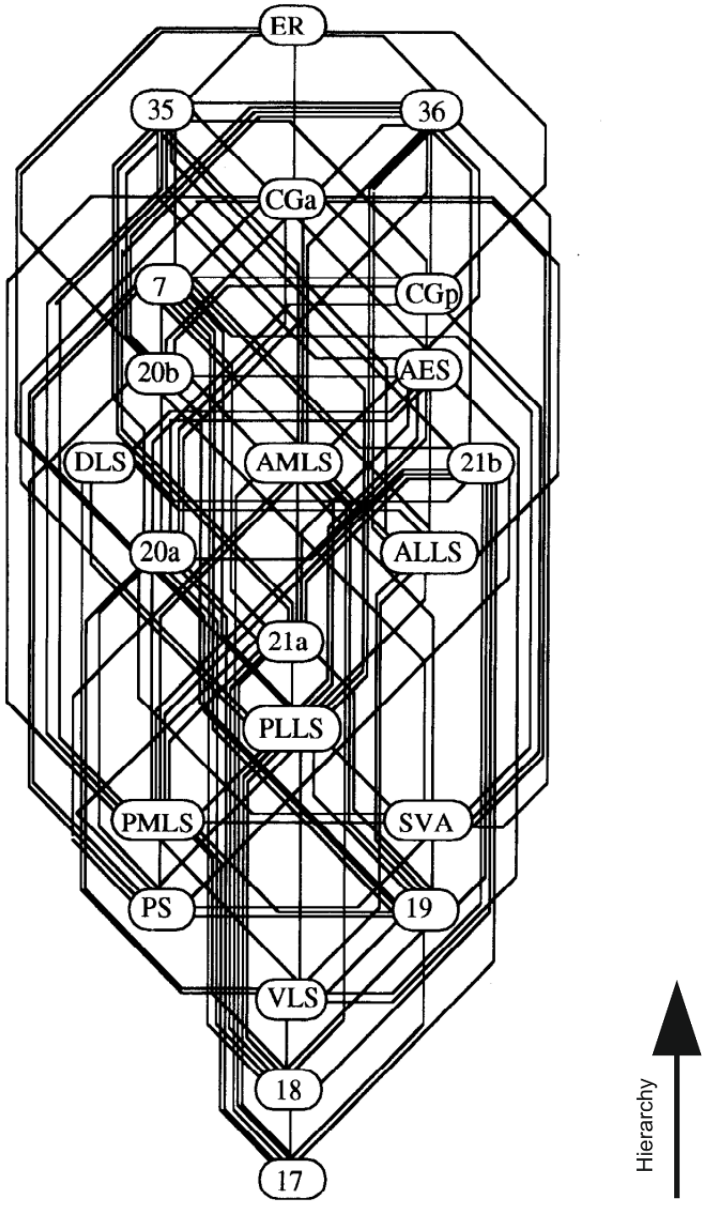

Figure 1.1.1: Hierarchical structure of cat visual system. The lower the area is on the figure the lower it is in the visual hierarchy (reprinted from Scannell et al., 1995).

Information flow for visual processing is predominantly organized in a hierarchical manner. Indeed, this flow initiates when light hits the photoreceptors in the retina, which transmits the sensory information to the visual region of the thalamus, the Lateral Geniculate Nucleus (LGN). LGN mainly projects to two cortical areas: Area 17 (A17) and area 18 (A18) that are both considered as primary visual cortices. These two areas send visual information to higher visual areas (see Figure 1.1.1).

Although the visual information propagates dominantly in a feedforward manner through the early visual system and then across the cortical mantle, processing is enriched by cortico-thalamic and cortico-cortical feedback as well as intrinsic intra-area projections (see Figures 1.1.1, 1.1.2 and 1.1.3).

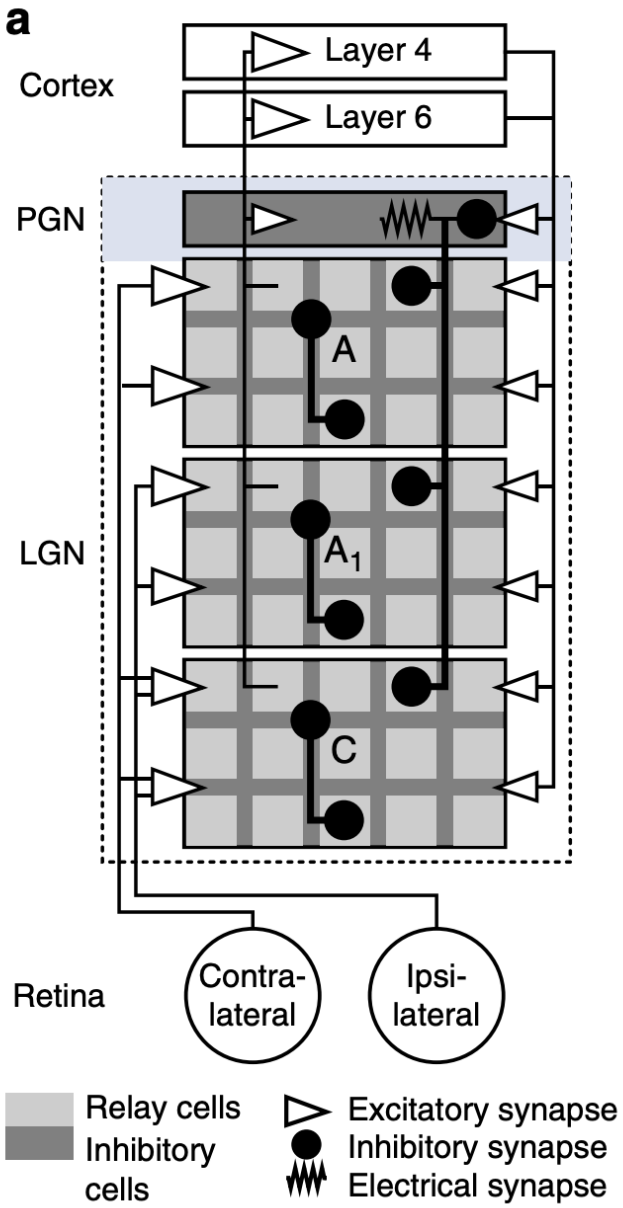

Figure 1.1.2. The early visual system. The PGN and main layers of the LGN drawn as rectangles including populations of excitatory (light fill) and inhibitory neurons (dark fill). Glutamatergic synapses (open arrows); GABAergic synapses (filled circles) and electrical synapses (resistor). (Reprinted from Soto-Sánchez et al., 2017)

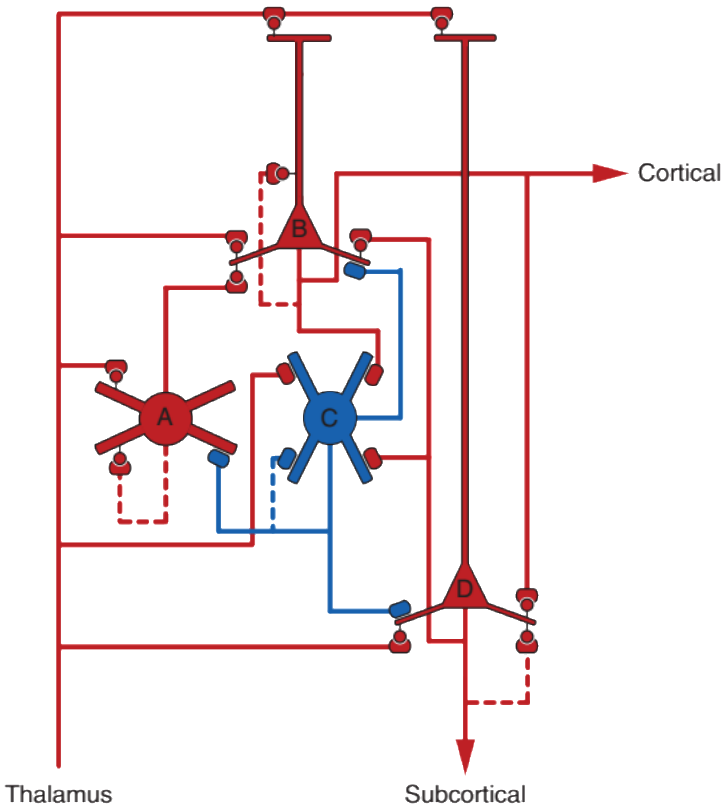

Figure 1.1.3. Example of connectivity within one layer of V1. Excitatory cells are in red and inhibitory cells in blue. A, B, C and D represent different neurons. (reprinted from Douglas and Martin, 2010)

The implication of the inputs projecting to V1 on visual processing will be developed in depth in section 3 of this chapter, but first it is important to describe the role of the two early visual areas preceding area 17.

1.2. The Early Visual System

1.2.1 The Retina

The retina, which is the first relay of the visual pathway, is composed of 80 different cell types distributed across three different layers (Cajal, 1883; Gollisch and Meister, 2010) At the output of the retina, the retinal ganglion cells perform essential visual processing and propagate information to higher visual centers. When visual information falls into their receptive field (RF), which is the particular region of the visual space in which a stimulus modifies the firing of that neuron (receptive fields are described in detail in section 5), the membrane potential of the cell changes and triggers a depolarization or a hyperpolarization. Two main types of ganglion cells are present in the retina: ON center-OFF surround and OFF center-ON surround (Sterling, 1983). A cell is considered as ON-center when a depolarization is triggered by a positive contrast change in its RF. Conversely, an OFF-center cell will be hyperpolarized by a negative contrast change in the RF (Kuffler, 1953)
Ganglion cells are divided into three morphologically distinct classes: alpha (α), beta (β) and gamma (γ). The approximate proportion of α, β and γ ganglion cells in the cat retina are 5%, 55% and 60%, respectively. These cells are also referred to as Y, X and W based on their spatial linear/non-linear summation properties, described hereafter. Y cells have large cell bodies and large dendritic trees.

They are also characterized by a complex spatio-temporal RF that cannot be linearly separated (Humphrey et al., 1985). The RF is large (0.5° to 2.5°) and responds preferentially to low spatial frequencies, high temporal frequencies, and high luminance contrast visual stimuli (Troy, 1987). Y-cells are involved in global aspects of spatial vision, in the detection of rapid visual transients in illumination and movement.
Conversely, X cells have small cell bodies, small dendritic trees and smaller receptive fields (0.2° to 1°). They have low luminance contrast and temporal frequency selectivity. X cells are able to report the position of a stimulus with great accuracy (Shapley and Victor, 1986). They also possess linear spatio-temporal receptive fields. These can be approximated by two linearly separable components: A spatial component modeled as a difference of two Gaussian functions for the concentrically opposing center and surround (Rodieck, 1965) and a temporal component modelled as the sum of two functions (Rodieck, 1965).
Finally, W cells have small cell bodies and are composed of a wide variety of dendritic trees. Their complex spatio-temporal receptive fields present very heterogeneous sizes (from 0.4° to 2.5°). To date, their contributions to vision are not well-defined (Rowe and Palmer, 1995).
The visual information processed by the retinal ganglion cells will be transmitted through their axons to the LGN via the optic tract.
Visual pathways emerge with the properties of these ganglion cells (Payne & Peters, 2002)

1.2.2 The Lateral Geniculate Nucleus

The signal coming from the optic tract is then directed to three main targets: the superior Colliculus, the pretectum and the LGN. Only LGN, which sends projections to primary visual cortex, the area of interest of this thesis, is considered here.
LGN is a sub-cortical structure composed of two main regions, the magnocellular region and the parvocellular region (in primates, a third region called koniocellular exists).
The magnocellular region is organized into three layers located on the dorsal part of LGN. These three main layers are named A, A1 and C. These layers are the ones classically considered in the study of the LGN (Figure 1.1.2).
The parvocellular region, located ventrally, is composed of three layers located under the C lamina. These three layers are referred as layers C1, C2 and C3 (Sherman and Spear, 1982). Each layer receives different types of inputs coming from retina. Fibers carrying Y-cell signals project to layers A, A1 and C. X-cells send their projections to layers A and A1. Finally, W cells project to layers C1, C2 and C3 (Sherman & Spear, 1982). Hence, the functional differences that are initiated in retina are preserved in LGN, as exemplified by the conservation in LGN of the circular shape (isotropy) and ON-OFF structure of retinal RFs. Thus, the properties of thalamic cells emerge from the properties of retinal ganglionic cells. Indeed, thalamic Y-cells respond more strongly to fast movements than X-cells, whereas X-cells are more sensitive to slow movements than Y-cells (Orban et al., 1985).
However, when considering geniculate Y and X cells, a novel functional property (compared to retina) emerges. They can respond to a visual stimulation in two different ways, X and Y cells either respond to a visual stimulus with a lag, they are then called “lagged cells”, or without a lag, and are called “non-lagged cells” (Sherman & Spear, 1982). One unique visual property that emerges from the thalamus is the higher spatial resolution for dark than light stimuli. This property is passed on to higher visual areas.

Thalamic cells project to three different areas: the X pathway projects to area 17, the Y pathway projects to areas 17 and 18 and the W pathway projects to areas 17, 18 and 19 (Sherman & Spear, 1982).

1.3. Structural and functional organization of cat primary visual cortex

In cat, areas 17 and 18 can both be considered primary visual cortices. because they both receive direct LGN inputs. However, area 18 also receives a strong input from area 17. This dual wiring is no longer found in V1 and V2 in non-human primates, where V2 receives most of its visual input from V1, becoming serially activated in the Felleman and Van Essen functional hierarchy. Area 19 also receives LGN inputs, but the number of projections is small, and connections are very weak, thus area 19 is not considered as a primary cortex (Payne & Peters, 2002).
Even if these two visual regions are primary visual cortices, they do not share equivalent functional properties. Area 17 is more selective to low temporal and high spatial frequencies with a dominance of “Simple” linear receptive fields, while area 18 is more selective to high temporal and low spatial frequencies with a dominance of Complex non-linear receptive fields. Moreover, area 18 receptive fields are bigger than those from area 17 (Friend and Baker, 1993).

As part of this thesis, we will only focus on area 17, hence from now on we will refer to it as primary visual cortex (V1). The next sections will aim to describe the structural and functional organization of cat primary visual cortex. Indeed, as described previously for early visual areas, the way V1 processes visual information is intrinsically linked to various factors such as the morphology and the intrinsic functional properties of the cells.

1.3.1 Cortical neuronal diversity

Cat primary visual cortex is organized into six layers, ranging from layer 1 (the most superficial) to layer 6 (the deepest) (Laminar organization is discussed in section 3). Three main classes of neurons have been distinguished based on their morphology and electrophysiological properties (Kelly and Van Essen, 1974; Nowak et al., 2003). Spiny stellate cells and pyramidal cells (that are dominantly) are the two kinds of excitatory neurons and inhibitory interneurons. Spiny stellate cells are mainly located in layer 4, pyramidal cells in layers 2, 3, 5 and 6 and interneurons in all layers. Excitatory cells represent about 70-80% of the cortical neurons and inhibitory cells the 20-30% remaining (Gabbott and Somogyi, 1986). This distribution is discussed in section 2.1.

- **Excitatory Neurons**

-Spiny stellate cells
Cat layer 4 is actually subdivided into two compartments: layer 4A and layer 4B that are respectively the superior and the inferior part of Layer 4 (Lund et al., 1979). The separation of layer 4 into two sub-layers is justified by the terminal location of the projections coming from LGN. The Layer 4A inputs are mainly composed by fibers carrying Y-visual signals, whereas layer 4B receives inputs almost exclusively from fibers carrying X-visual signals. Lamina 4A contains small and medium spiny stellate cells and few pyramidal cells. Lamina 4B contains small spiny stellate cells and a few pyramidal cells. Neurons are more spaced in layer 4A than in layer 4B. Stellate cells have spiny dendrites that extend radially from their cell bodies and they do not possess apical dendrites (Meyer

and Albus, 1981). Their axonal projections form a diffuse projection of collaterals that can reach either layers 2/3 or layers 5/6.

-Star pyramidal cells

Star pyramidal cells have a shape in between stellate cells and pyramidal cells (Lorente de No, 1949). They possess a thin apical dendrite in addition to basal dendrites surrounding their cell body and wide axonal projections (Martin and Whitteridge, 1984).

According to Peters & Payne (1993) only a small amount of star pyramidal cells are located in the upper portion of layer 4. However, in electrophysiological recordings in layer 4 Martin & Whitteridge (also Tarczy-Hornoch et al., 1998) observed a higher number of star pyramid cells than those stated by Peters & Payne.

-Pyramidal cells

Pyramidal cells are present in all cortical layers except in layer 4. The pyramidal cell is a class of excitatory neurons that sends projections to sub-cortical areas or other cortical regions.

Layers 2/3 Pyramidal cells:

Small pyramidal cells are located at the top of layer 2. With increasing depth, the size of the pyramidal cells increases. Because of this linear increase in size, it is very difficult to determine a clear border between layers 2 and 3, hence these two layers are considered together. However, according to O'Leary (1941) a difference between layer 2 and layer 3 pyramidal cells can be made. Indeed, layer 2 cells have short axons, whereas layer 3 cells have axons that extend into the white matter.

Many studies have showed that layer 2/3 pyramidal neurons have complex projections. Indeed, they send projections to other visual areas (ipsilateral projections) but also towards the other hemisphere (callosal projections) (Einstein and Fitzpatrick, 1991). In addition to these projections, axons from pyramidal cells form collaterals that extend horizontally inside layer 2/3 (Kisvárday et al., 1986). These horizontal connections target other layer 2/3 pyramidal cells (the functional impact of these horizontal connections is discussed in sections 3 and 5.5 of this thesis) and local inhibitory interneurons.

Layer 5 Pyramidal cells:

Two classes of pyramidal cells are present in layer 5:

- Small pyramidal cells, which have axons that extend basally for a short distance before arching upwards into layer 2/3 (Hübener et al., 1990).
- Large pyramidal cells, which have apical dendrites that connect in layer 4 and layer 2/3 and form a large terminal tuft in layer 1. Basal dendrites emerge from these neurons and make connections in layers 5 and 6 (Hübener et al., 1990).

Layer 6 Pyramidal cells:

Three sub-populations of pyramidal cells have been identified in layer 6 (Katz, 1987).

- The first population (about 50% of the cells) sends projections to LGN and has collaterals in layer 4.
- The second population (about 30% of the cells) sends axonal projections to a sub cortical structure called the claustrum. They also have collaterals that arborize in layer 6 and in lower layer 5.
- The third population (about 30% of the cells) sends its axonal projections only to layers 6 and 4.

- **Inhibitory neurons**

Inhibitory interneurons represent between 20% and 30% of the cortical neurons in V1 (Gabbott and Somogyi, 1986). These non-pyramidal neurons are present in every cortical layer and use GABA as their principal neurotransmitter. Their diversity is manifested in every aspect of their phenotype. Differences are found in morphological, electrophysiological and biochemical features (Markram et al., 2004; Petilla Interneuron Nomenclature Group et al., 2008). Because of these numerous features, in 2006, a group of studies (*i.e.* "The Petilla Interneuron Nomenclature Group") proposed a nomenclature in order to allow a precise and universal classification of the various interneurons found in cortex (The Petilla Interneuron Nomenclature Group, 2008). The Petilla group classified the interneurons based on three main features: morphological, molecular and physiological. Each feature is organized in a logical hierarchical fashion. Figure 1.1.4 gives a summary of how the nomenclature is organized.

Despite this vast number of different classes, a simpler classification linking both morphology and synaptic target criteria has been made (Tamás et al., 1997). From this classification, three main groups of inhibitory interneurons appear. Because of the complexity of the interneuron classification, we will only focus on these three main groups.

-Chandelier cells

The defining property of this neuronal type is the axon, which is very extensive and gives rise to a vertically oriented string of boutons (about 300 hundred) located in layer 2/3. These boutons will synapse with the initial axon segment of pyramidal cells (because of these connections, chandelier cells are also called axo-axonic cells). One cell makes about 10 axo-axonic contacts in the initial segment and one cell contacts around 150 pyramidal cells (Somogyi et al., 1985).

Box 2 | **Summary of morphological, molecular and physiological features**

Morphological features

- Soma: shape; size; orientation; other
- Dendrite: arborization polarity; branch metrics; fine structure; postsynaptic element; other
- Axon: initial segment; arbor trajectory; terminal shape; branch metrics; boutons; synaptic targets; other
- Connections: chemical and electrical; source; location and distribution; other

Molecular features

- Transcription factors
- Neurotransmitters or their synthesizing enzymes
- Neuropeptides
- Calcium-binding proteins
- Receptors: ionotropic; metabotropic
- Structural proteins
- Cell-surface markers
- Ion-channels
- Connexins
- Transporters: plasma membrane; vesicular
- Others

Physiological features

- Passive or subthreshold parameters: resting membrane potential; membrane time constants; input resistance; oscillation and resonance; rheobase and chronaxie; rectification
- Action potential (AP) measurements: amplitude; threshold; half-width; afterhyperpolarization; afterdepolarization; changes in AP waveform during train.
- Dendritic backpropagation
- Depolarizing plateaus
- Firing pattern: oscillatory and resonant behaviour; onset response to depolarizing step; steady-state response to depolarizing step
- Response to hyperpolarizing step: rectification; rebound
- Spiking recorded extracellularly: phase relationship to oscillations; functional response specificity; cross-correlation and other dynamics
- Postsynaptic responses: spontaneous and evoked; ratio of receptor subtypes; spatial and temporal summation; short- and long-term plasticity; gap junctions

Figure 1.1.4. Summary of morphological, molecular and physiological features adopted by the Petilla classification.

-Basket Cells
Basket cells can be divided into two categories: Large basket cells and small basket cells:

-Large basket cells are located from layer 2 to layer 6, have an oval and elongated cell body, spineless dendrites and a long axon (Somogyi et al., 1998). Their main target is the soma of pyramidal cells (Kisvarday et al., 1993). However, they also target other basket cells. Therefore, it has been suggested that the inhibition of basket cells could facilitate the activation of sets of pyramidal cells (Kisvárday et al., 1993).

-Small basket cells, also called “clutch cells”, are mainly located in layer 4. Their dendrites are smooth and their axons form clusters around cell bodies in layer 4.

-Double bouquet cells
Double bouquet cells are multipolar cells located in layer 2/3. They have smooth dendrites and their axons give rise to several descending bundles that go from layer 2 to layer 4 (Peters and Regidor, 1981). Because of this descending axon, it is assumed that double bouquet cells are involved in vertical inhibition. Somogyi and colleagues (1998) have shown that this type of cell forms synapses with dendritic spines (about 70% of them) and with dendritic shafts (about 30% of them).

In this first section, we described the early visual pathway, from the retina to the primary visual cortex. We looked in particular detail at the neuronal anatomy of V1, the visual area that is going to be studied in this thesis. As stated above, in addition to their morphological differences, both interneurons and excitatory neurons present segregating intrinsic properties. These intrinsic properties are more easily available to the experimenter than the morphology, thereby the description of these properties is a key point for the understanding of the results obtained during electrophysiological experiments.

2. ELECTROPHYSIOLOGICAL RECORDINGS OF CORTICAL ACTIVITY

2.1. Diversity of discharge types among cortical neurons

As discussed in the section above, neurons can be characterized by their morphology. However, each type of neuron also has its own physiological properties. During *in vivo* recordings of V1, only the physiological properties of the recorded neurons are immediately available to the experimenter. Therefore, by linking the neuronal morphology to its discharge type, evoked by injecting a pulse of depolarizing current and observing its current-voltage transfer function, one can more easily identify the type of cell being recorded.

Two main classifications, linked to the recording technique, exist: An intracellular classification and an extracellular one.
As described in annex 1, intracellular recordings allow the experimenter to inject a controlled amount of current, which in return, gives precise measurements of the electrical variations of a neuron. Hence, a very accurate characterization of the different spiking behavior is possible. However, it is important to keep in mind that intracellular solutions in the recording pipettes can perturb the firing of a neuron during whole cell patch recordings, and mechanical pressure of the tip on the membrane can alter firing recorded with sharp electrodes. Moreover, independently of the recording technique, the discharge type is not invariant. Indeed, the state of depolarization of the neuron can change its expressed conductance repertoire, thus changing the discharge type. On the other hand, extracellular recordings measure the potential difference between a reference and the extracellular medium. Therefore, a less precise description of the action potential of a single neuron can be made. In this section, we will describe the different neuronal characterizations that have been established for intracellular and extracellular recordings.

2.1.1 Intracellular Classification

In order to characterize the different discharge modes of V1 cells in the anesthetized cat, Nowak and colleagues (2003) performed a very precise and methodic classification that took advantage of the fact that intracellular sharp recordings allow the injection of a controlled amount of current or voltage. They were able to clearly distinguish four classes of neurons:

- Regular Spiking neurons (RS)
- Fast Spiking neurons (FS)
- Intrinsic bursting neurons (IB)
- Chattering neurons (CH)

An example of firing behavior for each neuron is shown in Figure 1.2.1
Their classification is based on the following criteria. First, they divided neurons into bursting and non-bursting neurons. Then, multiple variables were required to accurately discriminate the different cell classes. Indeed, using only one variable like the action potential width resulted in a big overlap between populations. In order to separate RS and FS neurons they examined the spike width and the spike frequency adaptation. Finally, to separate CH neurons from IB neurons (that both are bursting classes) the two-variable criteria applied was the careful examination of both action potential width and intra-burst frequency (another two-variable test that meticulously separates CH from IB is the intra-bust frequency and the burst inactivation indices).

Their careful analysis of the physiological properties of these four classes of neurons gave rise to different conclusions. Before discussing their results, it is important to note that the intracellular *in vivo* classification of neuronal classes is more complex than the *in vitro* one. Indeed, intracellular *in vivo* recordings are very complicated to perform, therefore reducing the number of recorded cells. Moreover, it is more complicated to have a good intracellular recording *in vivo* than *in vitro*. Finally, the synaptic activity (for example the neuromodulation) present *in vivo* can modulate the neuronal activity, in particular the bursting (Monier et al., 2008). The specificities of each recording technique can lead to a difference in the neuronal classification. Thus, when characterizing the electrophysiological properties of cortical interneurons, the advantages and limitations of every technique should be considered.

-Regular Spiking neurons

Regular spiking cells, like fast spiking cells are non-bursting neurons. In order to separate these two neuronal groups, a two-variable criterion has to be applied. When a train of action potentials is generated, RS cells show spike frequency adaptation and have spike widths that are, on average, broader than those of FS (or CH neurons). Their two-variable classification method allowed them to divide RS cells into two subclasses: Thin RS cells and “classic” RS cells. Thin RS cells have briefer action potentials and show less adaptation.

Intracellular recordings allow the injection of biocytin, a neuronal stain that labels the soma, the dendrites and the axons of the recorded cell. By injecting biocytin many authors have been able to identify the cell type and locate the recorded RS cells across the cortex (Tamás et al., 1997)
RS cells represent a vast variety of excitatory neurons: pyramidal cells in layers 2-6, spiny stellate cells in layer 4 and polymorphic cells in layer 6.

However, this classification may lead to an overestimation of the % of excitatory cells, since it has been shown, *in vitro,* that inhibitory interneurons can have the characteristics of a RS cell (Markram et al., 2004)

-Fast Spiking neurons

Another identified electrophysiological class are the fast spiking neurons.
They are non-bursting cells, with trains of action potentials that shows very little spike frequency adaptation, have a spike width thinner than RS cells and present a steep slope when the firing rate vs. current intensity is plotted (f-I curves). Two subclasses of FS cells, based on the differences of the f-I curve, have been identified: The classic FS cells that have a steep f-I curve and the “less steep f-I” FS cells.
FS neurons seem to be only GABAergic neurons, in particular basket cells and paravalbumin positive neurons (Nowak *et al.*, 2003). However, it is important to keep in mind that all FS cells seem to be interneurons, but not all interneurons are FS cells (Markram *et al.*, 2004).

-Chattering neurons

As stated in the section above, chattering cells are a subclass of bursting neurons. They are characterized by a spike width less than 0,5 ms and an intra-burst frequency greater than 350 Hz. By blocking ionic channels in visual cortex slices, Brumberg et al. (2000) showed that chattering is mediated by sodium and potassium currents and does not rely on calcium currents. Two subclasses of chattering neurons, CH1 and CH2, have been identified with a two-variable criteria. CH cells have been identified in many different areas and species like raccoon, ferrets or other cat cortices

(Brumberg et al., 2000; Istvan and Zarzecki, 1994; Steriade et al., 1998). They do not seem to be very common in rodents, however an *in vitro* study reported CH cells (called “fast rhythmic bursting neurons”) in slices of rat primary and secondary auditory cortices (Cunningham et al., 2004). Chattering cells have been mostly identified as pyramidal cells in layer 2/3. These cells send their projections to higher cortical areas or to many cortical regions in the contralateral hemisphere.
Chattering cells can also be identified extracellularly and seem to be linked with the generation of synchronous gamma oscillations in networks of cortical neurons (Gray and McCormick, 1996). The extracellular classification of CH neurons will be discussed in the following section.

-Intrinsic Bursting neurons

Intrinsic Bursting cells, like chattering cells, are bursting neurons. These groups are separated based on two criteria. IB neurons have a spike width greater than 0.5 ms and an intra-burst frequency less than 350 Hz. The burst itself is very stereotyped, with a high amplitude first action potential followed by smaller amplitude action potentials. *In vitro* results seem to indicate that bursting is linked to the activation of an intrinsic sodium current (Nishimura et al., 2001) whereas the end of bursting is linked to the inactivation of potassium and sodium channels (McCormick et al., 1985). Their two-variable classification method separated IB neurons into three different subclasses: IB1, IB2, IB3 (Nowak et al., 2003).
Intrinsic bursting cells have been identified as pyramidal cells in many cortical regions of different species, in layers 2/3, 5 and 6 (Agmon and Connors, 1989; Chen et al., 1996; Nishimura et al., 2001). Even though IB neurons are found in many layers, they are essentially present in layer 5. These pyramidal neurons possess an apical dendrite extending to layer 1 and horizontal axon collaterals in layers 5 and 6. Some of these neurons send their projections to subcortical areas.

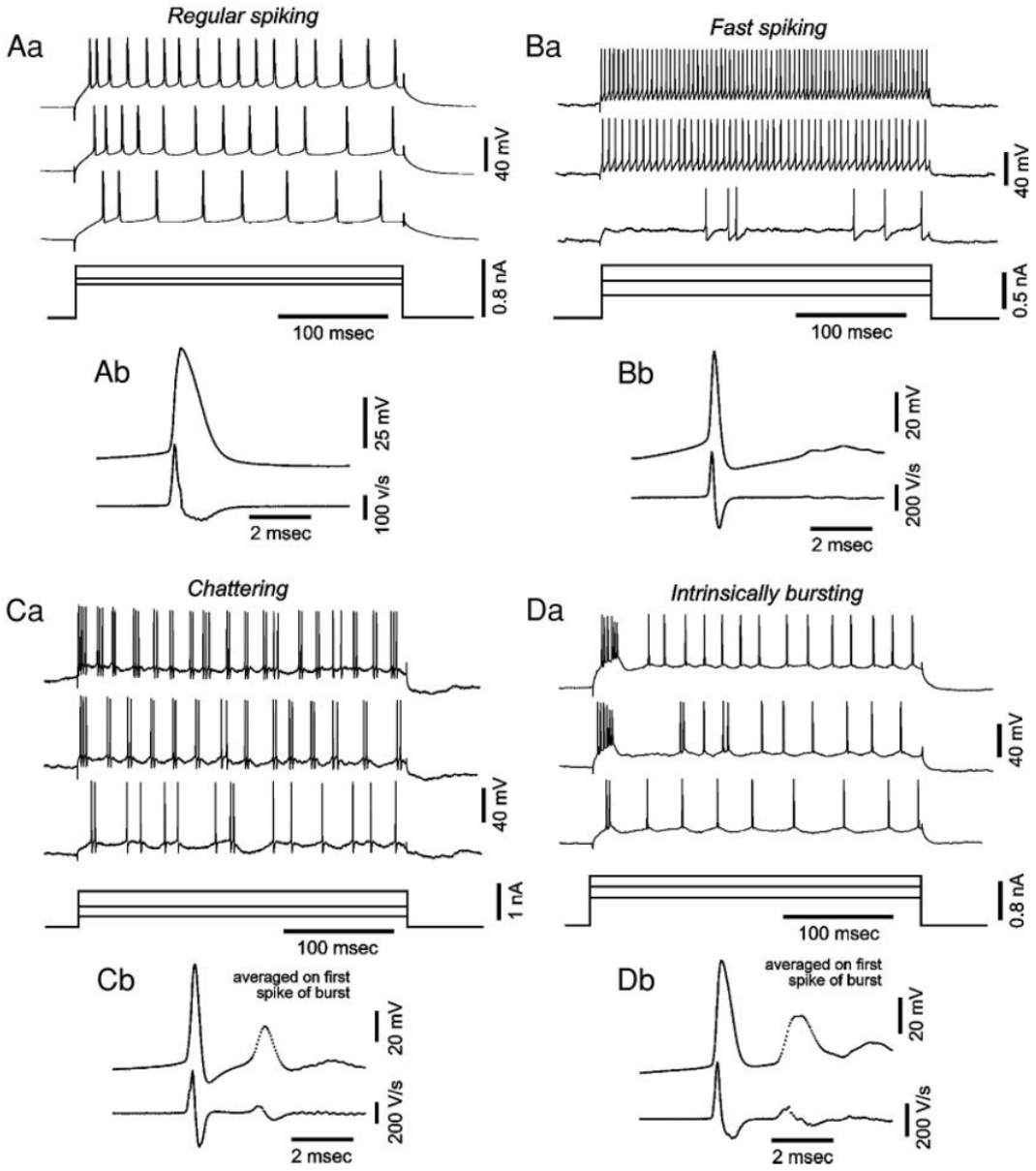

Figure 1.2.1: example of action potential responses to depolarizing currents (reprinted from Nowak *et al.*, 2003). **Aa:** Regular spiking cells recorded intracellularly. **Ab:** averaged spiking activity. **Ba:** Fast spiking cells recorded intracellularly. **Bb:** averaged spiking activity. **Ca:** Chattering cells recorded intracellularly. **Cb:** averaged spiking activity. **Da:** Intrinsically bursting cells recorded intracellularly. **Db:** averaged spiking activity (reprinted from Nowak *et al.*, 2003)

2.1.2 Extracellular Classification

As discussed in annex 1, extracellular recordings measure the potential difference between the local recording site in the extracellular medium and a “ground” reference and cannot be used to inject current in the neighboring cell as can be done intracellularly. The capacitive derivation of the recorded and injected currents depends greatly on the distance from the axon hillock and the geometry of the axon relative to the electrode (Houk et al., 1995). Hence, the classification of extracellular spiking activity into the four subtypes described above becomes a “risky business” since many criteria rely on direct measures of I/V relationships in response to test current patterns (McCormick et al., 1985; Nowak et al., 2003).

However, Nowak and colleagues (2003) suggest that some of their two-variable criteria can be used to separate CH cells and IB cells even when recorded extracellularly. Indeed, extracellular studies in the past identified CH-like neurons (Gray and McCormick, 1996) and described cells possessing the bursting properties of CH cells (Friedman-Hill et al., 2000; Gray and Singer, 1989). With the emergence of silicon probes, allowing simultaneous recordings of dozens of neurons, neuron classification has become more and more common (Barthó et al., 2004; Cardin et al., 2009; in rodents; Peyrache et al., 2012 in humans; but see Bachatene et al., 2012; Chen et al., 2015 for a classification in cat primary visual cortex). Yet, these extracellular studies only classified two types of cells: regular spiking and fast spiking neurons.

The bursting activity of the cells can vary depending on what anesthetic, depth of anesthesia, or type of stimulation is used. Unlike intracellular recordings, extracellular recordings do not allow a modulation of the spiking activity by current injection. Therefore, it is impossible to rely on the bursting activity to reliably classify neurons, hence reducing the number of neuronal classes (Bartho et al., 2004). In addition, CH cells are very rare in primary visual cortex (Nowak et al., 2003). Because of this methodological constraint, in this section, we will only focus on the two main neuronal classes described in extracellular studies: Regular Spiking neurons and Fast Spiking neurons.

-Regular Spiking Neurons

Extracellularly, RS neurons are identified using many parameters. Like the intracellular classification, two-variable criteria are always used. Many different measures can be paired in order to efficiently discriminate RS cells. The most commonly used two-variable criteria are spike width vs firing rate (Guo *et al.*, 2014, study performed on rodents), peak to peak value vs firing rate (Chen *et al.*, 2015, study performed on cats) and peak to peak vs half peak width (Peyrache *et al.*, 2012, study performed on humans). All the measurements made on the waveforms are detailed in Figure 1.2.3. It is important to note that some studies only use peak to peak to determine if neurons are RS of FS (Isett et al., 2018 study performed on rodents). Despite the fact that the intrinsic properties of the cells are not equivalent across species (Mochizuki et al., 2016), these criteria allow a discrimination between RS and FS neurons in all species. Indeed, in all species, regular spiking neurons present a lower firing rate, a higher peak to peak value, and a higher half peak width than fast spiking neurons.

Extracellularly, regular spiking neurons are commonly accepted as excitatory neurons (Peyrache et al., 2012; Chen et al., 2015) but as described in the above section, some interneurons can display characteristics of an RS cell. Risks for this potential mistake highlight the requirement for controls, such as the one performed by Peyrache and colleagues (2012). Indeed, by computing the cross-

correlations between cells, these authors were able to evaluate if the recorded FS or RS cells were inhibitory or excitatory, respectively.

-Fast Spiking Neurons

Extracellularly, FS neurons are identified by applying the same set of parameters used for RS classification.

Fast spiking neurons present a higher firing rate, a lower peak to peak value and a lower half peak width compared to FS neurons. Fast Spiking neurons are often thought of as inhibitory neurons. Indeed, as we described above, when the classification is made intracellularly, all the FS cells are inhibitory neurons (Nowak *et al.*, 2003). Yet, since extracellular classification focuses mainly on the waveform and its shape, because of their very close width at half height, chattering cells can easily be classified as fast spiking cells (see Figure 1.2.1 for the waveforms and Nowak *et al.*, 2003 for the spike width). Considering that, it is very important to be careful when drawing conclusions about the recorded cells. One cannot state that they are recording exclusively inhibitory neurons when speaking about FS cells.

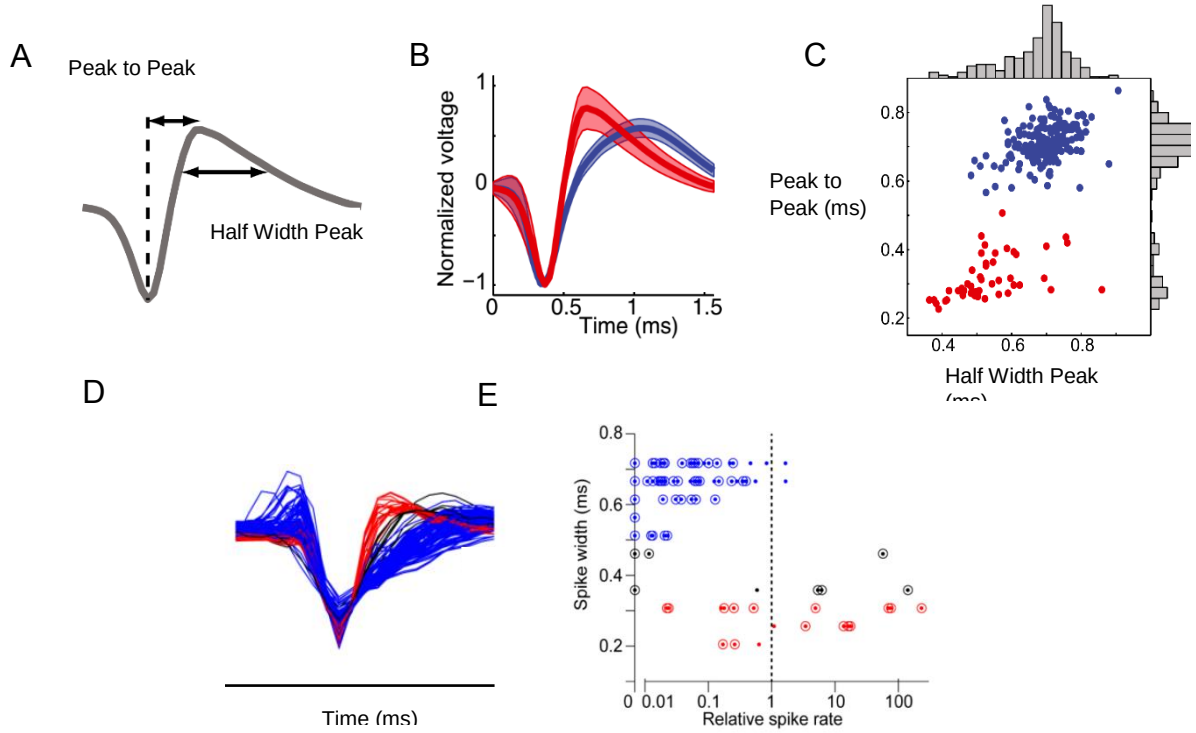

Figure 1.2.3: Examples of extracellular RS/FS classification. **A.** Measurements used in order to classify the recorded neurons. **B.** Regular spiking neurons (in blue) and fast spiking neurons (in red) recorded with a Utah array. **C.** Example of classification using a two-criteria test. **D.** Regular spiking neurons (in blue) and fast spiking neurons (in red) recorded with a silicon probe (in black, waveforms not classfied). **E.** Example of classification using another two-criteria test. (A, B, C: modified from Peyrache *et al.*, 2012; D, E: modified from Guo *et al.*, 2014)

In Figure 1.2.3, we show a panel of classical plots obtained when different two-criteria tests are applied to separate FS neurons from RS neurons. In Figure 1.2.3-B, these waveforms have been obtained with the Utah array (Peyrache et al., 2012), whereas the waveforms in 2.2-D are obtained with silicon probes (Guo et al., 2014). These figures highlight the fact that the waveform shape also depends highly on the type of probe that is used. Indeed, waveforms recorded with Utah arrays and

silicon probes are different (Lewicki, 1998). As the classification relies on the waveform shape, variations of the tools complicate the comparison of neuronal classification used across different studies.
Despite the described criteria being the most popular ones, other methods allow neuronal classification. In this thesis, we used a novel technique based on principal components analysis (PCA). The PCA is a statistical procedure that uses an orthogonal transformation to convert a set of observations of possibly correlated variables into a set of values of linearly uncorrelated variables. We performed this PCA on seven different features present in the waveforms. This novel technique is described in detail in the methods section.

The above description of intrinsic properties of V1 neurons is not sufficient *per se* to understand how V1 works. In this regard, one needs to understand how the cortical microcircuitry is organized. Indeed, the different neuronal types in V1 are connected together into complex but partially stereotyped circuits. This connectivity was first studied by Douglas and Martin (1991). By performing intracellular recordings in cat primary visual cortex, they developed a model of V1 microcircuitry that simulated their experimental data. Since this first publication, the knowledge about these microcircuits has been updated (see Frégnac and Bathellier, 2015; Harris and Mrsic-Flogel, 2013 for review). These authors showed that visual processing implies other circuits such as the thalamic and intra-cortical ones but also the feedback connectivity from higher areas. Thus, in order to understand how microcircuits participate in visual processing, a description of these is necessary.

3. FUNCTIONAL MICROCIRCUITS OF CAT PRIMARY VISUAL CORTEX

In this section, we will describe the general organization of the cortical microcircuit and the different steps of visual processing linked to this organization. We will first focus on how the visual information flows from the thalamus to V1, then how this information is processed within V1. Finally, we will describe primary visual cortex feedforward and feedback inputs.

3.1. Visual processing intrinsic to V1

3.1.1 Thalamic inputs

Neocortical circuits have been extensively studied in the past 60 years. Cat and primate sensory cortices have been the most studied models. From these studies, a general pattern of cortical organization and functional architecture in primary sensory areas, developed hereafter, has emerged.

Cat primary visual cortex receives visual information from LGN (Wilson and Cragg, 1967). Three visual streams come from this structure and project to V1: X-visual stream, Y-visual stream and W-visual stream. X-cells located in layers A and A1 of LGN send their projections to layer 4, in particular layer 4B, and layer 6. Y-cells which are also located in layers A and A1 of LGN, project to the bottom of layer 3, layer 4A and layer 6.
X-cell and Y-cell inputs compose the majority of the thalamic inputs received by V1, about 40% each, with the remaining 20% being W-cell projections. These W-cells are located in thalamic layers C1, C2 and C3 and send their projections to layer 1, the bottom of layer 3 and the top of layer 5 (LeVay and Gilbert, 1976) in V1. Figure 1.3.1 illustrates the thalamic inputs coming to V1.
Despite being the principal recipient of thalamic projections, only 5% of layer 4 synapses are derived from LGN. However, these synapses drive very strongly the visual response in V1, implying that they are potent effectors of excitation (Peters and Payne, 1993).

3.1.2 Intra V1 inputs

Based on their intracellular recordings and intracellular staining, Gilbert and Wiesel, 1983 provided one of the first descriptions of the “vertical” information flow intrinsic to the anatomy of each columnar subunit.

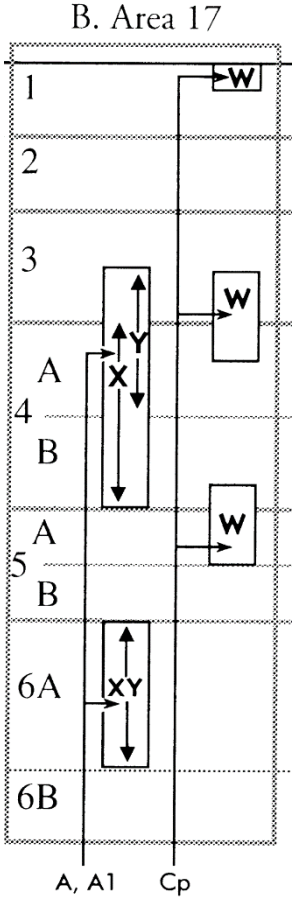

Figure 1.3.1: Diagrams of thalamic innervation in area 17 of cat visual cortex (reprinted from Payne and Peters, 2002). X corresponds to X-cell thalamic inputs, Y corresponds to Y-cell thalamic inputs, W corresponds to W-cell thalamic inputs. A, A1 and Cp correspond to the different thalamic layers.

Visual information arrives in layer 4 and layer 6 through thalamic inputs coming from LGN. The excitatory cells in layer 4 project to superficial layers. Layer 2/3 pyramidal neurons project to layer 5 which in turn projects to layer 6 and superficial layers. The loop is closed with projections from layer 6 to layer 4, but also to superficial layers (Gilbert and Wiesel, 1983, 1989; Hirsch et al., 1998; Lund et al., 1979).

In addition to these “vertical” connections, a plexus of horizontal connections linking distant columns across the V1 network is found originating mostly in layers 2/3, layers 5 and 6. In layer 2/3, pyramidal neurons have collaterals that extend horizontally and connect to other pyramidal neurons up to 8mm apart (Gilbert & Wiesel, 1989). Intracellular studies by the group of Frégnac showed, on the basis of electrophysiological measurements, that these long-distance connections intrinsic to V1 most likely send their message through unmyelinated axons (Bringuier et al., 1999; Frégnac, 2012; Gerard-Mercier et al., 2016). The apparent propagation speed of the message through horizontal connections is around 0.1-0.4 m/s. This speed of propagation is around ten times slower than the one observed for X-thalamic axons and one hundred times slower than what is observed for Y-thalamic axons (for review see Fregnac, 2012). Initially, the lateral connections were thought to make connections with neurons sharing the same functional properties. This has been proved to be more complicated. A recent study performed by Martin and colleagues (2014) showed, intracellularly and with optical recordings, that lateral connections also exist between neurons that do not share the same functional properties. In addition, a study performed by the laboratory (Gerard-Mercier *et al.*,

2016) showed that neurons receive predominantly iso-oriented inputs from neighboring V1 hypercolumns, with gradually weaker and more radially biased inputs the further away from the RF center. A more recent study from Frégnac's laboratory has inferred that precise spatiotemporal constraints can lead to the boosting of sensory responsiveness that depends on the relative timing (imposed by the visual input pattern) of the feedforward and horizontal inputs to the same V1 neuron (Le Bec, 2017). These subthreshold responses could play a role in the genesis of different visual processes such as figure-ground segregation, collinearity detection, and global motion flow sensitivity at saccadic speeds.
In parallel with supra-granular connections, some horizontal connections arise from laterally extending axons of layer 6 pyramidal cells that arborize in layers 5 and 6 (Katz, 1987) and may be fast conducting. The functional role of all the horizontal connections is described in sections 5 and 7 of this introduction.

3.2. Feedforward and feedback connectivity

We have described so far, the connectivity intrinsic to cat primary visual cortex, however some projections involve different areas. They are usually classified in two types: Feedforward and feedback connections.

Feedforward projections to other cortical areas originate from layer 2/3 pyramidal neurons and target layer 4 of higher visual areas, such as A18, 19, A20 or A21a (Einstein & Fitzpatrick, 1991; Scannell *et al.*, 1995; Huan *et al.*, 2007).
Layer 5 pyramidal neurons send their feedback projections to subcortical structures like the superior colliculus, whereas layer 6 pyramidal cells project to the LGN (Thomson and Lamy, 2007).
Cat primary visual cortex also receives feedback inputs coming from higher visual areas. These inputs target layers 2/3 and layers 5/6 (Binzegger et al., 2004). Primary visual cortex receives feedback inputs from areas 18, 19, 20 and 21a but also from the posteromedial lateral suprasylvian area (PLMS; Bullier et al., 1984). In addition, it has been found that other sensory cortices, such as primary auditory cortex project to V1 (Hall and Lomber, 2008). Callosal projections also connect the primary visual cortices of the two cortical hemispheres (Houzel et al., 1994). The interactions between two cortical areas are summarized in Figure 1.3.2.

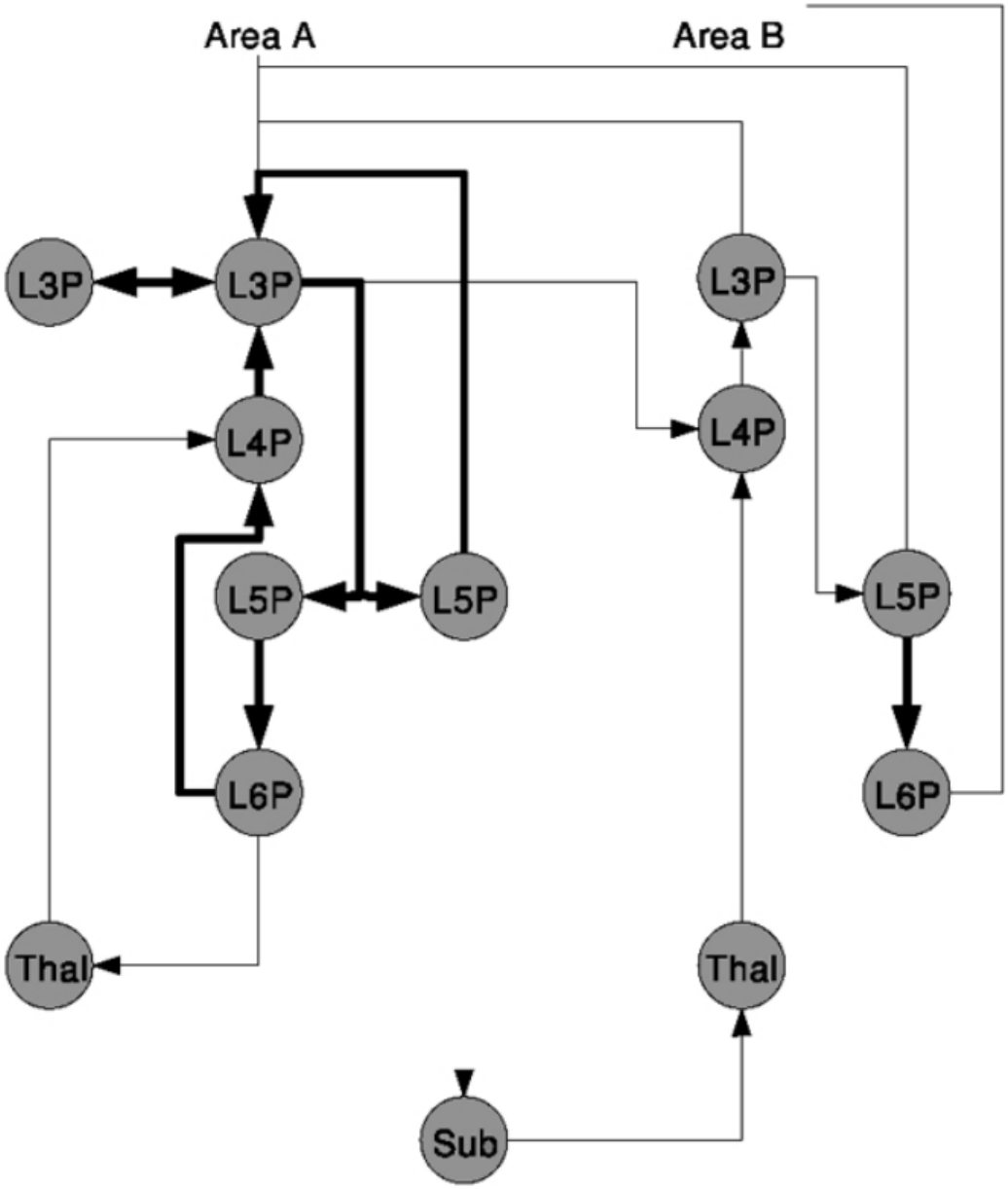

Figure 1.3.2: Graph of the dominant interactions between significant excitatory cell types in neocortex and their subcortical relations (reprinted from Douglas and Martin, 2004).Area A and B refer to two different cortical areas, with area A being the lowest in the visual hierarchy. *LX* refers to the layer, P refers to excitatory neurons, *Thal* to the thalamus and *Sub* to other subcortical structures.

3.3. LAMINAR PROCESSING WITHIN THE CORTICAL COLUMN

Depending on the type of stimulus used, the anatomical organization of the cortical circuitry can result in a very stereotyped visual response. Indeed, a strong activation of the thalamic inputs, either electrically or visually, will lead to strong responses in the layers receiving thalamic inputs followed by a response in the other layers (Watabe *et al.*, 1966; Mitzdorf, 1985). With the emergence of multi-electrode arrays, in particular linear silicon probes, recordings across all cortical layers have become more and more common, allowing the instantiation of current source density (CSD) analysis (Jin et al., 2011a, 2008; Mitzdorf, 1985). Linear silicon probes allowed experimenters to easily identify each

layer by recording the LFP across the whole cortex during simple stimulation protocolsand then computing the CSD of the responses (see Annex 1). We will describe the classical CSD pattern in cat V1 and link it to the anatomical data we described.

The most common way to identify cortical layers in a primary cortex is to take advantage of the geniculate inputs coming to layers 4 and 6. These projections create an early and stereotypical “sink” signature in these two layers and a strong “source” signal in layer 5 (layer 2/3 is deducted based on these clues, see Figure 1.3.3). It is then necessary to strongly activate the thalamic neurons projecting to V1. Two possible methods can be used to fulfill this purpose. The first one resides in the electrical stimulation of the LGN which leads to a strong activation of thalamic inputs projecting to primary visual cortex. This stimulation is characterized by a strong sink in layers 4 and 6 but also by a source current in layer 5 (Jin *et al.*, 2011 and Figure 1.3.3). The second option consists in the use of a visual stimulation that will activate the LGN fibers projecting to V1 in a stereotypical manner. The most commonly used stimuli are fast flashes of white or black squares (see the results section of this thesis for examples in cat V1).

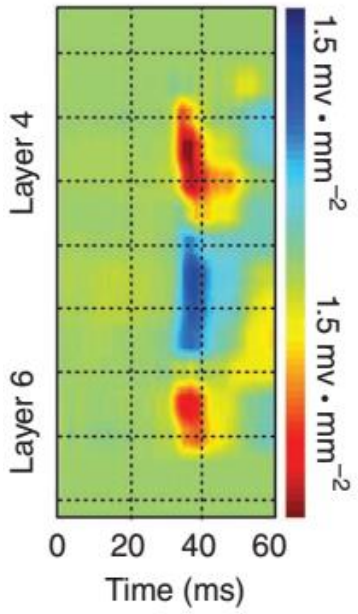

Figure 1.3.3: Current source density on cat primary visual cortex (reprinted from Jin *et al.*, 2011). In red sink currents, in blue source currents. Time 0 correspond to the electrical stimulation of the LFN.

Even though CSD is often used to perform an experimental layer identification, this technique can be exploited for other analysis. For example, in primates, Bijanzadeh and colleagues (2018) revealed with a CSD analysis how horizontal connections were activated after a surround visual stimulation, that was designed in order to preferentially activate these horizontal connections (Figure 1.3.4; the impact of the surround on visual processing is discussed in section 5.3).

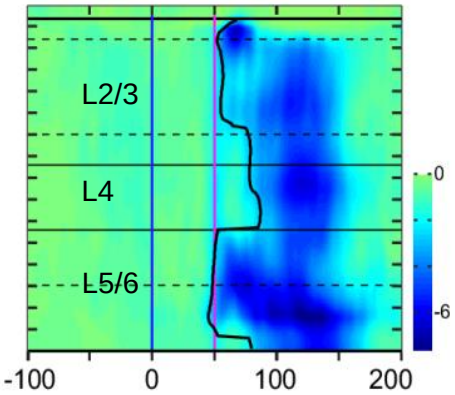

Figure 1.3.4: Example of current source density on primate primary visual cortex after a stimulation activating preferentially L2/3 and L5/6. In blue: sink (reprinted from Bijanzadeh et al., 2018).

In this section, we described the organization of the visual cortical microcircuit. We showed that these microcircuits are composed of different anatomical pathways from which different cortical responses could emerge. The stimulation of this circuitry with very simple stimuli such as black and white squares induces a very stereotyped response reflecting a well-identified circuit. However, other stimuli will likely evoke different patterns of activation, relying on other mechanisms and circuits like those recruited by the center surround interactions (described in detail in section 5). The use and characterization of more complex stimuli is then necessary to deepen our understanding of the visual circuitry. The next section will aim at deciphering how these complex stimuli lead to the identification of new functional mechanisms and an explanation of these mechanisms will take place in the next sections. Important points about the features that need to be tested and how they can be tested will follow these descriptions in all following sections.

4. VISUAL STIMULATION

The pioneering work of Hubel and Wiesel (1959), that revealed the existence of RFs in V1, was performed with very simple visual stimuli like bars and dots. For almost 30 years, this type of visual stimulation was repeatedly used (Olshausen, 2013). However, at the end of the 1980's, more complex stimuli, such as natural images, emerged in the field. Every stimulus has its own statistical properties and can be defined mathematically. We will distinguish, somewhat arbitrarily, four types of visual stimulation.

The first one is the artificial stimuli that have been widely used for the past 60 years by sensory electrophysiologists. The most common ones are point-like light or dark impulses, bars, dots, sine waves or noise. The choice of such stimulus obeys principles of linear systems theory for impulse-like stimuli, since if the system is linear, the response will be the transfer function. Moreover, Fourier analysis can be used for characterizing the modulation transfer function, as employed in optical systems. One important aspect of artificial stimulation is that the experimenter can define and control parametrically the statistics of the stimulus, allowing the precise knowledge of the features that modulate the neuronal response

A second class of stimulus is derived from ethological biology principles and is based on the working assumption that some features represent invariant universals shared in a given species (see for instance (Eckert and Zeil, 2001)). These highly specific features regroup low-level features known to imprint social behavior or trigger feeding, mating and survival reflexes in a species-specific way. The "worm" is a stereotypical shape encoded by retinal and collicular trigger features. The "predator" feature encoding can be suppressed by inverting the direction of movement of the stimulus, transforming it, for example, from a frightening hawk to a friendly goose. Such stimuli have been used across lower vertebrates with great success in retina, colliculus and other subcortical structures.

The third type is defined by natural scene statistics which correspond to scenes from our environment. A singular characteristic of natural scenes is that their spectral power falls with frequency "*f*", according to a power law "α", which leads to a power spectrum of $1/ f^{\alpha}$ (Tolhurst et al., 1992). Different theories emerged in order to explain why natural images follow this power law. The most common one is the scale invariance of the visual world. This means that the statistical properties of the image should not change if one changes the observation scale (Simoncelli and Olshausen, 2001). Spatially rescaling the coordinates of an image by a factor of α leads to a rescaling of the corresponding Fourier domain axes by a factor of $1/\alpha$. Only a spectrum that falls as a power law will retain its shape under this transformation. Another common theory is that the power spectrum of natural scenes emerges from the presence of edges in images since their power spectrum follows a $1/f^2$ power law (Simoncelli and Olshausen, 2001). The edges present in natural images hold also another interesting property. Indeed, Geisler et al., (2001) reported that edges present in natural images showed a strong co-occurrence. These co-occurrences form a "binding strength" allowing the visual processing of the image.

A fourth category of stimulus can also be defined by its closeness to natural statistics. As described earlier, one important aspect of artificial stimuli is the fact that the experimenter can define and control parametrically the statistics of the stimulus. However, performing this fine control with natural images is impossible. Therefore, when studying natural scenes, the experimenter has few cues

about the key feature of the visual statistics that induced the response and new composition methods for creating “artificial” with partial natural statistics need to be developed (Rust and Movshon, 2005). New stimuli containing some features of natural images have been developed in the past years (Goris et al., 2015; Leon et al., 2012; Vacher et al., 2018). These stimuli, such as motion clouds (MC), which have been implemented in our laboratory (Vacher *et al.*, 2018), allow the dynamic control of texture movies where many parameters such as speed, direction, orientation are parametrized experimentally in order to match the statistics of natural scenes. Therefore, these stimuli allow the precise study of naturalistic features but cannot be considered as natural stimuli nor artificial stimuli.

In this section, we will review more in depth three of the four types of stimuli (since they apply to the experimental work of the thesis) and their use in visual cortical neurosciences. We will describe studies performed in cats, but when needed we will also mention primate (both human and non-human) and rodent studies.

4.1. Artificial Stimuli

One of the major studies performed in cat primary visual cortex is the RF study by Hubel and Wiesel (1959; 1962; 1968). They discovered many functional properties in V1 by using very simple artificial stimuli: bars and squares. Rather than using isotropic stimuli (dots and annuli) used in retinal and thalamic sutides, they discovered by accident (slip of the negative film border in the slide projector) that anisotropic stimuli such as white or black bars were much more efficient at triggering spiking activity in visual cortical neurons. By flashing and moving small black or white squares on a grey screen, the existence of receptive fields in cat primary visual cortex was revealed. The bars that were shown at different orientations and moved in different directions allowed them to highlight two important functional properties of V1: Orientation and direction preference of V1 neurons (these functional properties will be discussed in section 5 of this manuscript).

With two very simple artificial stimuli, Hubel and Wiesel made fundamental discoveries about V1. However, despite being a primary sensory region, V1 is a highly complex visual area. In order to be able to study its other functional properties, more complex visual stimuli were needed. The most common artificial stimuli in vision are Drifting Gratings (DG) and Dense Noise (DN).
DG are sinusoidal gratings that drift in a direction perpendicular to the orientation of the grating. Like bars, they permit to test the orientation and the direction preference of the recorded cells but also to explore other functional properties like temporal frequency, spatial frequency, contrast, or phase (these functional properties will be discussed in detail later on the next section of this thesis).

DN, also called pixel white noise, is a stimulus where the luminance of each pixel on a screen is chosen randomly and independently of all other pixels in the same or any other stimulus frame. DN is used for the identification of receptive fields. The luminance’s alternation of the dense noise can be binary (black and white), ternary (black, grey (mean luminance) and white) and even more discretized. However, researchers have mainly used binary and ternary dense noise.

Figure 1.4.1 gives a both description of the spatio-temporal properties of the DG and DN and their frequency content. DG have a very simple spatio-temporal content and show high power spectral density (PSD) only on the frequency of the grating (and its harmonics). On the other hand, DN have a very complex spatio-temporal profile and a flat PSD.

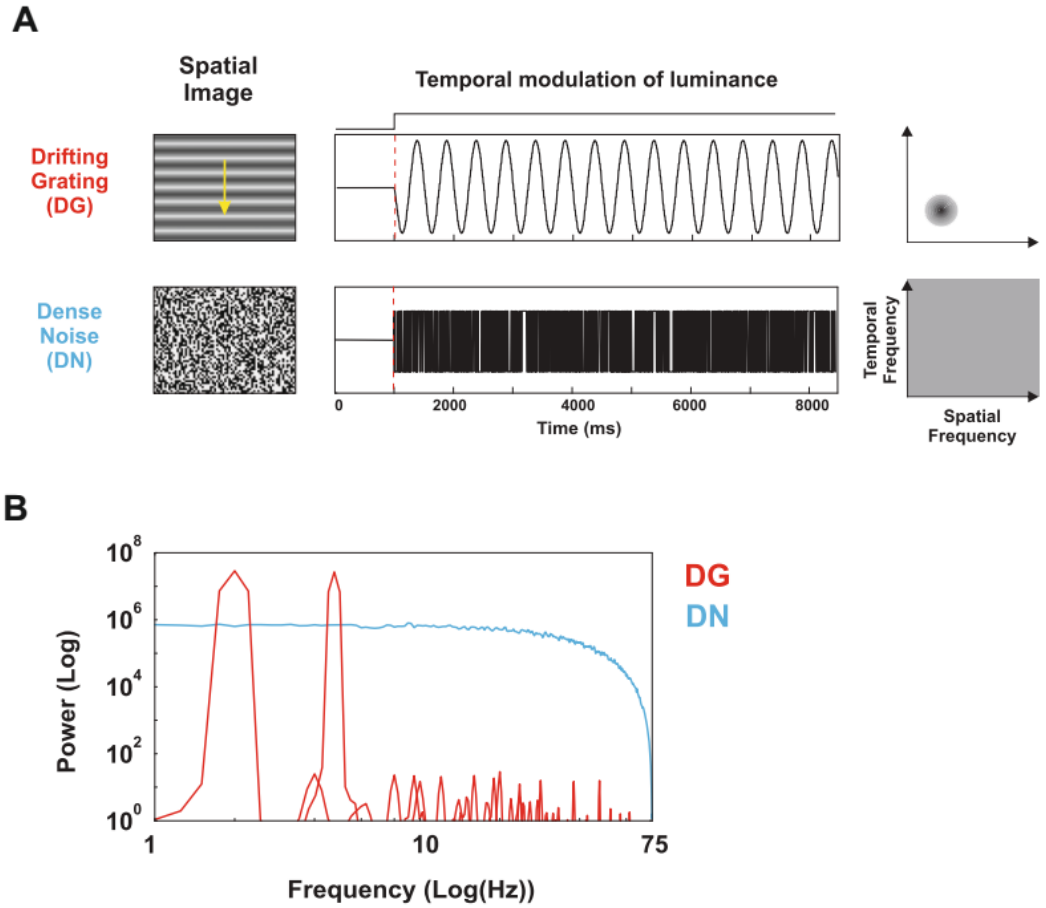

Figure 1.4.1 A. Left column: Example of two artificial stimuli. Middle column: Temporal variation of a given pixel. Right column: Spatio temporal power spectrum for each stimulus. Yellow arrow: direction of the drift. B. Average power spectrum of the luminance for one pixel (modified from Baudot et al., 2013).

4.2. Natural Stimuli

Despite the complexity of artificial stimuli, their statistical properties are far from those observed in natural images. Indeed, the latter are a complex mixture of many different visual features present in artificial stimuli like orientation, contrast, luminance or spatial and temporal frequencies. Among these statistics we can separate first order statistics (*i.e.* the local luminance distribution), and higher order statistics (*i.e.* the covariance; Geisler, 2008; Simoncelli and Olshausen, 2001). The first insights into complex statistics of visual stimuli came from a study by Brunswik (1943). His psychophysical experiments, in humans with natural images, demonstrated that size estimates were more related to object measurements than retinal size and hence provided evidence for the phenomenon of size constancy, implying that the visual system is adapted to the natural statistics of the environment.
Indeed, the hidden assumption is that the functional features of our visual system adapt to the "natural environment" through adaptive changes, most of which occur during one or several "critical" periods of postnatal development (Pecka et al., 2014).

Since the end of the 1990's, interest in the statistics of natural scenes has grown. Three main characteristics of natural images have emerged and will be explained hereafter.

4.2.1 Luminance and contrast

Contrast of edges, luminance polarity and to a lesser extent luminance level are visual features that are encoded by V1 neurons. Many studies have focused on the effects of local contrast and contextual luminance changes on neurons. In Figure 1.4.2-A, an example of luminance and contrast across a natural image is shown. The distribution of local luminance within a natural scene is classically obtained by dividing the luminance at each pixel by the average luminance of the whole image. Figure 1.4.2-B shows a classical luminance distribution. Relative to the mean luminance, there are more dark pixels than bright pixels (Brady and Field, 2000). There are many definitions of local contrast. One of the most used is the distribution of local root-mean-squared contrast, which corresponds to the standard deviation of luminance divided by the mean luminance (Mante et al., 2005). Figure 1.4.2-C shows a typical contrast distribution for a natural scene.

As shown in Figure 1.4.2-A there are large variations of contrast and luminance in a natural image. These variations in local luminance and contrast are nearly statistically independent. (Mante et al., 2005). For example, the joint distribution of luminance and contrast of the natural scene in Figure 1.4.2-A has a small positive correlation ($r = 0.15$; see Figure 1.4.2-D). This statistical independence is directly linked to the typical phase of natural images, indeed 1/f noise does not have this property (Mante et al., 2005).

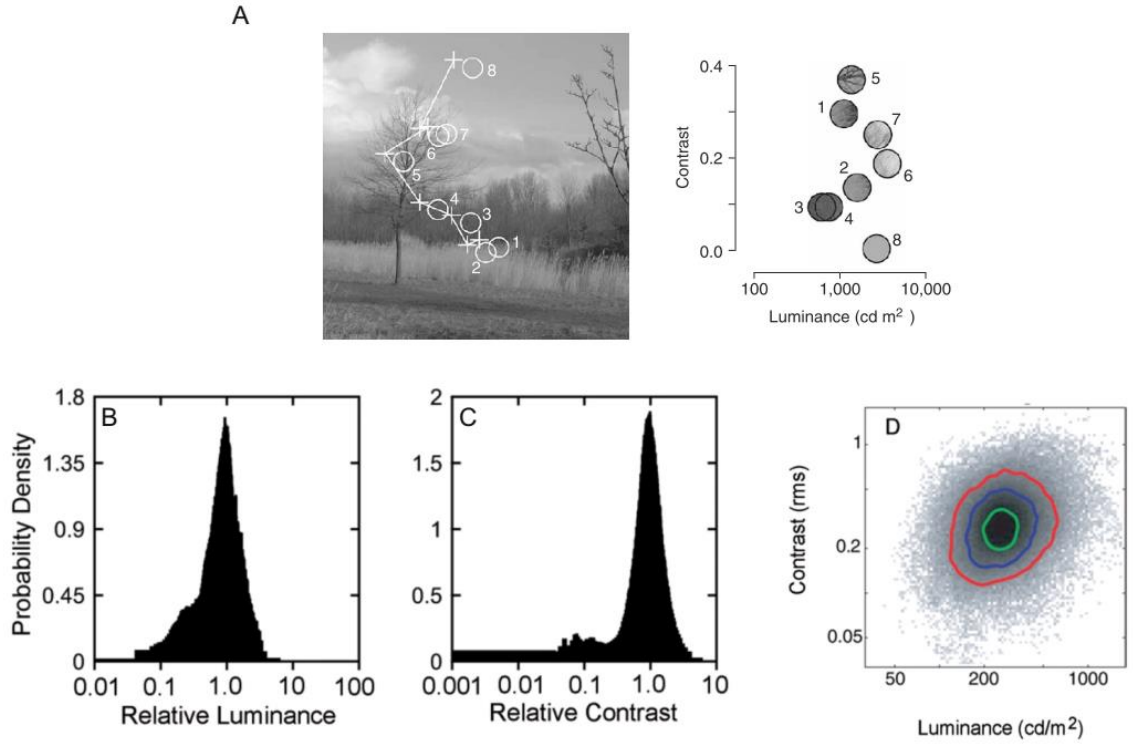

Figure 1.4.2. A. Example of a natural image and its contrast and luminance distribution. **B.** Typical luminance distribution for a natural scene. **C.** Typical contrast distribution for a natural scene. **D.** Joint distribution of luminance and contrast. (A: reprinted from Mante *et al.*, 2005; B,C,D: reprinted from Geisler, 2008).

4.2.2 Spatial Statistics

The majority of the visual information extracted by the retina is contained in the spatial pattern of luminance (Geisler, 2008). A spatial characteristic of natural images, which is consistent across scenes, is the Fourier amplitude spectrum. The classical amplitude power spectrum obtained for natural images is $1/f^{\alpha}$ where f is the spatial frequency and α is the value of the slope (Field, 1987; Rikhye and Sur, 2015a; Ruderman and Bialek, 1994). Based on this finding, a simple spatial model of natural images will be one with a 1/f amplitude spectrum and a random phase spectrum. This artificial image is also called 1/f noise because it corresponds to a sample of filtered Gaussian noise. Such an image does not contain any edges, orientation or any other structure expected in a natural scene (Figure 1.4.3-A). One can wonder if this type of image is adapted to the study of natural scenes. When we compare the response of a Gabor filter (a simple model of V1 neurons) to the 1/f noise and a natural image the distribution is not a Gaussian for the natural image. Indeed, if natural images were Gaussian, their whitening would result in an image without any correlations. Yet, a whitened natural image still contains obvious structures like edges, lines or contours (Figure 1.4.3-B).

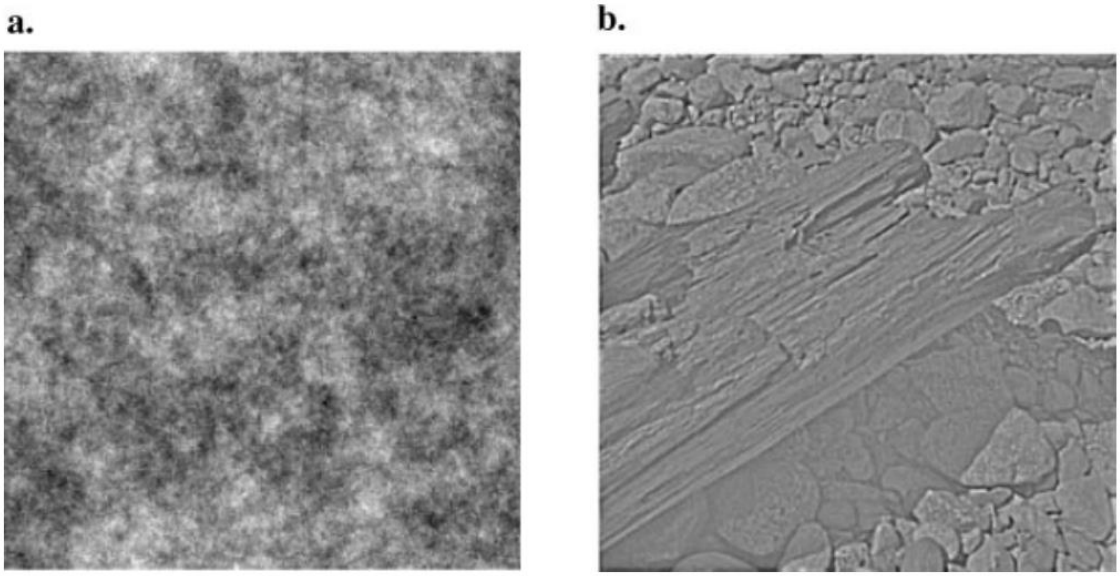

Figure 1.3.4. A. 1/f Gaussian noise. **B.** Whitened natural image (reprinted from Simoncelli & Olshausen, 2001)

Because of all this remaining structure, a more complete description of the spatial structure of natural images can be obtained by examining the joint statistics of responses from pairs of local sensors. For example, if there is a large response from an oriented edge sensor, then it is likely, because of the regularities found in natural scenes, that a neighboring collinear edge sensor also has a large response. Indeed, natural scenes contain many contours that tend to be relatively smooth and to have a significant spatial extent. Edges that are parallels but not collinear are also observed. This is linked to the fact that natural images have a strong occurrence of parallel features. However, even when there is no correlation between the responses, these parallel features are often statistically dependent (Geisler, 2008). The responses of two sensors, RF1 and RF2, are uncorrelated but RF2's variance increases as a function of RF1's magnitude. This shows that strong features tend to cluster in natural scenes. Therefore, when a strong response happens, other strong responses tend to occur nearby.

Another way to produce a complete description of natural images is to examine the joint statistics of the natural image (Felsen et al., 2005; Geisler, 2008). For example, if we compare the orientation of a central patch (or pixels) to the orientation of surrounding patches, the probability that their orientation is the same is high (Figure 1.4.4-A; 4.4-B). Dimensionality reduction approaches such as PCA and ICA (independent component analysis) are used for characterizing these joint statistics (Geisler, 2008).

A study performed by Rikhye and Sur (2015) showed that spatial correlations are necessary in order to obtain a reliable response in mouse V1. In addition, Coen-Cagli and colleagues (2015) found that the spatial correlations have a strong impact on the center-surround modulations. These results highlight the crucial role of spatial correlations in the encoding of natural scenes.

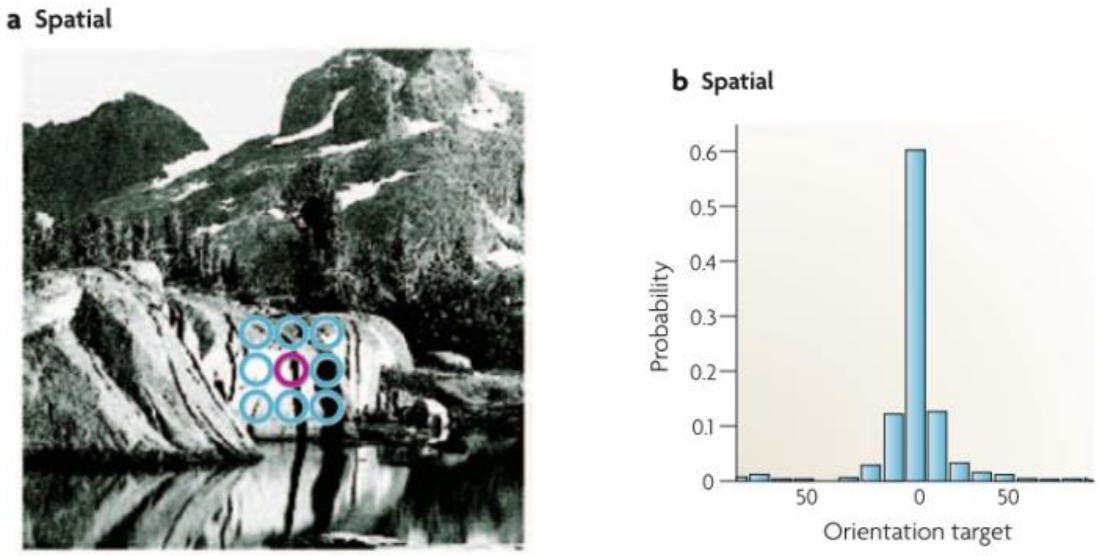

Figure 1.4.4 A. Example of a natural image. Magenta corresponds to the target patch and blue to the context patches. **B.** Probability that the context and the target patches have the same orientation (reprinted from Schwartz et al., 2007).

4.2.3 Temporal Statistics

The measurement of temporal statistics in natural scenes is much more difficult and trickier than for spatial statistics. Indeed, in order to obtain realistic time varying description of the retinal input, it requires tracking of the eye, head and body while the animal explores its environment. Additionally, one needs to account for the motion effects of the visual scene unrelated to the observer.

Some studies managed to fulfill some of these requirements. Kayser and colleagues (2001) mounted a camera on a cat's head in order to obtain movies capturing the temporal statistics of a cat environment. Despite the difficulty to obtain exact representations of temporal statistics, reasonable approximations have been made using video clips from movies or cameras. Dong and Atick (1995) computed the three-dimensional Fourier transform on short movie segments in order to estimate the spatio-temporal power spectrum of natural scenes and highlighted a dependency between spatial and temporal frequencies. For both spatial and temporal frequencies, the slope of the power spectrum becomes shallower for high frequencies (Figure 1.4.6).

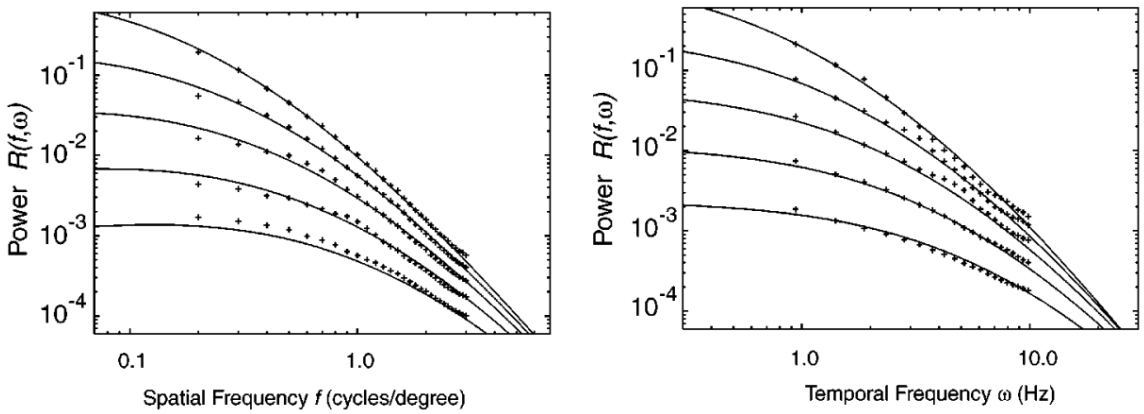

Figure 1.4.6. Spatiotemporal power spectra of natural images. Left panel: Spatial power spectra measured at different temporal frequencies (1.4, 2.3, 3.8, 6, and 10 Hz, from top to bottom). Right Panel: Temporal spectra measured at different spatial frequencies (0.3, 0.5, 0.8, 1.3, and 2.1 cpd, from top to bottom). The solid curves show the expected spectra if the world is modeled as collection of patches of spatial 1/ f noise that are each undergoing translation locally at some random velocity. Reprinted from Geisler (2008)

Similar to spatial statistics, temporal statistics are highly correlated in neighboring pixels. If we compare the orientation of a central patch (or pixels) to the orientation of surrounding patches across time, the probability that their orientation is the same is high (Figure 1.4.7-A; 1.4.7-B).

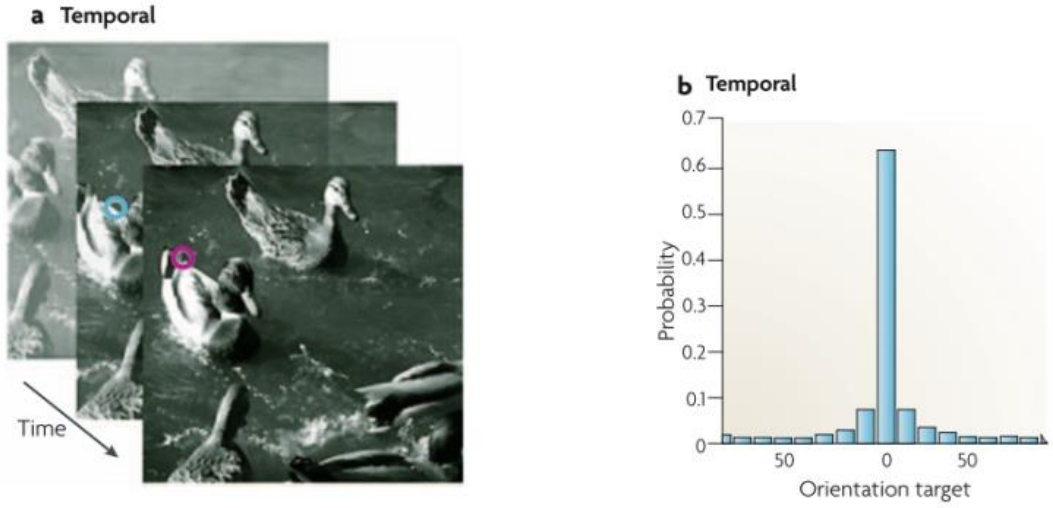

Figure 1.4.7. **A.** Example of a natural image. Magenta corresponds to the target patch and blue to the context patches. **B.** Probability that the context and the target patches have the same orientation (reprinted from Schwartz *et al.*, 2007).

One very important aspect that should not be neglected is the reflex (nystagmus) or voluntary movements linked to eye-head-body coordination. Indeed, mammals, from primates to rodent, perform eye and head movements while exploring a visual scene (Samonds et al., 2018). Eye movements are composed of drifts, tremors, micro-saccades and saccades (Baudot *et al.*, 2013), that drastically influence the visual inputs. Indeed, making a saccade will bring a new visual input uncorrelated with the previous one (Samonds *et al.*, 2018). The saccades are thought to be calibrated as a function of the environment in order to optimize the visual processing of the scene (Samonds et al., 2018). All mammals perform saccades and head movements to process a visual scene. However, the exploration strategy can differ depending on the species. Higher mammals, such as cats or primates use head movements for very large shifts in gaze (Guitton et al., 1984;

Morasso et al., 1973). However, marmosets also use head movements for small shifts in gaze, similar to the ones performed with saccades (Mitchell et al., 2014).
Contrary to higher mammals that explore their surroundings in a binocular manner, rodents (which are prey), disconjugate their eyes in a natural environment (Wallace et al. 2013). To do so, one eye processes the information coming from the close environment, while the other one processes the information coming from the visual field above the animal, to anticipate predator attacks.
Because cats, the experimental model of this work, only perform head movements for large shifts, we will not look at their impact on visual processing. However, previous studies (Baudot *et al.*, 2013; Samonds *et al.*, 2018 but also Vinje & Gallant, 2000) showed the importance of eye movements for visual processing. These studies showed in anesthetized and awake animals that eye movements have a strong impact on the efficiency of the coding (results commented in section 7). Therefore, it is essential to develop a model of natural stimuli where these eye movements are simulated in order to account for the natural behavior of the studied model.

In a paper called *A natural approach to studying vision*, Felsen and Dan (2005) claim that the best way to understand how V1 responds to natural images is to use natural stimuli. By using these stimuli, one can identify which features of natural scenes drive the neuronal response.
This approach, namely the exploratory approach, allows the observation of the system in its natural state. It leads to the development of new theories that will be tested with the development of stimuli containing precise features that showed to be relevant to explain the observed behavior. Moreover, the exploratory approach gives us the possibility to discover surprising new phenomena. One famous example of the exploratory approach is the somewhat opportunistic discovery of orientation selectivity.
Contrary to Felsen and Dan, in a paper called *In Praise of Artifice*, Rust and Movshon (2005) affirm that the best way to understand natural images is to develop stimuli containing some of the naturalistic features present in natural scenes. By understanding how V1 responds to each of these individual features, one will be able to understand how V1 encodes natural scenes.
This approach, that has been used for years in neuroscience, requires different parameters to be reunited in order to efficiently answer a question. Indeed, in order to define a hypothesis, one needs to identify features that are shown to be relevant. An example of a well-formed hypothesis is present in the work Rikhye and Sur (2015). They hypothesized that spatial correlations have an impact on the levels of reliability, which proved to be true. However, the formulation of this hypothesis was only possible because other studies (Baudot et al., 2013a; Haider et al., 2010; Vinje and Gallant, 2000) investigated, in an exploratory manner, how primary visual cortex responds to natural scenes.
Another important issue raised with this approach is that sometimes the questions asked are so precise that the obtained data is not useful when investigating other issues. Therefore, an interplay between a hypothesis-driven approach and a second approach is essential for the understanding of visual processing (Olshausen, 2013).
In summary, both approaches are essential and complementary. The exploratory approach will allow the emergence of new theories that will be tested with the hypothesis-driven approach. This is particularly true for natural images, since our knowledge about how V1 responds to them is limited.

Therefore, different studies performed with natural images opted for an exploratory approach. One of the most famous studies performed in V1 with natural images, performed by Vinje & Gallant, was exploratory. We can also cite other studies such as Haider et al., (2010), Baudot et al., (2013), and Froudarakis et al., (2014). All these studies investigated the impact of unaltered natural scenes on

visual processing and used simple controls like the randomization of the phase in order to confirm what they observed (these studies are discussed in detail in section 7).
Many new findings were made with the hypothesis-driven approach, based on results obtained with the exploratory approach. Notably, by using the hypothesis-driven approach, Movshon's group made significant contributions to the understanding of responses to natural images (Freeman et al., 2013; Ziemba et al., 2016, 2018). For this purpose and based on Portilla and Simoncelli (2000), they developed two sets of synthetic stimuli using a novel algorithmic approach (*i.e.* a model of naturalistic textures).
-The first set consists of spectrally matched noise images. The original texture is analyzed with linear filters and energy filters (corresponding to V1 simple and complex cells, respectively) tuned to different orientations, spatial frequencies and spatial positions. Noise images contain the same spatially averaged orientation and frequency structure as the original but lack many of the more complex features *i.e.* the high order statistics such as correlations between features in the image (Figure 1.4.8).
-The second set represents naturalistic textures. Here, correlations are computed by taking products of linear and energy filter responses across different orientations, spatial frequencies and positions. Images are synthesized to match both the spatially averaged filter responses and the spatially averaged correlations between filter responses. The resulting texture images contain many more of the naturalistic features from the original (Figure 1.4.8). With these different types of stimuli, the groups of Movshon and Simoncelli were able to show that the two synthetic stimuli elicited the same response in V1, while V2 responded more strongly to naturalistic stimuli. By using these two sets of stimuli, they showed that V2 has a particular functional role for the representation of natural image structure.

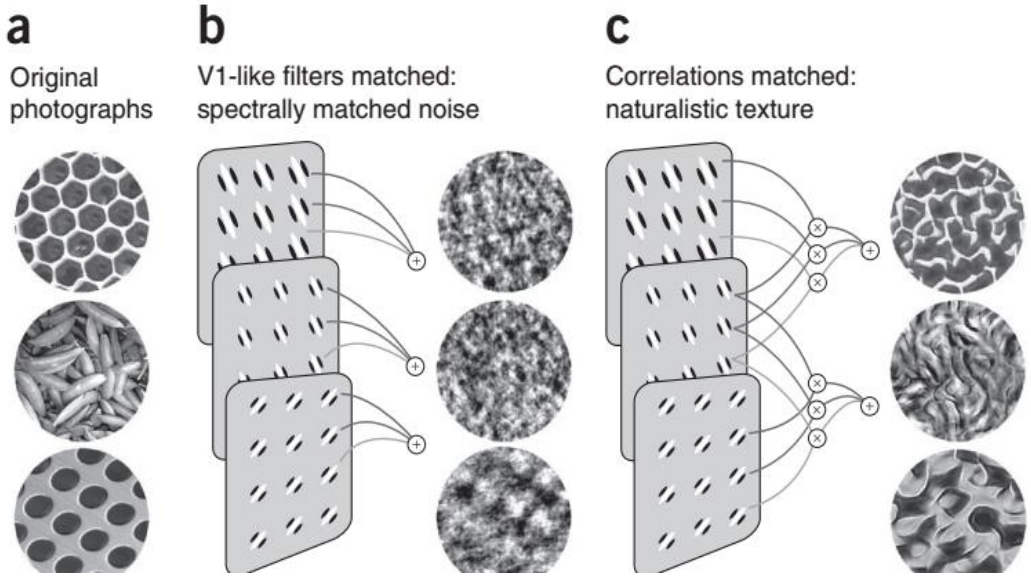

Figure 1.4.8. Generation of synthetic stimuli. **A.** Original natural textures. **B.** Spectrally matched noise images. **C.** Naturalistic texture images (Reprinted from Freeman *et al.*, 2013).

Recently, new algorithms for natural-like stimulus design have been developed (Galerne et al., 2011; for a natural-like stimulus developed in the laboratory see Vacher *et al.*, 2018). These stimuli, called motion clouds, allow the dynamic control of texture movies where many parameters such as speed, direction, and orientation are parametrized experimentally in order to match the statistics of natural scenes. Therefore, the experimenter can dynamically modify one specific parameter such as direction and directly address its impact on the response.

Other techniques to generate synthetic stimuli were also developed. Indeed, with the new deep convolutional models, new types of naturalistic stimuli can be synthetized (Gatys et al., 2015). Indeed, unlike Portilla & Simoncelli's (2000) model, which worked only with textures, deep networks are able to generate naturalistic images from complex images such as paintings (Figure 1.4.9). This allows the testing of a new class of stimuli, containing more naturalistic features than the ones previously generated. Because of this increased control of naturalistic features present in the generated stimulus, the experimenter can easily test more hypotheses than what was possible with the classic synthetic stimuli.

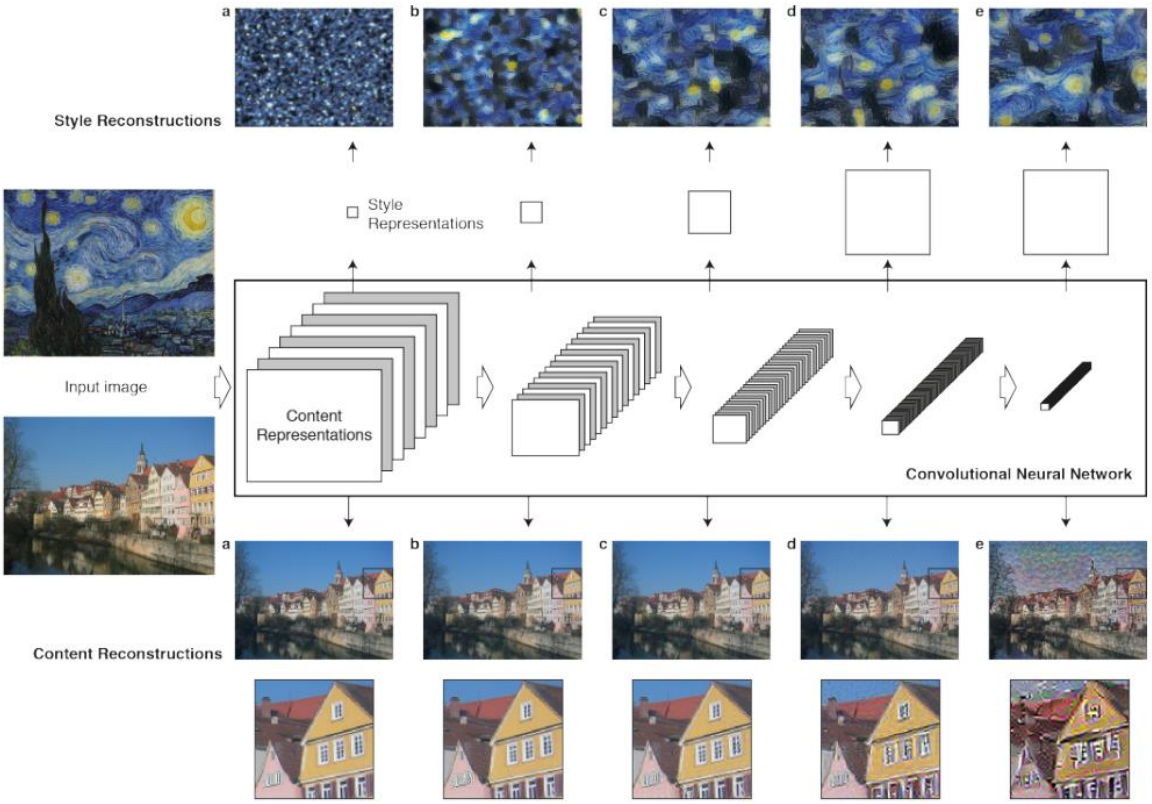

Figure 1.4.9. Generation of natural images based on deep convolutional networks (reprinted from Gatys *et al.*, 2015).

In conclusion, the exploratory approach led to a first characterization of the functional organization of the primary visual cortex, thereby allowing the emergence of hypothesis-driven studies. In the next section, we will describe these functional properties and how a functional organization emerged from them.

5. FUNCTIONAL ORGANIZATION OF CAT PRIMARY VISUAL CORTEX

The functional study of cat primary visual cortex started with the work of Hubel and Wiesel (1959, 1961). This seminal work showed that V1 neurons have different types of receptive fields. Additionally, these neurons are sensitive to different orientations, directions, spatial frequencies and contrast. In the following years, many other functional properties of V1 neurons have been discovered. Among them, spatial frequency selectivity (Enroth-Cugell and Robson, 1966); temporal frequency selectivity (Ikeda and Wright, 1975) and contrast selectivity (Ikeda and Wright, 1974; Movshon et al., 1978) emerged as remarkable hallmarks. Another notable, but not exclusive, functional feature of V1 resides in the organization of neurons sharing functional properties into functional columns (Hubel and Wiesel, 1969; Mountcastle, 1957). The functional properties of primary visual cortex, described above, emerge directly from the receptive field properties.

5.1. Receptive fields

The concept of receptive field has evolved over the years. It was introduced 70 years ago by Hartline (1938) who defined the RF as the region of the retina where a change in light brightness modifies the firing rate of a retinal ganglion cell. This definition is now applied to all visual structures. By stimulating with black and white bars, Hubel and Wiesel (1962) described two types of receptive fields in primary visual cortex: simple receptive fields and complex receptive fields. Their description of the receptive field was purely spatial. However, since the spatial structure of RFs is dynamic (DeAngelis et al., 1995), the complete characterization of the functional properties of a visual neuron has to include the temporal aspect.

The study of the receptive field became a standard procedure in understanding V1. Indeed, many studies considered the RF as a system that will transform the visual stimulus (the input) into a neuronal activity (the output) through a transfer function. Here the RF is considered as a “black box”: the focus is not on what happens inside the system but rather on how the input will induce the output. This approach allows a functional study of the system. Since the RF can be defined within spatiotemporal dimensions, the transfer function has to be characterized in both space and time.

We will describe below how simple and complex receptive fields have been characterized, both mathematically and experimentally, over the years.

5.1.1 Simple receptive fields

Both ganglion cells in the retina and thalamic cells in the LGN display circular receptive fields organized as a pair of concentric opponent sub-regions, defining a center (ON or OFF) and its antagonist surround (respectively OFF or ON). These two regions are defined by the fact that the OFF sub-region is sensitive to a negative contrast change (such as introducing a dark stimulus on a uniform background) while the ON sub-region is sensible to a positive contrast change (*i.e.* bright stimuli). In their pioneering papers on cat primary visual cortex, Hubel and Wiesel (1959, 1962), described two classes of receptive fields in cat V1 by recording extracellularly the neuronal responses to flashed stimuli: Simple and Complex.

According to their seminal work, simple cells are composed of spatially segregated ON and OFF regions of the same main axis orientation and are identified according to four criteria:

1. They are subdivided into distinct ON and OFF regions.
2. There is spatial summation within the separate ON and OFF regions.
3. There is an inhibitory antagonism between ON and OFF regions (also called push-pull; *i.e* within each subregion, stimuli of the opposite contrast evoke synaptic responses of the opposite sign).
4. It is possible from the spatial arrangement of ON and OFF regions to predict responses to any stimulus

All cells that do not adhere to these four criteria are considered as complex cells. However, Hubel and Wiesel did not provide a quantitative test to clearly separate simple and complex receptive fields. In order to overcome this problem, many quantitative classifications have been tested. These classification methods are based on new parameters such as the overlap of ON and OFF regions, spontaneous activity levels, response to moving light and dark bars and many others (Martinez and Alonso, 2003). Yet, these techniques were not able to clearly classify simple and complex cells. Indeed, for the same response some would classify them as simple RFs, while others as complex RFs. For example, simple cells presenting a partial overlap between ON and OFF subregions are considered as nonlinear simple cells and would have been called complex by Hubel and Wiesel.

A different quantitative test was introduced by De Valois and colleagues (1982) and later improved by Skottun and colleagues (1991). These authors used larger grating stimuli covering the RF (imposing a sinusoidal luminance contrast pattern, whose phase, spatial and temporal frequencies could be controlled by the experimenter), without changing the mean luminance of the view field. Although static gratings were first used in the retina and the thalamus by Enroth-Cuggel and Robson (1966) to test the linearity or non-linearity of spatial summation, De Valois et al. used sinusoidal drifting gratings and quantified simple and complex cells based on their response modulation index. The modulation index (F1/F0) is given by the ratio between the first Fourier harmonic (F1) of the response and the mean spike rate (F0). Simple cells modulate their firing rate in phase with the stimulus, while complex cells are not (or very little) modulated. Hence, when F1/F0 is above one, cells are considered as simple. Despite being used to discriminate between simple and complex cells in V1, the “response modulation” quantitative test failed to provide any information about the receptive field geometry. Therefore, in order to classify simple cells, it is necessary to include more than one parameter.

While Hubel and Wiesel proposed a spatial characterization of the receptive field, other studies showed that the RF can also be described spatiotemporally. Indeed, space and time can interact in two different ways, RFs can be space-time separable or space-time inseparable. Defined formally, space time separability means that the three dimensional RF, R(x,y,t) can be described as a product of two independent functions. A spatial profile, G(x,y), and a temporal profile, H(t), where the response, R(x,y,t), is equal to G(x,y) x H(t). In practical terms, this means that the spatial arrangement of RF subregions is fixed but their strength and polarities are modulated over time. In order to effectively map a simple receptive field, sparse noise (which consists of a pattern of black and white dots or squares presented alternatively on the screen) and dense noise stimulation are classically used. Therefore, if a cell has is space-time inseparable, it is not possible to subdivide it into a spatial and a temporal component (DeAngelis *et al.*, 1995). Spatiotemporal profiles are described in Figure 1.5.1.

The spatiotemporal organization of the RF is linked with other functional properties, like orientation or direction selectivity.

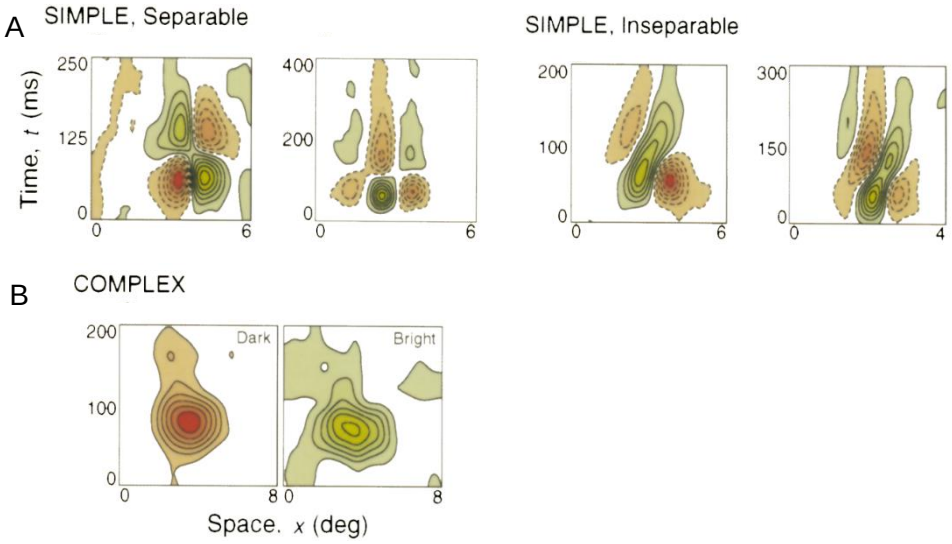

Figure 1.5.1. Spatiotemporal receptive fields. Y axis represents time and X axis space. Green contours correspond to light excitatory regions. Red contours correspond to dark excitatory regions. A. Two types of simple receptive fields. Left panel represents a separable RF, right panel represents an inseparable RF. B. Complex Receptive Field (reprinted from DeAngelis *et al.*, 1995)

It is well established that RFs are not static invariant structures. Indeed, Fournier and colleagues (2011, 2014) from Frégnac's lab demonstrated that the Simple/Complex nature of the RF depends on the visual statistics used to probe it. For each cell (intracellularly recorded), they computed the Volterra first and second order kernels and defined a "simpleness index" (SI). This index measures the spatiotemporal energy of the linear first kernel relative to the sum of the first and diagonal of the second kernel. If the SI is higher than 0.5 the cell is considered simple, whereas if the SI is lower than 0.5 the cell is complex. They found that, for the same cell, this index changes according to the test stimulus: if the stimulus is of high dimensionality (dense noise), the receptive field looks dominantly linear (simple-like), whereas if the stimulus is of lower dimensionality (sparse noise), the receptive field looks dominantly non-linear (complex-like). According to their decomposition scheme, the functional expression of the receptive field in a given context relies on the relative weights between simple-like and complex-like synaptic contributions. This stimulus dependence of the receptive field is discussed in section 6 of this chapter.

In their original study, Hubel and Wiesel (1962) proposed a hierarchical model explaining how simple and complex receptive fields emerge in V1. According to their model, simple receptive fields are constructed from the convergence of geniculate inputs with receptive fields of the same type (ON or OFF) aligned in the visual space. In turn, complex receptive fields are constructed from the convergence of simple cells sharing the same orientation preference but partially overlapping regions (Figure 1.5.2-A). However, over the years the scientific community has criticized this model and questioned the nature of the cortical microcircuit. Indeed, as previously described in section 1.3, only 10% of layer 4 synapses in V1 are thalamocortical. Therefore, cortical responses should also be shaped by cortical inputs and not only by geniculate inputs.

Based on a series of heroic intracellular studies, Douglas and Martin (1991) developed a new conceptual framework for receptive fields, known as the recurrent model. This model rests on three key assumptions

1. Only 10% of synapses in layer 4 are thalamocortical
2. Cortical excitation from neighboring neurons is very strong.
3. Cortical inhibition controls the gain of excitatory neurons.

Despite these three statements being true, one cannot reduce the contribution of LGN in the construction of simple receptive fields. Indeed, thalamic synapses represent only 10% of the synapses in layer 4 but they strongly drive cortical cells. In addition, an inactivation of a small region of LGN is enough to silence the activity of the majority of cortical cells in layer 4 (Martinez & Alonso, 2003).

Therefore, a new experimental framework has started to emerge. New models are taking into account both cortical recurrence and hierarchical organization (Figure 1.5.2-B; Antolík et al., 2016). In these new models, cortical recurrence is taken into account as well as other very important parameters like push-pull connectivity, untuned cells in layer 4, and also the ON-OFF relationship that gives rise to simple receptive fields (Kremkow et al., 2016a).

Many insights from both models (*i.e.* the old hierarchical model and its revision) came from computational studies. Indeed, responses from simple cells, both spatial and temporal, can be predicted with a linear function and have been widely used to validate different hypotheses about V1. A more detailed description of the results obtained with these models will be discussed later in this manuscript.

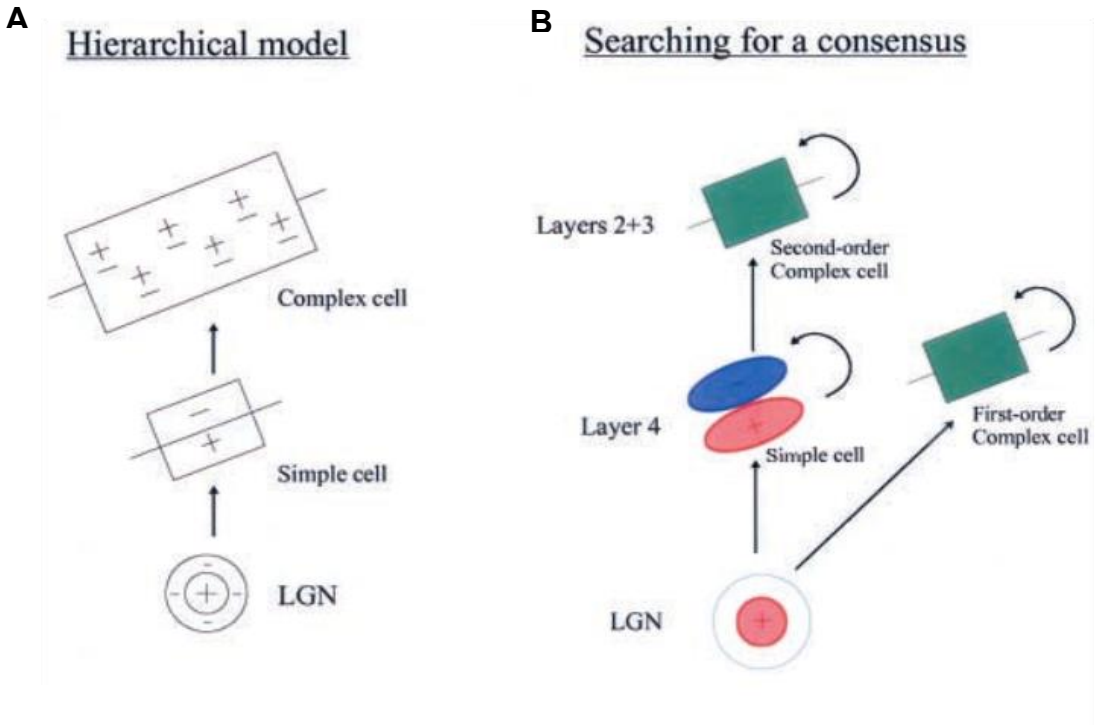

Figure 1.5.2. A. Hierarchical model of V1 receptive fields as described by Hubel and Wiesel. **B.** New model for the emergence of receptive fields in V1, taking into account the hierarchical, parallel and recurrent theories (Modified from Martinez and Alonso, 2003).

5.1.2 Complex Receptive Fields

According to Hubel and Wiesel (1962), all the cells that do not match their four-criteria classification are complex cells. As for simple receptive fields, their classification does not give a quantitative test to clearly separate simple and complex cells. A good way to classify complex cells is to use the test developed by Skottun and colleagues (1991). In response to a sinusoidal drifting grating, complex cells will show no, or very little, modulation. Hence, the modulation ratio will be less than one for complex cells. This test classifies complex cells in a very reliable way. Yet, in order to obtain the spatial and temporal structure of the complex RF, a spatiotemporal mapping technique is necessary. The spatiotemporal profile of complex cells is very different from those obtained with simple cells. They present non-elongated, overlapping ON and OFF regions (DeAngelis *et al.*, 1995; Figure 1.5.1-B).

Based on the hierarchical model of Hubel and Wiesel (1962), complex cells are generated from the convergence of simple cells sharing the same orientation preference. However, many studies found that some complex cells received direct thalamic inputs (Bullier and Henry, 1979; Martin and Whitteridge, 1984; Tanaka, 1983). This criticism of the purely serial/hierarchical Hubel and Wiesel model gave rise to a new class of V1 models, (Martinez and Alonso, 2003). This so-called “parallel model” proposed that simple and complex cells are generated through concurrent activation of separate thalamocortical pathways (Stone, 1965). In the retina, X-cells are simple-like cells and Y cells are complex-like cells. Retina projects to thalamus and geniculate projections converge in V1. The parallel model states that simple cells are built from the convergence of thalamic X-cells inputs while complex cells are built from the convergence of thalamic Y-cells inputs.

As discussed above, the scientific community could not ignore the findings that go against the hierarchical model. Therefore, a consensus taking into account the hierarchical model, the parallel model and the recurrent model has emerged (Martinez and Alonso, 2003; Figure 1.5.2). Many insights into complex cells came from computational studies. Indeed, both spatial and temporal responses of complex cells can be predicted with nonlinear functions and have been widely used to validate different hypotheses about V1. A more detailed description of the results obtained with these models will be discussed in section 6.
All the receptive field properties discussed above were obtained from single unit studies. However, their study can also be performed at multi-unit or mesoscopic scales.

5.1.3 Mesoscopic receptive fields

Receptive fields can also be obtained with the multi-unit activity (MUA) and the local field potential (LFP) that are mesoscopic signals (Land et al., 2013; Xing et al., 2009; see Annex 1 for a description of these measurements). Since these signals correspond to a local aggregate of neuronal responses, classifying them as simple or complex is not appropriate. A direct consequence of the fact that these signals capture global activity is that the size of the receptive fields are higher than the ones observed for isolated single units. A description of their functional properties and the differences between single unit activity, MUA and LFP will be done later in this section.

5.2. Laminar distribution of receptive fields

Functional studies have investigated the location of simple and complex receptive fields. A large body of evidence indicates that anatomical organization and laminar distribution of simple and complex receptive fields are correlated. Since simple cells originate from thalamic inputs, based on V1 anatomical studies, they should be located in layers 4 and 6 whereas complex cells should be located in layers 2/3 and 5 (See section 1.3 of this chapter). Indeed, the majority of spiny stellate cells (located in layer 4 of cat V1, see section 1.3) are simple cells (Martinez et al., 2002). Moreover, an intracellular study performed by Martinez and colleagues (2005) explored carefully the laminar distribution of simple and complex receptive fields. By coupling intracellular staining and whole-cell recordings they were able to determine the laminar localization of simple and complex receptive fields and established a classification using two criteria, the index of overlap between ON and OFF subregions and a push-pull index. According to this classification, if a stimulus of the opposite contrast evoked comparable amounts of push and pull, the index value is equal to 0, a value of 1 indicates push-null and a score of 2 denotes push-push. Cells showing ON/OFF subregion separation and a push-pull index lower than 1 are considered as simple. Their results indicate that simple cells are only located in layers 4 and 6 that receive thalamic inputs (Figure 1.5.3; Figure 1.5.4), whereas complex cells are located in all layers of the cortical microcircuit (Figure 1.5.3).
The characterization of the complex and simple cells is possible because a stimulus presented on the visual field is going to elicit a visual response. The region responding to this stimulation is called the center of the receptive field. However, the receptive field is a more complex structure that is also composed of a supposedly silent region, called the surround.

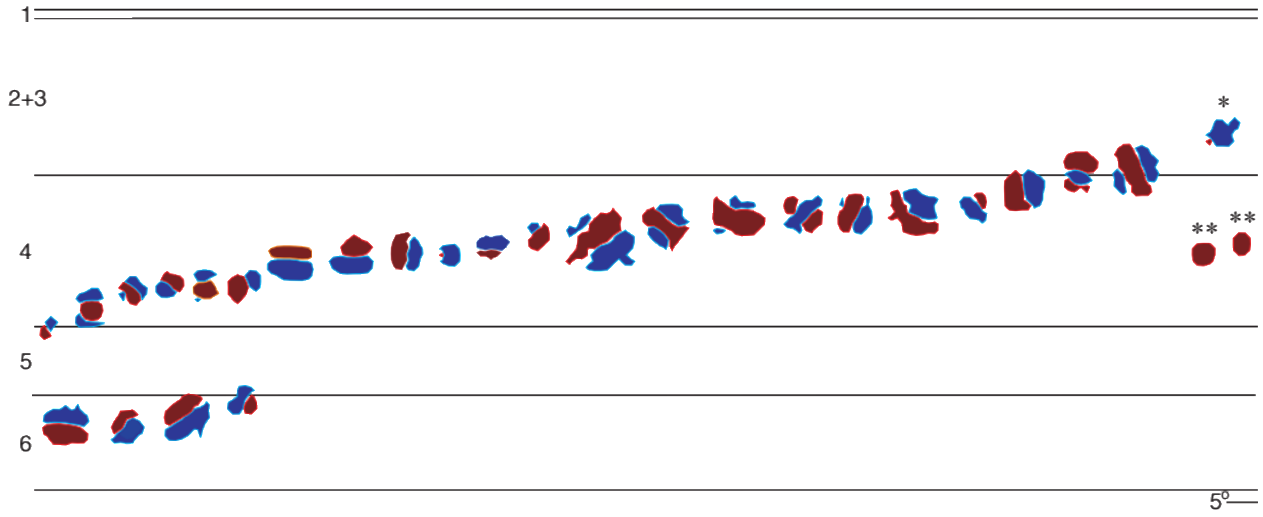

Figure 1.5.3. Laminar distribution of simple Receptive Fields in Cat primary visual cortex. Simple cells are only located in layers 4 and 6. Except for one cell in layer 2/3. In blue: OFF region; In red: ON region. Scale bar: 5°. (Reprinted from Martinez et al., 2005).

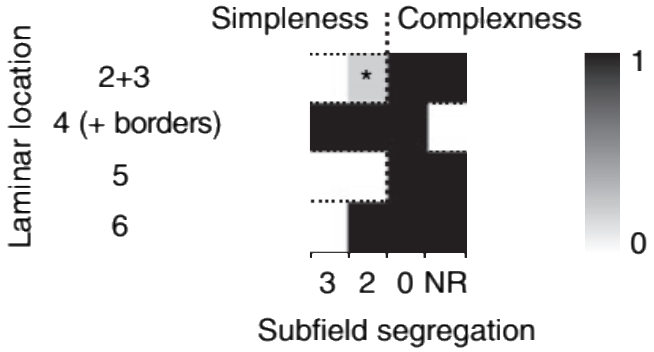

Figure 1.5.4. Laminar distribution of simple and complex cells in cat primary visual cortex. NR: no response. (reprinted from Martinez *et al.*, 2005).

5.3. Receptive field surround

The center of the RF is considered as the region that is going to elicit a response while stimulated. When probed with an impulse-like stimulus minimizing spatial summation, its extent defines the minimum discharge field (MDF). The region around the RF center is called the surround and is by definition the region where a stimulus presentation is not going to elicit any neuronal response (this region is also called the non-classical RF or “silent surround” (review in Frégnac and Bringuier, 1996; Seriès et al., 2003). Therefore, center-surround interactions are nonlinear because the sum of the surround response and the center response is not equal to the response of a simultaneous stimulation of the center and the surround. Because of these properties, many studies investigated, with a large number of different stimuli, the effect of simultaneous center-surround stimulation.
Different functional features emerge directly from the properties of the receptive field described in previous sections, for example, simple cell orientation selectivity originates from the organization of the ON and OFF subregions. In the next section, we describe V1 functional properties and how they are linked to the receptive field spatio-temporal characteristics.

5.4. Neuronal Functional Selectivity

Hubel and Wiesel’s pioneering studies (1959, 1962) showed that V1 neurons have simple and complex receptive fields, but also that neurons are selective to particular directions and orientations. V1 neurons are also sensitive to other parameters. Among them, there are spatial frequency (Enroth-Cugell & Robson, 1966) and temporal frequency (Ikeda & Wright, 1975).

5.4.1 Spatial Frequency Selectivity

The best way to measure spatial frequency selectivity is to present, at the preferred orientation of the cell, various sinusoidal drifting gratings having different spatial frequencies.

In cat primary visual cortex, neurons are sensitive to spatial frequencies (SF) ranging from 0.7 to 3.2 cycles per degree (c/deg). Whereas Movshon and colleagues (1978) reported that the mean spatial frequency selectivity is around 0.9 c/deg for both simple and complex cells. Other studies, like the one conducted by Chavane and colleagues (2011), performed visual stimulation with sinusoidal drifting gratings having a spatial frequency set at 0.6 c/deg (see Figure 1.5.5 for an example of responses to various SF). These discrepancies across studies show that a large range of spatial frequency sensitivity exists in V1. In this regard, Molotchnikoff and colleagues (2007) showed that nearby neurons do not necessarily exhibit the same optimal SF, thus highlighting the necessity to compute the spatial frequency tuning curve of the recorded neuron.

The spatial structure of simple receptive fields is correlated with the spatial frequency tuning. Indeed, by determining the width of the ON and OFF areas, the optimal SF can be computed. Several methods exist to predict the optimal SF. The first one consists of computing the responses to simple bright and dark bars presented at different positions in the visual field. These responses are then compared with the responses predicted by the inverse Fourier transform of the selectivity curve to spatial frequencies obtained with sinusoidal drifting gratings (Movshon *et al.*, 1978; Dean and Tolhurst, 1983). This function can be expressed as a Gabor function. The latter is a Gaussian function multiplied either by a sine or by a cosine. The pass band of the SF tuning curve determines the envelope of the Gaussian function, whereas the optimal frequency determines the width of the

cosine or sine function *(i.e.* the number of ON and OFF subregions; see examples of Gabor functions in Figure 1.5.6). For simple cells with non-overlapping subregions, this function gives an accurate description of the RF profile (Movshon *et al.*, 1978; Dean & Tolhurst, 1983). However, for nonlinear simple cells (with overlapping subregions) the result is less precise because of the RF non-linearity.

Another method for studying the spatial frequency tuning consists of computing the RF spatial profile with moving bars. These spatial profiles are then used to predict the SF tuning curve (Kulikowski and Bishop, 1981). Finally, with the combination of these two methods, Jones and Palmer (1987a, 1987b) investigated the correlation between the SF and the RF structure. They found that simple receptive fields can be modeled by 2D Gabor filters and that these filters can be used to measure the simple cell's linearity.

Unlike simple cells, complex cells are nonlinear. Movshon and colleagues (1978) investigated the complex cell response to the interaction between two bars presented at the same time but in different locations of the RF. According to the authors, the obtained response profile defines the RF sub-units. These spatial properties of these sub-units determine the SF selectivity. To model these complex responses with Gabor functions one needs to sum them in quadrature.

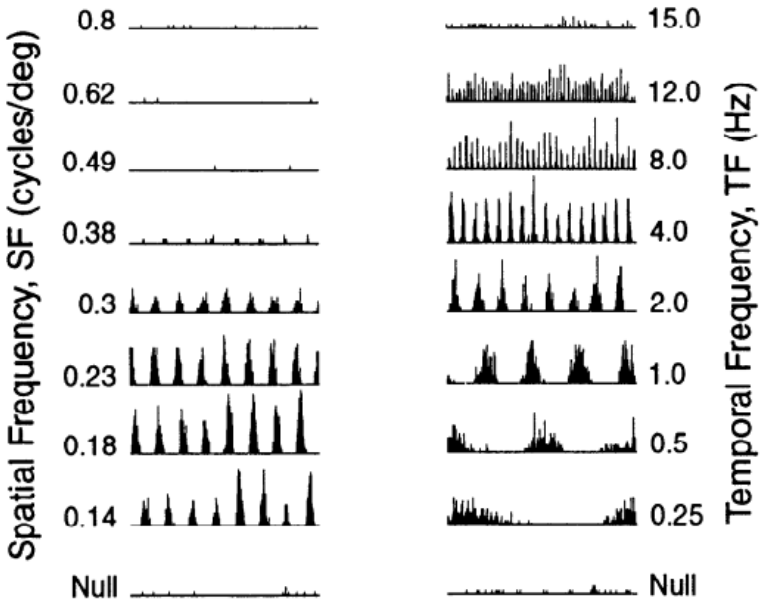

Figure 1.5.5. Influence of spatial and temporal frequencies on neuronal responses to sinusoidal drifting gratings. Left panel: Responses of one neuron to a DG at different spatial frequencies. Right panel: Responses of one neuron to a DG at different temporal frequencies (reprinted from DeAngelis *et al.*, 1993).

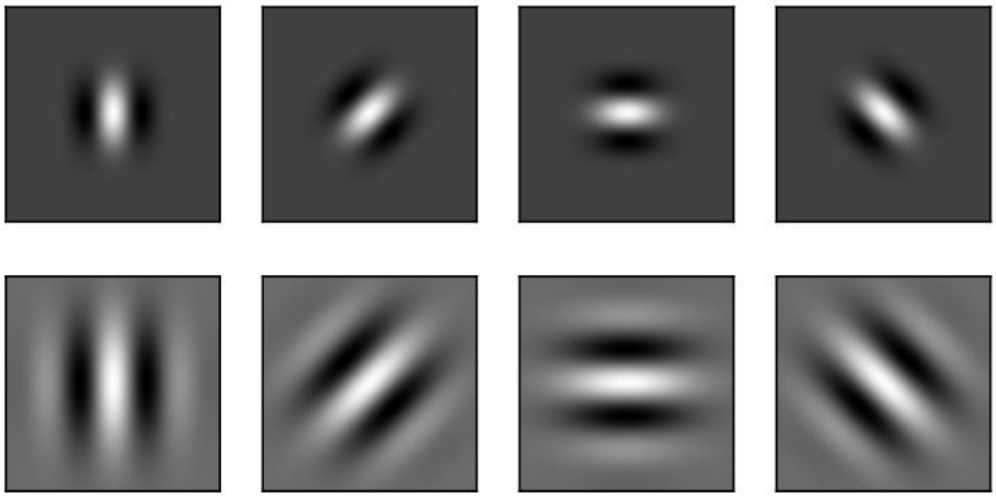

Figure 1.5.6. Examples of different Gabor functions at different spatial frequencies (reprinted from Vacher, 2017).

5.4.2 Temporal Frequency Selectivity

V1 cortical cells are selective for the temporal frequency (TF) of a stimulus. The tuning curve for spatial frequency ranges from 0.25 to 12 Hz (DeAngelis et al., 1993b). However, the optimal TF ranges between 2 and 4 Hz (Movshon *et al.*, 1978; Chavane *et al.*, 2011; See Figure 1.5.5, right panel, for a response to different temporal frequencies)

De Angelis and colleagues (1993b) have studied the linear aspect of TF. By performing a Fourier transform of the space-time graph, they were able to define a linear transfer function in the frequency domain. This function allows the prediction of the TF tuning curve. They compared the predicted results to the experimental ones and the correlation between the two of them was generally high. Indeed, some cells showed a difference between the predicted and the measured response. Their results show that a linear function can predict most of the simple cell responses.

Many studies have shown that both simple and complex cells are selective to speed. Cells that have a small receptive field tend to prefer slower speeds, whereas cells that have a large receptive field prefer high speeds (Baker, 1988; see Figure 1.5.7).

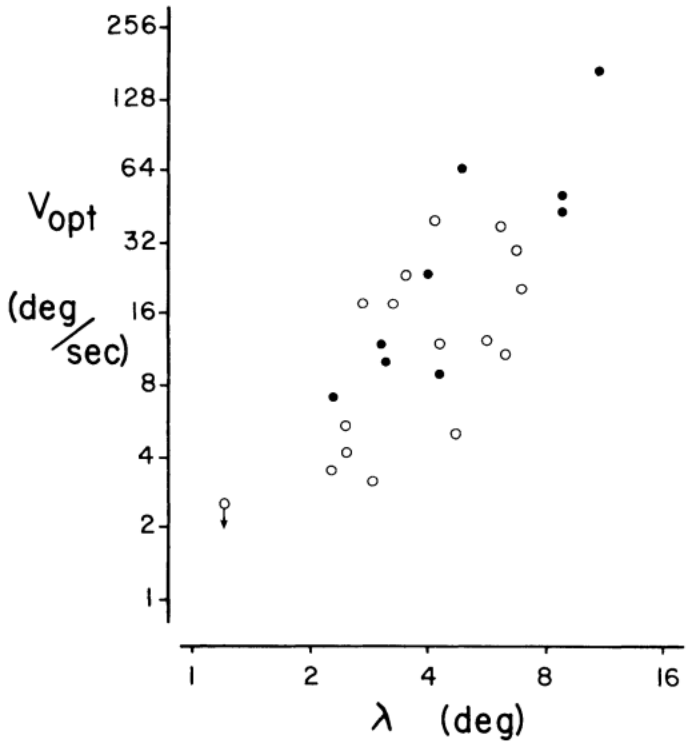

Figure 1.5.7. Relationship between receptive field size and speed preference. White dots: simple cells; Black dots: complex cells (Reprinted from Baker, 1988).

There is a direct link between spatial frequency and speed. Indeed, the speed of a sinusoidal drifting grating is defined by the ratio between temporal frequency and spatial frequency. Therefore, if cells are selective to SF and TF instead of speed, their sensitivity functions should be independent. Many studies proved this assumption to be true (Foster et al., 1985; Hamilton et al., 1989; Tolhurst and Movshon, 1975). However, Baker (1990) found that cells sensitive to low spatial frequencies tend to be sensitive to low temporal frequencies. This study also showed that, as expected, cells responding preferentially to high SF prefer high speeds, whereas cells sensitive to low SF prefer low speeds.

Baker also shows that we can predict the optimal speed of a moving bar by computing the ratio between the preferred TF and the preferred SF

5.4.3 Orientation Selectivity

There are many ways to determine a neuron's orientation selectivity. Hubel and Wiesel presented static bars at different orientations on the receptive field. Another classical way to measure orientation selectivity is to use moving bars. A moving bar displays a speed and a direction, in addition to an orientation. This will have an influence on the response, since, as mentioned before, receptive fields are sensitive to these parameters. Indeed, the way that ON and OFF subregions are organized determines cell's selectivity.

Sinusoidal drifting gratings or Gabor functions can also be used to determine the preferred orientation of a cell (DeAngelis *et al.*, 1993; see the results section of this manuscript). Both simple and complex cells are orientation selective. Among cortical populations, some cells respond only to a narrow range of orientations and are therefore considered sharply tuned. Conversely, other cells respond to a wide range of orientations, these cells are considered broadly tuned. Figure 1.5.8-A shows an example of sharply and broadly tuned cells. This difference in selectivity is quantified by a measure called: Orientation Selectivity Index (OSI). A sharply tuned cell exhibits an OSI close to 1 and a broadly tuned cell has an OSI close to 0 (Figure 1.5.8-B illustrates three different OSI). Primary visual cortex neurons exhibit a variety of OSIs as illustrated in Figure 1.5.8-C).

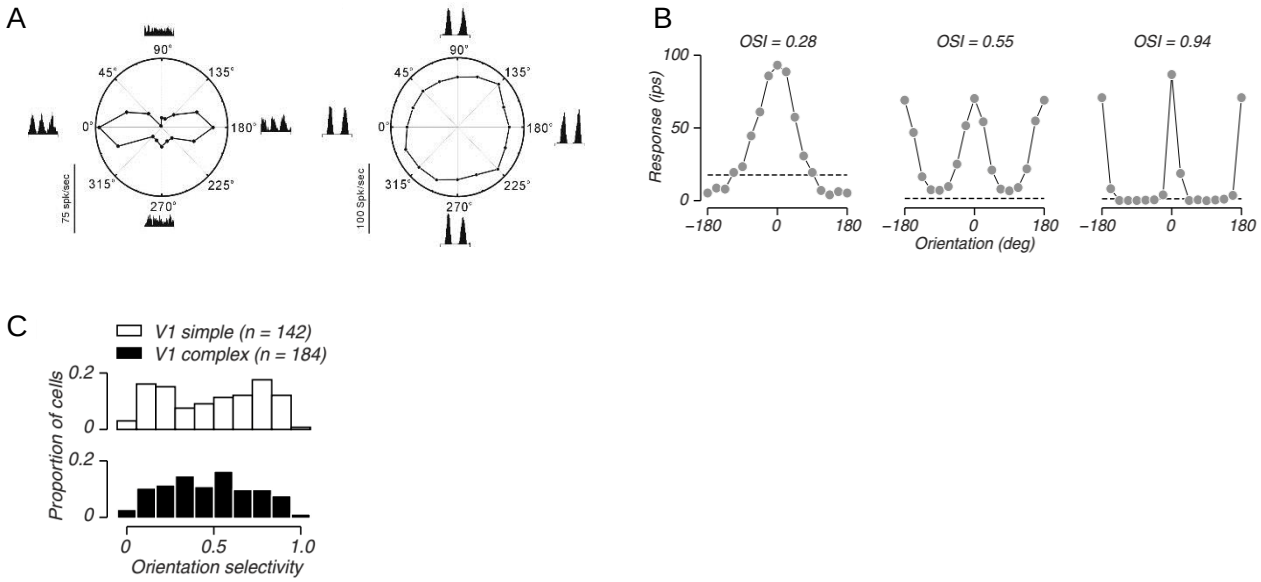

Figure 1.5.8. A. Polar plot of two V1 cells. Left panel represents a sharply tuned cell. Right panel represents a broadly tuned cell (reprinted from Scholarpedia-Receptive Field web page). B. Example of three cells having different OSIs in V1. C. Distribution of OSI for simple and complex cells in V1 (reprinted from Goris *et al.*,2015).

As discussed before, simple and complex cells can be quantified by looking at the response to sinusoidal drifting gratings. Indeed, when presented at the preferred orientation these two types of cells are going to respond in a very different manner to the stimulus. Simple cells are going to be modulated by the sinusoidal changes in luminance (described in Figure 1.5.9). Their response to DG is a rectified sinusoidal response (which is a linear replica of the stimulus). On the other hand, at the preferred orientation, complex cells only increase their mean firing rate (Figure 1.5.9 illustrates simple and complex cell responses to a DG at the optimal orientation).

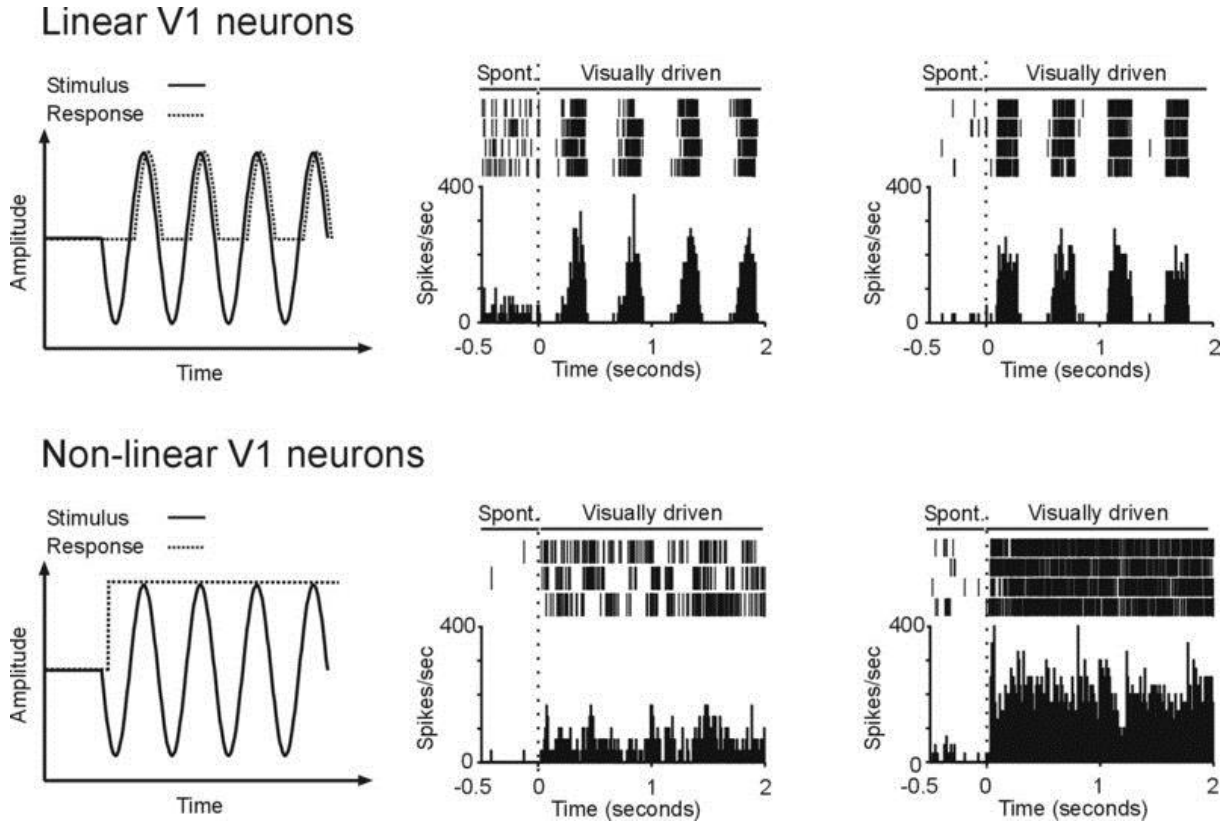

Figure 1.5.9. Example of simple and complex cell responses to a sinusoidal drifting grating (reprinted from Scholarpedia-Receptive Field web page).

Since the receptive field structure varies according to the layer, we can expect a difference in the laminar processing of stimulus orientation in V1. Martinez and colleagues (2002) investigated it with intracellular recordings. They found that for all layers, except layer 5, the excitatory and inhibitory inputs share the same orientation preference. In layer 5, the inhibitory and excitatory peaks are displaced.

Simple cells receiving direct thalamic inputs are modeled with a Gabor function (Jones & Palmer, 1987). However, simple cells also receive cortical inputs, and some studies claim these inputs play a role in orientation selectivity (Sillito, 1975; Somers et al., 1995). Because of this combination of different inputs, Gardner and colleagues (1999) investigated the linear and nonlinear contributions to orientation tuning in simple cells. They first defined the RF profile with dense noise. With a linear function, they predicted an orientation-tuning curve, representing the linear contribution of the RF. The nonlinear contribution is estimated as the difference between the predicted tuning curve and the experimental one, obtained by recording simple cell responses to DG. They found that measured tuning curves are more sharply tuned than the predicted ones. This indicates that linear mechanisms

are insufficient to account for the response to DG. They explained the non-linear mechanisms by adding an exponential to the linear function. This nonlinear mechanism is very homogenous. Indeed, the exponent varies between 0.15 and 15. They also showed that the nonlinearity makes the orientation tuning less dependent on the shape and size of the RF. Therefore, linearities do not explain orientation selectivity and non-linearities are needed to fully capture simple cell responses.

The complex cell responses can be predicted with a nonlinear function (Gaska et al., 1994; Goris et al., 2015; Szulborski and Palmer, 1990). Gaska and colleagues (1994) showed that experimental tuning curves for orientation, direction and SF could be predicted by computing the Fourier transform of second order spatio-temporal responses obtained with a dense noise stimulation.

5.4.4 Direction Selectivity

In order to study direction selectivity, two types of stimuli are classically used, namely moving bars passing through the receptive field in all directions and sinusoidal gratings drifting in all directions. In 1984, Orban stated that a neuron shows direction selectivity if the response to the optimal direction is 3 times higher than the response to its opposite direction. In a series of papers, Orban and colleagues (Orban et al., 1981a, 1981b) showed that the speed of the moving bar (or the DG) influences direction selectivity. According to their results, 30% of cells in area 17 are direction selective and are modulated by speed whereas 70% of cells in area 18 are modulated by speed. As described before (section 3.1), area 18 receives more thalamic inputs from Y-cells than area 17. As Y-cells display sensitivity to movement, this could explain the difference observed between these two areas.

Direction selectivity is partly dictated by the type of stimulus. Indeed, Casanova and colleagues (1992) showed that simple cells show a higher direction selectivity index (DSI) when a moving bar is used. A cell that shows a direction selectivity with gratings shares the same selectivity with a moving bar, but the opposite is not true. For complex cells, the stimulus has no influence on the DSI. In order to explore direction selectivity, the choice of the stimulus matters and has to be considered.

Direction and orientation selectivity are generally not observed in cat LGN (but see Kelly et al., 2014; Vidyasagar and Urbas, 1982), which means that these functional properties emerge from specific arrangements of thalamic afferents or are generated by intra-cortical inputs (Thompson et al., 1994). Many models of direction selectivity have been proposed and linearity of the response has been assumed (De Valois et al., 2000; Peterson and Freeman, 2004). However, when predicted with a linear function, direction selectivity is generally weaker than the one obtained experimentally with DG (DeAngelis et al., 1993; Peterson and freeman 2004). This shows that nonlinear mechanisms are involved in direction selectivity. Moreover, a study by Kim and Freeman (2016) showed that this non-linearity is layer dependent. In layer 4, predicted linear responses generally matched the experimental one. Yet, in supragranular and infragranular layers, the predicted DSI was lower than the measured one.

As discussed above the linear predicted response of simple cells direction selectivity does not fit perfectly with all the measured responses. Many studies noted that a proportion of simple cell direction selectivity is explained by a linear function (Hamilton et al., 1989; Kim and Freeman, 2016; Peterson et al., 2004). In order to explain accurately the DSI obtained, a nonlinearity needs to be added to the prediction function. By adding, an exponent to the linear function that takes into account

the temporal phase differences, Peterson and colleagues (2004) were able to predict a DSI that matched the measured direction selectivity.

The study of complex cell direction selectivity has been performed after mapping receptive fields with dense noise. This allows the experimenter to extract the first and second order interactions. The second order interactions participate in the direction selectivity of V1 complex cells (Emerson et al., 1987) and the predicted DSI based on these interactions matches the experimental DSI.
In this section, we described the principal functional properties of cat primary visual cortex. We also explained how it is possible to predict them with linear functions directly derived from the simple RF structure. All the results described above have been obtained by analyzing extracellular single units or intracellular recordings.

However, mesoscopic signals also present functional properties, similar or not, to the ones observed for microscopic signals (Berens et al., 2008; Lashgari et al., 2012). While the multi-unit activity shows functional properties similar to single units, this is not always the case for the local field potential.

Berens and colleagues (2008) show that, in the gamma range (see annex 1 for the description of frequency decomposition of the mesoscopic signal), the MUA and the LFP show very weak correlations in their preferred orientation. Moreover, the OSI obtained with LFP is always lower than the one obtained with SUA or MUA. However, they observed a strong correlation between MUA and LFP when they compared the ocular preferences. Lashgari *et al.* (2012) showed that LFP signals are tuned to orientation, direction, size, spatial phase and temporal frequencies. They divided the LFP into low and high frequency bands and observed that high frequency bands match the SUA stimulus preferences while this is not the case for low frequencies. They claim that this is linked to the fact that gamma frequencies come from locally synchronized neurons while low frequencies come from another population of cells.

5.5. Cortical maps in cat primary visual cortex

In the previous section, we described the feature selectivity that emerges from the functional properties of V1 neurons. However, as described in section 3, primary visual cortex has complex microcircuitry from which different properties might emerge. In the next section, we will focus on the mesoscopic functional organization of V1 that arises from the individual neuronal properties and the organization of the cortical microcircuit.

5.5.1 Retinotopy

One very important dimension to map in the visual cortex is the retinal position of the stimulus. In cats, a large portion of V1 is devoted to mapping central retina, with a nearly equal split between upper and lower visual fields (Figure 1.5.10-A). These retinotopic arrangements are possible because regions represented nearby in the retina are represented nearby in LGN and in V1. The cortical retinotopy is strongly determined by the density of thalamic afferents sampling different parts of the visual cortex (Azzopardi & Cowey, 1996). These thalamic afferents replicate the density of retinal afferents sampling the whole visual field (Adams and Horton, 2003; Azzopardi and Cowey, 1996). Figure 1.5.10-B illustrates the fact the foveal region is represented in a larger cortical area than the periphery.

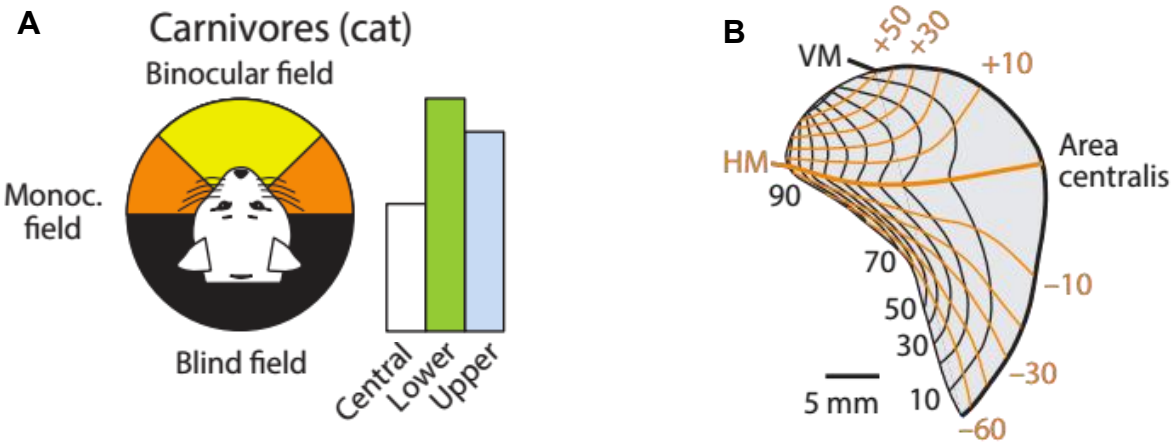

Figure 1.5.10. A. Visual field in cats where the binocular (yellow), monocular (orange), and blind (black) fields are represented. The bar graphs on the right show the percentage of V1 devoted to central vision (white, central 10◦) and the lower (green) and upper (blue) visual fields. **B.** Retinotopic map of V1 in cat primary visual cortex. VM: vertical meridian. HM: horizontal meridian (adapted from Kremkow and Alonso, 2018).

5.5.2 Ocular Dominance

Another crucial dimension to map in the visual cortex is eye inputs. Ocular dominance was first observed by Hubel and Wiesel along with orientation selectivity (1959). They showed that the majority of cells in cat primary visual cortex are binocular but respond strongly when one eye is masked. They also found that some cells in Layer 4 only respond to one eye. Cats (and primates) have most of their cortex devoted to binocular vision, yet the ratio of contralateral and ipsilateral axonal projections shows a bias toward the contralateral eye (Anderson *et al.*, 1998; Adams *et al.*, 2007). Later on, Hubel and Wiesel (1969) demonstrated by recording neuronal activity with perpendicular penetrations to the cortical surface, that ocular dominance is organized in columns. This was confirmed with anatomical and optical imaging studies (Anderson et al., 1988; Crair et al., 1998).

5.5.3 Light-Dark polarity

Another important map in cat visual cortex that has been identified only very recently, is the alternation of light-dark polarity domains. Indeed, cats discriminate patterns of dark and light in addition to the stimulus. An accurate map of light-dark polarity requires the splitting of the retinotopic map in four different copies: one for each eye and one for each polarity (Figure 1.5.11; Kremkow and Alonso, 2018). In cat primary visual cortex, eye input changes approximately every 0.5 mm along the eye axis and polarity also changes every 0.5 mm along the polarity axis (Figure 1.5.11). This means that within 1 mm² of primary visual cortex almost all combinations of polarity and eye input are represented for each position of visual space. Moreover, retinotopy changes within the cortex at a rate of 0.5 RF per millimeter (Kremkow *et al.*, 2016), implying that among this 1 mm² of cortical space, all neurons can represent the same region of visual space.
In addition to the bias toward the contralateral eye, there is a bias toward OFF geniculate inputs. OFF cortical responses are stronger, have a better spatiotemporal resolution, and show less scatter

in cortical retinotopy than ON cortical responses (Jin et al., 2008; Kremkow et al., 2014; Wang et al., 2015).
These ON-OFF asymmetries in spatial resolution could originate from the retina. Indeed, for both V1 and retina, the luminance-response saturation within the ON pathway causes a neuronal blur (Chichilnisky and Kalmar, 2002; Kremkow et al., 2014). Therefore, just like for retinotopy the ON-OFF polarity map amplifies visual phenomena already present in the retina.

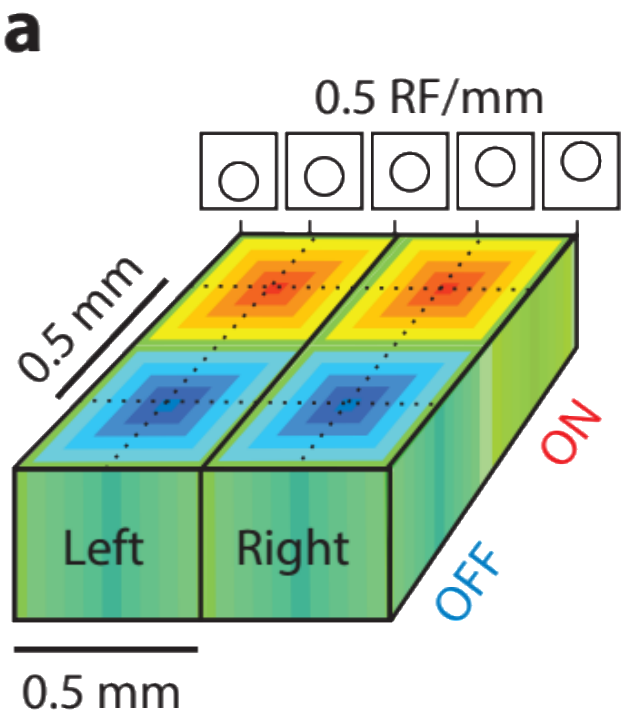

Figure 1.5.11. Eye–polarity grid and the multidimensional map of stimulus space. Cortical organization for retinotopy, eye input, and ON–OFF contrast polarity. Retinotopy illustrated as circular RFs changing position on the vertical axis at a slow rate of 0.5 RF/mm. The orthogonal arrangement of geniculate afferents sorted by eye input and ON–OFF polarity forms ocular dominance columns and ON–OFF cortical domains (reprinted from Kremkow and Alonso, 2018).

5.5.4 Orientation Map

Hubel and Wiesel (1977) observed that neurons in V1 are orientation selective, they also reported that this property was mapped at the cortical surface as a continuous gradient of orientation preference in space. These findings were confirmed later with optical imaging experiments (Bonhoeffer and Grinvald, 1991, 1993). Intrinsic imaging and voltage sensitive dye imaging (VSDi) allow the recording of neuronal activity in a whole cortical area. With these techniques, it was shown that neurons with similar orientations are clustered together and form orientation columns that are organized in a crystal-like orientation map (see Figure 1.5.12, where each color corresponds to a region tuned to a particular orientation; Bonhoeffer and Grinvald 1991, 1993).

The orientation maps are composed of “linear zones”, which represent the continuity in orientation of orientation columns. These linear zones are segregated by discontinuity regions. Discontinuities smaller than 90° are “one dimensional fractures”, whereas discontinuities greater than 90° are called pinwheels (Bonhoeffer and Grinvald 1991, 1993). Orientation domains rotate from 0° to 180° around the pinwheel. This large range of orientation selectivity arises from the fact that neurons at the center

of the pinwheel are clustered into different orientation preferences (Ohki et al., 2005). However, it is important to keep in mind that the computation of the orientation is invariant across the cortical surface. Indeed, Nauhaus et al., (2008) confirmed the proposal of Mariño et al., (2005) that in both cats and monkeys the neurons are more sharply tuned for orientation outside pinwheels than inside them. This result, *i.e.* the location of neurons (and its associated properties) within functional maps, explains the fact that we observe heterogeneity in the receptive field properties.

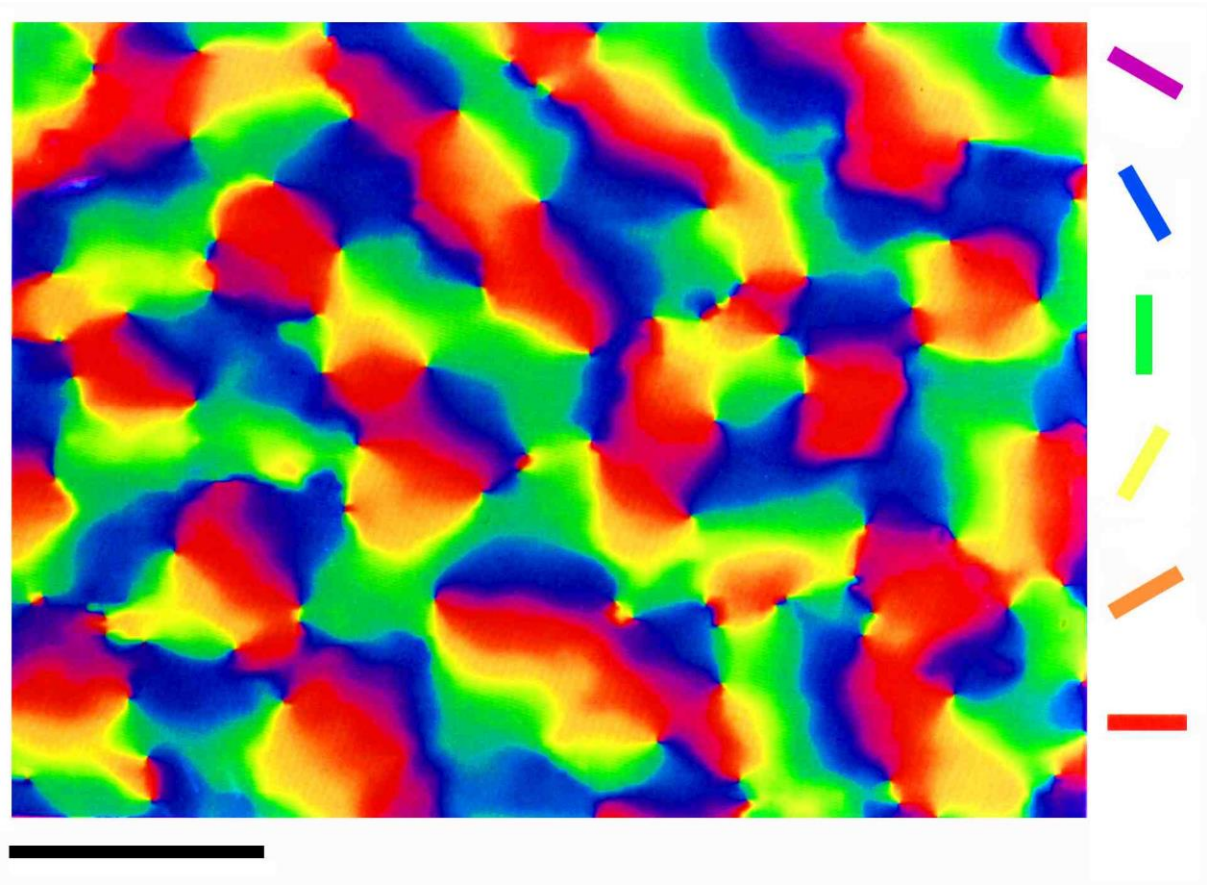

Figure 1.5.12. Layout of orientation preference observed in area V1 of macaque monkey. Scale bar = 1 mm. Modified from Blasdel & Salama (1986).

5.5.5 Direction Map

Despite the fact that direction selectivity is a well-described property of V1 cells, its clustering has been debated. Some studies found that direction-selective cells are not clustered in V1 (Bonhoeffer *et al.*, 1995; DeAngelis *et al.*, 1999) whereas other studies reported that a weak clustering exists (Swindale *et al.*, 1987; Shmuel and Grinvald, 1996).
Many optical imaging studies (Shmuel and Grinvald, 1996; Kisvárday *et al.*, 2001; Swindale *et al.*, 2003) showed that direction maps do exist in cat primary visual cortex. In V1, regions that are selective to two opposite directions are separated by sharp direction fractures. In area 18, Okhi *et al.* (2005) observed that boundaries between two regions are one or two cells wide and the cells in these dividing regions are not direction selective. A recent two-photon study observed the presence of direction maps in cat area 17 and gave new insights into their origin (Mariño et al., (2005)). Direction maps are composed of highly ordered direction columns, which are formed by clusters of direction-selective neurons. However, they observed that direction maps are not homogeneously distributed across V1. They tend to be located in cortical domains more sensitive to low spatial frequencies.

5.5.6 Spatial Frequency Map

Another dimension that organizes itself in maps is spatial frequency. Indeed, several reports found that SF selectivity may be clustered in cat primary visual cortex (Shoham et al., 1997). Spatial frequency domains are organized continuously along the cortical surface. Some studies (Everson et al., 1998) suggest that spatial frequency regions are organized around pinwheels while others claim that is not the case (Issa et al., 2000).
However, recent findings confirmed the presence of spatial frequency maps in cat primary visual cortex (Ribot et al., 2013; Sirovich and Uglesich, 2004). These authors reported that spatial frequency is topographically organized in primary visual cortex. In addition, they developed a model showing that this organization arises from the properties of X and Y thalamic cells, which are sensitive to high and low spatial frequencies, respectively. In addition to these results, modeling work suggests that orientation, direction and spatial frequency maps are a direct consequence of the eye-polarity grid formed by the geniculate inputs. Cortical regions can be dominated either by ON or OFF regions. In regions dominated by OFF inputs, ON subregions rotate around the OFF subregions, and in regions dominated by ON inputs, OFF subregions rotate around the ON subregions (Kremkow *et al.*, 2016). This rotation has an influence on the emergence of the orientation and direction maps (Figure 1.5.13-B). In addition, the balance between weak and balanced ON-OFF response antagonism shapes both orientation and spatial frequency selectivity (Figure 1.5.13-A; Kremkow & Alonso, 2018).

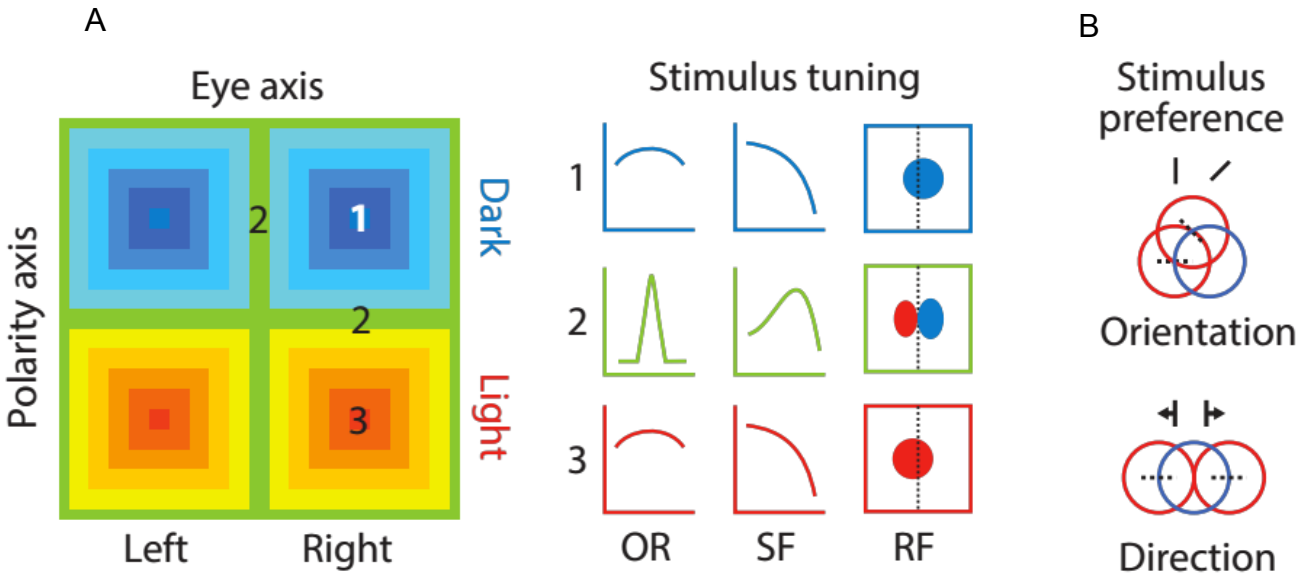

Figure 1.5.13. A. Cortical responses within the eye–polarity grid can be OFF dominated (blue), ON dominated (red), or ON–OFF balanced (green). Changes in ON–OFF balance should be associated with changes in OR, SF, and spatial resolution (spatial frequency cutoff). The OR, SF, and spatial resolution should be lowest at the center of ON and OFF domains and increase in surrounding regions. (B) Changes in ON and OFF retinotopy (red and blue circles) are associated with changes in orientation (lines above circles) and direction preference (lines with arrows above circles) within the cortex.

6. STIMULUS DEPENDENCE OF THE FUNCTIONAL RESPONSE

The diversity of contextual effects present in V1 does not allow the reduction of the receptive field to an ensemble of invariant filters. Multiple experimental approaches proved that strong gain control phenomena complexify or renormalize V1 receptive fields (Carandini et al., 1999; Schwartz and Simoncelli, 2001). These gain control phenomena can happen at the scale of the network or at the scale of the single cell. At the network scale for each stimulus class, the complete network is modified and the coupling between cells is changed. At the single cell scale, each cell is associated to a multipotent receptive field that is going to be recruited in a different way for each stimulus class (Fournier *et al.*, 2011, 2014: see section 5.1.1).

In the previous section, we described V1 functional responses to simple features of artificial stimuli. These responses have been intensively investigated and linear-nonlinear (LN) models of V1 neurons emerged (Carandini et al., 2005). Despite their good performance in predicting responses to simple artificial stimuli, these models performed poorly in predicting the response to more complex stimuli (Carandini *et al.*, 2005, Baudot *et al.*, 2013), as stated above.

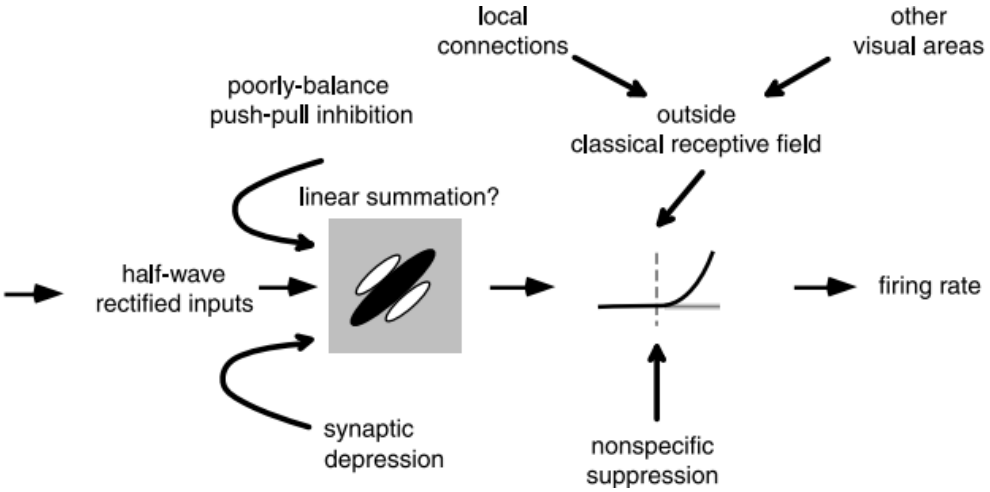

Figure 1.6.1 Toward a complete model of V1 simple cells that includes nonlinear phenomena modulating its response (reprinted from Carandini *et al.*, 2005)

Indeed, as soon as the stimulus becomes more complex, additional neuronal mechanisms will shape the response of both simple and complex cells. Figure 1.6.1 gives an example of all additional nonlinear phenomena that can modulate the response of a simple cell. Because of this increase in nonlinearity, the prediction of the response becomes more complicated. According to Rust & Movshon (2005), simple cells are predicted with a linear spatiotemporal filter and complex cells are predicted with two linear functions that have a quadrature phase relationship in both space and time. For both simple and complex cell models, a nonlinearity transforms the membrane potential into spikes. Yet, to predict all the nonlinear phenomena present in more complex stimuli it is necessary to add many spatiotemporal filters, combine them with a nonlinearity and finally add all the additional mechanisms that modulate the response (see Figure 1.6.2).
Because of the mechanisms modulating the neuronal activity, both computational neuroscientists and experimenters build new models in order to predict the responses to these complex artificial and natural stimuli.

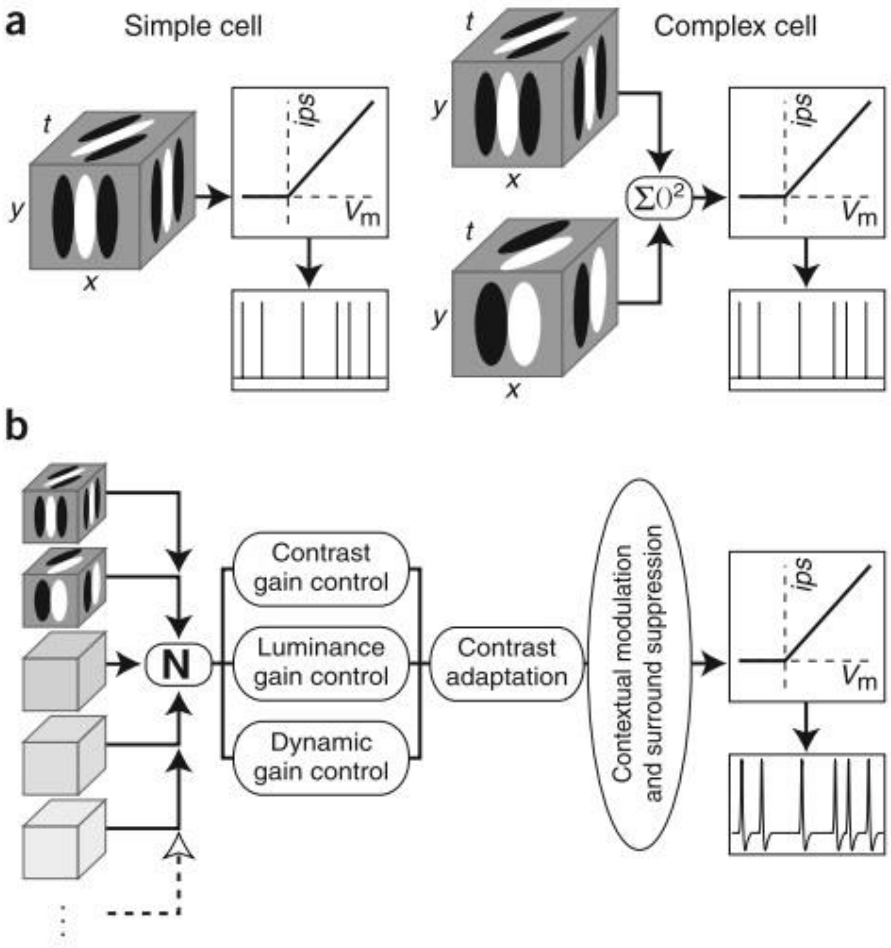

Figure 1.6.2. Examples of V1 models. **A.** Simple and complex cell standard models. **B.** New models taking into account nonlinearity induced by complex stimuli (reprinted from Rust & Movshon, 2005; see also Frégnac and Bathellier, 2015; Figure 2).

6.1. Artificial Stimuli and functional responses

6.1.1 Surround Modulation

One of the most studied nonlinear interactions occurring in primary visual cortex is the modulation of the response by the “silent surround”. Surround Modulation (SM) can either facilitate or suppress the response of V1 neurons. In this section, we will describe results obtained in both cats and macaques. The effects of stimulating both center and surround with artificial stimuli can be summarized in five main properties (Angelucci et al., 2017).

1. Surround modulation is spatially extensive. In primates, surround can be divided into the near surround and the far surround. Different cortical circuits generate the properties of these two surrounds. Contributions from near surround are thought to originate from thalamic inputs, horizontal connections and feedback projections from higher cortical areas, whereas far surround only reflects feedback projections (Angelucci *et al.*, 2002, 2017). This difference in circuitry gives rise to different functional properties. Near surround modulation is more strongly suppressive and more sharply tuned than far surround modulation (Shushruth et al., 2009, 2013).

2. In both primates and cats, surround modulation is tuned to specific parameters. Suppression or facilitation of the neuronal response is induced when both center and surround are stimulated. A strong suppression occurs when the stimulus in the center and surround have the same orientation, spatial frequency, direction and speed. A weak suppression or a facilitation occurs when stimuli of orthogonal parameters are presented (DeAngelis *et al.*, 1994; Li & Li, 1994; Durand *et al.*, 2007; Angelucci *et al.*, 2017). The surround also modulates Local Field Potential. Indeed, both surround suppression and facilitation have been reported in cat primary visual cortex (Zhang and Li, 2013).

3. A lone stimulation of the surround is considered to not elicit any spiking response, although synaptic responses can be elicited 4 to 8° outside the classical RF (Bringuier *et al.*, 1999; Gerard-Mercier *et al.*, 2016). Surprisingly, our results (chapter III) show that surround-only stimulation, using natural scenes, can modulate the spiking activity. On the other hand, it is documented that LFP is modulated by a surround-only stimulation (Angelucci *et al.*, 2017).

4. Surround modulation is contrast-dependent. When the center stimulus is of high contrast and at the same orientation as the surround, the stimulation of the latter is suppressive but can be facilitatory when the center stimulus is of low contrast (DeAngelis et al., 1994a; Levitt and Lund, 1997).

5. Surround modulation is layer dependent. In layer 4C of primates (receiving direct thalamic inputs), surround modulation is weaker and untuned for orientation, in contrary to supragranular and infragranular layers where surround modulation is strong and sharply tuned (Sceniak et al., 2001; Ichida *et al.*, 2007; but see the results section of this manuscript for data obtained in cat primary visual cortex).

Because surround modulation is a fundamental property in primary visual cortex, many computational models tried to understand the mechanisms underlying it. Numerous models (Series *et al.*, 2003; Haider *et al.*, 2010; Schushruth *et al.*, 2012) took into account V1 anatomical organization. Indeed, a local recurrent network composed of excitatory and inhibitory neurons constitutes each orientation column. Far and near surround stimulation activates feedback and horizontal connections that directly modulate the activity of inhibitory neurons and indirectly modulate the activity of the excitatory ones (Figure 1.6.3. describes the model of orientation-tuned surround suppression).

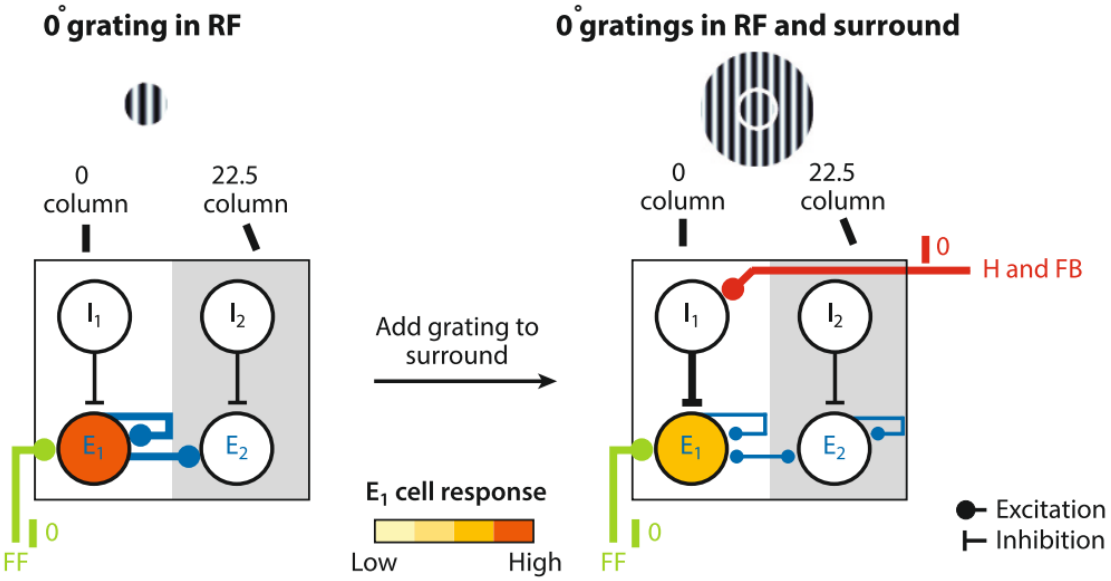

Figure 1.6.3. Model of orientation-tuned surround suppression. Left Panel: Mechanisms underlying the response to a grating in the RF. Right Panel: Mechanisms underlying the response to a grating both in the center of the RF and its surround. FF: feedforward projections; H: horizontal connections; FB: feedback projections. Line thickness indicates input strength (modfied from Angelucci *et al.*, 2017)

Even if this model predicts many biological responses (Fino and Yuste, 2011; Hofer et al., 2011; Ozeki et al., 2009), it does not predict all of them. For example, surround modulation induced by natural images or layer dependency of the center-surround interactions are not well-predicted because they are not well characterized (Angelucci *et al.*, 2017). The layer dependency of the surround modulation evoked by natural scenes will be addressed in the results section of this thesis.

6.1.2 Linear nonlinear models

As described above, we cannot consider V1 receptive fields as a sum of invariant filters. Many other mechanisms modulate the receptive field. Some of these mechanisms have been mathematically described as gain controls. However, adding gain controls does not explain the underlying structure of the observed physiological responses. Therefore, in the recent years computational scientists have elaborated complex models capable of predicting and explaining the biological response to complex artificial stimuli.

These advanced models have been developed in order to capture complex V1 responses (Touryan et al., 2002; Rust *et al.*, 2005). Touryan and colleagues used a method called spike-triggered covariance (STC), which computes the eigenvalues and eigenvectors of the second-order moments of the spike-eliciting stimulus events. They were then able analyze the responses of cortical complex cells to random-bar stimuli aligned to the preferred orientation of the cell.
They extracted two types of features: *relevant* and *null*. In particular, they found a small number of relevant features and a large number of null features. They claim that the basic operations in visual cortical processing originates from the observed additive and divisive interactions between these two features. Yet, their method only focused on the analysis of the responses to bar-stimuli and did not investigate the responses to more complex stimuli.

A recent example of how these advanced models are used to predict complex responses to complex stimuli can be found in the work of Goris and colleagues (2015). They investigated how cells in V1 (and V2) respond to classic DG and gratings with different orientation mixtures (Figure 1.6.4 gives an example of their stimuli). It appears that neurons with different degrees of selectivity are adapted to encode information from particular types of image contents. Indeed, they found that neurons with high orientation selectivity index responded better to stimuli containing one orientation while less selective neurons responded better to stimuli containing a mixture of orientations. They hypothesized that this diversity in the neuronal population is essential for the processing of complex visual stimuli. In order to test their hypothesis, they developed a linear-nonlinear-linear-nonlinear (LN-LN) cascade model.

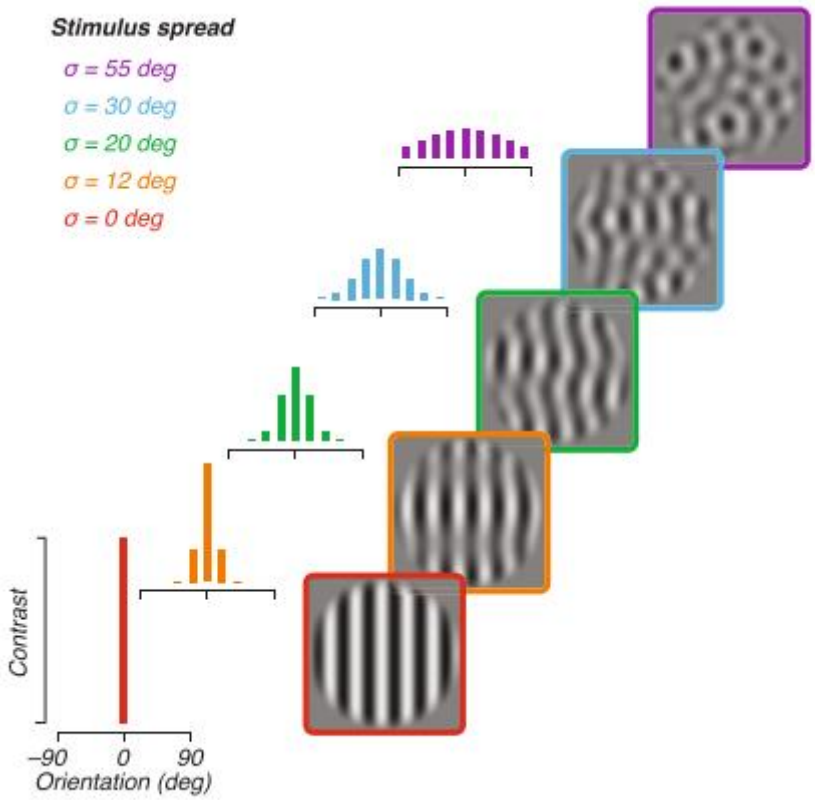

Figure 1.6.4. Each stimulus consisted of a windowed sum of drifting sinusoidal gratings, with drift directions drawn from one of five unimodal distributions (colored histograms), centered around a randomly selected primary direction. All gratings had the same spatial frequency, optimized for the cell (Reprinted from Goris *et al.*, 2015)

The initial linear stage creates orientation tuning, which is then modulated by nonlinearities that capture the effects of untuned suppression and spike threshold. As described in Figure 1.6.2 many filters and nonlinearities are added in order to explain a complex cortical behavior. Their model predicted accurately the diversity of orientation selectivities in V1 and V2. Then, they investigated if their model, containing a heterogeneous range of orientation selectivity, provides a better discrimination of natural images (*i.e.* complex stimuli) than models containing homogeneous populations of any particular selectivity. Their results argue that orientation diversity is beneficial for visual coding because their model allowed a better discrimination of patches of natural images. Their

study favors a model whereby, as claimed by Rust and Movshon (2005), the understanding of natural scene processing by V1 has to be studied through the use of artificial stimuli. However, the discriminability index of the model was not always the same according to the tested natural image. Indeed, natural images are composed of a mixture of orientations (*i.e.* what has been tested by Goris and colleagues) but also other features that are encoded by V1 neurons, such as spatial and temporal frequencies, phase or size. All these attributes interact together and shape how V1 responds. Their patches of natural images contained different statistics that interacted differently, thus modifying the discrimination performance of the model. A detailed analysis of the statistical content of the natural images, in particular of the orientations, would have been necessary in order to draw clearer conclusions about how their model (and V1) performs.

Other models take advantage of different design features of primary visual cortex, such as the functional properties emerging from the anatomy. One of them is the Hierarchical Structural Model (HSM), inspired by Hubel & Wiesel's hierarchical model. This model, developed by Antolik and colleagues (2016) in Mrsic-Flogel and Frégnac's labs, takes advantage of the functional hierarchy imposed by feedforward connections. It considers constraints from the anatomy of visual cortex, specifically the fact that only a limited number of thalamic inputs project to simple cells. The simple cells are considered as a first layer composed of the center-surround thalamo-cortical inputs. The second layer is composed of neurons that sum the linear inputs from simple cells to form both simple and complex-like RFs (Figure 1.6.5). This population model was developed in order to work with a population of simultaneously recorded neurons. It takes advantage of the receptive field redundancies among nearby V1 neurons, by simultaneously fitting the entire local population of recorded cells. The model was initially tested on mouse primary visual cortex using two-photon imaging (Antolik *et al.*, 2016). The authors obtained better predictions of the measured response to natural scenes than other models. This increase in performance also originates from the hierarchical features of the model that accounts for a great diversity of receptive field structures (within and between simple and complex cells), as observed in V1.
This model has also been used to predict extracellular neuronal responses in cat primary visual cortex (Larroche *et al.*, poster at FENS, 2018). Results obtained in cat primary visual cortex show that, depending on the set of images used to train the network, this model performs better than classical LN models to predict the measured response both for complex artificial and natural stimuli. Generalization is better achieved on new stimuli after training with animated natural scenes (respecting spatial and temporal coherence across successive frames).
Despite following the anatomical layout of primary visual cortex, the hierarchical model discussed above only considered feedforward connections. As presented in section 3, the neuronal activity is modulated by other cortical inputs such as horizontal and feedback connections. In the future, models need to include V1 anatomical features in order to improve their prediction performance. Another way to improve critically the HSM is by considering the invariant properties of the receptive field and its stimulus dependence (work in progress by Larroche and colleagues).

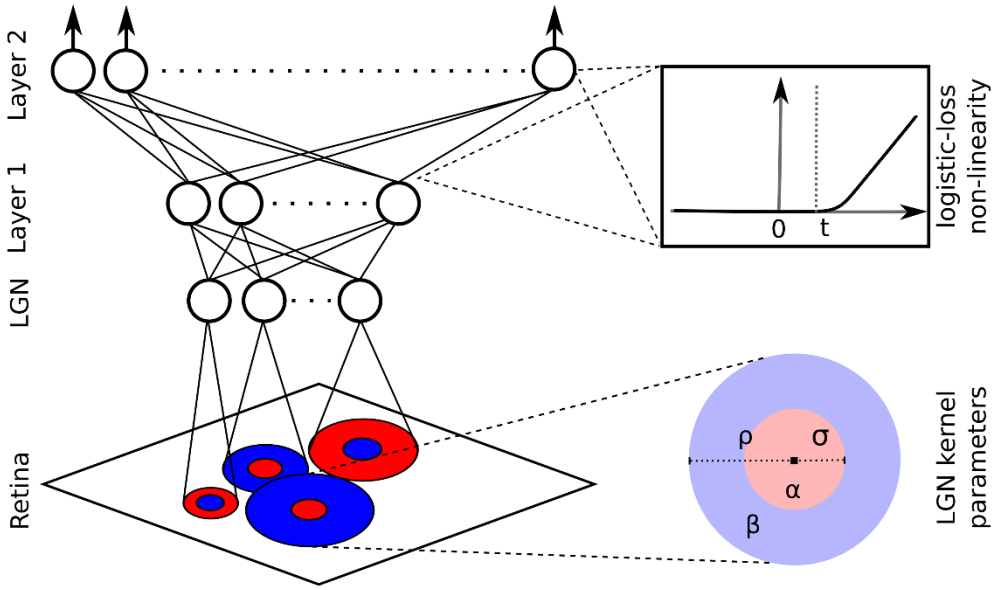

Figure 1.6.5. Architecture of the HSM. The model consists of a limited number of difference-of-Gaussian kernels. The LGN layer is followed by two cortical layers. Layer 1 is composed of linear filters and layer 2 contains nonlinearities. The two layers are inter-connected by all-to-all connections and the first layer has all-to-all connections from the LGN units (reprinted from Antolik *et al.*, (2016).

6.1.3 Stimulus dependence of Simple and Complex cells.

A neuron in primary visual cortex can adapt its response to different types of stimuli. However, few studies investigated if the functional properties of a receptive field can be modulated by the spatiotemporal statistics of the presented stimulus. Fournier and colleagues (2011) performed an intracellular study in cat primary visual cortex where they showed that receptive fields change according to the statistical properties of the visual input. While recording the same cell, they presented three types of stimuli: Sparse noise, ternary dense noise and Gabor noise. In order to show that the RF is modified by the stimulus statistics, they computed the relative power of the simple-like (linear) and the complex-like (non-linear) excitatory and inhibitory subcomponents of the RF. They also computed a modified simpleness index (SI*), which measures the balance between the compound synaptic contributions of simple-like and complex-like subunits once the stimulus-dependent receptive fields have been convolved with the corresponding stimulus sequences. Their results indicate that for all stimuli, the SI* was identical for the three stimuli. Their intracellular recordings indicate that, a normalization of the simpleness of the visually evoked synaptic activity happens in V1 cells. In a more recent papier, Fournier et al., (2014) showed that the functional expression of the simple or complex nature of changes according to the test stimulus: if the stimulus is of high dimensionality (dense noise), the receptive field looks dominantly linear (simple-like), whereas if the stimulus is of lower dimensionality (sparse noise), the receptive field looks dominantly non-linear (complex-like). According to their decomposition schema, the functional expression of the receptive field in a given context relies on the relative weight between simple-like and complex-like synaptic contributions.

They developed different models in order to predict this adaptive response. Their first model was a parallel Linear-nonlinear cascade receptive field architecture composed of many linear filters. Each filter corresponds to a feature of the stimulus. The outputs of these filters are then passed through a

nonlinearity (as described by Rust & Movshon, 2005; Figure 1.6.2). This first model failed to capture the adaptive response measured experimentally. In order to overcome this problem, they added gain control mechanisms to their model, which account for the branch-specific division of the simple-like and complex-like receptive field components, respectively, when switching from sparse to dense noise. They were able to predict the reorganization of simple-like and complex-like spatiotemporal profiles between sparse and dense noise by adding more filters to the model. However, they claim that more advanced models, capturing the computations occurring in V1 (inhibition, adaptation, depression) are necessary to predict complex responses.

This stimulus dependence of the RF also reflects some layer dependency. Yeh *et al.*, (2009) stimulated the primary visual cortex of primates with two types of stimuli: sparse noise and Hartley stimuli, which are a particular set of sinusoidal grating patches. They showed that receptive fields of neurons in layer 2/3 (*i.e.* in "output layers" that receive cortical inputs) were stimulus-dependent unlike neurons in layer 4C (*i.e.* in "input layers" that receive thalamic inputs). They argue that the difference observed in layer 2/3 arises from the fact that Hartley stimuli drive both inhibitory and excitatory cells more strongly than sparse noise. In addition, as confirmed by the findings obtained in Frégnac's group (Fournier *et al.*, 2011, 2014), their results support the idea that even simple cells can be highly nonlinear (*i.e.* "complex-like"). In addition, they conclude that to model the responses to more complex stimuli, in particular in output layers, one must consider rich models containing features such as recurrent nonlinear networks that can modify the spatiotemporal profile of the receptive field.
These studies showed, with simple and complex artificial stimuli, that the structure of the receptive field varies. However, how the structure of the receptive field changes in response to natural scenes was not investigated. Indeed, natural scenes contain a mixture of spatio-temporal statistics (section 3), thus based on the results previously discussed, one can expect that the receptive field structure will be different between an artificial and a natural stimulation. In the next section, we will describe and discuss the receptive field features obtained with natural stimulations.

6.2. Natural stimuli and functional responses

Barlow (1961) hypothesized that V1 should be optimized to treat natural statistics. Thus, it is legitimate to wonder how natural scenes shape V1 receptive fields and how one can model them.
In a study performed by Frégnac's group, using intracellular responses to dense noise, Baudot and colleagues (2013) tried to predict the responses to natural images animated with eye movements, drifting gratings, gratings animated with eye movements and other dense noise (a different stimulus seed than the one used for prediction). By computing the expected and predicted coherence, they determined the percentage of the coherence that the model explained. The linear prediction explained more than 80% of the response to drifting gratings but less than 20% of the response to natural images and animated gratings. Thus, they demonstrated that the response to natural images is not simple linear transformations of the eye-movement animated stimuli. Rather, eye-movement statistics appear particularly efficient for activating V1 non-linearities. This study investigated both spatial and temporal statistics of the stimuli.

Other studies, but this time based on extracellular recordings, looked at the linear and nonlinear properties of the RF in response to the spatio-temporal statistics of natural scenes and then performed a cross prediction (David et al., 2004; Felsen et al., 2005; Touryan et al., 2005). David and colleagues (2004) investigated how natural stimuli alter the receptive field structure of V1

neurons in primates. They concluded that natural scenes and DG do not induce the same spatiotemporal receptive field (STRF) structure. Based on these measurements, two nonlinear STRF models were developed, one based on the RF structure when DG were presented and the other based on the RF structure after natural scene presentation. The model based on the STRF obtained with natural images predicted the response to natural scenes significantly better than the STRF obtained with gratings (the natural images presented to compute the RF are not the same set of images that were used for the response prediction). Notably, some sets of natural scenes were very poorly predicted even with the STRF model based on natural images. These poor predictions could be linked to the fact that natural scenes evoke a very sparse neuronal activation in primary visual cortex. Indeed, a recent two-photon study (Tang et al., 2018) showed that different natural scenes activate small and different subsets of the neuronal population. David and colleagues (2004) only recorded 74 well isolated single units, this small population might not have been activated by the poorly predicted sets of natural scenes. Finally, by controlling the temporal and the spatial properties of their natural stimuli, they demonstrated that natural temporal stimulus statistics modulate both spatial and temporal response properties. Natural spatial statistics modulate spatial response properties, but do not influence temporal response properties (Figure 1.6.6). These results imply a crucial role for temporal statistics, yet they are often neglected because it is difficult to mathematically characterize them (see section 4.2). New studies need to take into account the temporal aspects of the natural stimulation in order to improve the understanding of their visual processing. Additionally, even if their model predicts better the measured response to some natural scenes, it is far from predicting it accurately. In this thesis, we explored V1 responses to the spatio-temporal statistics of natural scenes in order to provide a better characterization of visual processing.

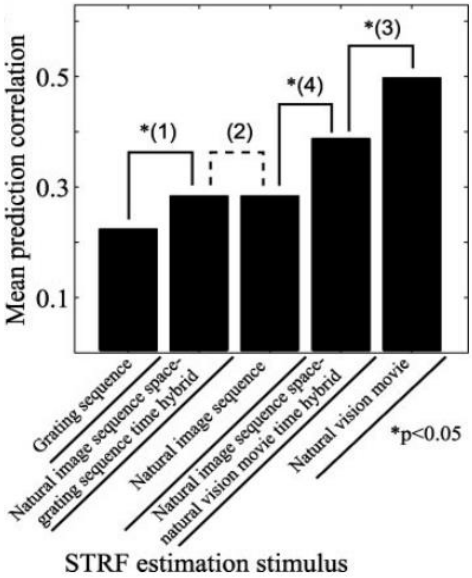

Figure 1.6.6. Sources of stimulus-dependent modulation. They compared the mean prediction of their STRF model to different stimuli where temporal and spatial properties where modulated (reprinted from David *et al.*, 2004).

Yang Dan's laboratory investigated extracellularly how spatial statistics of natural images impact the spatial structure of the receptive field (Touryan *et al.*, 2005). By using a modified spike-triggered covariance technique (STC), that takes into account the spatial correlations in the natural images, a detailed analysis of the complex receptive field spatial structure was computed. The fine spatial structure allowed a better prediction of the orientation and the spatial frequency preferences of the recorded cell than the one predicted with artificial stimuli.

As performed by Touryan and colleagues (2005), other extracellular studies focused on the benefits of natural scenes to the estimation and prediction of complex stimuli. Talebi and Baker performed two studies (2012, 2016) on cat primary visual cortex. They probed the receptive fields of neurons with artificial and natural stimuli. The natural image-derived receptive field models were better at predicting responses to other stimuli than other models based on RFs estimated with artificial stimuli. Notably, these predictions also provided good tuning curves for sinewave gratings.
Another modulation factor, evoked by both artificial and natural stimuli, is surround modulation (Haider et al., 2010a; Pecka et al., 2014; Vinje and Gallant, 2000). In order to increase the prediction to all classes of stimuli, this modulation needs to be better understood. Coen-Cagli and colleagues (2015) made a step towards it. By extracellularly recording the activity of hundreds of neurons in macaque V1 in response to 270 static natural images and optimized DG, they were able to understand why, compared to gratings, natural images induce less surround suppression. Despite the reduced amount of suppression observed for natural scenes, depending on the presented image, surround modulation either induces a suppression or a facilitation (Figure 1.6.7-B. Modulation ratio values smaller than 1 correspond to surround suppression; values larger than 1 to facilitation). They tried to predict the observed response with a model, also used by others (Cavanaugh et al., 2002; Webb et al., 2005), that takes into account divisive normalization (Figure 1.6.7-A, left panel) but failed to capture the diversity of responses to different natural images, particularly surround facilitation (Figure 1.6.7-B). By analyzing the statistics of the image, they concluded that regions in visual stimuli can be considered homogenous or heterogeneous. A homogenous image implies that neighboring locations in this image contain spatially redundant information. A heterogeneous image is characterized by the absence of spatial correlation between two neighboring regions. Heterogeneous natural images induce surround facilitation (“ON surround”) while homogenous natural images induce surround suppression (“OFF surround”). Based on these results, a new model was developed, in which the flexible neuronal responses linked to homogenous/heterogeneous regions are taken in account (Figure 1.6.7-A, right panel). The prediction improved greatly, particularly when the presented images were a mixture of homogenous and heterogeneous ones (Figure 1.6.7-B-C). In summary, their results argue in favor of the addition of a gain control mechanism, taking into account the homogeneity of the stimulus, in order to predict the response to natural images.

While their approach is purely functional, a hypothesis of the mechanisms underlying surround modulation with orientated gratings could be drawn when both center and surround have the same orientation, the image is spatially redundant *i.e.* homogenous, thus activating the same normalization pool. To the contrary, when center and surround orientation do not match, the spatial correlation is not present anymore, the image is heterogeneous and activates two different normalization pools. This could explain the surround context dependency of suppression and facilitation observed with oriented gratings.

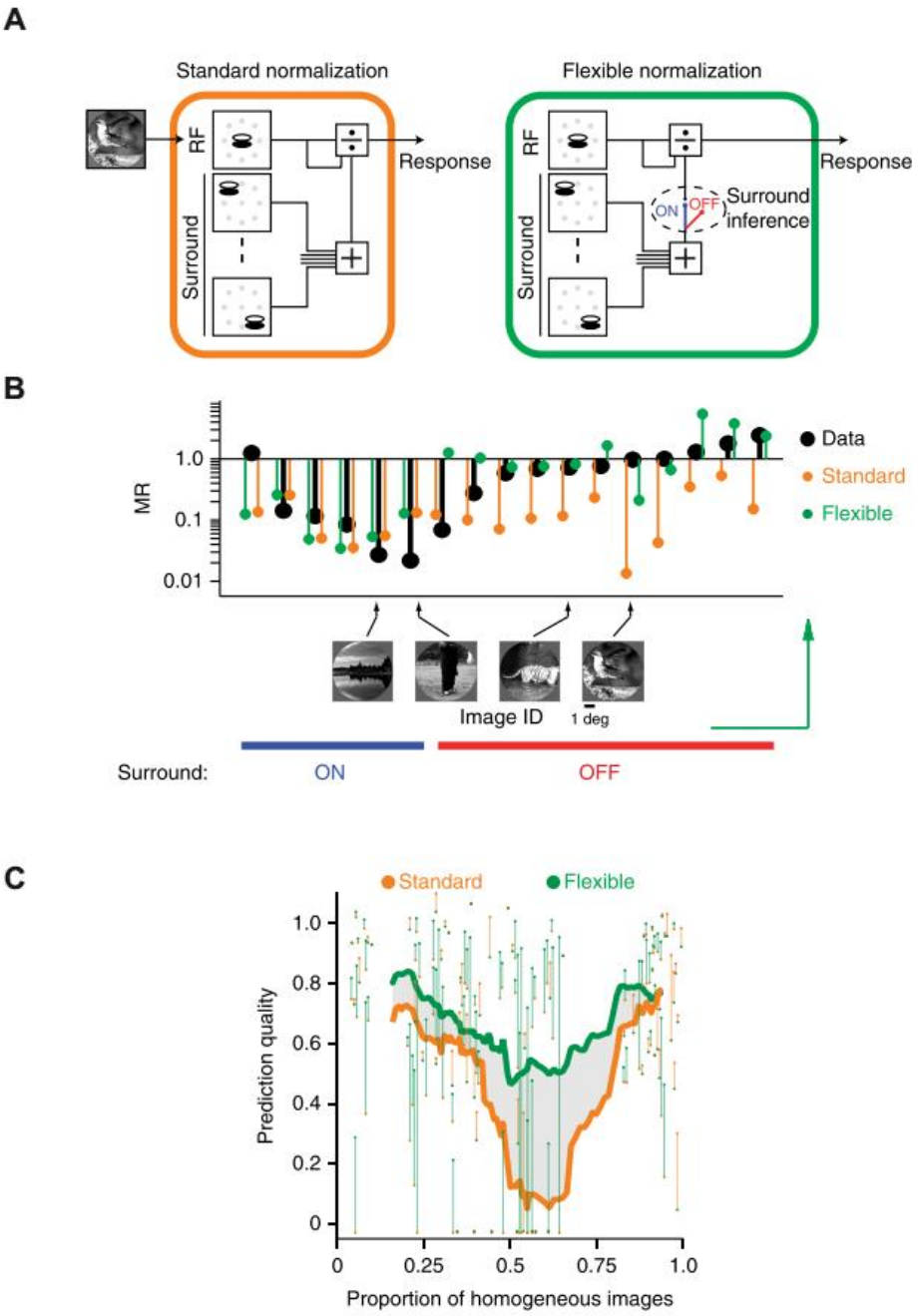

Figure 1.6.7. Standard and flexible normalization models and their performance. **A.** Left panel: Standard normalization model. Right panel: Flexible normalization model where surround can be considered as ON or OFF. **B.** Model performance for one neuron in response to an ensemble of images (MR: Modulation ratio). **C.** Prediction quality of the two models as a function of the proportion of homogenous and heterogeneous images (Reprinted from Coen-Cagli et al., 2015).

The work of Coen-Cagli and colleagues (2015) showed how a particular feature of spatial statistics impacts the response. However, other spatial statistical features, such as its correlations also modulate the visual response.

Rikhye and Sur (2015) explored in mouse primary visual cortex, with 2-photon imaging, how spatial correlations impact neuronal trial-to-trial reliability. By taking advantage of the $1/f^{\alpha}$ power spectrum of natural images, they were able to either increase or decrease their spatial correlations (Figure 1.6.8). Images with strong spatial correlations induced reliable responses in mouse V1 neurons and increased the correlation between ensembles of neurons. These differences in reliability mainly originate from low spatial frequency content. Indeed, the alteration of these has a stronger effect on the response than the alteration of the high spatial frequency content. They developed two linear-nonlinear cascade models in order to predict the neuronal response to the different types of natural scenes. The first model, called “independent model” because it does not include a normalization phenomenon, failed to predict accurately the measured responses. The second model, called “normalization model” because it does include a normalization phenomenon, predicted more accurately the measured responses. They concluded that strong stimulus correlations activate strongly V1 neurons and changing their correlations changes the normalization pool, which induces reliable responses (Figure 1.6.9).

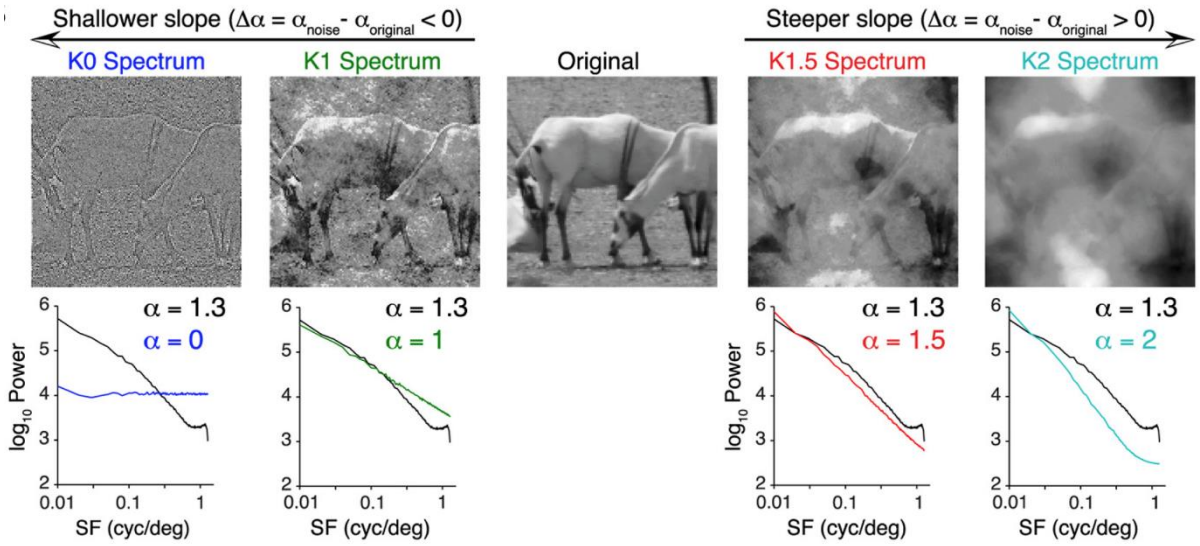

Figure 1.6.8. Perturbing spatial correlations in movies. By changing the slope of the spatial frequency power spectrum, the authors were able to reduce or increase spatial correlations (reprinted from Rikhye & Sur, 2015).

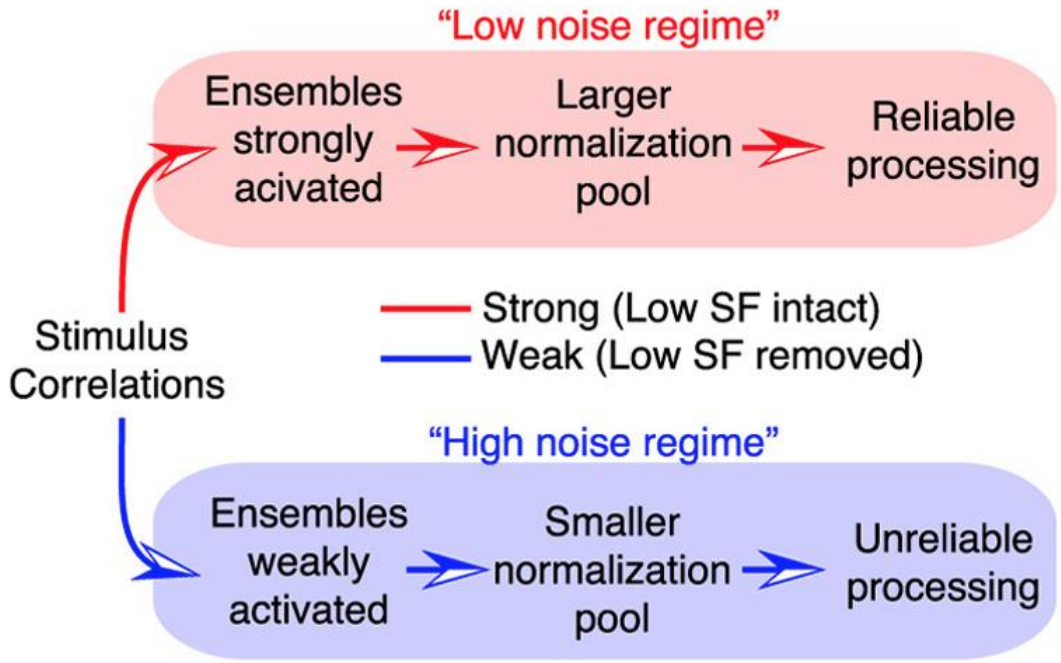

Figure 1.6.9. Schematic summarizing the findings of Rikhye & Sur (2015) when spatial correlations are increased or decreased in natural scenes.

We discussed the fact that receptive fields are stimulus dependent and how they have been modeled. Different studies demonstrated that receptive field models based on natural images result in a better prediction of the neuronal response than the ones based on artificial stimuli. However, despite the increased performance, these models did not fully capture V1 behavior. These mixed performances originate from the fact that we do not fully understand how natural images are encoded by primary visual cortex. This was very clear in David and colleagues' study (2004), where their model predicted very poorly the response to some sets of natural scenes, without any identified reason. Therefore, in order to model accurately the response to natural scenes, new research needs to investigate how they modulate visual activity. In this manuscript, we investigated carefully how natural images modulate the neuronal activity in cat V1. Others, such as Coen-Cagli *et al.* (2015), made a step towards this understanding by demonstrating some mechanisms underlying center-surround modulation for both natural and artificial conditions. However, other modulatory processes take place in V1, such as the impact of natural images in response variability. As studied by Rikhye & Sur (2015), spatial correlations activate strongly V1 neurons and change their correlations, which leads to a more reliable response, mediated by a change in the normalization pool. However, one cannot reduce the reliability modulation to a normalization process. Indeed, other mechanisms are actively involved in the variability changes observed in V1. The characterization of the mechanisms underlying cortical variability dynamics, and how they are affected by artificial and natural stimuli, is a mandatory step towards the understanding of visual processing. In this thesis work, we tried to understand some of these mechanisms (see results section).

7. CORTICAL VARIABILITY DYNAMICS

Cortical neurons are often considered “noisy” and have been compared to the communication channel described by Shannon (1948). In this communication channel, a message is converted into a signal. This signal is sent through the channel to a receiver. However, in the communication channel, the signal is mixed with some noise. Therefore, the received message is a combination of the signal plus an added noise. This is true when the neurons are in a silent network (*in vitro* slices for example) and their membrane potential is at a voltage value distant from the spiking threshold. This situation will generate a highly variable response. However, when the membrane potential is just below the spiking threshold, its spiking pattern becomes more reliable, as observed *in vitro* by Mainen and Sejnowski (1995). They maintained the neuron close to the depolarization threshold, added a pseudo-noise similar to synaptic activity, and compared it to a continuous stimulation. The addition of the pseudo-noise induced very reliable spike trains while the continuous stimulation elicited variable responses (Figure 1.7.1)

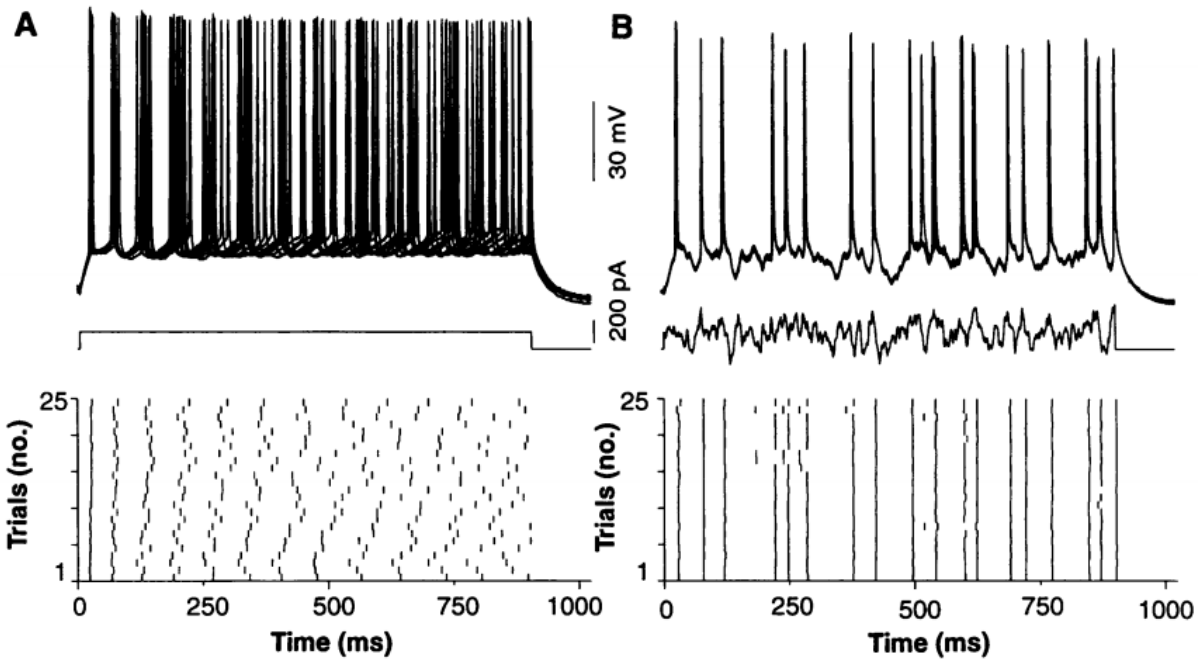

Figure 1.7.1. Reliability of firing patterns of cortical neurons evoked by two types of currents. A. Firing pattern evoked by a continuous dc current pulse. The response is very variable. B. Firing pattern evoked by a pseudo-noise. The response is very reliable (reprinted from: Mainen & Sejnowski 1995).

In another *in vitro* study, Nowak and Bullier (1997) injected different types of currents and investigated how the frequency content of these currents affected the reliability and the precision of the response. When the injected current contained a mixture of low and high frequencies, the spiking activity was more reliable and more temporally precise than a current containing only high or low frequencies. This indicates that reliable spiking activity is elicited when a cell receives a reproducible mixture of low and high frequencies. However, since these studies were performed *in vitro*, it is legitimate to wonder if neurons behave similarly *in vivo,* and which visual stimulations elicit reliable and precise responses.

A popular computational hypothesis called *efficient coding* suggests that visual processing in early sensory systems is optimized and adapted to the statistical properties of the sensory environment. This should result in a redundancy reduction between neurons (a decorrelation between neuronal response), associated with an increase in the sparseness of the population activity and a decrease in the response variability (Barlow, 1961). Thus, one could expect to observe the *in vitro* results obtained by Mainen & Sejnowski (1995) and Nowak and colleagues (1997) in primary visual cortex. Indeed, since artificial and natural stimuli are composed of a mixture of high and low frequencies, as the injected currents previously described, different stimulus statistics should evoke different levels of reliability.
In this section, we will describe the impact of both artificial and natural stimuli on V1 cortical variability and how these results match (or not) the efficient coding theory.

7.1. Stimulus-independent sources of neuronal variability

Due to the influence of neuronal variability on the encoding of visual information, a first step towards its understanding is to identify how this variability is shaped by intrinsic and evoked cortical dynamics. How much is driven by the stimulus or reflects covariations shared across the network, reflecting its internal state or predictions from higher cortical areas?
The sources of variability are numerous, internal signals such as attention or arousal can have an impact on the variability. Another important source of variability is the brain state. Indeed, if the animal is awake, lightly or deeply anesthetized the cortical dynamics are likely to vary. The visual stimulation also constitutes a source of variability. Two different stimuli will activate the system in two different ways and modulate the cortical variability. For example, natural images and drifting gratings do not have the same statistics, thus do no stimulate the inputs in the same way. This results in a visual context-dependent modulation of the cortical variability (Baudot *et al.*, 2013).
In a recent study, Goris and colleagues (2014) showed that internal signals in the brain, which are not purely sensory in origin, could affect the neuronal response. These signals are for example, adaptation, arousal or attention. A simple model provided a new view on cortical response variability. Whereas classical models assume that variability of an average sensory response is a random noise arising from presynaptic neurons or local circuits (Shadlen and Newsome, 1998; van Vreeswijk and Sompolinsky, 1996), Goris *et al.* hypothesized that variability is induced by a multiplicative modulatory gain. The simulation concludes that their model predicts accurately the variability along primate visual areas (LGN, V1, V2 and MT). Under anesthesia, the classical Poisson model predicts 20-30% of the variability while their gain fluctuation model predicts 70% of the cortical response variability in primary visual cortex. Fluctuations in excitability are less strong and have higher frequency content in awake animals performing an attentional task than they are in anesthetized animals, implying that different mechanisms occur during these two brain states. Goris *et al.*, (2015) proposed that the correlations between neurons are generated by two components, point process

correlations, which are the result of shared inputs within local cortical circuits and gain correlations which arise from fluctuations in the modulatory signal, that are shared across large population of neurons. This study pointed out the mechanisms underlying the variability caused by internal signals.

Although Goris *et al.* showed that anesthesia had no impact on the reported effects, one cannot neglect the impact of anesthesia, and brain states in general, on the cortical variability. Indeed, a study conducted by Ecker et al., (2014) compared the correlation structure of V1 neurons in anesthetized monkeys or awake monkeys performing a fixation task. They investigated how noise correlations *i.e.* the shared variability of pairs of neurons not related to the stimulus (this method is described in detail in section 7.2.1 and in the results section of this manuscript) was influenced by the state of the animal. Both experimental and modelling results indicate that, under anesthesia, noise correlations are dominated by a common modulatory factor, impacting all cells, explaining the high values of noise correlation that they obtained. On the other hand, during fixation, noise correlations are very low, and this common modulatory factor is absent, confirming that different cortical states induce different modulatory factors and modulate the variability of cortical dynamics.
During anesthesia, brain activity can change spontaneously from a synchronized to a desynchronized state (or from a desynchronized to a synchronized state). Spacek and Swindale investigated how noise correlations are impacted by the ongoing changes in brain states and found for both states rather low values of noise correlation (although significantly lower during the desynchronized state (0.015 vs 0.031)). The impact of the cortical synchronization relates directly to the common modulatory factor described by Goris *et al*.
This argues for the fact that brain states need to be monitored and taken into account during experiments. Indeed, between two brain states, the values of noise correlation were doubled. One can wonder how many similar experiments drew different conclusions because the brain was in different states (see Cohen and Kohn, (2011) and section 7 for a review of various noise correlation values across studies).
These latter studies drew conclusions about variability by focusing on single units or pairs of units. Others (Cui et al., 2016; Lin et al., 2015) investigated how variability is shared across a large neuronal population.
- Lin *et al.* analyzed the variability of a neuronal population recorded in the primary visual cortex of anesthetized cats and awake mice. In both species, they recorded simultaneously the responses of hundreds of neurons to sinusoidal drifting gratings. Their results show that response variability is shared across neurons in primary visual cortex. However, in contrast to Goris *et al.*, they claim that this variability is explained by an additive and a multiplicative gain modulation and that these two gain factors determine neuronal correlations.
- Instead of recording hundreds of neurons, Cui and colleagues (2016) took advantage of the fact that LFP and MUA provide population signals reflecting variability sources unrelated to the sensory drive. The model, based on recordings in primate MT, performs five times on predicting better cortical variability than models only taking into account predictions obtained from the stimulus.

All the previously mentioned studies investigated the stimulus-independent variability when visual cortex was stimulated with simple artificial stimuli (*i.e.* drifting gratings). As described in section 4, DG are simple stimuli with very simple spatio-temporal statistics. Yet, different studies showed that the stimulus-dependent variability changes as a function of the stimulus statistics (Martin & Schröder, 2008: Baudot *et al.*, 2013). Thus, we can suppose that the non-stimulus dependent variability will also be impacted, since an interplay between these two sources of variability occurs in cortex (Goris

et al., 2014). Therefore, in order to understand the non-stimulus dependent variability, a better understanding of the stimulus dependent variability is mandatory.

7.2. Stimulus-dependent sources of variability

Since drifting gratings are very simple stimuli, one could suppose that their impact on the variability is limited. However, Kohn and Smith (2005) proved that assumption to be false. By presenting DG at different contrasts while recording in the primary visual cortex of awake monkey, they reported that noise correlations between pairs of neurons change as a function of the stimulus, highlighting the stimulus dependence of the cortical variability, even for simple stimuli.

Additionally, an intracellular study performed on the primary visual cortex of the anesthetized and paralyzed cat investigated how stimuli of increasing complexity affected the sparseness and the reliability of the response (Baudot *et al.*, 2013). Four different stimuli were presented: drifting gratings, dense noise, gratings animated with artificial eye movements and natural images animated with artificial eye movements. They demonstrated that both the sparseness and the variability of the neuronal activity is stimulus-dependent and that this modulation of the variability is linked to the global statistics of the full field visual stimulation.

Taken together, the aforementioned studies investigated cortical variability in three ways, by computing the correlations, the sparseness and the variability of the neuronal activity. In order to describe the stimulus dependence of the cortical variability, these three aspects of the cortical response require a thorough investigation. Additionally, as previously stated, efficient coding implies a modulation of these three factors, and this theory is directly linked to cortical variability. Therefore, it is crucial to discuss how experimenters investigated the sparseness and the reliability of the response, the cortical dynamics and how their results match, or not, Barlow's efficient coding theory.

7.2.1 Correlations

Correlation is a simple statistical measure of association between two variables. Thereby, different types of correlations can be computed. Brain activity dynamics are mainly studied with three types of correlation:
- The first one, *signal correlation*, is used to quantify the degree to which different neurons have similar functional properties. For instance, one can quantify the similarity between the tuning curves of two different V1 neurons. In order to measure these correlations, many presentations of the same stimulus is needed. Indeed, signal correlation is the correlation between the mean responses of two neurons (Kohn et al., 2016).
- The second type of correlation is called *noise correlation*. This type of correlation captures the degree of response variability shared between pairs of neurons. Noise correlation is computed as the correlation of the remaining spike counts after mean subtraction to repeated presentations of the same stimulus (Kohn *et al.*, 2016).
- The last type of correlation, *pattern correlation*, is the correlation of the mean response of two neurons to different stimuli. Pattern correlation is used to capture the similarity in the response to two different stimuli (Kohn *et al.*, 2016). This type of correlation has been used in studies investigating the dynamics of olfactory cortex (Friedrich, 2013).

Primary visual cortex studies have focused primarily on *signal* and *noise correlations.* As described in this manuscript (see sections 2 and 5 of this chapter), the anatomical properties of primary visual cortex are linked to its functional properties. Indeed, primary visual cortex is organized into functional columns, while, within these columns, each layer can be considered as an individual functional unit. Because of this anatomical organization, we should expect that neurons spatially close or far (*i.e.* inside or outside of the same functional unit) show different values of correlation.
Tanaka and colleagues (2014) investigated the spatial range of signal correlations in the cat primary visual cortex. They recorded both horizontally (within the same layer) and vertically (within the same column), in cat primary visual cortex with a multi-shank linear silicon probe (similar to the one shown in Annex 1). Their results showed that correlated responses to drifting gratings are spatially dependent. Indeed, between pairs of neurons separated horizontally, the correlations tend to drop drastically within 400µm (see table 1.7.1). While similar values of correlation were found for pairs of neurons located 400 or 800µm, it was not the case for neurons separated by 1200µm. It has been proven that for short distances (less than 500-800µm, *i.e.* within the hypercolumn), horizontal connections preferentially link neurons that are not iso-oriented, while they link iso-oriented neurons for higher distances (*i.e.* outside the hypercolumn; Kisvárday et al., 1993 a,b). Therefore, the correlation is higher for neurons separated by 1200µm because they share functional properties, which is not the case for neurons located at 800µm or less.
Vertical correlations also dropped sharply within 400µm. However, unlike what has been reported horizontally, the correlations did not increase for very distant pairs (1200µm apart; see table 1.7.1). Indeed, each layer is a functional unit with different properties (see sections 2 and 5), and unlike what is observed horizontally, distant neurons are less likely to share functional properties.

Tanaka *et al.* (2014) only investigated the signal correlations in response to drifting gratings. However, as discussed previously in this manuscript (section 6), V1 responses are stimulus-dependent. Are the correlations, and the spatial decay, observed by Tanaka and colleagues similar with complex stimuli?
Martin and Schröder (2013) explored extracellularly, in cat primary visual cortex, the impact of different stimuli on the signal correlations. Their study on cat primary visual cortex compared the synchrony of the response to drifting gratings, visual noise and natural images. Some neighboring pairs gave a very high value of signal correlation for these three types of stimuli (above 0.8). On average, natural images induced a higher value of synchrony than the other stimuli (values of signal correlation are gathered in table 1.7.1). However, the signal correlations between all pairs gave a median value close to zero for the three classes of stimuli. Moreover, the absolute strength of signal correlations for 50% of the pairs (interquartile range) stayed well below 0.5, no matter which stimulus class was presented. Martin and Schröder reported signal correlation values in cat V1 in response to natural movies in the same range as those observed , by Yen et al., (2007) (see table 1.7.1).
Their findings confirm that the level of synchrony between two neurons is stimulus-dependent. However, heterogeneous responses where some pairs of neurons are highly correlated and others are uncorrelated were also observed. This lack of correlation tends to confirm the efficient coding theory. Yet, the very low correlations observed for artificial stimuli, tends to contradict Barlow's theory. Another result in contradiction with the efficient coding hypothesis is the very high correlation values of some pairs (above 0.5), observed for all stimuli, in particular for natural movies. The fact that only a small neuronal population was recorded (46 pair of neurons), makes it difficult to conclude if their results supportthe efficient coding theory. Moreover, no link between the statistics of the different movies and the values of correlations was made. One could suppose that some pairs of

neurons were very responsive to many movies while others only to a few, leading to these differences in correlation.
This was shown in a two-photon study, performed in mouse primary visual cortex. Rikhye and Sur (2015) investigated how the properties of natural scenes affect signal correlations in a large number of neurons. Natural images with strong spatial correlations evoke stronger signal correlations than the ones displaying low spatial correlations. In addition, across the population of neurons, different clusters in the population, based on the mean signal correlation between neurons, were established. They observed clusters displaying high correlations, while others displayed very low ones (see table 1.7.1). This correlation clustering could also explain the high and low correlations observed by Martin & Schröder. Indeed, some pairs of neurons might have been recorded within highly correlated clusters while others in poorly correlated clusters. However, these results need to be confirmed in higher mammals.

Other studies investigated, in higher mammals, the impact of the visual statistics on the signal correlation. Vinje and Gallant (2002) investigated, in awake behaving primates (fixation task), the impact of the center surround interactions on the heterogeneity of the response. To do so, a stimulation of both the center and the surround of the receptive field was performed. Different natural images were presented, while the response of V1 neurons was recorded extracellularly. When both center and surround were stimulated, the responses of pairs of neurons were more decorrelated than the response obtained with a stimulation restricted to the RF center (see table 1.7.1). Consequently, the increase of the stimulation size appears to enhance the statistically independent information carried by each neuron. However, unlike in a following study of Gallant's group (David *et al.*, 2004), they did not comment if all presented images evoked the same degree of decorrelation. Based on the results of David and colleagues (and others such as Rikhye & Sur (2015); Tang *et al.*, (2018)), one can expect that not all natural images presented by Vinje & Gallant (2000) evoked the same response in V1, hence not all pairs displayed the same degree of synchrony.
We discussed how signal correlations have been studied in primary visual cortex However, studies mainly focused on the correlated trial-to-trial response variability, namely, the *noise correlations.*

Study	Model	State	Values of signal correlation	Comments
Tanaka *et al.*, (2014)	Cat	Anesthetized	Horizontal correlations: **0.01** (for pairs separated by 0μm) **0.05** (for pairs separated by 0.4 and 0.8μm) **0.07** (for pairs separated by 1200μm) Vertical correlations: **0.01** (for pairs separated by 0μm) **0.05** (for pairs separated by 0.4 and 0.8μm) **0.001** (for pairs separated by 1200μm)	Visual stimulation: Gratings. They subtracted the shift predictor from the signal correlation. Leading to low values of correlation
Yen *et al.*, (2007)	Cat	Anesthetized	Natural Images: **0.18**	
Martin and Schröder (2013)	Cat	Anesthetized	Gratings: **0.2** Visual noise: **0.3** Natural Images: **0.4**	
Vinje and Gallant (2000)	Primate	Awake (Fixation)	Center stimulation: **67°** Center Surround stimulation: **51°**	Signal correlation computed as the separation angle between neurons
Rikhye and Sur (2015)	Rodent	Awake	High correlation cluster: **0.45** Low correlation cluster: **0.05**	Values of signal correlation for natural scenes

Table 1.7.1. Values of signal correlations across different studies.

Noise correlations are thought to originate from common synaptic inputs (Goris *et al.*, 2014). In section 7.1, we described different studies that evaluated the non-stimulus dependence of cortical dynamics, by computing the noise correlation. However, noise correlation is also very useful when it to comes to evaluating the stimulus-dependent variability. Many studies investigated the noise correlations in primary visual cortex, leading to different reported values, ranging from 0.01 to 0.3 (see table 1.7.2 and Cohen & Kohn, 2011 for a review). A study performed by Ecker et al., (2010) in awake monkeys reported surprising noise correlation values. They recorded the activity of neighboring pairs of V1 neurons in response to drifting gratings. The noise correlation values that they reported are almost 10 to 30 times lower than the ones reported in the literature. They affirm that their recordings are better than the ones performed previously by other groups, and that these differences rely on technical improvements. Indeed, by recording with chronically implanted tetrodes they obtain more stable recordings while the tetrodes allow optimal single unit isolation. However, another study performed in the awake monkey in similar conditions as the ones of Ecker and colleagues, extended their results. In this study, despite evidence ofthe laminar processing of visual information, Ecker and colleagues did not consider the laminar position of their electrode as a factor that could influence the noise correlations.

This issue was studied by Hansen et al., (2012) by recording in the awake monkey the single unit activity across all layers with a linear silicon probe chronically implanted. The responses were recorded during a fixation task, where drifting gratings were presented. In this study, the cortical layers were divided into three compartments, supragranular layers corresponding to layer 2/3, the granular layer corresponding to layer 4, and infragranular layers corresponding to layers 5 and 6. The granular layer, which receives the majority of the thalamic inputs, has very low noise correlations (according to their own terms, “Granular layer showed virtually no correlated variability”) close to the ones observed by Ecker *et al.* In contrast, supragranular and infragranular layers exhibited strong noise correlations (Figure 1.7.2; table 1.7.2), closer to the ones classically observed in the literature. A model based on these results was developed, and it suggests that the low values of noise correlations observed in the granular layer decreases the orientation discrimination threshold. This decrease in decorrelation in the trial-to-trial variability should be beneficial for sensory discrimination. In light of the results obtained by Hansel and colleagues, one can assume that the very low noise correlations observed by Ecker and colleagues originates from an oversampling of the granular layer. The laminar differences observed by Hansel *et al.* could originate from the anatomical properties of V1. Indeed, layer 4 receives inputs from the thalamus, which are known to be very reliable (Kumbhani et al., 2007; Reinagel and Reid, 2000). Since noise correlations are a measure of the trial-to-trial variability caused by the neuronal presynaptic activity (Ecker *et al.*, 2014), noise correlations should be reduced if the synaptic inputs are less variable. To the contrary, layers 2/3 and 5/6 receive less reliable inputs (Hirsch et al., 2002), which can lead to these higher correlation values.

Study	Model	State	Values of Noise correlation	Comments
Kohn and Smith (2005)	Primate	Anesthetized	Drifting Gratings: **0.2**	
Rasch *et al.*, (2011)	Primate	Anesthetized	Natural stimuli: **0.26**	
Ecker *et al.*, (2010)	Primate	Awake (fixation)	Drifting gratings: **0.01** Natural images: **0.001**	
Ecker et al., (2013)	Primate	Anesthetized	Drifting gratings: **0.05**	
Hansen *et al.*, (2012)	Primate	Awake (fixation)	Layer 2/3: **0.27** Layer 4: **0.05** Layer 5/6: **0.26**	They computed noise correlation in response to drifting gratings, in 3 different laminar compartments
Martin and Schröder (2013)	Cat	Anesthetized	Gratings: **0.05** Visual noise: **0.05** Natural Images: **0.05**	They found a very heterogeneous distribution of noise correlations in a very small sample of neurons (15)
Rikhye and Sur (2015)	Rodent	Awake	High correlation cluster: **0.07** Low correlation cluster: **0.03**	Values of noise correlation for natural scenes

Table 1.7.2. Values of noise correlations across different studies.

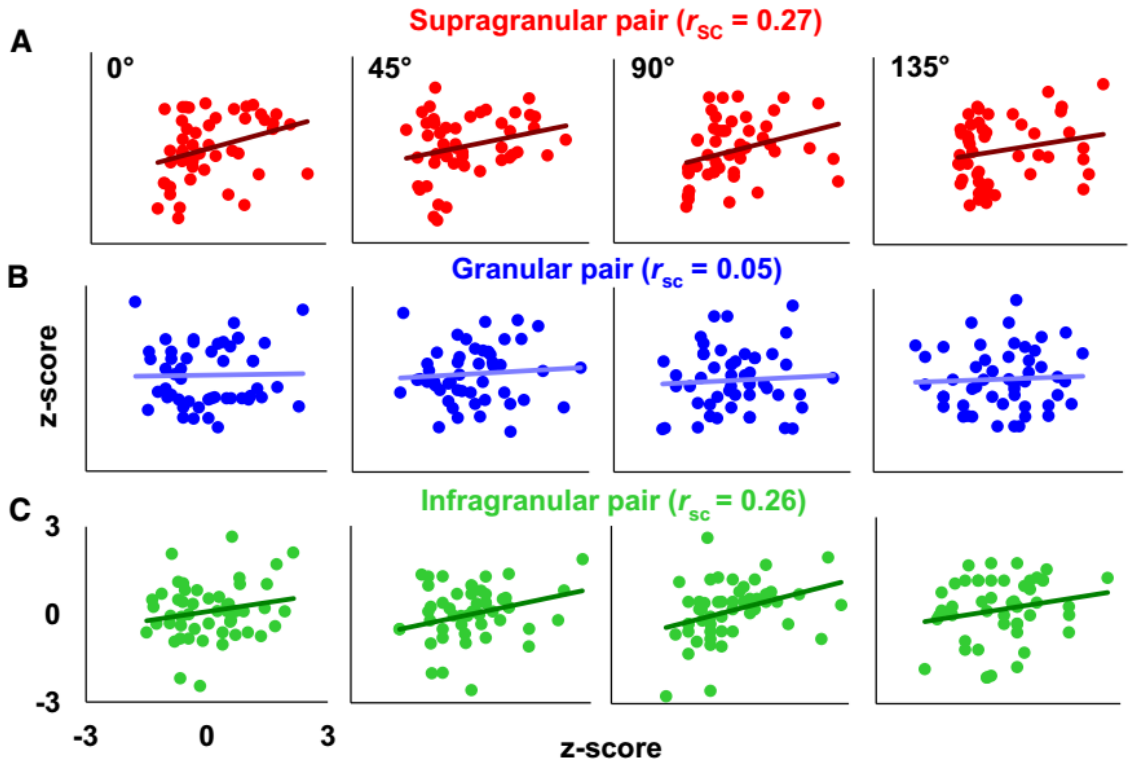

Figure 1.7.2. Each scatter plot represents the Z-score-transformed responses for three example pairs of cells recorded simultaneously in supragranular (A), granular (B), or infragranular (C) layers during the presentation of a particular stimulus orientation. The trend line represents the linear regression fit for each pair of cells; rSC for each layer represents the noise correlation extracted from all eight-stimulus orientations (reprinted from Hansen *et al.*, 2012)

In their study, Ecker *et al.* (2013) also investigated the noise correlations in response to natural images. They reported even lower values than the ones observed for a drifting grating stimulation (0.001 for natural images vs 0.01 for DG), arguing for a maximization of the coding efficiency as suggested by Barlow.

Surprisingly, Martin and Schröder (2013), who compared, in anesthetized cats, the values of noise correlations for different stimuli, did not find the same results. Drifting gratings, visual noise and natural images evoked similar noise correlation levels (table 1.7.2). However, even if the mean noise correlations were similar for different stimuli, a major difference was observed in the tails of the distribution of noise correlations. Indeed, unlike natural movies, artificial stimuli evoked, in some pairs of neurons, noise correlations above 0.1. Therefore, the similarities in the noise correlation levels might come from a low sampling of the neuronal population (only 15 pairs were used to compute the noise correlations evoked by natural scenes). New techniques, such as two-photon microscopy, can overcome the low sampling observed in Martin and Schröder study.

Rikhye & Sur (2015) also investigated the noise correlations in response to different types of natural scenes. They observed that natural images with strong spatial correlations induce lower levels of noise correlation than images with less spatial correlations. In addition, clusters of high signal correlations showed a higher noise correlation than the clusters of low signal correlation. These ensembles of highly correlated neurons (which represents 30% of the population) performed as well as the entire population in encoding various movies, supporting the notion of a sparse population code.

7.2.2 Sparseness

The efficient coding hypothesis predicts that neuronal population activity should be sparse. Indeed, a sparse code implies that single action potentials carry a lot of information. A perfectly sparse code has a sparseness value of 1 while a non-sparse code has a value of 0. Two types of sparseness can be computed: *Lifetime sparseness*, which is the sparseness of one neuron for many stimuli and *Population sparseness*, which is the sparseness of many neurons for one stimulus (Willmore and Tolhurst, 2001). Most of the studies that investigated sparseness measured lifetime sparseness (Baudot et al., 2013; Haider et al., 2010; Spacek and Swindale, 2016; Vinje and Gallant, 2000; Willmore et al., 2011; Yao et al., 2007) and then inferred population sparseness. However, some studies investigated population sparseness either with electrophysiological recordings (Weliky et al., 2003; Yen et al., 2007a) or 2-photon microscopy (Froudarakis et al., 2014; Tang et al., 2018). Due to its importance in the efficient coding hypothesis, researchers mainly focused on the sparseness of the response to natural scenes. Yet, in order to be able to determine if the sparseness of the response is optimized for natural scenes, it is necessary to determine the sparseness of the response to other stimuli as well.

Vinje & Gallant (2000) performed one of the first studies to investigate the sparseness. By presenting natural scenes on the receptive field but also on the receptive field and its surround, they observed that the concomitant stimulation of the center and the surround of the receptive field increases the sparseness of the response, implying an increase in the efficiency of the response as defined by the efficient coding theory. They hypothesized that this increase in sparseness was linked to the attentional effects caused by the fixation task. However, an extracellular study and two intracellular studies performed on the anesthetized and paralyzed cat showed that the sparseness is linked to the statistics of the stimuli (Baudot et al., 2013; Haider et al., 2010; Yao et al., 2007). Among these studies, the one of Haider and colleagues (2010) investigated intracellularly, in the cat, the effect of a center and surround natural stimulation on lifetime sparseness. As observed by Vinje & Gallant, the stimulation of the surround increases the sparseness of the response. However, the intracellular recordings allowed the discrimination of the mechanisms underlying this modulation. Indeed, the center surround stimulation increased the activity of fast spiking inhibitory neurons and increased the Inhibitory postsynaptic potentials in regular spiking cells, which leads to an inhibition of the response, thus an increase of the sparseness.
Additionally, the fact that the recordings were performed in anesthetized cats proved that the increase of the sparseness is not linked to the attentional effects. It is important to note that in this study Haider and colleagues reported an increase of sparseness only for classical RS neurons.
Their study identified the mechanisms underlying the increase in coding efficiency, mediated by center surround interactions (*i.e.* the statistics of the stimulus as described by Coen-Cagli *et al.* (2015)).

An intracellular study performed in the anesthetized and paralyzed cat, in Frégnac's lab (Baudot *et al.*, 2013), went a step further and investigated if sparseness is impacted in the same way by artificial and natural stimuli. By computing the lifetime sparseness of the response for each stimulus, they demonstrated that natural images animated with eye movements induces a sparser response than the other stimuli (Figure 1.7.3). The sparseness evoked by natural images arises from irregular and highly reproducible membrane potential trajectories.

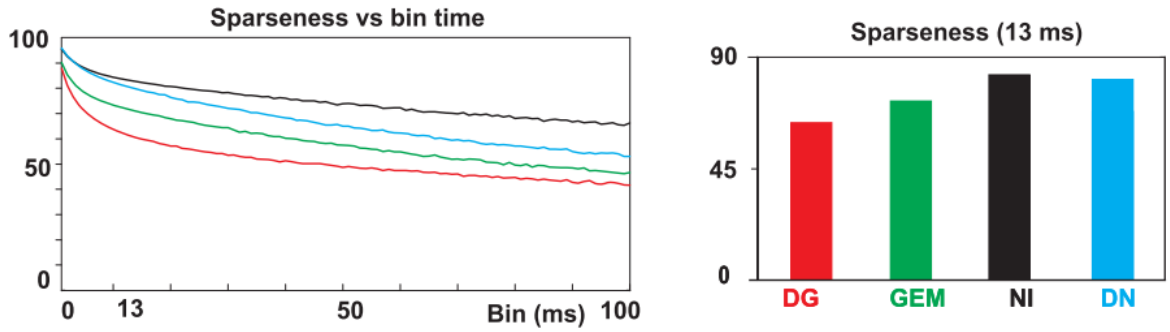

Figure 1.7.3. Sparseness index computed for each condition. Left panel: Sparseness temporal evolution is shown for bin durations ranging from 1 to 100 ms (step of 1 ms). Right panel: the sparseness mean values, averaged over the whole stimulus presentation for a bin equal to twice the refresh rate of the screen. DG: sinusoidal drifting gratings; GEM: gratings animated with simulated eye movements; NI: natural images animated with simulated eye movements; DN: ternary dense noise (reprinted from Baudot *et al.*, 2013)

Haider *et al.* (2010) and *Baudot* et al. (2013) both investigated intracellularly the sparseness in response to natural images. However, Baudot *et al.* found a higher mean sparseness value than Haider *et al*. This could be caused by many factors. First, the anesthesia is not the same in the two studies (Althesin for Baudot *et al.* and Isoflurane for Haider *et al.*). It is known that anesthetics have different effects on cortical dynamics, hence this difference in anesthesia could affect sparseness. In addition, the two studies differ by the type of presented natural images, especially in the temporal frequency content. Indeed, the images used by Haider *et al.* are not animated with eye movements and these could have an important impact on sparseness. Notably, in Baudot's study, the natural image was presented on the whole screen, meaning that the surround of all cells was stimulated (even those with bigger receptive fields), implying a stimulation of both near and far surround, while Haider and colleagues only stimulated the near surround. This larger stimulation of the surround could also explain the different sparseness between these two studies. Additionally, Baudot and colleagues did not classify the recorded cells into different RS/FS/IB/CH subtypes.
Finally, another factor is the low amount of recorded cells in both studies. Indeed, intracellular recordings are labor intensive and not as efficient in terms of quantity of recorded cells as extracellular ones. Thus, the differences between these two studies could arise from the low neuronal sampling in both situations.

Additional limitations caused by the number of recorded cells resides in the fact that these studies could only compute the *lifetime sparseness*. However, with the emergence of the imaging techniques such as two photon microscopy, the *population sparseness* can now be easily computed. Therefore, it is legitimate to wonder if the results observed for the lifetime sparseness are reproduced when population sparseness is computed.

In this line, Froudarakis and colleagues (2014) recorded with 2-photon recordings the neuronal activity in both anesthetized and awake mouse primary visual cortex. They wanted to investigate if population sparseness was higher when natural movies or when phase-scrambled movies were presented. Natural movies induced a sparser code at the population level and this sparseness facilitated the readout of natural scenes. In the same study, Froudarakis *et al.*, (2014) also developed a model that takes into account the brain state of the animal and concluded that brain state can increase or decrease the population sparseness, *i.e.* the encoding of natural scenes. This confirms our previous statement, in which we affirm that brain states need to be monitored continuously throughout experiments.

Similar results were found in higher mammals, arguing for a mechanism shared across species. Indeed, a study, performed on awake monkeys, investigated the sparseness of thousands of V1 neurons recorded with 2-photon imaging (Tang *et al.*, 2018). The recording of the neuronal responses to 2250 different natural images showed that only 0.5% of neurons respond strongly to any given natural image. However, this population activity is sufficient to discriminate visual stimuli with high efficiency. According to these authors, primary visual cortex is “super-sparse” because of these extremely high values of sparseness. These findings highlight the absolute necessity for the experimenters to characterize the response to every natural scene used for stimulation.

Notably, Froudarakis and colleagues (2014) did not find such high sparseness values. One possible explanation for such discrepancies may reside in the fact that Tang and colleagues’ two-photon recordings were performed with GCaMP6 that saturates when firing rates are above 60Hz. They overcame this technical issue by using GCamP5, which allows a precise measurement of neuronal response and their sparseness. The two-photon results also differ from those obtained with electrophysiological recordings because unlike electrophysiology, two-photon recordings can even track cells that are not responding to the stimulus.

All the studies discussed in this section investigated either the *population sparseness* or the *lifetime sparseness*, very few of them compared directly the two measurements. Indeed, the lifetime sparseness studies always assume that, by computing it on a high number of neurons, one could estimate the population sparseness.
In a recent report, the Allen institute (De Vries et al., 2018) compared the lifetime and population sparseness evoked by artificial and natural stimuli in the primary visual cortex of awake mice and confirmed the assumptions made about lifetime and population sparseness. Indeed, the correlation the two measurements turned out to be very high, which allows the experimenter to draw similar conclusions. Thus, they observed that natural scenes evoked a higher population and lifetime sparseness than drifting gratings. These findings argue for a very well-preserved mechanism of cortical processing across mammals.

De Vries and colleagues (2018), along with other studies (Haider *et al.*, (2010); Baudot *et al.*, (2013)), observed that the increase in sparseness is always associated with an increase in the reliability of the response. Remarkably, Baudot and colleagues found that the increase in sparseness is mediated by an increase in reliability of the membrane potential trajectories.

7.2.3 Reliability

One can consider that a neuron is extremely reliable if the repeated presentation of the same stimulus always evokes the same response. However, due to inherent variability present in primary visual cortex, one needs to present the same stimulus many times in order to obtain probabilistic estimates (mean, variance) of the stimulus-locked response. Figure 1.7.4 illustrates the response of a simple cell to a DG presented at the preferred orientation. It is clear that if we only analyze different trials (one row on the figure) the response is never the same, but we can observe that the temporal pattern of the response is modulated by the temporal frequency of the stimulus. However, if we average the responses across trials, a deterministic functional response emerges (black curve at the bottom of the figure). By computing the mean firing rate, experimenters can overcome the additional variability of cortical dynamics.

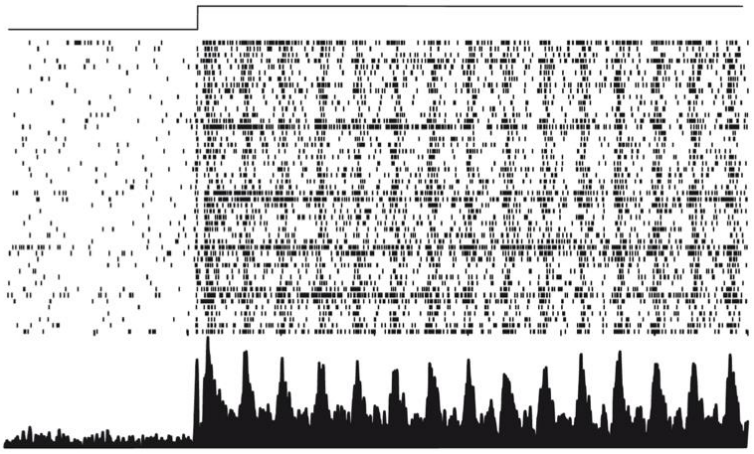

Figure 1.7.4 Response of a simple cell to a DG presented at the preferred orientation. Each row represents a trial. Black curve represents the mean of all the trials (reprinted from Cyril Monier, personal communication)

In order to further quantify the variability of the firing rate, different techniques have been developed. Among them we can cite the Fano Factor which is the variance of the response divided by its mean. Notably, the Fano Factor is biased by the firing rate of the cell (Churchland et al., 2010; Ecker et al., 2014). Thus, this method has to be used carefully. For example, in Baudot and colleagues (2013) work, cells below a certain firing rate were not included in the Fano Factor analysis. Yet, in the previous section, we discussed the fact that neuronal activity can be sparse, which leads to low firing rates. Excluding these cells from their analysis might have biased their results. Despite this technical limitation, neuronal responses in many cortical areas have been modeled with a Poisson process, which assumes that the Fano factor is equal to 1.

Yet, experimental reality is more complex than the theoretical one. Indeed, the Fano Factor can be modulated by different influences such as the global excitability state of the cortex. Indeed, since FF is a variability measure, it seems natural to think that the modulatory factors evoked by Goris *et al.* influences it. Ecker and colleagues (2014) compared the FF values between awake and anesthetized animals. They recorded the single unit activity in response to DG and observed that for both anesthetized and awake animals, neuronal responses display a great variety of Fano Factors. In awake animals, cells have Fano Factors above and below 1, but the mean FF of the population is above 1. In anesthetized animals, very few cells have a Fano Factor under 1 and the mean FF is higher than the one observed in awake animals (Figure 1.7.5).

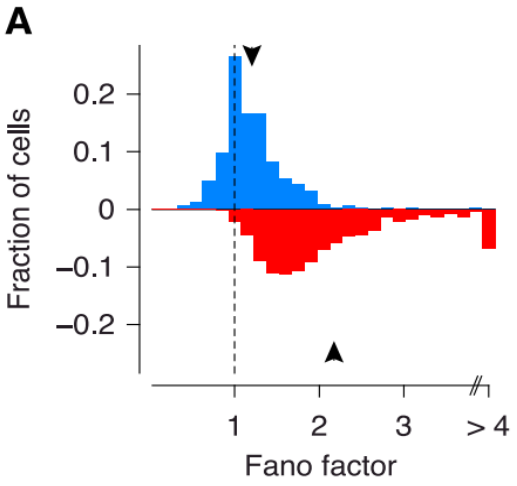

Figure 1.7.5 Fano Factor of V1 cells in awake and anesthetized primates. **A.** Distribution of Fano Factors (arrow indicates mean). (reprinted from Ecker *et al.*, 2014)

Thus, demonstrating that anesthesia has a great impact on the variability of the response is crucial and implies that reliability studies should include this modulatory factor. Surprisingly, a study performed by Kara et al., (2000) found very different results from those of Ecker and colleagues. Indeed, Kara and colleagues recorded in anesthetized and paralyzed cats, simultaneously, from retinal, thalamic and cortical (V1) cells and found that in these three structures, the Fano Factor was sub-Poissonian (below 1) but increased along the visual hierarchy (retina: 0.15; LGN: 0.33; V1: 0.52). These surprising results can be explained by the fact that they only recorded cells receiving monosynaptic inputs from the LGN. Indeed, layer 4 receives inputs from the thalamus, which are known to be very reliable (Vries et al., 2018). This leads to very reliable responses in cells monosynaptically connected to LGN. On the contrary, layers 2/3 and 5/6 receive less reliable inputs (Hirsch *et al.*, 2002), which can lead to these higher reliability values. Therefore, the Fano Factors below 1 observed by Ecker and colleagues (2014) could originate from neurons receiving monosynaptic inputs from the LGN

The previous studies investigated V1 variability with drifting gratings as a visual stimulation. Yet, as shown throughout this manuscript, visual responses are modulated differently as a function of the stimulus statistics. An intracellular study performed on cat primary visual cortex investigated the stimulus dependency of the reliability by presenting a set of artificial and natural stimuli (Baudot *et al.*, 2013). According to the results of these authors, all stimuli evoked a sub-Poissonian Fano Factor, with natural images evoking the most reliable response. However, only cells with a firing rate above 5Hz were considered in this study. Kara and colleagues (2000) demonstrated that variability decreases when firing rate increases. Thus, by eliminating 5 cells for the natural stimulation and 11 cells from the artificial stimulation, they might have biased their results towards low Fano Factor values. Another explanation for their low Fano Factors could be an oversampling of cells in layer 4 receiving monosynaptic thalamic inputs. However, Baudot and colleagues overcame the problems linked to the Fano Factor analysis by measuring the reliability with another method, the trial-to-trial correlation of the response. This method allowed the confirmation of the results obtained with the Fano Factor, *i.e.* natural movies animated with eye movements evoke a more reliable response than the artificial stimuli, both at the subthreshold (membrane potential) and spiking level. To determine which statistics were the most important in this increase in reliability, they randomized either the

spatial (altering spatial correlations) or the temporal statistics (altering temporal correlations) of the natural scene. Based on the Rikhye & Sur (2015) findings, a difference in reliability between the unaltered image and the one with altered spatial correlations is expected. Surprisingly, no difference in reliability between the three stimuli was observed, possibly originating from the small number of neurons used for this comparison (11 cells).

An interpretation of the increase of variability evoked by natural statistics is given by Baudot and colleagues, that natural animated scenes change the dynamics of the instantaneous balance between excitation and inhibition by creating highly selective "temporal windows of spiking opportunity" allowing reliable events to happen. This feature is reminiscent of the demonstration *in vitro* by Nawrot et al., (2009) Synaptic signals originating from spatially distinct sources in specific temporal sequences are integrated in a very reliable and precise manner. Thus, natural images, with their mixture of low and high frequencies may allow the integration of the synaptic signals in a very deterministic manner leading to a very reliable response.

A slightly different interpretation is put forward by Haider and colleagues (2010). They investigated intracellularly, in the anesthetized and paralyzed cat, how natural images and center surround interactions affect the reliability of the response. To do so, the trial-to-trial correlation of the response was computed. Regarding classic regular spiking cells, the concomitant stimulation of the center and the surround increases the reliability of the response, both at the spiking and subthreshold level. On the other hand, fast spiking neuron reliability is not modulated by center surround interactions. This increase in reliability may originate from an increase in the amplitude of inhibitory postsynaptic potentials (IPSPs) and an increase in the trial-to-trial reliability of excitatory postsynaptic potentials (EPSPs). Interestingly, these synaptic events were mirrored by spiking activity recorded in thin RS cells and FS cells.

Strikingly, Haider and colleagues found quite different values of reliability for the spiking activity than Baudot *et al.* (2013) (0.2 vs 0.04). Similar results, on a bigger population, have already been observed in mouse primary visual cortex (Kampa et al., 2011). In this study, following presentation of different natural scenes to anesthetized mice and recording the neuronal activity with two-photon imaging, the observation was made that among hundreds of neurons, only a fraction of the population displayed high levels of reliability in response to the natural stimulation. Based on these findings, it is likely that among their small sample of recorded cells, Baudot and colleagues recorded a higher fraction of less reliable cells while Haider and colleagues recorded a higher fraction of reliable cells. Because of the heterogeneity of the reliability observed in Kampa's work, in this thesis work we used a more adapted representation of the variability by using box plots instead of histograms. In this PhD, we investigated this issue by recording hundreds of neurons, the results are reported in Chapter III.

Throughout this manuscript, we reported different results proving the stimulus dependence of the neuronal response. However, one property that has been set aside is how the frequency content of the visual response matches the statistics of the stimulus. As discussed above, Baudot *et al.* showed that natural images animated with eye movements induced a more reliable response than artificial stimuli (*i.e.* drifting gratings, dense noise, gratings animated with eye movements). In addition to this reliability analysis, a wavelet analysis of their recordings was performed, which allowed the computation of the signal to noise ratio (SNR, which is a measure of reliability) for each stimulus. This analysis leads to two observations. On one hand, neurons responding to natural scenes have

a strong SNR for low frequencies (natural scenes have a strong power spectrum density in the low frequency range). Note that the natural scenes can be seen as an input generator mixing reproducible low and high frequency events, in a way similar to the current pattern injected by Nowak and colleagues (1997) or Mainen and Sejnowski (1995).
On the other hand, in response to DG, the SNR value was very high only for the frequency of the grating. This confirms that the stimulus statistics have an important influence on the response of V1 neurons. Indeed, these statistics recruit the inputs of the neurons and constrain their responses. Natural scenes induce a more reliable response than DG because they are statistically richer and induce a higher constraint on the neuronal activity. This higher constraint prevents the modulatory factors described in the previous section from increasing the variability of the response. These findings are consistent with the results obtained by Rikhye and Sur (2015) that highlighted the link between low frequencies and reliable responses (Figure 1.6.9).

In this introduction, we described the anatomical and functional properties of primary visual cortex. We focused our discussion on the fact that V1 is a highly complex structure, composed of different functional units (*i.e.* the laminar compartments), and that within these structures the visual responses are strongly modulated by the statistics of the visual input. We reported the fact that the dynamics of cortical variability are different if artificial or natural stimuli were presented. The results obtained so far tend to confirm and contradict some of the predictions of Barlow's efficient coding theory. For example, natural statistics increase the sparseness of the response but also evoke high correlations between pairs of neurons. In order to understand visual processing, the characterization of these responses is crucial. This comprehension of visual processing requires different steps of investigation. Indeed, how the different layers process natural statistics remains unknown. Moreover, which are statistics that modulate the cortical variability dynamics? An exploratory approach investigating these aspects would pave the way for many hypothesis-driven studies, which will deepen our understanding of primary visual cortex.
The work reported in this PhD manuscript investigated the laminar dependency of cortical dynamics of variability and how this is modulated by the spatio-temporal statistics of natural stimuli.

II. METHODS

In this section, we will review all the experimental and technical procedures used in the Results section of this PhD work.

1. ANIMAL PREPARATION

All experiments were performed in anesthetized and paralyzed adult cats of either sex, according to the American Physiological Society's Guiding Principles for the Care and Use of Animals. The animals used in the experiments were bred in the Central Centre National de la Recherche Scientifique Animal Care facilities of the Campus of Gif-sur-Yvette (French Agriculture Ministry Authorization: B91-272-105) under required veterinary and National Ethical Committee supervision.

Cats were hosted in the animal facility of Gif sur Yvette in specific rooms. The facility is composed of free spaces where the animals can move freely. The environment is supplemented with natural and artificial platforms, toys and balls for their well-being. They have access to natural light. Males and females are separated by a metallic grid. For reproduction, the light cycle is fixed at 14 hours of light per day and two females in heat are mated with a male in a separate room. Females and their litter are kept isolated until the new-borns are weaned. A quarantine room allows separating exterior animals arriving to the facility from the rest of the colony until a veterinarian confirms the absence of pathogens. Animals are in contact with humans daily, their food, water and litter box are changed every day. A veterinarian keeps up to date the vaccination of each animal, visiting the facility every two months.

In all experiments, adult cats of either sex weighing between 2 and 4kg were initially anesthetized with an intramuscular injection of Alfaxolone (1mL/kg). An intravenous catheter was inserted in the femoral vein in order to maintain the anesthesia during the rest of the surgical procedure. After tracheotomy, animals were placed onto a stereotaxic apparatus and head-fixed with ear bars coated with Xylocaine (5%), eye bars and a palate bar were also placed to maintain optimal head-fixation. The stereotaxic apparatus was mounted on a pneumatically controlled air table to avoid vibrations.

Once in the apparatus, paralysis was induced and maintained during the experiment with an intravenous injection of a synthetic curare: rocuronium bromure (4mg/kg/h), mixed with glucose (10%) and sodium chloride (0,9%). Animals were placed under artificial respiration, and anesthesia was maintained with Isoflurane (0.5-1.5%) in a mixture of 70% N_2O and 30% $O_{2.1.}$ Body temperature was monitored with a rectal probe and maintained at 38°C by a thermal blanket. Expired PCO_2, EEG and EKG are informative about the physiological state and anesthesia of animals and were monitored during the whole experiment. PC02 was maintained between 3.5 and 4.5%. Contact lenses filled with "viskyal" (Sodium hyaluronate) were placed immediately after paralysis in order to avoid any drying of the cornea and were later filled with atropine.

A local anesthetic (Xylocaine) was injected subcutaneously at the top of the head before cutting the skin in order to expose the skull. Stereotaxic coordinates of the area centralis were determined

according to the atlas of Tusa and Rosenquist (1979) and bilateral craniotomy was achieved by drilling holes (3-4 mm diameter) on the skull surface above Brodmann's area A17 (coordinates between P=-2, L=2 and P=-5, L=3), following the curvature of the cat primary visual cortex. A chamber was placed on the skull and fixed with dental cement. The chamber was filled with ACSF in order to keep the cortex hydrated. Finally, in order to access the cortex, the dura mater and other membranes were removed with a micro-surgical knife.

2. EXTRACELLULAR RECORDINGS

Extracellular data was recorded using three different types of silicon probes manufactured by Neuronexus. The three Neuronexus probes that we used are: 2x16 (A2x16-10mm-100-500-177) and 1x64 (A1x64-Poly2-6mm-23s-160) The electrodes were lowered through the cortex using a micromanipulator (Luigs & Neumann). In order to minimize tissue damage as much as possible, advancement through the brain was made very slowly 1µm at a time (~0.4 µm per second).

Data was acquired with a Blackrock Cerebus system. Signal from the probes was amplified, filtered and digitized by an amplifier, then transmitted to a Neural Signal Processor (NSP) via an optical fiber. The amplifier filters the signals with a first order Butterworth high pass filter at 0.3 Hz and a third-order Butterworth low-pass filter at 7.5 kHz. The filtered neural signals from each electrode are digitized with 16-bit resolution at 1 uV per bit with a sampling rate of 30,000 samples/sec. The analog filtering of the electrode signals allows both low frequency local field potentials and extracellular spike signals to pass through. The neural signals are later separated into low frequency (filtering between 1-250Hz) and spike signals (filtering high pass filter at 1 kHz) by digital filtering in the Neural Signal Processor (NSP). The NSP does an online analysis and then transmits the processed data to a host system via an Ethernet cable. On the host PC, a homemade software, Elphy (G.Sadoc, CNRS), was in communication with the Blackrock system in order to save the acquired data.

3. VISUAL STIMULATION

Nictitating membranes were retracted with Phenylephrine (1%) and pupils were dilated with atropine (0.5%) to perform a fundus examination. Projection of the fundus allowed us to perform a visual correction with additional contact lenses positioned in front of the eyes, if needed, and to precisely draw the blind spot of each eye and then determine the coordinates of the *area centralis.*

An LCD screen with a resolution of 1920x1080 pixels and a refreshing rate of 144Hz was placed 57 cm from the animal (distance for which 1cm on the screen is equal to one visual degree). All visual stimuli were generated with ELPHY, maximum and background luminance were set at 40cd/cm² and 12cd/m² respectively.

- **Sparse Noise stimulation**

The precise position and spatial organization of the RF was measured with sparse binary noise presented in a square matrix encompassing the identified area of interest. This matrix was divided into100 regions (10x10) where visual responses were identified (hence approximately 0,5 by 0,5° of visual angle for a square of 5°). This formed a grid in which bright (40 cd/m²) and dark (1 cd/m²) small squares were sequentially flashed in each position, one position and luminance at a time, in a pseudo random fashion against a uniform background luminance (20 cd/m²). The duration of presentation of each square was 48 ms.
The map of visually evoked responses was obtained using a forward correlation method. Each trial sequence was repeated between 10 and 30 times. Several successive mappings were often necessary to adjust the size and position of the area totally enclosing the local field potential and multi-unit receptive fields.
Once the location and spatial extent of the RF were assessed, the ocular dominance was probed and the following stimulation sequences were restricted to the dominant eye only (monocular viewing).

- **Drifting Gabor stimulation**

To determine the preferred orientation, spatial frequency and temporal frequency of the receptive fields, Gabor patches (GP) were obtained by convolving sinusoidal gratings with a Gaussian envelope. GP that covered the receptive fields were drifted at 12 orientations ranging from 0 to 360° by 30° incremental steps for 6 spatial periods: 0.2, 0.4, 0.6, 0.8, 1.2 and 1.6 cycles per degree of visual angle.

- **Dense Noise Stimulation**

White noise consisted of a dynamic sequence (13.3 ms refresh period) of high spatial definition (50 * 50 pixels of 0.39°) ternary dense noise. This formed a grid in which bright (40 cd/m²), dark (1 cd/m²) and grey (20 cd/m²) small squares were simultaneously flashed in each position, in a pseudo random form. The duration of presentation of each square was of 48 ms.

- **Natural Image Stimulation**

The following stimulation sequences consisted of two main protocols.
For the first protocol, four types of stimuli with increasing complexity were used: Drifting Gratings (DG), Gratings with simulated Eye Movements (GEM), Natural Images with simulated eye movements (NI) and Dense Noise (DN) (Figure 2.1.1).

Eye-movements are classically decomposed into intermittent ballistic movements, i.e. saccades, of large but variable amplitude, separated by fixation episodes. During fixation, the mean position of the eye drifts slowly in time, with superimposed very low amplitude tremors at high frequency (40–100 Hz range) as well as microsaccades. In order to simulate in a realistic way the continuous changes imposed by eye-movements during natural scanning of visual scenes, we built a model of the retinal flow (example in Figure 1C) whose kinematic parameters were fitted on the basis of

measurements previously made in the freely behaving cat (Pritchard and Heron, 1960; Collewijn, 1977; Olivier et al., 1993). A more detailed description follows:

Saccades

The saccade amplitudes and intersaccadic intervals were chosen randomly from the distribution established for saccadic and head gaze movements in the freely behaving cat (Collewijn, 1977). An estimate of the duration of the saccade (D_S) was made by using the best linear fit between saccadic amplitude (A_S) and duration:

$$D_S = 1.9 \times A_S + 63 \quad (1)$$

where D_S is expressed in ms and A_S in steradian degrees (°) of visual angle. The saccadic spatio-temporal profile was modeled by the following sigmoidal function F(t):

$$F(t) = -\lambda A_S + (A_S + 2\lambda A_S)/(1 + e^{(-2-\lambda)/(D_S(D_S/2-t))}) \quad (2)$$

where λ is a constant threshold fixed at 5%. The direction of the movement was chosen randomly from a uniform [0°, 360°] distribution. Since most saccadic paths present small drifts of directional angle during their execution (Yarbus, 1967; Rucci and Desbordes, 2003), an ad-hoc sinusoidal variation of direction during the drift path was fitted to real recordings:

$$f(t) = \Delta\theta \sin(2.\pi t.\tau/D_S) \quad (3)$$

where the amplitude of direction change (Δθ) was chosen randomly from a uniform distribution between 0° and 4°, and the fraction of during which it operated (τ) was chosen randomly between 0.5 and 1 (relative to the full saccade duration).

Drifts

The drift amplitude (A_D) was chosen randomly from a Gaussian distribution with a mean of 1.21° and a standard deviation of 0.63°. The duration (D_D) was derived from the best linear fit with A_D. These parameter values were taken from measures in the behaving cat (Olivier et al., 1993):

$$D_D = 41.7 \times A_D + 53.7 \quad (4)$$

where D_D is expressed in ms and A_D in °.

The direction of drift movement was chosen randomly from a uniform [0°, 360°] distribution. The same ad-hoc sinusoidal variation of direction during the drift path (Equation 3) was fitted to real recordings, but with direction change chosen randomly between 0 and 29°.

Tremors (during drifts)

Tremor eye-movements are typically of miniature amplitude, ranging from 0.001 to 0.017° [0.006–0.013° in Rucci and Desbordes (2003); 0.005° in Ratliff and Riggs (1950); 0.001°–0.004° in Ditchburn and Ginsborg (1952); Ditchburn (1973)], with a mean amplitude of 0.007° in the cat (Pritchard and Heron, 1960). The simulation of tremor was constrained by the spatial discretization of the screen (1024 × 768 pixels) and the imposed viewing distance (57 cm). In the present experiments, the smallest programmable distance between two neighboring pixels was 0.039°. For spectral characteristics, we chose to remove most of the tremor energy due to low amplitude micro-movements while keeping its highest amplitude components. This was achieved by using a white noise signal through a Bessel filter, between 40 and 80 Hz (Eizenman et al., 1985). The sequence movement thus obtained was then discretized, using only three possible inter-pixel amplitude values (−1, 0, 1), and low-pass filtered.

Microsaccades

Microsaccades are particularly rare in cats (Körding et al., 2001) and our modeled “frozen” eye movement sample sequence contains only three of them positioned at the end of a tremor. Their amplitude was chosen randomly from a Gaussian distribution with mean and standard deviation both set to 1°, thresholded for amplitudes less than 0.02°, as found in humans (Ditchburn, 1973). An estimate of their duration (Dms) on the basis of Ditchburn's observations in humans (Ditchburn, 1973), was given by the best linear fit between micro-saccadic amplitude Ams and duration:

$$D_{ms}=2.25\times A_{ms}+20 \quad (5)$$

where D_{ms} is expressed in ms and A_{ms} in ° of visual angle.

The microsaccadic spatio-temporal profile, direction and variation of angle during the microsaccade were modeled as for saccades.

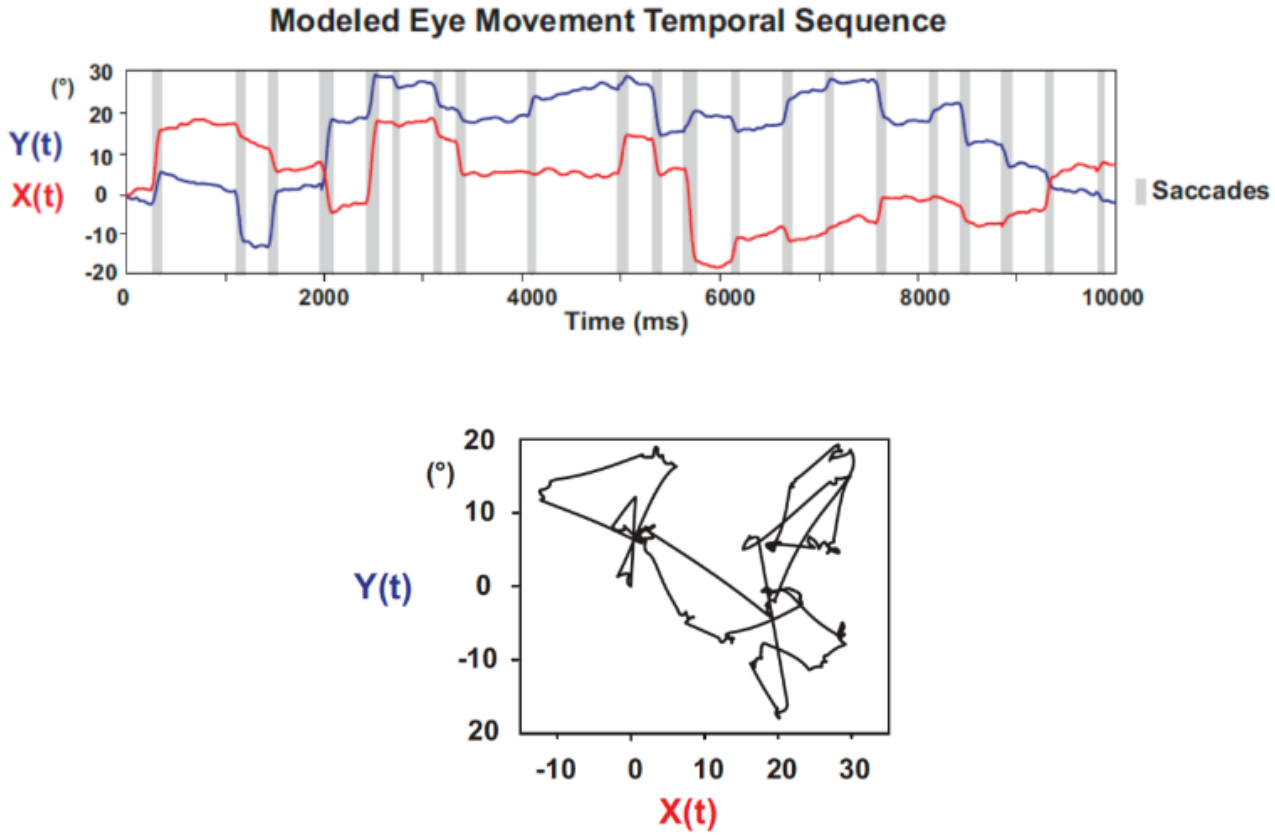

Figure 2.1.1: Temporal profile of the X and Y coordinates of the modeled eye-movement sequence. Saccadic episodes are indicated by a shaded box. Scan path generated by the modeled eye movement sequence. The natural scene image is centered on the RF center at the start of the animation and the same displacement pattern is applied to all experiments.

Each stimulus was presented at least 20 times, in three different conditions:

-The center only stimulation (C), stimuli were only showed on the RF.

-The surround only stimulation (S), stimuli were showed on the whole screen except for the RF center, which was masked.

-The full field stimulation (CS), stimuli were showed both on the center and on the surround of the RF.

The mean luminance and contrast of each movie were equalized to differ only in their higher-order statistics.

For the second protocol, we developed four control natural images where the spatial and temporal frequencies were modified.

- Natural images where the spatial frequencies, *i.e.* the phase, were randomized in order to remove the high order correlations from the image (NI-RS).
- Natural images where the temporal frequencies, *i.e.* the pattern of the eye movements, were randomized in order to remove its high order correlations (NI-RT).
- Natural images where both temporal and spatial frequencies were randomized in order to remove their high order correlations (NI-RST).
- Natural images where eye movements were only saccades (NI-SAC).

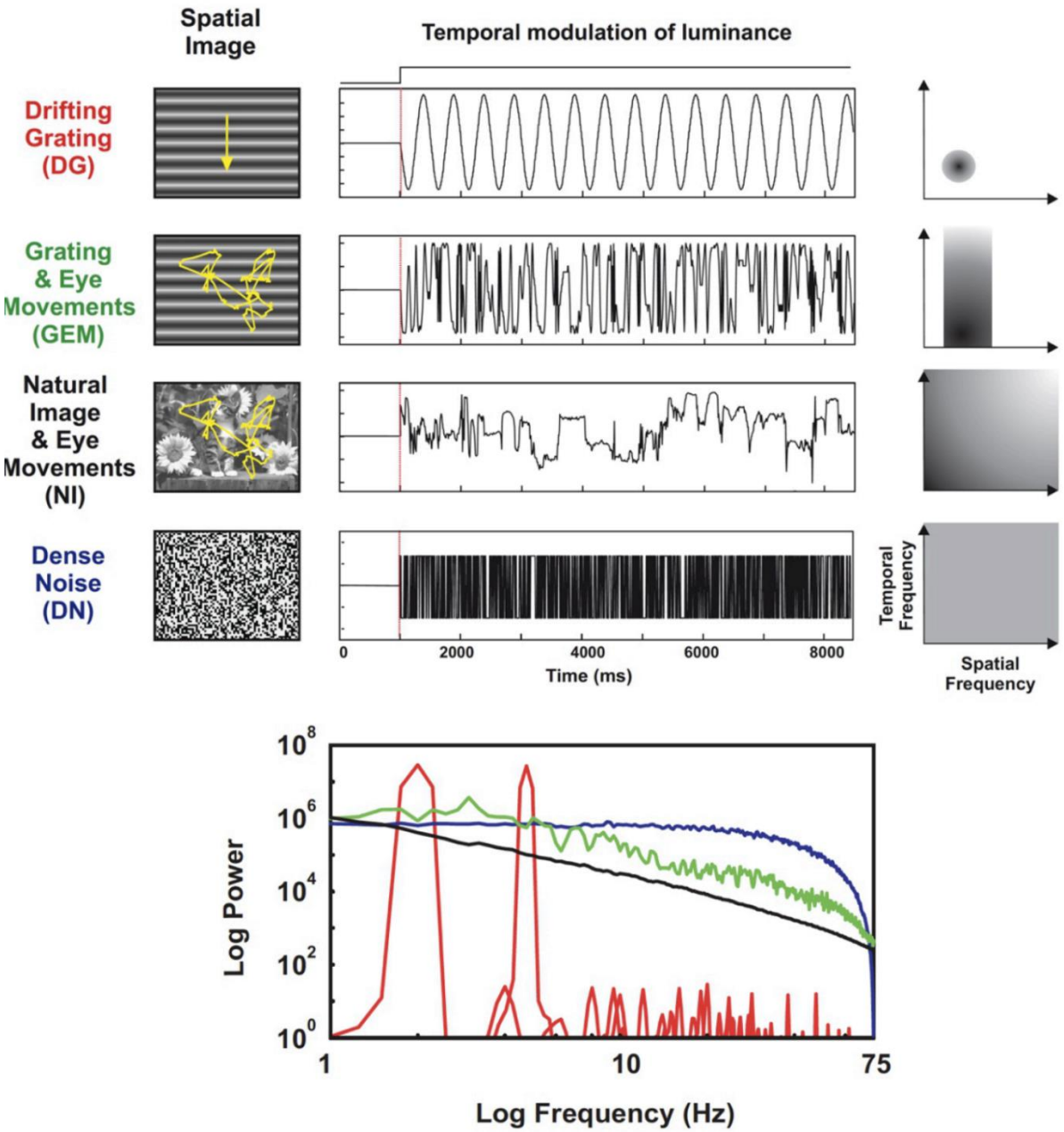

Figure 2.1.2 Spatio-temporal statistics of the four stimuli that were presented (reprinted from Baudot *et al.,* 2013).

4. HISTOLOGY

For all experiments, probes were covered with DiI ($DiIC_{18}(3)$), a lipophilic membrane dye that stains the cells and allows us to locate where the probe was in the cortex. At the end of the experiment, animals were euthanized with a lethal dose of T61 (Embutramide, 0.3mL/kg). Then an intracardiac perfusion was made with paraformaldehyde (4%) in order to fix brain tissue. After perfusion the pertinent part of the brain is removed, sliced and a DAPI or cytochrome oxidase staining is made on all the slices in order to mark neurons. Cytochrome oxidase stains the cell bodies in layer 4 and allows a more precise layer identification than DAPI. DiI and DAPI staining were visible under fluorescence with an adapted microscope. These procedures allow us to precisely locate the position of the probe in the cortex.

5. SPIKE SORTING

Spike sorting was performed automatically with the klusta suite (Rossant *et al.*, 2016). The quality of separation was based on a clear refractory period and cluster separation. Unit stability, in terms of waveforms, amplitude and drifting, was also checked across the whole recording session. All clusters were checked manually after the automatic sorting.

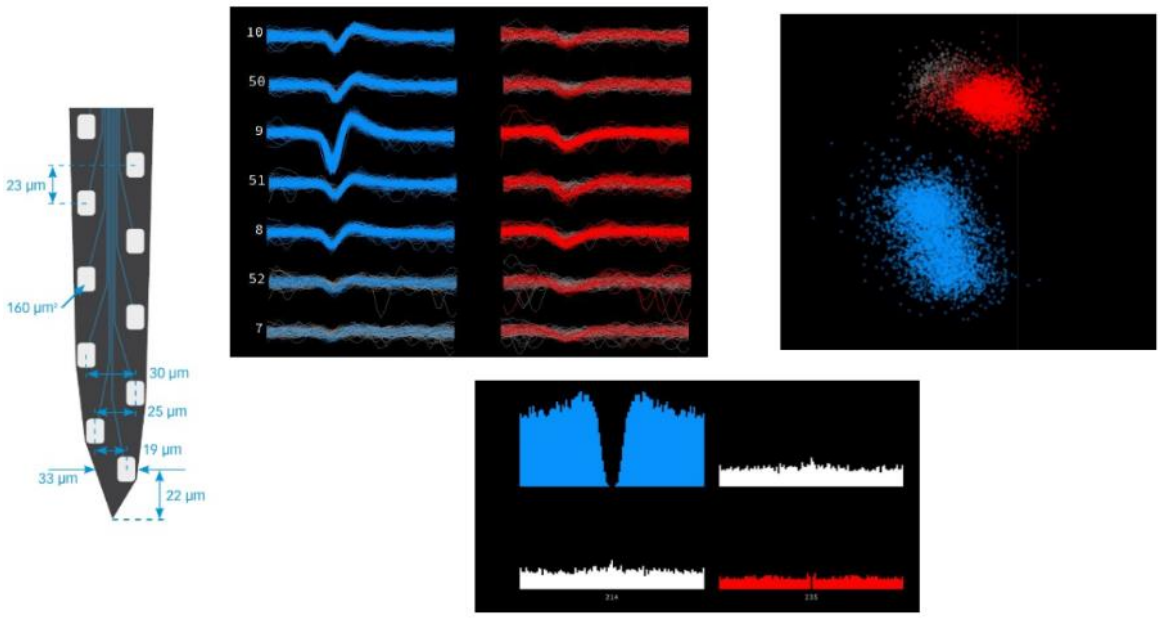

Figure 2.1.3. Example of manual curation after spike sorting with the klusta suite. On the left: spacing between the recording sites of the 1x64 probe. The other panels illustrate the sorting of a neuron based on a clear refractory period and cluster separation.

6. NEURONAL CLASSIFICATION

Neuronal classification from extracellular recordings relies on the careful quantification of the spike waveform shape. This classification separates units into the usually denominated fast spiking (FS) and regular spiking (RS) units. FS cells are normally thought of as inhibitory neurons, while the RS cells are recognized as dominantly excitatory. Using high impedance tungsten electrodes allows the clustering of the recorded spiking units by their bimodal distribution of spike widths, which is the peak to trough time (Goldin and Mindlin, 2017). Sometimes, the use of another variable is needed for better separation, and the firing rate is often selected as the second measure. However, this rate can be dependent on the type of stimulus used or may change during long experiments, so many studies have selected different measures. For example, the afterhyperpolarization width (Bruno and Simons 2002, high impedance tungsten electrodes) or the peak to trough amplitude ratio (Cardin et al. 2009, tetrodes or stereotrodes) have been successfully used for unit separation. Some studies have tried to further separate neuronal types within the mentioned RS and FS, for which they looked for more subtle differences. Using as many as 7 spike shape features followed by a principal component analysis (PCA) and subsequent clustering (Rauske et al. 2003, Pt-Ir electrodes), units have been classified into five different families.

The advent of silicon probes has enhanced the capacity of researchers to measure with multiple electrodes simultaneously. Whereas the spikes measured with these devices retain their prominent shape characteristics, a quick glance at their shapes shows a much bigger overlap between spikes of the RS and FS type than what is found with tungsten electrodes. For this reason, in order to have separated groups, ambiguous units have to be discarded from the analysis (Zengcai et al. 2014, silicon probes).

In our work, we decided to make a conservative classification of the units recorded, for which we quantified seven spike features. Five of the seven features are widths, all referenced to the time at the minimum peak of the spike. The five features are: the peak to peak width (prel2), the total width (width p2p), the width of first and second peaks relative to the minimum (peak1 and peak1-2) and the width between the two crossing points (crel1). Finally, the two peak values normalized to the minimum were used (peak trough ratio). An example for an RS and an FS with the mentioned features can be seen in figure 2.1.4-B.

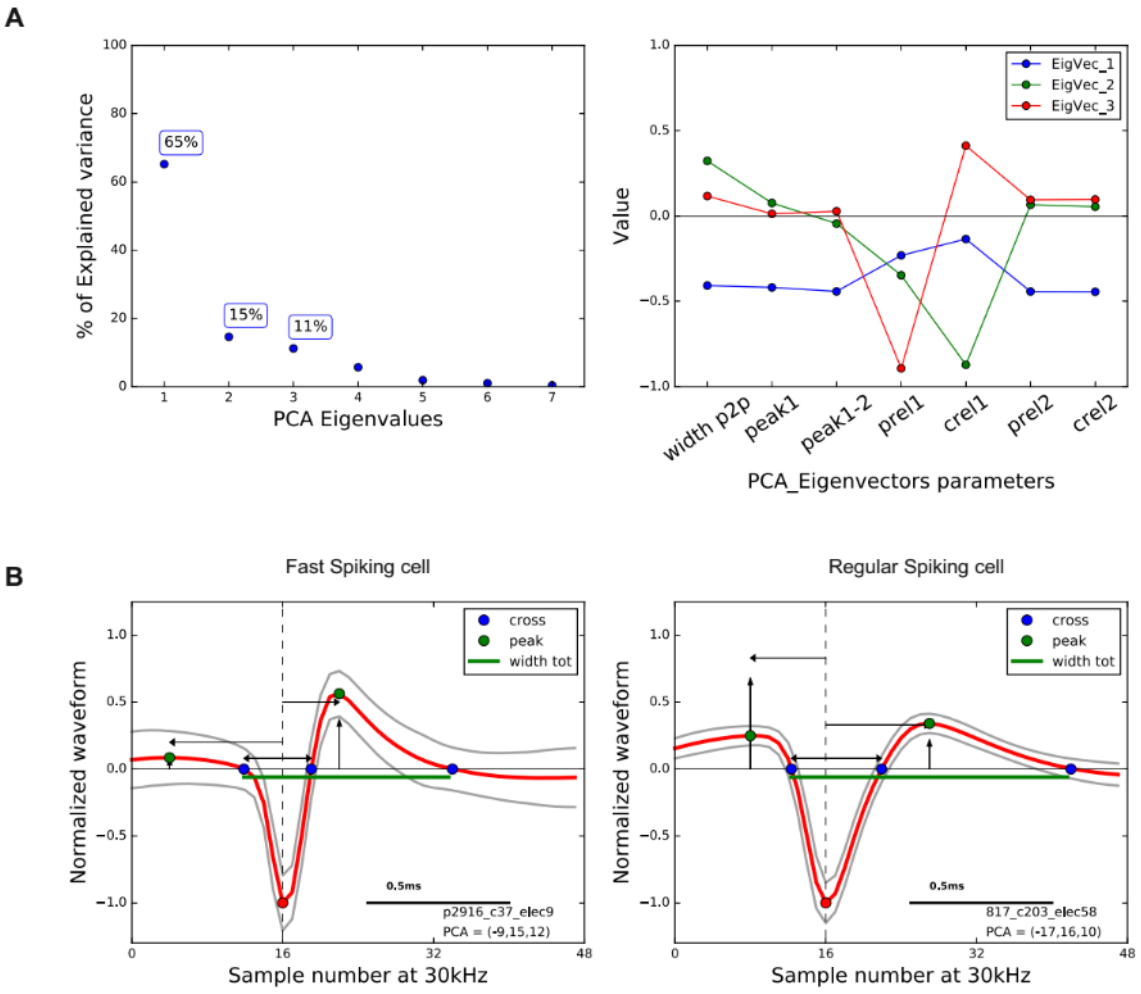

Figure 2.1.4. Features and PCA of our classification method. A. left panel: Percentage of variance explained by the PCA components. Right panel: Weights of each feature in these three eigenvectors. B. Selected features for spike classification.

7. SIGNAL ANALYSIS

In this section, we will describe the analysis performed for this PhD work. Unless specified all these analyses have been performed on all extracellular signals (SUA, MUA and LFP).

7.1. Current Source Density

We computed the current source density (CSD) based on the work of Mitzdorf (1985). He formulated a one-dimensional CSD based on the following equation:

$$CSD(x) = -\sigma \cdot \frac{\phi(x-h) - 2\phi(x) + \phi(x+h)}{h^2}$$

Where ϕ is the voltage, x is the point at which CSD is calculated, h is the spacing of electrodes for computation, and σ is the conductivity of cortical tissue. In order to be able to use this equation, the electrode must be perpendicular to the cortical surface. We took advantage of the black and white squares of the sparse noise stimulation to compute the CSD and experimentally identify cortical layers. We estimated layer 4 as the region where the earliest sink occurred after visual stimulation.

7.2. Trial-to-trial Cross Correlation

The reliability of the responses is measured by computing the cross-correlation (CC)—across trials—of the spiking responses (Multi unit and single unit activity), and of local field potential responses. The reliability was given by the CC peak amplitude at time zero and the temporal precision by the standard deviation of the Gaussian fit.

7.3. Correlations

-Signal correlation (SC) is the correlation between the mean response of two different neurons (SUA or MUA) in response to the same stimulus. The SC defined as:

$$SC = \bar{r_1} \cdot \bar{r_2}$$

Where $\bar{r}$ is the mean response of the neuron.

-Noise correlation (NC) is the correlation of each trial response (after mean subtraction) between two different neurons (SUA or MUA) in response to the same stimulus. Noise correlation is defined as:

$$NC = \sum_{i=1}^{N} (r_1^i - \bar{r_1}) \cdot (r_2^i - \bar{r_2})$$

Where $\bar{r}$ is the mean response of the neuron, N is the number of trials and r_j^i is the firing rate of cell j in trial i.

7.4. Power Spectral Density

LFP frequency analysis was performed using a fast Fourier transform analysis. The magnitude of the spectrum was computed using Welch's method. The signal was split into Hamming windows, the magnitude of each window was then computed and averaged in order to obtain the power spectral density (PSD). To obtain the relative power spectral density (R-PSD), we divided the mean PSD at each recording site by the mean PSD of the spontaneous activity across all channels.

7.5. Coherence

The coherence, $Coh(f)$, measures the degree of the linear relationship between two LFP signals $s_1(t)$ and $s_2(t)$ in the Fourier space, and is defined by:

$$\mathrm{Coh}_{S_1,S_2}(f) = \frac{| < S_1(f).S_2^*(f) >_t |^2}{< |S_1(f)|^2 >_t . < |S_2(f)|^2 >_t}$$

where S_1 and S_2 are the Fourier transforms of s_1 and s_2. The angular brackets symbolize window averaging (1 s-long Hann windows shifted by 1 s steps in the present study). The coherence equals one for linearly related signals and decreases below one when the signals are non-linearly related, and/or corrupted by noise. A coherence of 1 implies a very synchronized signal while a coherence of 0 a very desynchronized one.

7.6. Sparseness

To quantify sparseness on SUA and MUA, we used a non-parametric index (Vinje and Gallant, 2000):

$$S = \left(1 - \left(\sum r_i/n\right)^2 \Big/ \sum (r_i^2/n)\right) / (1 - (1/n))$$

where r_i is the response to the ith frame of a movie (averaged across trials) and n is the number of movie frames. S values range between 0 (0%) for a dense code, to 1 (100%) for a sparse code. The duration of the movie frame is 13.3 ms. The sparseness index was calculated also as a function of bin width values ranging between 1 and 250 ms (with a step of 1 ms).

7.7. Fano Factor

To quantify the Fano Factor, spike counts were computed by dividing the time axis in successive 15 ms bins. We then computed the variance (across trials) and the mean of the spike count. A scatter plot of the variance vs. the mean was compiled, with one point per time window, for the whole duration of the stimulation (10 s). The raw Fano factor was given by the slope of the regression line relating the variance to the mean.

7.8. Stimulus-Locked Time-Frequency Analysis

We applied here measurement methods developed by Baudot et al (2013) for intracellular and extracellular signals. Extracellular signals were convolved for each trial (one repeat of the same movie clip) with an array of complex-valued normalized Gabor functions $\psi_f(\tau)$

$$\Psi_f(\tau) = (a/\sqrt{f}) \cdot \exp(-2.\pi.i.f.\tau) \cdot \exp\left(-\frac{\tau^2}{\sigma^2}\right)$$

where a is a constant such that the energy of the wavelet is equal to 1. To improve the readability of the time-frequency representation, the Gabor decomposition presented here is largely oversampled: the Gabor filter bank is non-orthogonal, with wavelet frequencies ranging from 1 to 150 Hz (with incremental steps of 1 Hz), and a temporal sampling period of 1 ms. To achieve a fine temporal resolution (important for spike events), the normalized Gabor function had a Gaussian window variance equal to two Gabor periods ($\sigma.f$ = 2). This time-frequency decomposition allows the extraction of Signal power, Noise power, and Signal to Noise ratio (SNR) power. This analysis can be viewed as an extension of the Signal and Noise estimation method proposed by (Croner et al., 1993) to the time-frequency domain.

We define $S(t,f)$ as the complex result, at time t and frequency f, of the convolution between the wavelet and the response $X(t)$ for each trial:

$$S(t,f) = \int X(t-\tau) \cdot \Psi_f(\tau) d\tau$$

The Signal power $S_{est}(t,f)$ of the stimulus-locked waveforms is given by:

$$S_{\text{est}}(t,f) = \left|\left\langle S_i(t,f)\right\rangle_i\right|$$

where angular brackets ⟨⟩ indicate the average across all trials i of the wavelet transform in the complex domain and straight brackets indicate the squared modulus.
The Noise power $N(t,f)$ is measured as the average distance between the individual trial vectors and the average vector of the wavelet transform in the complex domain:

$$N(t,f) = \left\langle \left| S_i(t,f) - \left\langle S_i(t,f)\right\rangle_i \right| \right\rangle_i$$

The Signal to Noise ratio $SNR(t,f)$ is calculated as:

$$SNR(t,f) = \frac{\left|\langle S_i(t,f)\rangle_i\right|}{\left\langle\left|S_i(t,f) - \langle S_i(t,f)\rangle_i\right|\right\rangle_i} = S_{\text{est}}(t,f)/N(t,f)$$

In the case of spike train signals, SNR was assigned a zero value for the times and frequencies when a total absence of activity was observed for all trials ($Si\ (t,f) = 0, \forall\ i$). Signal, Noise, and SNR power spectra are obtained by averaging the squared functions over time:

$$F_{\text{SNR}}(f) = \int_{t_{\text{start}}}^{t_{\text{end}}} \left(\text{SNR}(t,f)\right)^2 / (t_{\text{end}} - t_{\text{start}})dt$$

$$F_{\text{Signal}}(f) = \int_{t_{\text{start}}}^{t_{\text{end}}} \left(S_{\text{est}}(t,f)\right)^2 / (t_{\text{end}} - t_{\text{start}})dt$$

$$F_{\text{Noise}}(f) = \int_{t_{\text{start}}}^{t_{\text{end}}} \left(N(t,f)\right)^2 / (t_{\text{end}} - t_{\text{start}})dt$$

These measures represent the average energy of the Signal, Noise and SNR at a given frequency

7.9. Results representation

Some analysis will result in a heterogeneous number of results. In order to represent, in the most authentic way, we will use boxplots.
A random distribution and the boxplots of this distribution are shown in figure 2.1.5.
On this boxplot the central black line represents the median, the extremities of the box are the first and third quartiles respectively. The whiskers represent the maximum and the minimum. In some cases, crosses will also be plotted, they represent the outliers (not show). Finally, a red square will indicate the mean (not shown)

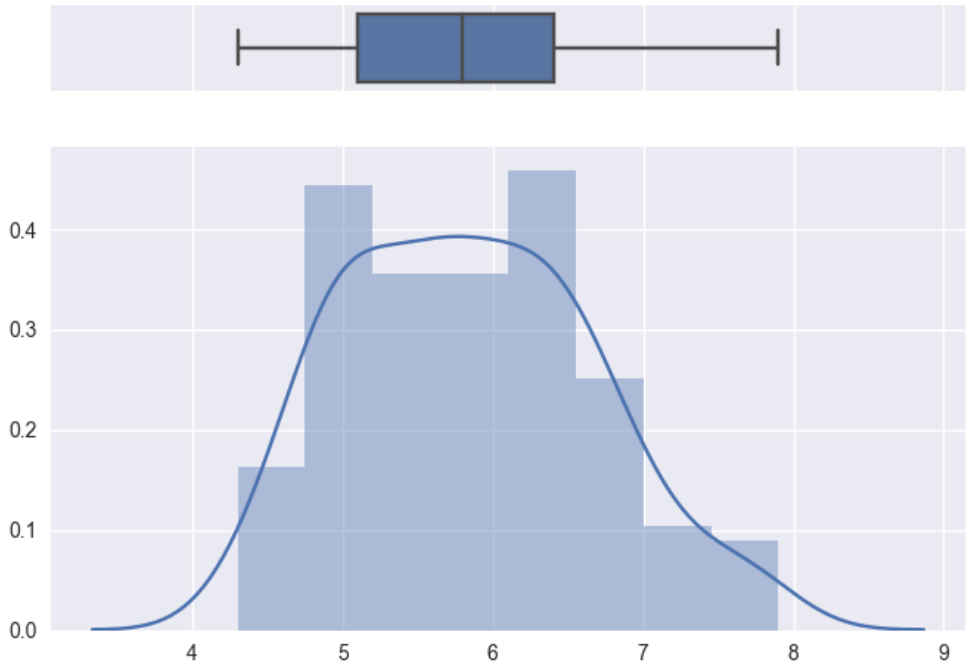

Figure 2.1.5: Example of a boxplot representation of a random distribution.

III. RESULTS

As described in the introduction, our aim is to investigate, in the cat primary visual cortex, the laminar dependency of cortical dynamics of variability and how this is modulated by the spatio-temporal statistics of natural stimuli. In order to answer these questions, we presented artificial (gratings and dense noise) and natural stimuli. Our stimulus set was presented on the whole screen (full field stimulation), on the receptive field (center stimulation) or only on the surround of the receptive field (surround stimulation). The neuronal activity evoked by these stimuli presented in these different conditions was recorded with high-density silicon probes. These probes allowed the recording of the spiking activity (single and multi-unit activities) and of the local field potential.
For each experiment, the first step was to determine the different receptive field properties of the recorded spiking activity and the laminar location of the probe.

1. CHARACTERIZING THE NEURONAL ACTIVITY

1.1. Receptive Field Mapping

We used 2x16 or 1x64 (shanks x sites per shank) silicon probes to record simultaneously local field potential (LFP), multi and single unit activity (MUA & SUA) across all cortical layers in cat primary visual cortex (V1). For each experiment, we determined the receptive fields (RFs) of the multi-unit activity along the silicon probe. The precise position and spatial organization of the RFs were measured with sparse binary noise presented in a square matrix encompassing the identified area of interest. This matrix was divided into 100 regions (10x10) where visual responses were identified (hence approximately 1° by 1° of visual angle for a square of 10°). Then, a map of visually evoked responses was obtained using a forward correlation method. Figure 3.1.1-A illustrates the receptive fields obtained across layers. Figure 3.1.1-B shows the overlap of the contour of all the receptive fields. Despite a small positional shift, all multi-unit and LFP receptive fields are co-registered, indicating that the recordings remain within a hypercolumn. After determining the RFs, a square mask of 5x5° covering all multi-unit receptive fields was defined. The purpose of this mask is to perform visual stimulation only inside the mask (“C” Center condition), which will only stimulate the aggregate spiking RFs of all the cells simultaneously recorded by the electrode. Stimulations outside the mask will stimulate their surround (“S”, surround condition). We also presented the visual stimuli on the whole screen (full field stimulation to stimulate simultaneously RF’s center and surround (“Full Field” condition)).
Because the LFP captures the neuronal activity from 500µm to 1mm around the recording site (Einevoll et al., 2013), it is legitmimate to wonder if we are also observing the response of cells that have their receptive fields in the surround? This is not the case. Indeed, our masks have a size of 5x5° (see results section) and are centered on the receptive fields. The first pixel of the surround stimulation is then located at 2.5°. In addition, our recordings are always performed in the *area centralis* ± 2-4° with the screen placed at 57cm from the cat. Based on the retinotopic map made by Tusa et al. (1978), at this cortical location the magnification factor is such that one visual degree is equal to 1mm. Since the first pixels of our stimuli are located a 2.5° and the maximum reach of our LFP signal is 1mm, we can exclude the fact that we are recording the activity from cells that have their receptive field in the surround. We also computed the size of the receptive field across layers (Figure 3.1.3). We observed that when we recorded within the area centralis, the bigger receptive fields were located in layer 5/6 and the smallest in layer 2/3 ($p < 0.01$, Kruskal-Wallis test).

We also computed the temporal profile of the receptive fields (Figure 3.1.1-C). We computed the temporal RF for different positions of the 10 x 10 matrix where the sparse noise was presented (Figure 3.1.1-B & C). As displayed in the figure, the positions that stimulated the center of the receptive field elicited a stronger response than the other positions. Based on this response, we were able to compute the current source density (CSD). We obtained a sink-source profile close to the one observed by Jin et al., (2011) with a sink in layer 4. However, in order to obtain a good CSD profile, the probe needs to be inserted perpendicularly to the cortical surface. Thus, in order to validate our electrophysiologically determined laminar profile, a histological confirmation was made after each experiment. Each probe was coated with fluorescent DiI before insertion in the cortex and cortical layer 4 location was labelled with cytochrome oxidase (Wong-Riley, 1979). As a result, we were able to determine with precision in which layers the probe was located (Figure 3.1.2). However, laminar identification was not always possible. Indeed, when the probe was not inserted perpendicularly to the cortical surface, laminar identification with CSD was impossible. Moreover, we were not always able to extract the cortical slice in order to perform the histological staining. Therefore, out of our 29 experiments, only 11 experiments meet the needed criteria in order to be included in our study. Table 3.1.1 illustrates the laminar position of each channel for every selected experiment and the number of recorded cells per experiment. It is important to note that the single units were identified after spike sorting which was performed after the experiments. This is why we only computed the receptive fields during the experiments using he multi-unit activity.

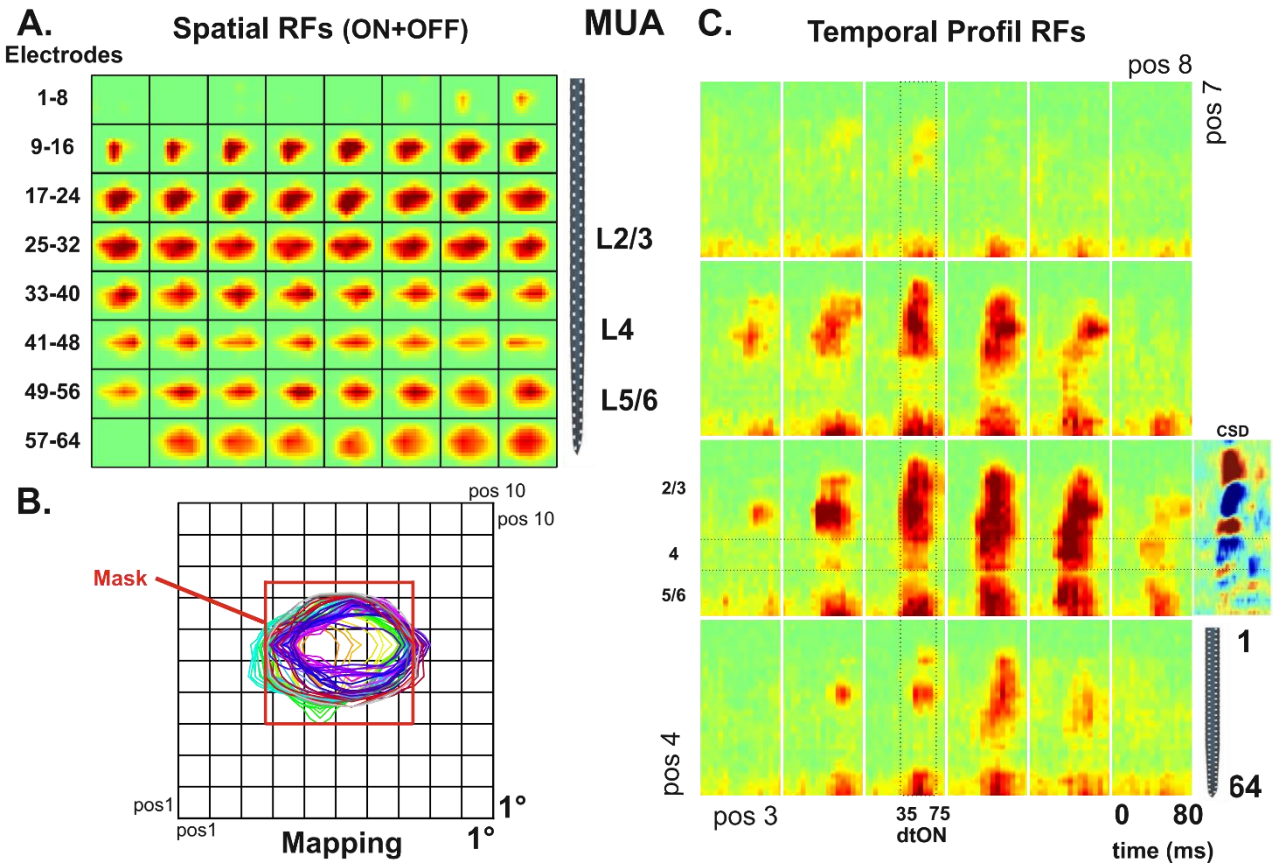

Figure 3.1.1: Receptive field mapping. Receptive Fields are mapped across all channels, spanning all layers. A. Spatial receptive field of the MUA recorded across 64 channels. B. Overlap of all the computed receptive fields. A mask corresponding to the center stimulation is then defined. C. Laminar Temporal profiles of the receptive field obtained for different positions of the sparse noise stimulation. The CSD correspond to the stimulation performed in position 6-6 *i.e.* the RFs center**.**

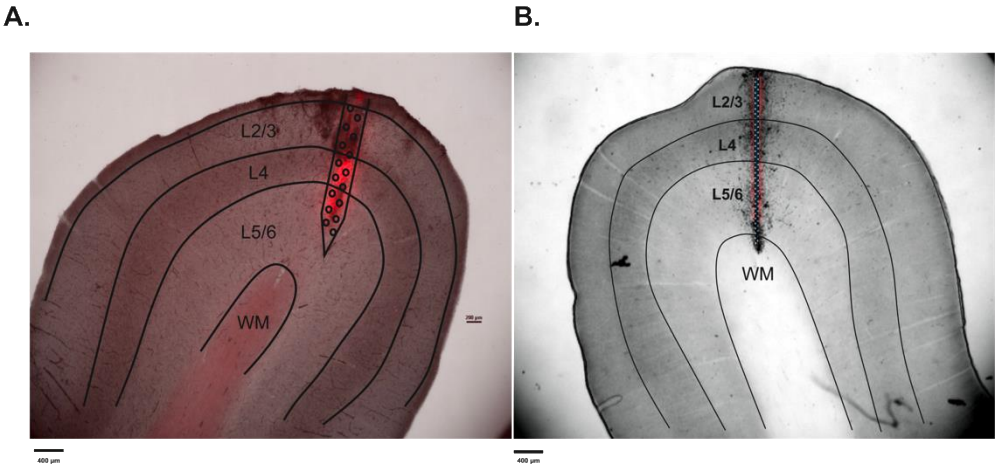

Figure 3.1.2. Histological Identification. Histological layer identification for two different experiments: Histological labelling with cytochrome oxidase. The probe was covered with DiI(red) (Histology performed by Guillaume Hucher)

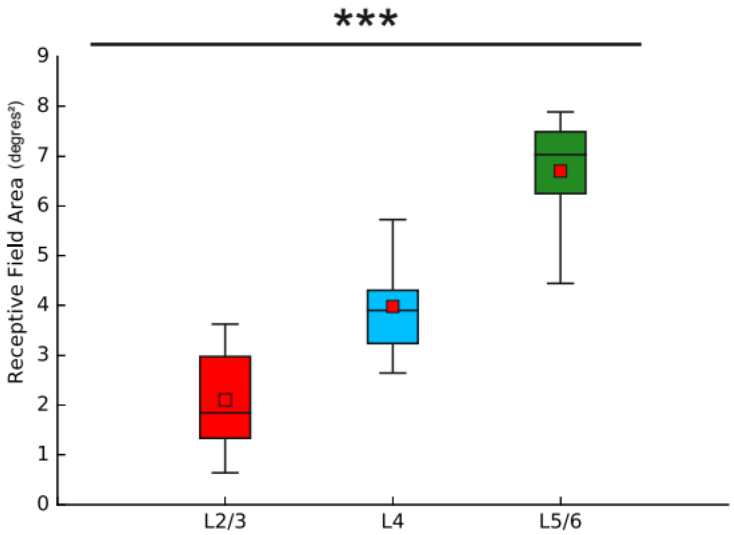

Figure 3.1.3. Receptive fields size. Differences in receptive sizes across layers. The RFs are the biggest in layer 5/6.

Recordings (w/y/side)	Electrodes				Recorded cells per layer		
	Layer 2/3	Layer 4	Layer 5/6		Layer 2/3	Layer 4	Layer 5/6
49 13 RIGHT	1--7	9--16	xxx		No SUA	No SUA	No SUA
17 14 LEFT	1--7	9--16	xxx		No SUA	No SUA	No SUA
15 16 RIGHT	1--12	13--37	38--64		No SUA	No SUA	No SUA
22 16 LEFT	1--12	13--37	38--64		No SUA	No SUA	No SUA
29 16 RIGHT	1--12	13--37	38--64		0	18	26
46 16 RIGHT	1--19	20--40	41--64		2	7	28
09 17 LEFT	1--13	14--40	41--64		17	59	49
28 17 LEFT	1--10	11--40	41--64		0	14	22
43 17 LEFT	1--16	17--50	51--64		0	16	21
03 18 LEFT	1--15	16--46	47--64		2	29	17
13 19 LEFT	1--20	21--42	43--64		14	40	22

Table 3.1.1. Laminar position of each channel for every selected experiment and the number of selected isolated single units after the semi-automatic spike sorting analysis

1.2. Characterizing the receptive field functional properties

After determining the spatial profiles of the receptive fields and their laminar locations, we investigated their functional properties. First, using gratings which elicit strong responses, we determined the orientation/direction and spatial frequency selectivities. To do this, we presented drifting Gabor functions on the RF at 12 different directions and 6 different spatial orientations (Figure 3.1.4). Figure 3.1.4-A shows the response (raster and PSTH) of one multi-unit site to the twelve different directions for one spatial frequency, while figure 3.1.4-B shows the response of the same multi-unit site to 6 different spatial frequencies for one direction. These results are summarized in figure 3.1.4-C. For this multi-unit site, the preferred orientation was 270° while the preferred spatial frequency was 0.8 Hz. This analysis was performed for all multi-unit sites along the probe (Figure 3.1.5). The population analysis allowed us to determine the functional properties that were shared by a majority of multi-unit sites along the probe. These shared properties were the ones that were used for the gratings stimulations in our later protocols.

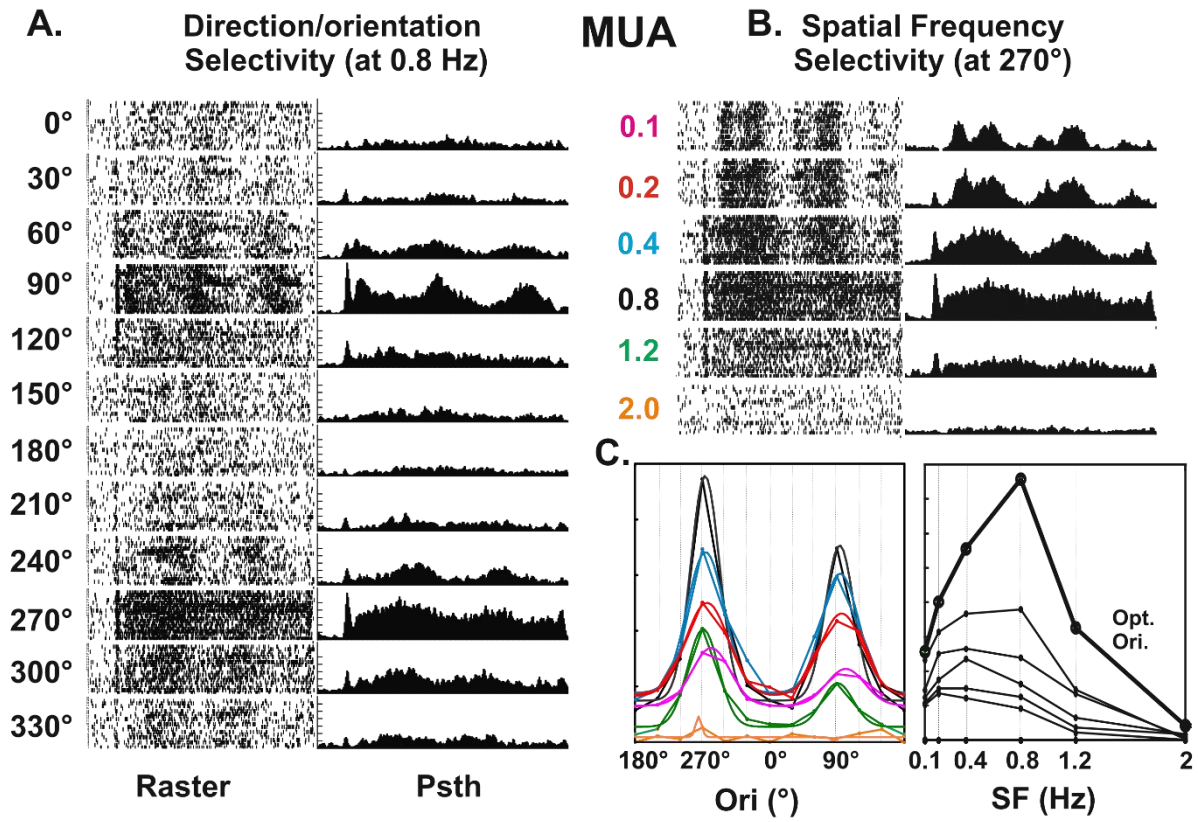

Figure 3.1.4: Estimation of the tuning properties for one site. Estimation of the preferred direction and spatial frequency for one recording site along our high-density silicon probe. A. Direction/Orientation selectivity. B. Spatial Frequency selectivity. C. Tuning curves of the preferred direction and spatial frequency. Each color corresponds to a different spatial frequency.

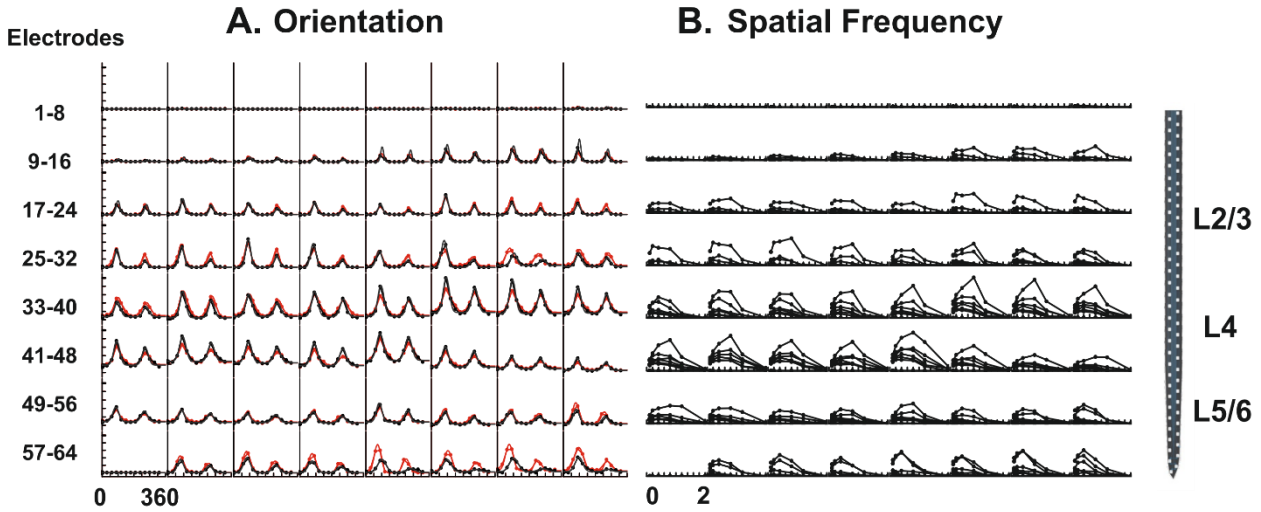

Figure 3.1.5: Estimation of the tuning properties across a population. Estimation of the preferred orientation/direction and spatial frequencies for all recording sites of the high-density silicon probe. A. Best orientation for two spatial frequencies. B. Best spatial frequency for the preferred orientation.

Recordings (w/y/side)	Direction (°)				Spatial Frequency (cycles/°)				Temporal Frequency (Hz)		
	Layer 2/3	Layer 4	Layer 5/6		Layer 2/3	Layer 4	Layer 5/6		Layer 2/3	Layer 4	Laye r 5/6
49 13 RIGHT	20	**20**	xxx		0.42	**0.42**	xxx		2	**2**	xxx
17 14 LEFT	240	**240**	xxx		0.42	**0.42**	xxx		2	**2**	xxx
15 16 RIGHT	140	**140**	140		0,42	**0,42**	0,42		2	**2**	2
22 16 LEFT	150	**200**	200		0,6	**0,6**	0,6		3	**3**	3
29 16 RIGHT	150	150	**300**		0,8	0,8	**0,6**		4	4	**4**
46 16 RIGHT	150	**150**	150		0,8	**0,8**	0,8		4	**4**	4
09 17 LEFT	260	**290**	290		0,4	**0,4**	0,4		2	**2**	2
28 17 LEFT	200	**200**	200		0,8	**0,8**	0,8		4	**4**	4
43 17 LEFT	300	**300**	300		1,2	**1,2**	1,2		5	**5**	5
03 18 LEFT	120	**120**	120		0,6	**0,6**	0,6		6	**6**	6
13 19 LEFT	270	**270**	270		0,8	**0,8**	0,8		5	**5**	5

Table 3.1.2: Tuning properties obtained with MUA within each layer, for each experiment. In bold, the chosen values for each experiment

1.3. Neuronal Classification

As described above, we also recorded the single unit activity. However, the precise single unit classifications were not available during the experiments. Indeed, a supplementary step (*i.e.* the spike sorting) was necessary in order to isolate the recorded single units. Our semi-automatic spike sorting analysis (see methods) allowed us to isolate 403 single units across the laminar compartments of cat primary visual cortex. However, among these 403 neurons some of them represent the activity recorded close to an axon. In addition, as described in chapter 1, the single unit population can be subdivided in two neuronal classes: regular and fast spiking neurons. It has been shown in cats (but also in rodents) that these two subclasses do not have the same intrinsic properties (Bachatene et al., 2011 and Chen et al., 2015). Therefore, we decided to perform this classification among our single unit population and to discard the axonal waveforms, that correspond to the thalamic activity coming from axons projecting to V1 (Sun et al, 2019; Society for Neuroscience conference). However, the available techniques in the literature rely too strongly on the firing rate and the peak-to-peak latency of the waveforms, which can lead to bad classifications. In order to overcome this problem, we developed with Matias Goldin and Evan Harrell (Shulz lab, ICN) a new classification method that uses several waveform features. We extracted seven features from the waveforms (see methods). The first three PCA components explain 90% of the variance of the spike shapes (Figure 3.1.6). The weights of each feature in these eigenvectors are shown in Figure 3.1.6. Then, a k-means clustering was made forcing the grouping of 12 clusters, followed by a manual merging step to ease the separation into two clusters. After plotting the projection of the twelve clusters into the first two PCA components, a manual assignment was made into the RS or the FS group, and to the middle unclassified group (*i.e.* axonal waveforms and single units finally classified as multi-units). The final resulting clusters and their waveforms are displayed in figure 3.1.7. There, we show that two separated clusters appear, whose waveform shapes match the ones encountered previously using silicon probes (Zengcai et al. 2014). With this method, we encountered 63% (225 cells) of RS neurons and 37% (131 cells) of FS neurons.

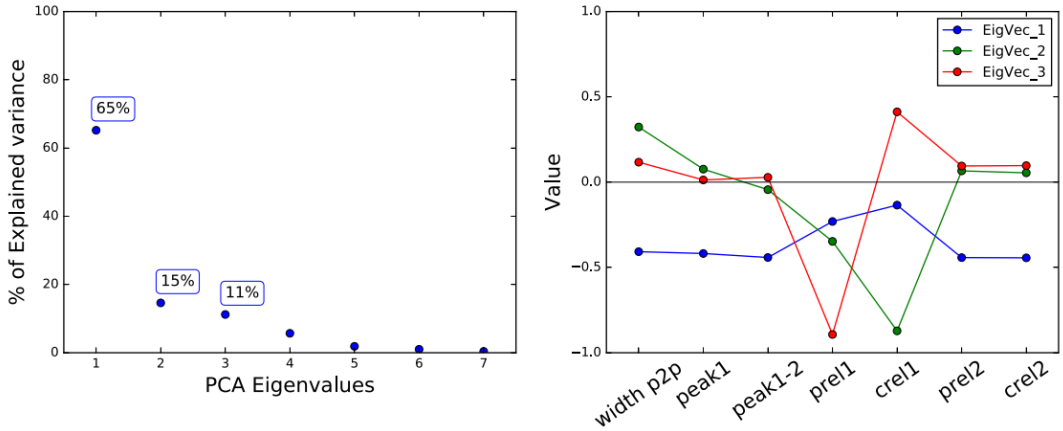

Figure 3.1.6 Features and PCA of our classification method. A. left panel: Percentage of variance explained by the PCA components. Right panel: Weights of each feature in these three eigenvectors

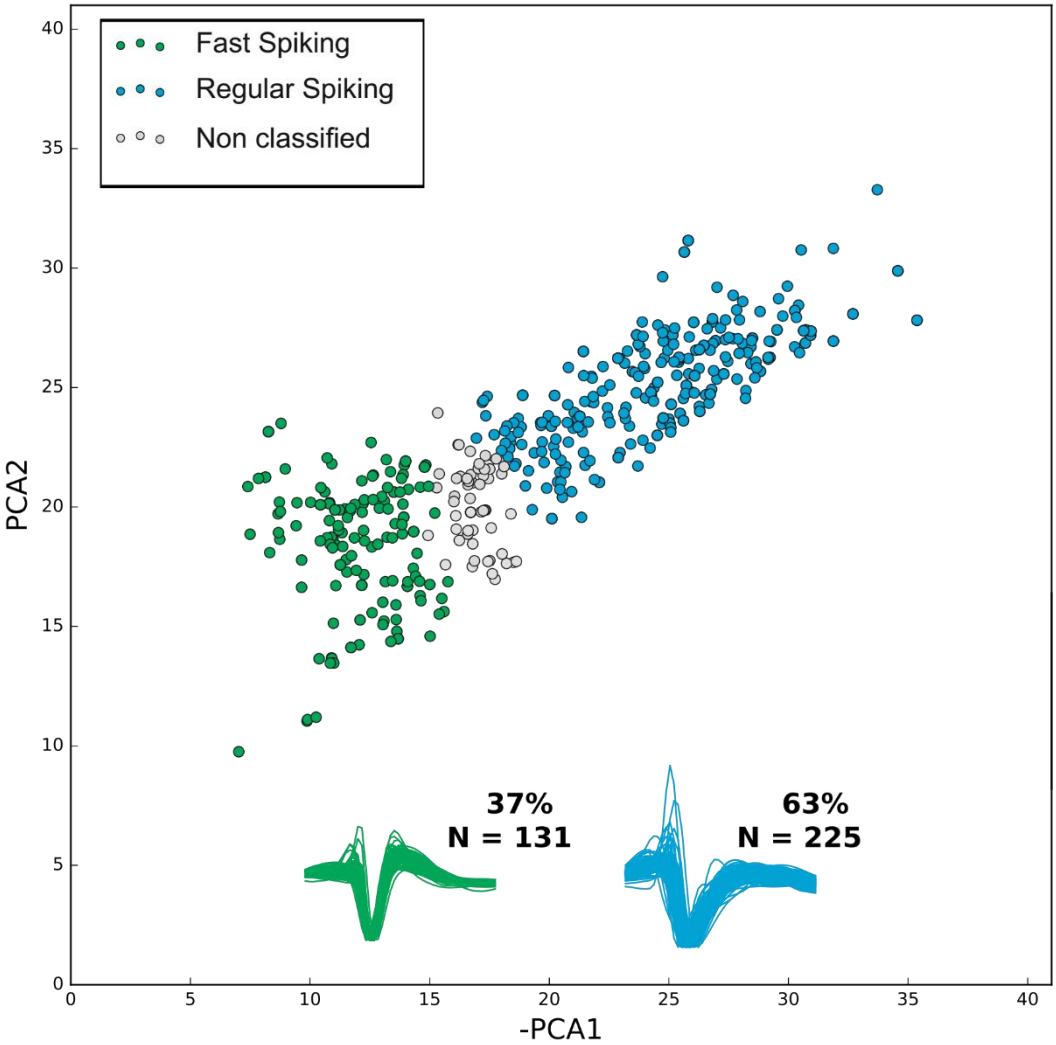

Figure 3.1.7. Cluster separation of regular spiking and fast spiking cells.

2. QUANTIFICATION OF THE VISUAL RESPONSE.

A previous intracellular study of the laboratory investigated the V1 responses to four different stimuli. These stimuli, calibrated both in their spatial and temporal domains, included classical artificial stimuli used to probe neuronal selectivity (drifting grating (DG), dense noise (DN)). They also contained more complex stimuli ((GEM) and natural images (NI), both animated with natural temporal statistics) that mimic the global retinal flow that occurs during the exploration of the natural environment. They showed that the retinal flow statistics imposed by simulated eye-movements evoke reliable, non-linear responses in V1, and that sparse spiking responses to natural stimuli arise from irregular but highly reproducible V_m trajectories. However, due to the difficulty imposed by intracellular recordings, they were able to only record 30 cells. The stability of the extracellular preparation allowed us to test additional parameters that were feasible in the intracellular study. We were able, with a linear silicon probe spanning all layers, to increase almost by a factor of 10 the number of recorded neurons (221 neurons), but also to record the neuronal activity at different scales by recording the multi-unit activity (377 sites) and the local field potential. These simultaneous recordings also allowed us to perform new analyses such as the computation of the correlations.
Moreover, we were able to present a set of control stimuli that was absent in the intracellular study. This set was composed of a natural image where the phase (spatial statistics) was randomized, a natural image where the eye movements (temporal statistics) were randomized, a natural image where both the phase and the eye movements were randomized and finally a natural image where the eye movements were only made of saccades.
The first step of this thesis was to validate the intracellular results previously obtained by the laboratory. Then, the geometry of the silicon probe allowed us to investigate the laminar dependency of the response variability at different scales. Finally, we wanted to link the responses to the natural image and its spatio-temporal statistics.

2.1. Impact of the full field response on the neuronal activity

2.1.1 Quantification of the spiking response

As described in section 3.1, we isolated 356 neurons. However, not all cells responded to visual stimulation. When a cell did not respond to natural images, no response to the other stimuli was observed either. Therefore, we excluded all the cells that did not display a visual response and showed activity similar to the spontaneous firing. In order to separate the responsive and unresponsive cells, we performed a selection based on the levels of reliability. Cells that displayed a reliability two times lower than the reliability of the spontaneous activity were not included in our study. The distribution of the spontaneous reliability is displayed in figure 3.2.1. Among our 356 neurons, 221 were included in the study (63%). One could expect a higher number of visually responsive cells. This ratio of responsive cells was also observed in rat somatosensory cortex (Goldin, Harrell, et al., 2018). This could be a signature of sensory cortices that was masked by single recording site probes. Another explanation of this ratio is that silicon probes are very big and cause damage in the brain when lowered, thus some functional connections might be destroyed during the probe descent and abolish the functional activity of some neurons. It is important to keep in mind that non-visually responsive cells are captured by the multi-unit activity.

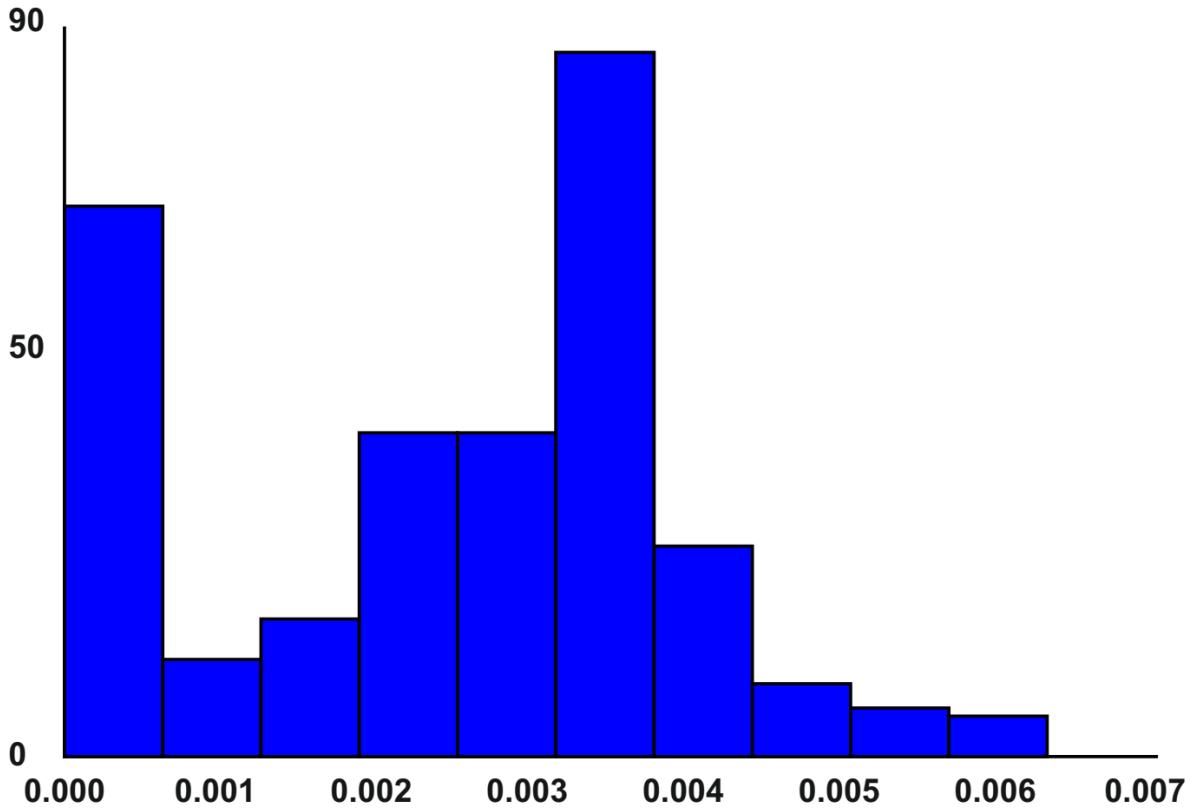

Figure 3.2.1: Distribution of two times the maximum standard deviation of the spontaneous activity reliability. Neurons presenting a reliability lower than the maximum 2*SD were not included in this study.

- **Comparison with the intracellular recordings**

As performed in the intracellular study we first characterized the spiking activity by computing the firing rate of the single and multi-unit activity. Figure 3.2.2 shows the response of a well-isolated neuron (Fast spiking cell) and of a multi-unit site to our four main stimuli presented 30 times. For both signals, the bin size of the PSTH was 5 ms.

As observed intracellularly, the presentation of an optimal DG (Figure 3.2.2 A & B, top row) evoked a strong modulation of the single unit response at the grating temporal and spatial frequencies (5Hz and 0.8 cycles/degree for this example; but see section 3.1 for the table containing all the preferred FS and FT). However, only simple cells are modulated by the frequencies of the drifting gratings. The presentation of a natural scene evoked strong and synchronized responses across the stimulus presentation (Figure 3.2.2). Figures 3.2.3 and 3.2.4 show the responses of many neurons (FS and RS) to both natural images and drifting gratings. We can observe that we have two classes of neurons. Those that do not respond to the visual stimulation and that are not selected by our criteria and neurons that are driven by the visual stimulation. Among the responsive neurons we observed different levels of response. This is particularly true for DG since, unlike what is performed intracellularly, it is impossible to choose the best parameters (phase, spatial and temporal frequencies) for all neurons simultaneously. We also computed the response of all neurons for each trial and plotted them in the same raster (Figures and 3.2.5 & 3.2.6). These raster plots show that across trials, the response is not always the same. This suggests that during our protocols, intrinsic processes, such as anesthesia, can modulate the responses (Ecker et al., 2014).

The same pattern was observed for the multi-unit but with increased activity compared to the SUA. This is not surprising since the MUA contains the activity of many neurons (Einevoll et al., 2007; Gray and Singer, 1989; Pettersen et al., 2008). As explained in the methods section, our MUA recordings correspond to all the events crossing the automatic threshold of our recording system for frequencies between 250Hz and 5Khz.

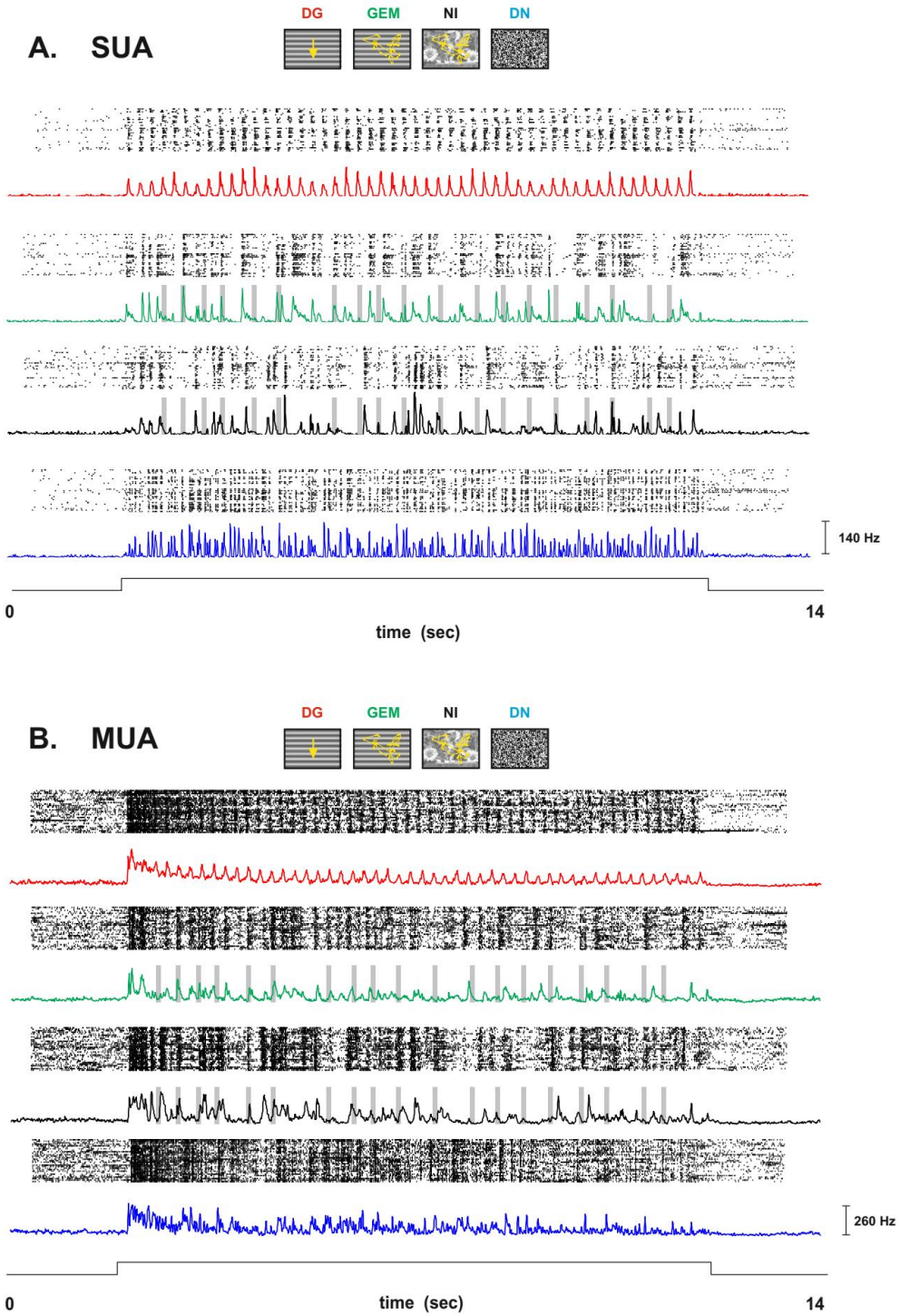

Figure 3.2.2 : Spiking Dynamics of the single unit and multi-unit responses as a function of visual input complexity. On the raster, each line represents a trial with the corresponding PSTH below (bin 5ms) **A.** Single unit response to our set of stimuli. **B.** Multi-unit response to our set of stimuli. Grey bars represent saccades.

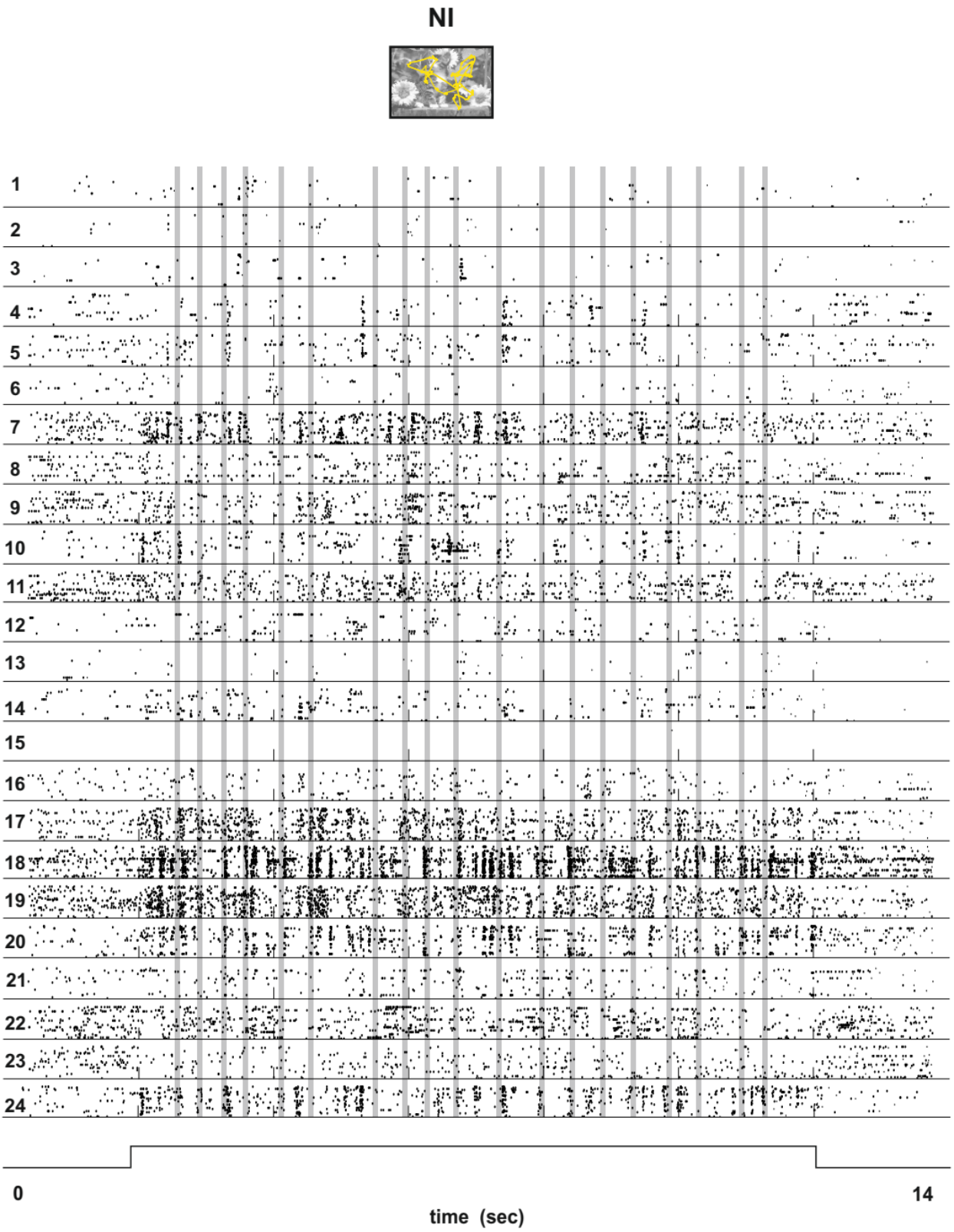

Figure 3.2.3: Spiking dynamics of the single unit activity evoked by Natural images animated with eye movements**.** Each raster represents a neuron.

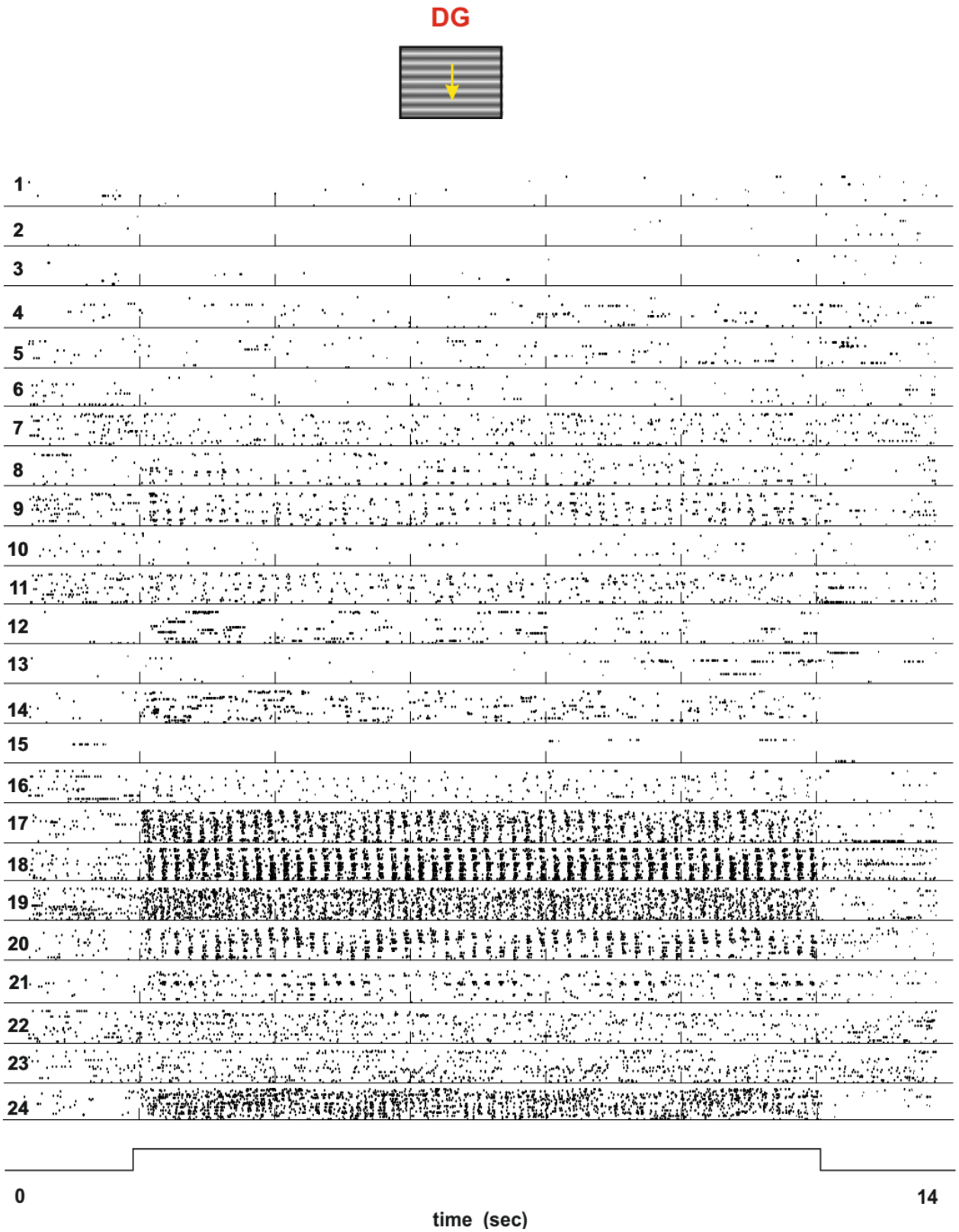

Figure 3.2.4: Spiking dynamics of the single unit activity evoked by Drifting Gratings. Each raster represents a neuron.

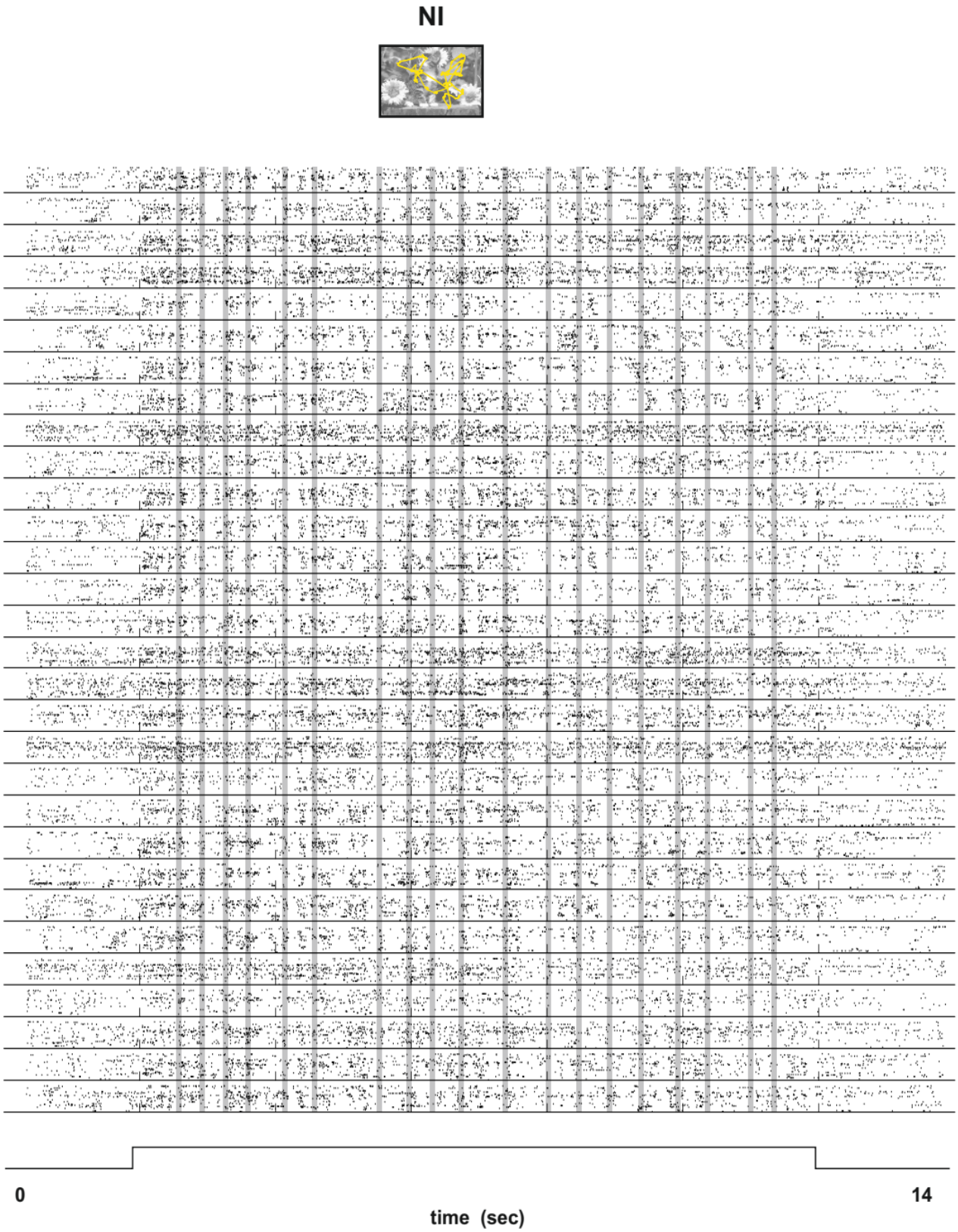

Figure 3.2.5: Spiking dynamics of the single unit activity for each trial evoked by Natural Images animated with eye movements. Each raster represents a trial and each line of the raster represent a neuron.

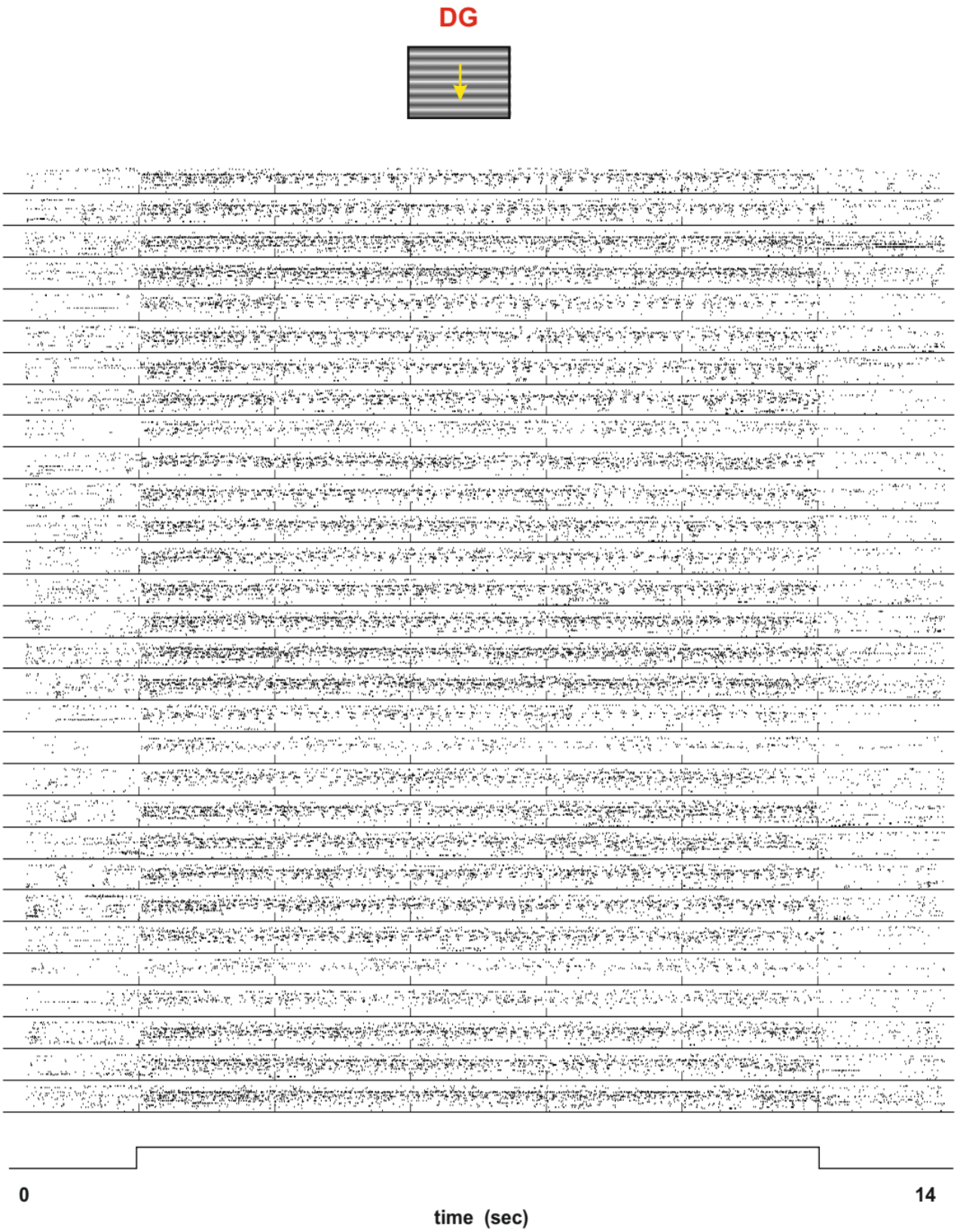

Figure 3.2.6: Spiking dynamics of the single unit activity for each trial evoked by Drifting Gratings. Each raster represents a trial and each line of the raster represent a neuron.

- **Comparison of the intracellular and extracellular results**

We then compared, at the population level, the firing rate of the SUA and the MUA to the one obtained in the intracellular study (Figure 3.2.7-A). For the first comparison the single unit activity was composed of 78 neurons responding both to the optimal DG and GEM (52 regular spiking neurons: 1 located in Layer 2/3, 30 in layer 4 and 21 in layer 5/6; 26 fast spiking neurons: 20 in layer 4 and 6 in layer 5). The mean response rate was the highest for the DG, the lowest for DN, while GEM and NI evoked similar firing rates (see table 3.2.1 located at the end of the section). This is different from the intracellular results where DG and GEM evoked a higher firing rate than the other stimuli. However, the MUA gave a similar response pattern to the intracellular study, but with higher firing rates (Figure 3.2.7-A, center and left; table 3.2.1). This difference might originate from the differences between intracellular and extracellular recording techniques. Indeed, intracellularly, one of the first steps of characterization of the cell, is the determination of the orientation tuning, the preferred spatial and temporal frequencies. Cells with smaller responses might have been discarded. On the other hand, since extracellularly, we recorded simultaneously dozens of neurons, we recorded cells for which the temporal and spatial frequencies were not optimal, as shown in figure 3.2.4. Moreover, low firing rate cells were not discarded, this results in a lower average firing rate. The pattern is probably the same between the intracellular spiking activity and the MUA because the latter gathers the response of many neurons, with some of them optimally responding to the gratings, therefore increasing the recorded activity (Gray and Singer, 1989; Einevoll *et al*, 2007; Pettersen *et al.*, 2008). We can rule out a difference caused by the anesthesia. Despite being performed with two different anesthetics (Alfaxolone and isoflurane respectively), the two studies resulted in similar values of firing rate for NI (5.5 Hz intracellularly vs 4.2 ± 0.8 Hz extracellularly). In summary, our extracellular results are similar to the ones obtained intracellularly despite a different anesthesia and a different recording technique.

- **Laminar results**

We also performed the same quantification on the single unit (221 neurons) and the multi-unit (377 sites) populations without GEM. Indeed, in some experiments the GEM, due to an error, were not presented at the optimal orientation. Thus, among our 221 neurons, only 78 neurons responded optimally to GEM. These 78 neurons do not allow us to perform a laminar and a neuronal subtype analysis. Thus, we performed supplementary analysis on the single-unit population without GEM. To do so we only focused on the response to DG, NI and DN.

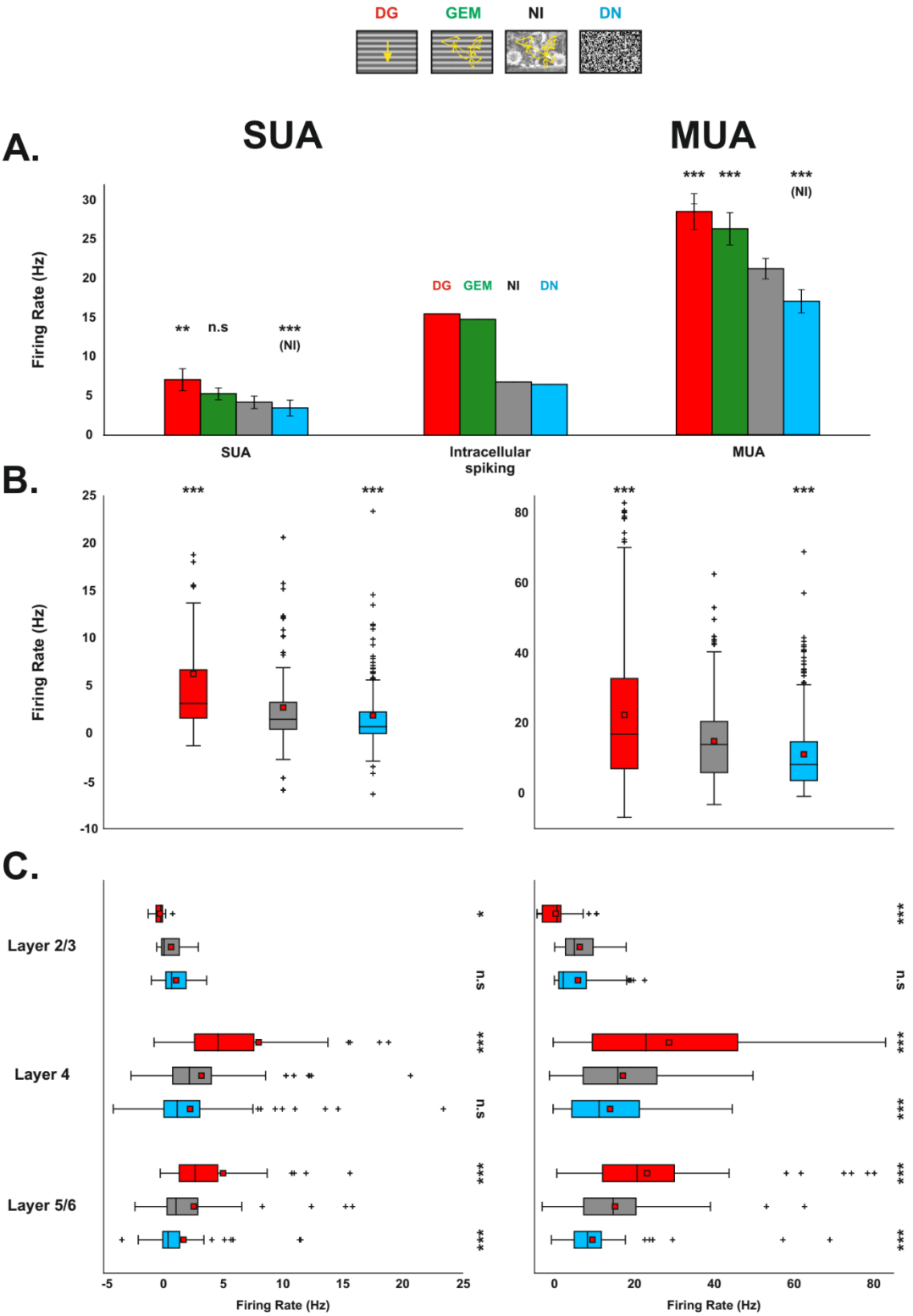

Figure 3.2.7: Single and multi-unit mean firing rate. A. Multiscale comparison of the mean evoked spike rates. Our extracellular results match the intracellular ones. Left: Single unit activity (n = 78), center: intracellular results. Right: Multi-unit activity (77 sites). **B.** Comparison of the mean evoked spike rates. DG evokes the highest firing rate. Left: single unit activity (n = 221), right: multi-unit activity (377 sites). **C.** laminar comparison of the mean evoked spike rates. Layer evokes the highest firing rates. Left: single unit activity (L2/3 = 10; L4 = 111; L5/6 = 99 neurons), right: multi-unit activity (L2/3 = 52; L4 = 187; L5/6 = 138 sites). Red squares: mean. Black line: median. Extremities of the box: first and third quartile. Whiskers: minimum and maximum. Crosses: outliers; Stars indicate values significantly different from NI. ***: $p < 0.001$

Within layers 4 and 5/6, drifting gratings evoked a higher firing rate than the other stimuli ($p < 0.05$ & $p < 0.001$; Friedman test). In layer 2/3, this low firing rate observed for DG can be explained by the fact that cells tend to adapt and reduce their firing rate very quickly. Since our visual stimulation lasts 10 seconds, the mean firing rate is reduced (Figure 3.2.9). Figure 3.2.9 shows the exponential fit of the response decay for the mean MUA in all layers (a + exp^(b +x) +c; where **a** is the value of the peak minus the baseline, **b** the value of the slope between the maximum peak and 500ms and **c** the baseline value). The higher b is the stronger the adaptation is. Our results show that b and c are the lowest in layer 2/3, thus we can conclude that the reduced firing rate evoked by DG in this layer is linked to a lower baseline firing rate but also to a faster adaptation of the response. Natural images and dense noise only exhibited a difference in firing rates in layer 5/6 (Figure 3.2.7-C, left panel; Table 3.2.1). Regarding the firing rate between layers, both NI and DG evoked different mean firing rates between layers; the highest firing rate was found in layer 4 and the lowest in layer 2/3 (Figure 3.2.7-C, left panel; Table 3.2.1; Kruskal-Wallis test).
The firing rate across the 377 multi-unit sites (52 sites in layer 2/3, 187 sites in layer 4, 138 sites in layer 5/6) exhibited the same pattern, with higher firing rates, as in the single unit activity. One difference was found in layer 4 where NI and DN were significantly different ($p < 0.001$; Friedman test; Figure 3.2.7-C, right panel; Table 3.2.1).
In summary, our results show that DG induce a higher firing rate in layers 4 and 5/6. On the other hand, natural images and dense noise evoke similar firing rates. The highest firing rates were found in layer 4.

As described in section 3.1, we developed an algorithm that classifies the single unit population into two subgroups: fast spiking and regular spiking cells. We recorded 83 FS cells (4 in layer 2/3, 61 in layer 4 and 18 in layer 5/6) and 138 RS cells (7 in layer 2/3, 50 in layer 4 and 81 in layer 5/6). Both FS and RS cells displayed the same firing rate pattern as the complete single unit population (Figure 3.2.10-A). However, for all stimuli respectively, FS neurons exhibited a higher mean firing rate than the RS cells and the total population ($p < 0.05$, Kruskal-Wallis test, Figure 3.2.10-A; table 3.2.2).
For the FS cells, we only observed a higher firing rate for DG in layer 4, this is probably linked to the number of cells recorded in layer 2/3 and 5/6. On the other hand, as observed for the whole population, DG evoked a higher spiking activity than the other stimuli while DN elicited the lowest one (Figure 3.2.10-B; table 3.2.2).
For both RS and FS cells and for all stimuli respectively, no laminar differences in the firing rate were observed ($p > 0.05$; Kruskal-Wallis test)

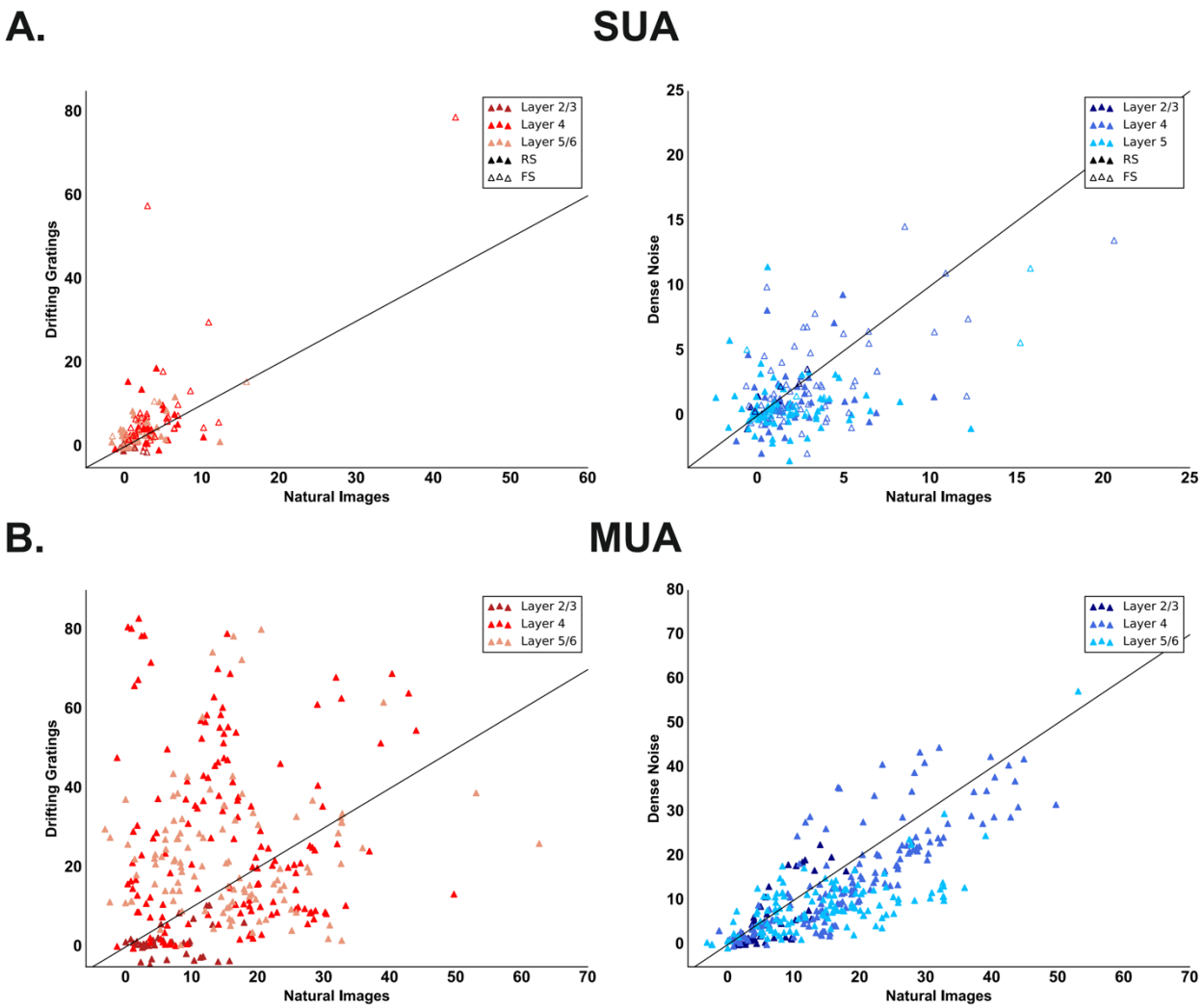

Figure 3.2.8: Firing Rate scatter plots. A. Single unit activity firing rate. Left: Natural images vs Drifting gratings. Right: Natural images vs Dense Noise. B. Multi-unit activity firing rate. Left: Natural images vs Drifting gratings. Right: Natural images vs Dense Noise. Empty symbols = FS. Full Symbols = RS or MUA.

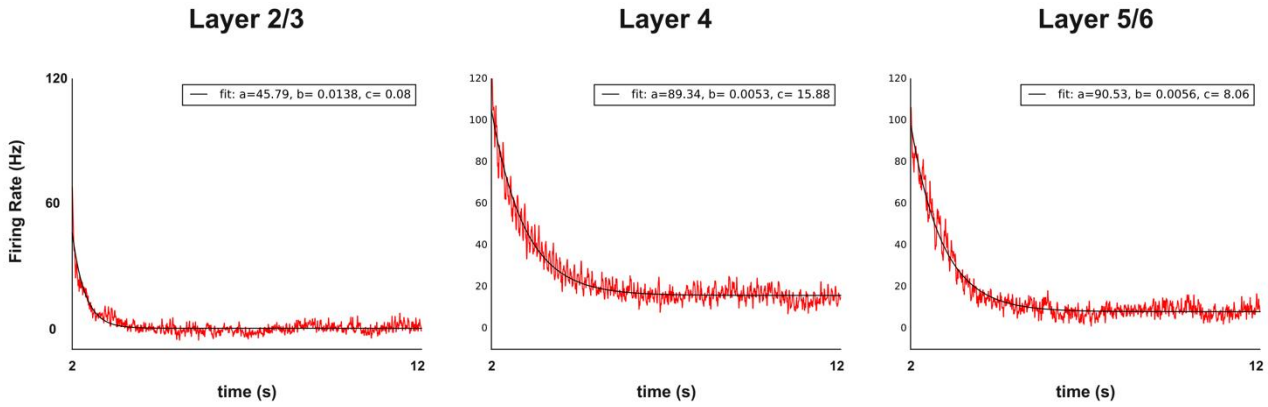

Figure 3.2.9: Firing rate adaptation. Mean firing rate for each layer and its level of adaptation quantified by an exponential fit.

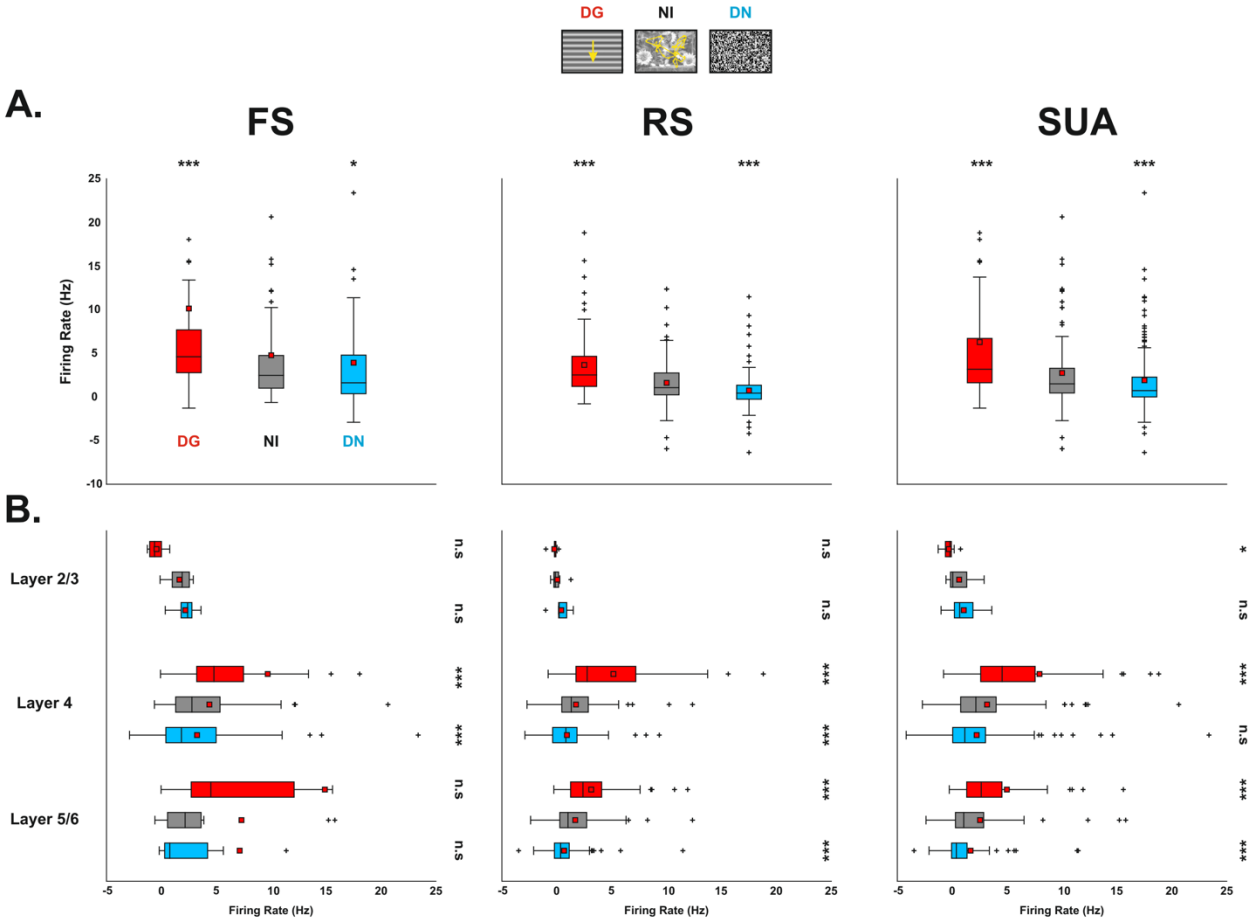

Figure 3.2.10: Single unit mean firing rate. A. Mean evoked spike rates for different subclasses of single units. Fast Spiking Neurons evoke a higher firing rate than regular spiking neurons. Left: Fast spiking neurons (n = 83), center: regular spiking neurons (n = 138). Right: single unit activity (n = 221). **B.** laminar comparison of the mean evoked spike rates across the single unit classes. Left: Fast spiking neurons (L2/3 = 4; L4 = 61; L5/6 = 18 neurons), center: regular spiking neurons (L2/3 = 7; L4 = 50; L5/6 = 81 neurons), right: single unit activity (L2/3 = 10; L4 = 111; L5/6 = 99 neurons). Black line: median. Extremities of the box: first and third quartile. Whiskers: minimum and maximum. Crosses: outliers; Stars indicate values significantly different from NI. *: $p < 0.05$; ***: $p < 0.001$

- **Impact of the natural statistics on the firing rate**

Finally, we investigated the impact of the spatio-temporal statistics of the natural image on the firing rate (Figure 3.2.10 & 3.2.11).
Figure 3.2.10 shows a response example for one cell and one multi-unit site in response to our control stimuli. In this example cell, Natural images (NI) and the natural images with randomized phase (NI-RS), natural images with randomized eye movements (NI-RT) and natural images where both phase and eye movements were randomized (NI-RST) seem to evoke a similar response pattern. On the other hand, the natural image animated only with saccades (NI-SAC) induced a reduced spiking activity compared to the other stimuli. The same observations were made for the multi-unit site.
We presented the control stimuli in 4 experiments and were able to record 124 well-isolated single units and 150 multi-unit sites. We computed the mean firing rate from these populations.
Our results on the population analysis showed that for both single unit and multi-unit activity, NI-SAC evoked a lower spiking activity than NI, implying that the other eye movements (drift, tremors, microsaccades) play a significant role in the neuronal activity ($p < 0.05$, Friedman test; Figure 3.2.12, table 3.2.3). The importance of the temporal structure of the eye movements in the generation of a spike is confirmed by the lower mean firing rate elicited by NI-RT ($p < 0.001$). In addition, NI and NI-RS have similar firing rates. This could mean that temporal statistics are more important than the spatial ones in the generation of the spiking activity.
However, since NI-RST and NI evoked similar firing rates for the SUA, one could argue that neither the spatial nor temporal frequencies are important. This absence of a difference could be linked to the number of recorded cells. Indeed, the firing rate obtained for the MUA is close but significantly higher for NI ($p < 0.001$, Friedman test). Another explanation could be That despite the absence of significance, NI-RS evokes a higher mean firing rate than NI, while NI-RT evokes a lower one. On the other hand, NI-RST evokes a higher firing rate than NI-RT. The reduction of activity induced by the randomization of the temporal statistics is compensated by the increase in activity evoked by the randomization of the spatial phase.

The pattern of response observed for the SUA was also observed for the regular spiking neurons ($n = 79$; Figure 3.2.12, table 3.2.3). However, for the fast spiking neurons ($n = 45$), only NI-RS showed a significantly different firing rate than NI ($p < 0.05$, Friedman test). This could be either linked to the number of cells or by the fact that fast spiking cells are less affected by the center surround interactions present in natural scenes (Haider *et al.*, 2010). This will be tested in the section 3.2.2 of this manuscript.

In summary, our results showed that both the single unit and the multi-unit activity exhibit a similar mean firing pattern (similar to the one obtained with intracellular recordings by Baudot *et al.*). Drifting gratings evoke a higher mean firing rate than the other stimuli. Regarding the layer specificity, layer 4 exhibits higher firing rates than the other layers. Finally, we showed that all the eye movements and not only saccades seem important for the generation of a spiking activity.

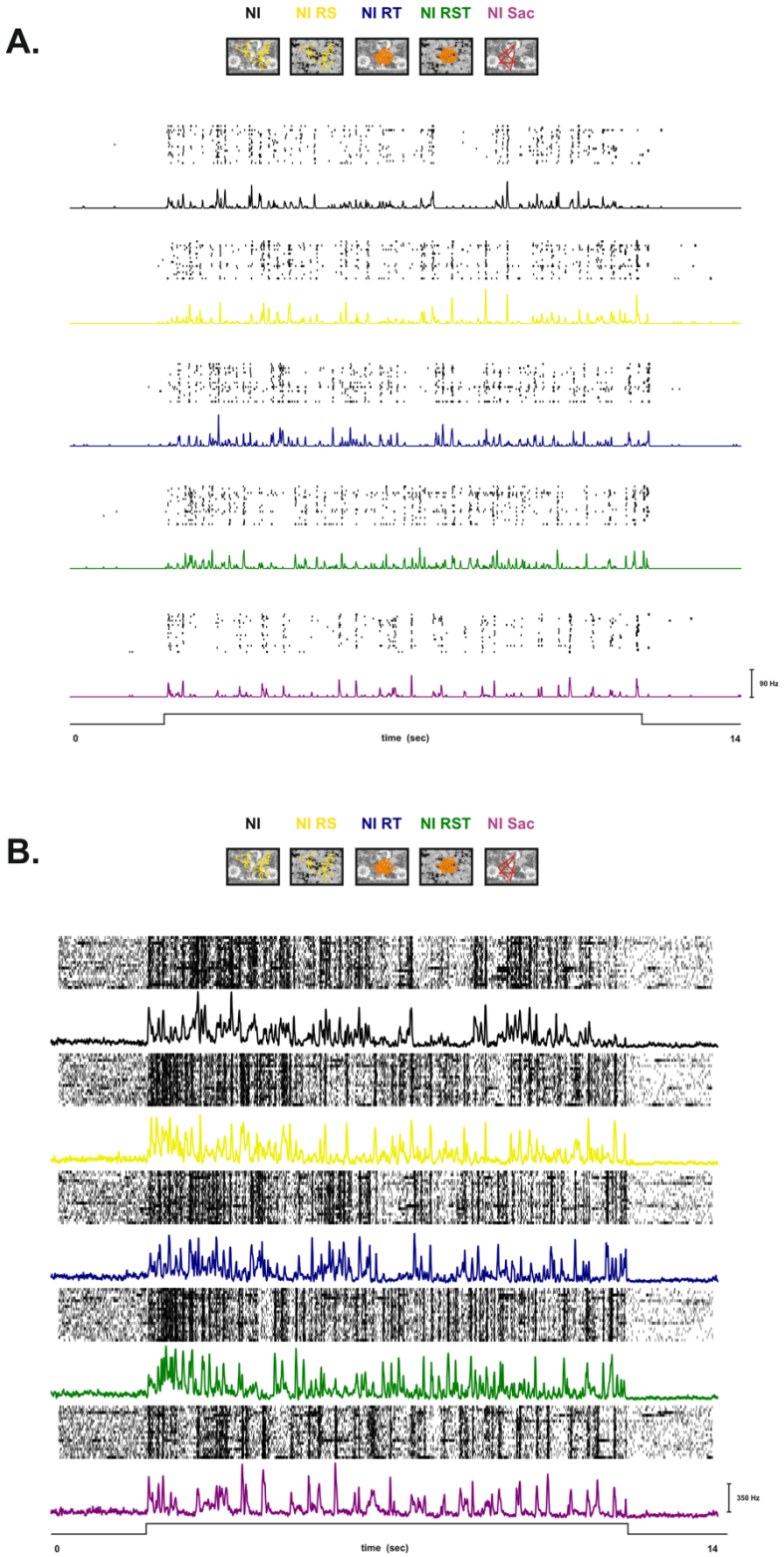

Figure 3.2.11: Spiking dynamics of the single unit and multi-unit responses for natural images and its controls. On the raster, each line represents a trial with the corresponding PSTH below **A.** Single unit response to our set of stimuli. **B.** Multi-unit response to our set of stimuli.

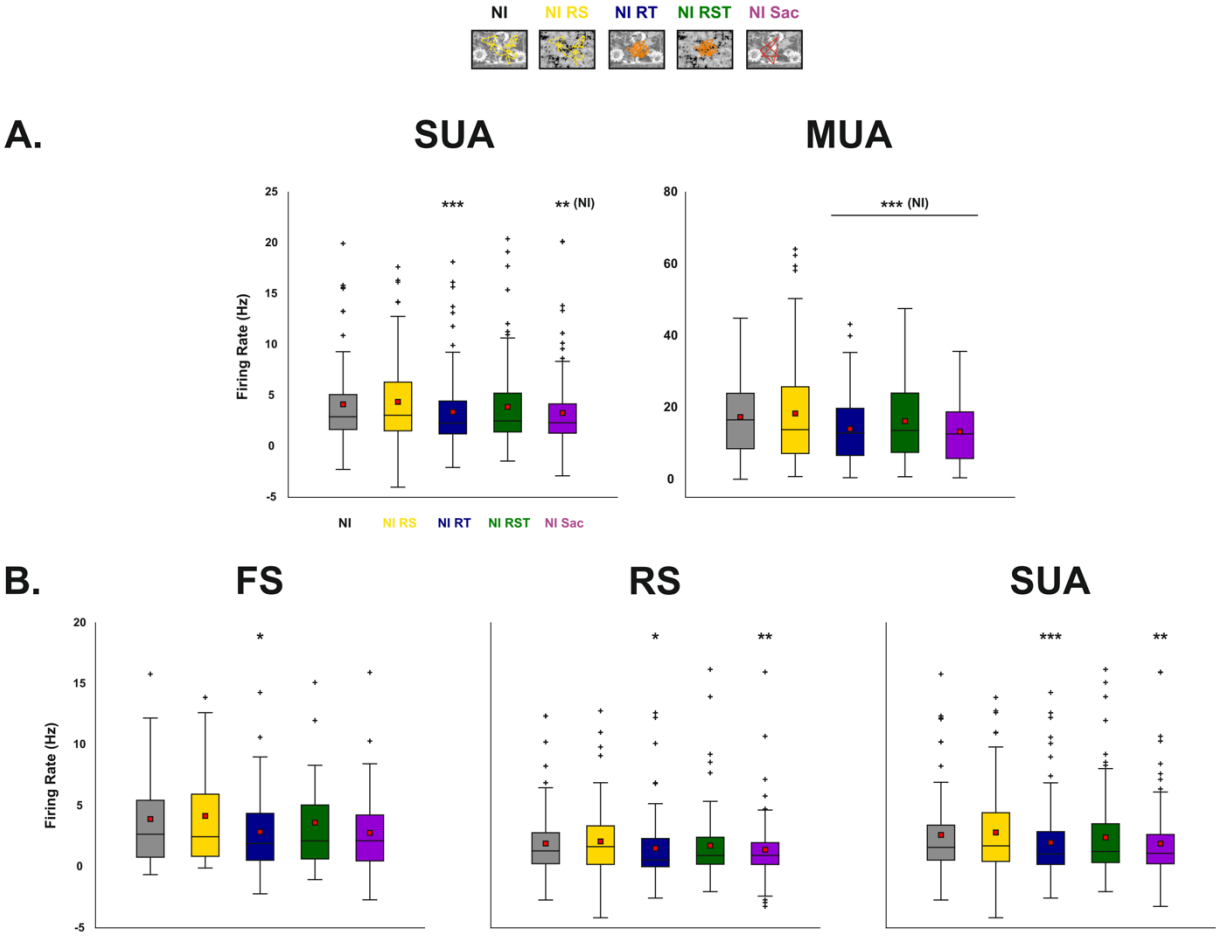

Figure 3.2.12: Single and multi-unit mean firing rate evoked by the control stimuli. **A.** Comparison of the mean evoked spike rates. Left: Single unit activity (n = 124), right: Multi-unit activity (150 sites). **B.** Comparison of the mean evoked spike rates across the single unit subtypes. Left: Fast spiking neurons (n = 45), center: regular spiking neurons (n = 79). Right: single unit activity (n = 124). ***** : $p < 0.05$; ** : $p < 0.01$; *** : $p < 0.001$

FULL FIELD	SUA			
	DG	GEM	NI	DN
Mean (w/ GEM)	7.1 ± 1.4	5.3 ± 0.8	4.2 ± 0.9	3.5 ± 1.0
Mean (w/o GEM)	6.3 ± 1.1		2.7 ± 0.4	1.9 ± 0.4
Layer 2/3	-0.3 ± 0.2		0.6 ± 0.4	1.1 ± 0.4
Layer 4	7.9 ± 1.6		3.2 ± 0.5	2.2 ± 0.4
Layer 5/6	5.0 ± 1.5		2.5 ± 0.7	1.7 ± 0.8

FULL FIELD	MUA			
	DG	GEM	NI	DN
Mean (w/ GEM)	28.6 ± 2.3	26.3 ± 2.1	21.2 ± 1.3	17.1 ± 1.5
Mean (w/o GEM)	22.5 ± 1.2		15.0 ± 0.6	11.2 ± 0.6
Layer 2/3	0.3 ± 0.6		6.3 ± 0.7	5.9 ± 1.0
Layer 4	28.7 ± 1.9		17.1 ± 0.9	13.9 ± 0.9
Layer 5/6	23.2 ± 1.5		15.2 ± 1.0	9.5 ± 0.8

Table 3.2.1: Mean firing rate values for the single and multi-unit activity (mean ± SEM)

FULL FIELD	FS		
	DG	NI	DN
Mean	10.1 ± 2.5	4.8 ± 1.0	3.9 ± 1.1
Layer 2/3	0.4 ± 0.5	1.6 ± 0.7	2.2 ± 0.7
Layer 4	9.7 ± 2.5	4.4 ± 0.9	3.2 ± 0.6
Layer 5/6	14.9 ± 9.2	7.3 ± 4.0	7.1 ± 5.1

FULL FIELD	RS		
	DG	NI	DN
Mean	3.7 ± 0.5	1.6 ± 0.2	0.7 ± 0.2
Layer 2/3	0.2 ± 0.1	0.1 ± 0.2	0.4 ± 0.3
Layer 4	5.2 ± 1.1	1.7 ± 0.5	0.9 ± 0.4
Layer 5/6	3.1 ± 0.4	1.7 ± 0.3	0.7 ± 0.2

Table 3.2.2: Mean firing rate values for the single unit activity and its subclasses (fast spiking and regular spiking cells; mean ± SEM)

FULL FIELD					
	NI	NI-RS	NI-RT	NI-RST	NI-SAC
FS	3.9 ± 0.7	4.2 ± 0.8	2.9 ± 0.5	3.6 ± 0.7	2.8 ± 0.5
RS	1.9 ± 0.3	2.1 ± 0.4	1.5 ± 0.3	1.7 ± 0.4	1.4 ± 0.3
SUA	2.6 ± 0.3	2.8 ± 0.4	2.0 ± 0.3	2.4 ± 0.3	1.9 ± 0.3
MUA	17.3 ± 0.9	18.3 ± 1.2	14.0 ± 0.8	16.2 ± 0.9	13.3 ± 0.7

Table 3.2.3: Mean firing rate values for the multi-unit activity, single unit activity and its subclasses (fast spiking and regular spiking cells; (mean ± SEM)

2.1.2 Quantification of the local field potential

As described in the methods section, the silicon probe allows the recording of the spiking activity (SUA, MUA) but also of a more global signal, the local field potential (LFP). The LFP is the combined activity of small neuronal populations located hundreds of microns around the electrode tip (Einevoll et al., 2013; Xing et al., 2009). It is important to note that a close correspondence between LFP and synaptic potentials has been found (Kamondi et al., 1998; Okun et al., 2010). Therefore, LFP has been considered as the summed activity of synaptic currents coming from cortical neurons, hundreds of microns around the recording site. However, recent papers (Meir et al., 2018; Tan et al., 2014), showed that this view needs to be reconsidered. These studies showed that the membrane potential and the LFP can either be correlated and decorrelated and that the correlation level depends on many factors such as the state of the animal or neuromodulation. The fact that the LFP switches from synchronous to asynchronous states has also been observed in the anesthetized cat (Spacek and Swindale, 2016). In addition to the different levels of correlation between the V_m and the LFP, it is important to keep in mind that even if synaptic currents are the major LFP contributors, action potentials (fast sodium spikes, slow calcium spikes and spike afterhyperpolarization) also participate in the signal formation (Einevoll et al., 2013). Thus, a high amplitude in the response is characteristic of highly synchronized neuronal activity while a low amplitude corresponds to poorly synchronized activity. An illustration of the mean LFP in response to all stimuli is shown in figure 3.2.13. This illustration shows that a very responsive SUA does not imply a strong LFP.

A better overview of the LFP across layers is shown in Figure 3.2.14. The mean response to NI seems to contain high amplitudes *i.e.* a more synchronized response. However, this observation needs to be quantified. A simple way to do it is to compute the energy of the mean stimulus-locked response and subtract the energy of the spontaneous activity. A highly synchronized response would result in high energy levels while an unsynchronized one would result in low energy levels. Figure 3.2.15 shows an example of the energy evoked by natural images and dense noise for two different experiments. For both experiments, NI evoked a higher energy than DN, however each experiment resulted in different values of energy. This is linked to the fact that the LFP is strongly dependent on the state of the animal (Spacek and Swindale, 2016) but also on how the ground reference is placed (Parabucki and Lampl, 2017). A determination of the synchronous and asynchronous states will be needed in the future.

We then computed the energy at the population level. We also computed the LFP of the GEM, even for the sites where it was not presented at the preferred orientation. Indeed, as shown in figure 3.2.16, the GEM elicited a similar response for the preferred and orthogonal orientations (we used the coherence as a marker of similarity, but the mean energy was also similar: 3.6×10^6 and 3.5×10^6 for the two responses).

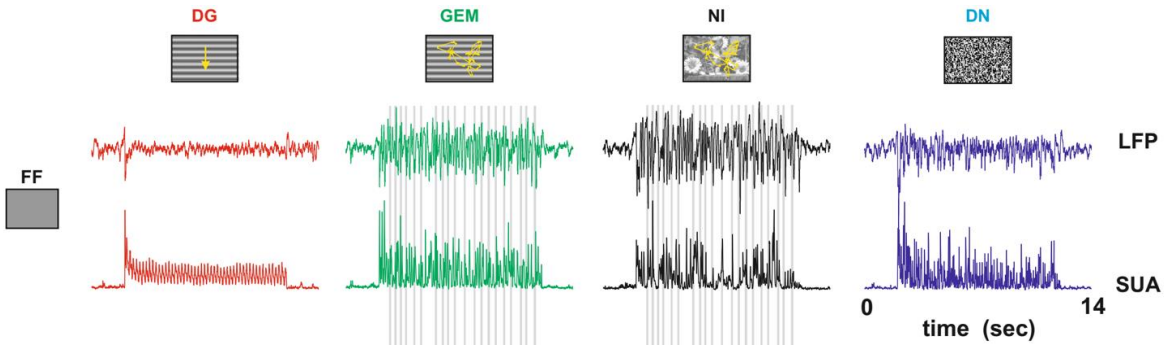

Figure 3.2.13: Example of the LFP and SUA response evoked by our set of stimuli.

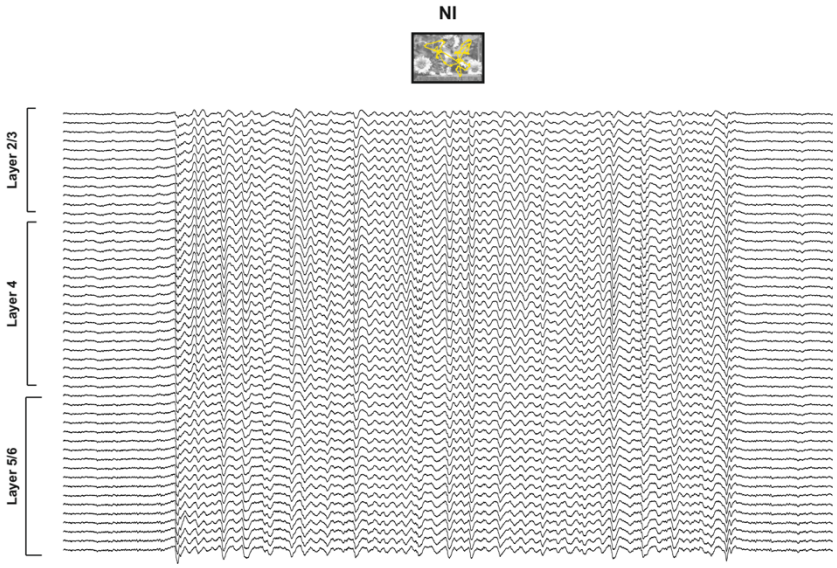

Figure 3.2.14: Mean LFP across layers. Mean LFP across layers in response to natural images.

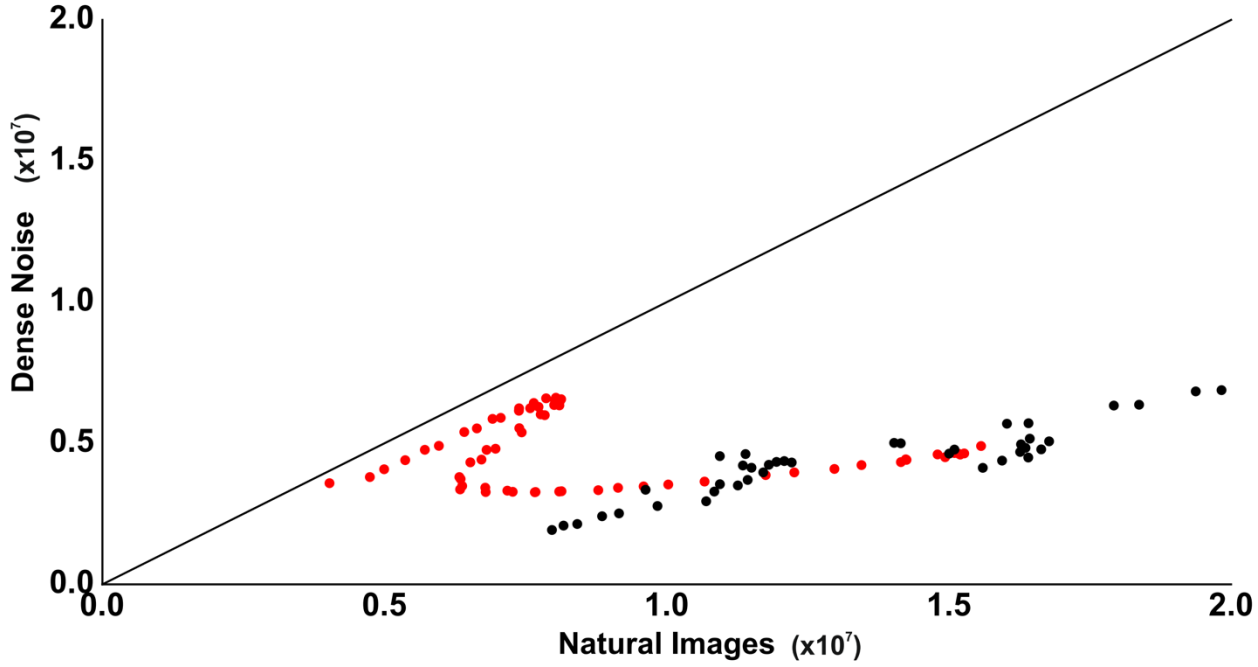

Figure 3.2.15: Scatter plot of the energy evoked by natural images and dense noise. The scatter plot represents two different experiments (black and red dots).

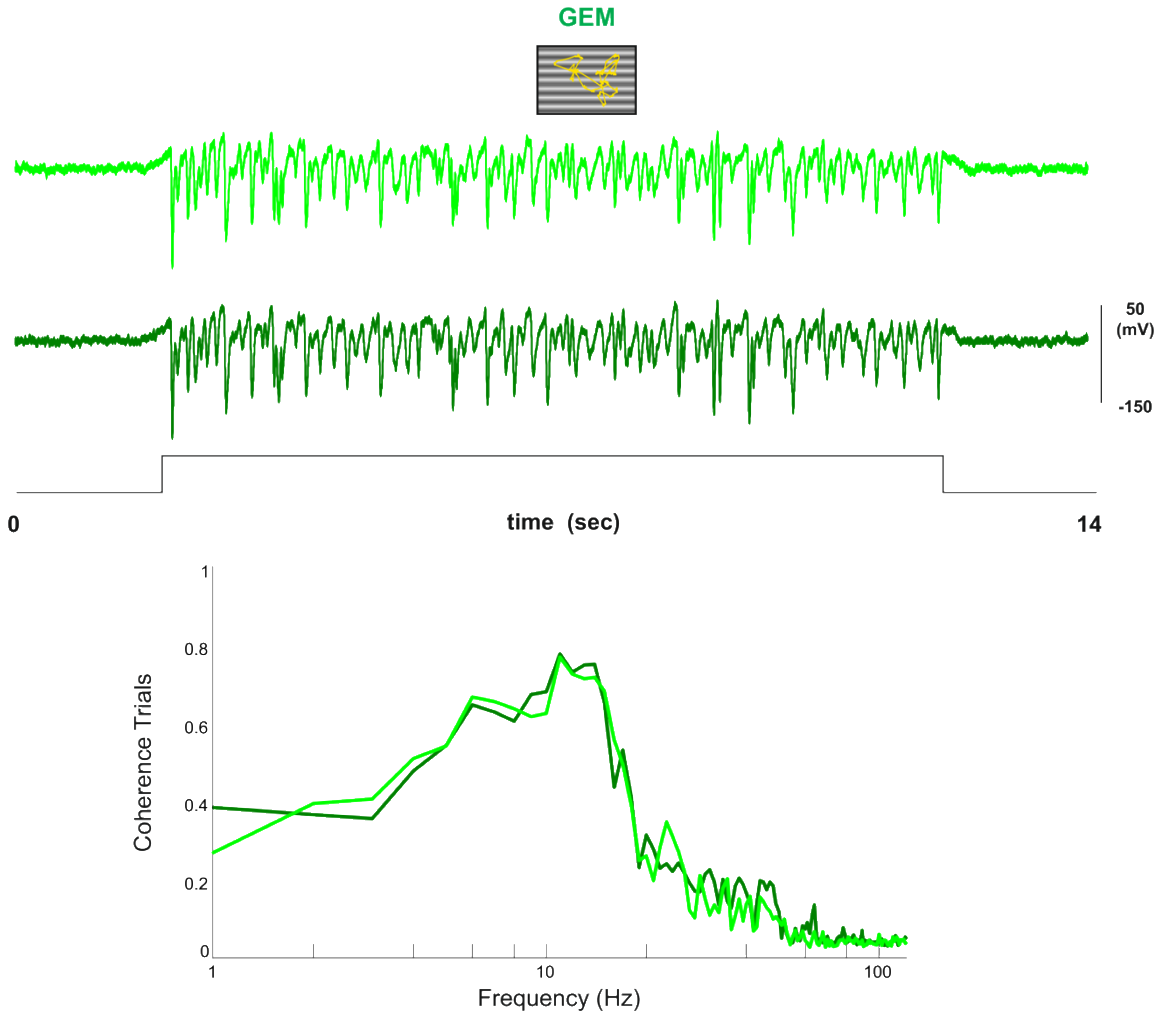

Figure 3.2.16: Comparison of the mean evoked LFP for two different animated gratings. Comparison of the LFP response when two animated gratings were presented at orthogonal orientations (top: mean LFP; bottom: mean coherence)

- **Mean Energy**

The computation of the energy mostly matches our observations. Indeed, we obtained a significantly higher energy when NI were presented compared to other stimuli, while and GEM elicited the highest energy among the artificial stimuli ($p < 0.001$; Friedman test; Figure 3.2.17, table 3.2.4). We also observed that drifting gratings evoked a much lower energy than the other stimuli. The LFP is a mean field signal that records the activity of many neurons, yet neurons responding to DG display are regrouped in phase columns and display a phase preference (Wang et al., 2015). Thus, the LFP correspond to a mixture of neurons displaying different phase preferences, which leads to a very desynchronized signal. Moreover, the neurons strongly adapt their response to DG as shown in the previous section, which is not the case for the other stimuli. This result in a total desynchronization of the LFP despite a spiking activity and a membrane potential locked to the stimulus (as shown in Baudot *et al.*, 2013; Figure 2). This suggests that the mesoscopic information carried by LFPs and the local integration of synaptic input activity realized by a single cell are clearly dissociated unlike what was claimed by Kamondi and colleagues (1998).

- **Energy across layers**

We then computed the energy of the LFP signal within each layer (Figures 3.2.17 and 3.2.18; table 3.2.4). Within each layer, we obtained the same pattern as the one observed for the mean energy ($p < 0.001$, Friedman test). However, we found a difference between layers ($p < 0.001$, Mann Whitney U test). For all stimuli, the lowest energy was found in layer 2/3. For NI and DG, the highest one was located in layer 5/6 while for DN and GEM it was layer 4. The great difference observed between layer 2/3 and the other layers can be explained by the fact that cells in the supragranular layer tend to spike in a sparser way than in other layers, therefore reducing the synchronization of the neuronal activity (Clancy et al., 2015; Tang et al., 2018). In addition, this high energy observed in granular and infragranular layers matches the strong sinks and sources that we observe when the CSD is computed.
A striking result that we obtained is the great heterogeneity of the energy for all stimuli and in all layers. As explained above, this can be caused by the placement of the electrode's reference during the experiment and by the state of the animal.
In summary, we found that natural images evoke a more synchronized signal than the other stimuli. These results are different from the intracellular findings of the laboratory (Baudot *et al.*, 2013), in particular for the mean LFP in response to DG that does not match the intracellular findings. This difference is the result of the intrinsic properties of the LFP.

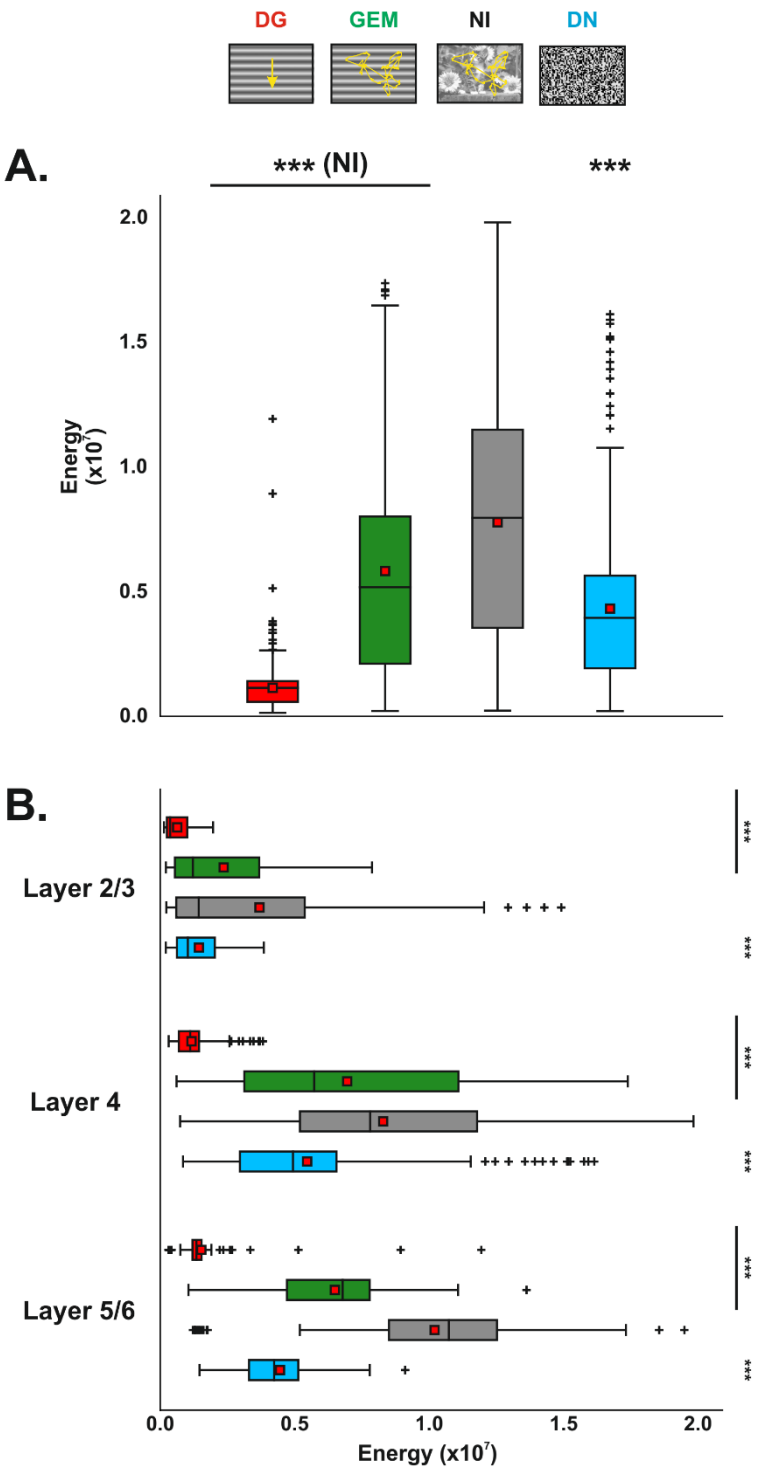

Figure 3.2.17: Mean energy of the LFP. Natural Images evoke the highest energy levels. A. Mean energy of the LFP in response to our set of stimuli. B. Mean laminar energy of the LFP in response to our set of stimuli. Red square: mean. Black line: median. Extremities of the box: first and third quartile. Whiskers: minimum and maximum. Crosses: outliers. ***: $p < 0.001$

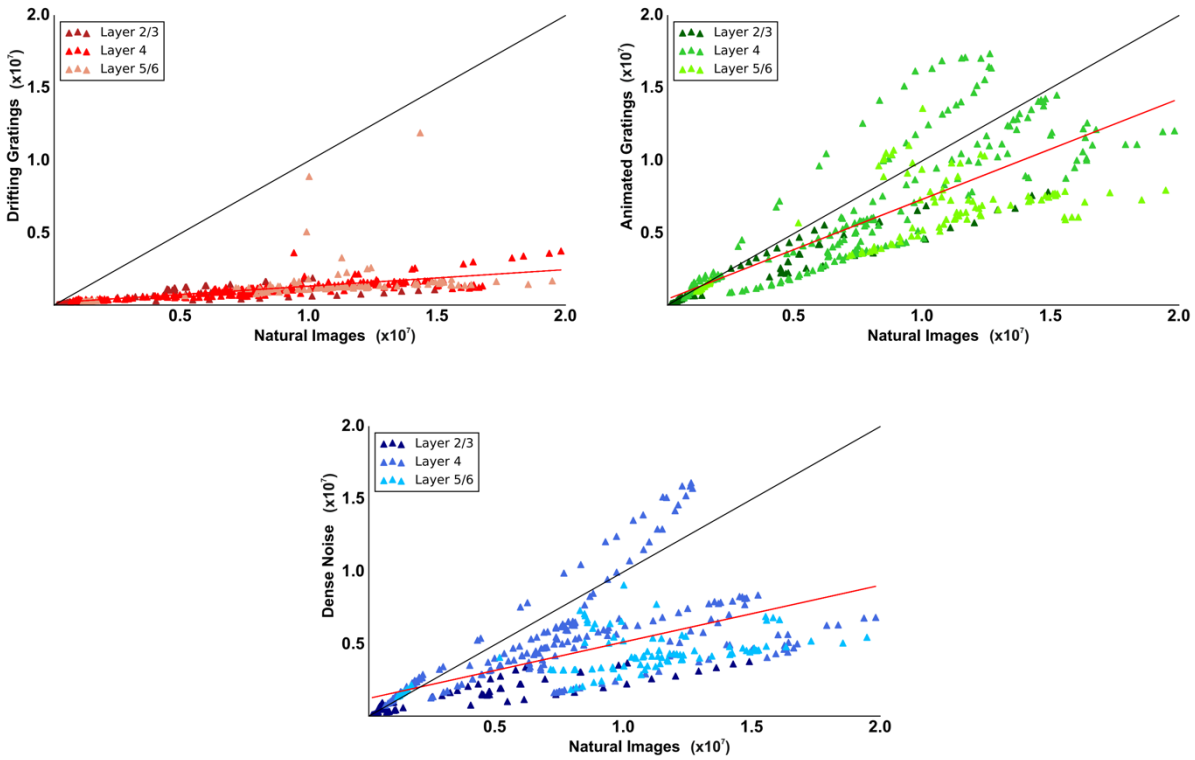

Figure 3.2.18: Energy correlation plots. Top left: Natural images vs drifting gratings; Top right: Natural images vs gratings animated with eye movements. Bottom: Natural images vs dense noise.

- **Impact of the natural statistics on the energy**

Finally, as performed for the spiking activity, we computed the energy from the responses to our control stimuli (Figure 3.2.19, table 3.2.5).
We did not obtain any differences between the unaltered natural image and the one where the spatial statistics were altered ($p > 0.05$; Friedman test). However, the natural image only animated with saccades elicited a higher mean energy than all the other stimuli while the NI and NI-RS evoked a higher energy than NI-RT and NI-RST ($p < 0.001$, Friedman test). The increase observed for NI-SAC is linked to the sole presence of saccades, which leads to a more synchronized response but also to reduced adaptation.
As mentioned in the previous section, the spiking activity does not seem to be impacted by the absence of higher order correlations in the spatio-temporal statistics. This is maybe not the case for LFP, thus for the synaptic activity, which might be impacted by the correlations in the temporal statistics.

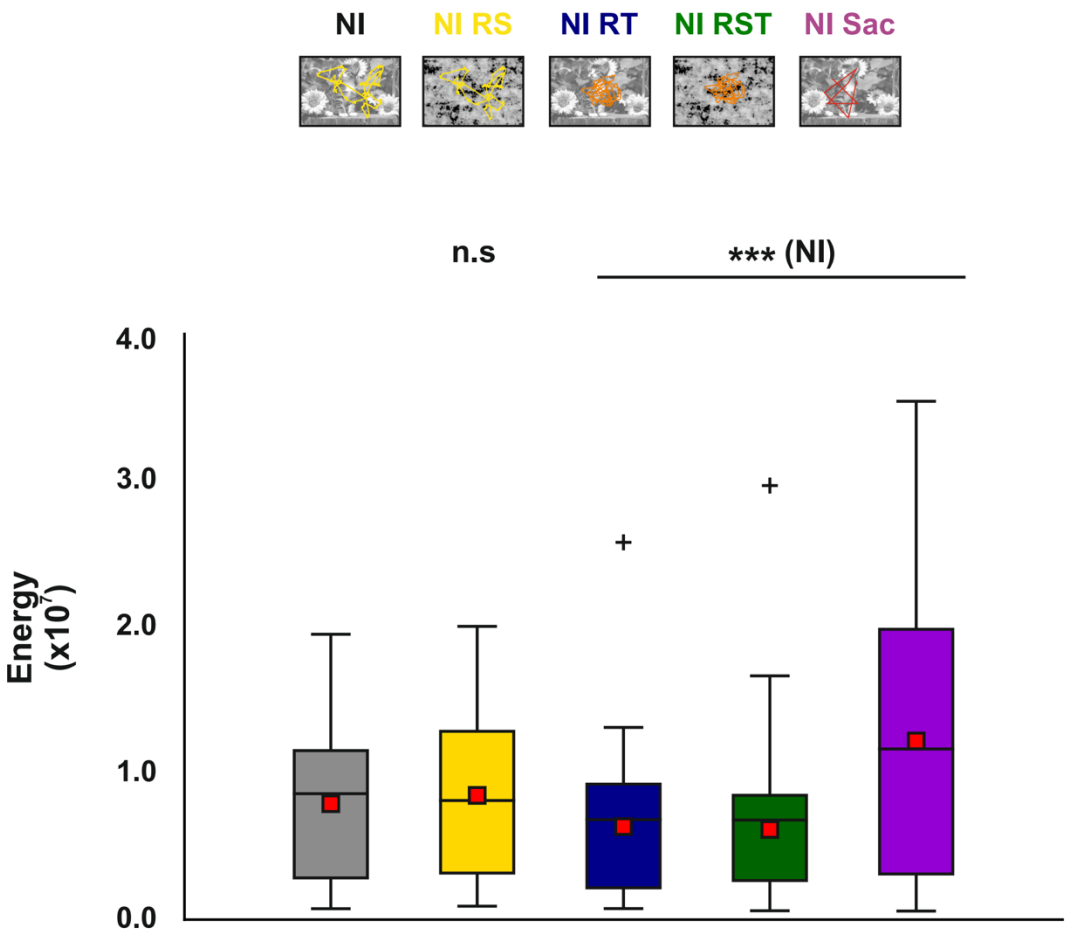

Figure 3.2.19: Mean energy of the LFP. Mean LFP energy in response to our control stimuli. Red squares: mean. Black line: median. Extremities of the box: first and third quartile. Whiskers: minimum and maximum. Crosses: outliers. n.s: non-significant; *** : $p < 0.001$

FULL FIELD	LFP			
	DG	GEM	NI	DN
Mean	1.1e+06 ± 4.9e+04	5.8e+06 ± 2.2e+05	7.8e+06 ± 2.5e+05	4.3e+06 ± 1.7e+05
Layer 2/3	6.3e+05 ± 5.4e+04	2.4e+06 ± 2.4e+05	3.7e+06 ± 4.3e+05	1.4e+06 ± 1.1e+05
Layer 4	1.2e+06 ± 4.5e+04	7.0e+06 ± 3.3e+05	8.3e+06 ± 3.3e+05	5.5e+06 ± 2.4e+05
Layer 5/6	1.5e+06 ± 1.4e+05	6.5e+06 ± 3.1e+05	1.0e+07 ± 4.3e+05	4.5e+06 ± 2.6e+05

Table 3.2.4: Evoked mean energy by our stimulus set (mean ± SEM)

	NI	NI-RS	NI-RT	NI-RST	NI-SAC
FULL FIELD	7.9e+06 ± 3.5e+05	8.5e+06 ± 3.7e+05	6.4e+06 ± 2.9e+05	6.2e+06 ± 2.9e+05	1.2e+07 ± 6.7e+05

Table 3.2.5: Evoked mean energy by our control stimulus set (mean ± SEM)

2.2. Impact of the center surround interactions on the neuronal activity

We investigated the impact natural and artificial full field stimulation on the neuronal activity. The full field (FF) stimulation is defined by the fact that both the center and the surround of the receptive field are stimulated simultaneously. Many studies showed that the concomitant stimulation of both center and surround induced a different response than the stimulation of the center alone (DeAngelis et al., 1994; Guo et al., 2005; Haider et al., 2010; Vinje and Gallant, 2000, see Angelucci et al., 2017 for a review). It is however important to note a lone stimulation of the surround is considered to not elicit any spiking response, although synaptic responses can be elicited 4 to 8° outside the classical RF (Bringuier *et al.*, 1999; Gerard-Mercier *et al.*, 2016). Despite this absence of response for a surround only stimulation, center surround interactions shape the response differently as a function of the type of stimulus.

Firstly, compared to the center stimulation, suppression or facilitation of the neuronal response is induced when both center and surround are stimulated with gratings. A strong suppression occurs when the grating in the center and surround have the same orientation, spatial frequency, direction and speed. A weak suppression or a facilitation occurs when stimuli of orthogonal parameters are presented (DeAngelis *et al.*, 1994; Li & Li, 1994; Durand *et al.*, 2007; Angelucci *et al.*, 2017).

Second, compared to the center stimulation, suppression of the neuronal response is usually induced when both center and surround are stimulated with natural images (Vinje and Gallant, 2000; Haider et al, 2010). However, a study on primates found that a facilitation or an absence of modulation of the neuronal response can also be induced when both center and surround are stimulated with natural scenes (Guo et al., 2005).

This stimulation of both center and surround with natural scenes also impacts other aspects of the visual response. Indeed, it has been shown that the concomitant stimulation of the center and the surround with natural scenes increases the sparseness and the reliability of the spiking activity both at the single and multi-unit levels (Vinje & Gallant, 2000; Haider et al., 2010) and decorrelates the single unit activity (Vinje & Gallant, 2000).

Despite these important results, in our knowledge, no study compares simultaneously the impact of the center surround interactions in both natural and artificial stimuli. In addition, none of the above-mentioned studies investigated the laminar distribution of the coding efficiency (*i.e.* the sparseness, the reliability and the correlation of the response) induced by natural image center surround interactions. Therefore, in this chapter we will investigate how the center surround interactions shape the neuronal response at the spiking level but also at the mesoscopic level (*i.e.* the LFP). Moreover, since a synaptic response can be elicited 4 to 8° outside the classical receptive field, we should expect a strong LFP response for a surround only stimulation. In order to answer these questions, we computed the same indices as in the previous sections.

2.2.1 Quantification of the spiking activity

As performed in the previous section, we will first quantify the firing rate of the single and multi-unit activity when only the center was stimulated with our stimulus set. Since we also investigated the impact of the lone stimulation of the surround on the LFP, we will also describe it for the spiking activity. As described in section 3.1, the center stimulation (C stimulation) was performed on a 5x5° square that was determined from the MUA receptive fields. The surround stimulation (S stimulation) was performed outside this mask and the center surround stimulation covered both the center and surround. In order to avoid any misunderstanding, the center surround stimulation, which corresponds to a full field stimulation will be named this way along this manuscript and will be abbreviated “FF stimulation”.

Haider and colleagues (2010), who performed intracellular recordings in cat primary visual cortex also investigated the impact of natural scene center surround interactions on the neuronal response. They showed that the concomitant stimulation of both center and surround with natural scenes resulted in a suppression of the neuronal activity.
Figure 3.2.20 shows an example of single unit activity evoked by all stimuli presented in the FF, C and S conditions. Unlike what is observed by others, compared to the center stimulation, the stimulation of the full field with natural images seems to increase the spiking activity of the neuron. However, for DG, the full field and center stimulations seem to induce the same activity. It has been shown that the suppression evoked by gratings’ center surround interactions tend to reach a plateau after a certain size of the surround (Ozeki et al., 2004). Surprisingly, the NI surround only stimulation evoked a small response across the duration of the stimulation also present for the FF and C conditions. However, this response was only observed in a very small number of neurons and did not change the mean firing rate of the response evoked by NI that stayed at the same level as the one evoked by the other stimuli. Therefore, we will not further comment this stimulation for the SUA and MUA.

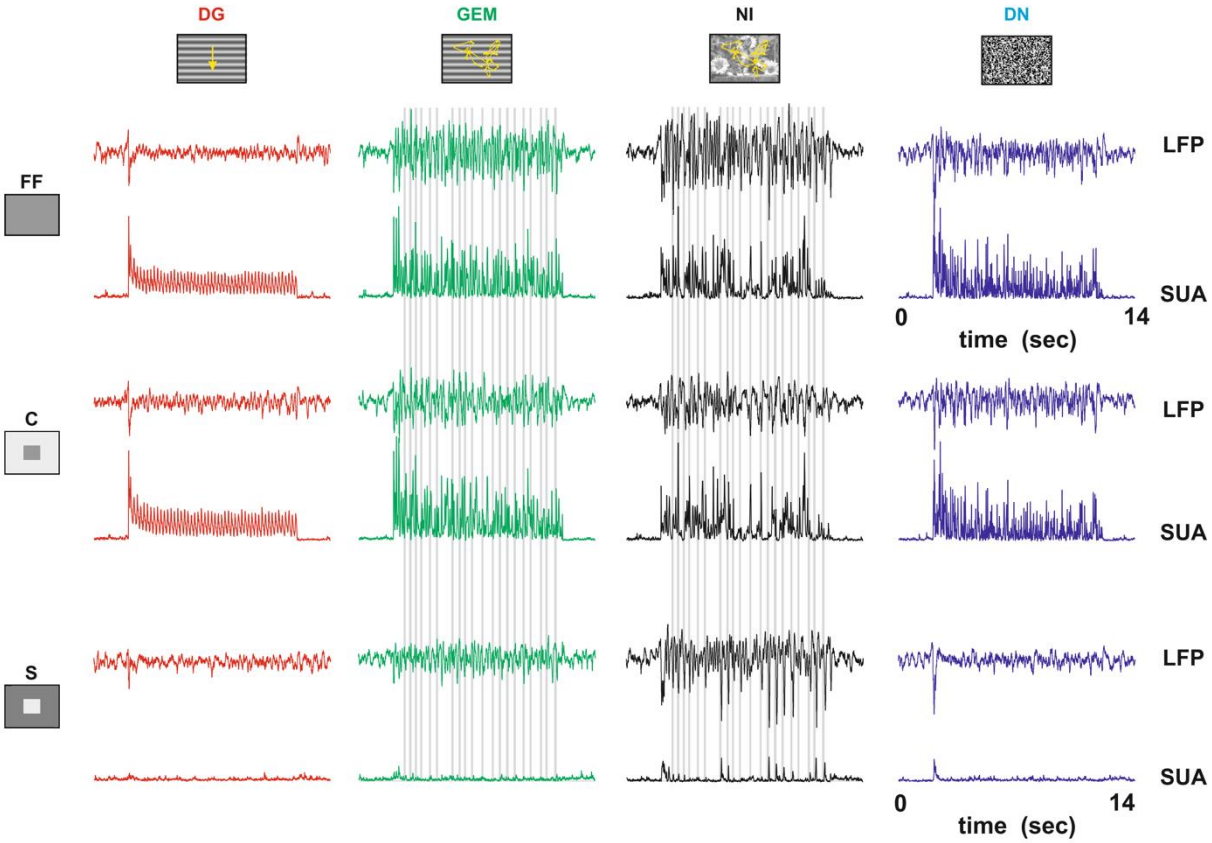

Figure 3.2.20: Example of a single unit and LFP response to our set of stimuli presented full field, center or surround.

- **Impact of the center surround interactions**

In order to be able to evaluate the impact of the center surround interactions on the firing rate we first computed the mean firing rate evoked by the center stimulation (figure 3.2.21; table 3.2.6). As observed for the full field stimulation, drifting gratings evoked the highest firing rate and dense noise the lowest one, for both SUA and MUA ($p < 0.001$; Friedman test).
We then compared the firing rates evoked by the full field and center stimulations. For the SUA, all stimuli evoked the same firing rate for the FF and the C stimulations ($p > 0.05$, Wilcoxon test). Again, as explained above, this is not surprising for drifting gratings. However, the lack of a difference for the NI condition is more surprising. Within our population, some neurons displayed a suppression while other a facilitation when both center and surround where stimulated (figure 3.2.21). This is probably linked to the size of our center stimulation. Indeed, in their paper, Haider and colleagues (2003) showed that natural images also evoke a plateau of maximum suppression. This plateau is reached for stimulations 3 times bigger than the size of the receptive field. However, they stopped their analysis at a stimulation 4 times higher than the size of the RF. Thus, with a 5° stimulation, we are above this 3-times limit. Surprisingly, the full field stimulation with dense noise evoked a higher firing rate than the center one ($p < 0.05$).
For all our multi-unit recordings, the full field stimulation induced a higher firing rate than the center stimulation ($p < 0.001$). However, the difference between the two conditions is small (table 3.2.6). Non-linear mechanisms might shape the response when a certain size of stimulation is reached. In addition, despite the absence of significance for the NI and DG conditions at the single unit level, the mean firing rates evoked by the FF stimulation tend to be higher than the one evoked by the C

condition. By increasing the number of recorded neurons, we might reach a pattern of response similar to the multi-unit one.
We also observed the impact of the center surround interactions on the FS and RS cells (Figure 3.2.21; table 3.2.7). Among RS cells, no difference was observed between the FF and C conditions for NI and DG ($p > 0.05$) while one was present for DN ($p < 0.01$). While FS cells displayed the same pattern of response as the single unit population. The absence of differences for RS neurons could be linked, as explained above, to the size of the center stimulation.

- **Laminar impact of the center surround interactions**

It is known that neurons in layers 2/3 and 5/6 receive horizontal connections coming from other neurons. These horizontal connections are strongly activated by the stimulation of the surround (Bringuier et al., 1999; Frégnac, 2012; Gerard-Mercier et al., 2016). Thus, we wondered if the laminar mean firing rate pattern evoked by the center stimulation was different from the one evoked by the full field one. The laminar pattern was the same except for the SUA, in layer 4, where NI evoked a higher firing rate than DN ($p < 0.001$; Friedman test). Regarding the laminar impact of the full field and center stimulations on the SUA, NI and DG evoked the same firing rate for both conditions, respectively ($p > 0.05$). However, dense noise evoked a higher firing rate for the C stimulation in layers 2/3 and 5/6, while no difference was observed in layer 4. This suggests that responses to dense noise are modulated by the horizontal connections present in these layers. On the other hand, for the MUA, for all stimuli respectively, the center stimulation evoked a lower firing rate than the full field one in all layers ($p < 0.001$).

For both RS and FS neurons, layer 2/3 will be excluded from this comparison because the number of neurons for each class does not allow us to perform any statistical analysis (Figure 3.2.21).
Fast spiking and regular spiking neurons showed no differences between the FF and the C conditions for each layer and each stimulus, respectively ($p > 0.05$, Wilcoxon test). The fact that for the whole SUA population, dense noise showed a difference in layer 5/6 (and 2/3) implies that among FS and RS neurons, some cells were sensitive to center surround interactions while others were not. In their intracellular paper, Haider and colleagues (2010) only recorded a small population of FS and RS cells and might have missed this greater diversity that is unveiled by dense extracellular recordings.

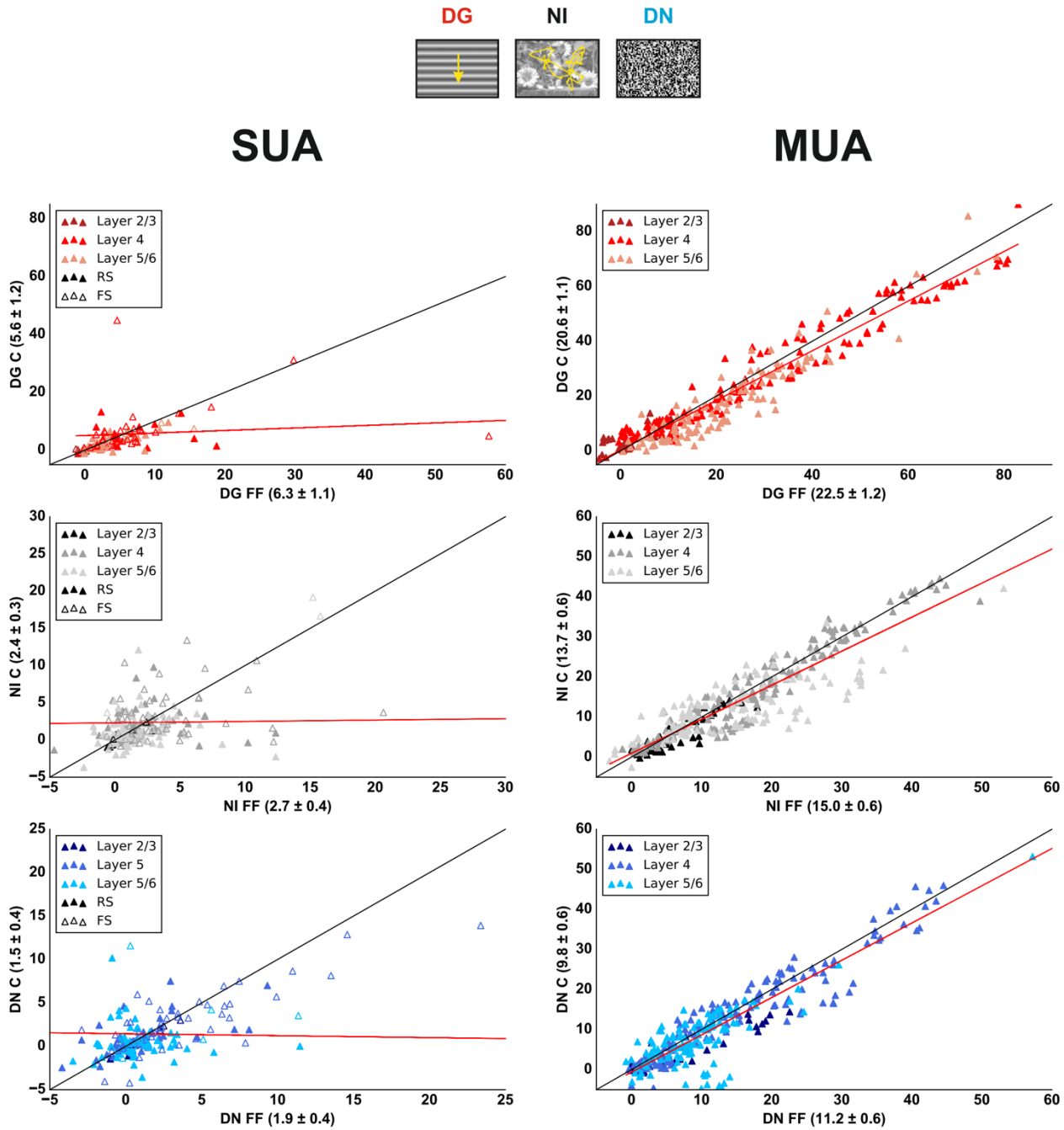

Figure 3.2.21: Firing rates evoked by the full field vs the center conditions. The center surround interactions have a small impact on the firing rate. Left column: single unit activity; Right column: multi-unit activity. Empty symbols = FS; Full symbols = RS or MUA.

- **Impact of the natural statistics on the center surround interactions**

In their work, Guo and colleagues (2015) showed that the center surround modulations are dependent of the spatial statistics of the surround and its higher order spatial correlations. However, their work was performed in the awake monkey. We wondered if these effects were also observed in cats. Based on our previous results, we can suppose that the temporal and spatial higher order correlations will have different levels of impact on the response. We first computed the mean firing rate for our spiking activity and investigated if the center stimulation elicits the same response pattern as the full field one (Figure 3.2.23; table 3.2.8). We found different patterns of response between the full field and center stimulations. Indeed, unlike what was observed for the FF condition, for the SUA when presented in the center only all stimuli evoked the same firing rate ($p > 0.05$; Friedman test). Regarding the MUA, all stimuli evoked a different response from NI except the natural image where both spatial and temporal statistics were altered. NI-RS evoked a higher firing rate than NI, while NI-RT and NI-SAC a lower one ($p < 0.05$).
We then compared the responses evoked by the FF and C conditions for both SUA and MUA (Figure 3.2.23). For the SUA, no difference was observed between the center and full field conditions for each stimulus, respectively ($p > 0.05$; Wilcoxon test).
For the MUA, all altered stimuli evoked a higher response for the center condition, respectively ($p < 0.001$; Wilcoxon test). However, the difference in firing rates remain small between two conditions. Only the unaltered natural images did not display any difference between the two conditions ($p > 0.05$). As explained previously, for NI the difference was very small between the FF and C stimulations. Since we performed our analysis on a reduced multi-unit population compared to the one in figure 3.2.21, there are not enough multi-unit sites to reach a significant response. These results suggest that the higher order correlations tend to have an impact on the center surround interactions that lead to an increase of the firing rate.
We also investigated the impact of the center surround interactions on the RS and FS neurons. No difference between the FF and C conditions was observed ($p > 0.05$: table 3.2.8).

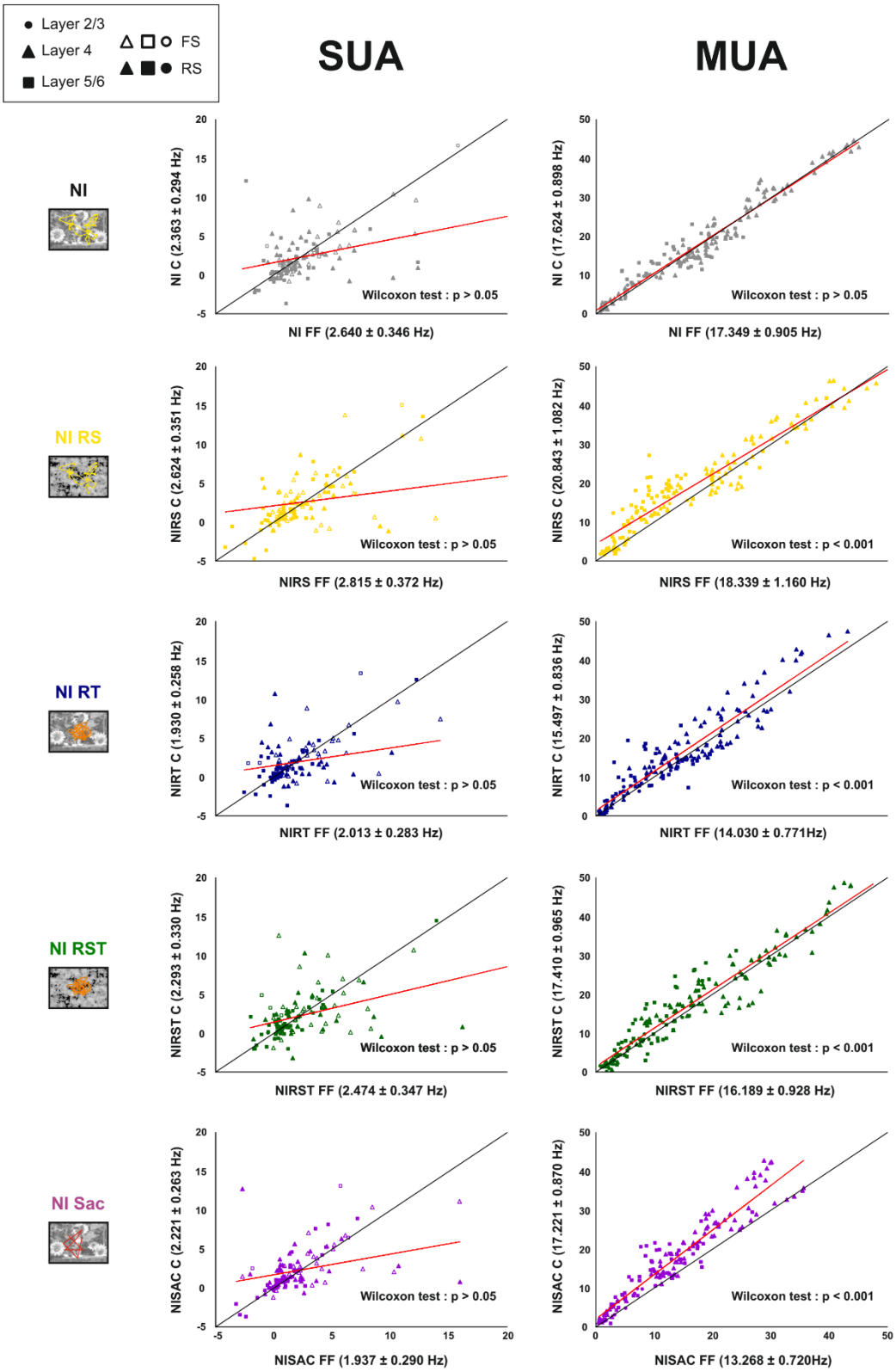

Figure 3.2.23: Firing rates evoked by the full field vs center stimulation. Left panel: Single unit activity firing rate. Right panel: Multi-unit activity firing rate. Red line: polynomial fit. Circles: Layer 2/3; Triangles: Layer 4; Squares: Layer 5/6. Empty symbols = FS. Full Symbols = RS or MUA.

FULL FIELD	SUA		
	DG	NI	DN
Mean (w/o GEM)	6.3 ± 1.1	2.7 ± 0.4	1.9 ± 0.4
Layer 2/3	-0.3 ± 0.2	0.6 ± 0.4	1.1 ± 0.4
Layer 4	7.9 ± 1.6	3.2 ± 0.5	2.2 ± 0.4
Layer 5/6	5.0 ± 1.5	2.5 ± 0.7	1.7 ± 0.8

CENTER	SUA		
	DG	NI	DN
Mean (w/o GEM)	5.6 ± 1.2	2.4 ± 0.3	1.5 ± 0.4
Layer 2/3	-0.1 ± 0.2	0.4 ± 0.3	0.5 ± 0.4
Layer 4	7.1 ± 1.6	2.8 ± 0.4	1.7 ± 0.3
Layer 5/6	4.4 ± 2.0	2.1 ± 0.6	1.4 ± 0.8

FULL FIELD	MUA		
	DG	NI	DN
Mean (w/o GEM)	22.5 ± 1.2	15.0 ± 0.6	11.2 ± 0.6
Layer 2/3	0.3 ± 0.6	6.3 ± 0.7	5.9 ± 1.0
Layer 4	28.7 ± 1.9	17.1 ± 0.9	13.9 ± 0.9
Layer 5/6	23.2 ± 1.5	15.2 ± 1.0	9.5 ± 0.8

CENTER	MUA		
	DG	NI	DN
Mean (w/o GEM)	20.6 ± 1.1	13.7 ± 0.6	9.8 ± 0.6
Layer 2/3	2.6 ± 0.5	5.4 ± 0.7	3.8 ± 0.7
Layer 4	27.3 ± 1.7	16.4 ± 0.9	13.0 ± 0.9
Layer 5/6	19.1 ± 1.7	13.0 ± 0.7	7.6 ± 0.8

Table 3.2.6: Mean firing rate values for the single and multi-unit activity.

FULL FIELD	FS		
	DG	NI	DN
Mean	10.1 ± 2.5	4.8 ± 1.0	3.9 ± 1.1
Layer 2/3	0.4 ± 0.5	1.6 ± 0.7	2.2 ± 0.7
Layer 4	9.7 ± 2.5	4.4 ± 0.9	3.2 ± 0.6
Layer 5/6	14.9 ± 9.2	7.3 ± 4.0	7.1 ± 5.1

CENTER	FS		
	DG	NI	DN
Mean	9.8 ± 2.8	4.1 ± 0.8	3.4 ± 1.0
Layer 2/3	0.4 ± 0.2	1.3 ± 0.5	1.9 ± 0.6
Layer 4	9.0 ± 2.5	3.5 ± 0.6	2.5 ± 0.5
Layer 5/6	15.7 ± 12.0	6.9 ± 3.6	7.0 ± 4.7

FULL FIELD	RS		
	DG	NI	DN
Mean	3.7 ± 0.5	1.6 ± 0.2	0.7 ± 0.2
Layer 2/3	0.2 ± 0.1	0.1 ± 0.2	0.4 ± 0.3
Layer 4	5.2 ± 1.1	1.7 ± 0.5	0.9 ± 0.4
Layer 5/6	3.1 ± 0.4	1.7 ± 0.3	0.7 ± 0.2

CENTER	RS		
	DG	NI	DN
Mean	2.7 ± 0.4	1.4 ± 0.2	0.4 ± 0.2
Layer 2/3	0.4 ± 0.1	0.1 ± 0.3	0.3 ± 0.3
Layer 4	4.0 ± 0.9	1.9 ± 0.4	0.7 ± 0.4
Layer 5/6	2.3 ± 0.4	1.2 ± 0.2	0.3 ± 0.2

Table 3.2.7: Mean firing rate values for the Fast and Regular spiking neurons.

FULL FIELD					
	NI	NI-RS	NI-RT	NI-RST	NI-SAC
FS	3.9 ± 0.7	4.2 ± 0.8	2.9 ± 0.5	3.6 ± 0.7	2.8 ± 0.5
RS	1.9 ± 0.3	2.1 ± 0.4	1.5 ± 0.3	1.7 ± 0.4	1.4 ± 0.3
SUA	2.6 ± 0.3	2.8 ± 0.4	2.0 ± 0.3	2.4 ± 0.3	1.9 ± 0.3
MUA	17.3 ± 0.9	18.3 ± 1.2	14.0 ± 0.8	16.2 ± 0.9	13.3 ± 0.7

CENTER					
	NI	NI-RS	NI-RT	NI-RST	NI-SAC
FS	3.6 ± 0.6	3.5 ± 0.7	2.8 ± 0.5	3.4 ± 0.7	3.0 ± 0.5
RS	1.7 ± 0.3	2.1 ± 0.4	1.4 ± 0.3	1.6 ± 0.3	1.8 ± 0.3
SUA	2.4 ± 0.3	2.6 ± 0.4	1.9 ± 0.3	2.3 ± 0.3	2.2 ± 0.3
MUA	17.6 ± 0.9	20.8 ± 1.1	15.5 ± 0.8	17.4 ± 1.0	17.2 ± 0.9

Table 3.2.8: Mean firing rate values evoked by our control stimuli.

2.2.2 Quantification of the local field potential

In the previous section, we showed that natural images evoke a higher energy than the artificial stimuli. We also showed that the spiking activity is modulated by the center surround interactions. Moreover, an intracellular study performed on the anesthetized and paralyzed cat showed that the evoked membrane potential by natural images is modulated by center surround interactions (Haider et al., 2010). Even if we showed that LFP and V_m are similar but different signals we wondered if we would observe an increase in energy for the LFP when natural scenes, but also artificial stimuli are presented in the full field condition compared to the center condition. In addition, while spiking activity evoked no response for the surround only stimulation, a lone stimulation of the surround can elicit a synaptic response (Bringuier *et al.*, 1999; Chavane et al., 2011; Gerard-Mercier *et al.*, 2016). Thus, we wondered if the sole stimulation of the surround also evokes a response. Our previous results also showed that the levels of energy are layer dependent. Will we observe a laminar dependence of the center surround interactions?

- **Impact of the center surround interactions**

Figure 3.20 (in the previous section) illustrates the LFP evoked by our set of stimuli in the full field, center and surround conditions.
In figure 3.2.24 (and table 3.2.9) we investigated the LFP energy evoked by of our set of stimuli presented on the center and surround conditions. We then compared the energy evoked by the full field, center and surround conditions for each stimulus, respectively. As observed for the full field condition, when presented in the center, natural images evoked the highest energy and DG the lowest, confirming our observations made in figure 3.2.17 ($p < 0.001$; Friedman test; Figure 3.2.24; table 3.2.9). We then wondered if the center surround interactions had an impact on the LFP energy (Figure 3.2.24). All LFPs displayed a higher energy when the stimulus was presented in the full field condition ($p < 0.001$; Wilcoxon test). However, natural images were more impacted by the center surround interactions than other stimuli. Indeed, as shown in figure 3.2.24 (and table 3.2.9), the difference between the FF and C conditions was higher for NI than for the other stimuli. For NI, the energy of the FF stimulation was about 2 times higher than the C stimulation. On the other hand, for artificial stimuli this difference was only about 1.5 times (Table 3.2.9).
Surprisingly, the surround condition also evoked a very synchronized LFP response, in particular when natural images are presented. Indeed, when only the surround is stimulated, natural images still evoked the highest energy among all the stimuli ($p < 0.001$; Friedman test). In this condition, the difference in energy between natural images and the other stimuli is increased while the difference between the artificial stimuli is decreased. This highlights a specific effect of the surround in the processing of natural scenes. Despite the strong response evoked by natural images when presented on the surround, the full field evoked the highest energy ($p < 0.001$; Wilcoxon test; Figure 3.2.24; table 3.2.9). This was also observed for the artificial stimuli. However, the difference in the evoked energy between the surround and full field conditions was higher for the artificial stimuli than the natural one (Table 3.2.9). We also investigated the difference in energy between the center and surround conditions. Unsurprisingly, the three artificial stimuli evoked a higher response for the center condition. However, natural images evoked the same energy for the surround condition as for the center one ($p < 0.05$; Wilcoxon test; Figure 3.2.24).
This was not observed for all LFP sites. Indeed, some sites displayed a higher energy for the center condition while others for the surround.

- **Laminar Impact of the center surround interactions**

Because each layer has its own properties, in particular layers 2/3 and 5/6 that are known to be more sensitive to surround interactions because of the horizontal connections present in these layers, we wondered if each laminar compartment is impacted the same way by the center surround interactions (figure 3.2.24; table 3.2.9). For both center and surround stimulations, we observed the same pattern of response as in the full field one (table 3.2.9). We computed, for each layer, the difference between the full field and center conditions. Again, the impact of the center surround modulation is stronger for natural images than for the artificial stimuli.
When presented on the surround, unlike what was observed for the center condition, natural images evoked the highest energy in layer 5/6 and the lowest one in layer 2/3. The fact that layer 5/6 displays a higher energy could be linked to the horizontal connections present in this layer. Layer 2/3, which also contains horizontal connections might display a lower energy because of the sparser activity of this layer. Within all layers, the natural images presented in the full field condition evoked a higher energy than the surround condition ($p < 0.001$; Wilcoxon test). Surprisingly, within all layers the surround condition evoked a higher energy than the center condition ($p < 0.001$; Wilcoxon test). The difference between the center and surround conditions was the highest in layers 2/3 and 5/6, which contain horizontal connections, suggesting an important role of these in the processing of the surround natural statistics.
In summary, we showed that when natural images are presented on the surround, a strong response is elicited. This response is higher than the one evoked by a center stimulation, highlighting the importance of the surround in the processing of natural scenes.

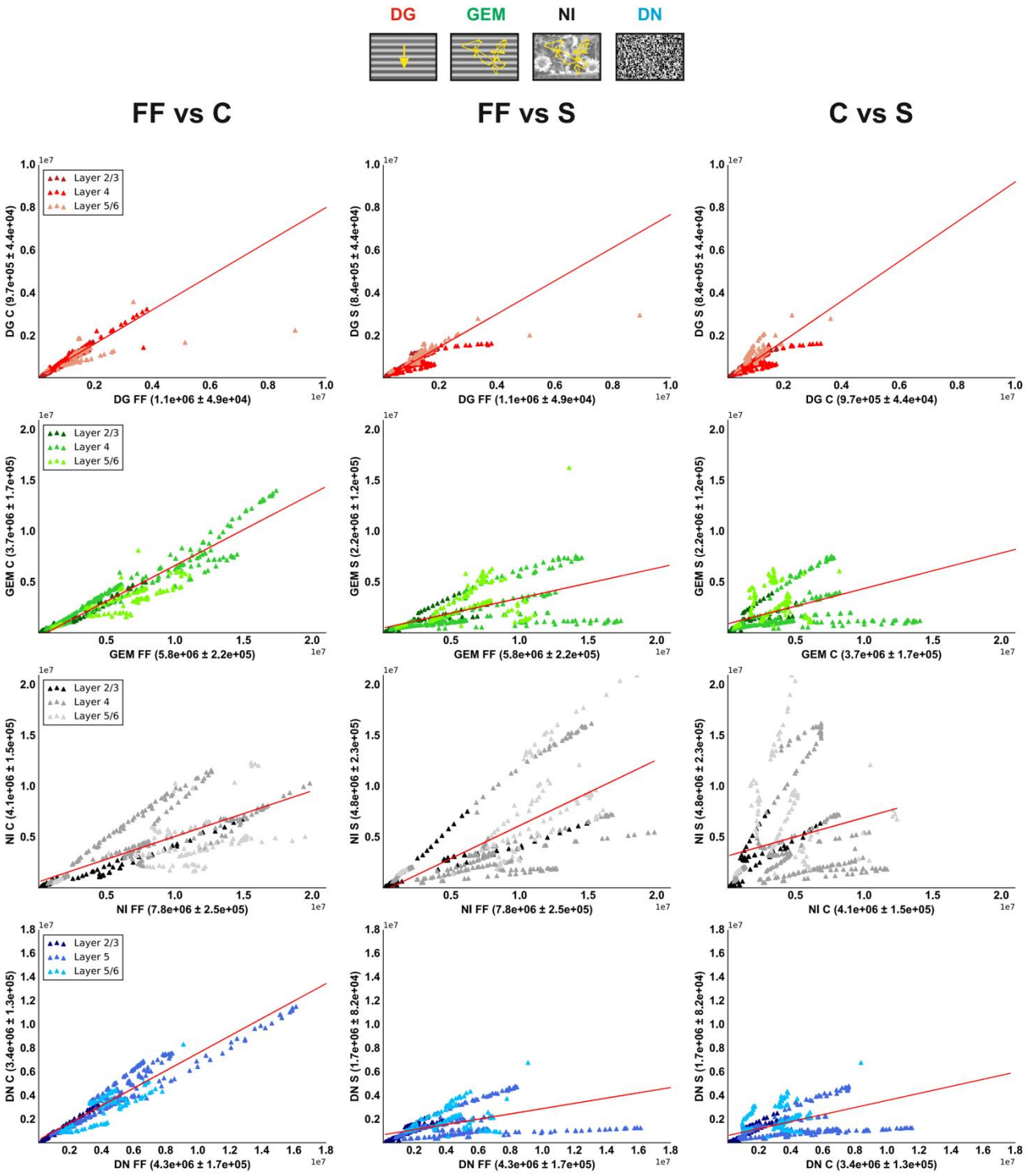

Figure 3.2.24: Correlation plots of the mean energy. LFP energy evoked by full field, center and surround stimulations. The surround of Natural images evokes high energy levels, in particular in layers 2/3 and 5/6. Left column: Full field vs center. Center column: Full field vs surround. Right column: center vs surround

- **Impact of the Natural Statistics on the center surround interactions**

Our previous results showed that the surround of natural images evokes a strong LFP response. This response is not only linked to the temporal statistics of the image since GEM did not show the same energy levels as NI. We wondered how spatio-temporal statistics shape the response and what their impact is on the energy levels. In order to answer this question, we computed the energy evoked by our set of control stimuli (figure 3.2.25; table 3.2.10).
Our results show that for the center condition, the unaltered and the altered natural scenes evoked the same energy ($p > 0.05$, Friedman test). In addition, all stimuli evoked a higher energy when presented full field. This confirms the importance of the full field on the processing of natural scenes, even if they have altered statistics.
However, for the surround condition, all stimuli except NI-RS evoked a different energy than the unaltered natural image. The natural image animated only with saccades evoked a higher energy than the unaltered natural image, while NI-RT and NI-RST evoked a lower energy than NI ($p < 0.001$; Wilcoxon test). This result highlights the importance of the surround in the processing of unaltered temporal statistics. In addition, the surround seems more suited to the processing of high-speed transitions, *i.e.* the saccades.
The full field condition evoked a higher energy than the center condition for all stimuli($p < 0.001$). However, there is no difference in energy between the center and surround conditions for NI, NI-RS and NI-SAC ($p > 0.05$). On the other hand, NI-RST and NI-RT evoked a higher energy for the center condition ($p < 0.001$). This suggests that the center is also suited to process the eye movements but that the surround processing of altered temporal statistics is not optimal.
In summary we showed that at the LFP level, the surround is not suited to the processing of altered temporal statistics unlike the center.

In this section we quantified the response of both spiking activity and local field potential. The spiking activity is the direct measurement of the neuronal activity while the LFP corresponds to a mean field that contains the summed transmembrane currents. This functional difference led to diverse behaviors between these two signals. Two striking aspects of these signals were observed. The first one is that a stimulus that evokes a strong response at the spiking level, such as drifting gratings, can induce a very small LFP. This is linked to the mean field properties of the local field potential. The second one is that the LFP is more sensitive to the center surround interactions than the spiking activity. This could be linked to the fact that the LFP gathers the activity of many cells, thus by increasing the number of responses we increase the visibility of the effect. Another explanation is that, since we know the membrane potential is strongly modulated by the surround (Bringuier et al, 1999; Chavane et al., 2011; Gerard-Mercier et al, 2014) the LFP might reflect the V_m response. A comparison of the spiking activity and the LFP will be needed in order to evaluate, in our data, the impact of the spiking activity on the LFP response. The recording of the membrane potential in response to our set of stimuli could also highlight the impact of this on the LFP.

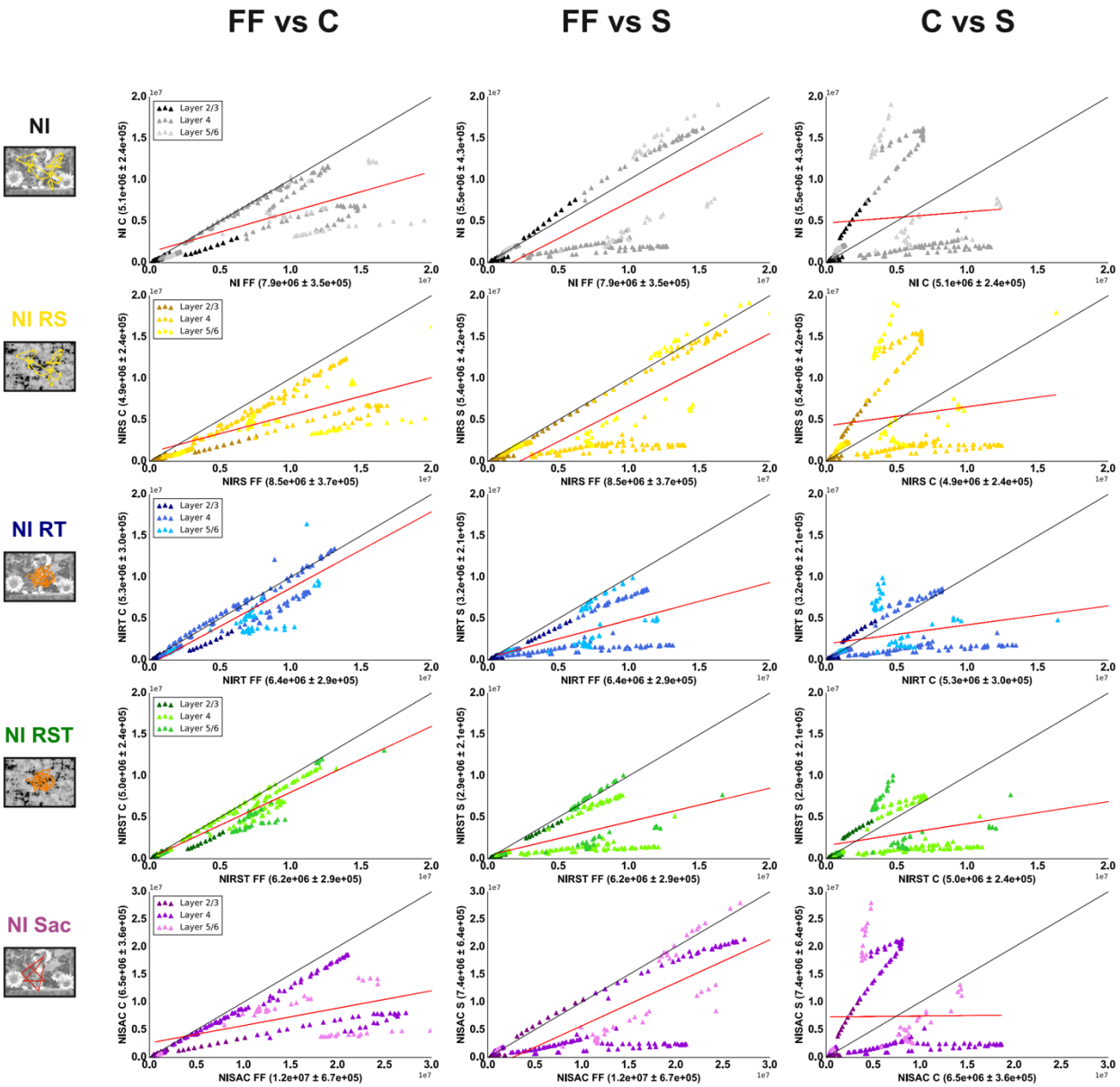

Figure 3.2.25: Correlation plots of the mean energy. LFP energy evoked by full field, center and surround stimulations. Left column: Full field vs center. Middle column: Full field vs surround. Right column: center versus surround. Red line: polynomial fit.

FULL FIELD	LFP			
	DG	GEM	NI	DN
Mean	1.1e+06 ± 4.9e+04	5.8e+06 ± 2.2e+05	7.8e+06 ± 2.5e+05	4.3e+06 ± 1.7e+05
Layer 2/3	6.3e+05 ± 5.4e+04	2.4e+06 ± 2.4e+05	3.7e+06 ± 4.3e+05	1.4e+06 ± 1.1e+05
Layer 4	1.2e+06 ± 4.5e+04	7.0e+06 ± 3.3e+05	8.3e+06 ± 3.3e+05	5.5e+06 ± 2.4e+05
Layer 5/6	1.5e+06 ± 1.4e+05	6.5e+06 ± 3.1e+05	1.0e+07 ± 4.3e+05	4.5e+06 ± 2.6e+05

CENTER	LFP			
	DG	GEM	NI	DN
Mean	9.7e+05 ± 4.4e+04	3.7e+06 ± 1.7e+05	4.1e+06 ± 1.5e+05	3.4e+06 ± 1.3e+05
Layer 2/3	5.8e+05 ± 5.1e+04	1.5e+06 ± 1.5e+05	1.6e+06 ± 1.8e+05	1.3e+06 ± 9.8e+04
Layer 4	1.0e+06 ± 3.7e+04	4.8e+06 ± 2.4e+05	5.2e+06 ± 2.1e+05	4.5e+06 ± 1.9e+05
Layer 5/6	1.2e+06 ± 1.4e+05	3.6e+06 ± 3.3e+05	4.2e+06 ± 2.6e+05	3.2e+06 ± 2.0e+05

SURROUND	LFP			
	DG	GEM	NI	DN
Mean	8.4e+05 ± 4.4e+04	2.2e+06 ± 1.2e+05	4.8e+06 ± 2.3e+05	1.7e+06 ± 8.2e+04
Layer 2/3	5.7e+05 ± 4.8e+04	1.2e+06 ± 1.1e+05	2.2e+06 ± 2.2e+05	9.6e+05 ± 7.5e+04
Layer 4	7.3e+05 ± 2.4e+04	2.1e+06 ± 1.4e+05	4.4e+06 ± 3.0e+05	1.6e+06 ± 8.1e+04
Layer 5/6	1.3e+06 ± 1.5e+05	3.3e+06 ± 3.0e+05	7.5e+06 ± 5.0e+05	2.4e+06 ± 2.4e+05

Table 3.2.9: Mean energy evoked by the presentation of our stimulus set on full field, on the center or the surround (mean ± SEM)

	NI	NI-RS	NI-RT	NI-RST	NI-SAC
FULL FIELD	7.9e+06 ± 3.5e+05	8.5e+06 ± 3.7e+05	6.4e+06 ± 2.9e+05	6.2e+06 ± 2.9e+05	1.2e+07 ± 6.7e+05
CENTER	5.1e+06 ± 2.4e+05	4.9e+06 ± 2.4e+05	5.3e+06 ± 3.0e+05	5.0e+06 ± 2.4e+05	6.5e+06 ± 3.6e+05
SURROUND	5.5e+06 ± 4.3e+05	5.4e+06 ± 4.2e+05	3.2e+06 ± 2.1e+05	2.9e+06 ± 2.1e+05	7.4e+06 ± 6.4e+05

Table 3.2.10: Mean energy evoked by the presentation of our control stimulus set on full field, on the center or the surround (mean ± SEM)

3. SPARSENESS AND RELIABILITY OF THE NEURONAL RESPONSE

The principle of efficient coding suggests that visual processing in early sensory systems is optimized and adapted to the statistical properties of the sensory environment. This should result in a redundancy reduction between neurons (a decorrelation between neuronal response), associated with an increase in the sparseness of the population activity and a decrease in the response variability (Barlow, 1961). In this section we will focus on the sparseness and the reliability of the response. Different studies showed that natural images increase the sparseness and the reliability of the response (Vinje and Gallant, 2000; Haider et al, 2010). However, in our knowledge, no multiscale laminar recordings performed in response to both artificial and natural stimuli have been performed.

3.1. Impact of the full field stimulation

3.1.1 Sparseness of the spiking activity

The analysis of the extracellular spiking activity highlighted the stimulus dependence of the firing rate. As shown in figure 3.2.2 the recorded neurons can display a dense or a sparse discharge pattern, which affects the mean firing rate. In their intracellular study, Baudot et al. (2013) showed that this discharge pattern is stimulus dependent. In order to quantify the density of the discharge pattern of the recorded activity we computed the sparseness of the single unit and multi-unit activity in response to our set of stimuli (and their controls) and compared it to the intracellular results obtained in the laboratory. We used the same sparseness measure as in the intracellular study (*i.e.* lifetime sparseness). The sparseness mean values were averaged over the whole stimulus presentation with a bin equal to the refresh rate of stimuli (15 ms). Figure 3.3.1 shows the sparseness evoked by our stimuli for a highly responsive neuron, a not very responsive neuron and the multi-unit activity. As observed intracellularly, the sparseness tends to decrease with the increase of the PSTH bin size. In these examples we also observed that natural images evoked the highest sparseness levels. Unsurprisingly, the MUA evoked a lower sparseness than the SUA.

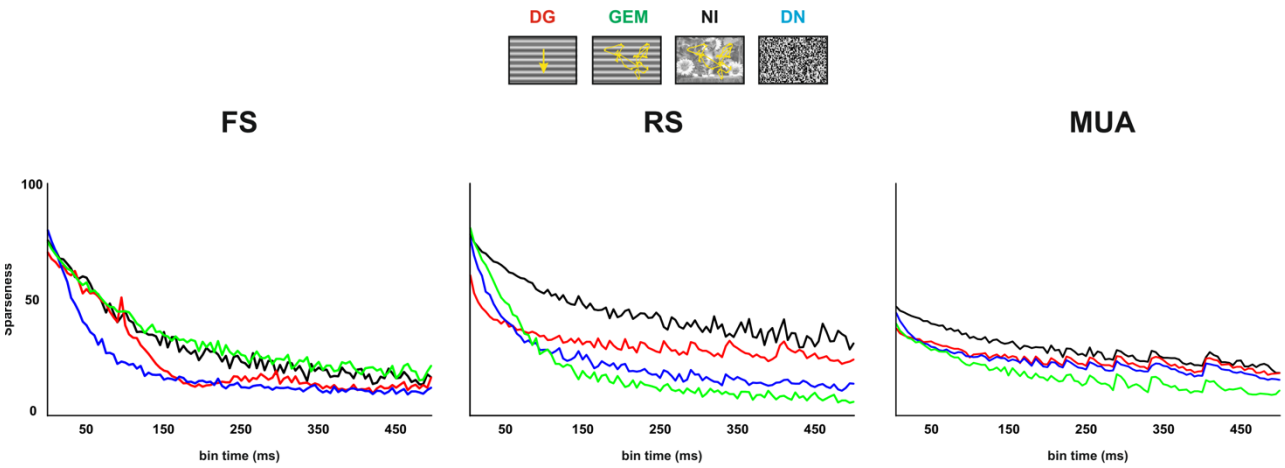

Figure 3.3.1: Sparseness vs bin size obtained for two single units (FS & RS cells) and multi-unit activity.

- **Comparison with the intracellular recordings**

As explained earlier we investigated the sparseness among two neuronal populations, one with GEM and one without GEM. At the level of the population with GEM, the single-unit sparseness and the one obtained with intracellular recordings displayed the same pattern *i.e.* natural images evoked the sparsest response while DG the lowest one (Figure 3.3.2-A; Table 3.3.1; $p < 0.001$, Friedman test). However, the intracellular study reported higher sparseness values. This is probably linked to the recording technique. As explained in the previous section, by not recording less responsive cells, intracellular recordings introduce a bias that is not present in the simultaneous recordings of the extracellular technique. The rasters and PSTHs displayed in figures 3.2.4 and 3.2.5 show that these cells are taken into account in our study. Another possible explanation is the difference in the anesthetics used. Indeed, Haider et al. (2010) who also recorded intracellularly the responses of cat V1 neurons to natural movies, presented on the center and the surround of the receptive field, but used Isoflurane as an anesthetic, found sparseness values similar to ours. Indeed, Althesin, the anesthetic used by Baudot and colleagues (2013), induces a higher post synaptic depression than isoflurane (El-Beheiry and Puil, 1989).Therefore, higher inhibition leads to a sparser spiking activity.

On the other hand, the MUA exhibited a much lower and different pattern of sparseness (Figure 3.2.2-A). Admittedly, as observed for the SUA and the intracellular recordings, natural images evoked the sparsest response. However, DG and GEM evoked an equivalent sparseness, higher than the one elicited by the dense noise stimulation (Figure 3.3.2-A, table 3.3.1). As explained in the previous section, our MUA measurement corresponds to all the signals between 250Hz and 5Khz, crossing an automatic threshold. Thus, the MUA corresponds to the summed activity of many single units, which densifies the response. We compared the sparseness of the summed activity of 4 single units and to the multi-unit and found very similar results. The sparseness reduction observed for MUA comes from a densification of the response. Regarding the sparseness evoked by dense noise, these results are explained by the response of some cells to white pixels while others respond to black ones. Since the MUA regroups these two types of cells, it will regroup these responses, leading to a densification of the response.
In summary, our extracellular results are close to the ones found with intracellular recordings by Baudot and colleagues (2013). Some differences are present that can either be explained by the number of cells recorded in our study or the difference in anesthetics between the two studies. It is important to note that our results are closer to another intracellular study (Haider et al., 2010) where the cats were anesthetized with isoflurane, as we do.

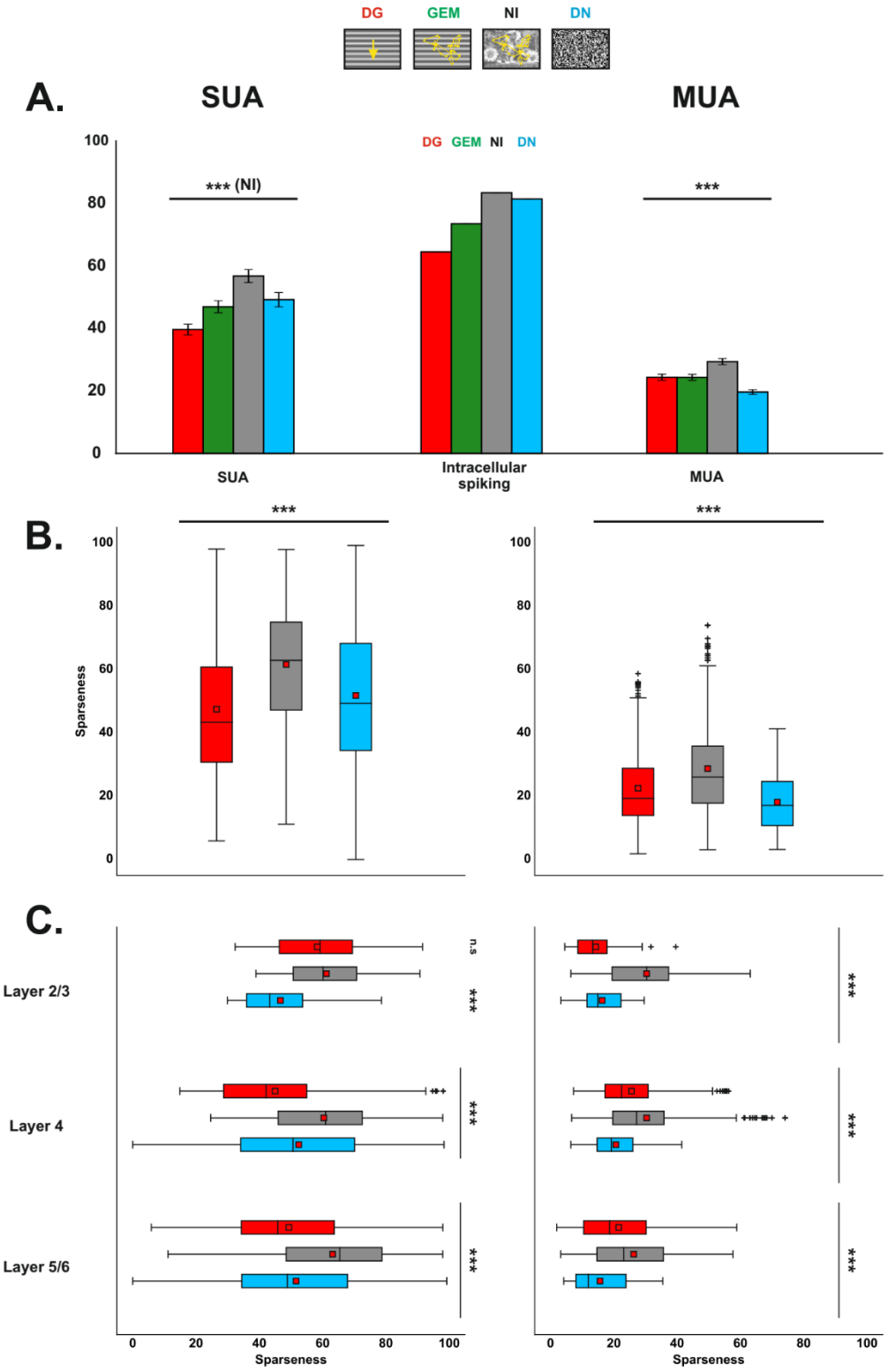

Figure 3.3.2: Single and multi-unit mean sparseness. A. Multiscale comparison of the mean sparseseness. Natural images evoke the sparsest responses. Left: Single unit activity (n = 78), center: intracellular results. Right: Multi-unit activity (77 sites). **B.** Comparison of the mean sparseness. Left: single unit activity (n = 221), right: multi-unit activity (377 sites). **C.** laminar comparison of the mean sparseness. Left: single unit activity (L2/3 = 10; L4 = 111; L5/6 = 99 neurons), right: multi-unit activity (L2/3 = 52; L4 = 187; L5/6 = 138 sites). Red squares: mean. Black line: median. Extremities of the box: first and third quartile. Whiskers: minimum and maximum. Crosses: outliers. Stars indicate values significantly different from the NI condition ***** : $p < 0.05$; ** : $p < 0.01$; *** : $p < 0.001$

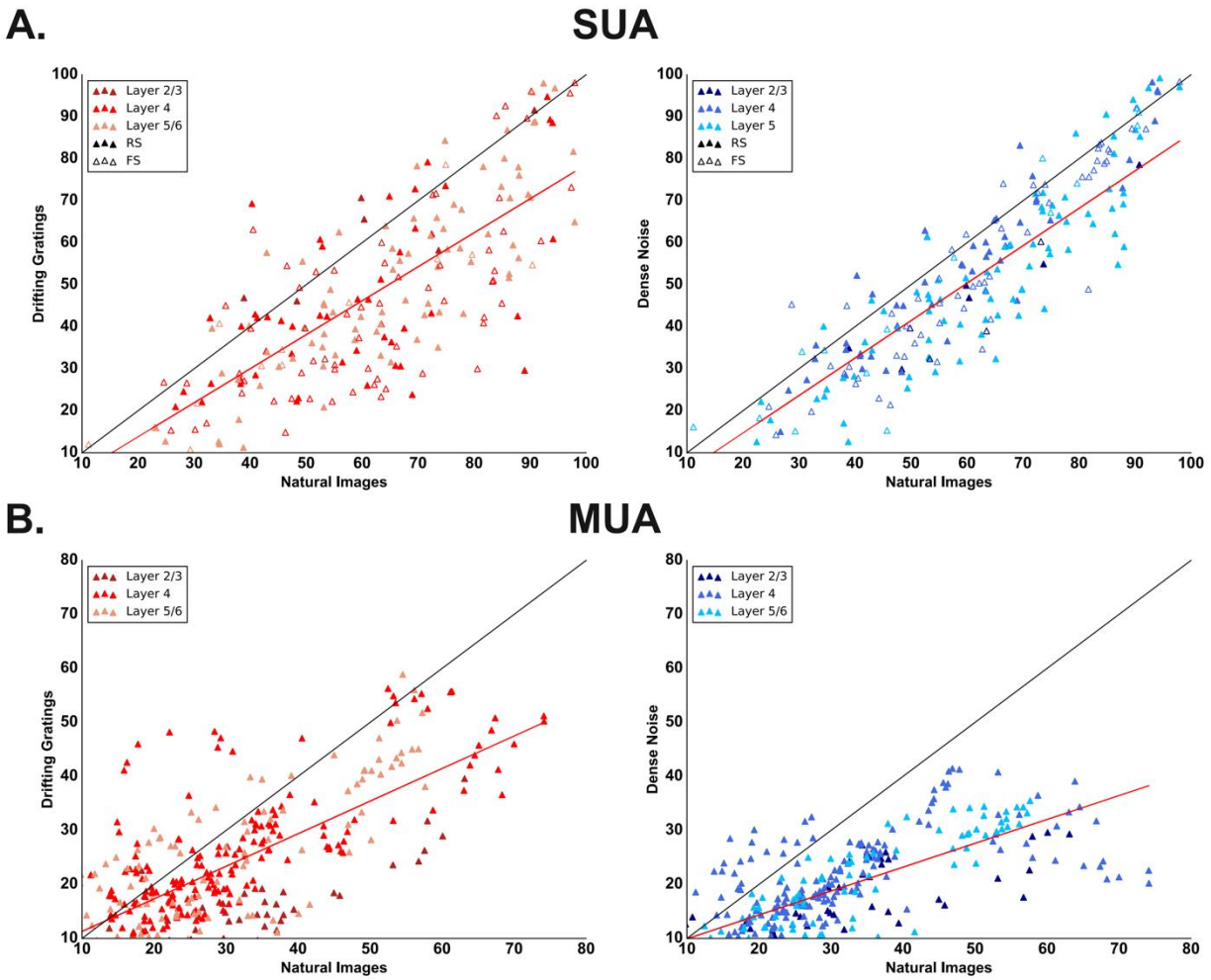

Figure 3.3.3: Sparseness correlation plots. A. Single unit activity sparseness. Left: Natural images vs Drifting gratings. Right: Natural images vs Dense Noise. B. Multi-unit activity sparseness. Left: Natural images vs Drifting gratings. Right: Natural images vs Dense Noise. Empty symbols = FS. Full Symbols = RS or MUA.

- **Mean Evoked Sparseness**

As described in the previous section, our extracellular recordings allow us to explore the sparseness across all layers. Therefore, we computed it on our 221 cells, without GEM (figure 3.3.2-B-C and figure 3.3.3 but see also table 3.3.1). We found the same pattern of sparseness as in our population of 78 single units *i.e.* natural images evoked the highest sparseness and drifting gratings the lowest one ($p < 0.001$, Friedman test; table 3.3.1). However, for each stimulus, the mean sparseness of the 221 cells was higher than the one with 78 cells. As shown in figure 3.3.3, different neurons display different sparseness levels. If the high sparseness cells are not present in both populations, this can affect the mean. In general, a cell displaying a low or high sparseness in response to one stimulus will display a high or low sparseness in response to the other stimuli (Figure 3.3.3). The same MUA sparseness pattern was observed when we increased the number of sites.

In their intracellular study, Haider and colleagues observed that RS and FS cells evoked different sparseness levels. Thus, we wondered if the same observations would be made with our extracellular classification. Despite a significant difference in their firing rates, the RS and FS populations displayed the same sparseness values as the mean SUA population ($p > 0.05$, Mann Whitney U test; Figures 3.3.3 and 3.3.4; table 3.3.2).

- **Laminar Sparseness**

We wondered if the observed heterogeneity was linked to a layer expressing a higher sparseness than the others. The laminar sparseness of the single unit activity presented a similar pattern as the mean population (table 3.3.1, Figure 3.3.2). Indeed, within all layers, natural images evoked the sparsest response ($p < 0.001$, Friedman test). However, in layer 2/3 we did not observe any differences between DG and NI. This is probably linked to the small number of cells recorded in this layer ($n = 10$). Regarding the artificial stimuli, they elicited an equivalent sparseness in layer 5/6 ($p = 0.06$), while in layer 4, DN evoked the sparsest response. Layer 4 and layer 5/6 cells showed high and low values of sparseness respectively (Figure 3.3.2-A), this heterogeneity lead to no significant differences in sparseness evoked by the same stimulus between layers ($p > 0.05$; Mann Whitney U test; table 3.3.1).
Regarding the multi-unit activity, natural images also evoked the sparsest activity within all layers ($p < 0.001$, Friendman test; Figures 3.3.2-C and 3.3.3; 3.3.1). Unlike the SUA, we observed a difference in sparseness between layers. Indeed, for all stimuli, the sparseness was higher in layer 4 than in layer 5/6 ($p < 0.05$, Mann Whitney U test).
Regarding RS and FS cells, the same absence of differences observed for the mean response was observed across layers. This difference might come from the low number of cells that they recorded. Indeed, for each neuronal subclass they recorded less than 15 neurons. As shown in figure 3.3.3 natural images evoke a great diversity of sparseness for both FS and RS cells. Thus, they could have recorded more cells with high sparseness for one population than the other, leading to this difference.

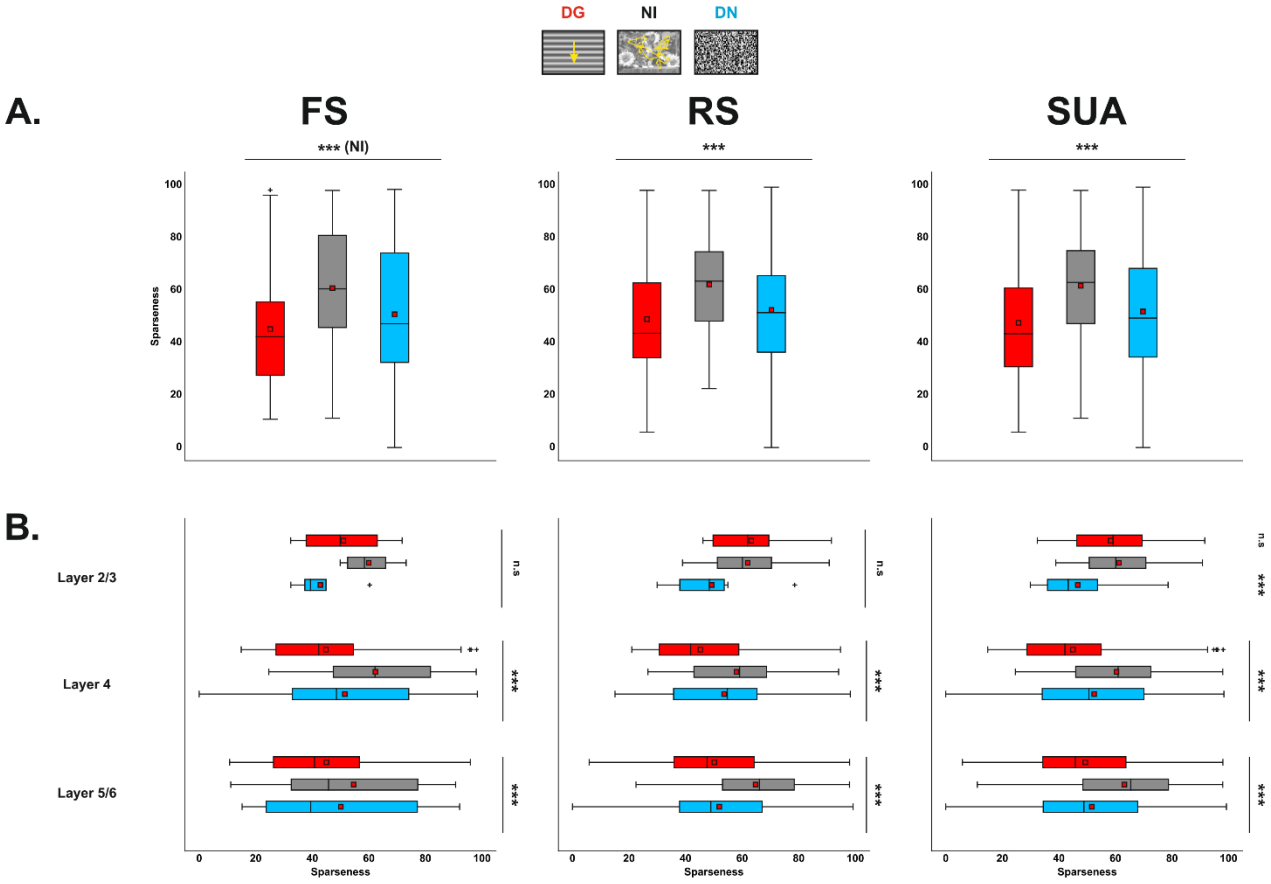

Figure 3.3.4: Single unit mean sparseness. A. Mean sparseness for different subclasses of single units. Left: Fast spiking neurons (n = 83), center: regular spiking neurons (n = 138). Right: single unit activity (n = 221). **B.** Laminar comparison of the mean sparseness across the single unit classes. Left: Fast spiking neurons (L2/3 = 4; L4 = 61; L5/6 = 18 neurons), center: regular spiking neurons (L2/3 = 7; L4 = 50; L5/6 = 81 neurons), right: single unit activity (L2/3 = 10; L4 = 111; L5/6 = 99 neurons). Red squares: mean. Black line: median. Extremities of the box: first and third quartile. Whiskers: minimum and maximum. Crosses: outliers. Stars indicate values significantly different from the NI condition. n.s : non significant; ***** : $p < 0.05$; *** : $p < 0.001$

- **Impact of the natural statistics on the sparseness**

Finally, we investigated with our control stimuli the impact of the spatio-temporal natural statistics on the sparseness (figure 3.3.5). For both the single unit and the multi-unit activity we did not observe any significant difference in the sparseness between the control stimuli and the unaltered NI. This absence of difference was also observed among the RS and FS subpopulations ($p > 0.05$; Friedman test; table 3.3.3). However, it is important to note that all unaltered stimuli evoked a higher sparseness than the artificial ones. Therefore, we can conclude that the high order correlations present in the natural spatio-temporal statistics have no impact on the sparseness of the neuronal activity.

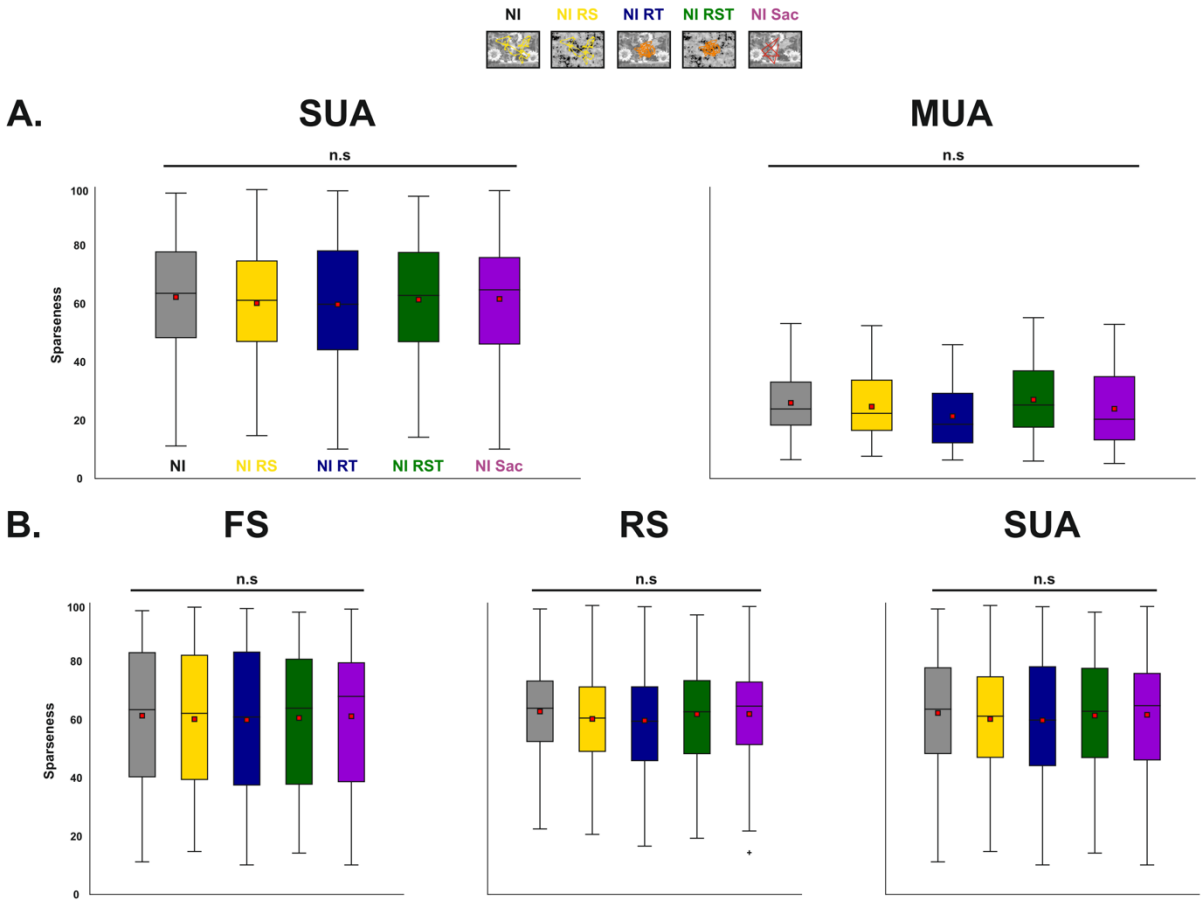

Figure 3.3.5: Single and multi-unit sparseness evoked by the control stimuli. A. Multi-scale comparison of the mean sparseness. Left: Single unit activity (n = 124), right: Multi-unit activity (150 sites). **B.** Comparison of the mean sparseness across the single unit subtypes. Left: Fast spiking neurons (n = 45), center: regular spiking neurons (n = 79). Right: single unit activity (n = 124). Red squares: mean. Black line: median. Extremities of the box: first and third quartile. Whiskers: minimum and maximum. Crosses: outliers n.s: non-significant

FULL FIELD	SUA			
	DG	GEM	NI	DN
Mean w/ GEM	39.6 ± 1.8	47.0 ± 2.0	56.8 ± 2.1	49.2 ± 2.3
Mean w/o GEM	47.5 ± 1.4		61.6 ± 1.3	51.8 ± 1.5
Layer 2/3	58.3 ± 5.6		61.2 ± 4.8	46.7 ± 4.7
Layer 4	45.0 ± 2.0		60.4 ± 1.8	52.5 ± 2.1
Layer 5/6	49.3 ± 2.3		63.2 ± 2.1	51.6 ± 2.4

FULL FIELD	MUA			
	DG	GEM	NI	DN
Mean w/ GEM	24.3 ± 1.0	24.3 ± 1.0	29.3 ± 1.0	19.7 ± 0.8
Mean w/o GEM	22.7 ± 0.6		28.9 ± 0.8	18.3 ± 0.5
Layer 2/3	14.3 ± 1.1		30.4 ± 2.2	16.3 ± 1.1
Layer 4	25.6 ± 0.9		30.4 ± 1.1	20.7 ± 0.6
Layer 5/6	21.6 ± 1.1		26.3 ± 1.3	15.7 ± 0.8

Table 3.3.1: Mean SUA and MUA sparseness evoked by our set of stimuli presented full field (Mean ± SEM)

FULL FIELD	FS		
	DG	NI	DN
Mean	45.1 ± 2.5	60.7 ± 2.4	50.8 ± 2.8
Layer 2/3	51.0 ± 9.1	60.0 ± 5.3	42.9 ± 6.0
Layer 4	44.8 ± 2.8	62.3 ± 2.6	51.5 ± 3.1
Layer 5/6	45.0 ± 7.0	54.6 ± 6.9	50.1 ± 7.7

FULL FIELD	RS		
	DG	NI	DN
Mean	48.9 ± 1.8	62.2 ± 1.6	52.4 ± 1.8
Layer 2/3	63.2 ± 7.0	62.0 ± 7.5	49.2 ± 7.0
Layer 4	45.2 ± 2.7	58.0 ± 2.6	53.7 ± 2.8
Layer 5/6	50.2 ± 2.3	64.8 ± 2.1	51.9 ± 2.4

Table 3.3.2: Mean FS and RS sparseness evoked by our set of stimuli presented full field (Mean ± SEM)

FULL FIELD					
	NI	NI-RS	NI-RT	NI-RST	NI-SAC
FS	61.3 ± 3.5	60.1 ± 3.6	59.9 ± 3.7	60.5 ± 3.5	61.1 ± 3.7
RS	62.8 ± 2.1	60.2 ± 2.2	59.7 ± 2.3	61.8 ± 2.2	61.9 ± 2.3
SUA	62.3 ± 1.8	60.2 ± 1.9	59.7 ± 1.9	61.4 ± 1.9	61.6 ± 2.0
MUA	26.0 ± 0.8	24.7 ± 0.9	21.4 ± 0.9	27.0 ± 1.0	23.9 ± 1.1

Table 3.3.3: Mean sparseness evoked by our set of control stimuli presented full field (Mean ± SEM)

3.1.2 Fano Factor

According to Barlow's theory of efficient coding, an increase of the evoked sparseness should be linked to an increase of the response reliability. A classic way to evaluate the variability of a neuronal response is to compute its Fano Factor. The fano factor (FanoFa) of the spiking activity corresponds to the spike-count variance divided by the spike-count mean. However, there are many ways to compute this ratio. In our study, we divided the time axis in successive 15 ms bins. We then computed the variance (across trials) and the mean of the spike count. A scatter plot of the variance vs. the mean was compiled, with one point per time window, for all the duration of the stimulation (10 s). The raw Fano factor was given by the slope of the regression line relating the variance to the mean (Baudot et al., 2013; Kara et al., 2000). Figure 3.3.6 shows an example of the scatter plots and the regression slope obtained for two cells in response to NI (bin 15ms). Figure 3.3.7 shows the impact of the bin on the evoked Fano Factor of these two same cells. The bin increase tends to increase the Fano Factors. Thus, before comparing the Fano Factors obtained in two different studies it is crucial to know the chosen bin. This explains the difference in Fano Factors between our (and Baudot's) studies and others (Ecker et al., 2014; Goris et al., 2014; Ouelhazi et al., 2019).

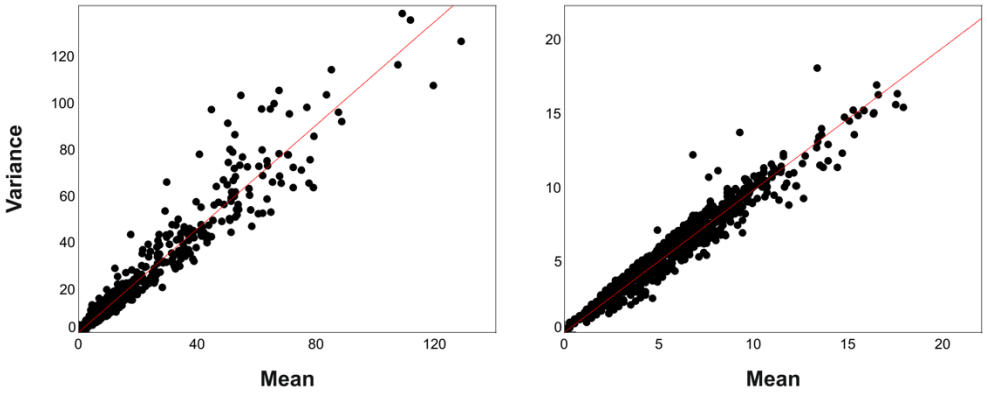

Figure 3.3.6: Mean firing rate vs Variance of the firing rate evoked by NI for two cells (PSTH bin = 14ms). Red line: regression curve. Left Panel: Fano Factor = 1.2; Right Panel: Fano Factor = 0.8

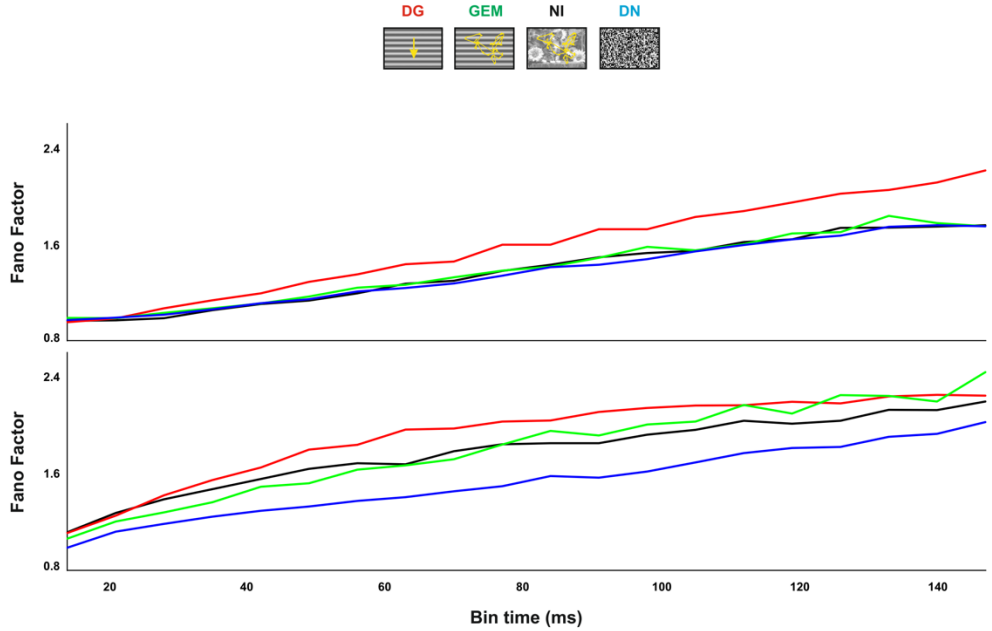

Figure 3.3.7: Example of the Fano Factor computed in function of the bin of the PSTH for two different cells.

- **Comparison with the intracellular recordings**

In their intracellular study, Baudot and colleagues (2013) obtained a mean sub-poissonian Fano Factor, in response to all stimuli. They chose a bin similar to ours (13.3 ms), therefore the comparison between our results and theirs is possible. We first computed the Fano Factor on the neuronal population without GEM (Figure 3.3.8-A). The Fano Factor values, of the SUA, that we obtained are different to theirs *i.e.* Natural images and animated gratings evoked a Fano Factor below 1 yet higher than the ones obtained intracellularly while DN and DG evoked values almost equal to 1 (see table 3.3.4). In addition, only DG evoked a FanoFa different from NI ($p < 0.05$; Friedman test). On the other hand, at the multi-unit level, all stimuli evoked Fano Factors below 1 (table 3.3.4). Animated gratings evoked the lowest FanoFa while DN the highest one ($p < 0.05$).
The difference between the intracellular and extracellular results has possible sources. The first one is, as stated in the previous sections, the number of cells between the two studies. As shown in figures 3.3.8 and 3.3.10 (but also in Ecker et al., 2014), among an important neuronal population some cells will exhibit a low Fano Factor (below 1) while others will exhibit a high one (above 1). The other source of variability between our two studies can come from the difference anesthetics (Isoflurane vs Alfaxolone). In their extracellular study on the anesthetized monkey (with fentanyl), Ecker et al., (2014) reported values of Fano Factor, in response to gratings, around 2. Anesthesia, by increasing the variance of the response, has a strong impact on the Fano Factor values.
Notably, the values of Fano Factor for the SUA and MUA are close but lower for the MUA, this is linked to the fact that despite a higher mean variance we also obtained an even higher mean firing rate at the multi-unit level (table 3.3.4, figure 3.3.8).

- **Mean Evoked Fano Factor**

We then computed the analysis on the population without GEM (Figure 3.3.8 and 3.3.10; table 3.3.4). Unlike what was observed for the population with GEM, both at the single and multi-unit levels Natural images evoked the lowest Fano Factors ($p < 0.001$; Friedman test). At the single unit level, all stimuli evoked a Fano Factor above 1 while at multi-unit the Fano Factors were below 1. As observed by Ecker et al (2014), we obtained a variety of Fano Factor values ranging from very low ones (0.4) to high ones (2.0). By increasing the number of recorded cells, we also increased the number of higher Fano Factors, which lead to the observed difference between the two populations. It is important to note that both the mean and median evoked values were around 1 (figure 3.3.8). As shown in Figure 3.3.9 the increase in firing rate is correlated with decrease in the Fano Factor.
In their intracellular study, Haider and colleagues (2010) showed that the reliability depends on the recorded cell type. In addition, we observed that Fano Factor is correlated with the firing rate. Since FS neurons displayed a higher firing rate than RS ones, we wondered if we would observe an impact on the Fano Factor. We first computed the Fano Factor within each neuronal subclass (Figure 3.3.11; Table 3.3.5). The regular spiking neurons displayed the same pattern as the single unit population. However, among FS neurons no difference was observed between the FanoFa evoked by NI and DN ($p > 0.05$; Friedman test). In addition, for each stimulus respectively, no difference was observed between the complete single unit population and the regular and fast spiking neurons ($p > 0.5$; Kruskal-Wallis test).

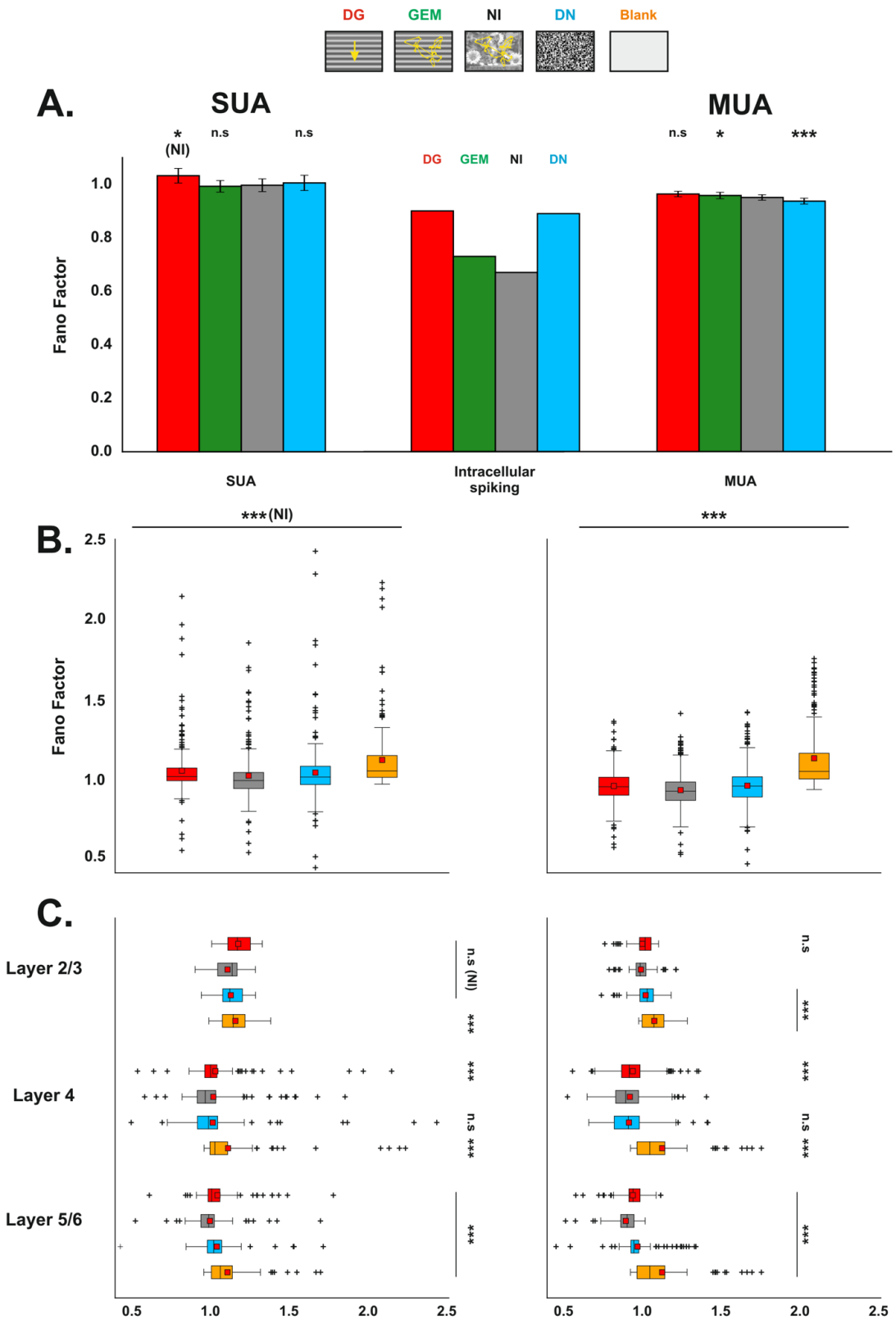

Figure 3.3.8: Single and multi-unit mean Fano Factor. A. Multiscale comparison of the mean Fano Factor. Natural images evoke the lowest Fano Factor. Left: Single unit activity (n = 78), center: intracellular results. Right: Multi-unit activity (77 sites). B. Comparison of the mean Fano Factor. Left: single unit activity (n = 221), right: multi-unit activity (377 sites). C. laminar comparison of the mean Factor. Left: single unit activity (L2/3 = 10; L4 = 111; L5/6 = 99 neurons), right: multi-unit activity (L2/3 = 52; L4 = 187; L5/6 = 138 sites). Red square: mean. Black line: median. Extremities of the box: first and third quartile. Whiskers: minimum and maximum. Crosses: outliers. Stars indicate values significantly different from the NI condition * : $p < 0.05$; ** : $p < 0.01$; *** : $p < 0.001$

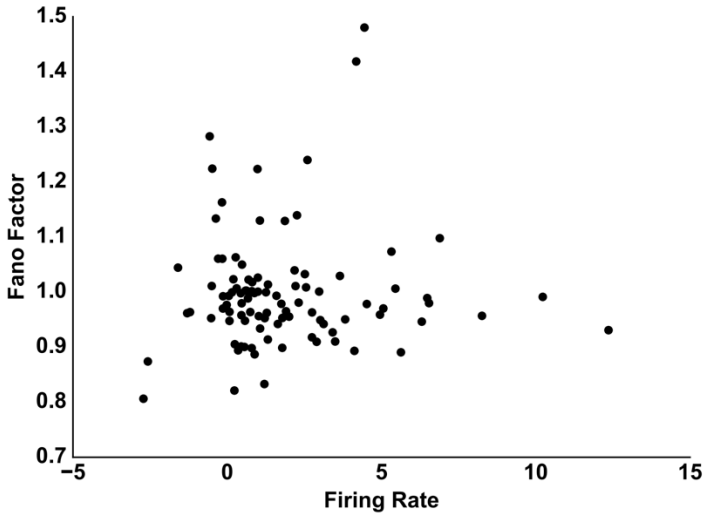

Figure 3.3.9: Impact of the firing rate on the Fano Factor evoked by NI at the single unit level

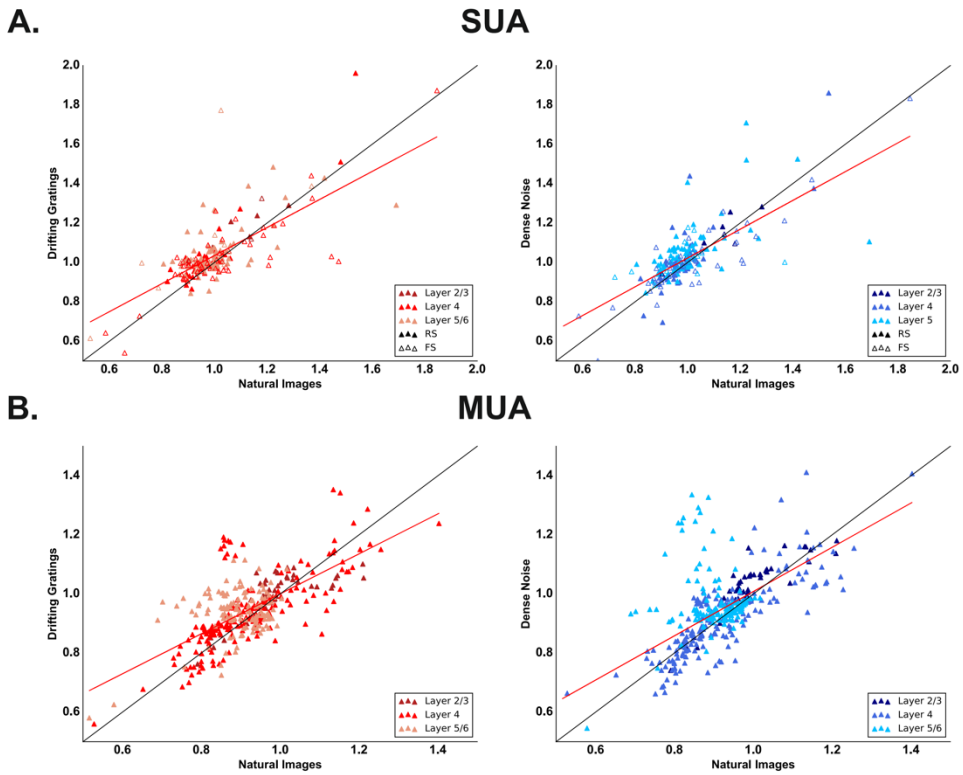

Figure 3.3.10: Fano Factor correlation plots. A. Single unit activity Fano Factor. Left: Natural images vs Drifting gratings. Right: Natural images vs Dense Noise. B. Multi-unit activity Fano Factor. Left: Natural images vs Drifting gratings. Right: Natural images vs Dense Noise. Empty symbols = FS. Full Symbols = RS or MUA.

- **Laminar Fano Factor**

The population without GEM allow us to explore the evoked Fano Factor within each layer. In their work, Kara and colleagues (2000) obtained very low Fano Factor values. They assumed that this was probably linked to the fact that their recordings were only performed in layer 4. We wondered if we would obtain lower Fano Factors value in layer 4 as observed by Kara et al (2000) (Figure 3.3.8 and 3.3.10). We first investigated the evoked Fano Factors within layers. At the single unit level, all stimuli evoked a similar FanoFa ($p > 0.05$; Friedman test). In layer 4, no difference was observed for the dense noise and natural images stimulation ($p > 0.05$), while DG evoked the lowest Fano Factor ($p < 0.001$; Table 3.3.4). Finally, in layer 5/6, NI evoked the lowest values ($p < 0.001$). The same response pattern was observed for the MUA, except in layer 2/3 where DN evoked the highest Fano Factor ($p < 0.001$).
We then investigated the Fano Factor between layers. At the single unit level, all stimuli evoked the highest FanoFa in layer 2/3 ($p < 0.001$; Kruskal-Wallis test). Both artificial stimuli evoked the highest reliability in layer 4 ($p < 0.001$). On the other hand, in response to NI, despite a lower mean Fano Factor evoked layer 5/6, no difference was observed between layers 4 and 5/6 ($p = 0.6$). At the multi-unit level, the same pattern was observed for artificial stimuli. However, in response to NI the highest values were observed in layer 2/3 and the lowest in layer 5/6, confirming the tendency observed at the single unit level ($p < 0.001$). It is important to note that in all layers we observed high a low Fano Factor values (figures 3.3.8 and 3.3.10). For both SUA and MUA, the differences between layers are small.
Regarding Fast and Regular spiking neurons, we observed within and between layers, a similar pattern as the one of the single unit population (Figure 3.3.11; table 3.3.5).
In summary, we showed that natural images evoke a more reliable response than the other stimuli. In addition, we do have a layer dependency of the Fano Factor, however this latter does not explain the heterogeneity observed among the populations.

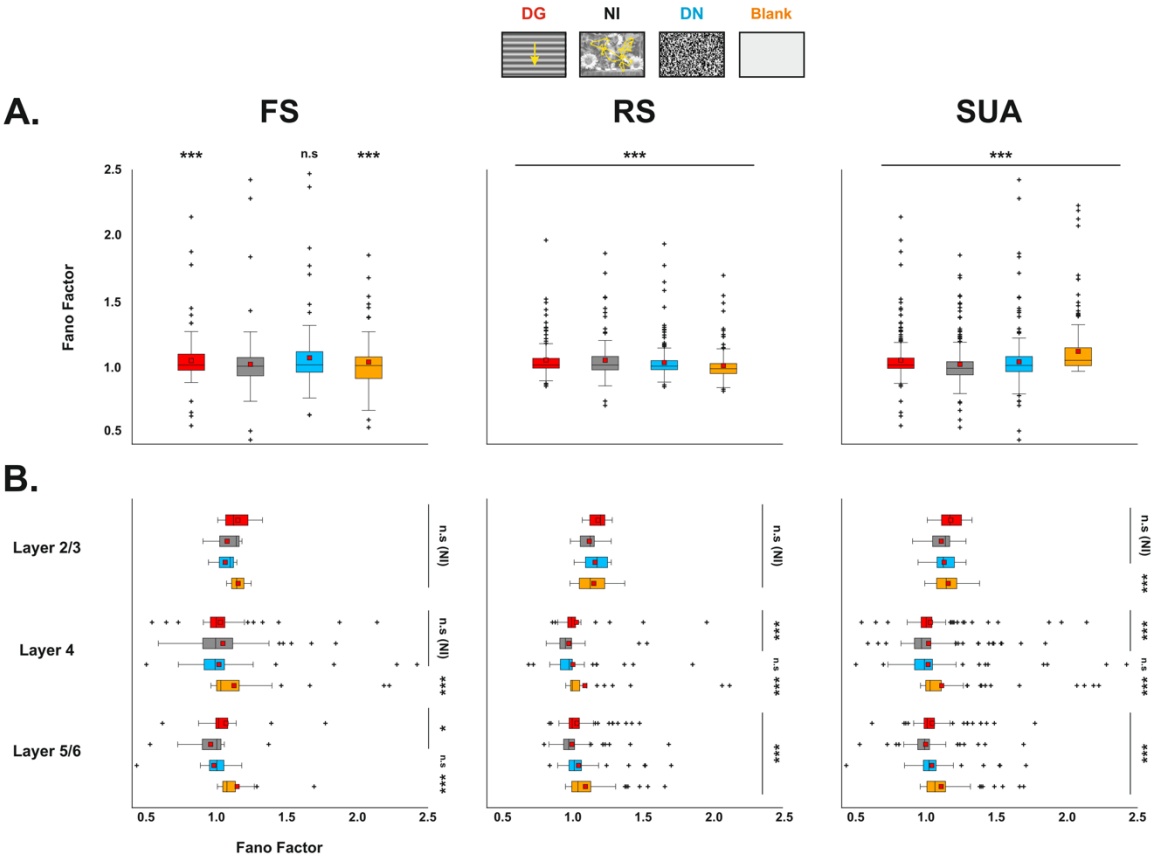

Figure 3.3.11: Single unit mean Fano Factor. A. Mean Fano Factor for different subclasses of single units. Left: Fast spiking neurons (n = 83), center: regular spiking neurons (n = 138). Right: single unit activity (n = 221). **B.** laminar comparison of the mean Fano Factor across the single unit classes. Left: Fast spiking neurons (L2/3 = 4; L4 = 61; L5/6 = 18 neurons), center: regular spiking neurons (L2/3 = 7; L4 = 50; L5/6 = 81 neurons), right: single unit activity (L2/3 = 10; L4 = 111; L5/6 = 99 neurons). Red square: mean. Black line: median. Extremities of the box: first and third quartile. Whiskers: minimum and maximum. Crosses: outliers. Stars indicate values significantly different from the NI condition. n.s : non significant; ***** : $p < 0.05$; *** : $p < 0.001$

- **Impact of the natural statistics on the Fano Factor**

Finally, we investigated the impact of the spatio-temporal statistics on the reliability of the response. Indeed, our previous results showed that the response is differently modulated by the randomization of not of the spatio-temporal statistics. Our results are reported in figure 3.3.11 and table 3.3.6. At the single unit level (and its subpopulations) all stimuli evoked the same Fano Factor ($p > 0.05$; Friedman test). However, at the multi-unit level, the natural image were both spatial and temporal statistics were randdomozed evoked a lower fano factor than the unalted natural image ($p < 0.001$) while the natural image animated only with saccades evoked a higher one. This tendency was also observed at the single unit level.

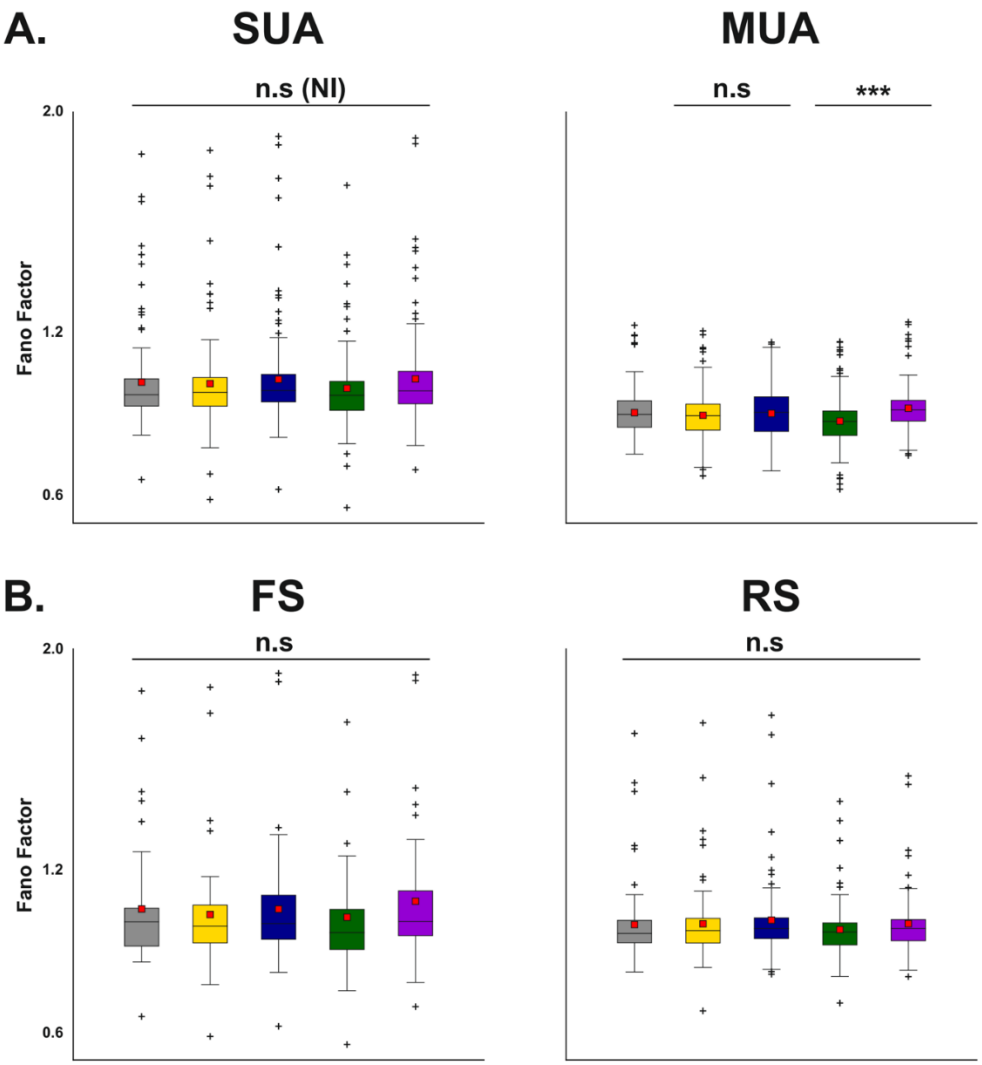

Figure 3.3.11: Single and multi-unit Fano Factor evoked by the control stimuli. A. Multi-scale comparison of the mean Fano Factor. Left: Single unit activity (n = 124), right: Multi-unit activity (150 sites). **B.** Comparison of the mean sparseness across the single unit subtypes. Left: Fast spiking neurons (n = 45), center: regular spiking neurons (n = 79). Right: single unit activity (n = 124). Red square: mean. Black line: median. Extremities of the box: first and third quartile. Whiskers: minimum and maximum. Crosses: outliers n.s: non-significant

FULL FIELD	SUA			
	DG	GEM	NI	DN
Mean w/ GEM	1.032 ± 0.027	0.993 ± 0.022	0.997 ± 0.024	1.005 ± 0.028
Mean w/o GEM	1.043 ± 0.014		1.011 ± 0.012	1.031 ± 0.016
Layer 2/3	1.175 ± 0.039		1.107 ± 0.042	1.128 ± 0.041
Layer 4	1.031 ± 0.023		1.018 ± 0.019	1.014 ± 0.030
Layer 5/6	1.044 ± 0.015		0.997 ± 0.014	1.040 ± 0.015

FULL FIELD	MUA			
	DG	GEM	NI	DN
Mean w/ GEM	0.963 ± 0.010	0.958 ± 0.012	0.950 ± 0.010	0.937 ± 0.011
Mean w/o GEM	0.947 ± 0.006		0.921 ± 0.006	0.949 ± 0.007
Layer 2/3	0.999 ± 0.011		0.990 ± 0.013	1.020 ± 0.014
Layer 4	0.939 ± 0.010		0.921 ± 0.009	0.915 ± 0.010
Layer 5/6	0.939 ± 0.007		0.895 ± 0.007	0.969 ± 0.010

Table 3.3.4: Mean SUA and MUA Fano Factor evoked by our set of stimuli presented full field (Mean ± SEM)

FULL FIELD	FS		
	DG	NI	DN
Mean	1.040 ± 0.030	1.029 ± 0.025	1.011 ± 0.038
Layer 2/3	1.151 ± 0.093	1.075 ± 0.086	1.061 ± 0.061
Layer 4	1.027 ± 0.036	1.045 ± 0.030	1.017 ± 0.048
Layer 5/6	1.067 ± 0.065	0.958 ± 0.048	0.981 ± 0.045

FULL FIELD	RS		
	DG	NI	DN
Mean	1.045 ± 0.012	1.001 ± 0.011	1.042 ± 0.014
Layer 2/3	1.189 ± 0.038	1.127 ± 0.049	1.168 ± 0.049
Layer 4	1.036 ± 0.027	0.982 ± 0.020	1.011 ± 0.028
Layer 5/6	1.040 ± 0.013	1.004 ± 0.014	1.051 ± 0.015

Table 3.3.5: Mean FS and RS Fano Factor evoked by our set of stimuli presented full field (Mean ± SEM)

FULL FIELD					
	NI	NI-RS	NI-RT	NI-RST	NI-SAC
FS	1.051 ± 0.034	1.031 ± 0.033	1.051 ± 0.035	1.021 ± 0.038	1.079 ± 0.037
RS	0.994 ± 0.016	0.997 ± 0.016	1.010 ± 0.018	0.976 ± 0.013	0.998 ± 0.013
SUA	1.014 ± 0.016	1.009 ± 0.016	1.025 ± 0.017	0.992 ± 0.016	1.027 ± 0.016
MUA	0.903 ± 0.007	0.893 ± 0.007	0.901 ± 0.007	0.872 ± 0.008	0.919 ± 0.007

Table 3.3.6: Mean Fano Factor evoked by our set of control stimuli presented full field (Mean ± SEM)

3.1.3 Reliability of the spiking activity

The Fano-Factor is a reliability measure that relies on the mean and the variance of the firing rate. This measure can be biased, and two different stimuli can lead to similar results if the ratio variance over mean is similar despite the fact that these two stimuli elicit very different firing rates. Therefore, as performed by Baudot and colleagues (2013) in their intracellular study we decided to compute another measure of reliability: the cross-correlation of the spiking response between trials. The reliability is given by the CC peak amplitude at time zero (Baudot et al., 2013; Butts et al., 2007).
Figure 3.3.12 show the trial to trial cross correlation for two cells (one fast spiking and one regular spiking neuron). Both cells elicited different values of reliability. One neuron evoked a very reliable response, for all stimuli, while the other one a much lower one. This result is not surprising, it has been observed V1 is composed of cells exhibiting different levels of reliability (Kampa et al, 2011; Rikhye and Sur 2015). However, no study investigated at the population level the levels of reliability evoked by artificial and natural stimuli.

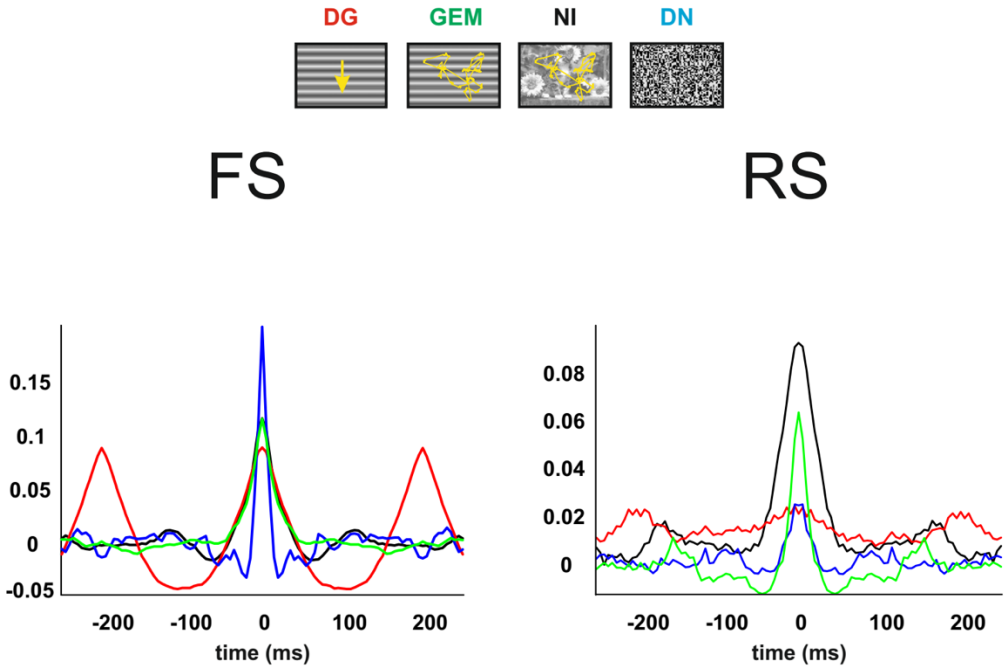

Figure 3.3.12: Example of the levels of reliability evoked by our set of stimuli on two different cells.

- **Comparison with the intracellular recordings**

In their intracellular study, Baudot and colleagues (2013) found that NI and GEM evoked a higher reliable spiking activity than the other stimuli. However, they did not observe a significant difference between NI and GEM. We found, for both SUA and MUA, a similar pattern of reliability as the one observed intracellularly (Figure 3.3.13-A; Table 3.3.7; $p < 0.01$, Friedman Test). Natural images and gratings animated with eye movements evoked the highest level of reliability for the single unit activity. However, the levels of reliability were different between the intracellular and the extracellular spiking activities. As explained for the other indexes quantifying the spiking activity, the extracellular recordings allowed us to record simultaneously a great number of cells, even those that tend to display a low response therefore low levels reliability. The barplots in figure 3.3.13 and the scatter plots in figure 3.3.14 give a good overview of the different levels of reliability that are found in V1. On the other hand, these low spiking cells were probably not taken in account in the intracellular study,

leading to this difference in reliability. We can eliminate a difference caused by the anesthesia because Haider et al. (2010), who used the same anesthetics as we did (Isoflurane) and also performed intracellular recordings in cat V1, found levels of reliability evoked by NI similar to those observed by Baudot and colleagues (2013).
Interestingly, the MUA reliability followed the same pattern as the one observed for the SUA. However, we obtained higher levels of reliability for all stimuli. This reliability was also higher than the one observed intracellularly (Figure 3.3.13-A; Table 3.3.7). This result is in agreement with the theories stating that the stimulus is efficiently encoded by the population and not by a single neuron (Deneve and Chalk, 2016; Yuste, 2015). Indeed, as described in the previous sections the MUA, particularly in our study, correspond to the spiking activity of many single neurons. In addition, these results correspond to our previous observations made with another the reliability measure, the Fano Factor.
In summary, we found similar results as the ones observed intracellularly, thus validating at different scales the observations previously made by the laboratory. We also showed that the multi-unit activity evokes a more reliable response than the single neuron.

- **Mean Evoked Reliability**

As described in the previous section, our extracellular recordings allowed us to record cells across all layers. Therefore, we computed the trial-to-trial correlation on the 221 recorded cells and the 377 multi-unit sites, without GEM (figure 3.3.13-B-C and figure 3.3.14 but see also table 3.3.7).
We first computed the mean reliability levels for both SUA and MUA. We obtained similar results as the ones reported in Figure 3.3.13-A. The boxplots and the scatter plots in figure 3.3.13-B show that our populations are composed of very reliable and very unreliable cells and multi-unit sites. Kampa et al. (2011) also observed this heterogeneity in layer 2/3 of mouse primary visual cortex. They reported that, in response to different stimuli, 20% of their cell population can be considered as reliable. We computed the reliability in function of the firing rate and observe that for a proportion of cells a high reliability is correlated to the firing rate. However, cells exhibiting a low firing rate can also induce high levels a reliability (Figure 3.3.15). The reliability of the spontaneous activity was always equal to 0, thus we decided to not plot it for this analysis (figure 3.2.1)
As performed for the other quantification indexes we computed the trial-to-trial cross correlation of our two neuronal subclasses: the regular and fast spiking cells (Figures 3.3.14 and 3.3.16-A; Table 3.3.8). We wondered if we would observe a difference in reliability between these two subclasses. The different stimuli evoked the same reliability in the regular spiking and fast spiking cells as in the complete SUA population ($p > 0.05$; Kruskal Wallis test). However, fast spiking cells displayed, for the same stimulus, higher levels of reliability than regular spiking cells ($p < 0.001$).

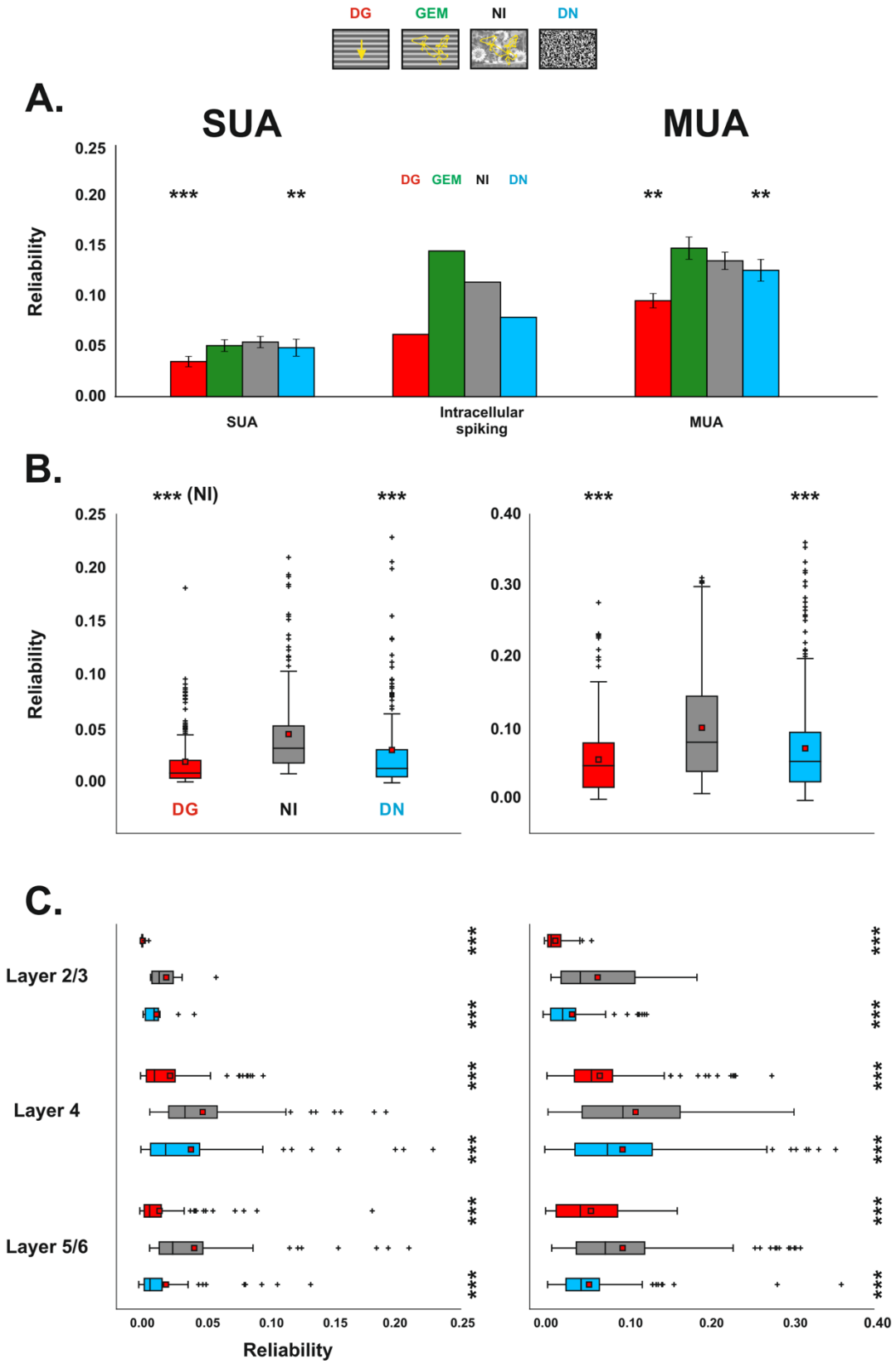

Figure 3.3.13: Single and multi-unit mean reliability. Natural Images evoke the highest levels of reliability. **A.** Multiscale comparison of the mean reliability Left: Single unit activity (n = 78), center: intracellular results. Right: Multi-unit activity (77 sites). **B.** Comparison of the mean reliability. Left: single unit activity (n = 221), right: multi-unit activity (377 sites). **C.** laminar comparison of the mean reliability. The most reliable response is in layer 4. Left: single unit activity (L2/3 = 10; L4 = 111; L5/6 = 99 neurons), right: multi-unit activity (L2/3 = 52; L4 = 187; L5/6 = 138 sites). Red square: mean. Black line: median. Extremities of the box: first and third quartile. Whiskers: minimum and maximum. Crosses: outliers. Stars indicate values significantly different from NI. n.s: non-significant; ***:** $p < 0.05$; **: $p < 0.01$; ***: $p < 0.001$

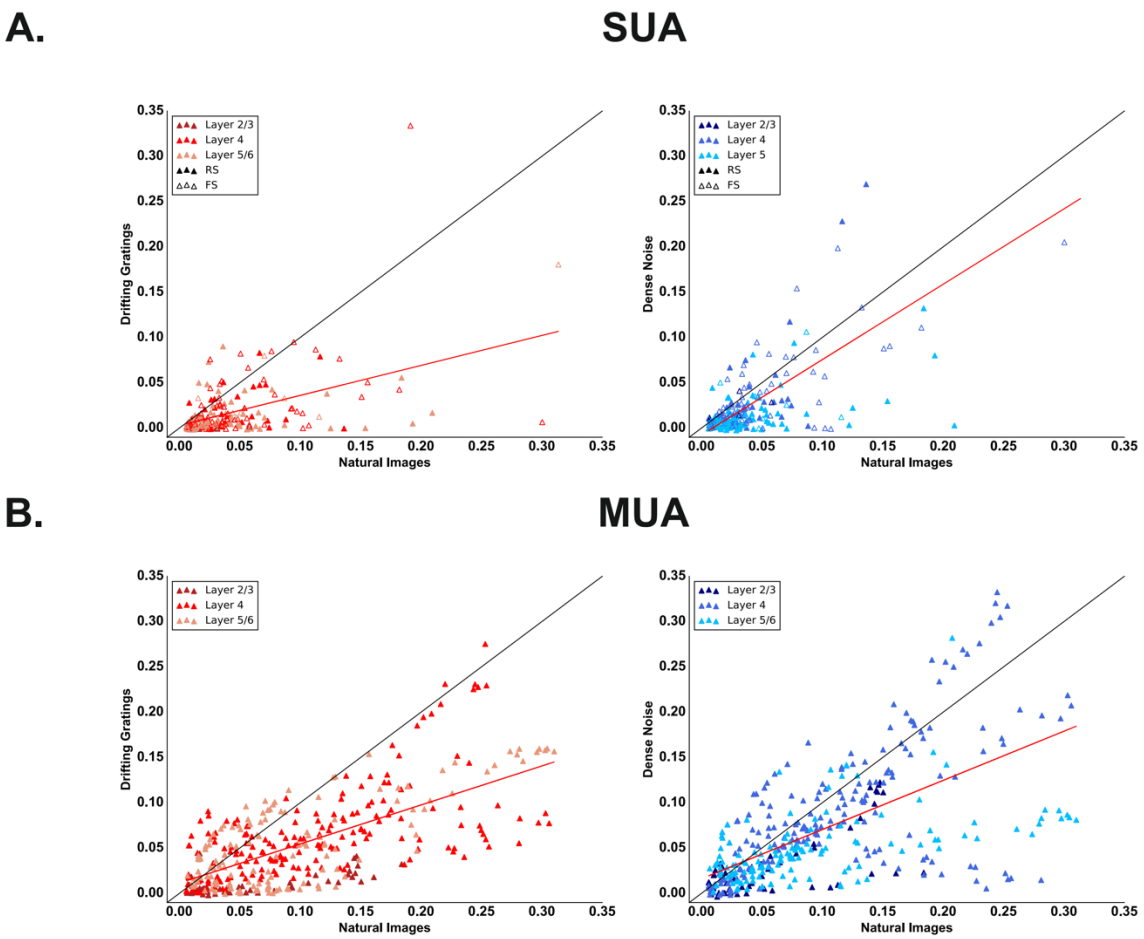

Figure 3.3.14: Reliability correlation plots. A. Single unit activity reliability. Left: Natural images vs Drifting gratings. Right: Natural images vs Dense Noise. B. Multi-unit activity reliability. Left: Natural images vs Drifting gratings. Right: Natural images vs Dense Noise. Empty symbols = FS. Full Symbols = RS or MUA.

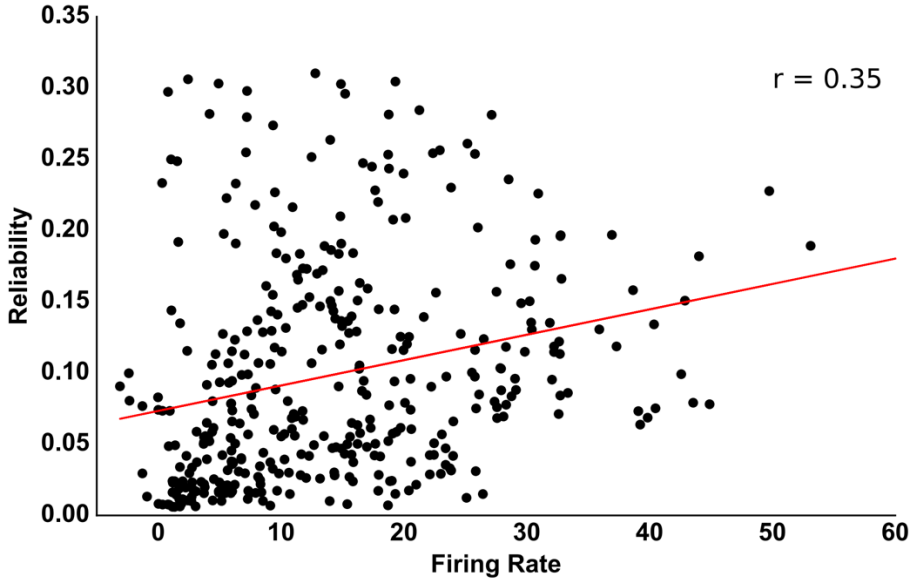

Figure 3.3.15: Reliability of the response in function of the cell firing rate (r: Spearman Correlation)

- **Laminar reliability**

We, and others (Hansen et al, 2012) showed that the reliability of the response is layer dependent. We wondered if this reliability analysis would result in the same laminar dependency as the one observed with the fano factor. For the SUA, our results show that within all layers, natural images evoked a more reliable spiking activity than the other stimuli ($p < 0.001$, Friedman test). DN displayed a higher reliable response than DG in layers 2/3 and 4 ($p < 0.001$). All stimuli evoked the highest level of reliability in layer 4 and the lowest one in layer 2/3 ($p < 0.05$; Mann-Whitney U test). This higher reliability observed in layer 4 could be linked to the dense and reliable thalamic inputs projecting to this layer (Wilson & Cragg, 1967; Kumbhani et al., 2007) or to inhibitory mechanisms (Zhu et al., 2015). We observed the same exact pattern for the multi-unit activity, apart from the reliability that was higher than the one observed for the SUA. Despite a significant difference, it is important to note that for both signals, NI evoked close reliability levels in layers 4 and 5/6.
Regarding the laminar reliability of the single unit subpopulations, natural images evoked the most reliable response within layers 4 and 5/6 among regular and fast spiking cells ($p < 0.01$; Friedman test). The number of cells recorded in layer 2/3 for both RS ($n = 4$) and FS ($n= 7$) cells did not allow us to perform a statistical analysis. However, if we increased the number of recorded cells in this layer, we could expect that NI would evoke a more reliable response than the other stimuli. For regular spiking cells, NI and DG evoked similar levels of reliability between layers 4 and 5/6, only DN evoked a more reliable response in layer 4 than in layer 5/6. Regarding fast spiking cells, the same stimuli evoked the same reliability in layers 4 and 5/6 (figures 3.3.14 and 3.3.16; table 3.3.8).
In summary, we showed that for the MUA and the SUA (and its subclasses) natural images evoked a more reliable response than the other stimuli. In addition, for the MUA, SUA and RS cells, layer 4 evoked the most reliable response for all stimuli.

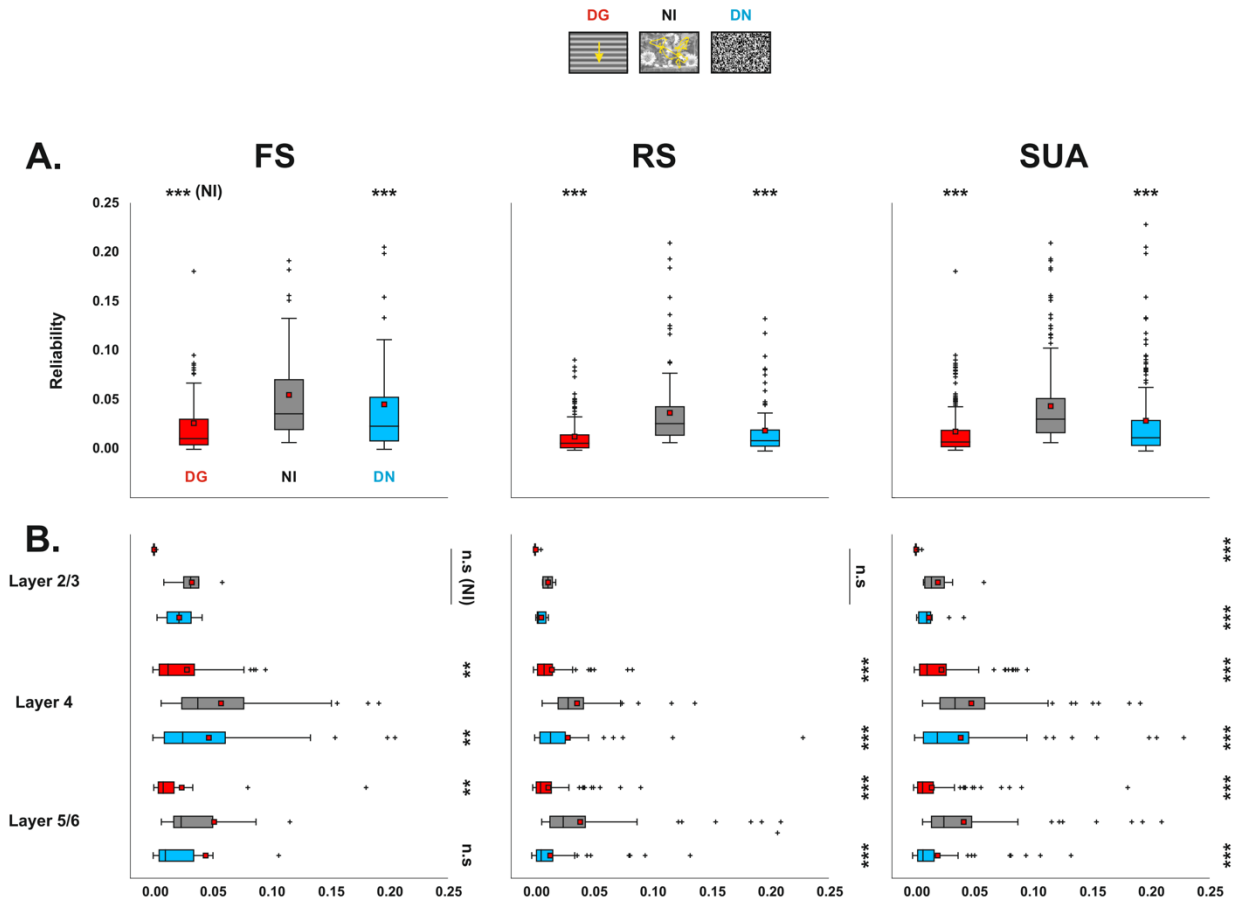

Figure 3.3.16: Single unit mean reliability. A. Mean reliability for different subclasses of single units. Fast spiking neurons evoke the highest reliability levels. Left: Fast spiking neurons (n = 83), center: regular spiking neurons (n = 138). Right: single unit activity (n = 221). **B.** laminar comparison of the mean reliability across the single unit classes. Left: Fast spiking neurons (L2/3 = 4; L4 = 61; L5/6 = 18 neurons), center: regular spiking neurons (L2/3 = 7; L4 = 50; L5/6 = 81 neurons), right: single unit activity (L2/3 = 10; L4 = 111; L5/6 = 99 neurons).Red square: mean. Black line: median. Extremities of the box: first and third quartile. Whiskers: minimum and maximum. Crosses: outliers. n.s : non-significant; ***** : $p < 0.05$; *** : $p < 0.001$

- **Impact of the natural statistics on the reliability**

Finally, we investigated, with our control stimuli, the impact of the spatio-temporal natural statistics on the reliability of the response (figure 3.3.17; table 3.3.9). For both the single unit and the multi-unit activity we did not observed any significant difference in the reliability. This absence of difference was also observed among the RS and FS subpopulations ($p > 0.05$; Friedman test; table 3.3.9). This absence of difference between the stimuli containing high order correlations in their spatio-temporal statistics or not matches the results of Freeman et al., 2013. They observed, in the primary visual cortex of awake primates, that V1 responds the same way to natural stimuli containing or not high order correlations in their spatial statistics. Based on our results, it seems that V1 reliability is modulated the same way by natural spatio-temporal frequencies containing or not high order correlations.

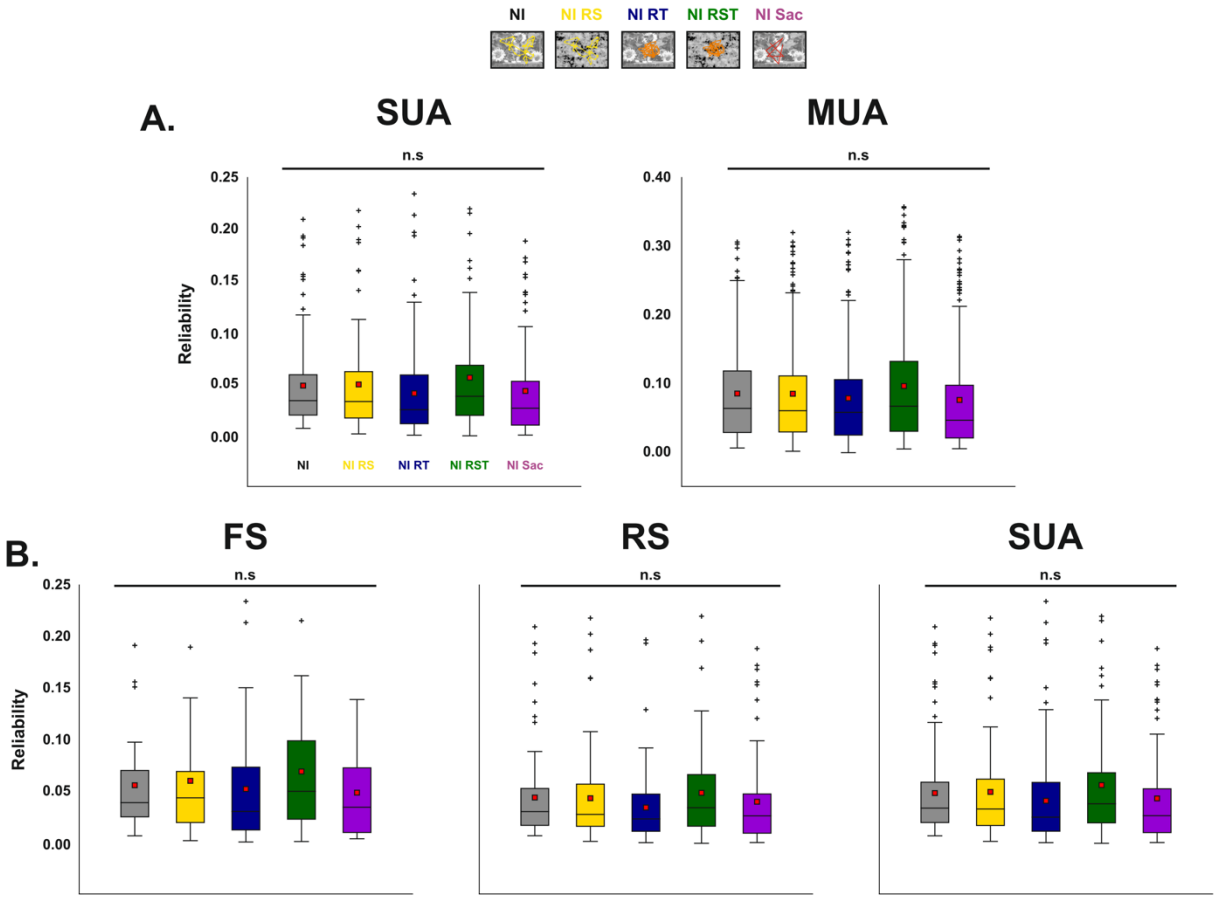

Figure 3.3.17: Single and multi-unit reliability evoked by the control stimuli. A. Multi-scale comparison of the mean reliability. Left: Single unit activity (n = 124), right: Multi-unit activity (150 sites). B. Comparison of the mean reliability across the single unit subtypes. Left: Fast spiking neurons (n = 45), center: regular spiking neurons (n = 79). Right: single unit activity (n = 124). Red square: mean. Black line: median. Extremities of the box: first and third quartile. Whiskers: minimum and maximum. Crosses: outliers n.s: non-significant

FULL FIELD	SUA			
	DG	GEM	NI	DN
Mean w/ GEM	0.035 ± 0.005	0.054 ± 0.006	0.049 ± 0.008	0.051 ± 0.006
Mean w/o GEM	0.017 ± 0.002		0.043 ± 0.003	0.028 ± 0.004
Layer 2/3	0.001 ± 0.001		0.019 ± 0.005	0.011 ± 0.004
Layer 4	0.022 ± 0.004		0.048 ± 0.005	0.038 ± 0.006
Layer 5/6	0.014 ± 0.002		0.041 ± 0.005	0.019 ± 0.005

FULL FIELD	MUA			
	DG	GEM	NI	DN
Mean w/ GEM	0.096 ± 0.007	0.135 ± 0.009	0.126 ± 0.011	0.148 ± 0.011
Mean w/o GEM	0.054 ± 0.003		0.099 ± 0.004	0.070 ± 0.003
Layer 2/3	0.011 ± 0.002		0.063 ± 0.007	0.032 ± 0.005
Layer 4	0.066 ± 0.004		0.113 ± 0.006	0.093 ± 0.006
Layer 5/6	0.055 ± 0.004		0.093 ± 0.007	0.052 ± 0.004

Table 3.3.7: Mean SUA and MUA reliability evoked by our set of stimuli presented full field (Mean ± SEM)

FULL FIELD	FS		
	DG	NI	DN
Mean w/o GEM	0.026 ± 0.005	0.055 ± 0.006	0.045 ± 0.008
Layer 2/3	0.000 ± 0.001	0.032 ± 0.010	0.022 ± 0.008
Layer 4	0.028 ± 0.006	0.057 ± 0.007	0.047 ± 0.008
Layer 5/6	0.024 ± 0.010	0.051 ± 0.017	0.044 ± 0.025

FULL FIELD	RS		
	DG	NI	DN
Mean w/o GEM	0.012 ± 0.002	0.036 ± 0.003	0.018 ± 0.003
Layer 2/3	0.001 ± 0.001	0.011 ± 0.002	0.006 ± 0.002
Layer 4	0.015 ± 0.003	0.036 ± 0.004	0.028 ± 0.007
Layer 5/6	0.012 ± 0.002	0.039 ± 0.005	0.013 ± 0.002

Table 3.3.8: Mean FS and RS reliability evoked by our set of stimuli presented full field (Mean ± SEM)

FULL FIELD					
	NI	NI-RS	NI-RT	NI-RST	NI-SAC
FS	0.056 ± 0.008	0.060 ± 0.010	0.052 ± 0.008	0.069 ± 0.011	0.048 ± 0.008
RS	0.044 ± 0.005	0.043 ± 0.005	0.034 ± 0.004	0.048 ± 0.006	0.040 ± 0.005
SUA	0.048 ± 0.004	0.049 ± 0.005	0.040 ± 0.004	0.056 ± 0.005	0.043 ± 0.004
MUA	0.085 ± 0.005	0.085 ± 0.005	0.078 ± 0.005	0.096 ± 0.006	0.076 ± 0.005

Table 3.3.9: Mean reliability evoked by our set of control stimuli presented full field (Mean ± SEM)

3.1.4 Reliability of the local field potential

In the previous sections, we quantified the reliability of the spiking response. In addition, we quantified the energy of the local field potential and showed that this mesoscopic signal integrates the synaptic information in a very different way than the single cell. Therefore, in order to continue our LFP quantification and the multiscale study of the evoked response we computed the reliability of the local field potential.

Figure 3.3.18-A shows an example of the mean LFP and all its trials for all stimuli. The mean LFP obtained in response to NI and GEM seem to follow the trial-to-trial response, while the mean DG is completely flat, but with a reduced standard deviation, as observed with the trials (in grey). As explained in the previous sections this is linked to the neuronal activity responding to the different phases of the grating. The reliability of this example shows that DG evokes low reliability levels while NI induce a reliable LFP (Figure 3.3.18-B). As performed for the energy, we computed the difference in reliability between NI and DN for two different experiments. As observed previously, each experiment result in different reliability levels (Figure 3.3.18-C).

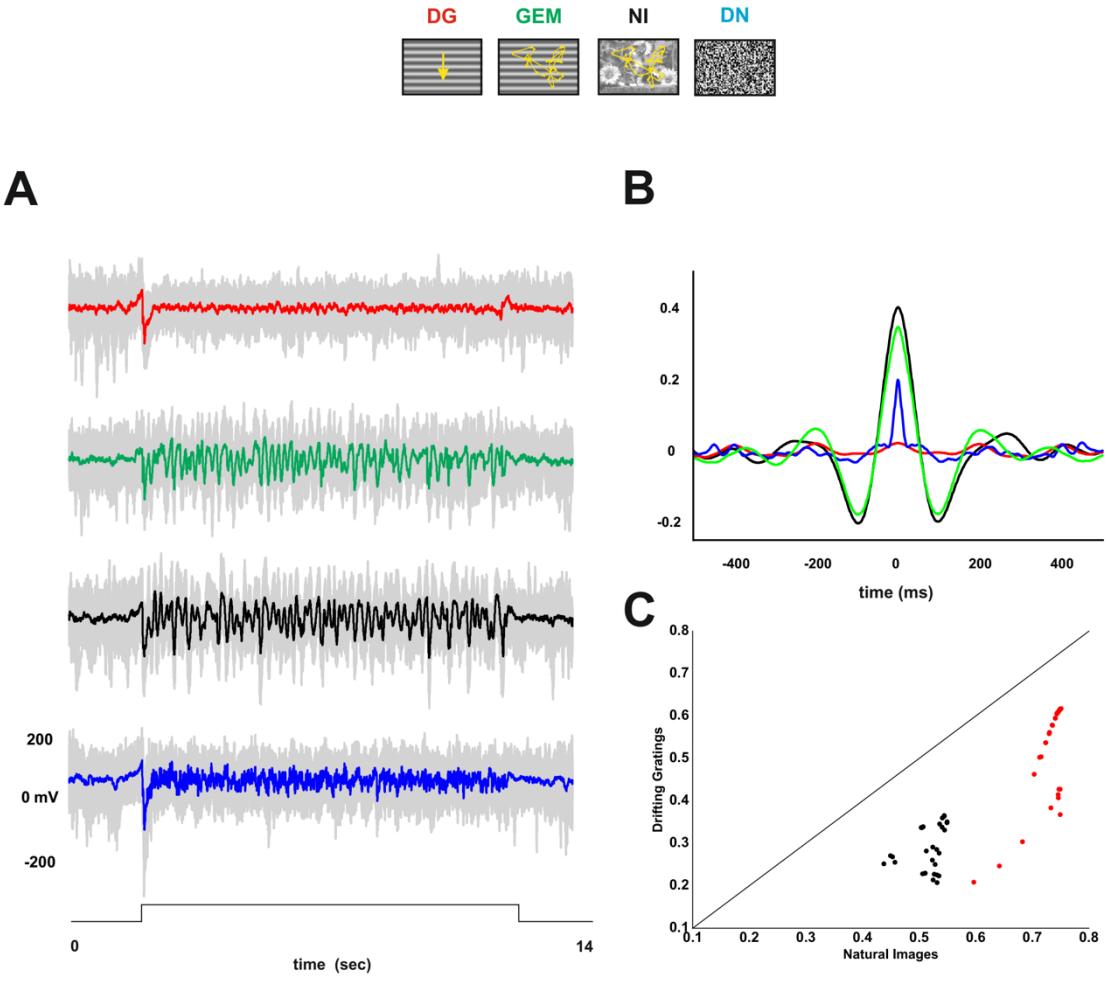

Figure 3.3.18: Mean and trials LFP. A: Mean LFP and its 30 trials in response to our set of stimuli. B: Trial-to-trial cross correlation of the LFP example C: Example of reliability values evoked by DN and NI for two experiments.

- **Comparison with the intracellular recordings**

The first step was to compare the reliability of the LFP and the Vm (Figure 3.3.19-A; table 3.3.10). For this analysis, we only took in account the sites where the 78 single units responded to GEM. We obtained a similar pattern of reliability intracellularly and extracellularly: Natural images elicited the most reliable LFP while GEM evoked the higher level of reliability among the artificial stimuli ($p < 0.001$, Friedman test). The reliability evoked by DG was very low. This confirm our observation made with the examples in figure 3.3.18 and corroborates our previous explanation, where we claimed that the energy evoked by DG is very low because the LFP captures the activity from many cells, responding to different phases. This mixture of signals lead to a very low reliability, lower than the one observed by the MUA (0.096 ± 0.007 for the MUA & 0.048 ± 0.002 for the LFP).

- **Mean evoked reliability**

We then investigated the reliability across all the recorded LFPs. As explained in the previous section we can use the LFP locked to the GEM, even when this latter was not presented at the preferred orientations. We obtained a similar pattern as the one observed for the reduced LFP population (Figures 3.3.19 and 3.3.20, table 3.3.10). However, the reliability levels were higher when computed across all the LFP sites. This is probably be caused by the fact that in this analysis we included sites from experiments were the global level reliability was a higher because of the electrode's reference placement.

- **Laminar reliability**

We obtained within layers, the same reliability pattern as the one observed for the mean population (Figures 3.3.19-C and 3.3.20; table 3.3.10). For all stimuli, the lowest levels of reliability were found in layer 2/3 ($p < 0.001$, Mann Whitney U test). While GEM and DN elicited their most reliable response in layer 4, we did not observe any difference in reliability between layers 4 and 5/6 for NI and DG ($p > 0.05$, Mann Whitney U test). As observed for the mean LFP, the laminar reliability is also highly stimulus dependent.

In summary, we found that natural images evoke a more reliable LFP response than the other stimuli. This result matches the intracellular findings of the laboratory (Baudot *et al.*, 2013) and our extracellular results. In addition, the very low levels of reliability evoked by DG confirms the fact that the integration at the LFP and the cellular level are different. With complementary analysis, Baudot and colleagues (2013) showed that the reliability needed to be measured in other ways. Indeed, they also observed a low level of reliability in response to gratings with the trial-to-trial correlation analysis but with a time frequency analysis they showed that gratings do evoke a reliable response but only at the grating frequency. Further in this manuscript, we will investigate the frequency-dependent reliability and put it in parallel with the results obtained in this section.

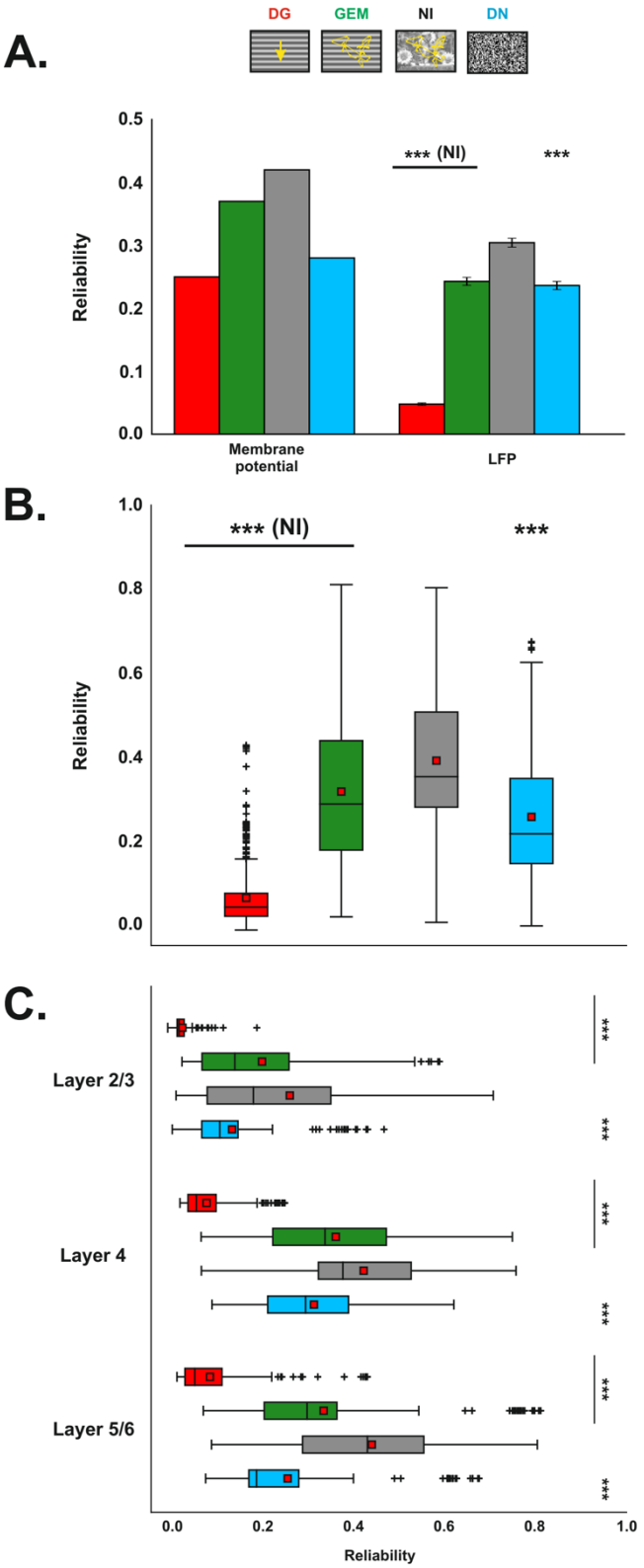

Figure 3.3.19: Local field potential mean reliability. Natural images evoke the most reliable response. A. Multiscale comparison of the mean reliability Left: intracellular results. Right: Local field potential. B. Comparison of the mean LFP reliability evoked by our stimulus set. C. laminar comparison of the mean reliability evoked by our stimulus set. The highest levels of reliability were observed in layer 4. Red square: mean. Black line: median. Extremities of the box: first and third quartile. Whiskers: minimum and maximum. Crosses: outliers; ***: $p < 0.001$

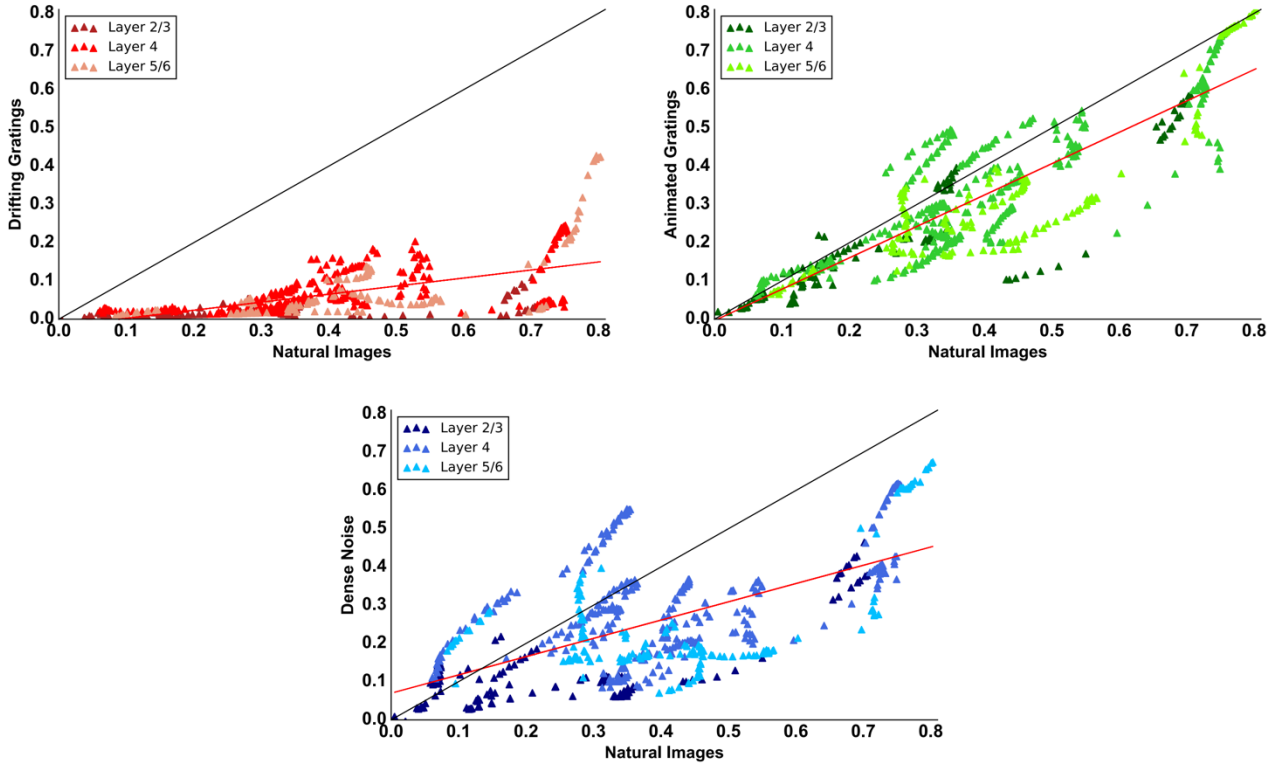

Figure 3.3.20: Reliability correlation plots. Top left: Natural images vs drifting gratings; Top right: Natural images vs gratings animated with eye movements. Bottom: Natural images vs dense noise. Circles: Layer 2/3; Triangles: Layer 4; Squares: Layer 5/6.

- **Impact of the natural statistics on the reliability**

Finally, as performed for the spiking activity, we computed the reliability levels obtained in response to our control stimuli (Figure 3.3.12, table 3.3.11). We did not obtain any difference between the unaltered natural image and the ones where the spatial and/or temporal statistics were altered ($p > 0.05$; Friedman test). Only the Natural image only animated with saccades evoked a higher reliability than the other stimuli ($p < 0.01$).
Unlike what was previously hypothesized, by looking at the LFP energy, it seems that the LFP is not strongly impacted by the absence of high order correlations in the spatio-temporal statistics. However, the increase of LFP reliability observed for the NI-SAC and its absence on the spiking activity could imply a saccadic impact on the neuronal activity that is only visible on a large population.

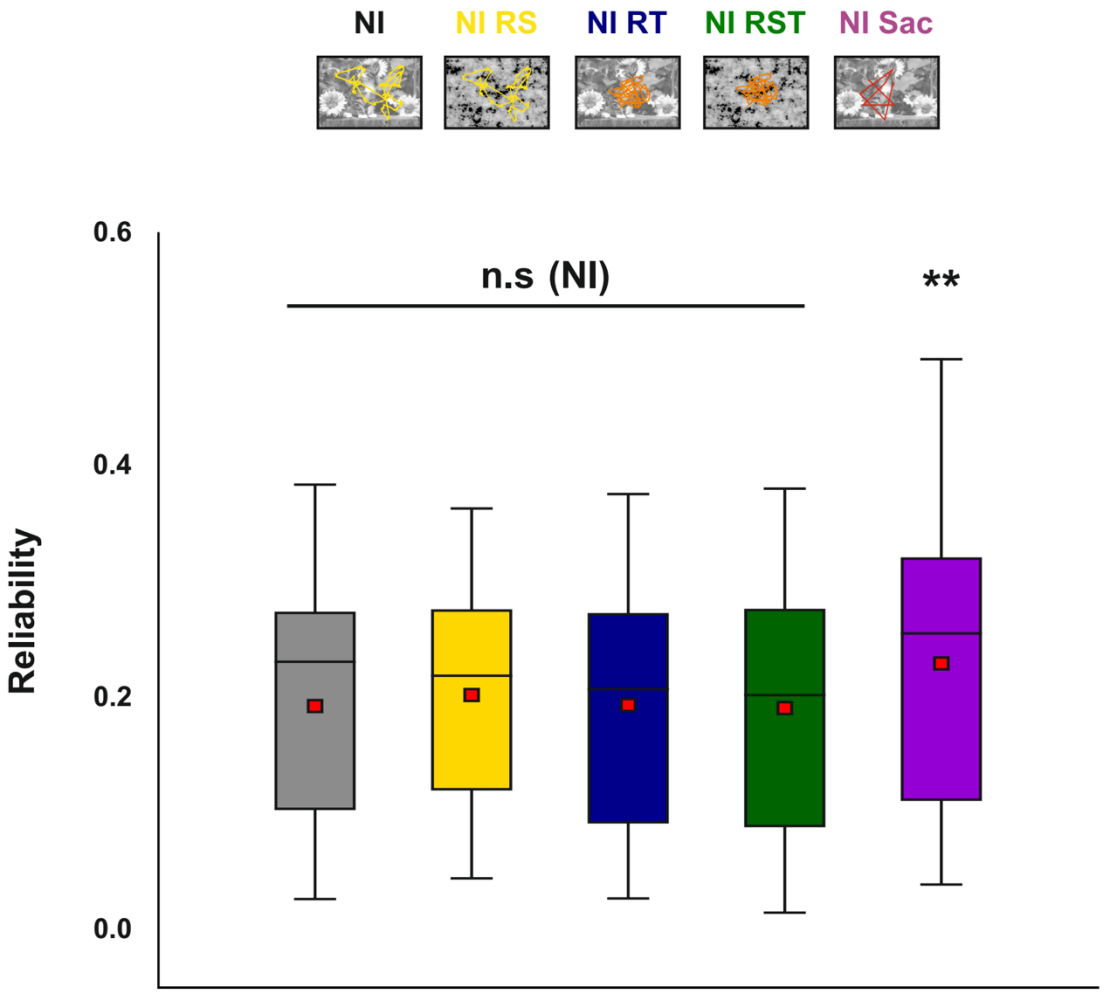

Figure 3.3.20: Mean reliability of the LFP evoked by the control stimuli. Mean LFP reliability in response to our control stimuli. Red square: mean. Black line: median. Extremities of the box: first and third quartile. Whiskers: minimum and maximum. Crosses: outliers. n.s: non-significant; ** : $p < 0.01$

FULL FIELD	LFP			
	DG	DN	GEM	NI
Mean tuned GEM	0.048 ± 0.002	0.243 ± 0.006	0.304 ± 0.007	0.236 ± 0.006
Mean all sites	0.063 ± 0.003	0.257 ± 0.006	0.317 ± 0.008	0.391 ± 0.008
Layer 2/3	0.019 ± 0.002	0.129 ± 0.010	0.195 ± 0.015	0.256 ± 0.019
Layer 4	0.072 ± 0.003	0.310 ± 0.008	0.358 ± 0.010	0.419 ± 0.010
Layer 5/6	0.080 ± 0.007	0.252 ± 0.012	0.331 ± 0.015	0.437 ± 0.015

Table 3.3.10: Mean LFP reliability evoked by our set of stimuli presented full field (Mean ± SEM)

	NI	NI-RS	NI-RT	NI-RST	NI-SAC
FULL FIELD	0.230 ± 0.007	0.241 ± 0.007	0.231 ± 0.007	0.228 ± 0.008	0.272 ± 0.009

Table 3.3.11: Mean LFP reliability evoked by our set of control stimuli presented full field (Mean ± SEM)

3.2. Impact of the Center Surround Interactions

As observed when quantifying the spiking activity and the local field potential responses, the concomitant stimulation of both center and surround has an impact on response. In addition, many studies showed that center surround interactions, in particular in natural images have modulate others aspect of the neuronal response. In their seminal study, Vinje and Gallant (2000) showed, in the primate, that the stimulation of both center and surround with a natural scene increases the response sparseness at the single unit level. This has also been observed, intracellularly and at the multi-unit level, on the cat by Haider and colleagues (2010). In addition, they showed that the stimulation of the surround with a natural scene increased the reliability of the spiking response. Based on these results, and ours, we decided to investigate the impact of the center surround interactions on the sparseness, reliability and precision of the response. In addition, we will be able to measure the impact of the center surround modulations evoked by artificial stimuli. Moreover, our dense recordings allowed us to record simultaneously across all layers.

3.2.1 Sparseness of the Spiking Activity

As described above, the center surround interactions have a strong impact on the sparseness of the response. We wondered if we would observe, across our single and multi-unit populations, the same sparseness increases between the FF and C stimulations. Moreover, since each layer has its unique properties, will the sparsening of the response be the same across layers? In addition, no study investigated the sparseness and the impact of the center surround interactions evoked by artificial stimuli. Figure 3.3.21 shows an example of sparseness evoked by the natural image presented on the full field, center conditions. We can observe that the FF stimulation evoked a sparser response than the center one. We observed no difference between the FF and C condition for drifting gratings. The spontaneous activity evoked a sparseness close to the stimulus. As stated in the previous section, the surround response evokes almost no response, thus will not be mentioned.

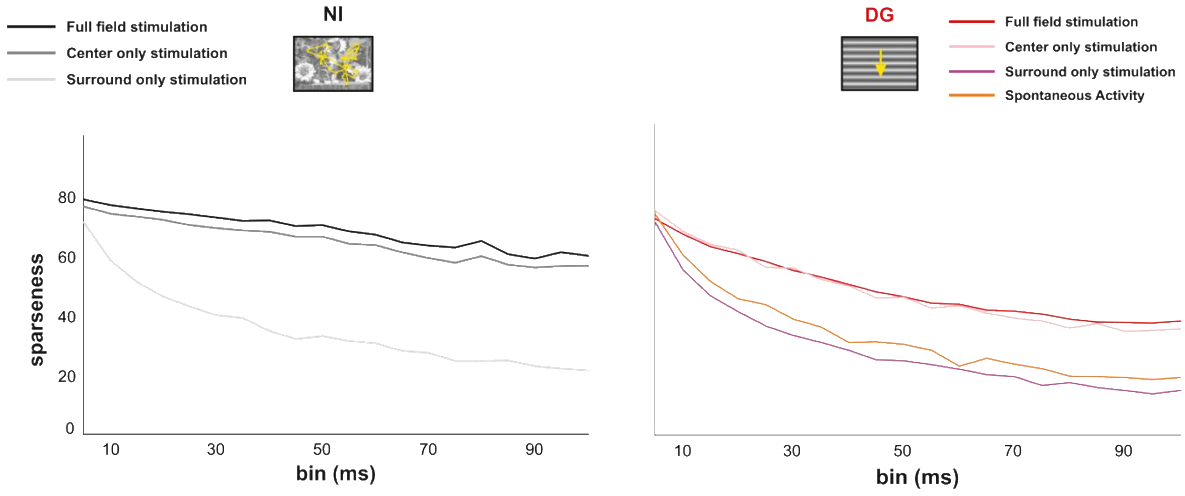

Figure 3.3.21: Example of evoked sparseness by natural images and drifting gratings for the full field, center and surround conditions.

- **Impact of the center surround interactions on the evoked sparseness**

At the single unit level, in response to NI, a sparsification of the response was observed when both center and surround were stimulated compared to a lone stimulation of the center (Figure 3.3.22; $p < 0.001$; Wilcoxon test). However, the difference between the FF and the C stimulation was very low (Table 3.3.12). This could be linked to the size of the center stimulation that we used. Indeed, a 5° stimulation already covers the surround of many cells. Regarding the artificial stimuli, no difference in sparseness between the full field and center conditions was observed. This suggests that the sparsening of the response is linked to the naturalness of the visual statistics.
We also compared the sparseness of the multi-unit activity (Figure 3.3.22). As observed for the SUA, natural images evoked a sparser response in the full field than in the center condition ($p<0.001$; Wilcoxon test). Surprising, the artificial stimuli evoked different sparsenesses between the FF and C conditions. While drifting gratings evoked a sparser response for the center condition ($p < 0.001$), dense noise evoked a sparser response the full field condition ($p < 0.001$). For all three stimuli, the difference between the center and center surround stimulations was very low (table 3.3.12). The fact that the artificial stimuli evoke a different sparseness between the FF and C conditions for the MUA but not for the SUA might come from the number of responses that is recorded in the MUA. Indeed, since the difference in sparseness between the two conditions is very low, a great number of responses is needed to reach a significant response. Another explanation could be that the sparsening of the response for artificial stimuli is present at a population level.
In their intracellular study, Haider *et al.* (2008) reported that, for natural images, the center surround interactions reduced the sparseness of FS and RS thin spike neurons compared to the center condition. On the other hand, RS neurons see their sparseness increase for the center and surround condition, compared with center condition. Therefore, we decided to compare the center surround and center only sparseness induced by natural images for both FS and RS neurons (Figure 3.3.22; table 3.3.12). As observed for the full field population, no difference in sparseness was observed between the two populations. We compared, for each stimulus, the sparseness evoked by the full field and the center conditions. The center surround interactions had no impact on the sparseness of FS cells (table 3.3.12; $p > 0.05$; Wilcoxon test). These results differ from those of Haider and colleagues (2010). However, among our FS population we do observe neurons displaying a higher sparseness for the center condition (figure 3.3.22). Only 9 neurons were recorded in Haider et al (2010) study, their results are not representative of the fast spiking population. Regarding the regular spiking population, we observed the same pattern as in the complete single unit, *i.e.* no difference between the FF and the C condition were observed for the artificial stimuli while NI evoked a higher sparseness when presented in the FF condition ($p < 0.001$; Wilcoxon test).

- **Laminar impact of the center surround interactions**

We showed that the sparseness is modulated by center surround interactions at the level of the complete population. However, since each layer display unique properties will we observe the same modulations within them. We first computed the sparseness of the spiking activity evoked by a center stimulation across layers (figure 3.3.22). We found the same pattern of response as in the full field condition. For the SUA and MUA, within all layers, natural images evoked the sparsest response. At the single unit level, for each stimulus, no difference in sparseness was observed in layer 2/3 ($p > 0.11$: Wilcoxon test). In layer 4, only DG were impacted by center surround interactions. Indeed, the center condition evoked a higher sparseness than the FF ($p < 0.05$). Finally, in layer 5/6, only NI were impacted by center surround interactions. Indeed, the full field condition evoked a higher

sparseness than the center ($p < 0.05$). Neurons in layer 5/6 are connected by horizontal connections. These latter are activated by surround stimulations. These results suggest that natural images evoked sparseness is modulated by these connections. These connections are also present in layer 2/3. However, the small number of neurons recorded on this layer might bias the response. It is important to note that for each stimulus, the difference of sparseness between the center and full field conditions is low (table 3.3.12).
At the multi-unit level, we observed the same pattern as in the global population for DG and NI. Indeed, natural images evoked a sparser response within all layers when a full field stimulation was performed ($p < 0.001$; Wilcoxon test), while gratings evoked a sparser response within all layers when a center stimulation was performed ($p < 0.001$). However, for DN, a difference between the FF and the C condition was only observed in layer 4 ($p < 0.001$). In this layer, the FF condition evoked a sparser response than the C condition. Again, for each stimulus, the difference of sparseness between the center and full field conditions is low (table 3.3.12).
For RS cells, as observed for the SUA, the only layer impacted by the natural images and its center surround interactions is layer 5/6. On the other hand, across layers, FS cells were not impacted by the center surround modulation (table 3.3.12).

Despite, this significant increase in sparseness evoked by NI when they were presented full field, the difference with the center condition remains low. Our results differ from the ones observed in the literature (Vinje and Gallant, 2000; Haider et al., 2010). This is probably linked to the difference in the size of the center stimulation between our study and theirs. Indeed, our center stimulation is performed on a mask of 5x5°. In Haider and colleagues studie, the center stimulation is performed on a mask of more or less 2°. Therefore, the small difference, that we observe, between the center surround and center firing sparseness might come from the fact that a 5° center stimulation also stimulates the surround. We are probably close to a limit where the sparseness will not be strongly modulated anymore by an increase of the stimulation size. A preliminary examination of the influence size of the stimulation mask and the sparseness values has been performed on the multi-unit activity. We computed a normalized sparseness with 100% being the value obtained for the full field condition (Figure 3.3.23). We observed that between a mask of 2x2° and 3x3° the difference in the normalized sparseness is about 20% (64% vs 84%). Then, a plateau is reached. Indeed, the sparseness values are very similar (3x3° = 84%; 5x5° = 85%; 7x7° = 90%). This tends to confirm that the increase in sparseness is not strongly modulated when we reach a certain stimulation size.

In conclusion, we showed that natural images are affected by center surround interactions. These interactions result in a sparsening of the response. However, the effect is very small. This effect was probably stronger at multi-unit level because of the higher number of responses that we recorded for this signal, compared to the SUA.

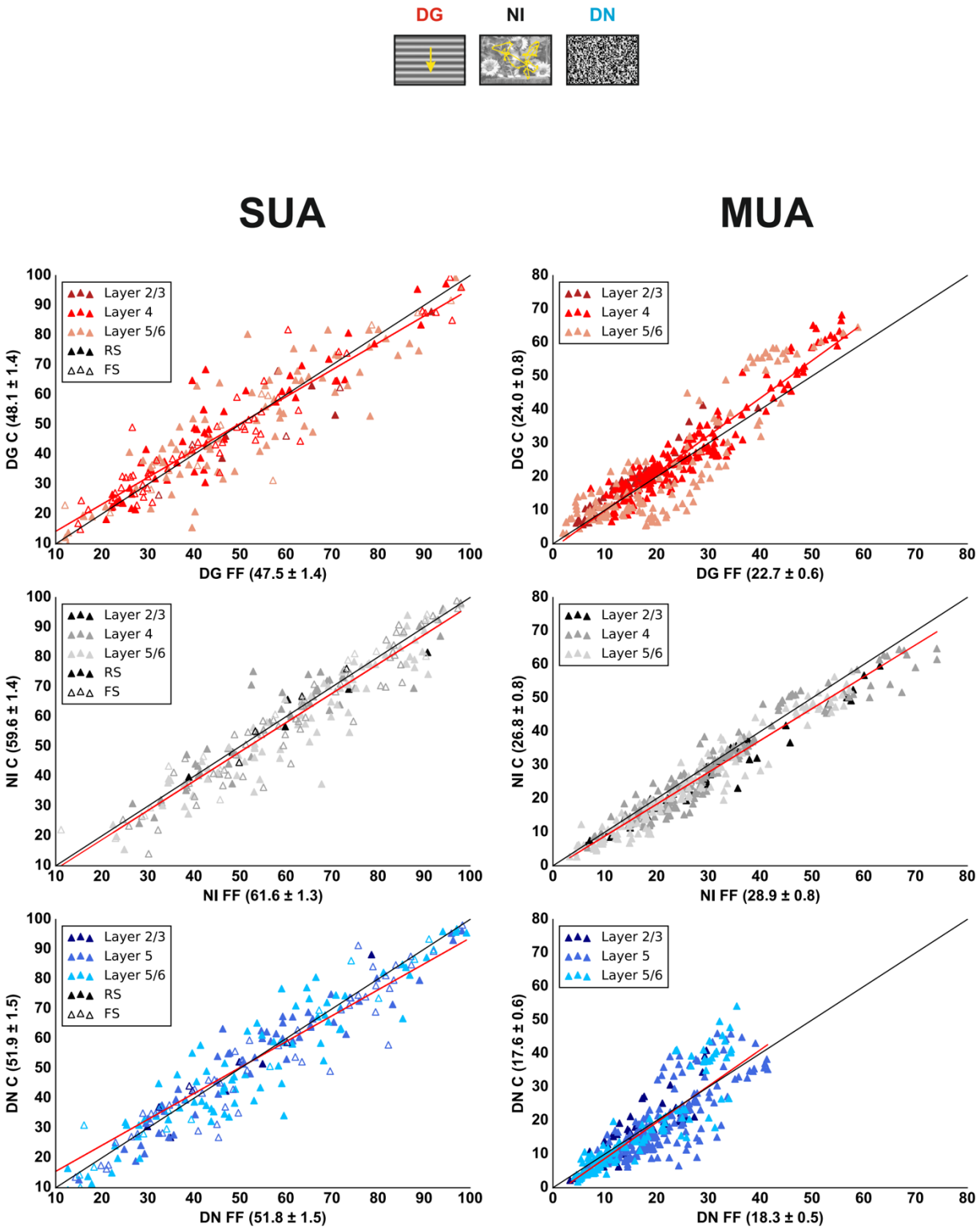

Figure 3.3.22: Full field vs center stimulation sparseness. The center surround interactions have a small impact on the sparseness. Left: Single unit sparseness Right: Multi-unit activity sparseness. Top row: Drifting Gratings. Middle row: Natural images. Bottom row: Dense Noise. Red line: polynomial fit. Empty symbols = FS. Full Symbols = RS or MUA.

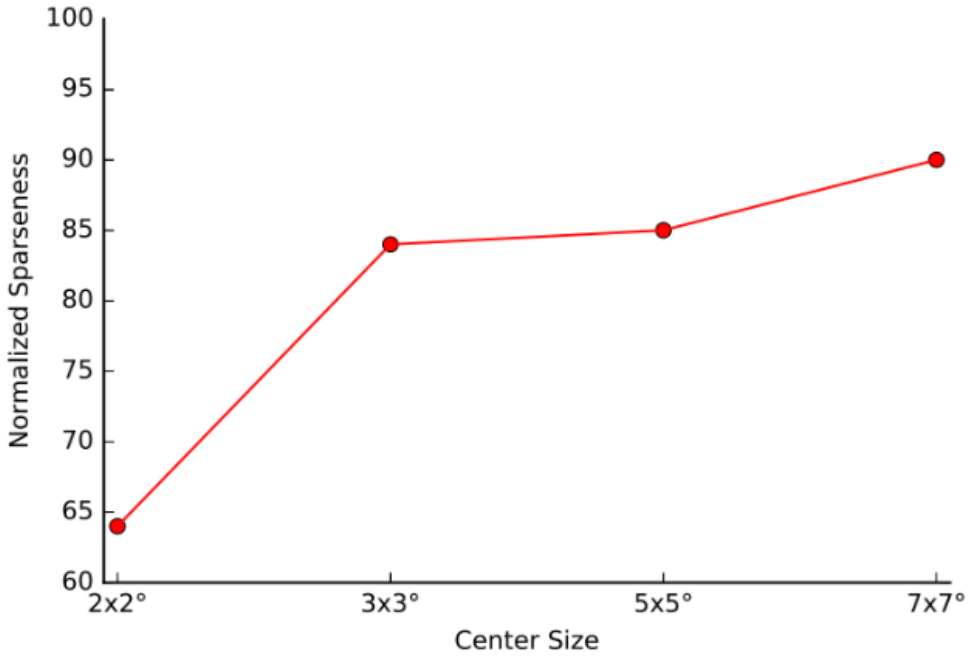

Figure 3.3.23: Normalized sparseness as a function of the stimulation size of the center condition. The sparsification of the response reach a plateau when the center stimulation reaches a certain size.

- **Impact of the natural statistics on the center surround interactions**

In their study, Guo and colleagues (2005) showed that the spiking activity of the cell is modulated by the naturalness of the surround statistics. Therefore, we wondered if the absence of spatial and/or high order correlations had an impact on the sparseness of the response (Figure 3.3.24 and table 3.3.13). As observed for the full field condition, all stimuli evoked the same level of sparseness for each signal ($p > 0.05$; Friedman test). At single unit level, all stimuli evoked a higher sparseness for the full field condition compared to the center one ($p > 0.05$; Wilcoxon test). However, at the multi-unit level only NI and NI-RST displayed a higher sparseness for the full field condition. The other stimuli (NI-RT and NI-SAC) displayed a higher sparseness for the center condition. As observed for the normal stimulus set, full field and center conditions evoked very similar values of sparseness, despite a significant difference. No difference between the FF and C condition was observed for the FS neurons ($p > 0.05$) while RS neurons displayed the same pattern as the complete SUA population.

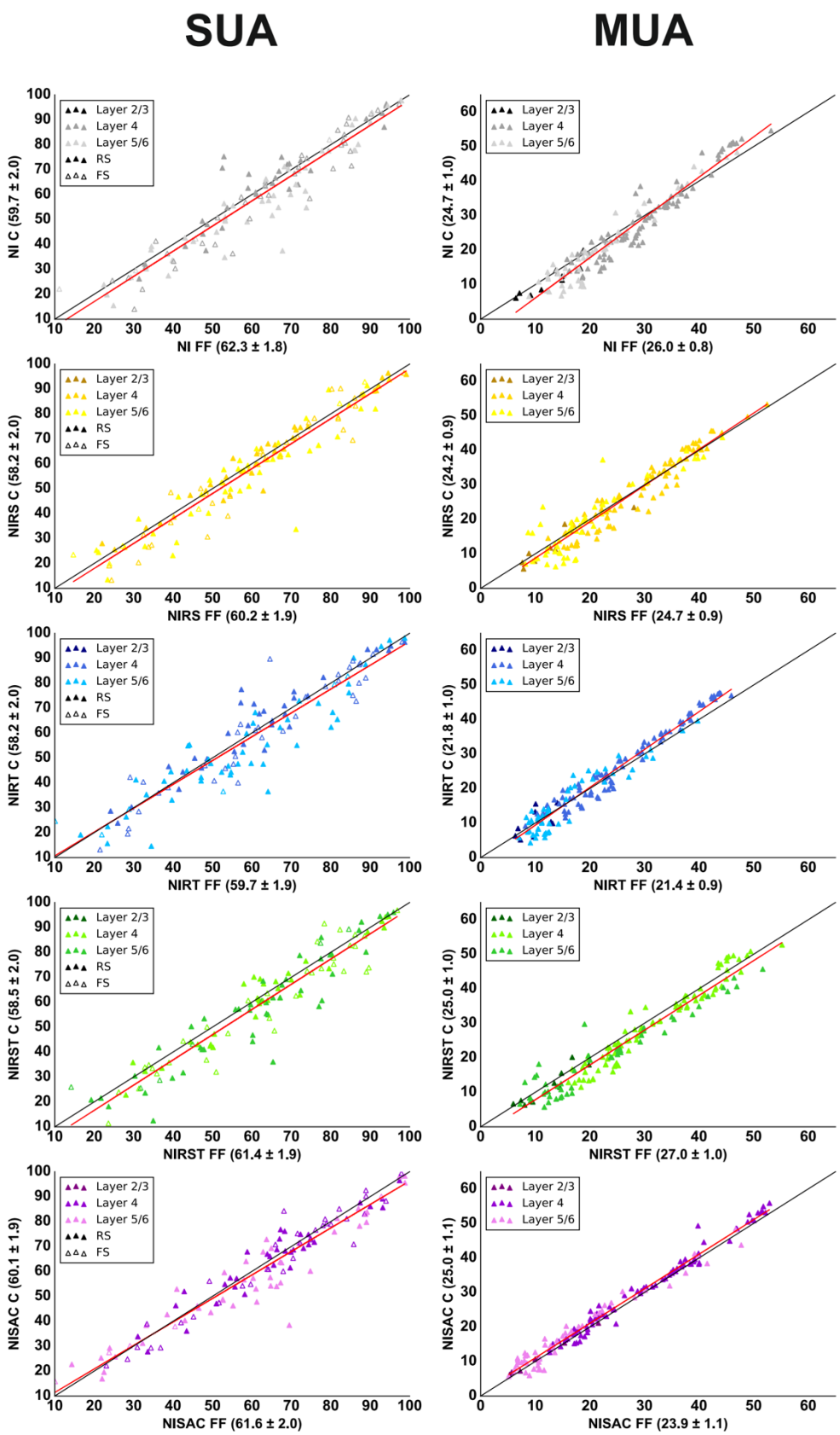

Figure 3.3.24: Full field vs center stimulation sparseness evoked by the control stimuli. Left panel: Single unit activity firing rate. Right panel: Multi-unit activity firing rate. Red line: polynomial fit. Empty symbols = FS. Full Symbols = RS or MUA.

FULL FIELD	SUA			FS		
	DG	NI	DN	DG	NI	DN
Layer 2/3	58.3 ± 5.6	61.2 ± 4.8	46.7 ± 4.7	51.0 ± 9.1	60.0 ± 5.3	42.9 ± 6.0
Layer 4	45.0 ± 2.0	60.4 ± 1.8	52.5 ± 2.1	44.8 ± 2.8	62.3 ± 2.6	51.5 ± 3.1
Layer 5/6	49.3 ± 2.3	63.2 ± 2.1	51.6 ± 2.4	45.0 ± 7.0	54.6 ± 6.9	50.1 ± 7.7
Mean	47.5 ± 1.4	61.6 ± 1.3	51.8 ± 1.5	45.1 ± 2.5	60.7 ± 2.4	50.8 ± 2.8

CENTER	SUA			FS		
	DG	NI	DN	DG	NI	DN
Layer 2/3	53.6 ± 5.5	60.4 ± 4.4	47.5 ± 5.5	44.6 ± 7.4	60.8 ± 6.9	45.7 ± 4.6
Layer 4	46.6 ± 1.9	59.2 ± 1.9	52.3 ± 2.1	45.8 ± 2.7	59.6 ± 2.8	51.2 ± 3.1
Layer 5/6	49.1 ± 2.2	60.0 ± 2.2	51.8 ± 2.4	44.8 ± 6.8	55.6 ± 7.0	50.0 ± 7.8
Mean	48.1 ± 1.4	59.6 ± 1.4	51.9 ± 1.5	45.5 ± 2.4	58.9 ± 2.5	50.7 ± 2.8

FULL FIELD	MUA			RS		
	DG	NI	DN	DG	NI	DN
Layer 2/3	14.3 ± 1.1	30.4 ± 2.2	16.3 ± 1.1	63.2 ± 7.0	62.0 ± 7.5	49.2 ± 7.0
Layer 4	25.6 ± 0.9	30.4 ± 1.1	20.7 ± 0.6	45.2 ± 2.7	58.0 ± 2.6	53.7 ± 2.8
Layer 5/6	21.6 ± 1.1	26.3 ± 1.3	15.7 ± 0.8	50.2 ± 2.3	64.8 ± 2.1	51.9 ± 2.4
Mean	22.7 ± 0.6	28.9 ± 0.8	18.3 ± 0.5	48.9 ± 1.8	62.2 ± 1.6	52.4 ± 1.8

CENTER	MUA			RS		
	DG	NI	DN	DG	NI	DN
Layer 2/3	16.9 ± 1.3	27.7 ± 2.0	17.1 ± 1.3	59.5 ± 7.2	60.2 ± 6.2	48.7 ± 9.0
Layer 4	27.3 ± 1.0	28.7 ± 1.1	18.9 ± 0.7	47.7 ± 2.8	58.6 ± 2.6	53.6 ± 2.9
Layer 5/6	22.1 ± 1.5	23.8 ± 1.3	16.0 ± 1.1	50.0 ± 2.3	60.9 ± 2.2	52.2 ± 2.5
Mean	24.0 ± 0.8	26.8 ± 0.8	17.6 ± 0.6	49.5 ± 1.8	60.0 ± 1.6	52.6 ± 1.8

Table 3.3.12: Mean SUA (and its subpopulations) and MUA sparseness evoked by our set of stimuli presented full field and center (Mean ± SEM)

FULL FIELD					
	NI	NI-RS	NI-RT	NI-RST	NI-SAC
FS	61.3 ± 3.5	60.1 ± 3.6	59.9 ± 3.7	60.5 ± 3.5	61.1 ± 3.7
RS	62.8 ± 2.1	60.2 ± 2.2	59.7 ± 2.3	61.8 ± 2.2	61.9 ± 2.3
SUA	62.3 ± 1.8	60.2 ± 1.9	59.7 ± 1.9	61.4 ± 1.9	61.6 ± 2.0
MUA	26.0 ± 0.8	24.7 ± 0.9	21.4 ± 0.9	27.0 ± 1.0	23.9 ± 1.1

CENTER					
	NI	NI-RS	NI-RT	NI-RST	NI-SAC
FS	58.5 ± 3.7	57.8 ± 3.8	58.2 ± 3.7	57.5 ± 3.6	59.9 ± 3.7
RS	60.4 ± 2.3	58.5 ± 2.3	58.2 ± 2.3	59.0 ± 2.4	60.2 ± 2.2
SUA	59.7 ± 2.0	58.2 ± 2.0	58.2 ± 2.0	58.5 ± 2.0	60.1 ± 1.9
MUA	24.7 ± 1.0	24.2 ± 0.9	21.8 ± 1.0	25.0 ± 1.0	25.0 ± 1.1

Table 3.3.13: Mean SUA (and its subpopulations) and MUA sparseness evoked by our set of control stimuli presented full field and center(Mean ± SEM)

3.2.2 Fano Factor

In the previous section, we showed that the Fano Factor, *i.e.* the reliability of the response was stimulus dependent. In their study, Haider and colleagues (2010) also showed that this reliability was modulated by the concomitant stimulation of both center and surround with natural images. However, they did not compute the Fano Factor. We wondered if we would observe an impact of the center surround interactions on the Fano Factor, when natural images are presented but also when artificial stimuli are presented. In addition, will we observe a laminar dependency of the center surround modulations of the Fano Factor? In order to test the impact of the center surround interactions we computed the Fano Factor when we presented our set of stimuli in the center and in the full field conditions.

- **Impact of the center surround interactions on the Fano Factor**

Before comparing the response evoked by the center and full field conditions, we compared the Fano Factors evoked by the different stimuli presented on the center (Figure 3.3.25; Table 3.3.14). For both single and multi-unit activities the center and the full field conditions evoked the same response pattern, *i.e.* natural images evoked the lowest Fano Factor for each signal $p < 0.001$; Friedman test). The comparison of the evoked Fano Factors by the full field and center conditions showed that Natural Images and Dense Noise displayed lower values for the Full field condition (*i.e.* a more reliable response), for both SUA and MUA (Figure 3.3.25; $p < 0.001$; Wilcoxon test). On the other hand, no significant difference was observed for DG ($p > 0.05$). Within layers, at the single unit level, no difference was observed between the conditions in layer 2/3. On the other hand, in layer 4 and 5/6, NI evoked a more reliable response for the FF condition ($p < 0.001$). At the multi-unit level, NI evoked, in all layers, a lower fano factor when presented full field ($p < 0.001$). This was also observed for DN in layers 4 and 5/6.
In their study, Haider and colleagues (2010) showed that FS and RS neurons were differently impacted by center surround interactions. Thus, we computed the Fano Factor among our RS and FS populations in order to evaluate how the concomitant stimulation of the center and the surround modulate their Fano Factors (Figures 3.3.25 and table 3.3.14). The center condition evoked a similar response pattern for each subclass as the one observed for the complete single unit population. We then compared the full field and center conditions.
Natural images evoked for both RS and FS cells a lower Fano Factor for the full field condition ($p < 0.001$). On the other hand, dense noise evoked a lower Fano Factor for the full field only among FS cells ($p < 0.001$). Within layers 4 and 5/6, for both RS and FS cells, natural images evoked a higher fano factor for the center condition than the full field.

- **Impact of the natural statistics on the center surround interactions**

Finally, we asked ourselves if the alteration of the spatial and temporal statistics would have an impact on the center surround interactions and on the response reliability (figures 3.3.26 and table 3.3.15). At the single unit level, only NI and NI-RST displayed a lower FanoFa for the full field condition ($p < 0.001$; Wilcoxon test), while no difference was observed for the other stimuli ($p > 0.05$). At the multi-unit level, all stimuli evoked a lower Fano Factor for the full field than the center condition ($p < 0.01$; Wilcoxon test). This suggest that reliability of natural images is modulated by the surround.

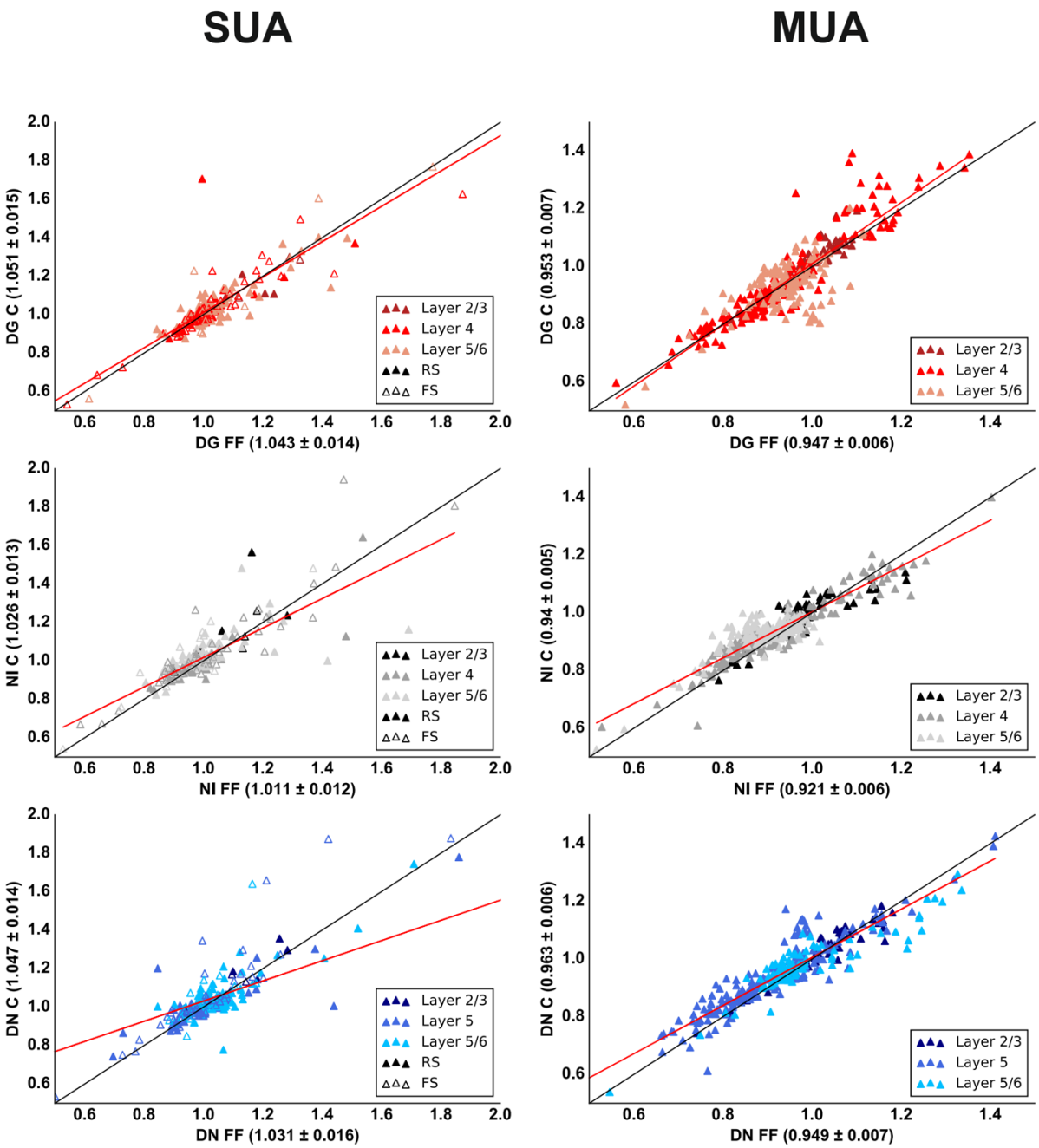

Figure 3.3.25: Full field vs center stimulation Fano Factor. Left: Single unit Fano Factor Right: Multi-unit activity sparseness. Top row: Drifting Gratings. Middle row: Natural images. Bottom row: Dense Noise.Red line: polynomial fit. Empty symbols = FS. Full Symbols = RS or MUA.

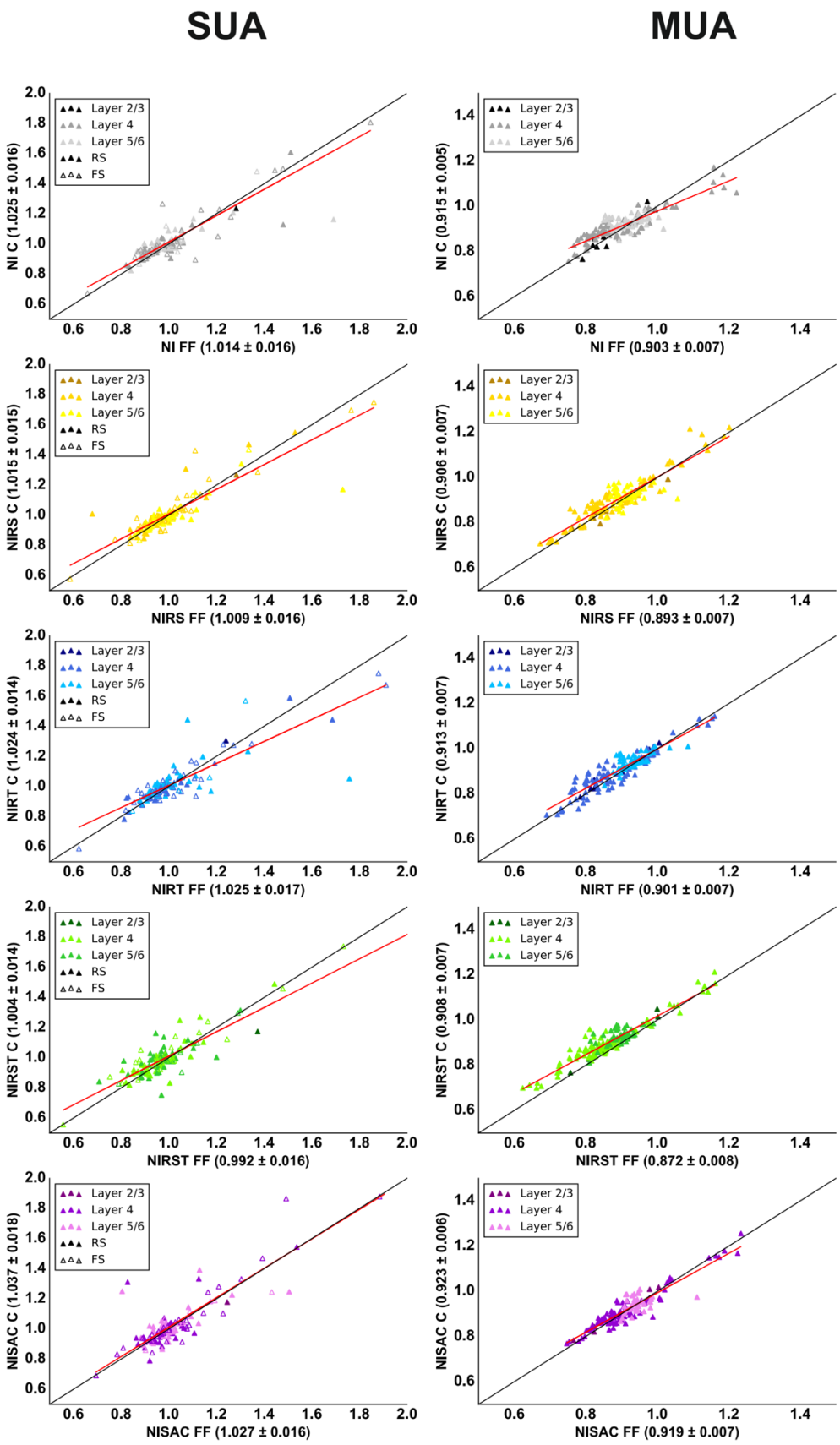

Figure 3.3.26: Full field vs center stimulation Fano Factor evoked by our set of control stimuli. Left panel: Single unit activity firing rate. Right panel: Multi-unit activity firing rate. Red line: polynomial fit. Empty symbols = FS. Full Symbols = RS or MUA.

FULL FIELD	SUA			FS		
	DG	NI	DN	DG	NI	DN
Mean	1.051 ± 0.015	1.026 ± 0.013	1.047 ± 0.014	1.057 ± 0.033	1.047 ± 0.032	1.069 ± 0.030
Layer 2/3	1.148 ± 0.039	1.177 ± 0.066	1.162 ± 0.044	1.119 ± 0.090	1.111 ± 0.092	1.093 ± 0.060
Layer 4	1.047 ± 0.026	1.023 ± 0.024	1.049 ± 0.023	1.046 ± 0.038	1.051 ± 0.039	1.077 ± 0.035
Layer 5/6	1.047 ± 0.015	1.017 ± 0.012	1.036 ± 0.018	1.086 ± 0.074	1.020 ± 0.055	1.036 ± 0.064

FULL FIELD	MUA			RS		
	DG	NI	DN	DG	NI	DN
Mean	0.953 ± 0.007	0.940 ± 0.005	0.963 ± 0.006	1.047 ± 0.013	1.014 ± 0.010	1.034 ± 0.014
Layer 2/3	1.017 ± 0.014	0.997 ± 0.012	1.022 ± 0.014	1.165 ± 0.039	1.217 ± 0.093	1.204 ± 0.057
Layer 4	0.951 ± 0.012	0.933 ± 0.008	0.941 ± 0.009	1.048 ± 0.032	0.985 ± 0.018	1.011 ± 0.023
Layer 5/6	0.932 ± 0.008	0.928 ± 0.006	0.971 ± 0.009	1.040 ± 0.012	1.016 ± 0.011	1.036 ± 0.019

Table 3.3.14: Mean SUA (and its subpopulations) and MUA Fano Factor evoked by our set of stimuli presented full field and center (Mean ± SEM)

FULL FIELD					
	NI	NI-RS	NI-RT	NI-RST	NI-SAC
FS	1.051 ± 0.034	1.031 ± 0.033	1.051 ± 0.035	1.021 ± 0.038	1.079 ± 0.037
RS	0.994 ± 0.016	0.997 ± 0.016	1.010 ± 0.018	0.976 ± 0.013	0.998 ± 0.013
SUA	1.014 ± 0.016	1.009 ± 0.016	1.025 ± 0.017	0.992 ± 0.016	1.027 ± 0.016
MUA	0.903 ± 0.007	0.893 ± 0.007	0.901 ± 0.007	0.872 ± 0.008	0.919 ± 0.007

CENTER					
	NI	NI-RS	NI-RT	NI-RST	NI-SAC
FS	1.075 ± 0.039	1.040 ± 0.033	1.045 ± 0.032	1.030 ± 0.032	1.089 ± 0.043
RS	0.998 ± 0.011	1.001 ± 0.014	1.013 ± 0.014	0.989 ± 0.013	1.009 ± 0.014
SUA	1.025 ± 0.016	1.015 ± 0.015	1.024 ± 0.014	1.004 ± 0.014	1.037 ± 0.018
MUA	0.915 ± 0.005	0.906 ± 0.007	0.913 ± 0.007	0.908 ± 0.007	0.923 ± 0.006

Table 3.3.15: Mean SUA (and its subpopulations) and MUA Fano Factor evoked by our set of control stimuli presented full field and center (Mean ± SEM)

3.2.3 Reliability of the Spiking Activity

In the previous chapter, we showed that natural images evoke a more reliable response than the artificial stimuli. These results were in agreement with the literature (Yao et al., 2007; Baudot et al., 2013). As shown in the previous sections, the spiking activity is modulated by the center surround interactions of natural statistics. An intracellular study performed on the anesthetized and paralyzed cat showed that the reliability evoked by natural images is modulated by center surround interactions (Haider et al., 2010). This modulation occurs both at the spiking and at the membrane potential level. They showed that levels of reliability evoked by classic regular spiking neurons are increased when both center and surround are stimulated with a natural scene. This reliability increase of the spiking activity is accompanied of an increase of the membrane potential reliability. On the other hand, they showed that thin spike regular spiking neurons display a decrease in reliability when both center and surround are stimulated while fast spiking neurons' reliability is not modulated by center surround interactions. They also showed that the reliability of the multi-unit activity is increased when both center and surround are stimulated. Based on these results we wondered if we would observe an increase in reliability for the spiking activity when natural scenes, but also artificial stimuli are presented in the full field condition compared to the center condition. Moreover, our previous results showed that the levels of reliability are layer dependent. We can wonder if this is the case for the center surround interactions. Finally, will we observe a different impact of the center surround modulations in function of the neuronal subclass?

Figure 3.3.27 shows an example of trial-to-trial correlation computed for single unit activity in response to DG and NI presented on the full field, center and surround conditions. The level of reliability corresponds to the peak at zero. On this example, both stimuli evoked higher levels of reliability for the full field condition than for the center. The surround stimulation and the spontaneous activity induced similar levels of reliability, almost equal to zero.

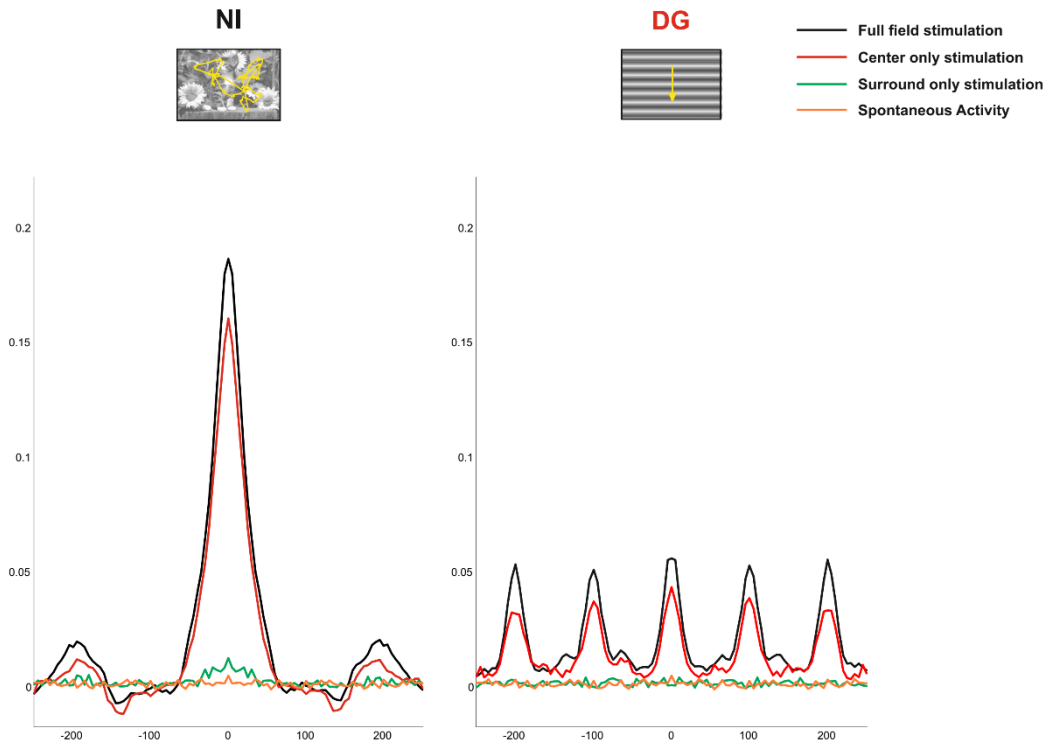

Figure 3.3.27: Example of trial-to-trial cross correlation evoked by natural images and drifting gratings presented on the full field, center and surround conditions.

- **Impact of the center surround interactions on the reliability**

The pattern of reliability that we obtained for the center condition is similar to the one obtained for the full field condition. We investigated the impact of the center surround interactions on the reliability (figure 3.2.28 and table 3.3.16). At the single unit level, both natural images and dense noise evoked higher levels of reliability when both center and surround were stimulated, compared to a center stimulation alone ($p < 0.001$; Wilcoxon test). On the other hand, despite a higher mean evoked by the center stimulation, DG showed no difference in reliability between the two conditions ($p > 0.05$). As observed for the full field condition, the levels of reliability are very heterogeneous with a group of cells being very reliable and another displaying very low values of reliability. This has already been observed on mice by Kampa and colleagues (2011). At the multi-unit level, both natural images and dense noise evoked higher levels of reliability when both center and surround were stimulated, compared to a center stimulation alone ($p < 0.001$; Wilcoxon test). Regarding DG, we confirmed the tendency observed at the single unit level since the center stimulation evoked a higher reliability than the full field one ($p < 0.001$). This increase observed for the center condition might be linked to the suppressive effect observed for gratings when both center and surround are stimulated. Indeed, the plateau observed for the sparseness (and possibly the firing rate) does not seem to be true for the reliability. This suggest that the reliability of spiking activity is less impacted by the size of the surround than the sparseness.
In their intracellular study, Haider and colleagues (2010) showed that center surround interactions do not modulate in the same way regular spiking neurons and fast spiking neurons reliability. In addition, we showed in the previous section that these two subtypes show different modulations to the center surround interactions. Will we observe a different modulation of the reliability for these two neuronal subclasses?
As observed for the full field condition, natural images evoked the highest mean reliability for both regular and fast spiking cells ($p < 0.001$; Wilcoxon test; Figure 3.3.28; table 3.3.16). Based on Haider and colleagues results natural images should evoke the same level of reliability between the two conditions for FS cells and higher one for the full field condition for RS cells. However, for both FS and RS cells, when natural images were presented the full field condition evoked higher levels of reliability compared to the center condition (Table 3.3.16; $p < 0.001$; Wilcoxon test). The difference between our two studies could be linked to the fact that they only recorded 9 FS cells. As shown in figure 3.3.28 some cells are not at all modulated by the center surround interactions while others show an increase in reliability for the center condition. Therefore, among these 9 cells they might have recorded some non-modulated cells combined with cells displaying a higher reliability for the FF and the C condition, which lead to an equal mean.
In summary, we showed that the reliability evoked by natural images is higher for the full field condition than the center condition.

- **Laminar impact of the center surround interactions**

We then wondered if the impact of the center surround interactions would be the same within each layer or if the different properties of the laminar compartments would lead to different center surround modulations. As observed for the full field condition, for both single and multi-unit activities, natural images evoked the highest level of reliability within all layers ($p < 0.001$, Friedman test; Figure 3.3.28; Table 3.3.16). At the single and multi-unit levels, all stimuli evoked their highest level of reliability in layer 4 and the lowest one in layer 2/3 ($p < 0.01$; Kruskal-Wallis test). We then wondered if the center surround interactions impacted the laminar reliability in an equivalent way (figure 3.3.28; table

3.3.16). At the single unit level, Natural images evoked a more reliable response for the full field condition in layers 4 and 5/6 ($p < 0.001$, Wilcoxon test). No difference was found in layer 2/3, despite a higher mean for the full field condition ($p = 0.07$). The absence of significance is probably linked to the small number of cells recorded in this layer (10). The difference in the single unit reliability between layers 4 and 5/6 was higher for the center condition than the full field condition (Table 3.3.16). As described in section 3.1, neurons in layer 5/6 are connected to each other by horizontal connections. Neurons that have their receptive field on the surround are stimulated by the surround stimulation and their horizontal connections project to the recorded neuron. This suggest that during the full field stimulation, layer 5/6 neurons' reliability is modulated by horizontal connections. Thus, when the surround is not stimulated the reliability is reduced. Within all layers, dense noise displayed a higher reliability for the full field condition while DG only displayed a higher reliability for the center condition in layer 4 ($p < 0.001$).

At the multi-unit level, both Natural images and dense noise evoked a more reliable response for the full field condition within all layers, respectively ($p < 0.001$; Wilcoxon test). This confirms the tendency observed in layer 2/3 for the single unit activity.

Another explanation of the difference observed for FS cells between our two studies could be the fact that their recordings oversampled one particular layer. Indeed, we showed that the center surround interactions evoked a stronger modulation in layer 5/6 than in layer 4. Therefore, the neurons that they recorded might have been located mainly in this layer. As observed for the full field condition, natural images evoked the most reliable response in layers 4 and 5/6 for both RS and FS neurons ($p < 0.01$; Wilcoxon test). No statistical analysis was possible in layer 2/3 because of the reduced number of cells recorded in this layer. Among the fast spiking neurons, no difference in reliability was observed between layers, for each stimulus respectively ($p > 0.1$; Mann Whitney U test). Among regular spiking cells, unlike what was observed for the full field condition where the two values were equal, natural images evoked higher levels of reliability in layer 4 than in layer 5/6 ($p > 0.001$; table 3.3.16). These results suggest that RS cells are modulated by horizontal connections while FS are not.

In summary, we showed that both FS and RS neurons are modulated by center surround interactions when natural images are presented. This modulation is present in all layers. The fact that this modulation is stronger in layer 5/6 for RS cells than FS cells combined to the fact that horizontal connections target only excitatory neurons suggest that regular spiking cells are modulated by horizontal connections while fast spiking neurons are modulated by intrinsic connections.

In conclusion, we showed that we also observe a center surround modulation across layers. For natural images this modulation seems more important, at the single unit level, in layer 5/6 where neurons are connected by horizontal connections.

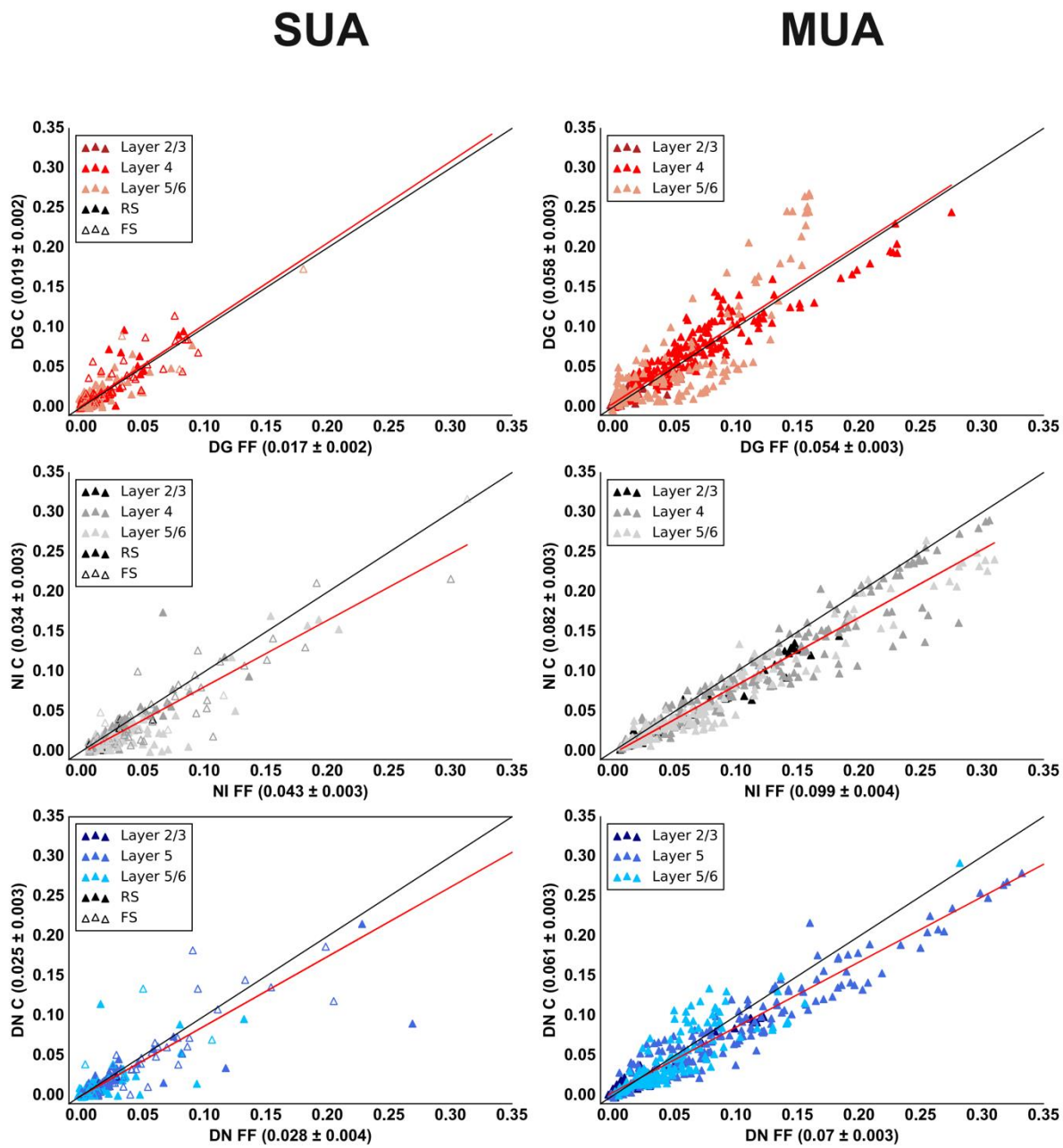

Figure 3.2.28: Full field vs center stimulation reliability. The center surround interactions increase the reliability in response to natural images. Left: Single unit reliability Right: Multi-unit activity reliability. Top row: Drifting Gratings. Middle row: Natural images. Bottom row: Dense Noise. Empty symbols = FS. Full Symbols = RS or MUA.

- **Impact of the natural statistics on the center surround interactions**

In their study, Guo et al, (2005) showed that the response of V1 neurons in primates were modulated by the alteration of the spatial statistics of the surround. Thus, will we observe a different modulation of the reliability if the spatial or temporal statistics are altered?
First, as observed for the full field condition, all stimuli displayed the same level of reliability, for all signals respectively, when they were only presented in the center ($p > 0.05$; Friedman Test; Figure 3.3.29 and table 3.3.17). Despite this absence of difference, at the single unit level, all unaltered images except NI-RT, evoked a higher level of reliability for the full field condition ($p < 0.01$; Wilcoxon test). The same observation was made for the regular spiking cells but not for the fast spiking ones. Indeed, for fast spiking cells only NI and NI-RST displayed a higher reliability for the full field condition, no difference was observed for the other stimuli. These results suggest that high order temporal correlations are more important than spatial ones for the reliability but also that spatial and temporal statistics lacking high order correlations interact in a similar way as unaltered spatial and temporal statistics. In addition, FS neurons need to have similar spatial and temporal statistics in order to be modulated by the center surround interactions. Similar observations were made for the multi-unit activity except that NISAC evoked no difference between the full field and center conditions.

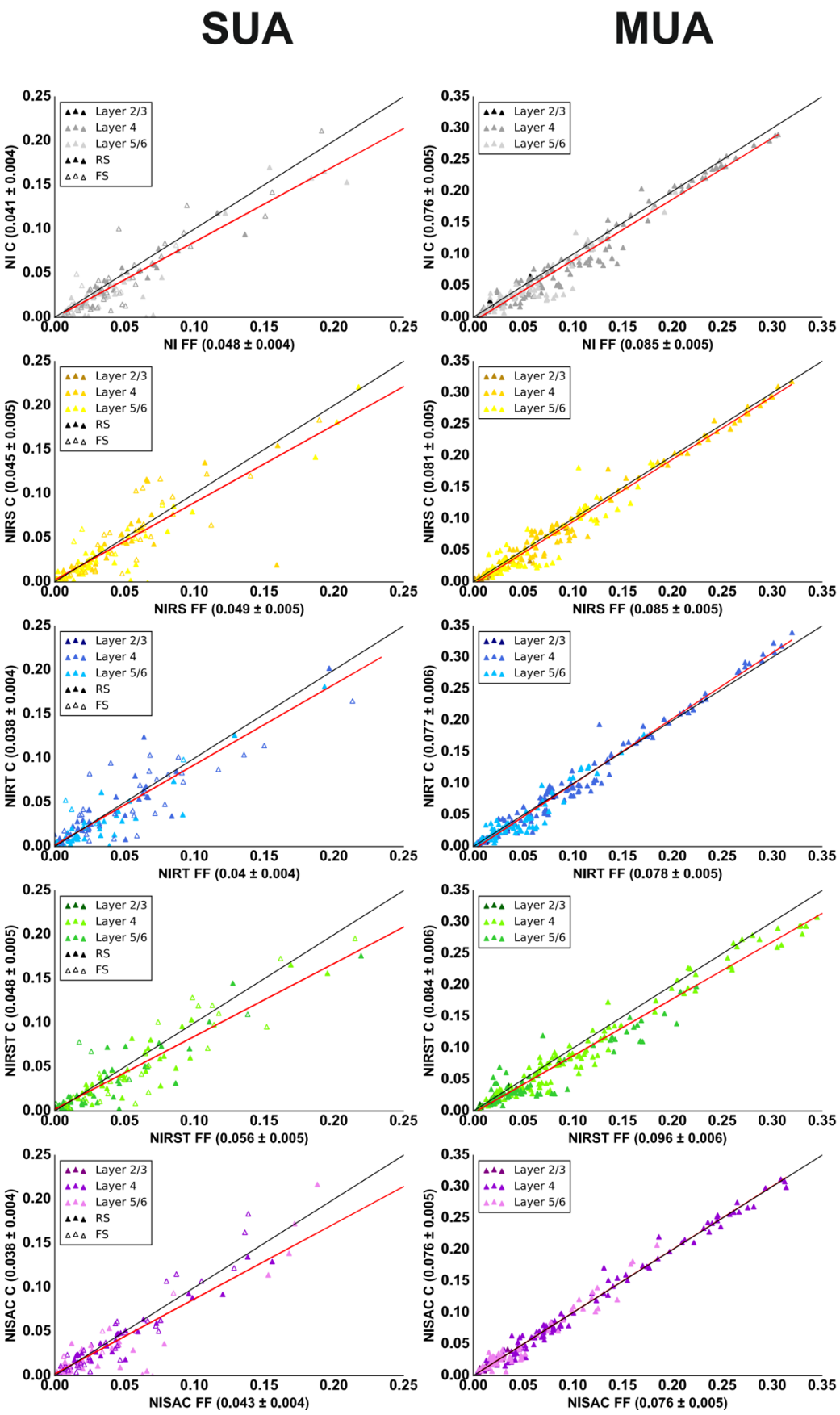

Figure 3.3.29: Full field vs center stimulation reliability evoked by the control stimuli. Left panel: Single unit activity firing rate. Right panel: Multi-unit activity firing rate. Red line: polynomial fit. Empty symbols = FS. Full Symbols = RS or MUA.

FULL FIELD	SUA			FS		
	DG	NI	DN	DG	NI	DN
Layer 2/3	0.001 ± 0.001	0.019 ± 0.005	0.011 ± 0.004	0.000 ± 0.001	0.032 ± 0.010	0.022 ± 0.008
Layer 4	0.022 ± 0.004	0.048 ± 0.005	0.038 ± 0.006	0.028 ± 0.006	0.057 ± 0.007	0.047 ± 0.008
Layer 5/6	0.014 ± 0.002	0.041 ± 0.005	0.019 ± 0.005	0.024 ± 0.010	0.051 ± 0.017	0.044 ± 0.025
Mean	0.017 ± 0.002	0.043 ± 0.003	0.028 ± 0.004	0.026 ± 0.005	0.055 ± 0.006	0.045 ± 0.008

CENTER	SUA			FS		
	DG	NI	DN	DG	NI	DN
Layer 2/3	0.003 ± 0.001	0.015 ± 0.004	0.008 ± 0.003	0.004 ± 0.001	0.029 ± 0.008	0.018 ± 0.007
Layer 4	0.025 ± 0.004	0.041 ± 0.004	0.033 ± 0.005	0.031 ± 0.007	0.047 ± 0.006	0.043 ± 0.008
Layer 5/6	0.014 ± 0.002	0.028 ± 0.004	0.017 ± 0.005	0.026 ± 0.010	0.043 ± 0.017	0.048 ± 0.025
Mean	0.019 ± 0.002	0.034 ± 0.003	0.025 ± 0.003	0.029 ± 0.005	0.054 ± 0.006	0.043 ± 0.008

FULL FIELD	MUA			RS		
	DG	NI	DN	DG	NI	DN
Layer 2/3	0.011 ± 0.002	0.063 ± 0.007	0.032 ± 0.005	0.001 ± 0.001	0.011 ± 0.002	0.006 ± 0.002
Layer 4	0.066 ± 0.004	0.113 ± 0.006	0.093 ± 0.006	0.015 ± 0.003	0.036 ± 0.004	0.028 ± 0.007
Layer 5/6	0.055 ± 0.004	0.093 ± 0.007	0.052 ± 0.004	0.012 ± 0.002	0.039 ± 0.005	0.013 ± 0.002
Mean	0.054 ± 0.003	0.099 ± 0.004	0.070 ± 0.003	0.012 ± 0.002	0.036 ± 0.003	0.018 ± 0.003

CENTER	MUA			RS		
	DG	NI	DN	DG	NI	DN
Layer 2/3	0.015 ± 0.002	0.050 ± 0.006	0.029 ± 0.004	0.002 ± 0.002	0.007 ± 0.001	0.003 ± 0.001
Layer 4	0.070 ± 0.003	0.096 ± 0.005	0.079 ± 0.005	0.018 ± 0.004	0.033 ± 0.005	0.021 ± 0.005
Layer 5/6	0.059 ± 0.006	0.074 ± 0.006	0.050 ± 0.004	0.012 ± 0.002	0.025 ± 0.004	0.010 ± 0.002
Mean	0.058 ± 0.003	0.082 ± 0.003	0.061 ± 0.003	0.013 ± 0.002	0.027 ± 0.003	0.014 ± 0.002

Table 3.3.16: Mean SUA (and its subpopulations) and MUA Reliability evoked by our set of stimuli presented full field and center (Mean ± SEM)

FULL FIELD					
	NI	NI-RS	NI-RT	NI-RST	NI-SAC
FS	0.056 ± 0.008	0.060 ± 0.010	0.052 ± 0.008	0.069 ± 0.011	0.048 ± 0.008
RS	0.044 ± 0.005	0.043 ± 0.005	0.034 ± 0.004	0.048 ± 0.006	0.040 ± 0.005
SUA	0.048 ± 0.004	0.049 ± 0.005	0.040 ± 0.004	0.056 ± 0.005	0.043 ± 0.004
MUA	0.085 ± 0.005	0.085 ± 0.005	0.078 ± 0.005	0.096 ± 0.006	0.076 ± 0.005

CENTER					
	NI	NI-RS	NI-RT	NI-RST	NI-SAC
FS	0.049 ± 0.007	0.059 ± 0.010	0.052 ± 0.008	0.062 ± 0.010	0.047 ± 0.008
RS	0.036 ± 0.005	0.037 ± 0.005	0.031 ± 0.004	0.040 ± 0.005	0.033 ± 0.005
SUA	0.041 ± 0.004	0.045 ± 0.005	0.038 ± 0.004	0.048 ± 0.005	0.038 ± 0.004
MUA	0.076 ± 0.005	0.081 ± 0.005	0.077 ± 0.006	0.084 ± 0.006	0.076 ± 0.005

Table 3.3.17: Mean SUA (and its subpopulations) and MUA Reliability evoked by our set of control stimuli presented full field and center (Mean ± SEM)

3.2.4 Reliability of the Local Field Potential

In the previous section, we showed that natural images evoke a more reliable response than the artificial stimuli at the local field potential level. In addition, we showed that the spiking activity is modulated by the center surround interactions. An intracellular study performed on the anesthetized and paralyzed cat showed that the reliability of the evoked membrane potential by natural images is modulated by center surround interactions (Haider et al., 2010). We observed that the LFP shows a similar, but not identical response, as the membrane potential. Based on these results we wondered if we would observe an increase in reliability for the LFP when natural scenes, but also artificial stimuli, are presented in the full field condition compared to the center condition. In addition, while spiking activity evoked no reliable response for the surround only stimulation, a lone stimulation of the surround can elicit a synaptic response. The surround only stimulation evoked a strong energy for the NI and GEM conditions. Thus, we wonder if this surround response is also reliable. Moreover, our previous results showed that the levels of reliability are layer dependent. We can wonder if this is the case for the center surround interactions. Figure 3.3.30 illustrates the trial-to-trial correlations (for one LFP site) evoked by our set of stimuli presented the full field, center and surround conditions. The reliability corresponds to the peak of the correlation at time 0. On this example, natural images evoke the highest correlations for all conditions. Interestingly, NI, evokes a higher reliability when presented in the surround condition than in the center.

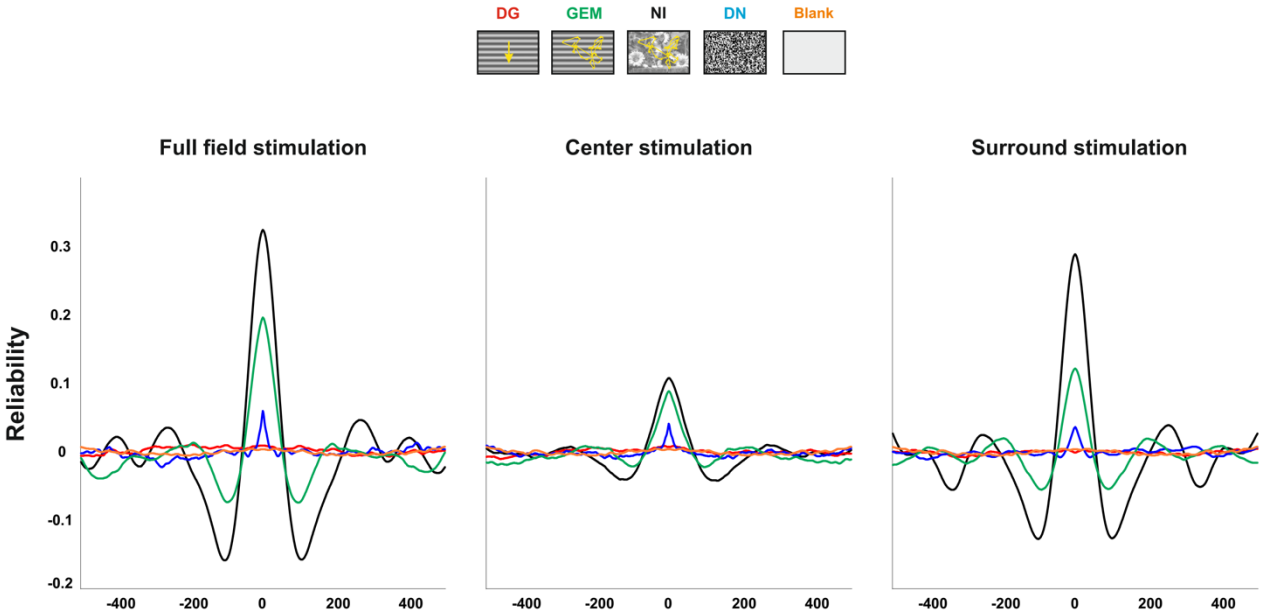

Figure 3.3.30: Example of LFP levels of reliability evoked in one recording site by our set of stimuli presented on the full field (left panel), center (middle panel) or surround (right panel) conditions.

- **Impact of the center surround interactions on the reliability**

Figure 3.3.31 compares the reliability evoked by the full field, center and surround conditions for each stimulus, respectively. Our results showed that both center and surround conditions evoked a similar pattern of reliability as the full field. when only the center was stimulated, natural images evoked the most reliable response ($p < 0.001$; Friedman test; Figure 3.3.31; table 3.3.18). Among the artificial stimuli, GEM evoked the most reliable response and DG the lowest one ($p < 0.001$). Compared to the full field stimulation, all stimuli evoked a lower reliability when presented in the center ($p < 0.001$; Wilcoxon test; Figure 3.3.31). This confirms the importance of the surround in the generation of a reliable response, in particular for natural images. We also investigated the impact of the lone stimulation of the surround. Indeed, since the LFP show a synchronized response when a surround stimulation is performed it might also impact the reliability. Our results show that for all stimuli the full field condition evoked a higher level of reliability than the surround condition ($p < 0.001$; Wilcoxon test). Interestingly, for natural images the difference between the full field and surround conditions is not as important as the one evoked by artificial stimuli (Figure 3.3.31; table 3.3.18). This confirms the key role of the surround in the processing of natural scenes, especially at a synaptic level. We also observed that the difference in reliability between NI and GEM was higher for the surround condition than for the center condition (table 3.3.18). Based on these results we wondered if the stimulation of the surround only will be higher than the center only. Natural images displayed higher levels of reliability for the surround condition compared to the center condition ($p < 0.001$). This was not the case for the artificial stimuli, arguing in favor to the fact that the processing of natural statistics is greatly mediated by the surround. It is important to note that we can exclude the fact that we are recording the LFP activity that has its receptive field on the surround. Indeed, one could legitimately ask itself: since the LFP captures the neuronal activity from 500µm to 1mm around the recording site (Einevoll *et al.*, 2013) are they not observing the response of cells that have their receptive fields in the surround? This is not the case. Indeed, our masks have a size of 5x5° (see section 3.1) and are centered on the receptive fields. The first pixel of the surround stimulation is located at 2.5° from the center. In addition, our recordings are always performed in the *area centralis* ± 2-4° with the screen placed at 57cm of the cat. Based on the retinotopic map made by Tusa et al. (1978) at this cortical location the magnification factor is such that one visual degree is equal to 1mm. Thus, the first pixels of our stimuli are located a 2.5°, *i.e.* it stimulates a cortical region 2,5mm apart from our recordings, and since the maximum reach of our LFP signal is 1mm we can exclude the fact that we are recording the activity from cells that have their receptive field on the surround.

- **Laminar impact of the center surround interactions**

We also computed the reliability evoked by the center condition across layers (Figure 3.3.31; table 3.3.18). Within all layers, natural images evoked the most reliable response ($p < 0.001$). In layer 2/3 NI and GEM evoked similar levels of reliability ($p = 0.8$). This suggests that horizontal connections are important in the generation of reliable response. The increased reliability that we observed for the full field condition at the population level is also present for each laminar compartment. Indeed, within all layers and for each stimulus, the full field condition evoked a more reliable response than the center condition ($p < 0.001$; Wilcoxon test).
We also investigated the laminar pattern of the surround only reliability. Indeed, since horizontal connections are present in layer 2/3 and 5/6 and that their effect is visible at the synaptic level (Bringuier et al., 1999) we wondered if all the layers would be impacted equally by surround

stimulation. For each layer, in response to natural scenes, the full field condition evoked a higher reliability than the surround condition (Figure 3.3.31; table 3.3.18; $p < 0.001$). When we compared the reliability evoked by the center and surround conditions, we observed that the surround condition evoked higher levels of reliability in layers 2/3 and 5/6 while no difference was observed in layer 4 ($p = 0.26$). This suggests that the increase in reliability observed for the surround condition is mediated by the horizontal connections present in these layers. In addition, the absence of difference in layer 4 underlies the importance of the surround in the processing of natural scenes. In summary, we showed that natural images reliability is increased by center surround modulations. In addition, the surround participates greatly at the natural scenes processing. This processing is mediated by horizontal connections in layers 2/3 and 5/6.

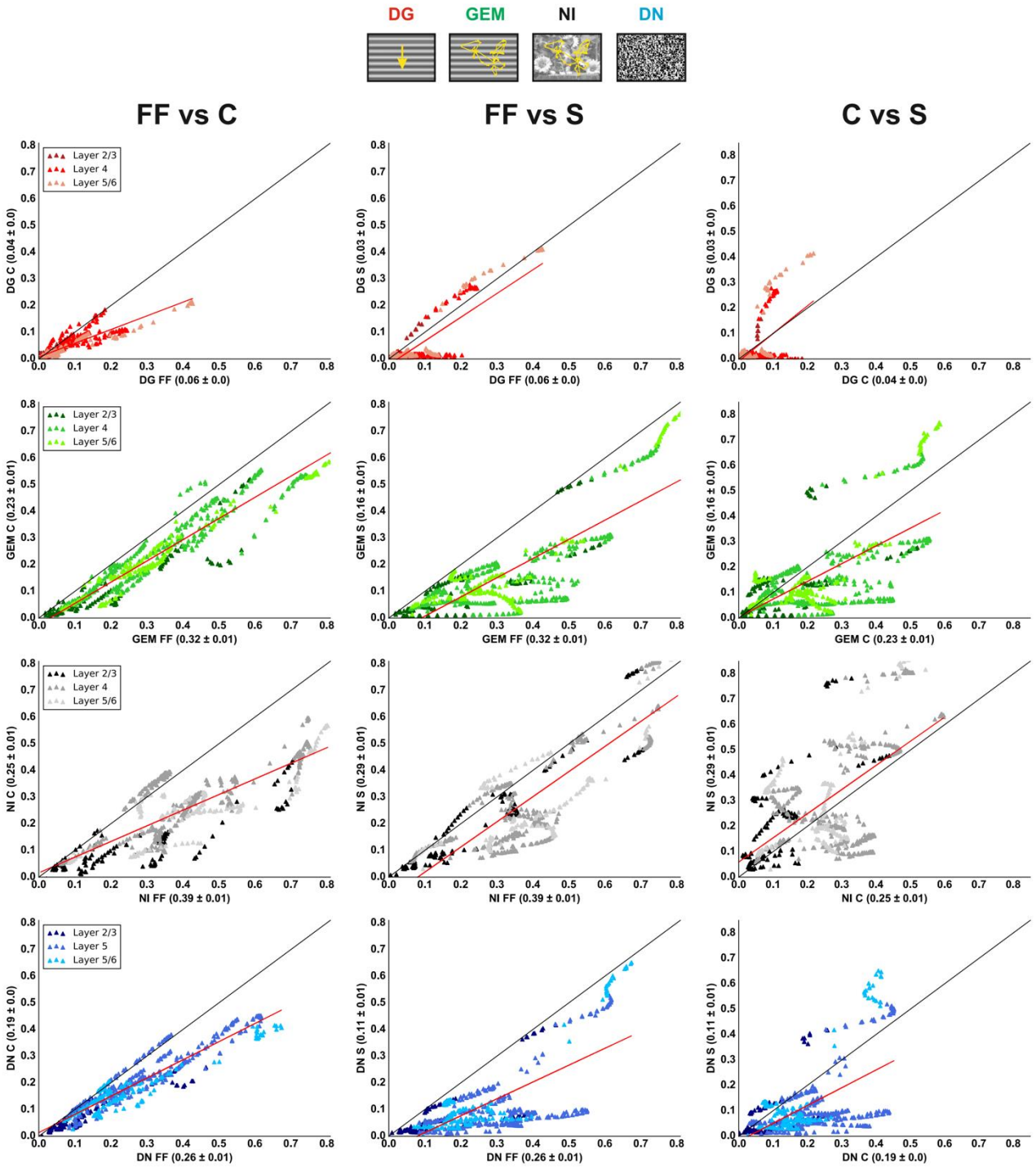

Figure 3.3.31: LFP reliability evoked by full field, center and surround stimulations. The center surround interactions increase the reliability in response to natural images. In addition, the surround only of NI evoke higher levels of reliability than the center, in layers 2/3 and 5/6. Left column: Full field vs center. Middle column: Full field vs surround. Right column: center versus surround. Red line: polynomial fit

- **Impact of the natural statistics on the center surround interactions**

Finally, we asked if the alteration of the spatial and temporal statistics would have an impact on the center surround interactions and on the response reliability. For the center condition all stimuli evoked the same levels of reliability (Figure 3.3.32; Table 3.3.19; $p > 0.05$; Mann Whitney U test). However, all stimuli evoked a higher reliability for the full field condition than the center ($p < 0.001$; Wilcoxon test). On the other hand, for the surround condition, the natural images containing altered temporal statistics (NI-RS and NI-RST) displayed a lower reliability than the unaltered natural image ($p < 0.001$; Friedman test). In addition, the natural image animated only with saccades evoked a less variable response than NI ($p < 0.001$). Finally, NI and NI-RS responses were equally reliable ($p = 0.9$). These results suggest that the surround mainly process the temporal statistics and that the high order correlations are necessary in order to elicit a reliable response. Moreover, the surround is also suited to the processing of fast movements, *i.e.* the saccades. The full field stimulation evoked a more reliable response than the surround one, as expected (Figure 3.3.32). However, unlike what we observed on a complete set of LFPs, for NI the center and surround conditions evoked the same levels of reliability ($p > 0.1$). This is probably caused by an increased number of LFPs recorded in layer 4 (55% of the sites were located in layer 4).
We did not observe any difference between the center and surround conditions for NI-RS while NI-RT and NI-RST evoked a higher reliability for the center condition ($p < 0.001$). This suggests that the center is also suited to process natural temporal statistics and altered spatial and temporal statistics while the surround cannot. NI-SAC evoked a higher reliability for the surround than the center condition, suggesting that the center is less suited to process fast movements ($p < 0.001$)
In summary we showed that surround is more sensitive the temporal statistics than the center that is suited to more efficiently process altered and unaltered statistics. Our results also showed that the center surround interactions do not have the same effect on the spiking activity and on the LFP. First, as observed for the full field stimulation the LFP is more reliable than the SUA and MUA for all stimuli. While on the SUA we observed a small (if no) impact of the center surround interactions the LFP was strongly modulated by the latter. In addition, the surround evoked almost no reliable spiking activity while a highly reliable LFP was observed. This suggest that the reliability observed for the LFP is mainly originating from the synaptic activity.

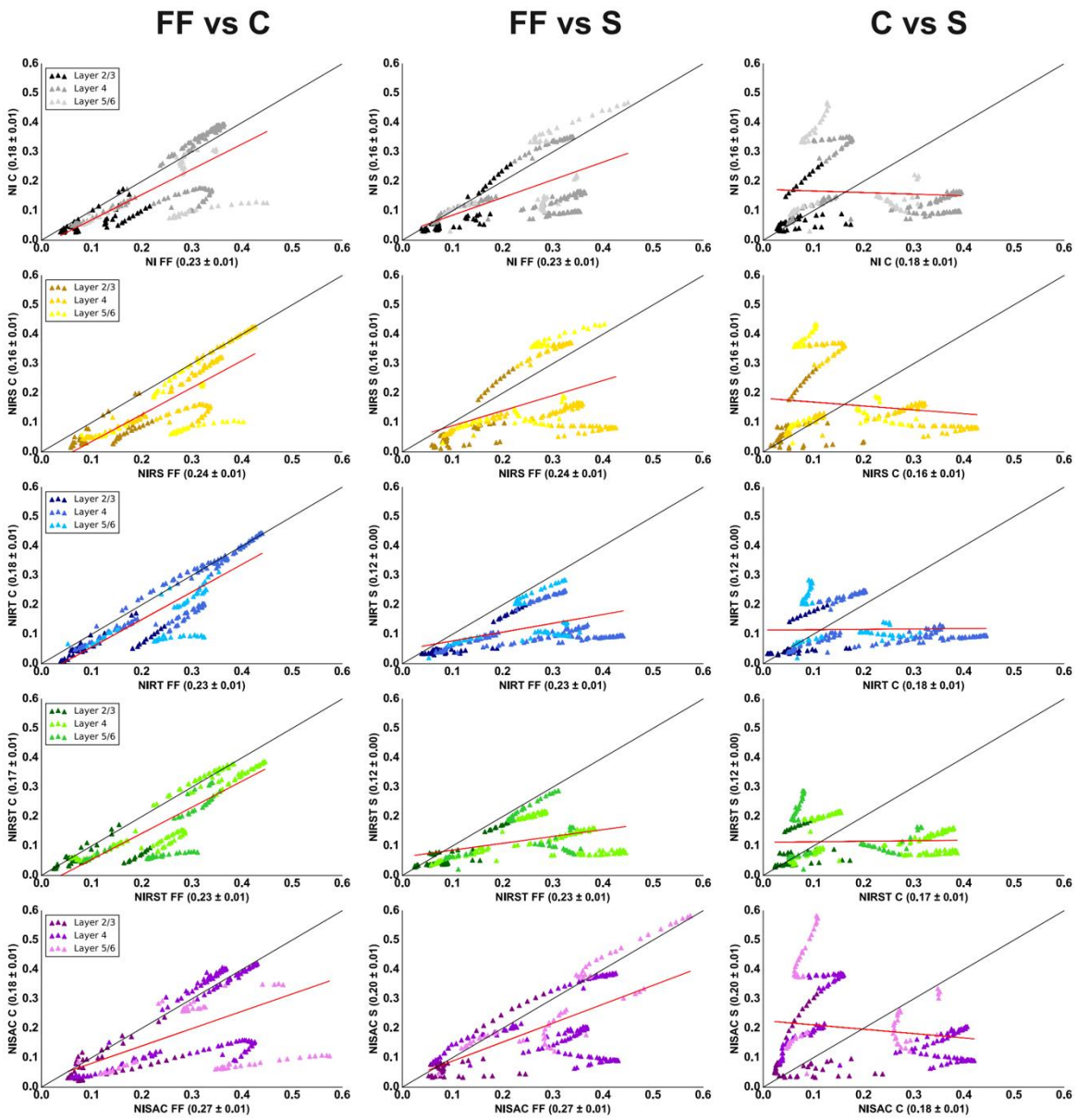

Figure 3.3.32: LFP reliability evoked by the control stimuli presented full field, center and surround. Left column: Full field vs center. Middle column: Full field vs surround. Right column: center versus surround. Red line: polynomial fit

FULL FIELD	LFP			
	DG	GEM	NI	DN
Layer 2/3	0.019 ± 0.002	0.195 ± 0.015	0.256 ± 0.019	0.129 ± 0.010
Layer 4	0.072 ± 0.003	0.358 ± 0.010	0.419 ± 0.010	0.310 ± 0.008
Layer 5/6	0.080 ± 0.007	0.331 ± 0.015	0.437 ± 0.015	0.252 ± 0.012
Mean	0.063 ± 0.003	0.317 ± 0.008	0.391 ± 0.008	0.257 ± 0.006

CENTER	LFP			
	DG	GEM	NI	DN
Layer 2/3	0.014 ± 0.002	0.112 ± 0.011	0.110 ± 0.010	0.086 ± 0.006
Layer 4	0.049 ± 0.002	0.274 ± 0.009	0.292 ± 0.007	0.237 ± 0.006
Layer 5/6	0.041 ± 0.004	0.225 ± 0.012	0.258 ± 0.010	0.173 ± 0.007
Mean	0.040 ± 0.002	0.227 ± 0.007	0.245 ± 0.006	0.188 ± 0.005

SURROUND	LFP			
	DG	GEM	NI	DN
Layer 2/3	0.015 ± 0.003	0.109 ± 0.011	0.211 ± 0.018	0.070 ± 0.008
Layer 4	0.031 ± 0.004	0.169 ± 0.009	0.306 ± 0.012	0.115 ± 0.007
Layer 5/6	0.057 ± 0.008	0.193 ± 0.016	0.329 ± 0.019	0.140 ± 0.014
Mean	0.035 ± 0.003	0.163 ± 0.007	0.293 ± 0.009	0.112 ± 0.006

Table 3.3.18: Mean LFP Reliability evoked by our set of stimuli presented full field, center and surround (Mean ± SEM)

	NI	NI-RS	NI-RT	NI-RST	NI-SAC
FULL FIELD	0.230 ± 0.007	0.241 ± 0.007	0.231 ± 0.007	0.228 ± 0.008	0.272 ± 0.009
CENTER	0.181 ± 0.008	0.164 ± 0.008	0.179 ± 0.008	0.168 ± 0.008	0.183 ± 0.009
SURROUND	0.163 ± 0.007	0.161 ± 0.008	0.117 ± 0.005	0.116 ± 0.004	0.200 ± 0.009

Table 3.3.18: Mean LFP Reliability evoked by our set of control stimuli presented full field, center and surround (Mean ± SEM)

4. TIME FREQUENCY ANALYSIS OF THE VISUAL RESPONSE

In their intracellular study, Baudot and colleagues (2013) quantified the reproducibility of the response by performing a time-frequency wavelet analysis of Vm responses. This analysis was performed because their reliability analysis depended on the timescale of the analyzed response. By computing this analysis, they were able to unveil some results that were not visible with the non-frequency dependent analysis. Therefore, we decided to perform the same analysis in our spiking and LFP recordings. In order to compute this analysis (method illustrated in figure 3.4.1), each of the individual trial-responses to a given stimulus was filtered by an array of complex Gabor wavelets whose temporal frequencies ranged from 1 to 150 Hz (It is important to note that in the Intracellular paper, Baudot and colleagues only computed the analysis from frequencies ranging from 1 to 75Hz) Then, a set of ten complex numbers (one for each trial of the same stimulus) was computed for each frequency band and point in time. The mean (the Signal) and standard deviation (the Noise) in the complex plane were used to build SNR matrices. The SNR measure captures transient and reproducible fluctuations that appear as “hot peaks” in the corresponding SNR matrix (Figures 3.4.1 and 3.4.4). This decomposition allows the extraction of several time-frequency dependent measures: Signal power, Noise power, and SNR power and the inforate of the signal, noise and SNR, as illustrated in Figure 3.4.2. The inforate is obtained by integrating the values over the frequencies (figure 3.4.2) while the power spectrum is obtained by integrating it over time.
We first investigated the frequency-based response evoked by the full field activity on both spiking activities and local field potential.

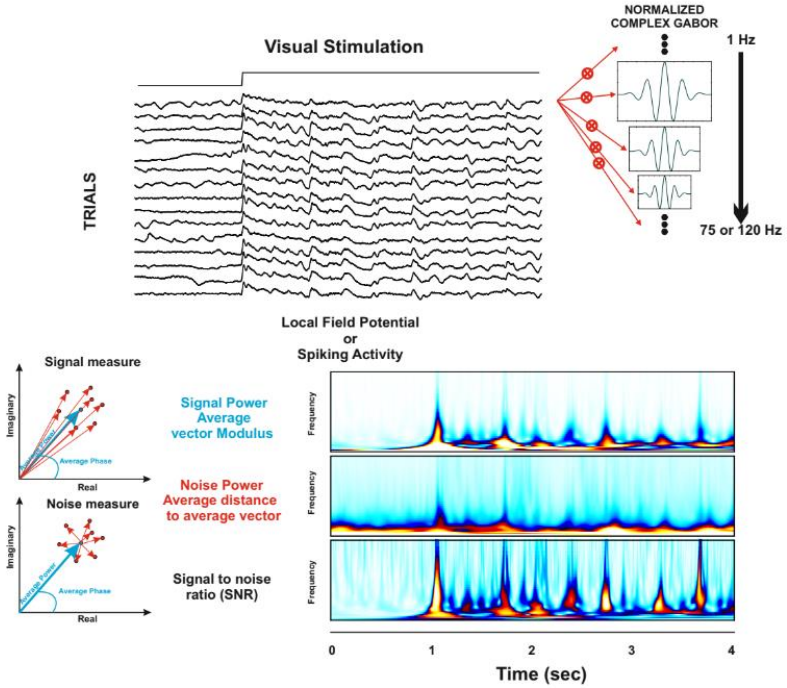

Figure 3.4.1. Time Frequency analysis of the reliability. Time-frequency analysis of the evoked Signal (upper matrix), the Noise (middle), and the SNR (bottom matrix), following the method of Croner et al. (1993). The repetition of the vectorial operations (detailed in the right panels) at all times and frequencies yields the Signal and Noise matrices. The SNR matrix is obtained from point-by-point division of the Signal matrix by the Noise matrix. Reliable events are signaled by hot (red) peaks straddling from low to high frequencies (1–150 Hz). Upper left panel: each red vector represents the result (in the complex plane) of the convolution of the signal with a given wavelet frequency for one particular point in time and a given trial. The blue vector represents the mean vector, averaged across all trials, and its squared modulus gives the estimated Signal power. Lower left panel: Noise is measured in the complex plane as the average distance (dispersion) of the individual trial vectors (blue vectors) from the mean (red).

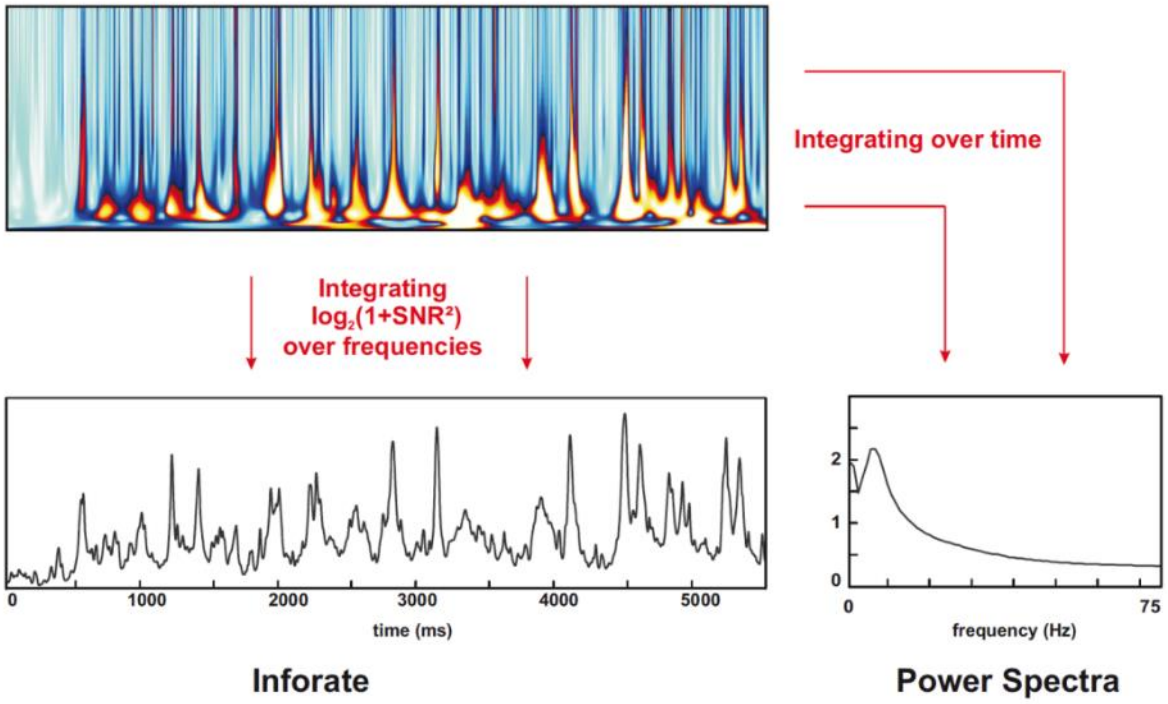

Figure 3.4.2. Obtaining of the SNR power spectra and inforate. Integration of the values over time or over frequencies in order to obtain the power spectra and the Inforate of the signal to noise ratio.

4.1. Impact of the Full Field Stimulation

4.1.1 Time Frequency Analysis of the Spiking Activity

In their study, Baudot and colleagues showed that the SNR displayed the same response pattern for the Vm and the spiking activity (Figure 3.4.3). In their results we can observe that the higher reliability evoked by natural images results from a lower signal but also a lower noise than animated gratings. In addition, they show that DG do elicit a reliable response but at the grating frequency.

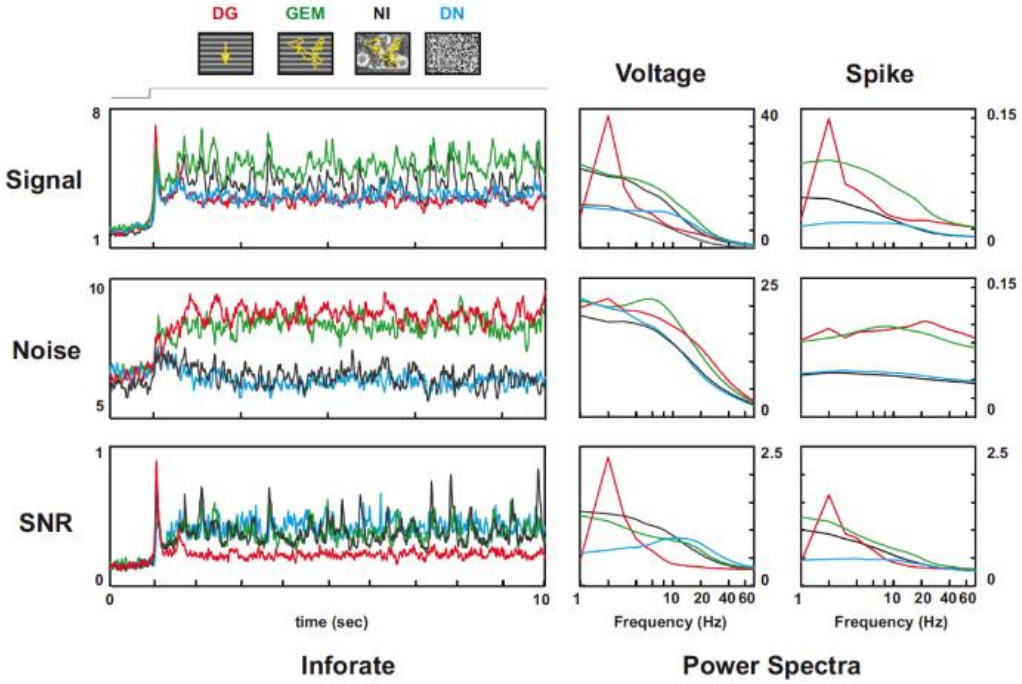

Figure 3.4.3: Mean SNR obtained intracellularly by Baudot and colleagues for both spiking activity and membrane potential (n =20). The inforate was computed from the voltage analysis.

We first wondered if we would observe the same responses in a large population of neurons. Unlike Baudot and colleagues we subtracted the Signal, Noise and SNR of the spontaneous activity to the mean response. Indeed, since we recorded the spontaneous activity, we were able to subtract the mean spontaneous activity from the mean stimulus locked response. Figure 3.4.4 shows two matrices, their corresponding spectra and the response of the neuron used as example. The DG and the NI result in very different SNR patterns. Drifting gratings elicited a “hot peak” at the grating frequency while NI elicited a hot peak across different frequencies (Figure 3.4.4). We then computed the SNR across the complete single unit and multi-unit population.

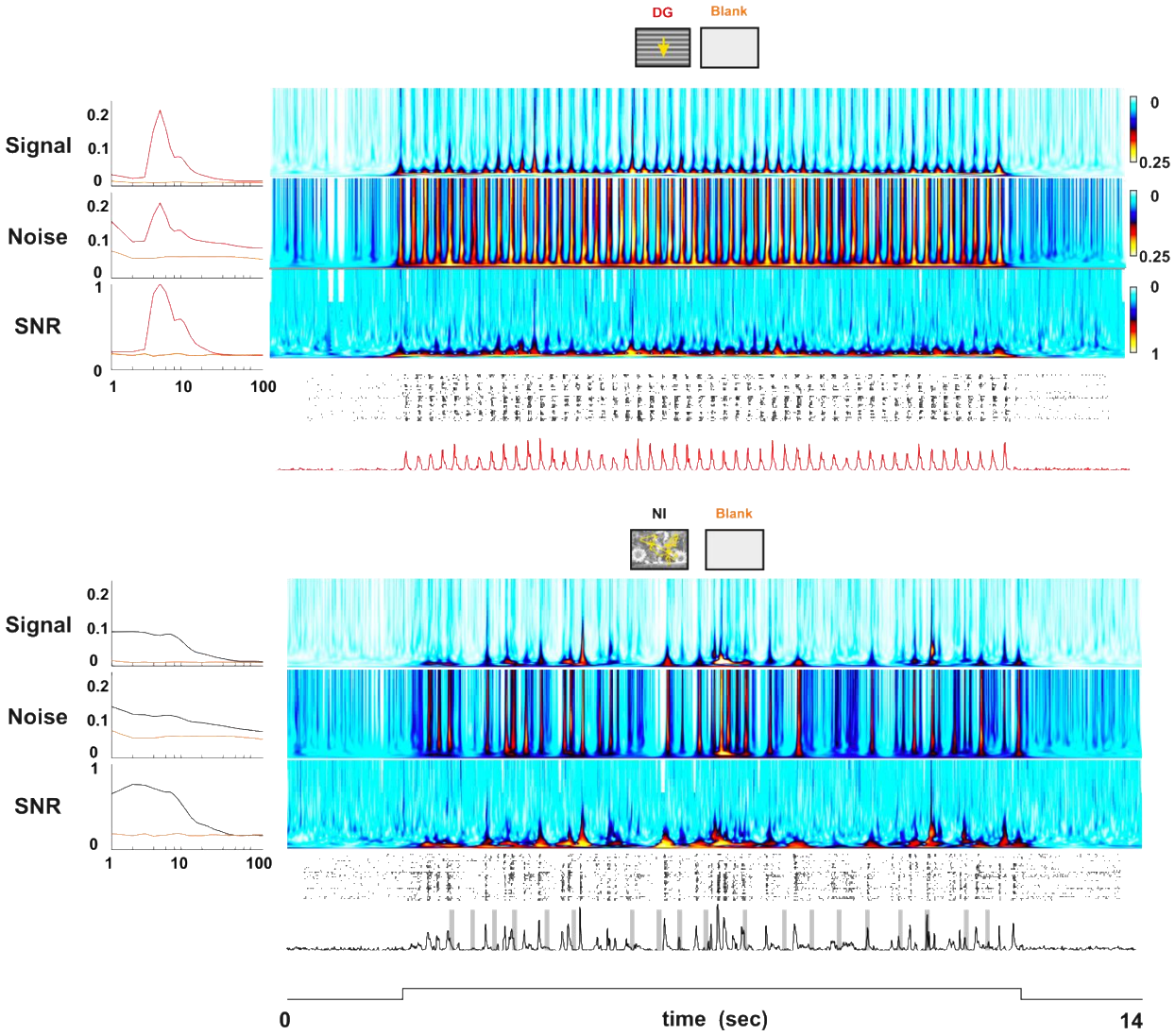

Figure 3.4.4: Example of signal, noise and SNR matrices and PSD evoked by NI, DG and for the spontaneous activity.

- **Comparison with the intracellular recordings**

As stated above, we focused on the SNR response after blank subtraction. Figure 3.4.5 shows an example of the mean Signal, Noise and SNR after and before subtraction of the blank (we only showed the mean MUA response because the SUA displayed the same response pattern).
We first computed the SNR of the population with GEM. As performed in Baudot's work, we divided the frequency into two main groups. The first one contains all the frequencies between 0.01 and 10 Hz, which correspond to Delta, Theta and Alpha rhythms. This frequency band will be referred as "**low frequency band**". The second one contains all the frequencies between 10.01 and 40 Hz *i.e.* Mu and Beta rhythms and will be referred as "**high frequency band**". Finally, we can also evoke a third band that will not be described in this section (but will be used in others), the "very high frequency band" that regroups the frequencies between 40.01 and 120 Hz (*i.e.* low and high gamma; Galambos, 1992; Rougeul-Buser and Buser, 1997; Steriade et al., 1993). We plotted the means signal/noise/SNR for these two frequencies band (Figure 3.4.6-A and B left panel). The Multi-unit activity displayed a noise, a signal and a SNR about two to three times higher than the ones computed for the SUA (table 3.4.1), yet for both SUA and MUA we found similar responses' patterns to our stimulus set.
Indeed, for both signals we observed that natural images evoked the highest signal in the low frequency band ($p < 0.01$; Friedman test; table 3.4.1). However, the difference in signal between the NI and GEM conditions was higher for the MUA. Indeed, for the MUA the mean signal of the NI condition was about two times higher than the GEM condition (table 3.4.1). We also observed a clear signal peak evoked by DG at the grating frequency. For the SUA, this peak was the maximum signal value obtained among all conditions (Figure 3.4.6-A). This maximal peak evoked by DG was also present in the noise, for both single and multi-unit activities. For both signals, drifting gratings evoked the highest noise values while dense noise the lowest ones (at all frequency bands). For the SUA no difference in noise was observed between the NI and GEM conditions ($p > 0.05$; Friedman test). However, for the MUA natural images evoked a higher noise than gratings animated with eye movements.
This led to a higher SNR, in the low frequency bands, for the NI condition compared to the other ones ($p < 0.001$; Friedman test). This was true for the two spiking signals (Figure 3.4.6). These results differ from the intracellular observations made by Baudot and colleagues (2013). Indeed, they also observed a higher reproducibility in response to NI. However, this increase was linked to a lower noise and not a higher signal. These results highlight a strong difference between the spiking activity observed intracellularly and the spiking activity recorded extracellularly. This difference could come from the difference in anesthetics between the two studies. Indeed, it has been shown that anesthesia affects the variability of the response thus two different anesthetics could affect the noise differently (Ecker et al; 2014).
Interestingly, the response to DN is more reliable than the other stimuli in the high frequency band. This is caused by the fact that dense noise evokes a higher signal than the other stimuli ($p < 0.01$; Friedman test). Finally, unlike what was observed for our other reliability indexes, when we computed the SNR of the spiking activity, NI evoke a more reliable response than GEM in the low frequency band, while no difference was observed for higher frequencies. We can conclude that our previous measurements are biased by the timescale of the response (*i.e.* the bin of the PSTH). The higher reliability observed for the multi-unit activity is in agreement with the population coding theory (Deneve & Chalk, 2016; Yuste, 2015). This theory states that the coding of the stimulus is performed at the population level (*i.e.* a group of neurons) and not at the single unit level. This aspect will be combined with our previous results and discussed at the end of this manuscript.

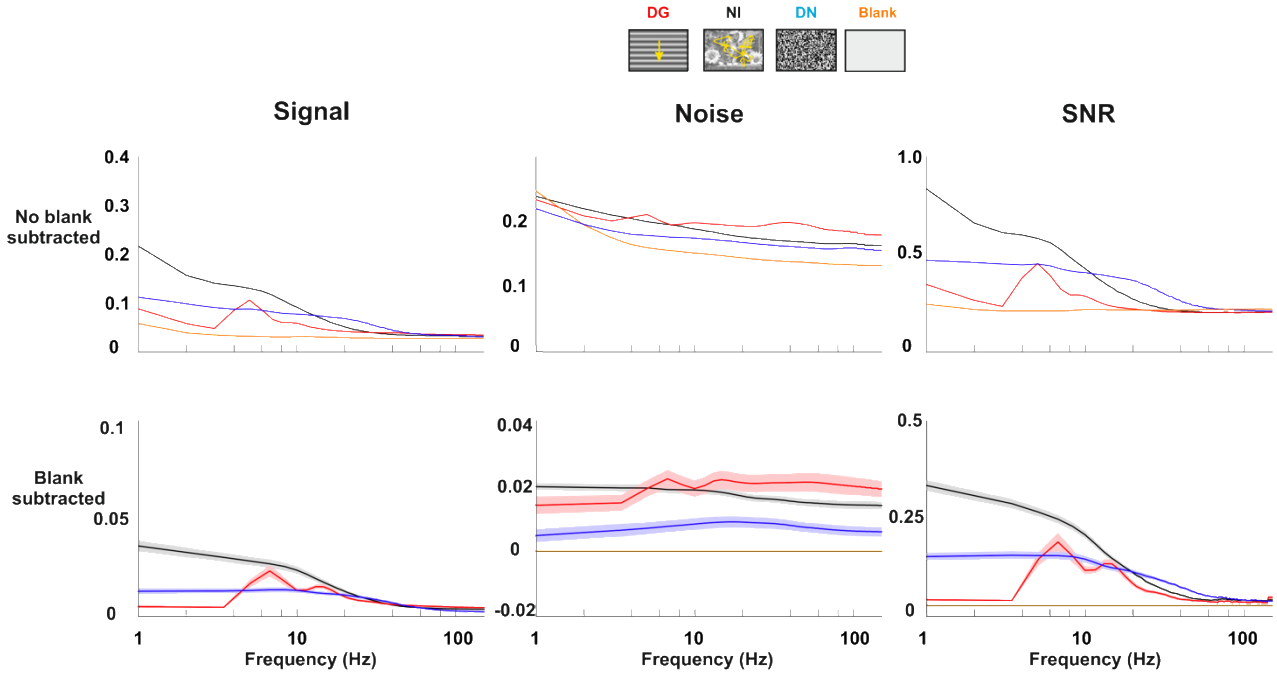

Figure 3.4.5: Signal, noise and SNR with or without blank subtraction

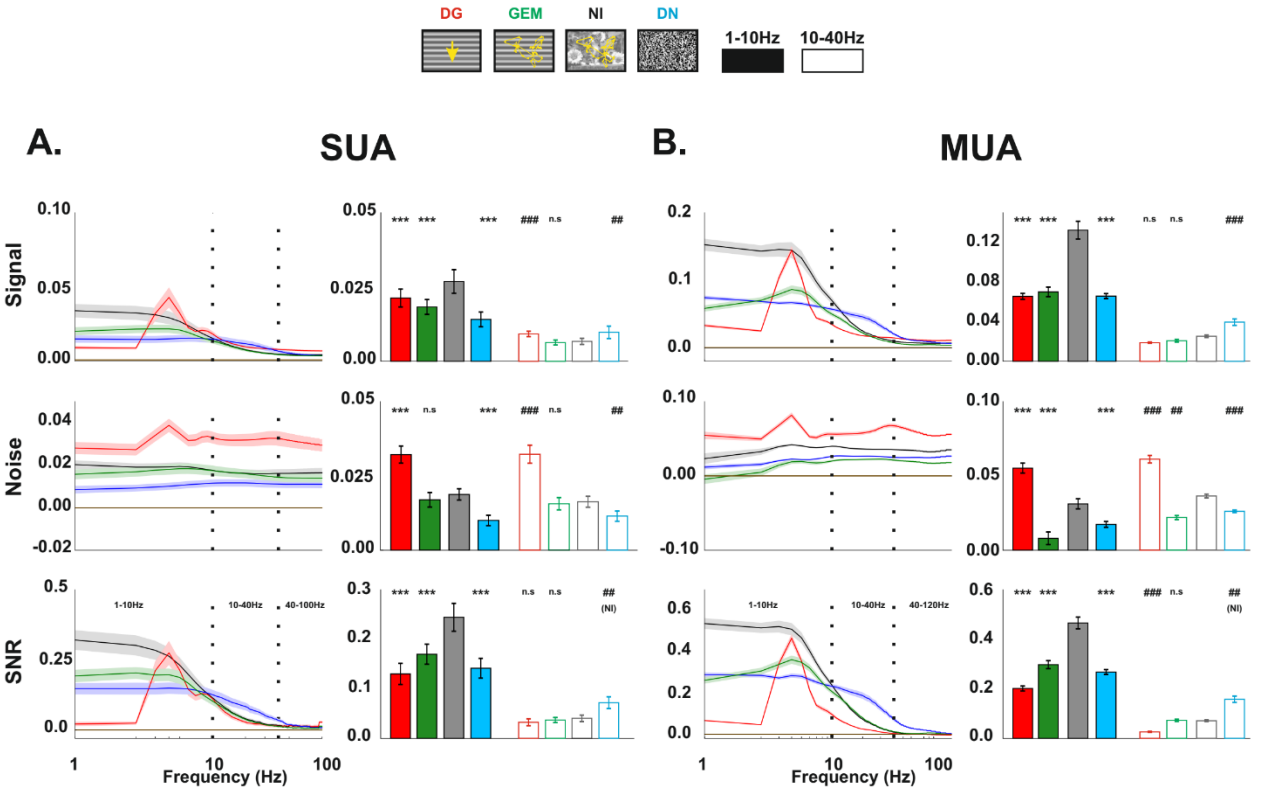

Figure 3.4.6: Signal, Noise and SNR of the single and multi-unit activities in response to our set of stimuli. Natural images evoke a reliable response in the low frequency range. **A. Left:** Mean signal (left), noise (center) and SNR (right) obtained for the single unit activity (n =78). **Right:** Bar plots of the low and high frequency means signal (left panel), noise (center) and SNR (right) obtained for the single unit activity in response to our set of stimuli. **B. Left:** Mean signal (left), noise (center) and SNR (right) obtained for the multi-unit activity (n =177 sites). **Right:** Bar plots of the low and high frequency means signal (left panel), noise (center) and SNR (right) obtained for the multi-unit activity in response to our set of stimuli. *: significantly different from NI low frequency;
: significantly different from NI high frequency. * : $p < 0.05$; ** $p < 0.01$; *** : $p < 0.001$; # : $p < 0.05$; ## $p < 0.01$; ### : $p < 0.001$. Error bars & shaded area: SEM.

- **Mean evoked SNR**

The previous results have been computed on a restricted population (78 cells and 138 multi-unit sites) that displays a strong response to our stimulus set (see previous sections). Will we observe the same SNR across the complete population (221 cells and 377 multi-unit sites)?
We computed the signal to noise ratio on both single unit and multi-unit activities (Figure 3.4.7 to 3.4.10). For both SUA and MUA, the mean signal, noise and SNR computed on the population without GEM were similar to the one computed on the population with GEM.
In the previous sections, we reported that these two single unit subtypes exhibited different properties, in particular fast spiking neurons evoked a higher firing rate and a more reliable response than regular spiking neurons. Since we showed that the SNR and our other analysis give similar but yet different results, will we observe a difference among the FS and RS cells? We did observe a difference between these two subtypes. Indeed, the fast spiking cells exhibited a higher signal, noise and SNR than the regular spiking cells ($p > 0.01$; Mann Whitney U test; Figures 3.4.11 to 3.4.14; table 3.4.2). Both subtypes displayed the same pattern of response as the complete SUA population.

- **Laminar Signal to Noise ratio**

Do we obtain the same patterns across layers? Indeed, as shown previously and by others (Bijanzadeh et al., 2018; Hansen et al., 2012) layers possess a unique signature at the spiking level. This left us wondering if we would observe a different SNR pattern across layers. The signal to noise ratio across all layers was computed for both spiking activities. We first focused on the signal across layers. As observed previously, the MUA's signal was about 2 to 3 times higher than the one obtained with the SUA. For both signals, within all layers, natural images evoked the strongest signal in the low frequency range ($p < 0.001$; Friedman test; table 4.3.1). However, the difference between the low frequency signal elicited by NI and the other stimuli was higher for the MUA than the SUA (almost 2.5 times higher for the MUA vs 1.5 times for the SUA). Remarkably, DG evoked a very low signal in layer 2/3. This is linked to the adaptation that we observed in the PSTH and the increased number of complex cells in this layer (figure 3.2.9). This strong adaptation of the signal is confirmed by the inforate, which evaluates the information sent by the response (Figures 3.4.15 and 3.4.16). The inforate will be discussed in detail later in this section. In layers 4 and 5/6 the strong peak at the grating frequency is still present (Figures 3.4.7 and 3.4.8). This peak originates from a higher number of simple cells in these two layers and corresponds to the modulation of these cells at the grating frequency. Between layers, at both SUA and MUA scales respectively, natural images evoked the same mean low frequency signal in granular and infragranular layers ($p > 0.35$), higher than the one observed in layer 2/3 ($p < 0.001$). This absence of difference between layers 4 and 5/6 was also observed for the DG and DN conditions (figures 3.4.7 to 3.4.10; table 3.4.1). These results are in line with the ones observed for the mean population.
We can wonder if the noise will also exhibit a similar pattern. Regarding the SUA, as observed for the mean noise, in layers 4 and 5/6 we did not observe any difference in the low frequency noise evoked by DG and NI while dense noise condition evoked the lower noise ($p < 0.001$). On the other hand, layer 2/3 exhibited a different behavior. Within this layer, DG evoked the lowest noise while NI and DN conditions were equal ($p > 0.05$). The laminar MUA also displayed a different pattern than the mean one (Figures 3.4.9 and 3.4.10). Indeed, in layers 4 and 5/6, drifting gratings and natural images evoked the same low frequency noise. Only layer 2/3 displayed the same pattern as the mean population. However, unlike the other stimuli, the noise evoked by DG in layer 2/3 is below the one evoked by the spontaneous activity. Again, it is important to keep in mind that, for both SUA and

MUA, the differences in noise evoked by the stimuli are very low, in particular in layers 4 and 5/6 (figures 3.4.7 to 3.4.10; table 3.4.1). When we compared noise values evoked by a stimulus across layers, we observed that for the SUA, natural images and dense noise evoked the same noise values between all layers. However, DG evoked its lowest noise in layer 2/3, while layers 4 and 5/6 did not exhibit any difference (table 3.4.1). On the other hand, the MUA responded in a very different way. Layers 4 and 5/6 evoked similar values in response to NI. Despite the absence of significance, the natural stimulation evoked the higher mean low frequency noise in layer 4 and the lowest in layer 5/6. This was also (significantly) true for DG and DN ($p < 0.01$; Friedman test).

These results allow us to refine the statements previously made about the SNR. As observed for the mean populations, at all spiking levels, natural images evoked the most reliable low frequency response within all layers and drifting gratings the lowest one ($p < 0.001$; table 3.4.1). On one hand, at both SUA and MUA levels, NI images evoked similar levels of reliability in layers 4 and 5/6. This is not surprising since the values of signal and noise were equal between these layers, leading to an equivalent ratio. On the other hand, we observed that both DG and DN evoked their highest levels of reliability (in the low frequency range) in layer 4 (table 3.4.1). The fact that neurons in layer 4 show higher levels of reliability in response to gratings has already been observed in awake monkeys. Indeed, Hansen et al. (2012) showed that the variability of the response to gratings is lower in layer 4 compared to the other layers. However, no study tested the laminar dependency of the reliability in response to natural scenes. We can imagine that neurons in layer 5/6 are recruited in a better way by natural statistics than by artificial ones, leading to this increase in reliability.

Regarding regular and fast spiking cells, we observed the same response pattern as for the SUA population and FS cells evoked a higher SNR than RS cells (Figures 3.4.11 to 3.4.14; table 4.3.2).

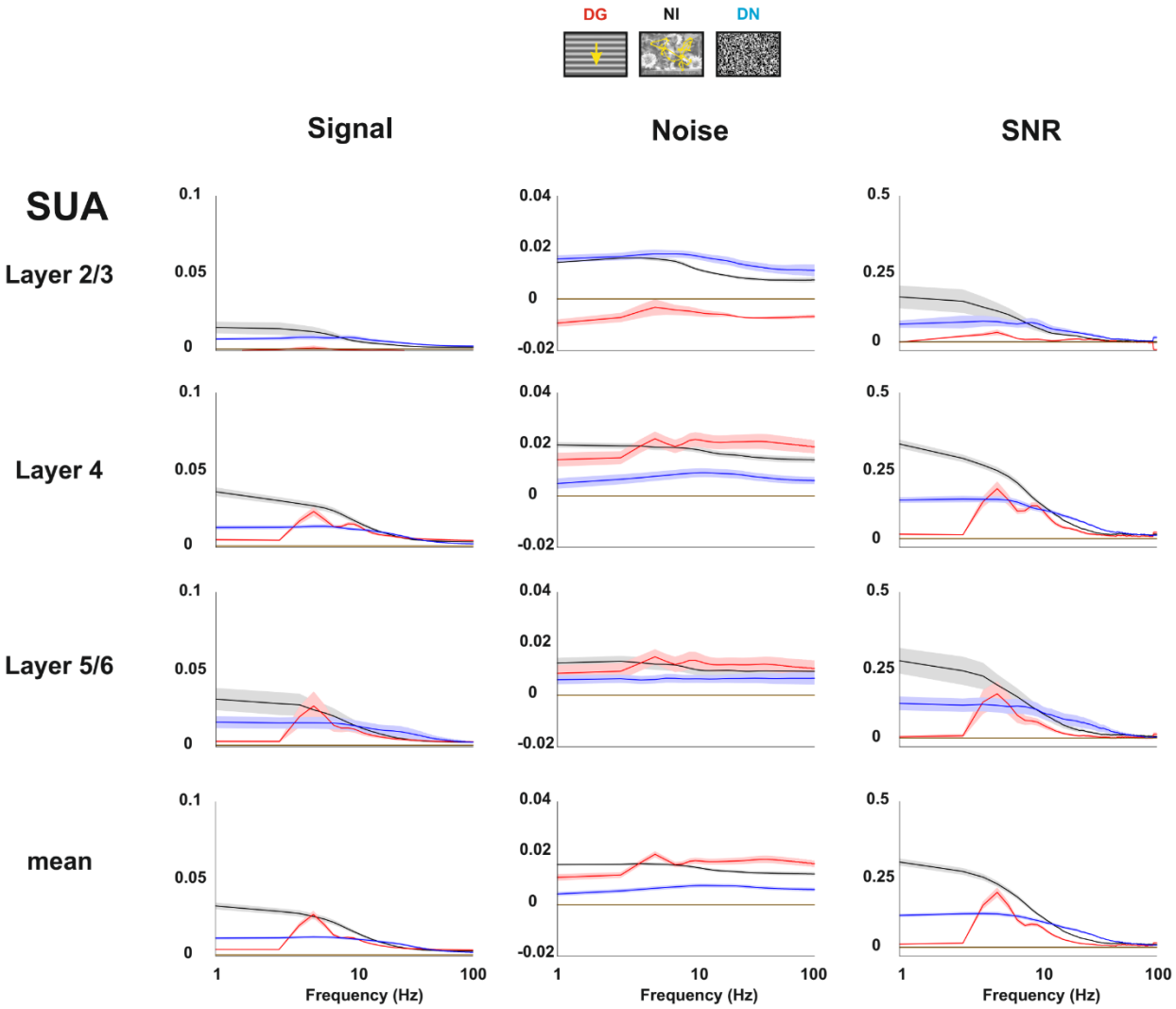

Figure 3.4.7: Mean and laminar SNR of the single unit activity. Natural images evoke a reliable response in the low frequency range. Mean signal (left), noise (center) and SNR (right) obtained for the single unit activity in response to our set of stimuli. (Number of neurons: L2/3 = 10; L4 = 111; L5/6 = 99 neurons; total= 221) Shaded area: SEM

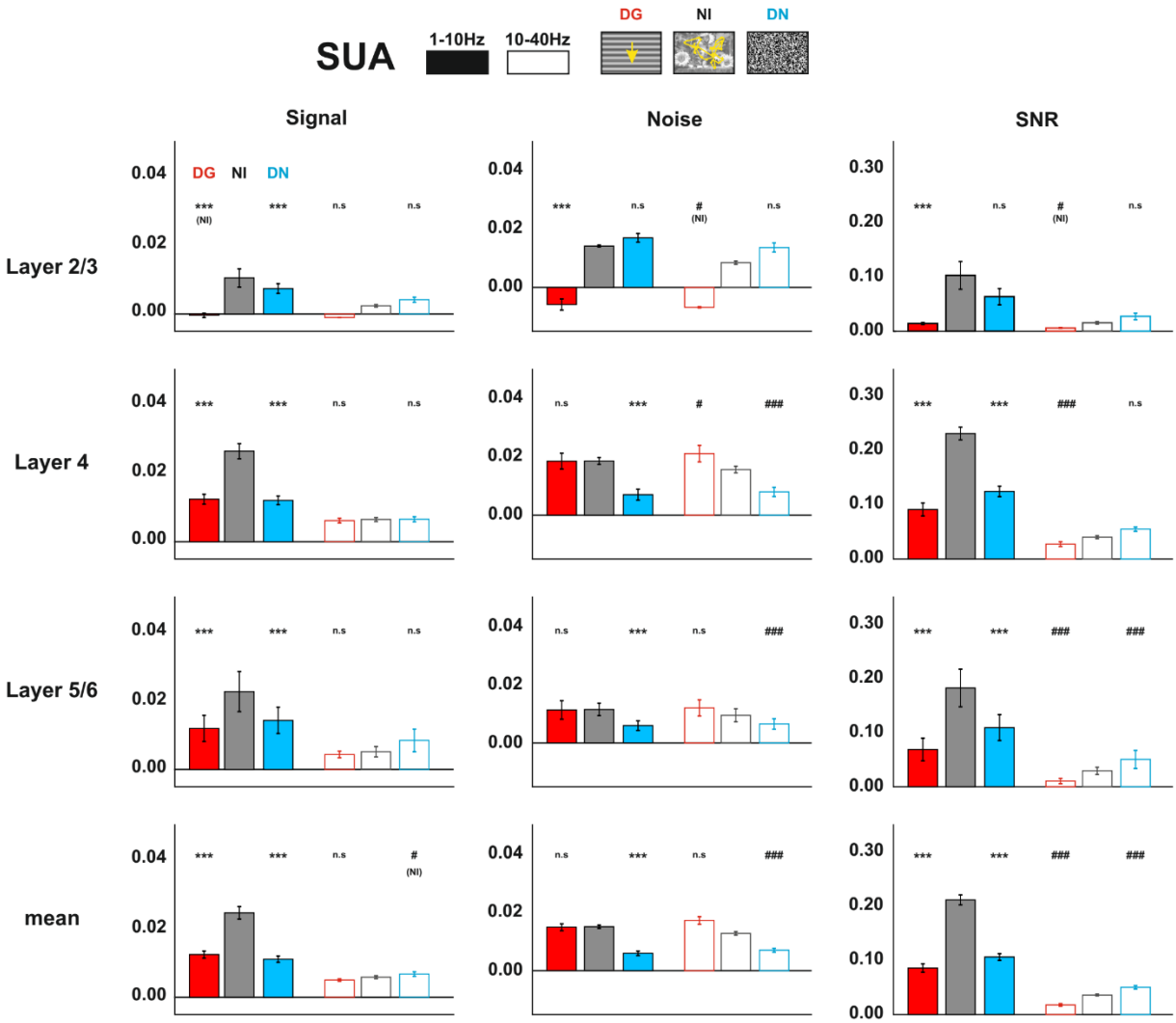

Figure 3.4.8: Bar plots of the low and high frequency single unit SNR. Signal (left panel), noise (center) and SNR (right) obtained for the single unit activity in response to our set of stimuli. (Number of neurons: L2/3 = 10; L4 = 111; L5/6 = 99 neurons; total= 221). *: significantly different from NI low frequency; # significantly different from NI high frequency. * : $p < 0.05$; ** : $p < 0.01$; *** : $p < 0.001$; # : $p < 0.05$; ## : $p < 0.01$; ### : $p < 0.001$. Error bars : SEM.

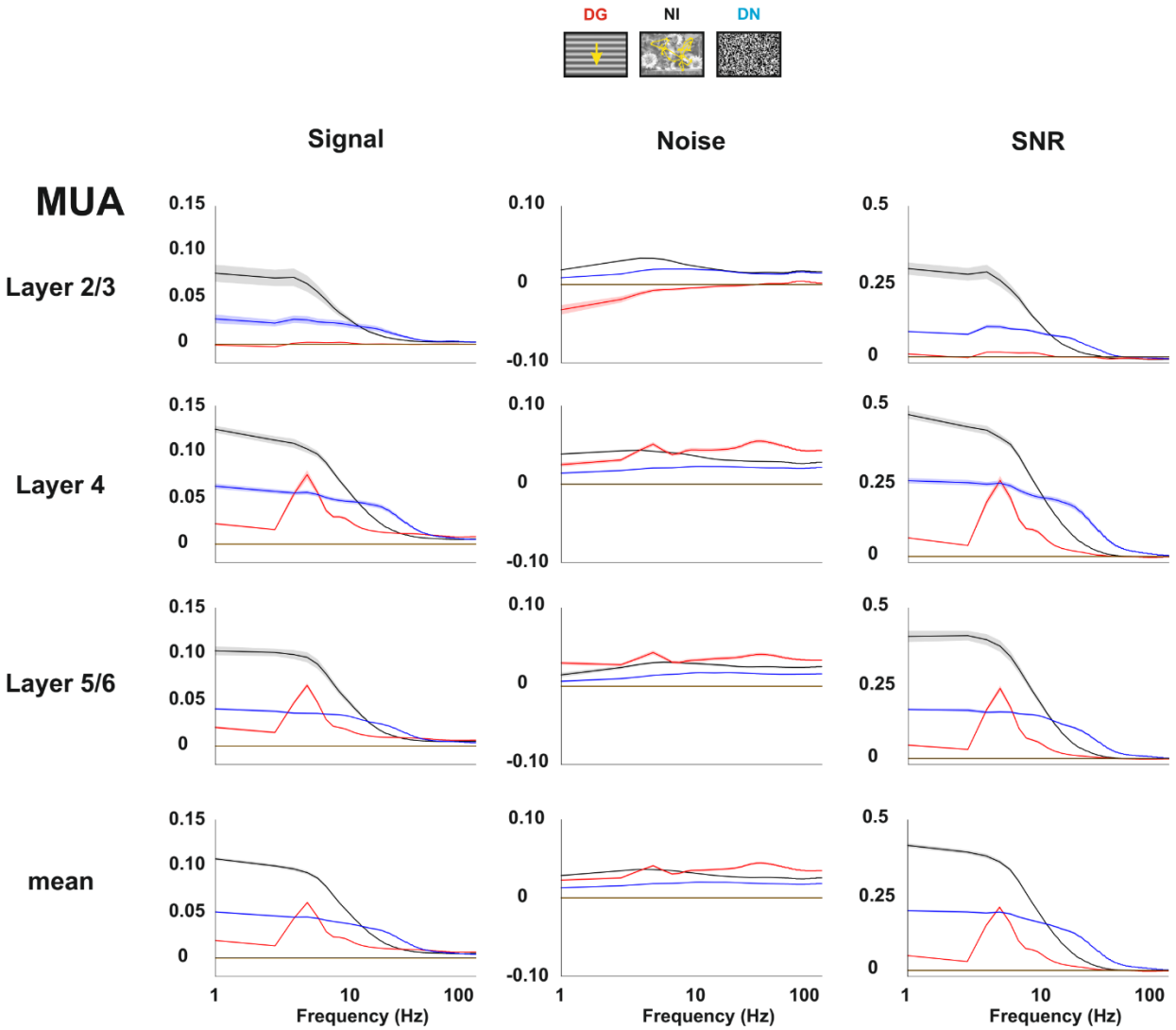

Figure 3.4.9: Mean and laminar SNR of the multi-unit activity. Mean signal (left), noise (center) and SNR (right) obtained for the multi-unit activity in response to our set of stimuli. (Number of sites: L2/3 = 52; L4 = 187; L5/6 = 138 sites; total= 378). Shaded area: SEM

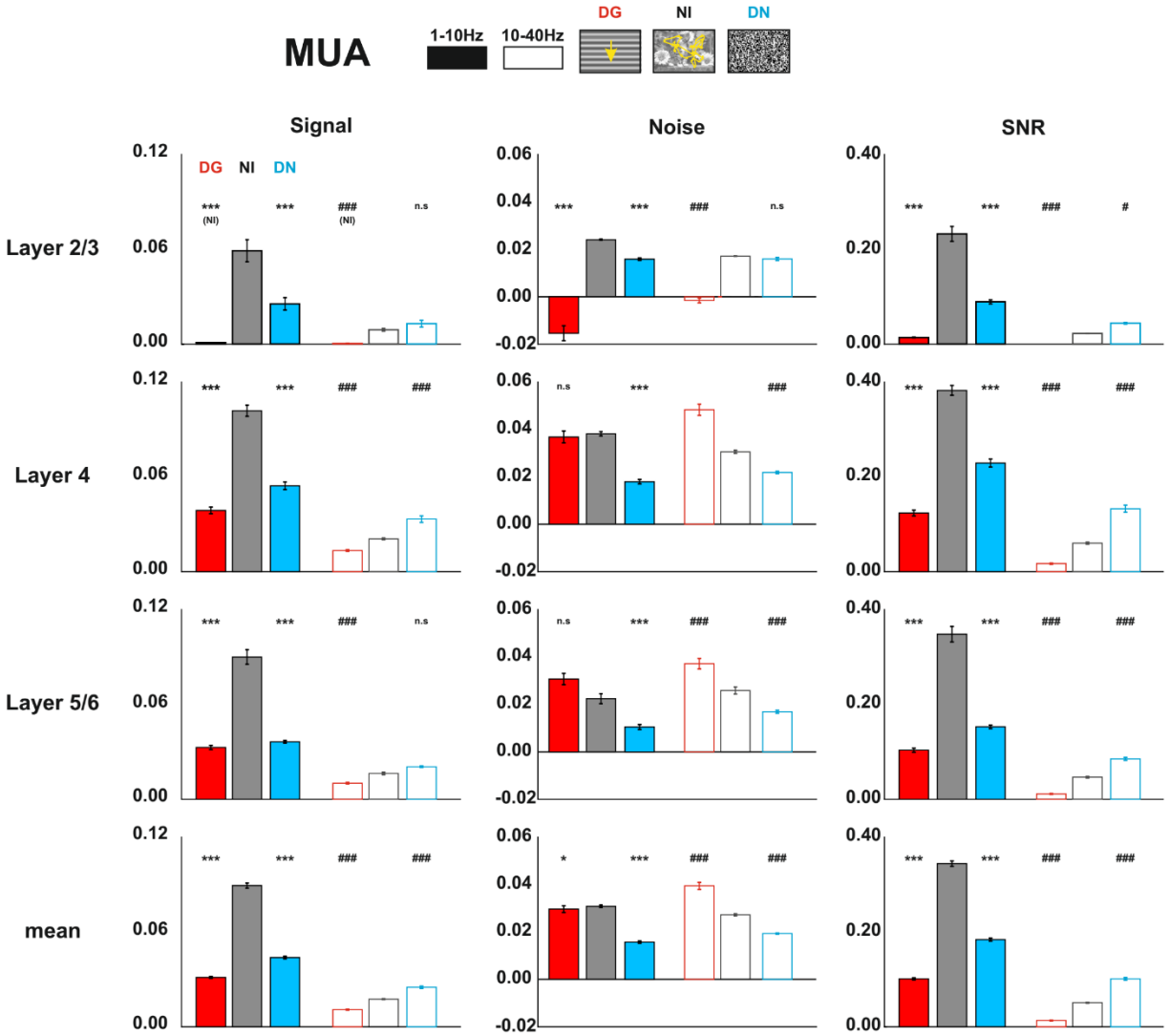

Figure 3.4.10 Bar plots of the low and high frequency multi-unit SNR. Signal (left panel), noise (center) and SNR (right) obtained for the multi-unit activity in response to our set of stimuli. (Number of neurons: L2/3 = 10; L4 = 111; L5/6 = 99 neurons; total= 221). *: significantly different from NI low frequency; # significantly different from NI high frequency. * : $p < 0.05$; ** : $p < 0.01$; *** : $p < 0.001$; # : $p < 0.05$; ## : $p < 0.01$; ### : $p < 0.001$. Error bars: SEM.

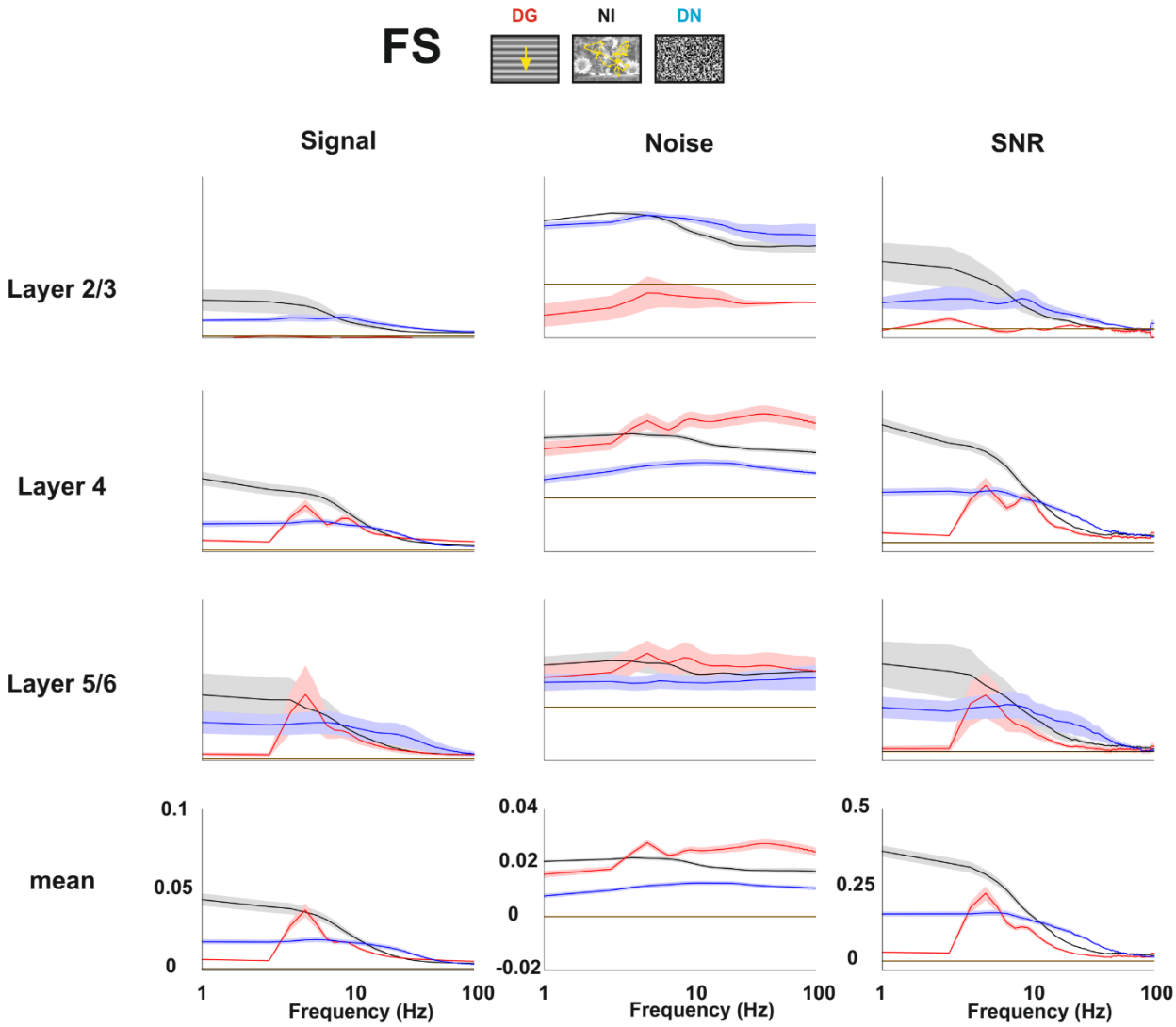

Figure 3.4.11: Mean and laminar SNR of the fast spiking neurons. Mean signal (left), noise (center) and SNR (right) obtained for the fast spiking neurons in response to our set of stimuli. (Number of neurons: L2/3 = 4; L4 = 61; L5/6 = 18 neurons; total= 83) Shaded area: SEM

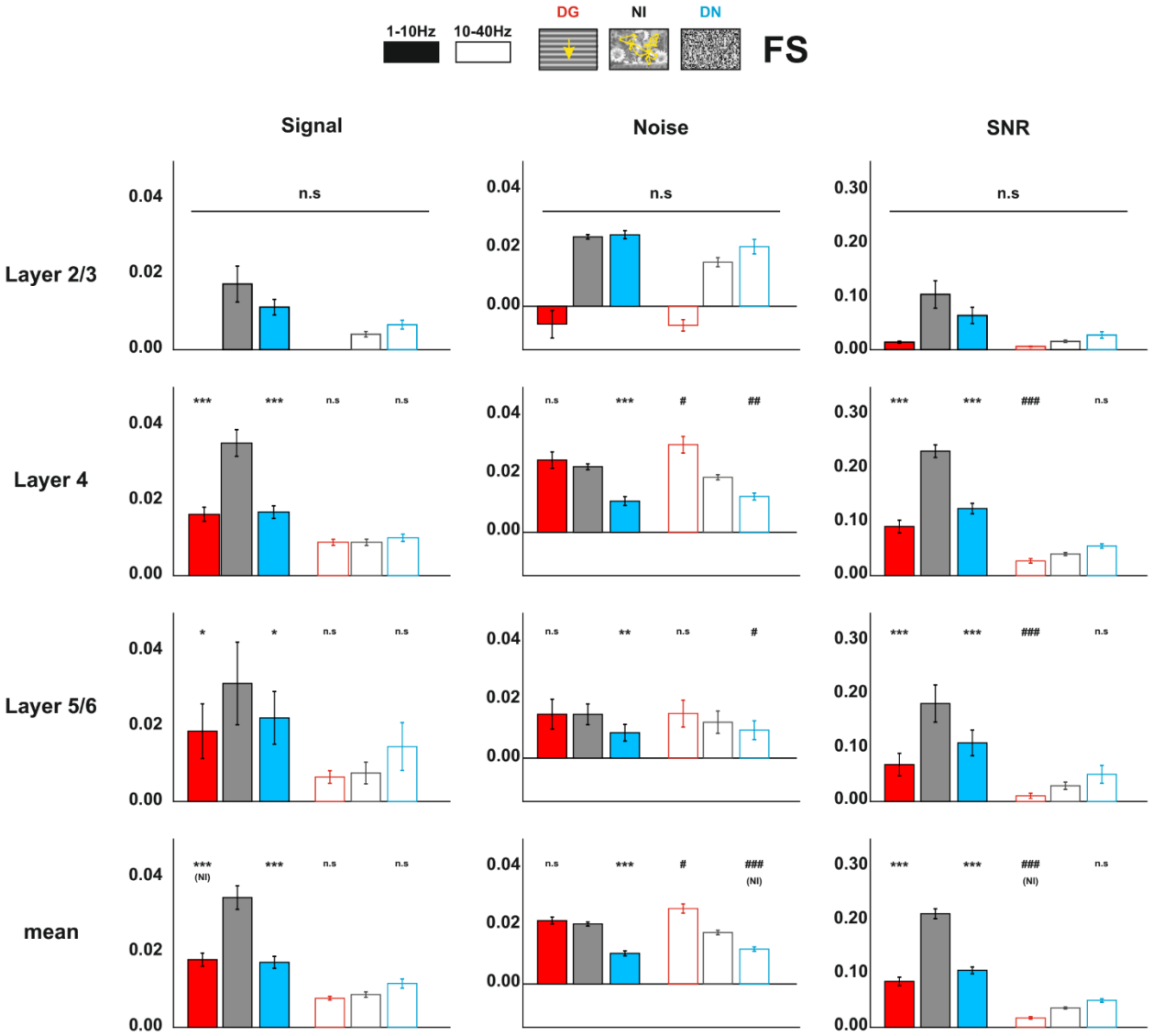

Figure 3.4.12: Bar plots of the low and high frequency fast spiking neurons SNR. Signal (left panel), noise (center) and SNR (right) obtained for the multi unit activity in response to our set of stimuli. (Number of neurons: L2/3 = 4; L4 = 61; L5/6 = 18 neurons; total= 83). *: significantly different from NI low frequency; # significantly different from NI high frequency. * : $p < 0.05$; ** : $p < 0.01$; *** : $p < 0.001$; # : $p < 0.05$; ## : $p < 0.01$; ### : $p < 0.001$. Error bars : SEM.

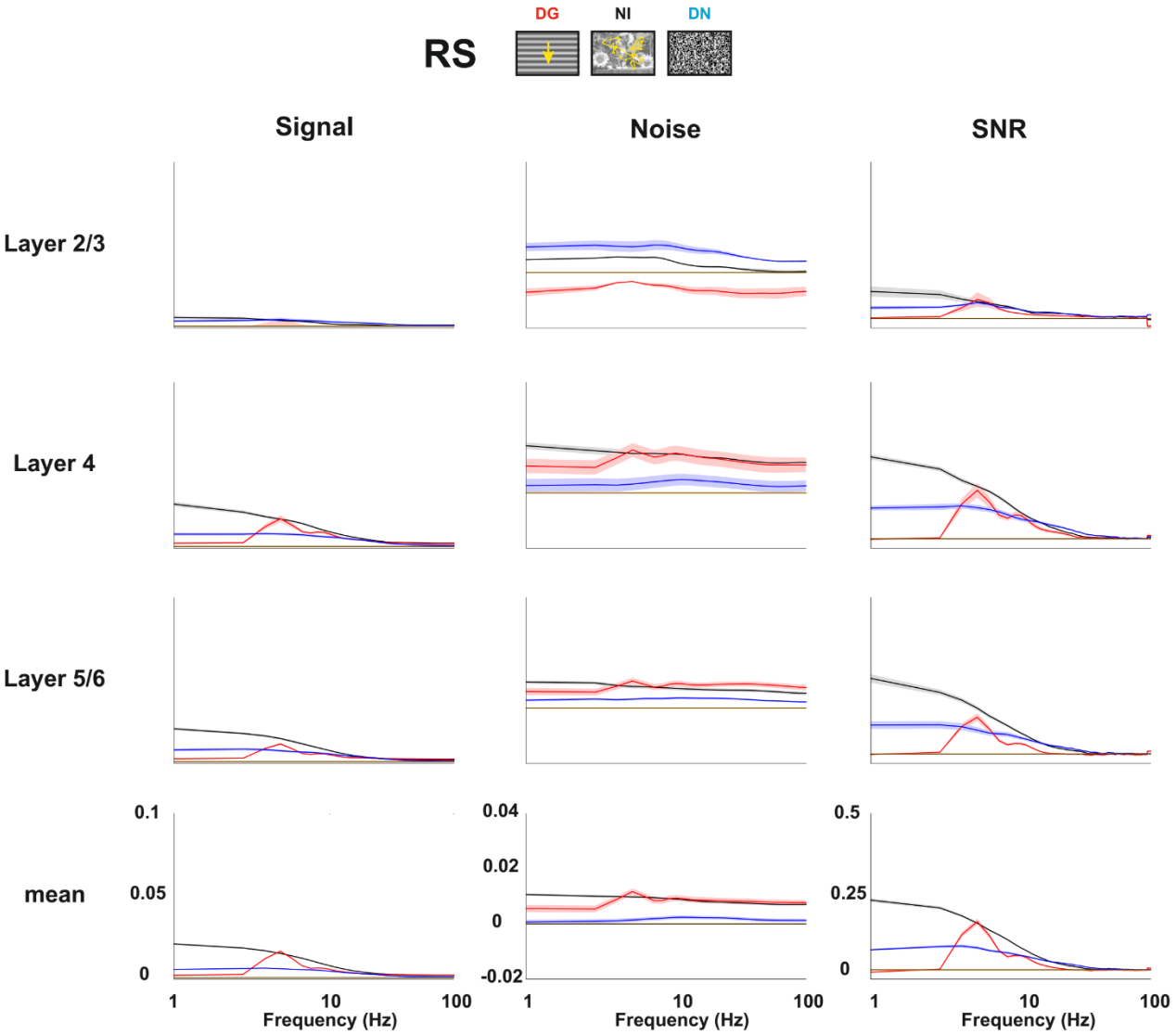

Figure 3.4.13: Mean and laminar SNR of the regular spiking neurons. Mean signal (left), noise (center) and SNR (right) obtained for the regular spiking neurons in response to our set of stimuli. (Number of neurons: L2/3 = 10; L4 = 111; L5/6 = 99 neurons; total= 138) Shaded area: SEM

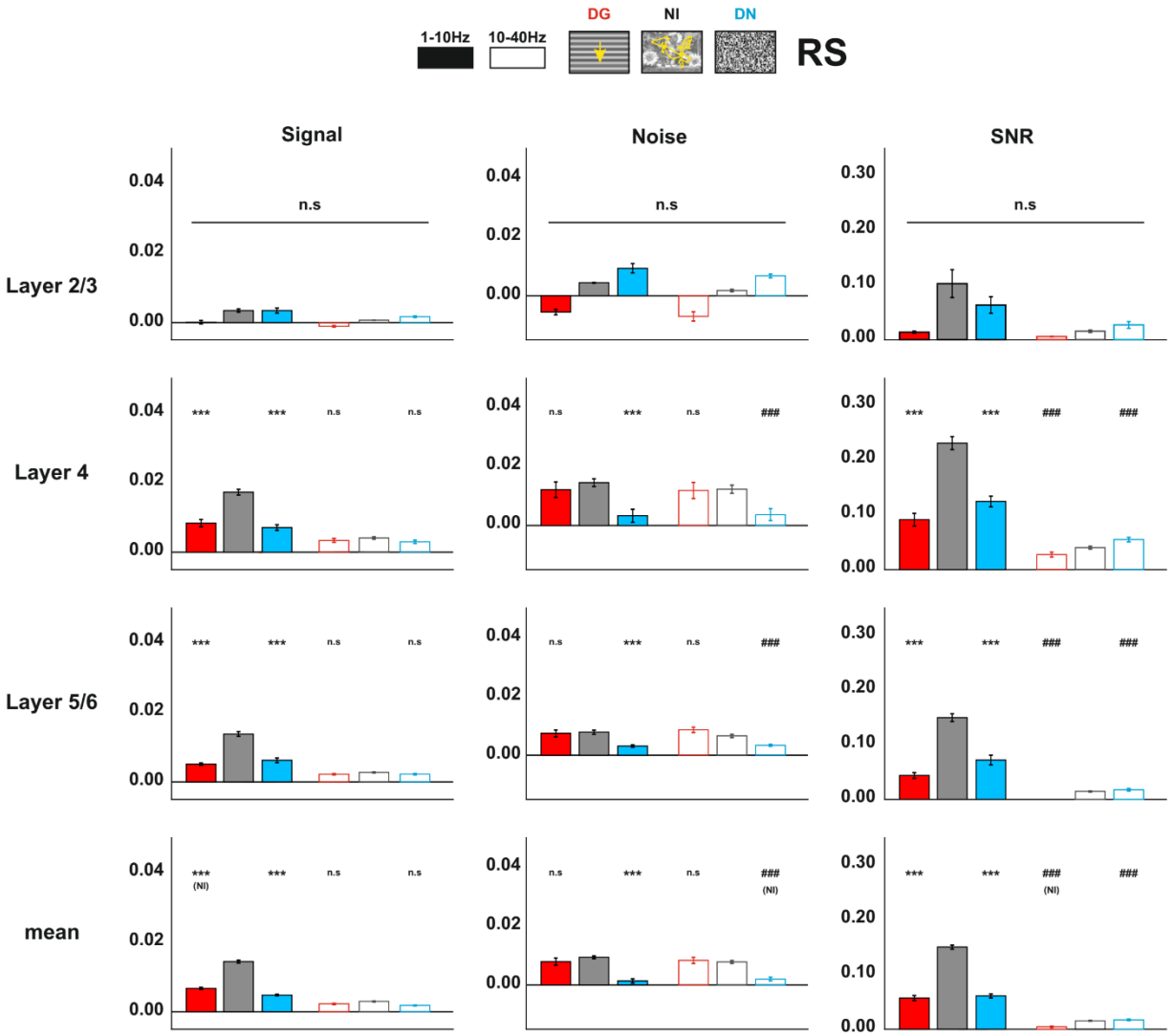

Figure 3.4.14: Bar plots of the low and high frequency regular spiking neurons SNR. Signal (left panel), noise (center) and SNR (right) obtained for the regular spiking neurons in response to our set of stimuli. (Number of neurons: L2/3 = 10; L4 = 111; L5/6 = 99 neurons; total= 138). *: significantly different from NI low frequency; # significantly different from NI high frequency. * : $p < 0.05$; ** : $p < 0.01$; *** : $p < 0.001$; # : $p < 0.05$; ## : $p < 0.01$; ### : $p < 0.001$. Error bars : SEM.

- **Information rate**

The principle of efficient coding introduced by Horace Barlow in 1961 suggests that visual processing in early sensory systems should be optimized to natural-like statistics. This will result, among others, in a decrease in stimulus-locked response variability at the single neuron level and an increase in the information carried by a single neuron. According to our results, the first statement appears to be true, but is it the case for the information carried by the neurons? In order to test this, we computed the information rate (inforate) carried by the spiking activity on the signal, noise and signal to noise ratio (Figures 3.4.15, 3.4.16 and table 3.4.3). As observed for the signal, the MUA exhibit a higher info rate than the SUA. In addition, our results show that for both SUA and MUA the mean information rate carried by the signal is similar between all stimuli. This is also true within all layers. Moreover, the different stimuli did not elicit a significant difference between layers 4 and 5/6. Regarding the noise inforate, the pattern of response was similar was the one observed for the signal, except for DG that evoked a higher noise (table 3.4.3). This led to a similar SNR inforate elicited by NI and DN, higher than the one evoked by DG. Our results contradict Barlow's theory regarding the amount of transmitted information. Yet, since the SNR is frequency dependent the inforate analysis should also be computed across our two main frequency ranges. Indeed, we observed that the DN condition is more reliable than the NI condition in the high frequencies while the opposite is true for low frequencies. Therefore, these two stimuli carry the information in two different frequency bands. In the future, a decomposition of the inforate into high and low frequency ranges will be performed.

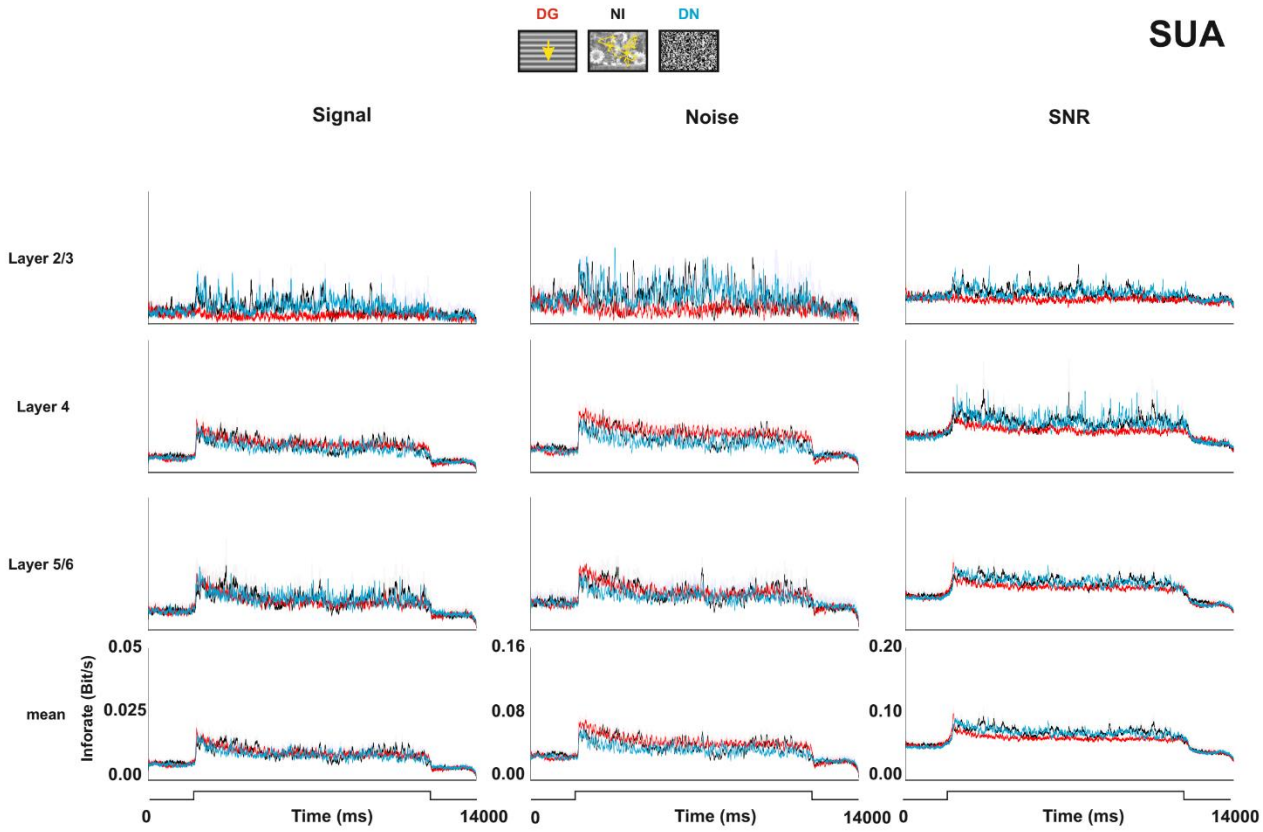

Figure 3.4.15: Information rate of the Signal, Noise and SNR of the single unit activity in response to our set of stimuli. Mean signal (left), noise (center) and SNR (right) obtained for the single unit activity in response to our set of stimuli (Number of neurons: L2/3 = 10; L4 = 111; L5/6 = 99; total = 221)

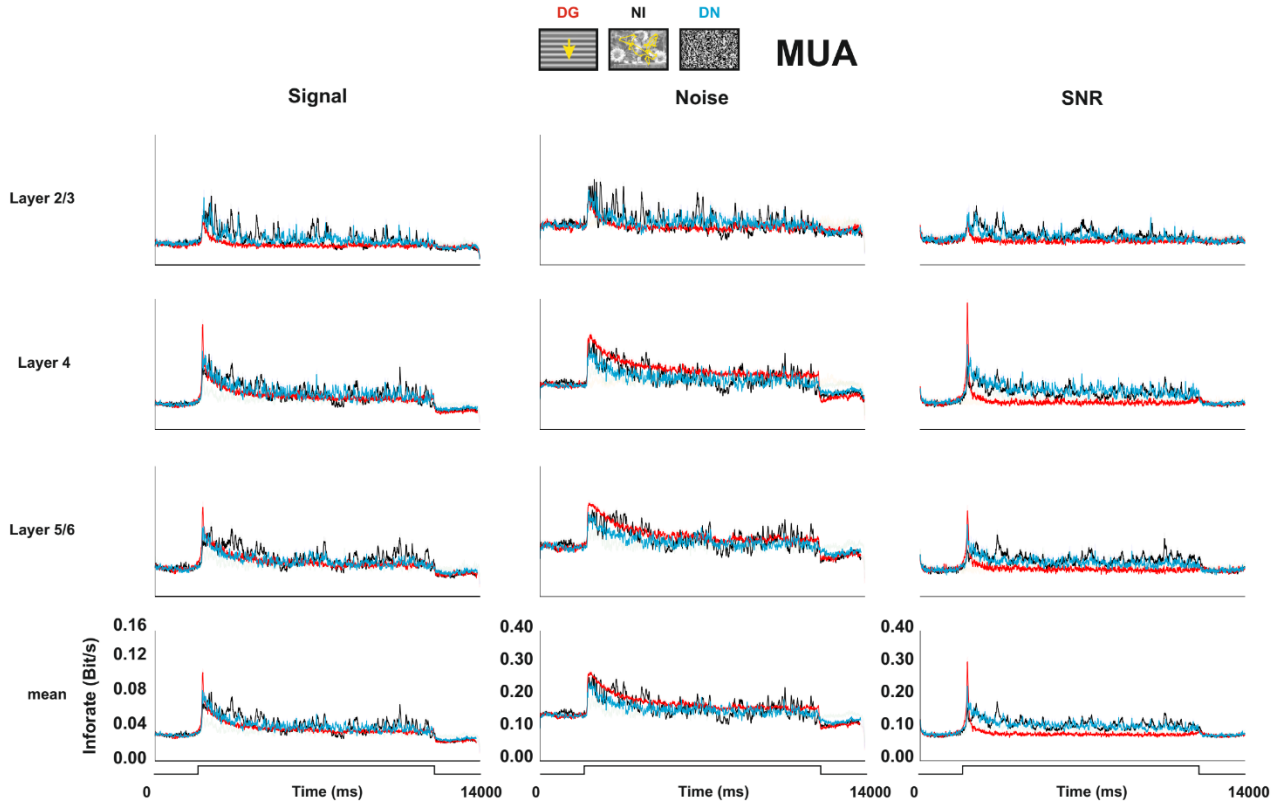

Figure 3.4.16: Information rate of the Signal, Noise and SNR of the multi- unit activity in response to our set of stimuli. Mean signal (left), noise (center) and SNR (right) obtained for the multi- unit activity in response to our set of stimuli (Number of sites: L2/3 = 52; L4 = 187; L5/6 = 138; total = 378)

- **Impact of the natural statistics on the signal to noise ratio**

Finally, we wondered if the wavelet analysis would allow us to have another insight on the reliability evoked by our control stimuli. Indeed, we did not find any difference in reliability between the unaltered natural image and its controls. However, among our set of stimuli the SNR analysis highlighted differences that were not visible when we computed the trial-to-trial correlation and the fano factor.

For the single unit and its subclasses, we did not find any difference between the signal, noise and SNR evoked by natural images and its controls (figures 3.4.17 and 3.4.18; table 3.4.4). However, a difference was observed for the multi-unit activity. Indeed, NI-RS and NI-RST evoked a higher low frequency signal than NI ($p < 0.001$; Friedman test) while NI-RT and NI-SAC evoked a lower one ($p < 0.001$). A difference was also observed for the noise. On one hand, NI-RS evoked a higher low frequency noise than the other stimuli. On the other hand, all the other altered natural images evoked a lower low frequency noise than the unaltered one ($p < 0.001$). This resulted in a lower low frequency SNR evoked by NI-RT and NI-SAC compared to the other stimuli, which evoked similar levels of reliability. This implies that V1 is actually sensitive to the high order correlations in the spatio-temporal statistics. Surprisingly, the natural images containing both spatial and temporal statistics and only spatial statistics lacking high order correlations showed a reliability similar as the unaltered natural image. Yet, the natural image lacking temporal high order correlations evoked a less reliable response than the other stimuli. The interaction between the spatio-temporal statistics probably plays a role in the response. Finally, NI-SAC was less reliable than the other stimuli, implying that not only saccades but that all eye movements are important in the generation of a reliable response. However, due to the small difference that we observed it is difficult to draw strong and definitive conclusions about the impact of the spatio-temporal statistics.

The fact that we observe a difference for the MUA and not the SUA, might be the effect of a population response that is not visible at the single cell level. Another option is that the effect is so small that the latter is only visible on a large number of cells. An increase in the number of recorded neurons and multi-unit sites is needed in order to clarify these results.

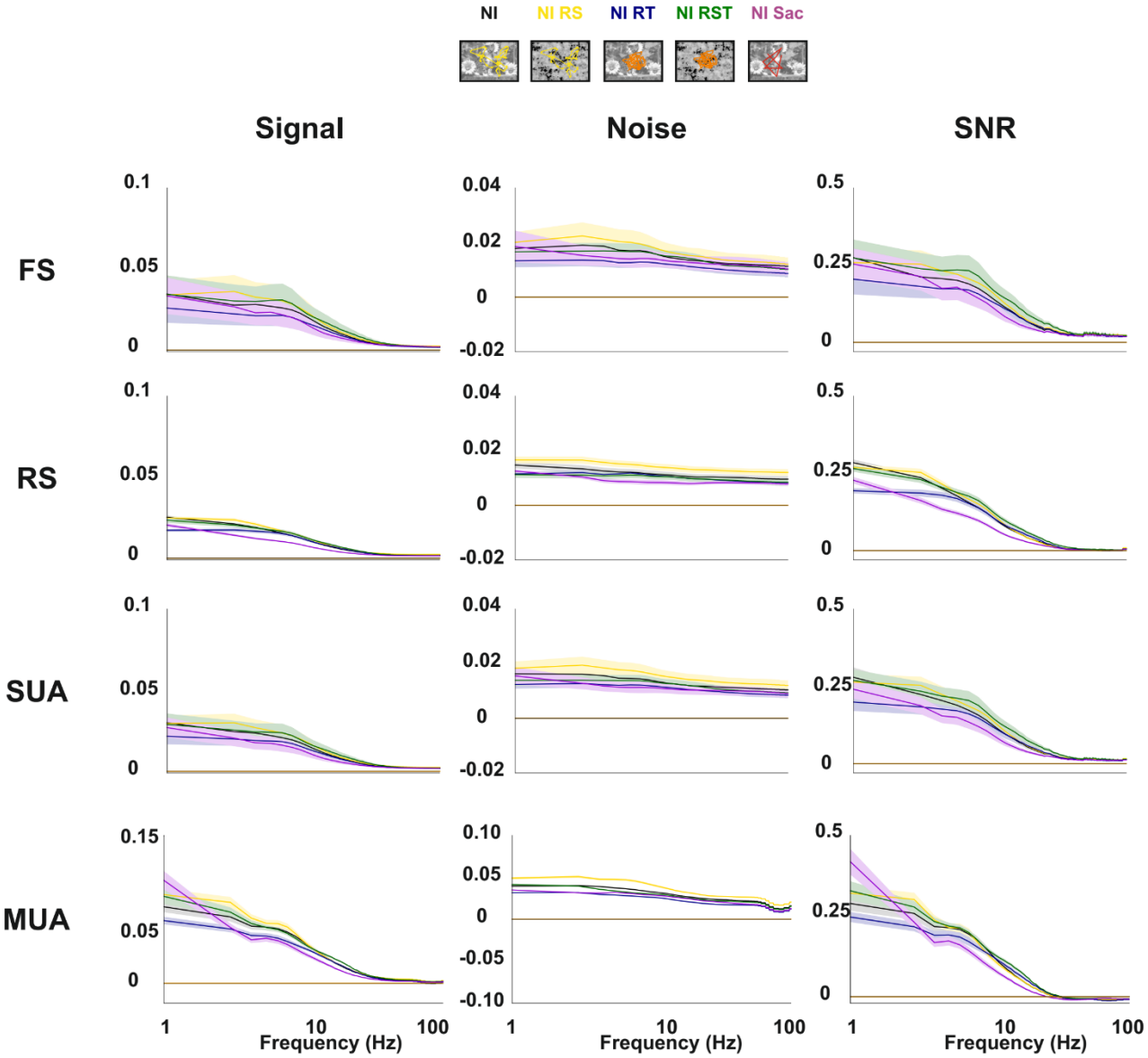

Figure 3.4.17: Mean SNR of the spiking activity in response to the control stimulus set.
Mean signal (left), noise (center) and SNR (right) obtained for the multi-unit activity, the single unit activity and its subclasses obtained in response to our set of control stimuli. Shaded area: SEM

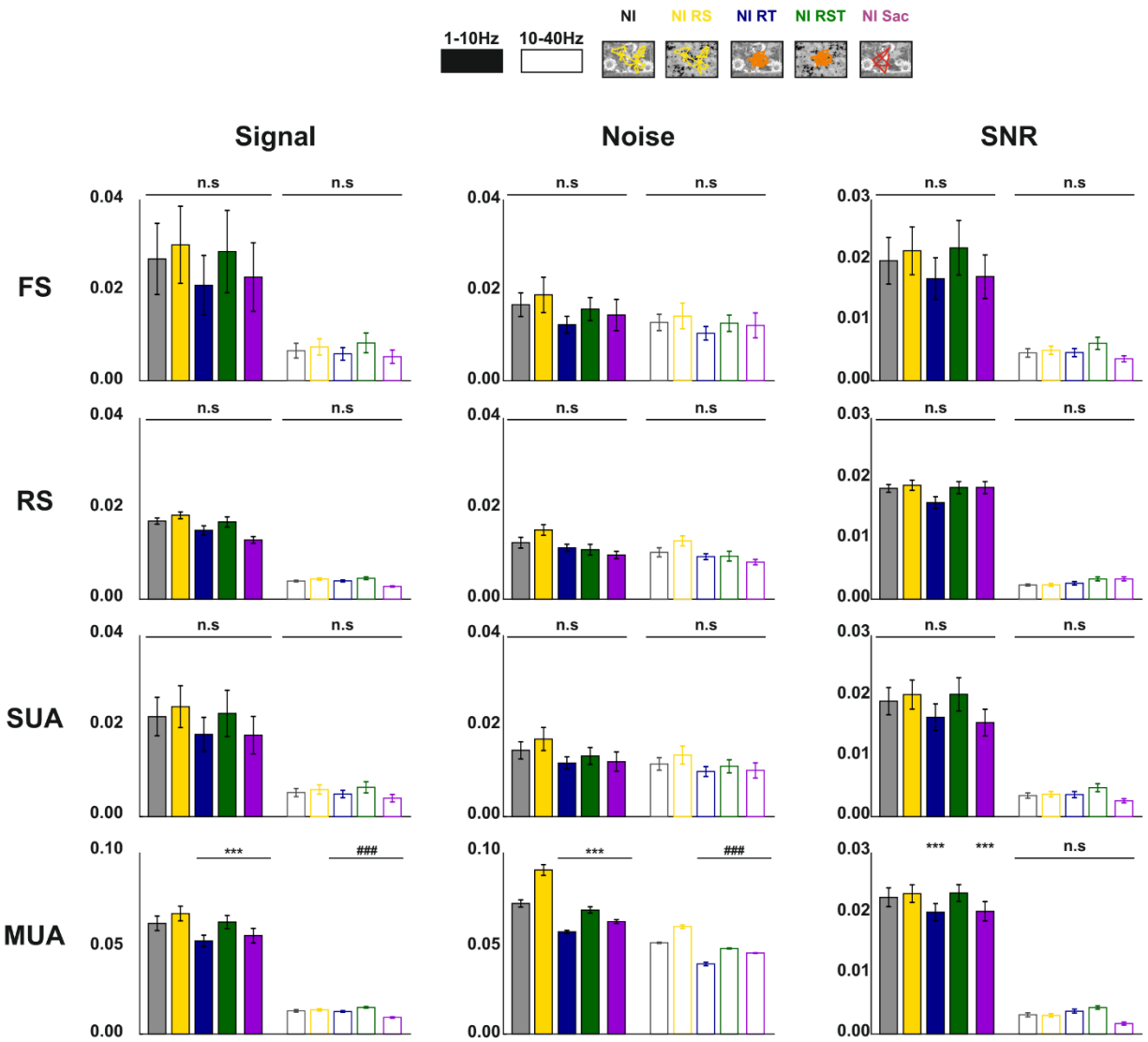

Figure 3.4.18: Bar plots of the low and high frequency SNR of the spiking activity evoked by the control stimuli. Signal (left panel), noise (center) and SNR (right) obtained for the multi-unit activity, the single unit activity and its subclasses in response to our set of control stimuli. (Number of neurons: L2/3 = 10; L4 = 111; L5/6 = 99 neurons; total= 138). *: significantly different from NI low frequency; # significantly different from NI high frequency. * : $p < 0.05$; ** : $p < 0.01$; *** : $p < 0.001$; # : $p < 0.05$; ## : $p < 0.01$; ### : $p < 0.001$. Error bars : SEM.

FULL FIELD	LOW FREQUENCY SIGNAL (SUA)			
	DG	GEM	NI	DN
Layer 2/3	0.000 ± 0.000		0.010 ± 0.002	0.007 ± 0.001
Layer 4	0.012 ± 0.001		0.026 ± 0.002	0.012 ± 0.001
Layer 5/6	0.012 ± 0.004		0.022 ± 0.005	0.014 ± 0.003
Mean w/o GEM	0.012 ± 0.001		0.024 ± 0.001	0.011 ± 0.001
Mean w/ GEM	0.021 ± 0.003	0.018 ± 0.002	0.026 ± 0.003	0.014 ± 0.002

HIGH FREQUENCY SIGNAL (SUA)			
DG	GEM	NI	DN
-0.001 ± 0.000		0.002 ± 0.000	0.004 ± 0.001
0.006 ± 0.001		0.006 ± 0.001	0.007 ± 0.001
0.004 ± 0.001		0.005 ± 0.002	0.008 ± 0.003
0.005 ± 0.000		0.006 ± 0.000	0.007 ± 0.001
0.009 ± 0.001	0.006 ± 0.001	0.007 ± 0.001	0.010 ± 0.002

FULL FIELD	LOW FREQUENCY NOISE (SUA)			
	DG	GEM	NI	DN
Layer 2/3	-0.005 ± 0.002		0.014 ± 0.000	0.017 ± 0.001
Layer 4	0.018 ± 0.002		0.018 ± 0.001	0.007 ± 0.001
Layer 5/6	0.011 ± 0.003		0.011 ± 0.002	0.006 ± 0.001
Mean w/o GEM	0.015 ± 0.001		0.015 ± 0.001	0.006 ± 0.001
Mean w/ GEM	0.032 ± 0.003	0.017 ± 0.002	0.018 ± 0.002	0.010 ± 0.001

HIGH FREQUENCY NOISE (SUA)			
DG	GEM	NI	DN
-0.007 ± 0.000		0.008 ± 0.001	0.014 ± 0.002
0.021 ± 0.003		0.016 ± 0.001	0.008 ± 0.002
0.012 ± 0.003		0.009 ± 0.002	0.007 ± 0.002
0.017 ± 0.001		0.013 ± 0.001	0.007 ± 0.001
0.032 ± 0.003	0.016 ± 0.002	0.016 ± 0.002	0.011 ± 0.002

FULL FIELD	LOW FREQUENCY SNR (SUA)			
	DG	GEM	NI	DN
Layer 2/3	0.014 ± 0.001		0.102 ± 0.025	0.063 ± 0.015
Layer 4	0.091 ± 0.011		0.231 ± 0.011	0.124 ± 0.009
Layer 5/6	0.068 ± 0.020		0.182 ± 0.034	0.109 ± 0.023
Mean w/o GEM	0.085 ± 0.007		0.211 ± 0.009	0.106 ± 0.006
Mean w/ GEM	0.130 ± 0.021	0.170 ± 0.020	0.244 ± 0.028	0.142 ± 0.020

HIGH FREQUENCY SNR (MUA)			
DG	GEM	NI	DN
0.006 ± - 0.001		0.016 ± 0.002	0.027 ± 0.006
0.027 ± 0.004		0.040 ± 0.003	0.055 ± 0.004
0.011 ± 0.005		0.029 ± 0.007	0.050 ± 0.017
0.018 ± 0.002		0.036 ± 0.002	0.050 ± 0.003
0.033 ± 0.007	0.037 ± 0.005	0.041 ± 0.007	0.072 ± 0.012

Table 3.4.1: Mean low and high frequency Signal, Noise and SNR of the single and multi-unit activities in response to our stimulus set (Mean ± SEM)

FULL FIELD	LOW FREQUENCY SIGNAL (MUA)			
	DG	GEM	NI	DN
Layer 2/3	0.001 ± 0.000		0.059 ± 0.007	0.025 ± 0.003
Layer 4	0.038 ± 0.002		0.101 ± 0.003	0.054 ± 0.002
Layer 5/6	0.032 ± 0.001		0.090 ± 0.004	0.036 ± 0.001
Mean w/o GEM	0.031 ± 0.001		0.089 ± 0.001	0.043 ± 0.001
Mean w/ GEM	0.065 ± 0.003	0.070 ± 0.004	0.132 ± 0.008	0.065 ± 0.002

HIGH FREQUENCY SIGNAL (MUA)			
DG	GEM	NI	DN
0.000 ± 0.000		0.009 ± 0.001	0.013 ± 0.002
0.013 ± 0.001		0.021 ± 0.001	0.033 ± 0.002
0.010 ± 0.000		0.016 ± 0.001	0.021 ± 0.001
0.011 ± 0.000		0.018 ± 0.000	0.025 ± 0.001
0.019 ± 0.001	0.021 ± 0.001	0.025 ± 0.001	0.039 ± 0.003

FULL FIELD	LOW FREQUENCY NOISE (MUA)			
	DG	GEM	NI	DN
Layer 2/3	-0.015 ± -0.003		0.024 ± 0.000	0.015 ± 0.001
Layer 4	0.036 ± 0.002		0.038 ± 0.001	0.017 ± 0.001
Layer 5/6	0.030 ± 0.002		0.022 ± 0.002	0.010 ± 0.001
Mean w/o GEM	0.029 ± 0.001		0.030 ± 0.001	0.015 ± 0.001
Mean w/ GEM	0.055 ± 0.003	0.008 ± 0.004	0.031 ± 0.003	0.017 ± 0.002

HIGH FREQUENCY NOISE (MUA)			
DG	GEM	NI	DN
-0.002 ± -0.001		0.017 ± -0.000	0.016 ± 0.001
0.048 ± 0.002		0.031 ± 0.001	0.022 ± 0.000
0.037 ± 0.002		0.026 ± 0.002	0.017 ± 0.001
0.039 ± 0.001		0.027 ± 0.000	0.019 ± 0.000
0.061 ± 0.003	0.022 ± 0.001	0.036 ± 0.001	0.026 ± 0.001

FULL FIELD	LOW FREQUENCY SNR (MUA)			
	DG	GEM	NI	DN
Layer 2/3	0.013 ± -0.000		0.232 ± 0.015	0.089 ± 0.004
Layer 4	0.123 ± 0.006		0.382 ± 0.010	0.229 ± 0.008
Layer 5/6	0.103 ± 0.004		0.342 ± 0.016	0.152 ± 0.003
Mean w/o GEM	0.101 ± 0.002		0.344 ± 0.005	0.184 ± 0.003
Mean w/ GEM	0.201 ± 0.010	0.297 ± 0.016	0.466 ± 0.023	0.268 ± 0.009

HIGH FREQUENCY SNR (MUA)			
DG	GEM	NI	DN
-0.001 ± -0.001		0.023 ± -0.000	0.044 ± 0.002
0.017 ± 0.001		0.060 ± 0.002	0.133 ± 0.008
0.011 ± 0.001		0.047 ± 0.002	0.085 ± 0.003
0.013 ± 0.001		0.051 ± 0.001	0.101 ± 0.003
0.026 ± 0.002	0.073 ± 0.005	0.071 ± 0.003	0.158 ± 0.013

Table 3.4.1: Mean low and high frequency Signal, Noise and SNR of the single and multi-unit activities in response to our stimulus set (Mean ± SEM)

FULL FIELD	LOW FREQUENCY SIGNAL (FS)			HIGH FREQUENCY SIGNAL (FS)		
	DG	NI	DN	DG	NI	DN
Layer 2/3	-0.001 ± 0.001	0.017 ± 0.004	0.011 ± 0.002	-0.001 ± 0.000	0.004 ± 0.001	0.007 ± 0.001
Layer 4	0.016 ± 0.001	0.035 ± 0.003	0.016 ± 0.001	0.009 ± 0.001	0.009 ± 0.001	0.010 ± 0.001
Layer 5/6	0.018 ± 0.007	0.031 ± 0.011	0.022 ± 0.007	0.006 ± 0.002	0.008 ± 0.003	0.015 ± 0.006
Mean w/o GEM	0.018 ± 0.001	0.034 ± 0.003	0.017 ± 0.001	0.008 ± 0.000	0.009 ± 0.001	0.012 ± 0.00

FULL FIELD	LOW FREQUENCY NOISE (FS)			HIGH FREQUENCY NOISE (FS)		
	DG	NI	DN	DG	NI	DN
Layer 2/3	-0.006 ± 0.004	0.024 ± 0.001	0.024 ± 0.001	-0.007 ± 0.002	0.015 ± 0.002	0.021 ± 0.003
Layer 4	0.024 ± 0.002	0.022 ± 0.001	0.010 ± 0.001	0.030 ± 0.003	0.019 ± 0.001	0.012 ± 0.001
Layer 5/6	0.015 ± 0.005	0.015 ± 0.003	0.008 ± 0.002	0.015 ± 0.005	0.012 ± 0.004	0.010 ± 0.003
Mean w/o GEM	0.021 ± 0.001	0.020 ± 0.001	0.010 ± 0.001	0.026 ± 0.002	0.018 ± 0.001	0.012 ± 0.001

FULL FIELD	LOW FREQUENCY SNR (FS)			HIGH FREQUENCY SNR (FS)		
	DG	NI	DN	DG	NI	DN
Layer 2/3	0.002 ± -0.001	0.150 ± 0.043	0.090 ± 0.026	0.004 ± 0.000	0.019 ± 0.005	0.042 ± 0.013
Layer 4	0.112 ± 0.012	0.287 ± 0.017	0.160 ± 0.011	0.040 ± 0.006	0.059 ± 0.003	0.082 ± 0.005
Layer 5/6	0.093 ± 0.036	0.214 ± 0.062	0.146 ± 0.038	0.020 ± 0.009	0.044 ± 0.012	0.083 ± 0.031
Mean w/o GEM	0.114 ± 0.010	0.272 ± 0.015	0.151 ± 0.008	0.031 ± 0.003	0.057 ± 0.003	0.083 ± 0.005

Table 3.4.2: Mean low and high frequency Signal, Noise and SNR of the regular and fast spiking neurons in response to our stimulus set (Mean ± SEM)

FULL FIELD	LOW FREQUENCY SIGNAL (RS)		
	DG	NI	DN
Layer 2/3	0.000 ± 0.000	0.003 ± 0.000	0.003 ± 0.001
Layer 4	0.008 ± 0.001	0.017 ± 0.001	0.007 ± 0.001
Layer 5/6	0.005 ± 0.000	0.013 ± 0.001	0.006 ± 0.001
Mean w/o GEM	0.006 ± 0.000	0.014 ± 0.000	0.004 ± 0.000

HIGH FREQUENCY SIGNAL (RS)		
DG	NI	DN
-0.001 ± -0.000	0.001 ± -0.000	0.002 ± 0.000
0.003 ± 0.001	0.004 ± 0.000	0.003 ± 0.000
0.002 ± 0.000	0.003 ± 0.000	0.002 ± 0.000
0.002 ± 0.000	0.003 ± 0.000	0.002 ± 0.000

FULL FIELD	LOW FREQUENCY NOISE (RS)		
	DG	NI	DN
Layer 2/3	-0.005 ± -0.001	0.004 ± 0.000	0.009 ± 0.001
Layer 4	0.012 ± 0.002	0.014 ± 0.001	0.003 ± 0.002
Layer 5/6	0.007 ± 0.001	0.007 ± 0.001	0.003 ± 0.000
Mean w/o GEM	0.007 ± 0.001	0.009 ± 0.001	0.001 ± 0.001

HIGH FREQUENCY NOISE (RS)		
DG	NI	DN
-0.007 ± -0.002	0.002 ± -0.000	0.007 ± 0.001
0.012 ± 0.003	0.012 ± 0.001	0.004 ± 0.002
0.009 ± 0.001	0.007 ± 0.001	0.003 ± 0.000
0.008 ± 0.001	0.008 ± 0.000	0.002 ± 0.001

FULL FIELD	LOW FREQUENCY SNR (RS)		
	DG	NI	DN
Layer 2/3	0.025 ± 0.005	0.055 ± 0.007	0.037 ± 0.003
Layer 4	0.070 ± 0.011	0.175 ± 0.006	0.089 ± 0.008
Layer 5/6	0.043 ± 0.005	0.149 ± 0.007	0.072 ± 0.008
Mean w/o GEM	0.057 ± 0.004	0.150 ± 0.003	0.060 ± 0.003

HIGH FREQUENCY SNR (RS)		
DG	NI	DN
0.008 ± -0.001	0.012 ± -0.001	0.013 ± -0.000
0.015 ± 0.003	0.021 ± 0.002	0.028 ± 0.003
0.002 ± 0.001	0.015 ± 0.001	0.018 ± 0.002
0.004 ± 0.001	0.015 ± 0.001	0.017 ± 0.001

Table 3.4.2: Mean low and high frequency Signal, Noise and SNR of the regular and fast spiking neurons in response to our stimulus set (Mean ± SEM)

FULL FIELD	SIGNAL (SUA)		
	DG	NI	DN
Layer 2/3	0.003 ± 0.001	0.006 ± 0.002	0.007 ± 0.002
Layer 4	0.011 ± 0.001	0.010 ± 0.001	0.009 ± 0.001
Layer 5/6	0.011 ± 0.002	0.012 ± 0.003	0.012 ± 0.004
Mean w/o GEM	0.010 ± 0.001	0.010 ± 0.001	0.010 ± 0.001

SIGNAL (MUA)		
DG	NI	DN
0.023 ± 0.001	0.028 ± 0.002	0.028 ± 0.002
0.039 ± 0.001	0.043 ± 0.002	0.043 ± 0.002
0.041 ± 0.001	0.046 ± 0.002	0.042 ± 0.001
0.037 ± 0.001	0.043 ± 0.001	0.040 ± 0.001

FULL FIELD	NOISE (SUA)		
	DG	NI	DN
Layer 2/3	0.017 ± 0.010	0.032 ± 0.013	0.036 ± 0.011
Layer 4	0.050 ± 0.007	0.044 ± 0.006	0.037 ± 0.005
Layer 5/6	0.048 ± 0.010	0.046 ± 0.010	0.041 ± 0.010
Mean w/o GEM	0.047 ± 0.005	0.043 ± 0.005	0.037 ± 0.004

NOISE (MUA)		
DG	NI	DN
0.117 ± 0.007	0.129 ± 0.008	0.127 ± 0.008
0.186 ± 0.007	0.168 ± 0.006	0.159 ± 0.006
0.192 ± 0.006	0.183 ± 0.005	0.172 ± 0.005
0.178 ± 0.004	0.169 ± 0.004	0.160 ± 0.003

FULL FIELD	SNR (SUA)		
	DG	NI	DN
Layer 2/3	0.037 ± 0.006	0.049 ± 0.008	0.047 ± 0.008
Layer 4	0.065 ± 0.005	0.074 ± 0.008	0.073 ± 0.006
Layer 5/6	0.065 ± 0.008	0.078 ± 0.019	0.078 ± 0.012
Mean w/o GEM	0.064 ± 0.004	0.073 ± 0.007	0.073 ± 0.005

SNR (MUA)		
DG	NI	DN
0.074 ± 0.005	0.089 ± 0.005	0.085 ± 0.005
0.085 ± 0.003	0.118 ± 0.004	0.123 ± 0.005
0.086 ± 0.004	0.116 ± 0.005	0.106 ± 0.006
0.084 ± 0.002	0.114 ± 0.003	0.111 ± 0.004

Table 3.4.3: Mean inforate of the Signal, Noise and SNR of the single and multi-unit activities in response to our stimulus set (Mean ± SEM)

FULL FIELD	SIGNAL				
	NI	NI-RS	NI-RT	NI-RST	NI-SAC
FS	0.027 ± 0.007	0.030 ± 0.008	0.021 ± 0.006	0.028 ± 0.009	0.023 ± 0.007
RS	0.017 ± 0.001	0.018 ± 0.001	0.015 ± 0.001	0.017 ± 0.001	0.013 ± 0.001
SUA	0.022 ± 0.004	0.024 ± 0.004	0.018 ± 0.003	0.022 ± 0.005	0.018 ± 0.004
MUA	0.061 ± 0.004	0.066 ± 0.004	0.051 ± 0.003	0.061 ± 0.003	0.054 ± 0.004

FULL FIELD	NOISE				
	NI	NI-RS	NI-RT	NI-RST	NI-SAC
FS	0.016 ± 0.002	0.019 ± 0.003	0.012 ± 0.001	0.015 ± 0.002	0.014 ± 0.003
RS	0.012 ± 0.001	0.015 ± 0.001	0.011 ± 0.001	0.011 ± 0.001	0.009 ± 0.001
SUA	0.014 ± 0.001	0.017 ± 0.002	0.011 ± 0.001	0.013 ± 0.001	0.012 ± 0.002
MUA	0.036 ± 0.001	0.045 ± 0.001	0.028 ± 0.001	0.034 ± 0.001	0.031 ± 0.001

FULL FIELD	SNR				
	NI	NI-RS	NI-RT	NI-RST	NI-SAC
FS	0.199 ± 0.038	0.215 ± 0.039	0.169 ± 0.034	0.220 ± 0.045	0.172 ± 0.036
RS	0.183 ± 0.006	0.189 ± 0.008	0.160 ± 0.009	0.185 ± 0.010	0.139 ± 0.008
SUA	0.191 ± 0.022	0.202 ± 0.024	0.164 ± 0.022	0.202 ± 0.027	0.156 ± 0.022
MUA	0.226 ± 0.015	0.232 ± 0.014	0.202 ± 0.014	0.233 ± 0.013	0.203 ± 0.016

Table 3.4.4: Mean low frequency Signal, Noise and SNR of the spiking activity in response to our control stimulus set (Mean ± SEM)

4.1.2 Time Frequency Analysis of the Local Field Potential

LFP is not a measure of the neuronal activity but it indicates it synchronization level. We obtained a highly synchronized signal in response to NI and unsynchronized one in response to DG. This resulted in poor reliability levels evoked by DG. However, as shown with our spiking results and the intracellular results of Baudot and colleagues (2013), drifting gratings do evoke a reliable response but only at the grating frequency. Thus, we can wonder if the wavelet analysis of local field potential will unveil some specific frequential aspects of the reliability. As performed for the spiking activity, we subtracted the SNR of the spontaneous activity to the evoked one. Figure 3.4.19 shows the SNR response without and with blank subtraction.
Our previous results showed that only choosing the LFP sites of the population with GEM or choosing all the sites, resulted in the same mean responses evoked by the animated gratings. Thus, for the time frequency analysis we decided to only perform our analysis on all the sites and not only the ones of the population with GEM. Since the LFPs were recorded across all layers, we will be able to investigate if, as observed for our previous indexes (sections 2 and 3 of this chapter), the different stimuli elicit different responses across layers. Moreover, we observed, at the spiking level, a difference between the SNR and the timescale dependent analysis. Yet, will these differences also be present at the LFP level (which was not the case for Vm in Baudot's study (2013)). In order to answer these questions, we computed the wavelet analysis across our recordings (Figures 3.4.20 to 3.4.22, table 3.4.5).

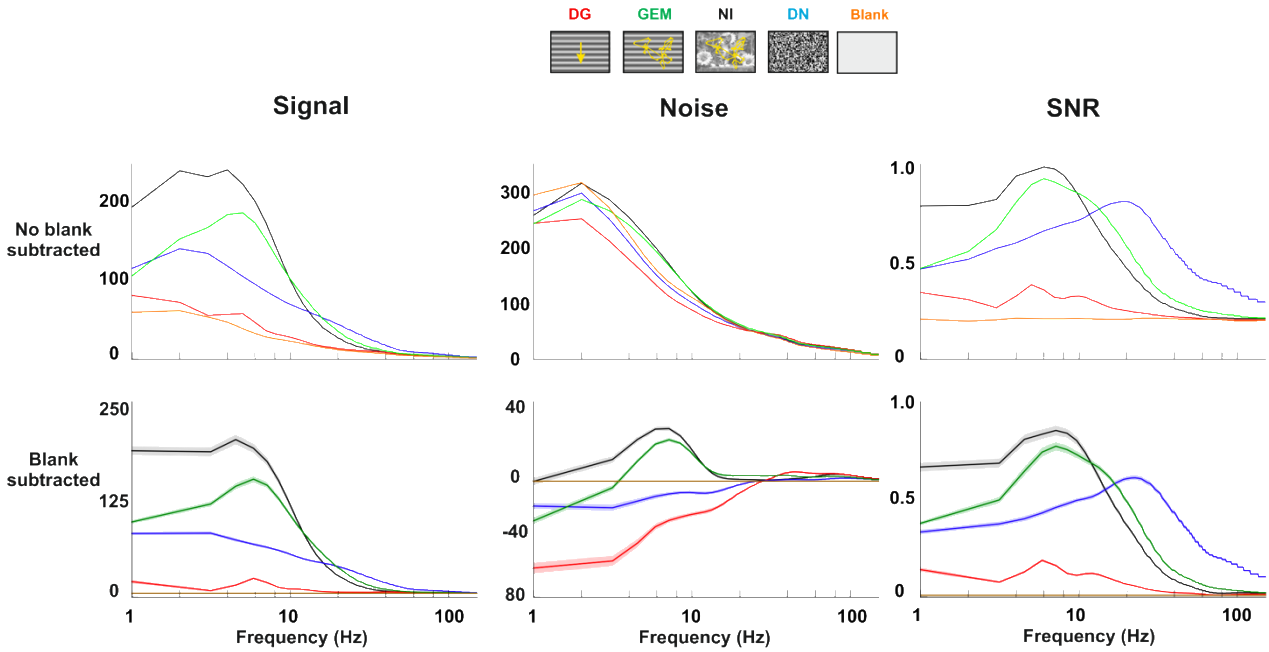

Figure 3.4.19: Signal, Noise and SNR with or without blank subtraction

- **Mean Evoked SNR**

As observed for the SUA and MUA, natural images are the stimulus that evoked the highest mean signal in the low frequency band ($p < 0.001$, Friedman test; Figures 3.4.20 and 3.4.21; table 3.4.5). Among the artificial stimuli, GEM evoked the highest signal and DG the lowest one ($p < 0.001$). The signal peak observed at the spiking level in the DG condition was almost absent for the LFP. This peak was present for the membrane potential. This result argues in favor of our previous observations and can be refined. Indeed, as stated before our results suggest that the mesoscopic

information carried by LFPs and the local integration of synaptic input activity realized by a single cell are clearly dissociated. This frequency-based analysis also suggests that during drifting grating stimulation, the response of each neuron is mainly driven by the stimulus (*i.e.* the peak) and that stochastic activity for frequencies different from the driving frequency are also present. In addition, at the LFP level, the peak is reduced since we also record the activity simple neurons that do not respond to the same phases and complex cells that do not display this modulation, thus no peak (Benucci et al., 2007). Regarding the high frequency signal, the GEM and DN condition were higher than NI ($p < 0.001$; Friedman test; Figures 3.4.20 and 3.4.22). However, it is important to note that, as observed intracellularly, the low frequency signal is usually ten times higher than the high frequency one.

The noise analysis resulted in very different results from the ones obtained intracellularly (Figure 3.4.20; table 3.4.5). Indeed, while Baudot and colleagues observed that DG and GEM evoked a higher low frequency noise than NI we observed the opposite. For the local field potential, natural images evoked the highest mean noise in the low frequency range ($p < 0.001$; Friedman test). Among the artificial stimuli, GEM evoked the highest mean low frequency noise, while DG the lowest. Surprising, DG and DN noise were much lower than the one obtained for the spontaneous activity (figure 3.4.20). At high frequencies, DG and DN still evoked negative values of noise yet close to 0. It is important to note that both the signal and the noise obtained for the LFP are in similar range of values as the ones obtained for Vm but almost 1000 times higher than the ones obtained for both SUA and MUA.

This led to different values of SNR both in high and low frequencies. First, as expected by the noise and signal values, natural images evoked the highest SNR in the low frequency range ($p < 0.001$; Friedman test). This result differs from the one obtained intracellularly. Indeed, Baudot and colleagues (2013) did not find any difference between the SNR evoked by the animated gratings and the natural images. Second, among the artificial stimuli, animated gratings evoked the highest low frequency levels of reliability while drifting gratings evoked the less reliable response ($p < 0.001$). The higher reliability obtained in response to GEM originates from the high signal evoked by the stimulus. Indeed, despite a lower noise, the dense noise condition did not evoke a signal strong enough to increase the reliability at the same level as GEM (GEM's mean signal being almost two times higher than the one elicited by DN whereas the difference in noise is not as important). Third, dense noise evoked the highest high frequency SNR ($p < 0.001$), this value was close to one observed for the low frequencies. This is not surprising since dense noise contain an important amount of high frequencies (see Chapter II: methods).

In conclusion, as observed for the spiking activity and with our other indexes of reliability we showed that natural images evoke a strong and reliable response. In addition, during the dense noise stimulation, a high SNR is observed for high frequencies. Finally, in some cases the analysis of LFP and the Vm allowed to draw similar conclusions while in the others no, arguing in favor for a fundamental difference between the Vm and the LFP.

- **Laminar Signal to Noise Ratio**

As stated before, our probes allowed us to perform laminar recordings. Our previous results showed a laminar processing of the visual inputs. Yet, we can wonder if we will observe the same laminar differences. In addition, will we observe a layer-specific frequency content? Within all layers, the signal, the noise and the SNR displayed the same pattern as the one observed for the mean over the population. Yet, we observed a clear laminar dependency of the response (Figures 3.4.20 to 3.4.22 table 3.4.5).

Indeed, natural images evoked its highest low frequency signal value in layer 5/6 and the lowest one in layer 2/3. However, the difference in signal between layers 4 and 5/6 is small (Table 3.4.5). On the other hand, the same artificial stimuli elicited an equivalent response in layers 4 and 5/6 ($p > 0.05$; Mann Whitney U test), higher than the ones observed in layer 2/3 ($p < 0.001$). For all stimuli, layers 4 and 5/6 showed a signal almost two times higher than the one observed in layer 2/3 (Table 3.4.5). Regarding the high frequency noise, dense noise evoked the highest value in layer 4 and the lowest in layer 2/3 ($p < 0.001$; Figure 3.4.22). The noise analysis did not reveal any difference between layers ($p > 0.05$; Mann Whitney U test). However, the highest mean noise values were found in layer 5/6. Therefore, one could suppose that the laminar values of the stimulus locked SNR are linked to the variations of the evoked signal. Yet, natural images evoked an equivalent low frequency SNR in layers 4 and 5/6 ($p = 0.95$), higher than the one in layer 2/3 ($p < 0.001$; confirming the results obtained with our other indexes). This result from a higher signal in layer 5/6 but a higher noise, while in layer 4 NI evoked a lower signal and a lower noise. Drifting gratings and dense noise stimulation evoked their highest levels of reliability in layer 4 and the lowest in layer 2/3 ($p < 0.001$). Only animated gratings elicited a SNR "matching" the signal and noise values (*i.e.* highest SNR in layer 4 and lower in layer 2/3). Dense noise evoked a higher high frequency SNR than a low frequency in layer 4 ($p < 0.01$). These results match the ones obtained with our previous (see section 3 of this chapter).

In conclusion, we confirmed the results that we obtained previously, *i.e.* natural images evoke a higher reliability than the other stimuli, across all layers. This originates from a high signal that overcomes the fact that NI are the stimuli eliciting the highest noise. In addition, we observed, for all stimuli, a laminar dependency of the signal but not for the noise. Therefore, the highest evoked signal and SNR were observed in layer 4. These strong signal and SNR might come from the numerous thalamic inputs present in this layer. Indeed, it is known that thalamic send strong and reliable inputs leading to this strong response in layer 4 (Kumbhani et al., 2007). Another explanation could be that the differences are linked to the intrinsic properties of the layers.

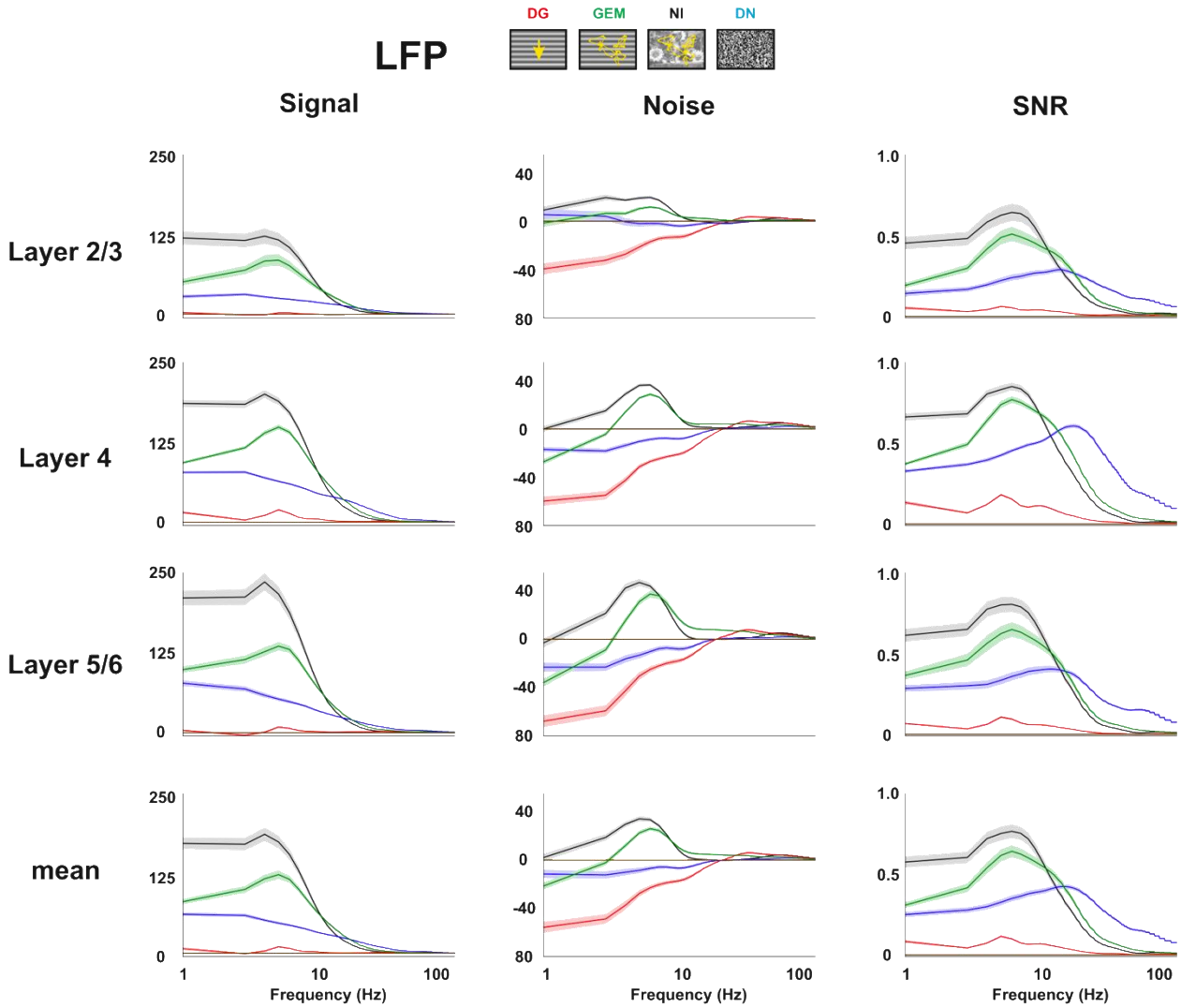

Figure 3.4.20: Mean and laminar SNR of the local field potential. Natural images evoke the most reliable response in the low frequency range. Signal (left), noise (center) and SNR (right) obtained for the single unit activity in response to our set of stimuli (shaded area : SEM)

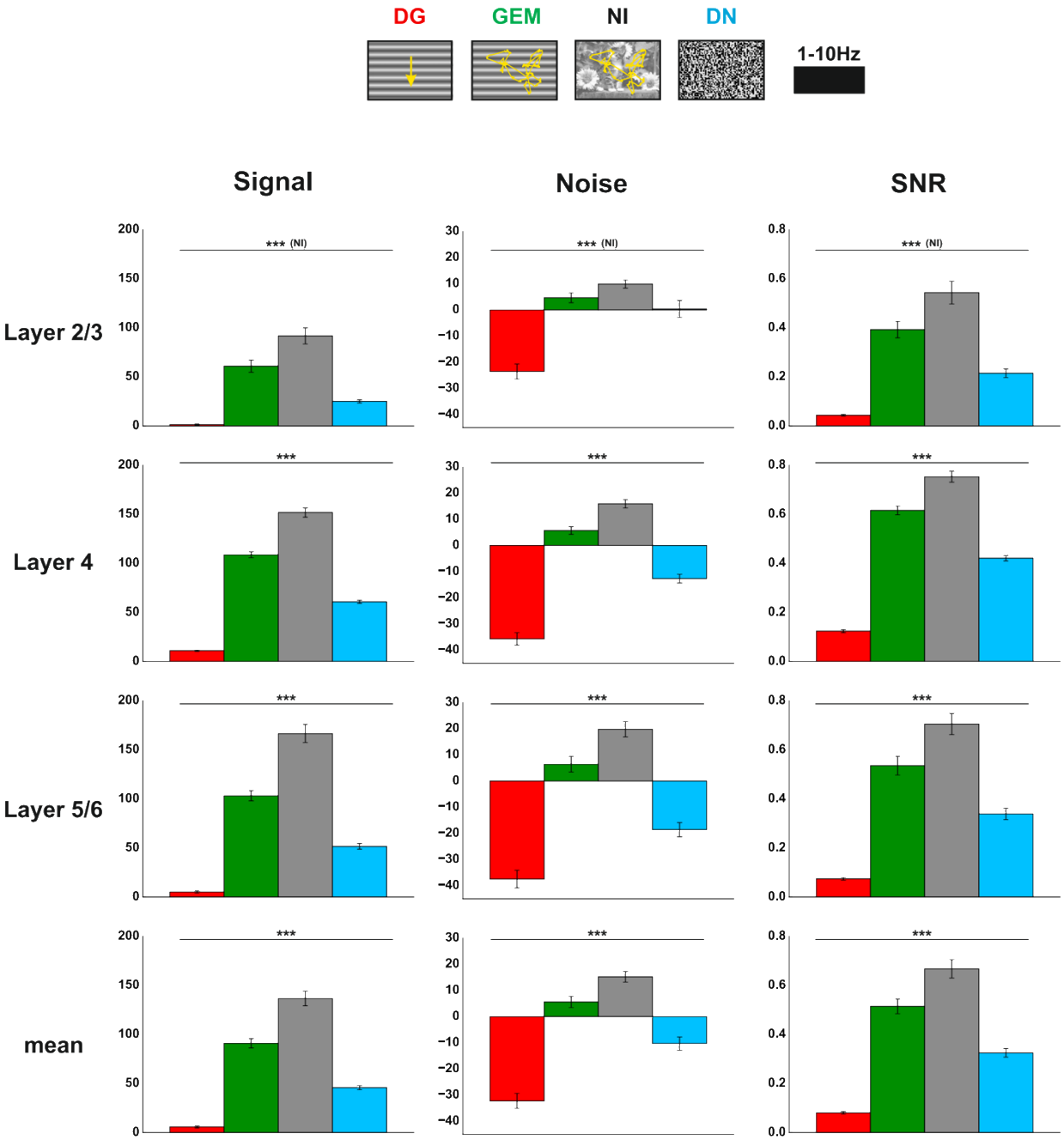

Figure 3.4.21: Bar plots of the low frequency local field potential SNR. Signal (left panel), noise (center) and SNR (right) obtained for the local field potential in response to our set of stimuli. *: significantly different from NI low frequency; # significantly different from NI high frequency. * : $p < 0.05$; ** : $p < 0.01$; *** : $p < 0.001$; # : $p < 0.05$; ## : $p < 0.01$; ### : $p < 0.001$. Error bars : SEM.

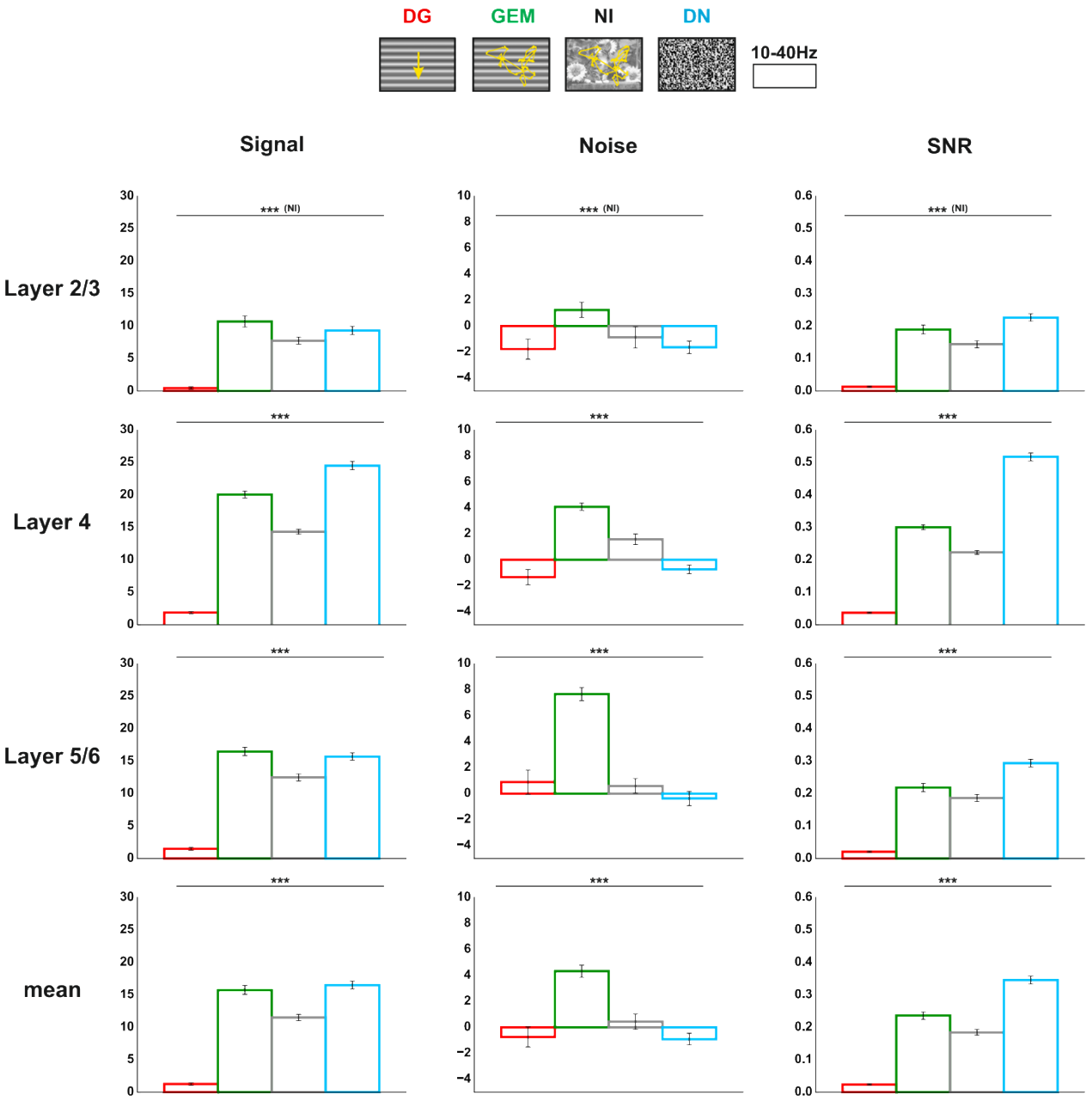

Figure 3.4.22: Bar plots of the high frequency local field potential SNR. Signal (left panel), noise (center) and SNR (right) obtained for the local field potential in response to our set of stimuli. *: significantly different from NI low frequency; # significantly different from NI high frequency. * : $p < 0.05$; ** : $p < 0.01$; *** : $p < 0.001$; # : $p < 0.05$; ## : $p < 0.01$; ### : $p < 0.001$. Error bars : SEM.

- **Information rate**

As performed for the spiking activity, we quantified the amount of information by computing the information rate (inforate) of the local field potential (figure 3.4.23)
Regarding the signal, Natural images and animated gratings evoked a similar signal, higher than dense noise and drifting gratings. The same pattern was found across layers, except for the DN condition in layer 4, which induced a similar inforate as GEM and NI. Again, one need to keep in mind that the inforate is computed for frequencies up to 150Hz (while Baudot and colleagues limited their analysis to 75Hz). Therefore, some stimuli, such as DN, can send the same amount of information as NI since they display a stronger signal for higher frequencies. Dense noise and drifting gratings evoked a similar mean inforate noise lower than NI and GEM. The same pattern was found across layers (figure 3.4.23). Finally, we obtained the highest SNR inforate for the DN while NI and GEM were equivalent and higher than the one induced by DG. These results come from the fact that the inforate is computed from frequencies ranging between 1 and 120Hz and as shown in figures 3.4.20 and 3.4.22, dense noise evokes a high SNR in the higher frequencies, while GEM's high frequency SNR is higher than the one evoked by NI. As stated in the previous section, an analysis of the inforate for our different frequency bands would confirm the results that we observed.

As performed by Baudot and colleagues (unpublished results; Figure 3.4.24), we compared the inforate of the SNR for our different signals. This allows to directly compare our different signals (Figure 3.4.25). Our results show that the local field potential was the most informative signal while the SUA was the lowest. Surprisingly, both the LFP and the MUA evoked a similar inforate in response to DG. For the three signals we can observe that the traces are very similar but at different amplitudes. A filtering between the LFP and the spiking activity seem to be performed. This was also observed intracellularly between the membrane potential and the spiking activity
We also plotted the different inforates for each layer (Figure 3.4.26). While layers 4 and 5/6 produce similar levels of information, an important decrease is observed in layer 2/3. This layer is the one sending projections to higher areas. Yet, our results suggest that a filtering of the pertinent information is performed. This reduction in the amount of information transmitted between two areas is also observed between the LGN and V1 (Sedigh-Sarvestani et al., 2019). Thus, the filtering of pertinent information might be a shared property in order to maximize information processing.

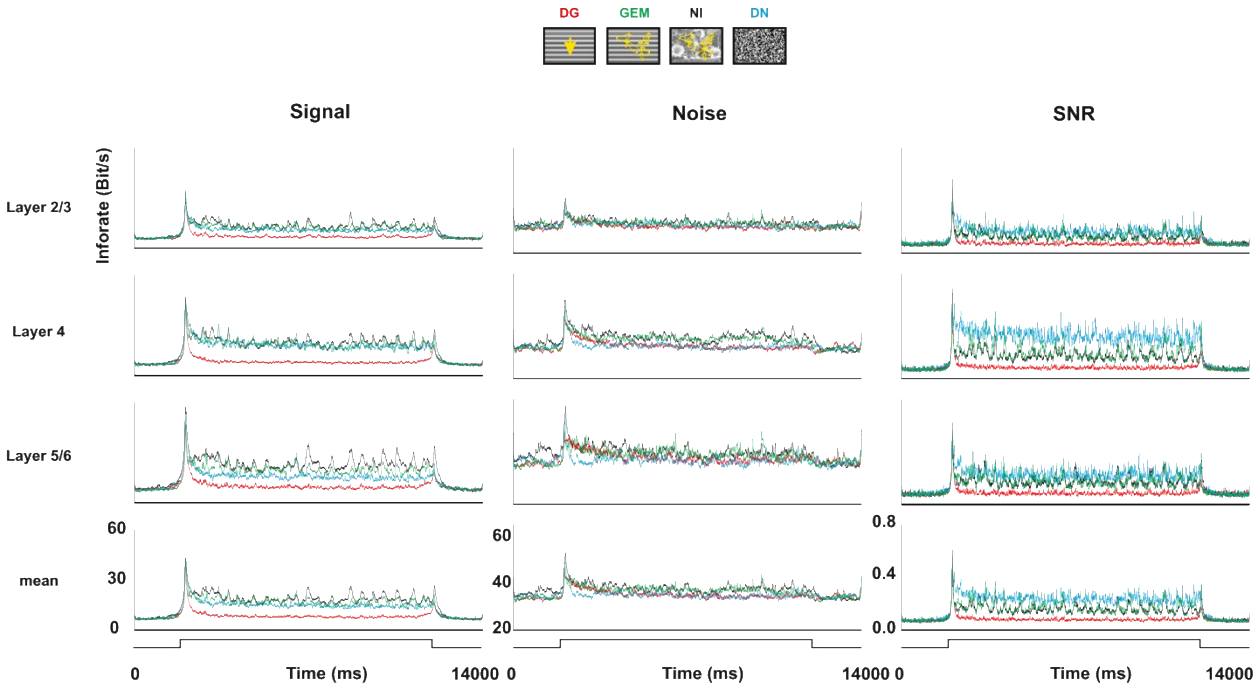

Figure 3.4.23: Mean information rate of the signal, noise and SNR of the local field potential in response to our stimulus set.

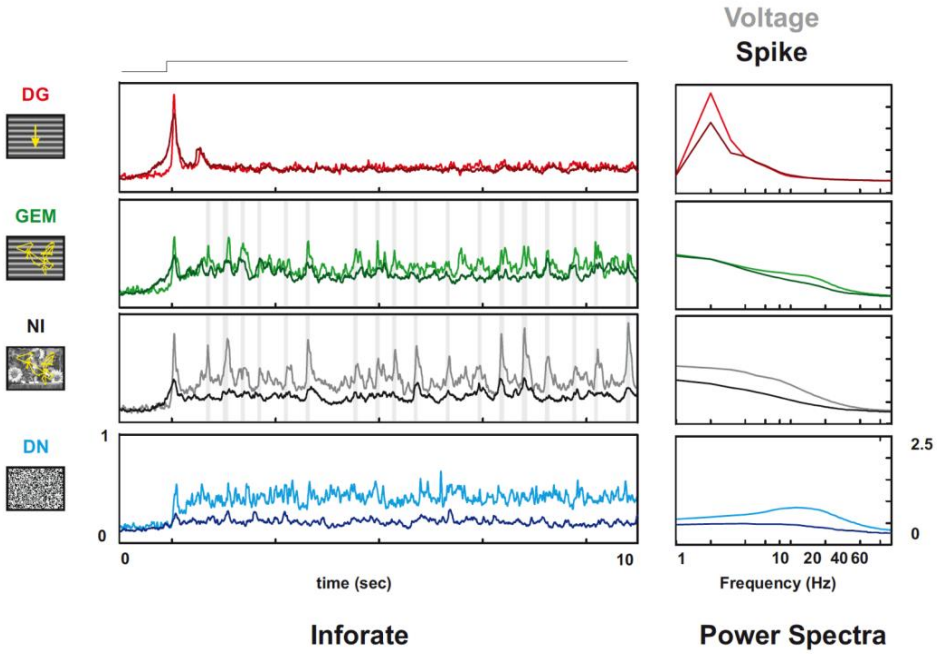

Figure 3.4.24: Mean information rate and power spectra of the membrane potential and intracellular spiking in response to our stimulus set.

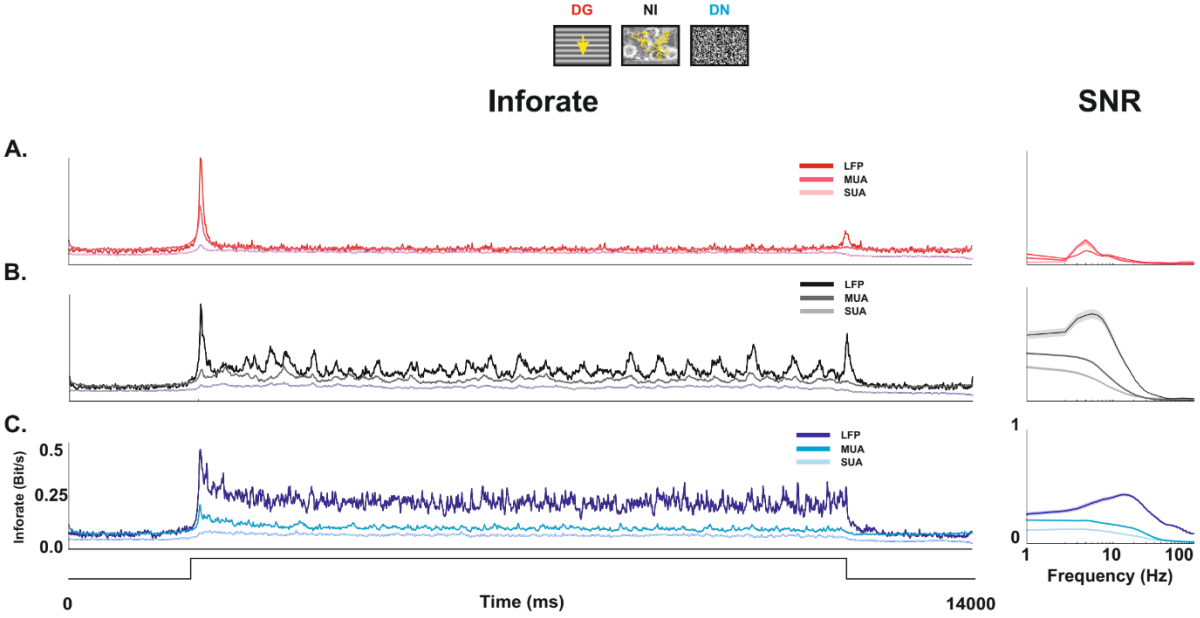

Figure 3.4.25: SNR power spectra and inforate of our three different signals. The local field potential evokes the highest inforate and the SUA the lowest one. LFP (red), MUA (green) and SUA (blue) in response to three stimuli of our stimulus set. **A.** Mean inforate evoked by drifting gratings. **B.** Mean inforate evoked by Natural images. **C.** Mean inforate evoked by Dense noise.

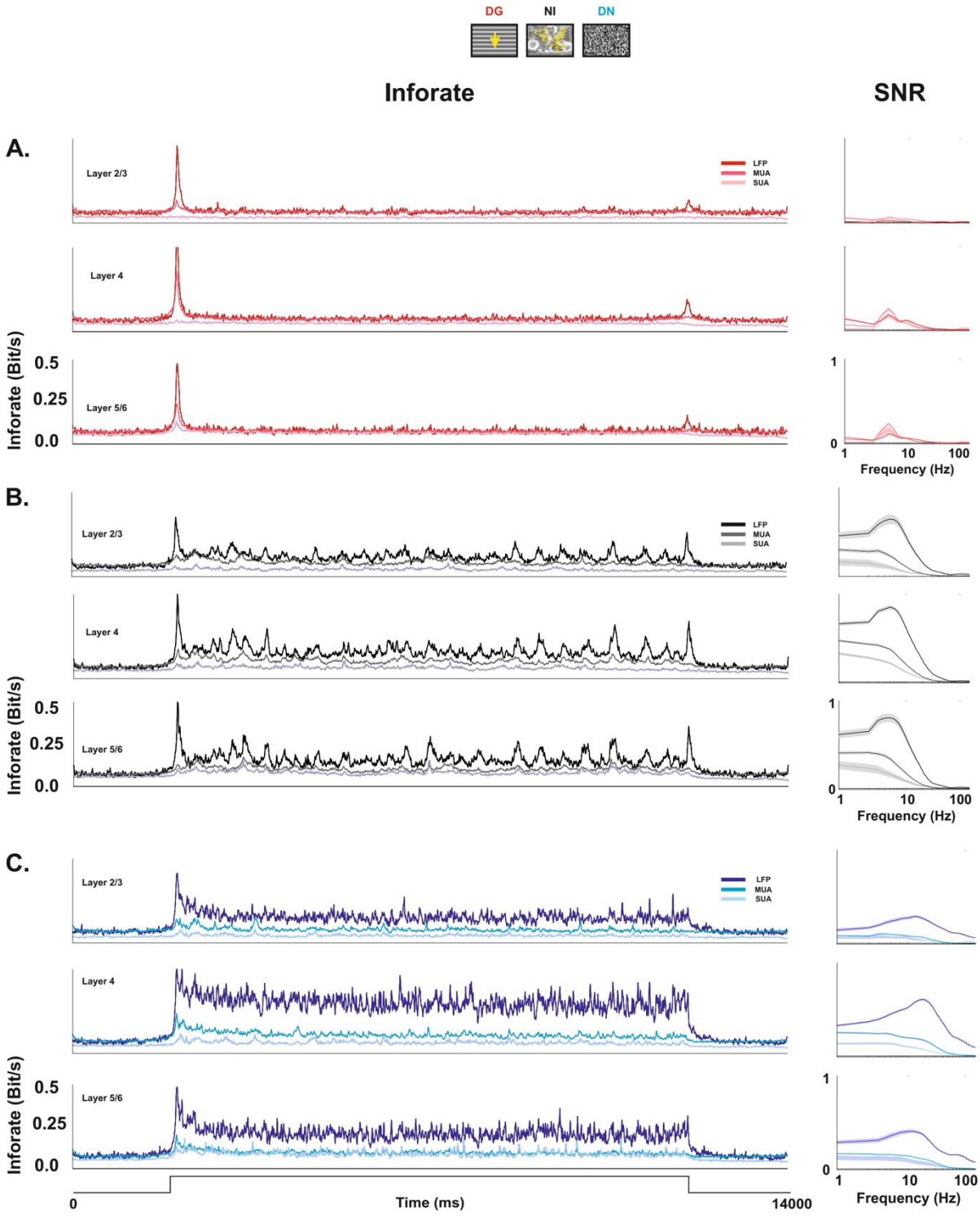

Figure 3.4.26: Mean laminar SNR power spectra and inforate of our three different signals. The local field potential evokes the highest inforate and the SUA the lowest one. LFP (red), MUA (green) and SUA (blue) in response to three stimuli of our stimulus set. **A.** Mean inforate evoked by drifting gratings. **B.** Mean inforate evoked by Natural images. **C.** Mean inforate evoked by Dense noise.

- **Impact of the natural statistics on the signal to noise ratio**

Finally, we wondered if the wavelet analysis would allow us to have another insight on the reliability evoked by our control stimuli. Indeed, we only found a difference in reliability between the Natural image animated only with saccades (NI-SAC) and the unaltered image. Moreover, do we observe different levels of signal and noise leading to a similar ratio or do the control stimuli evoke the same values of noise and signal?

We first computed the signal (Figure 3.4.27; table 3.4.6). The natural images where the spatial statistics were altered (NI-RS) evoked the same levels of signal as the unaltered natural image, for both low and high frequencies ($p > 0.05$). However, all the other stimuli evoked different signal values. On one hand, the natural images where the temporal statistics were altered (NI-RT) and the one where both spatial and temporal statistics were randomized (NI-RST) evoked a lower low frequency signal and higher high frequency signal than NI ($p < 0.001$). On the other hand, NI-SAC evoked higher low frequency signal than NI, but a lower high frequency signal ($p < 0.001$). This increase in the low frequencies originates from the very low frequencies and is absent for the other stimuli. This suggest that the saccades alone increase the amount of low frequencies and that the addition of other eye movements tend to attenuate this increase. This increase could be linked to the fact that saccades reduce the adaptation of the response resulting in a stronger impact of low frequency content present in NI-SAC. Surprisingly, for the spiking scale, NI-SAC evoked a lower signal than the unaltered NI. One could wonder if the low frequency increase observed for the LFP is linked to the membrane potential. All stimuli evoked a different low frequency noise than NI ($p < 0.001$) while no difference was observed for the high frequency noise ($p > 0.05$). Both NI-RS and NI-SAC elicited a higher noise than NI while NI-RT and NI-RST a lower one (figure 3.4.27). This led to different SNRs for our different stimuli condition. First, despite the higher noise, NI-RS and NI evoked the same low frequency SNR (and high frequency one, $p > 0.05$). This absence of difference probably originates from the fact that the evoked noise by NI-RS was very variable. Second, NI-RT and NI-RST evoked a lower low frequency SNR than NI but a higher high frequency one (as expected based on the signal and noise values). Third, NI-SAC evoked a higher low frequency SNR but a lower high frequency one. These patterns of low and high frequency responses might explain why we were not able to detect any difference in the evoked levels of variability when we computed the trial-to-trial correlation. In addition, since these differences are absent at the spiking level, we can suppose that they do not have an impact on the spiking activity. Finally, these results allow us to refine our previous statements. Indeed, these findings suggest that V1 is sensitive to the frequencies present in the eye movements. On the first hand, eye movements increase the low frequency signal and reliability. They also decrease the response for higher frequencies. Saccades seem to have a strong impact on this interplay between high and low frequencies. On the other hand, V1 show a more reliable response, in the low frequency range, when the phase is not randomized. However, it is important to note that the difference between the evoked reliability levels is small.

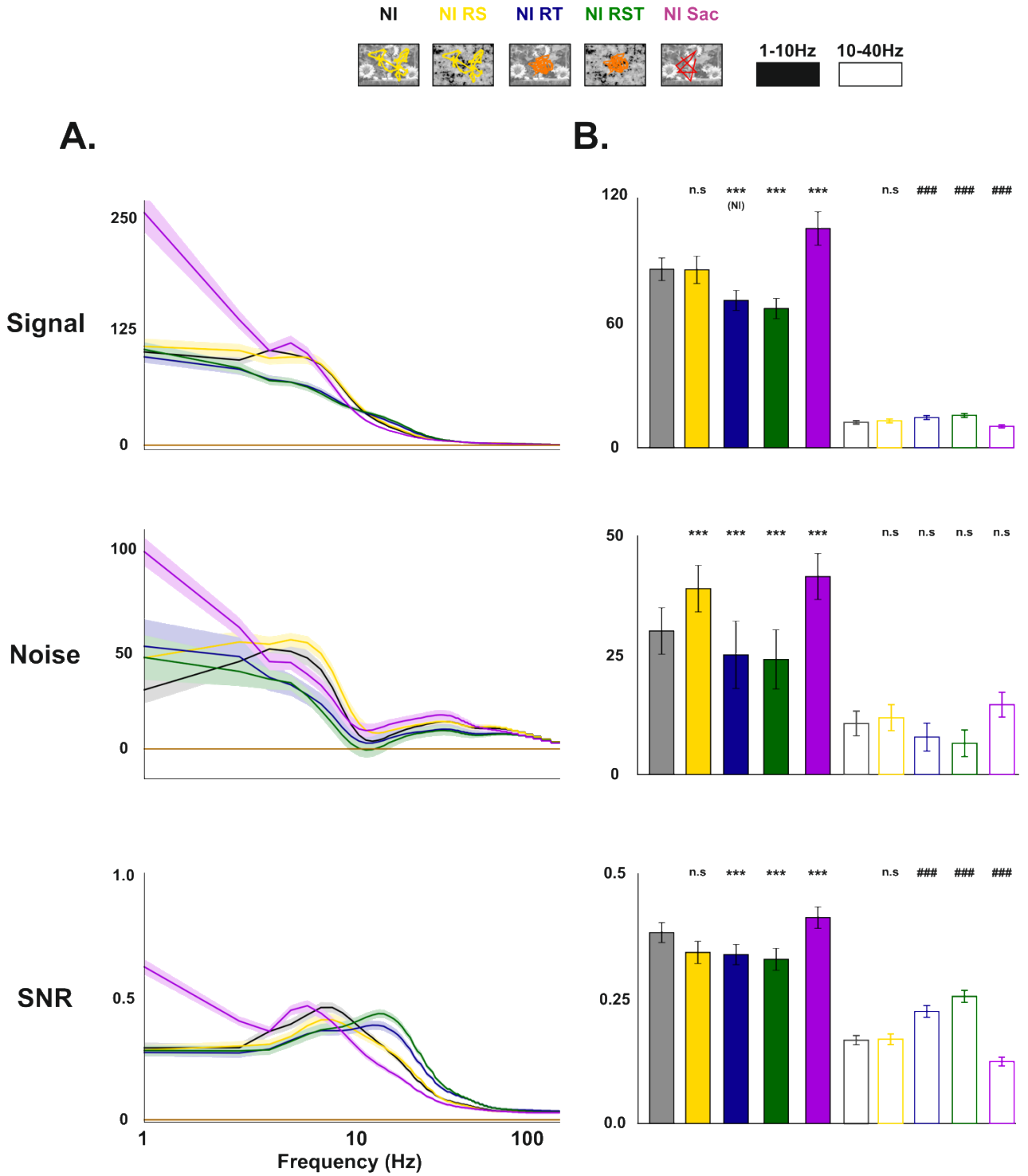

Figure 3.4.27: Mean SNR of the local field potential in response to our control stimuli. A. Mean signal (top row), noise (middle row) and SNR (bottom row) obtained for local field potential in response to our set of control stimuli (shaded area: SEM). **B.** Barplots of the mean signal (top row), noise (middle row) and SNR (bottom row) obtained for local field potential in response to our set of control stimuli *: significantly different from NI low frequency; # significantly different from NI high frequency. * : $p < 0.05$; ** : $p < 0.01$; *** : $p < 0.001$; # : $p < 0.05$; ## : $p < 0.01$; ### : $p < 0.001$. n.s: no significant difference. Error bars : SEM.

FULL FIELD	LOW FREQUENCY SIGNAL			
	DG	GEM	NI	DN
Layer 2/3	1.3 ± 0.7	60.9 ± 6.2	91.7 ± 8.3	25.1 ± 1.7
Layer 4	11.0 ± 0.9	108.7 ± 3.0	151.8 ± 4.7	60.8 ± 1.6
Layer 5/6	5.1 ± 1.1	103.2 ± 5.1	166.6 ± 9.2	51.5 ± 2.9
Mean	5.8 ± 0.9	90.9 ± 4.8	136.7 ± 7.4	45.8 ± 2.1

HIGH FREQUENCY SIGNAL			
DG	GEM	NI	DN
0.4 ± 0.2	10.7 ± 0.9	7.7 ± 0.6	9.3 ± 0.6
1.9 ± 0.2	20.1 ± 0.5	14.3 ± 0.4	24.5 ± 0.6
1.5 ± 0.2	16.5 ± 0.6	12.5 ± 0.6	15.7 ± 0.6
1.3 ± 0.2	15.7 ± 0.7	11.5 ± 0.5	16.5 ± 0.6

FULL FIELD	LOW FREQUENCY NOISE			
	DG	GEM	NI	DN
Layer 2/3	-23.5 ± 2.9	4.6 ± 1.9	9.9 ± 1.6	0.3 ± 3.2
Layer 4	-35.7 ± 2.4	5.7 ± 1.4	15.9 ± 1.6	-12.7 ± 1.7
Layer 5/6	-37.4 ± 3.4	6.4 ± 3.0	19.8 ± 2.9	-18.6 ± 2.7
Mean	-32.2 ± 2.9	5.6 ± 2.1	15.2 ± 2.0	-10.3 ± 2.5

HIGH FREQUENCY NOISE			
DG	GEM	NI	DN
-1.8 ± 0.8	1.2 ± 0.6	-0.9 ± 0.8	-1.6 ± 0.5
-1.3 ± 0.6	4.1 ± 0.3	1.6 ± 0.4	-0.7 ± 0.3
0.9 ± 0.9	7.7 ± 0.5	0.6 ± 0.6	-0.4 ± 0.5
-0.7 ± 0.8	4.3 ± 0.5	0.4 ± 0.6	-0.9 ± 0.5

FULL FIELD	LOW FREQUENCY SNR			
	DG	GEM	NI	DN
Layer 2/3	0.04 ± 0.00	0.39 ± 0.03	0.54 ± 0.05	0.21 ± 0.02
Layer 4	0.12 ± 0.01	0.62 ± 0.02	0.75 ± 0.02	0.42 ± 0.01
Layer 5/6	0.07 ± 0.01	0.54 ± 0.04	0.70 ± 0.04	0.34 ± 0.02
Mean	0.08 ± 0.00	0.51 ± 0.03	0.67 ± 0.0	0.32 ± 0.02

HIGH FREQUENCY SNR			
DG	GEM	NI	DN
0.01 ± 0.00	0.19 ± 0.01	0.14 ± 0.01	0.23 ± 0.01
0.04 ± 0.00	0.30 ± 0.01	0.22 ± 0.01	0.52 ± 0.01
0.02 ± 0.00	0.22 ± 0.01	0.19 ± 0.01	0.29 ± 0.01
0.02 ± 0.00	0.24 ± 0.01	0.18 ± 0.01	0.35 ± 0.01

Table 3.4.5: Mean low and high frequency Signal, Noise and SNR of the LFP in response to our stimulus set (Mean ± SEM)

FULL FIELD	LFP				
	NI	NI-RS	NI-RT	NI-RST	NI-SAC
SIGNAL	85.7 ± 5.4	85.4 ± 6.5	70.7 ± 4.8	66.8 ± 4.8	105.3 ± 8.0
NOISE	30.0 ± 4.8	38.9 ± 4.8	25.0 ± 7.0	24.1 ± 6.2	41.4 ± 4.8
SNR	0.38 ± 0.02	0.34 ± 0.02	0.33 ± 0.02	0.32 ± 0.02	0.41 ± 0.02

Table 3.4.6: Mean low frequency Signal, Noise and SNR of the LFP in response to our control stimulus set (Mean ± SEM)

4.1.3 Power Spectral Density and Reliability of the Local Field Potential

Our previous results showed that each stimulus elicits different levels of reliability. In particular, the local field potential that possesses different frequency signatures. The study of the LFP is based on a frequency-based decomposition of the response. These different frequencies have been linked to different tasks in visual processing. High frequencies, in particular gamma, have been linked to the filtering the irrelevant information of the stimulus representation (Brunet et al., 2015, 2014; Desimone, 1996; Gray and Singer, 1989) while low frequencies convey the most information about the stimulus (Belitski et al., 2008). Because of the importance of the different frequency bands in the LFP, we decided to extend the frequency-based analysis of this signal. A classic analysis performed on the LFP is to compute its power spectrum density (PSD). By performing a Fourier transform on the LFP signal, we obtain the distribution of power into frequency components composing the LFP. We can wonder if the frequencies eliciting the highest PSD are also the most reliable ones (The reliability of the response will be measured by computing the coherence and the SNR). Moreover, based on the frequencies linked to feedback and feedforward interactions, will we observe an increase of these frequencies in the layers associated to these interactions? We computed the mean PSD and the relative mean PSD (R-PSD) for the complete population and for each layer (Figure 3.4.28-A). The relative R-PSD was computed by dividing the mean PSD of the spontaneous activity of each recording site to the mean evoked PSD of the same recording site. As performed for the SNR we divided the frequencies in 3 bands. The low frequency band ranging from 1 to 10 Hz, the high frequency band ranging from 11 to 40 Hz and a very high frequency band, *i.e.* the gamma band, ranging from 41 to 150 Hz.

- **Mean Evoked Power Spectral Density**

Regarding the mean PSD and R-PSD (Figures 3.4.28 to 3.4.30; Tables 3.4.7 and 3.4.8) we observed that natural images evoked the highest power spectral density in the low frequency range ($p < 0.001$; Wilcoxon test). Animated gratings evoked a higher PSD, in the low frequency range, than dense noise and drifting gratings. For low frequencies, DG elicited a PSD above the one of the spontaneous activity only at the grating frequency (and its harmonics). This result has been observed in the literature (Kayser et al, 2003). The PSD in the high frequency range displayed the same pattern, but with lower values, as the one observed for the low frequencies. Surprisingly, all the stimuli evoked the same PSD in the gamma range ($p > 0.05$; Wilcoxon test). Our results show that the suppression of low frequencies by the visual stimulation is stimulus dependent.
A few differences are present between the PSD and R-PSD this is linked to the fact that we divided the mean PSD of the spontaneous activity for each channel instead of using the global mean that is plotted on figure 3.4.28.

- **Laminar Power Spectral Density**

We then investigated the laminar power spectrum density. Within layers, we found the same pattern as in the mean response, with the exception of GEM and NI that evoked a similar high frequency PSD (but not R-PSD) within layers 2/3 and 5/6 ($p > 0.05$). As observed in the other sections, the evoked PSD presented a laminar dependency. All stimuli evoked the highest low frequency PSD in layer 5/6 while the lowest one was in layer 2/3 ($p < 0.001$). This is probably linked to the intrinsic properties of each layer. Indeed layer 5/6 also evoked the highest PSD for the spontaneous activity. Thus, when we computed the R-PSD we were able to reduce the impact of the intrinsic properties

of each layer. This resulted in a different laminar response: natural images evoked the highest low frequency R-PSD in layers 4 and 5/6 ($p < 0.001$; Mann Whitney U test). On the other hand, the highest low frequency R-PSD evoked by the artificial stimuli was found in layer 4 while the lowest one was in layer 2/3 ($p < 0.001$). This laminar difference between natural and artificial stimuli was also observed in the previous sections. In conclusion, we observed, once again, that natural images induce a stronger response than the other stimuli. Based on the SNR results obtained in the previous section, it would appear that a high PSD in the low frequency range is linked to high levels of reliability at the same frequencies. Yet, this does not seem to be true for higher frequencies.

- **Frequency Based Reliability**

In order to confirm (or infirm) these observations we computed another frequency-based reliability measurement, the trial-to-trial coherence. The coherence measures the degree of the linear relationship between two LFP signals in the Fourier space. A coherence of 1 implies a very synchronized (*i.e.* reliable) for a chosen frequency while a coherence of 0 a very desynchronized (*i.e.* variable) one. The coherence and SNR results are reported in figures 3.4.28-C-D, 3.4.29-C-D and 3.4.30-C-D (see also tables 3.4.7 and 3.4.8). These two-analysis resulted in the same observations. First, as observed for the SNR natural images evoked the highest coherence in the low frequency range ($p < 0.001$, Wilcoxon test). Second, among the artificial stimuli, animated gratings evoked the highest low frequency levels of reliability while drifting gratings evoked the less reliable response ($p < 0.001$). Third, dense noise evoked the highest high frequency reliability ($p < 0.001$). The peak value observed at 70Hz for DN, and absent for the other stimuli, might be linked to the stimulus frequency. Indeed, dense noise is the only stimulus to evoke a locked and reliable LFP response in these frequencies. Unlike the other stimuli, dense noise contains an important amount of high frequencies. Another notable difference was the fact that dense noise evoked a low R-PSD for frequencies between 10 and 40Hz but a reliable response in this frequency band. This suggest that a strong spectral density does not imply a strong reliability and that a locked and reliable response to the stimulus does not always evoke an increase in PSD higher than the one observed for the spontaneous activity. Thus, only a frequential analysis of the reliability can highlight these specific modulations. Regarding the laminar reliability, natural images evoked an equivalent low frequency coherence in layers 4 and 5/6 ($p = 0.14$), higher than the one in layer 2/3 ($p < 0.001$). The artificial stimuli evoked their highest levels of reliability in layer 4 and the lowest in layer 2/3 ($p < 0.001$). Dense noise evoked the highest high frequency coherence in layer 4. In addition, when dense noise was presented, the LFPs in layer 4 evoked a more reliable response in the high frequency range than in the low frequency one ($p < 0.01$). In conclusion, our coherence results confirm the ones obtained by computing the signal to noise ratio and show that the stimuli modulate the response reliability in a specific way.

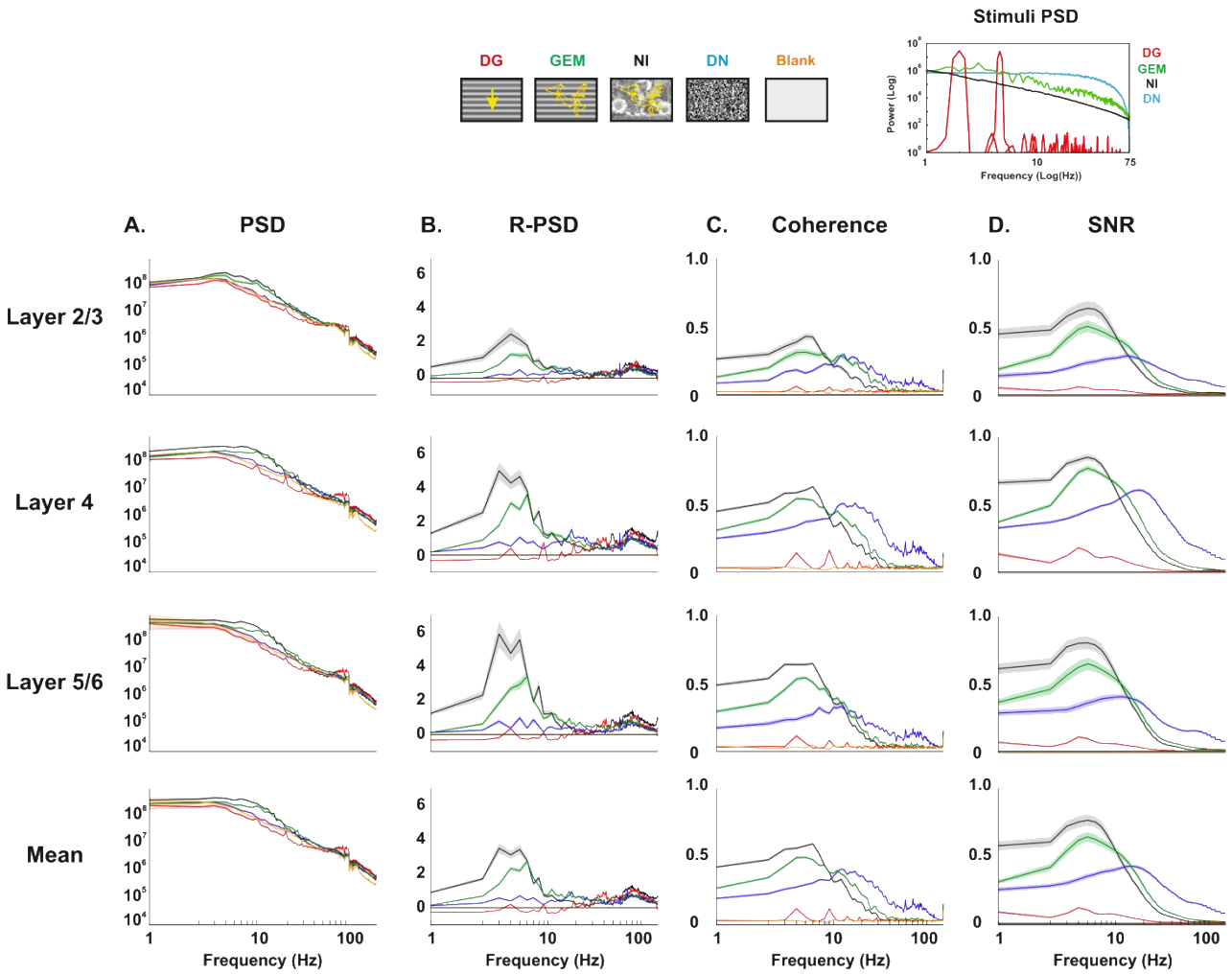

Figure 3.4.28: Frequency based analysis of the local field potential in response to our set of stimuli. For all analysis, natural images display an increase in the low frequency range. **A.** Mean Power Spectrum Density across layers and for the complete population. **B.** Mean Relative Power Spectrum Density across layers and for the complete population**. C.** Mean Coherence across layers and for the complete population. **D.** Mean SNR across layers and for the complete population.

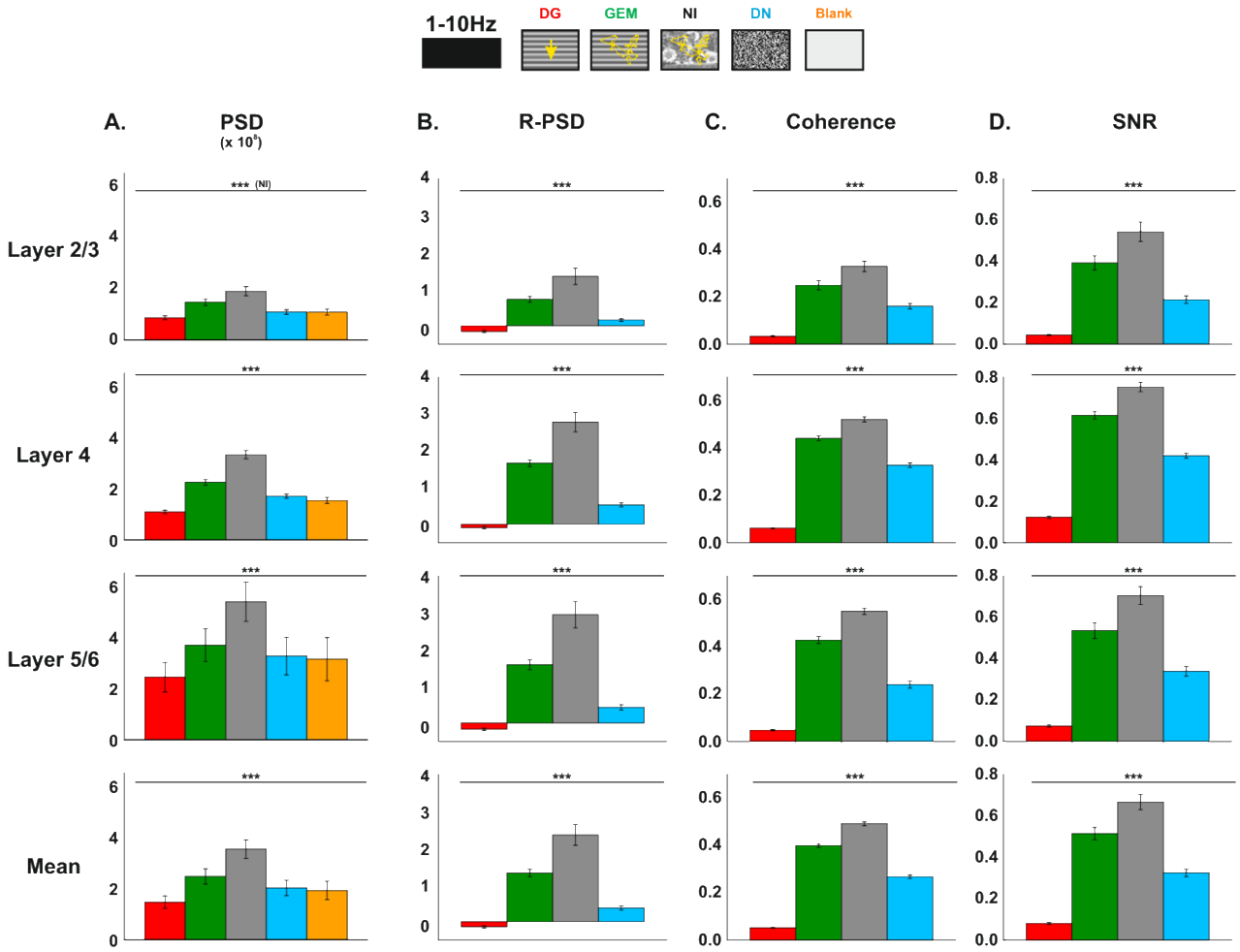

Figure 3.4.29: Bar plots of the low frequency-based analysis of the LFP in response to our stimulus set. A. Mean Power Spectrum Density across layers and for the complete population. **B.** Mean Relative Power Spectrum Density across layers and for the complete population. **C.** Mean Coherence across layers and for the complete population. **D.** Mean SNR across layers and for the complete population. *: significantly different from NI * : $p < 0.05$; ** : $p < 0.01$; *** : $p < 0.001$. Error bars : SEM.

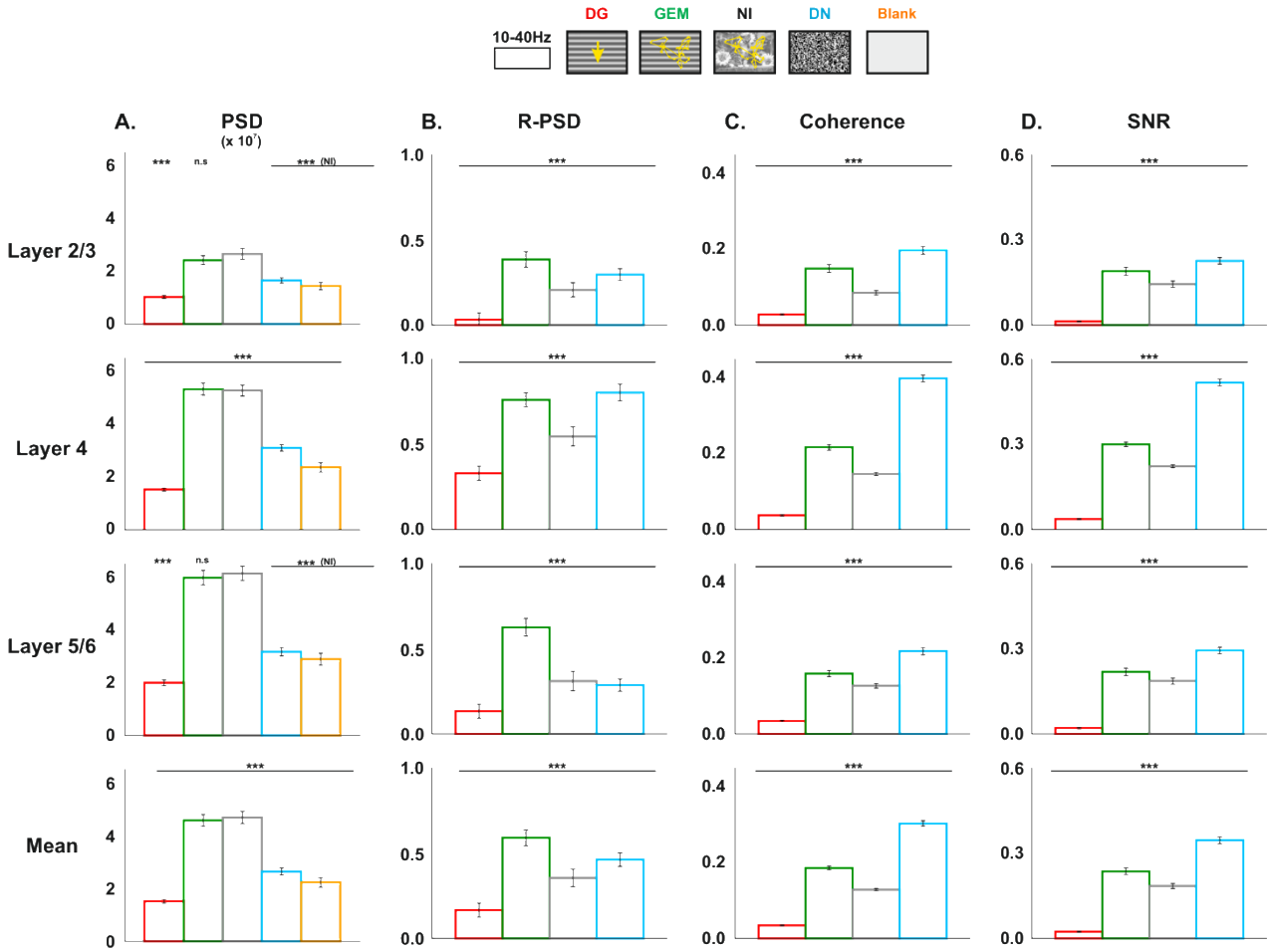

Figure 3.4.30: Bar plots of the high frequency-based analysis of the LFP in response to our stimulus set. A. Mean Power Spectrum Density across layers and for the complete population. **B.** Mean Relative Power Spectrum Density across layers and for the complete population. **C.** Mean Coherence across layers and for the complete population. **D.** Mean SNR across layers and for the complete population. *: significantly different from NI * : $p < 0.05$; ** : $p < 0.01$; *** : $p < 0.001$. Error bars : SEM.

- **Impact of the natural statistics on the power spectral density**

Since we observed the control stimuli evoked differences in reliability at different frequency ranges we wondered if an impact would be observed on the PSD (and R-PSD). For both PSD and R-PSD, all altered natural images evoked different power than the unaltered natural image ($p < 0.001$, Wilcoxon test, Figure 3.4.31, table 3.4.9). At the low frequency range, NI-SAC evoked the strongest response while NI-RT and NI-RST the lowest one. Unlike what was observed for the SNR, NI-RS evoked a higher low frequency response than the unaltered NI ($p < 0.001$). At the high frequency range, NI-SAC evoked the highest PSD while NI-RT and NI-RST the lowest ones. ($p < 0.001$). Finally, at the very high frequency range, all stimuli evoked the same PSD ($p > 0.05$).
We then computed the coherence evoked by our control stimuli in order to compare it to the SNR. Again, both analyses resulted in the same patterns except between NI-RS and NI. Indeed, with the coherence analysis, the unaltered natural images evoked a more reliable response in the low frequency range than NI-RS but a less reliable one in the high frequency range ($p < 0.001$). However the levels of reliability evoked by these stimuli are very similar.
In conclusion, our coherence results confirm the ones obtained by computing the signal to noise ratio and validate our previous statements.

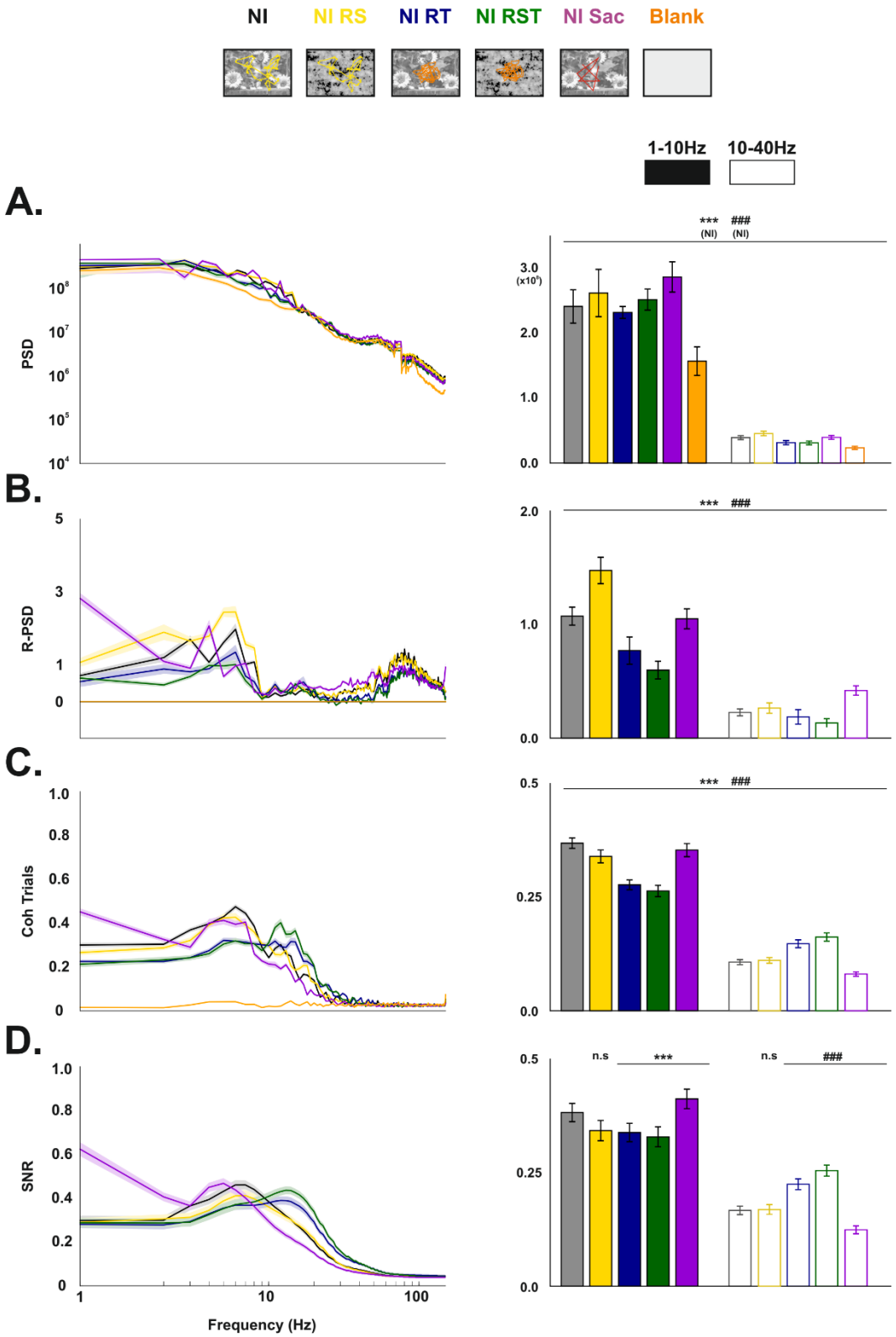

Figure 3.4.31: A. Mean PSD and barplots for low and high frequencies on response to the set of control stimuli. **B.** Mean R-PSD and barplots for low and high frequencies on response to the set of control stimuli. **C.** Mean Coherence and barplots for low and high frequencies on response to the set of control stimuli. **D.** Mean SNR and barplots for low and high frequencies on response to the set of control stimuli *: significantly different from NI low frequency; # significantly different from NI high frequency. * : $p < 0.05$; ** : $p < 0.01$; *** : $p < 0.001$; # : $p < 0.05$; ## : $p < 0.01$; ### : $p < 0.001$. n.s: no significant difference. Error bars and shaded area : SEM

.

FULL FIELD	LOW FREQUENCY PSD				
	DG	GEM	NI	DN	BLK
Layer 2/3	8.6e+07 ± 8.3e+06	1.5e+08 ± 1.4e+07	1.9e+08 ± 1.8e+07	1.1e+08 ± 9.2e+06	1.1e+08 ± 1.2e+07
Layer 4	1.1e+08 ± 7.3e+06	2.2e+08 ± 1.1e+07	3.3e+08 ± 1.6e+07	1.7e+08 ± 8.1e+06	1.5e+08 ± 1.2e+07
Layer 5/6	2.4e+08 ± 5.7e+07	3.7e+08 ± 6.4e+07	5.4e+08 ± 7.6e+07	3.3e+08 ± 7.3e+07	3.1e+08 ± 8.4e+07
Mean	1.5e+08 ± 2.4e+07	2.5e+08 ± 3.0e+07	3.5e+08 ± 3.7e+07	2.0e+08 ± 3.0e+07	1.9e+08 ± 3.6e+07

FULL FIELD	LOW FREQUENCY Coherence			
	DG	GEM	NI	DN
Layer 2/3	0.03 ± 0.00	0.25 ± 0.02	0.33 ± 0.02	0.16 ± 0.01
Layer 4	0.06 ± 0.00	0.44 ± 0.01	0.52 ± 0.01	0.33 ± 0.01
Layer 5/6	0.05 ± 0.00	0.43 ± 0.01	0.55 ± 0.01	0.24 ± 0.02
Mean	0.05 ± 0.00	0.40 ± 0.01	0.49 ± 0.01	0.27 ± 0.01

FULL FIELD	LOW FREQUENCY R-PSD			
	DG	GEM	NI	DN
Layer 2/3	-0.16 ± 0.03	0.72 ± 0.07	1.34 ± 0.22	0.16 ± 0.04
Layer 4	-0.09 ± 0.03	1.66 ± 0.09	2.78 ± 0.26	0.53 ± 0.06
Layer 5/6	-0.17 ± 0.03	1.58 ± 0.14	2.94 ± 0.36	0.43 ± 0.07
Mean	-0.14 ± 0.02	1.31 ± 0.07	1.95 ± 0.15	0.36 ± 0.03

FULL FIELD	LOW FREQUENCY SNR			
	DG	GEM	NI	DN
Layer 2/3	0.04 ± 0.00	0.39 ± 0.03	0.54 ± 0.05	0.21 ± 0.02
Layer 4	0.12 ± 0.01	0.62 ± 0.02	0.75 ± 0.02	0.42 ± 0.01
Layer 5/6	0.07 ± 0.01	0.54 ± 0.04	0.70 ± 0.04	0.34 ± 0.02
Mean	0.08 ± 0.00	0.51 ± 0.03	0.67 ± 0.0	0.32 ± 0.02

Figure 3.4.7: Mean low frequency PSD, R-PSD, Coherence and SNR in response to our stimulus set (Mean ± SEM)

FULL FIELD	HIGH FREQUENCY PSD				
	DG	GEM	NI	DN	BLK
Layer 2/3	1.0e+07 ± 6.0e+05	2.4e+07 ± 1.7e+06	2.7e+07 ± 2.1e+06	1.6e+07 ± 1.1e+06	1.4e+07 ± 1.4e+06
Layer 4	1.5e+07 ± 5.5e+05	5.3e+07 ± 2.3e+06	5.3e+07 ± 2.0e+06	3.1e+07 ± 1.2e+06	2.4e+07 ± 1.7e+06
Layer 5/6	2.0e+07 ± 1.1e+06	6.0e+07 ± 2.8e+06	6.1e+07 ± 2.7e+06	3.2e+07 ± 1.6e+06	2.9e+07 ± 2.3e+06
Mean	1.5e+07 ± 7.6e+05	4.6e+07 ± 2.2e+06	4.7e+07 ± 2.3e+06	2.6e+07 ± 1.3e+06	2.2e+07 ± 1.8e+06

FULL FIELD	HIGH FREQUENCY R-PSD			
	DG	GEM	NI	DN
Layer 2/3	0.03 ± 0.04	0.38 ± 0.05	0.21 ± 0.04	0.30 ± 0.04
Layer 4	0.33 ± 0.04	0.76 ± 0.04	0.55 ± 0.06	0.80 ± 0.05
Layer 5/6	0.13 ± 0.04	0.63 ± 0.05	0.31 ± 0.06	0.29 ± 0.04
Mean	0.21 ± 0.03	0.59 ± 0.03	0.30 ± 0.03	0.50 ± 0.03

FULL FIELD	HIGH FREQUENCY Coherence			
	DG	GEM	NI	DN
Layer 2/3	0.03 ± 0.00	0.15 ± 0.01	0.09 ± 0.01	0.20 ± 0.01
Layer 4	0.04 ± 0.00	0.22 ± 0.01	0.15 ± 0.00	0.40 ± 0.01
Layer 5/6	0.03 ± 0.00	0.16 ± 0.01	0.13 ± 0.01	0.22 ± 0.01
Mean	0.03 ± 0.00	0.19 ± 0.01	0.13 ± 0.00	0.30 ± 0.01

FULL FIELD	HIGH FREQUENCY SNR			
	DG	GEM	NI	DN
Layer 2/3	0.01 ± 0.00	0.19 ± 0.01	0.14 ± 0.01	0.23 ± 0.01
Layer 4	0.04 ± 0.00	0.30 ± 0.01	0.22 ± 0.01	0.52 ± 0.01
Layer 5/6	0.02 ± 0.00	0.22 ± 0.01	0.19 ± 0.01	0.29 ± 0.01
Mean	0.02 ± 0.00	0.24 ± 0.01	0.18 ± 0.01	0.35 ± 0.01

Figure 3.4.8: Mean high frequency PSD, R-PSD, Coherence and SNR in response to our stimulus set (Mean ± SEM)

	FULL FIELD					
	NI	NI-RS	NI-RT	NI-RST	NI-SAC	BLK
PSD	2.4e+08 ± 2.5e+07	2.6e+08 ± 3.6e+07	2.3e+08 ± 9.2e+06	2.5e+08 ± 1.6e+07	2.8e+08 ± 2.3e+07	1.5e+08 ± 2.2e+07
R-PSD	1.07 ± 0.07	1.47 ± 0.11	0.77 ± 0.12	0.59 ± 0.07	1.05 ± 0.08	X
Coherence	0.37 ± 0.01	0.34 ± 0.01	0.28 ± 0.01	0.26 ± 0.01	0.35 ± 0.01	X
SNR	0.38 ± 0.02	0.34 ± 0.02	0.34 ± 0.02	0.33 ± 0.02	0.41 ± 0.02	X

Figure 3.4.9: Mean high frequency PSD, R-PSD, Coherence and SNR in response to our control stimulus set (Mean ± SEM)

4.1.4 Spectral Analysis of the Unlocked Local Field Potential

We also computed the frequency content of the non-locked stimulus dependent part of the signal. Indeed, by subtracting the mean evoked LFP over trials from each trial, we separated the component of the LFP that is stimulus-locked by the stimulus from the component evoked by the presence of the stimuli but unlocked to its presentation. Will the different stimuli elicit a particular unlocked response or are will they be equivalent? In order to investigate the link between the LFP the unlocked LFP and our stimuli we computed the PSD and the R-PSD. To obtain the relative power spectrum density (R-PSD), we divided from the mean PSD at each recording site the mean PSD of the spontaneous activity. Low and high frequencies have respectively been linked to feedback and feedforward processing (Bastos et al., 2015; van Kerkoerle et al., 2014). Precisely, feedback has been associated to alpha (Van Kerkoerle et al, 2014) or beta bands (Bastos et al, 2015) while feedforward has been associated with gamma bands. Based on these results, we should expect a stronger gamma band in the layers receiving feedforward inputs i.e. layers 4 and 6 while a stronger alpha/beta band should be observed in layers 2/3 and 5. One could argue that feedback is not present in anesthetized animals, however recent studies observed feedback interactions on anesthetized monkeys (Bijanzadeh et al., 2018).

- **Mean evoked Unlocked PSD**

Our results are reported in figures 3.4.32 and 3.4.33 table 3.4.10. All stimuli evoked an equally negative relative power spectrum density between 1 and 4 Hz. In addition, our results show that the main responses are between 4-20 Hz and 40-150 Hz. Therefore, we modified the frequency bands of interest. We focused on a mixture between low and high frequencies, ranging from 4 to 20Hz, *i.e.* the alpha band and on a very high frequency band ranging from 40 to 150 Hz *i.e.* the gamma band. These frequencies correspond to the frequencies linked to feedback and feedforward activities, respectively (Van Kerkoerle et al. 2014).
We first computed the mean PSD (and R-PSD) across the complete population. The mean PSD of the unlocked LFP resulted in an increase of the power in the alpha for the NI and GEM conditions while DN and GEM evoked a PSD lower than the spontaneous one ($p < 0.001$; Friedman test test). Animated gratings and natural images evoked close PSD values in these frequencies. However, GEM value was significantly higher than the NI one ($p < 0.001$). Because only the stimuli that are animated with eye movement show this increase, it suggests that the “uncertainty” brought by the eye movements this increase. The eye movements might create prediction error message that is conveyed by feedback, thus inducing an increase in the alpha band (VanRullen et al., 2011). In the gamma band, DG evoked the highest power spectral density. In addition, NI evoked a higher PSD than GEM and DN (but GEM and NI power spectrums are similar, as observed for the intermediate frequencies ($p < 0.001$)). Interestingly, NI and DG evoke the same PSD for frequencies above 100 Hz. The main difference comes from frequencies between 60 and 100Hz. This could be linked to the fact that the repeated presentation of gratings induce an increase in this frequency band (Brunet et al., 2011).

- **Laminar Unlocked PSD**

We observed a laminar dependency of the response when we investigated the PSD of the stimulus locked LFP. In addition, if feedback messages are visible in the alpha band, the layers receiving these inputs should display a strong PSD for these frequencies.

We computed the PSD and R-PSD of the unlocked LFP across all layers. Within each layer, the power spectrum density resulted in the same pattern of response as the one observed in for the mean, except for two exceptions. Indeed, in layer 2/3, GEM and NI evoked the same PSD in the alpha band while DG and NI displayed the same PSD in the gamma band ($p > 0.05$). We then compared the PSD between layers. Regarding the PSD, for all stimuli respectively (and for alpha and gamma bands), we observed the highest power in layer 5/6 and the lowest in layer 2/3 ($p < 0.001$; Kruskal-Wallis test). These results match the findings of Van Kerkoerle and colleagues (2014), with a strong PSD in the alpha band, linked to the feedback interactions. However, as observed for the locked response, we also observed evoked the highest PSD of the spontaneous activity in layer 5/6. Therefore, by computing the relative PSD we were able to reduce the impact of the spontaneous activity on the response. This led to a different PSD pattern in the alpha band. Indeed, for GEM and NI, the highest power spectrum was found in layer 4 and the lowest in layer 5/6. At these frequencies, DG and DN showed a similar laminar pattern of PSD and R-PSD. Alpha has been linked to prediction error messages and eye movements induce unpredictable responses (VanRullen et al., 2011). The fact that only animated gratings and natural images display an increase in the alpha band suggest that this boost is linked to a prediction error message. It is important to note that we computed the PSD of the complete 10 seconds of stimulation. By computing the PSD right after the saccades we might obtain a different laminar pattern with higher PSDs in the layers receiving feedback inputs (2/3 and 5/6). On the other hand, at the gamma band, all stimuli evoked the highest R-PSD in layer 4 and the lowest in layer 2/3, matching again the observations of Van Kerkoerle and colleagues (2014). In conclusion, the unlocked LFP unveiled a possible prediction error message induced by eye movements transmitted through feedback. We also observed the supposedly impact of the feedforward interactions through the increase in the gamma band.

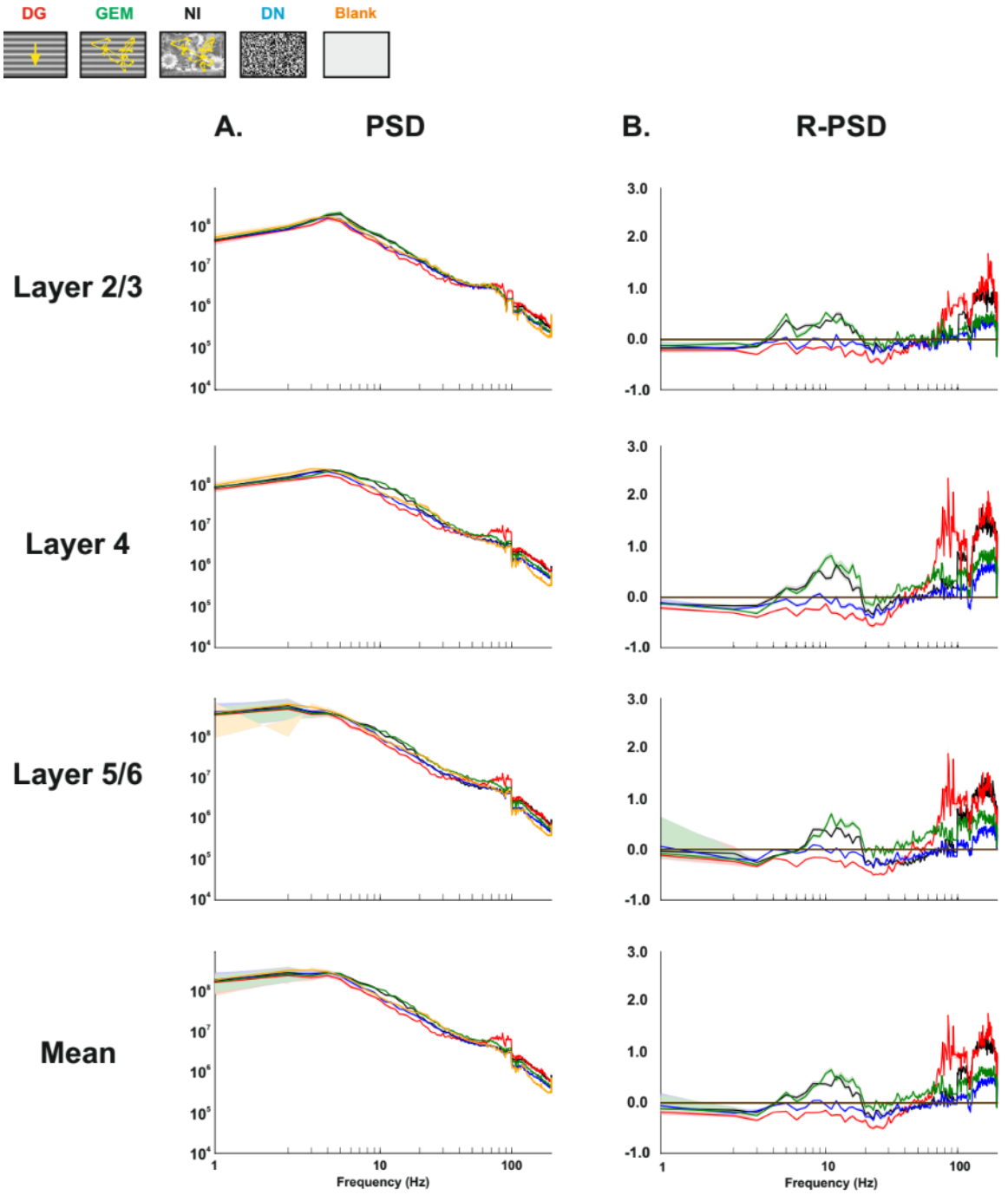

Figure 3.4.32: Spectral density of the unlocked LFP in response to our set of stimuli. An increase in the frequencies linked to feedback is observed for GEM and NI. All stimuli displayed an increased linked to the feedforward frequencies. **A**. Spectral density across the population and within layers**. B.** relative spectral density across the population and within layers.

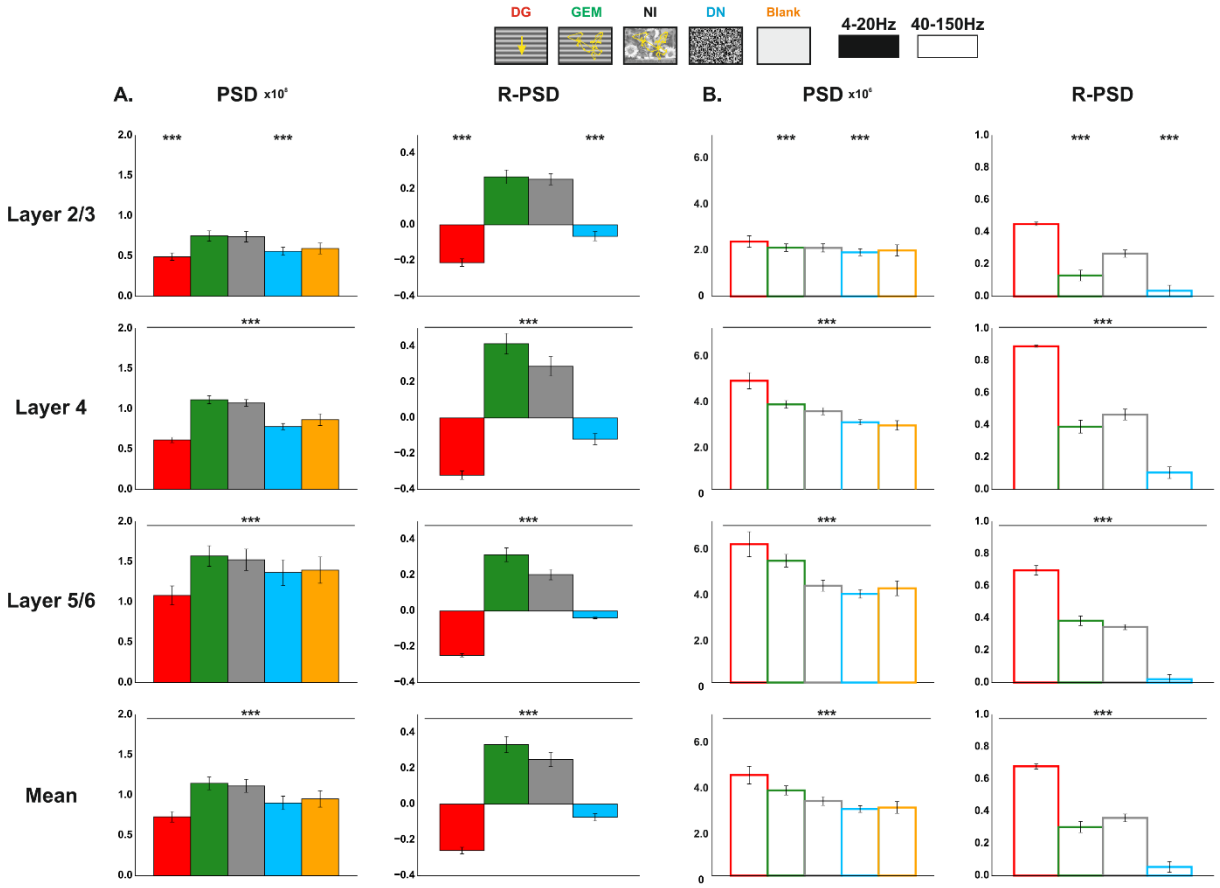

Figure 3.4.33: Barplots of the spectral density analysis of the unlocked PSD. A. Bar plots obtained for the alpha band. B. Bar plots obtained for the gamma band.

- **Impact of the natural statistics on the unlocked LFP**

However, we need to confirm that this increase in PSD observed for both GEM and NI is linked to the eye movements. In order to investigate this question, we computed the PSD of the unlocked LFP that we obtained in response to our control stimuli (Figure 3.4.34; table 3.4.11).
Again, we did not observe any difference between the stimuli between 1 and 4Hz ($p > 0.05$).
For the alpha band, natural images PSD (and R-PSD) was higher than the ones evoked by NI-RT and NI-RST ($p < 0.001$; Wilcoxon test). NI-RS evoked a higher power spectrum than NI. This result is in agreement with the prediction error theory. Indeed, by randomizing the phase of the image we increase the error messages. Interestingly, the mean PSD of the NI and NI-SAC conditions were equal. However, NI-SAC displayed 3 peaks, one at 4Hz, one at 9H and one around 20Hz, absent in the NI condition. The natural images showed a smoother response, without peaks. This suggest that these peaks are linked to the saccades. In the alpha band, the PSD was or less powerful if the spatio-temporal statistics were both altered. Thus, the natural images containing unaltered eye movements or only saccades displayed the most powerful densities. This suggest a strong impact of the eye movements in the prediction error message. In conclusion, we showed that the PSD increase observed for NI and GEM in the intermediate frequencies could be linked to the prediction error message induced of the eye movements.

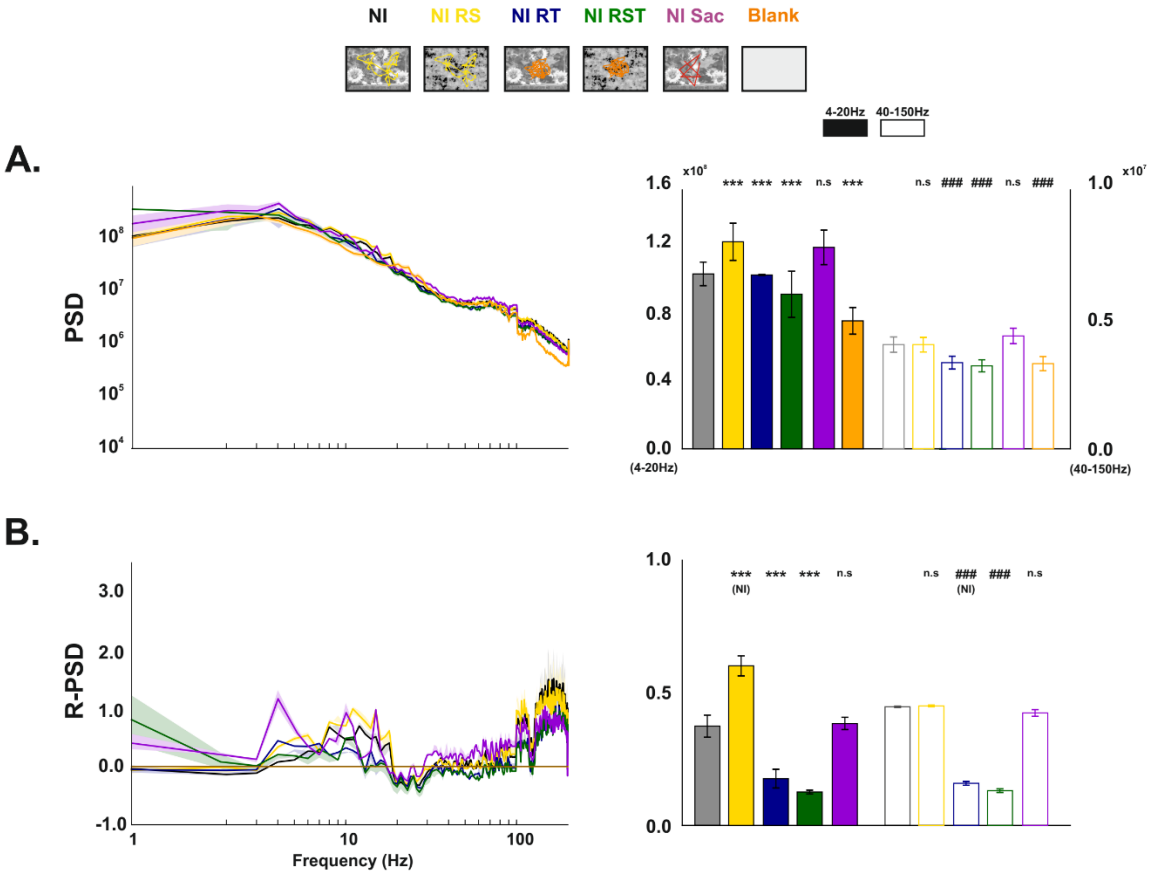

Figure 3.4.34: Frequency based analysis of the contextual local field potential in response to our set of control stimuli. A. Mean Power Spectrum Density for the complete population. Left panels: Mean PSD. Right Panels: Barplots of the mean PSD for frequencies between 4-20Hz and 40-150Hz. B. Mean Relative Power Spectrum Density for the complete population. Left panels: Mean R-PSD. Right Panels: Barplots of the mean R-PSD for frequencies between 4-20Hz and 40-150Hz.*: significantly different from NI intermediate frequency; # significantly different from NI very high frequency. * : $p < 0.05$; ** : $p < 0.01$; *** : $p < 0.001$; # : $p < 0.05$; ## : $p < 0.01$; ### : $p < 0.001$. n.s: no significant difference. Error bars and shaded area: SEM.

FULL FIELD	ALPHA BAND PSD				
	DG	GEM	NI	DN	BLK
Layer 2/3	4.9e+07 ± 4.6e+06	7.5e+07 ± 6.4e+06	7.4e+07 ± 6.6e+06	5.6e+07 ± 5.0e+06	6.0e+07 ± 6.8e+06
Layer 4	6.1e+07 ± 3.3e+06	1.1e+08 ± 4.9e+06	1.1e+08 ± 4.2e+06	7.8e+07 ± 3.9e+06	8.7e+07 ± 7.4e+06
Layer 5/6	1.1e+08 ± 1.2e+07	1.6e+08 ± 1.3e+07	1.5e+08 ± 1.3e+07	1.4e+08 ± 1.6e+07	1.4e+08 ± 1.6e+07
Mean	7.3e+07 ± 6.5e+06	1.1e+08 ± 8.0e+06	1.1e+08 ± 8.0e+06	9.0e+07 ± 8.2e+06	9.5e+07 ± 1.0e+07

FULL FIELD	ALPHA BAND R-PSD			
	DG	GEM	NI	DN
Layer 2/3	-0.21 ± -0.02	0.27 ± -0.04	0.25 ± -0.03	-0.06 ± -0.03
Layer 4	-0.32 ± -0.02	0.42 ± -0.06	0.29 ± -0.05	-0.12 ± -0.03
Layer 5/6	-0.25 ± -0.01	0.31 ± -0.04	0.20 ± -0.03	-0.04 ± -0.00
Mean	-0.26 ± -0.02	0.33 ± -0.04	0.25 ± -0.04	-0.07 ± -0.02

FULL FIELD	GAMMA BAND PSD				
	DG	GEM	NI	DN	BLK
Layer 2/3	2.4e+06 ± 2.5e+05	2.1e+06 ± 1.6e+05	2.1e+06 ± 1.8e+05	1.9e+06 ± 1.5e+05	2.0e+06 ± 2.4e+05
Layer 4	4.7e+06 ± 3.5e+05	3.7e+06 ± 1.7e+05	3.4e+06 ± 1.6e+05	2.9e+06 ± 1.2e+05	2.8e+06 ± 2.0e+05
Layer 5/6	6.0e+06 ± 5.4e+05	5.3e+06 ± 2.8e+05	4.2e+06 ± 2.4e+05	3.9e+06 ± 1.8e+05	4.1e+06 ± 3.2e+05
Mean	4.4e+06 ± 3.8e+05	3.7e+06 ± 2.0e+05	3.2e+06 ± 1.9e+05	2.9e+06 ± 1.5e+05	3.0e+06 ± 2.6e+05

FULL FIELD	GAMMA BAND R-PSD			
	DG	GEM	NI	DN
Layer 2/3	0.45 ± 0.01	0.13 ± -0.03	0.27 ± -0.02	0.04 ± -0.03
Layer 4	0.89 ± 0.01	0.39 ± -0.04	0.47 ± -0.03	0.10 ± -0.04
Layer 5/6	0.70 ± 0.03	0.38 ± -0.03	0.34 ± -0.02	0.02 ± -0.03
Mean	0.68 ± 0.02	0.30 ± -0.03	0.36 ± -0.02	0.05 ± -0.03

Table 3.4.10: Mean low and high frequency unlocked PSD and R-PSD in response to our stimulus set (Mean ± SEM)

FULL FIELD (ALPHA BAND)						
	NI	NI-RS	NI-RT	NI-RST	NI-SAC	BLK
PSD	1.01e+08 ± 6.83e+06	1.20e+08 ± 1.08e+07	1.01e+08 ± -2.99e+05	8.95e+07 ± 1.34e+07	1.17e+08 ± 1.00e+07	7.42e+07 ± 7.71e+06
R-PSD	0.374 ± -0.042	0.601 ± -0.038	0.176 ± 0.035	0.126 ± 0.007	0.384 ± -0.023	X

FULL FIELD (GAMMA BAND)						
	NI	NI-RS	NI-RT	NI-RST	NI-SAC	BLK
PSD	4.03e+06 ± 2.94e+05	4.02e+06 ± 2.83e+05	3.33e+06 ± 2.49e+05	3.21e+06 ± 2.34e+05	4.36e+06 ± 2.97e+05	3.29e+06 ± 2.74e+05
R-PSD	0.447 ± 0.003	0.451 ± -0.003	0.158 ± -0.007	0.131 ± -0.007	0.424 ± -0.013	X

Table 3.4.11: Mean low and high frequency unlocked PSD and R-PSD in response to our control stimulus set (Mean ± SEM)

4.2. Impact of the center surround interactions

In the previous sections, we showed that the center surround interactions modulate the spiking activity, in particular when natural images are presented. In addition, we showed, by computing a time frequency analysis, that natural images presented full field evoked a reliable response between 1-10Hz at the opposite of drifting gratings that only evoked a reliable response at the grating frequency. Based on these results, we wondered if the center surround interactions modulate the reliability in this frequency range or if a different behavior will be observed. In addition, it is known that layer 4 responses contain more high frequencies than the other layers (Maier et al., 2010) will these center surround interactions impact all the layers in the same frequency ranges?

4.2.1 Time Frequency Analysis of the Spiking Activity

We computed the time frequency analysis of the spiking activity (SUA & MUA) evoked by our set of stimuli presented full field or only on the center (Figures 3.4.44 to 3.4.49 & Tables 3.4.12 and 3.4.13) We did not investigate the response to the surround because, as showed in the previous sections, the latter evokes no stimulus locked response.

- **Impact of the center surround interactions on the SNR**

The time frequency analysis of the spiking activity (both SUA & MUA) showed that the center conditions evoked a similar response pattern as the full field. Thus, we will only focus on the impact of the center surround interactions for each stimulus, respectively. The concomitant stimulation of both center and surround with natural images evoked a more reliable response, in the low frequency range, than the sole stimulation of the center ($p < 0.001$; Wilcoxon test). This increase is linked to a higher signal evoked by the full field condition, but also a higher noise. Yet, the increase in noise is not a strong as the one observed for the signal, leading to a higher SNR for the full field condition (Figures 3.4.44 & 3.4.45; table 3.4.12). Dense noise also evoked higher levels of reliability, in the low frequency range, for the full field condition. As observed for NI, this is linked to the fact that the FF condition evoked a higher signal and noise ($p < 0.001$). Finally, no significant difference was observed between the FF and C conditions when drifting gratings were presented despite a higher mean low frequency SNR being observed for the center.
At the multi-unit level (Figures 3.4.48 & 3.4.49; table 3.4.13), in response to natural images and dense noise, we observed the same impact of the center surround interactions as in the single unit population. At this scale, drifting gratings evoked a significantly higher low frequency signal and noise when presented in the center ($p < 0.001$). This simultaneous increase led to an absence of difference in reliability between the FF and C conditions.
Our previous results showed that both fast spiking and regular spiking and fast spiking neurons were impacted by center surround interactions when natural images were presented. Based on these results we wondered if the same pattern would be observed by computing a time frequency analysis (Figures 3.4.50 to 3.4.53; Table 3.4.14 and 3.4.15).The two neuronal subtypes displayed the same pattern of center surround modulations, in the low frequency range, as the complete single unit population.
At the high frequency level (and for both SUA and MUA), dense noise and natural images evoked higher levels of reliability when presented full field. This higher reliability originates from the generation a higher noise and a higher signal when both center and surround were stimulate ($p < 0.001$). No difference was observed for DG.

- **Laminar impact of the center surround interactions**

Our previous results showed that the center surround interactions also modulated the reliability levels across layers. This was also observed for the signal to noise ratio.
Indeed, at the single unit level (Figures 3.4.44 & 3.4.45; table 3.4.12), the full field presentation of natural images evoked the highest low frequency SNR in both layers 4 and 5/6 ($p < 0.001$). In both layers, this is linked to a higher low frequency signal evoked by the FF condition. The FF condition also evoked a higher low frequency noise in layer 4, while no difference was observed between the two conditions in layer 5/6 (despite a higher mean low frequency noise evoked by the FF). On the other hand, no significant difference in reliability was observed in layer 2/3. This is probably linked to the small number of neurons recorded in this layer (10). The Dense noise displayed the same response pattern as natural excepts with one exception: the full field condition evoked higher levels of reliability in layer 2/3 ($p < 0.05$). Finally, as observed for the mean population, no significant difference in reliability between the two conditions was observed in response to DG (despite a higher mean reliability evoked by the center condition). The almost same pattern of responses was observed at the multi-unit level. The main difference lied on the fact the differences that were not significant for the single unit are for the MUA (Figures 3.4.48 & 3.4.49; table 3.4.13). It is important to note that the difference in reliability evoked by the presentation of natural images full field or only on the center are higher in the layers containing horizontal connections (table 3.4.13). This suggest that in these layers (2/3 and 5/6), these connections play an important part in the generation of a reliable response.
Regarding the single unit subpopulations, regular spiking cells displayed the same modulation as the complete population. On the other hand, fast spiking cells were only modulated by the center surround interactions in layer 4.
Across layers, for both SUA and MUA, the high frequency reliability displayed the same pattern as the one observed for the complete population ((Figures 3.4.44 & 3.4.46; 3.4.47 & 3.4.49; tables 3.4.12 and 3.4.13).

In summary, we showed that the spiking activity is modulated by the center surround interactions. This modulation is particularly visible at the low frequency range. This suggests that the modulations that we observed with non-frequency measurements originate from these frequencies. The reliability observed for natural images is the result of the generation of a strong signal in these low frequency bands that compensates the noise increase. Finally, we showed again, that the multi-unit activity is a more reliable signal than the single unit activity. This suggest that in order to process a visual input and transmit it to different visual areas, the activity of many neurons might be needed.

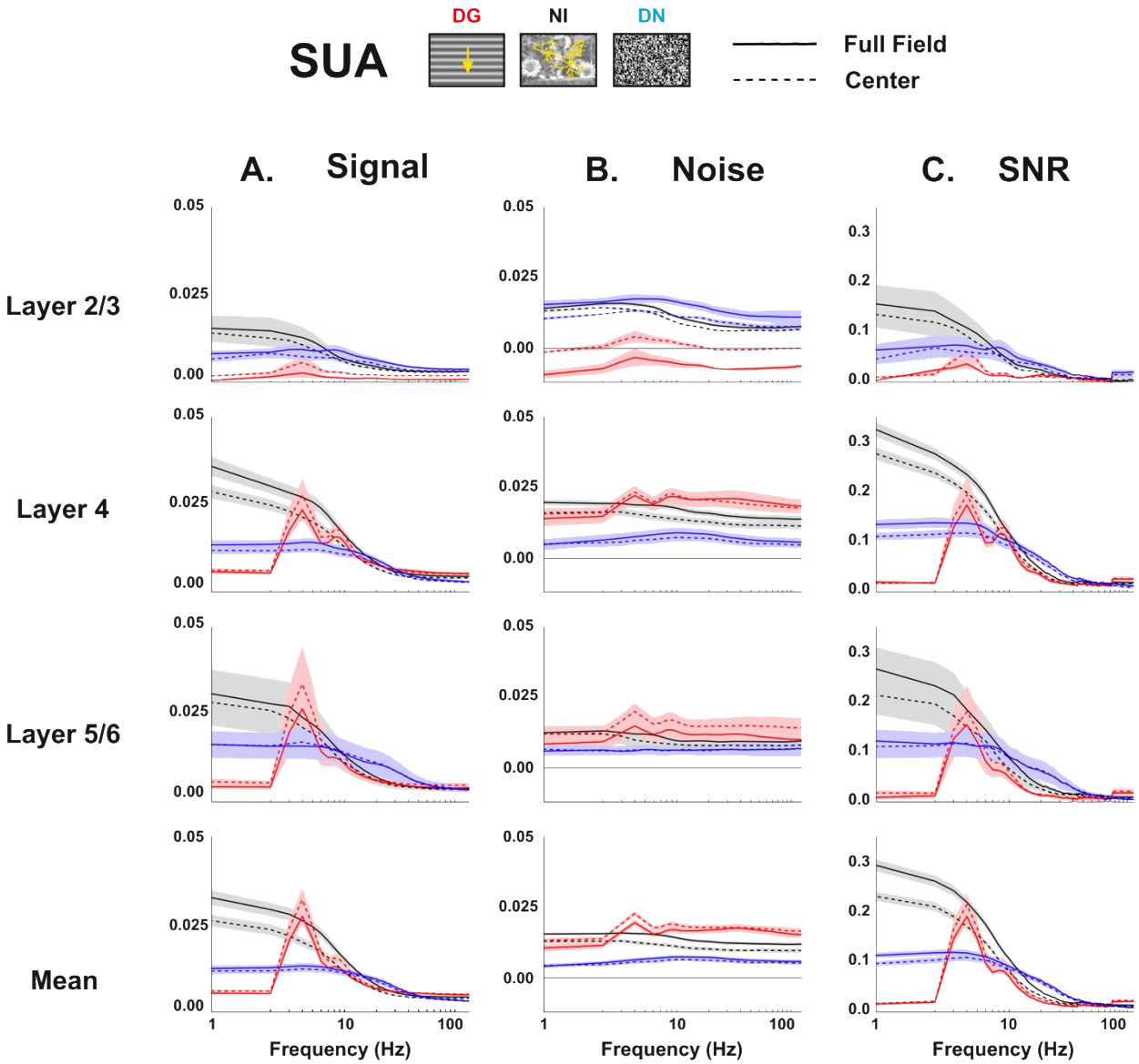

Figure 3.4.44.: Mean and laminar SNR of the single unit activity in response to natural and artificial stimuli presented on the full field (full line) and center (big dashed lines) conditions. The center surround interactions increase the reliability evoked by Natural Images.

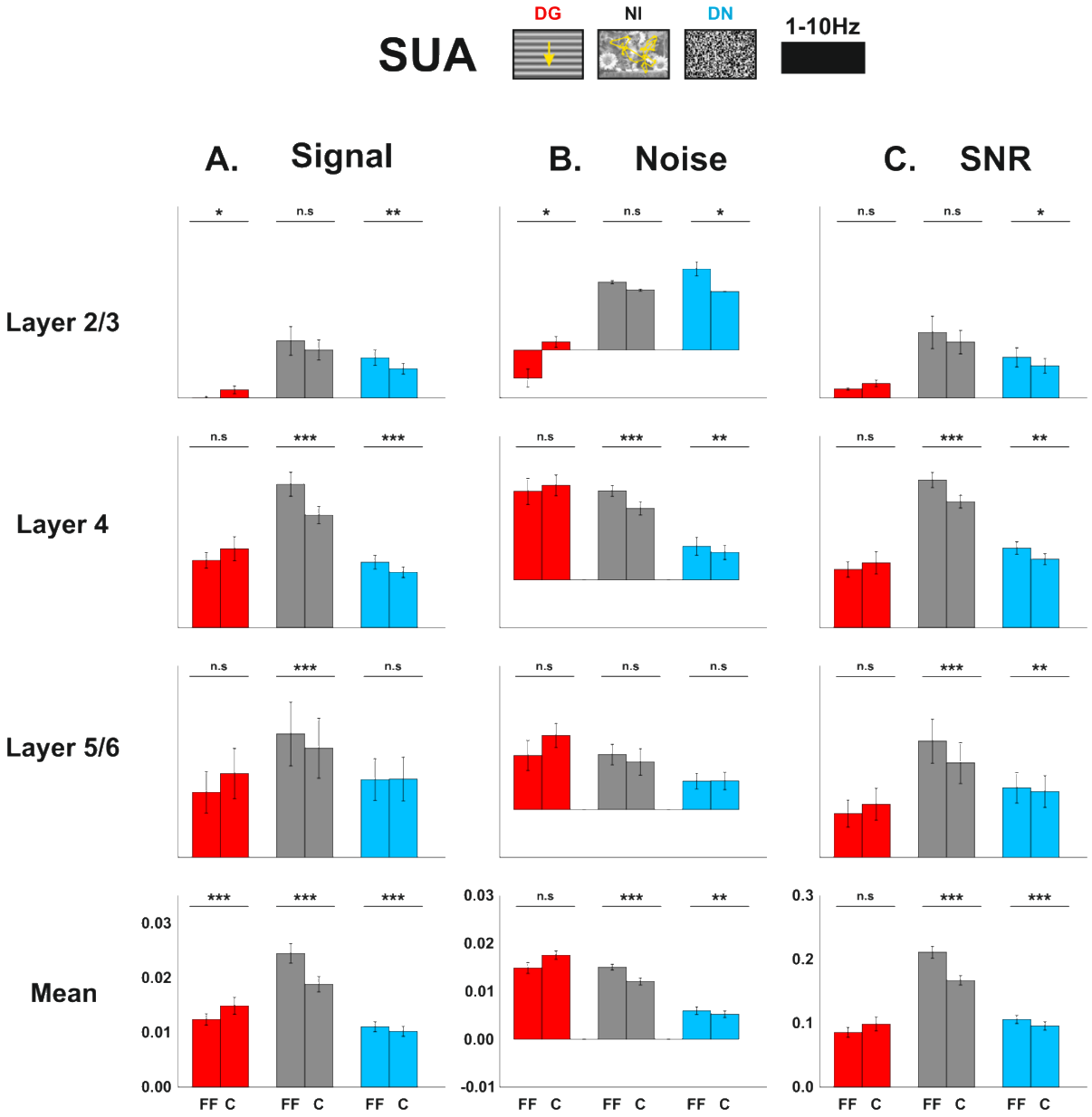

Figure 3.4.45: Bar plots of the low frequency SNR of the single unit activity in response to our stimulus set. A. Mean low frequency Signal across layers and for the complete population. **B.** Mean low frequency Noise across layers and for the complete population. **C.** Mean low frequency SNR across layers and for the complete population.(Total neurons = 221; L2/3 = 10; L4 = 111; L5/6 = 99 neurons) *: all conditions are significantly different from each other; * : $p < 0.05$; ** : $p < 0.01$; *** : $p < 0.001$; Error bars : SEM.

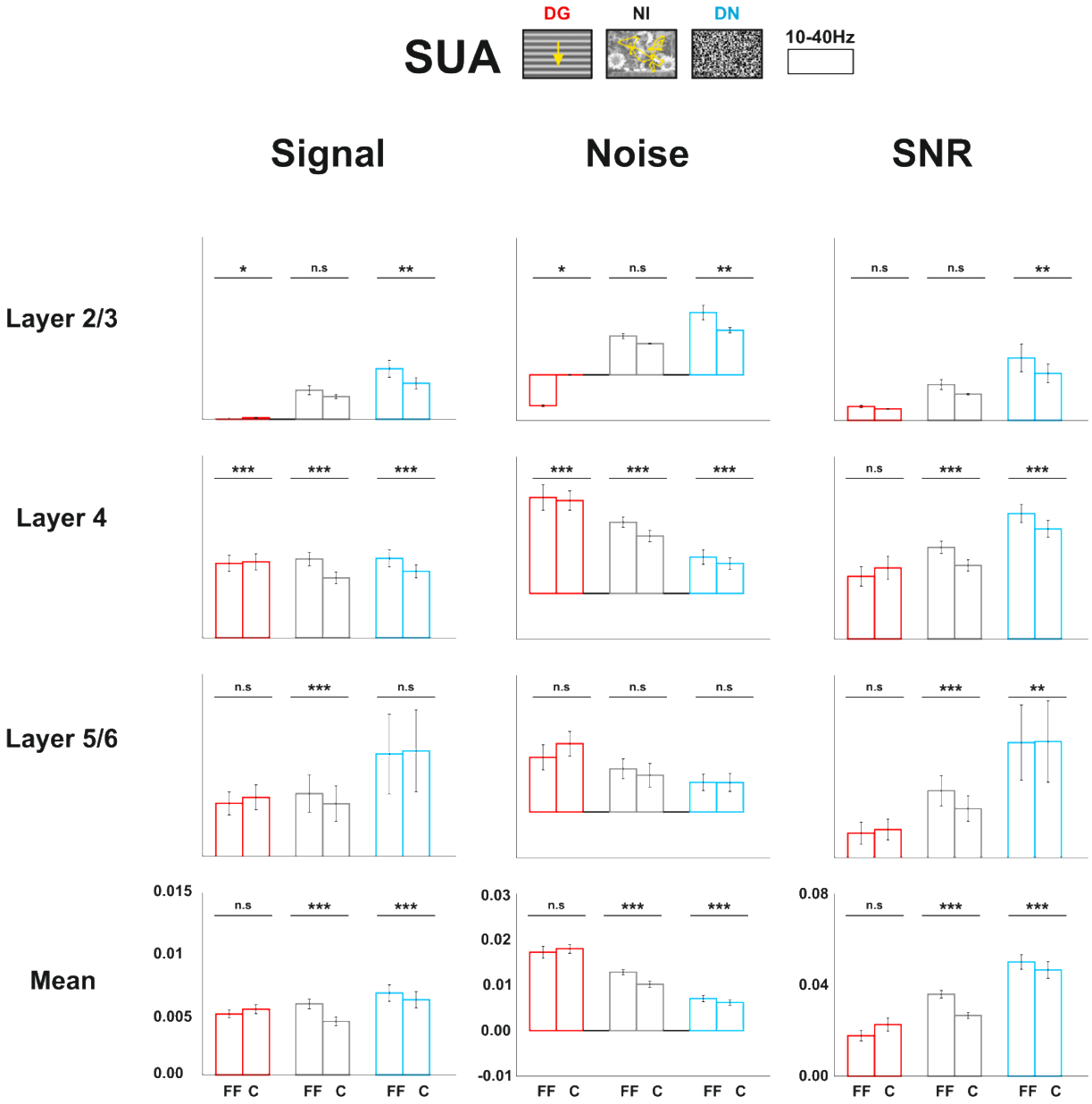

Figure 3.4.46: Bar plots of the high frequency SNR of the single unit activity in response to our stimulus set. A. Mean high frequency Signal across layers and for the complete population. **B.** Mean high frequency Noise across layers and for the complete population. **C.** Mean high frequency SNR across layers and for the complete population.(Total neurons = 221; L2/3 = 10; L4 = 111; L5/6 = 99 neurons). *: all conditions are significantly different from each other; * : $p < 0.05$; ** : $p < 0.01$; *** : $p < 0.001$; Error bars : SEM.

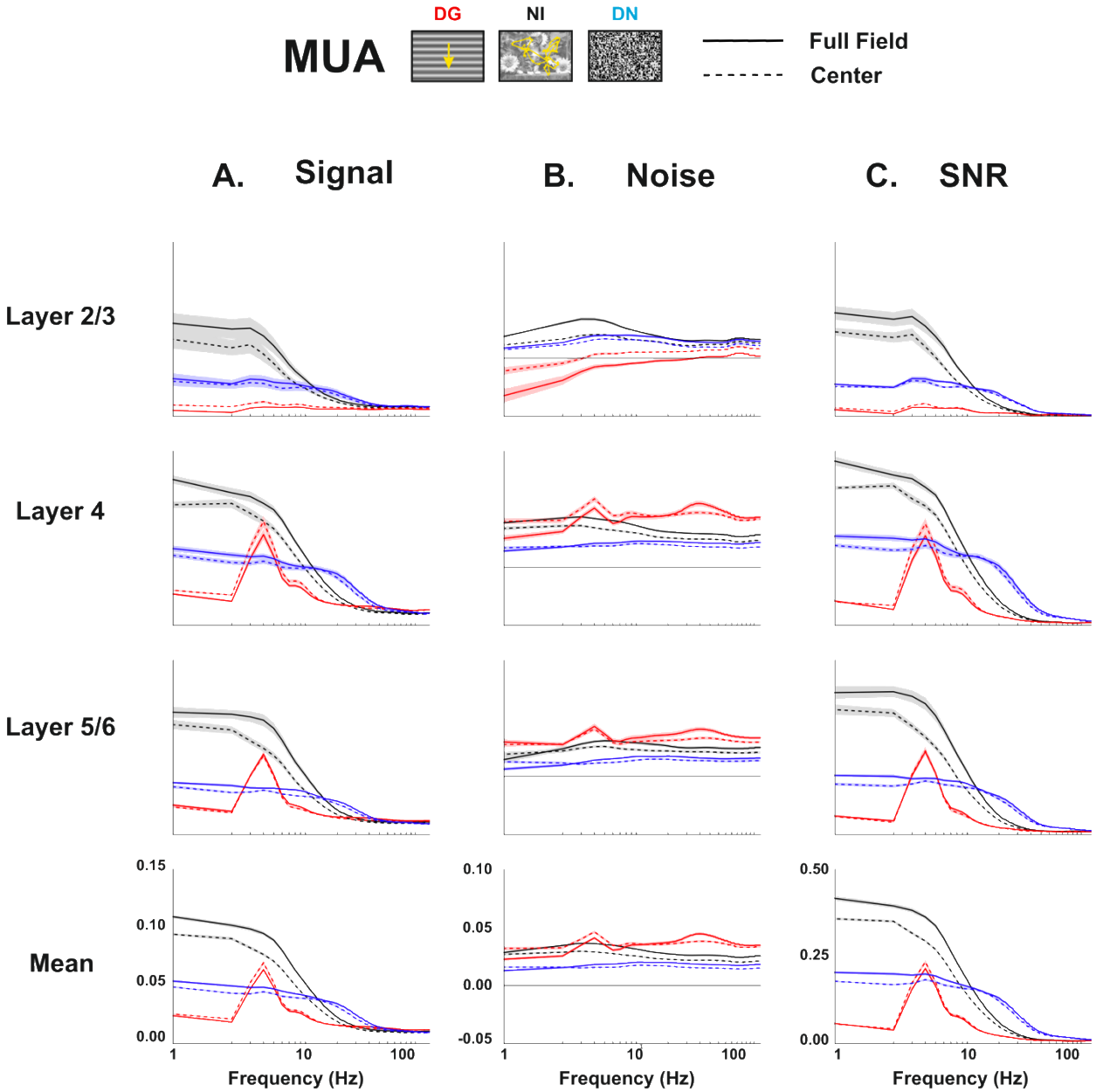

Figure 3.4.47: Mean and laminar SNR of the multi-unit activity in response to natural and artificial stimuli presented on the full field (full line) and center (big dashed lines) conditions.

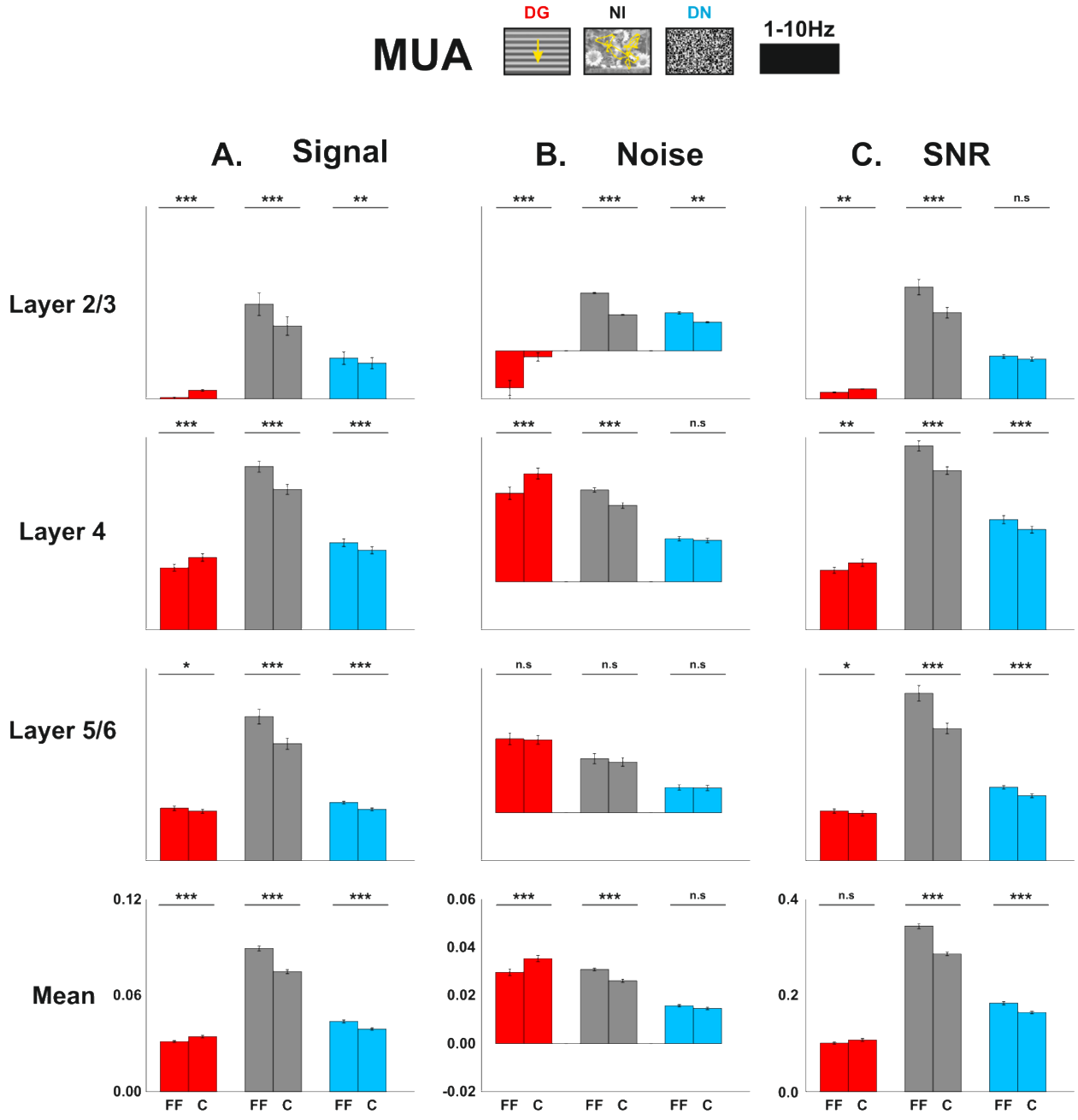

Figure 3.4.48: Bar plots of the low frequency SNR of the MUA in response to our stimulus set. A. Mean low frequency Signal across layers and for the complete population. **B.** Mean low frequency Noise across layers and for the complete population. **C.** Mean low frequency SNR across layers and for the complete population. (Total sites = 377; L2/3 = 52; L4 = 187; L5/6 = 138 sites). *: all conditions are significantly different from each other; * : $p < 0.05$; ** : $p < 0.01$; *** : $p < 0.001$; Error bars : SEM.

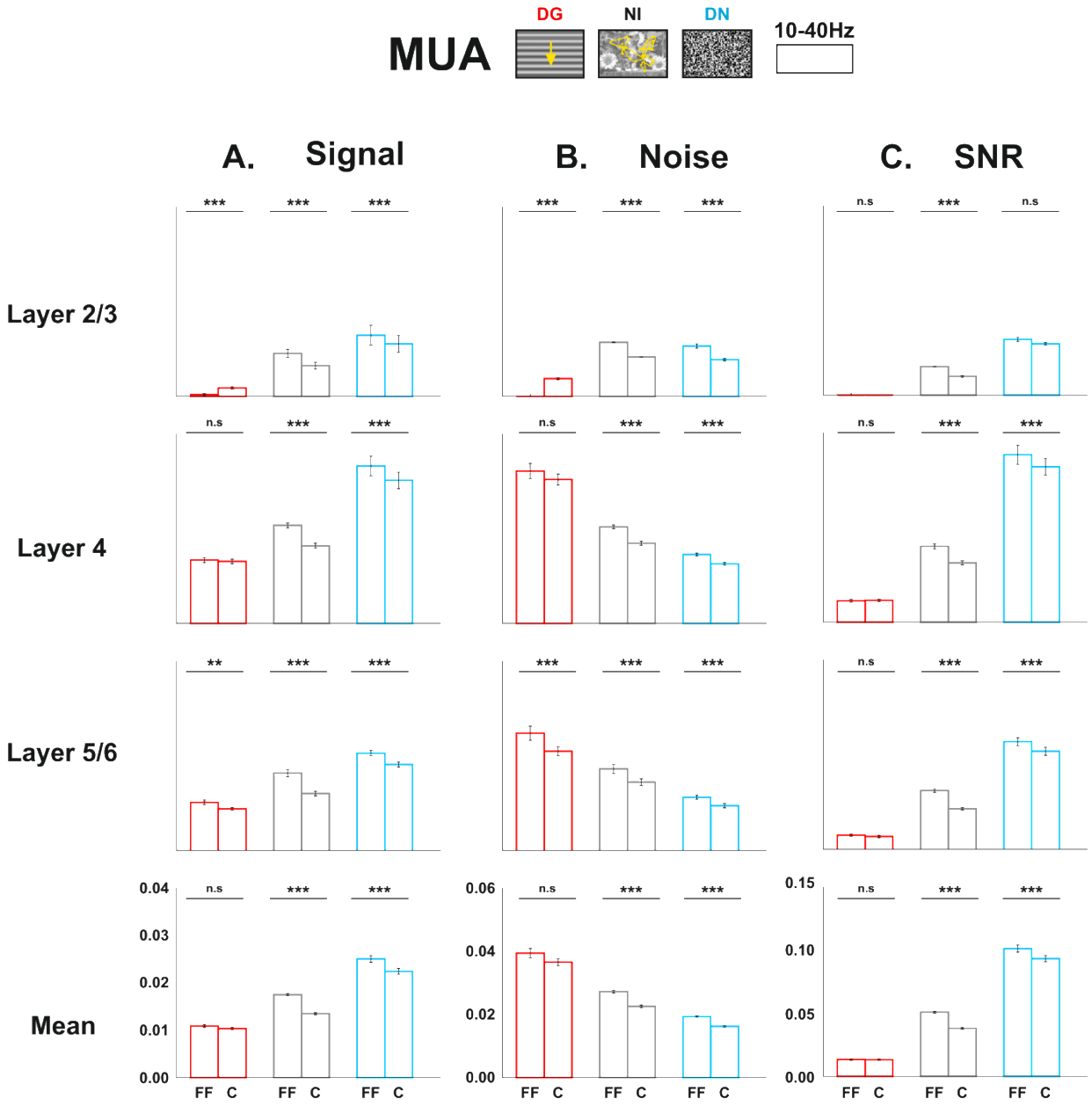

Figure 3.4.49: Bar plots of the high frequency SNR of MUA in response to our stimulus set. A. Mean high frequency Signal across layers and for the complete population. **B.** Mean high frequency Noise across layers and for the complete population. **C.** Mean high frequency SNR across layers and for the complete population.(Total sites = 377; L2/3 = 52; L4 = 187; L5/6 = 138 sites). *: all conditions are significantly different from each other; * : $p < 0.05$; ** : $p < 0.01$; *** : $p < 0.001$; Error bars : SEM.

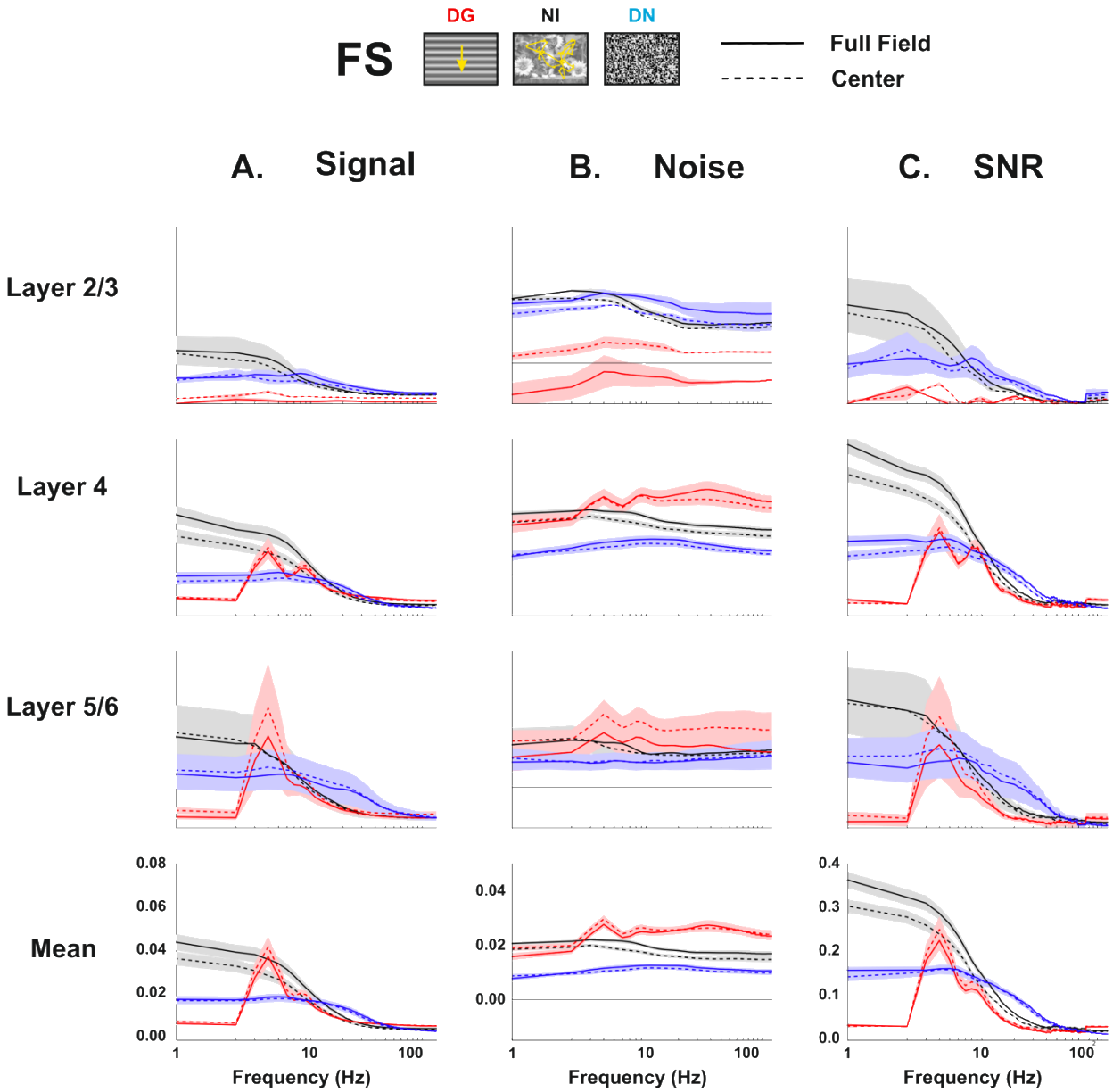

Figure 3.4.50: Mean and laminar SNR of the fast spiking cells in response to natural and artificial stimuli presented on the full field (full line) and center (big dashed lines) conditions.

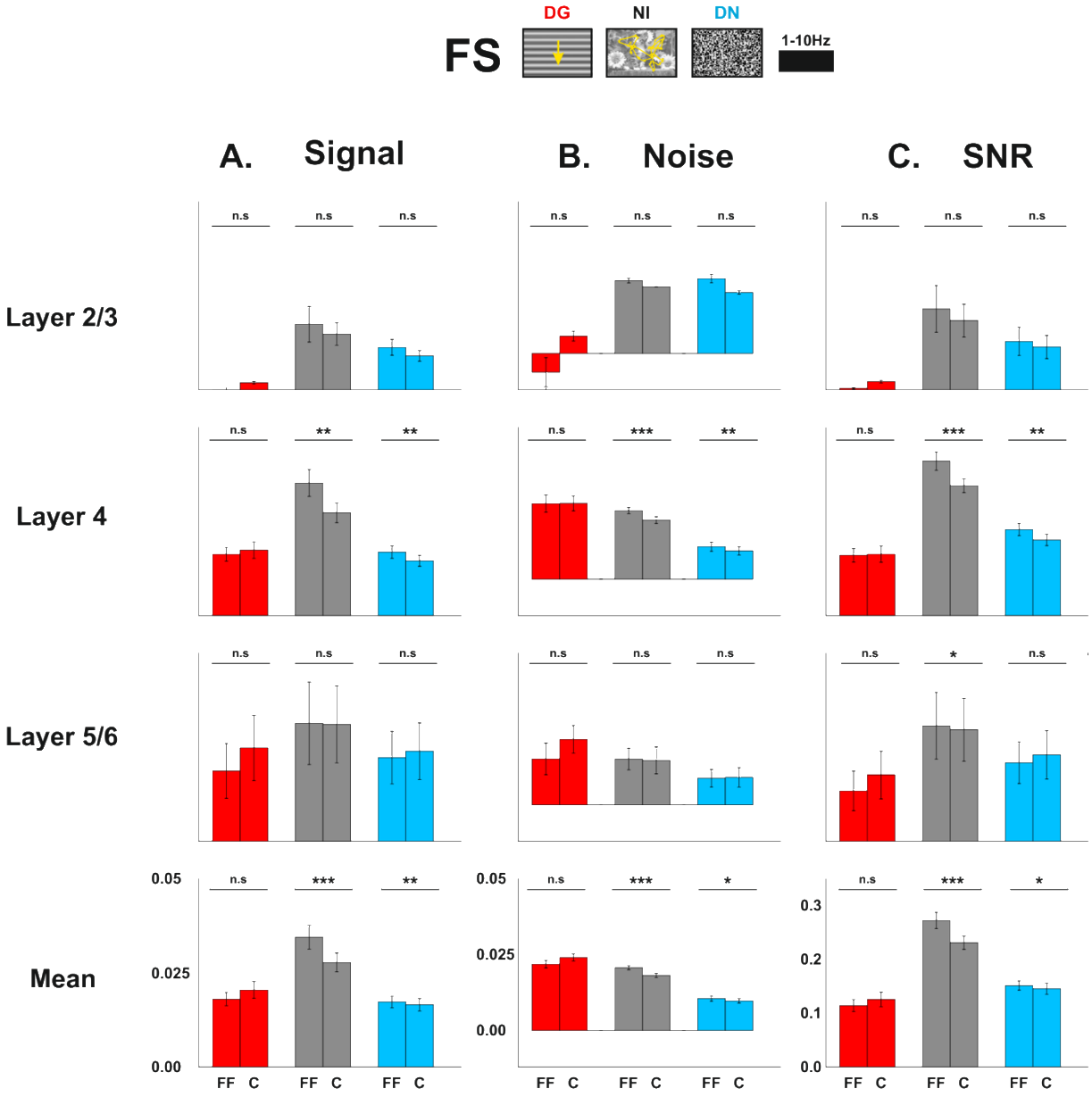

Figure 3.4.51: Bar plots of the low frequency SNR of FS cells in response to our stimulus set. A. Mean low frequency Signal across layers and for the complete population. **B.** Mean low frequency Noise across layers and for the complete population. **C.** Mean low frequency SNR across layers and for the complete population. (Total neurons = 83; L2/3 = 4; L4 = 61; L5/6 = 18 neurons). *: all conditions are significantly different from each other; * : $p < 0.05$; ** : $p < 0.01$; *** : $p < 0.001$; Error bars : SEM.

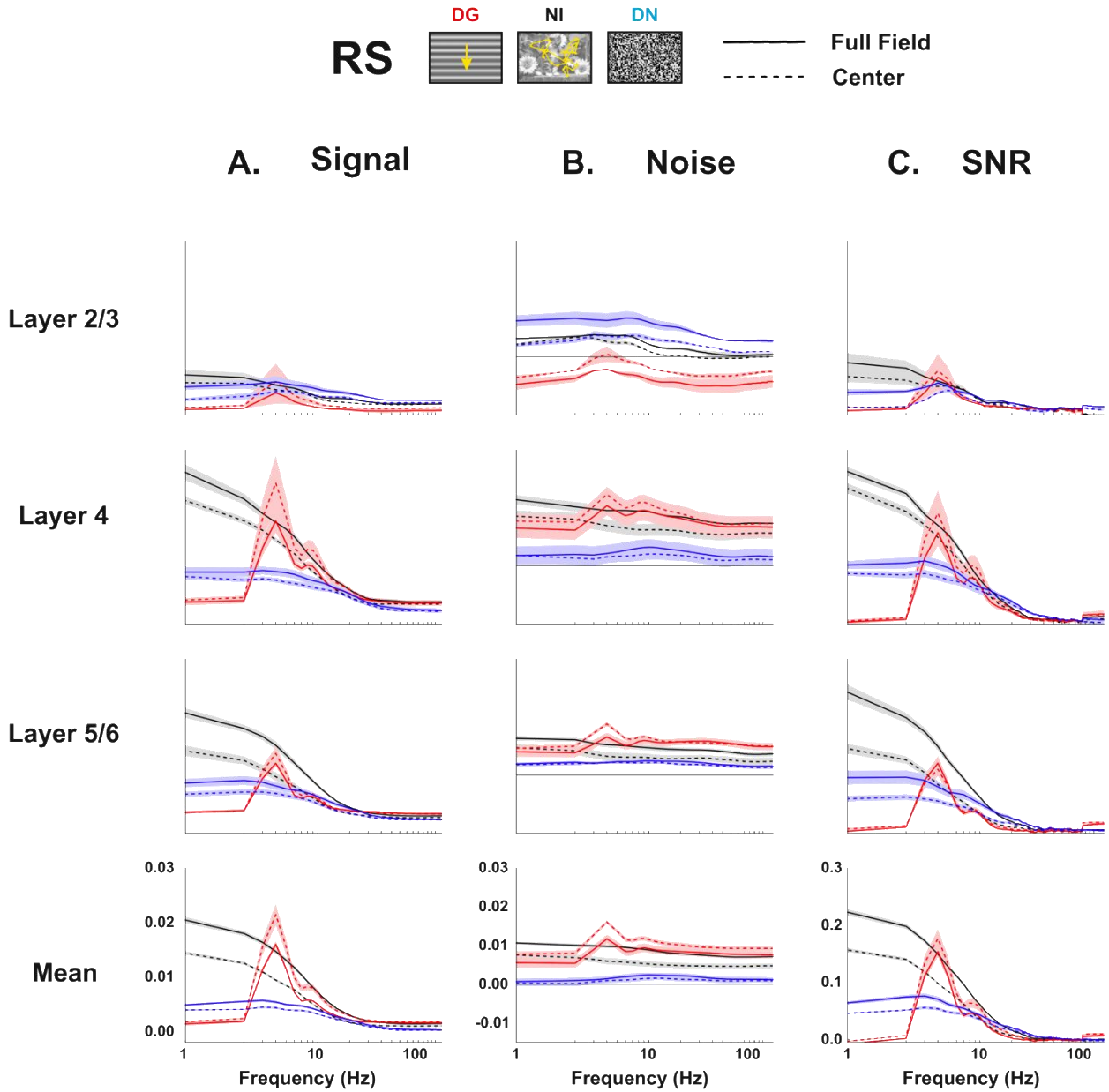

Figure 3.4.52: Mean laminar and SNR of the regular spiking cells in response to natural and artificial stimuli presented on the full field (full line) and center (big dashed lines) conditions.

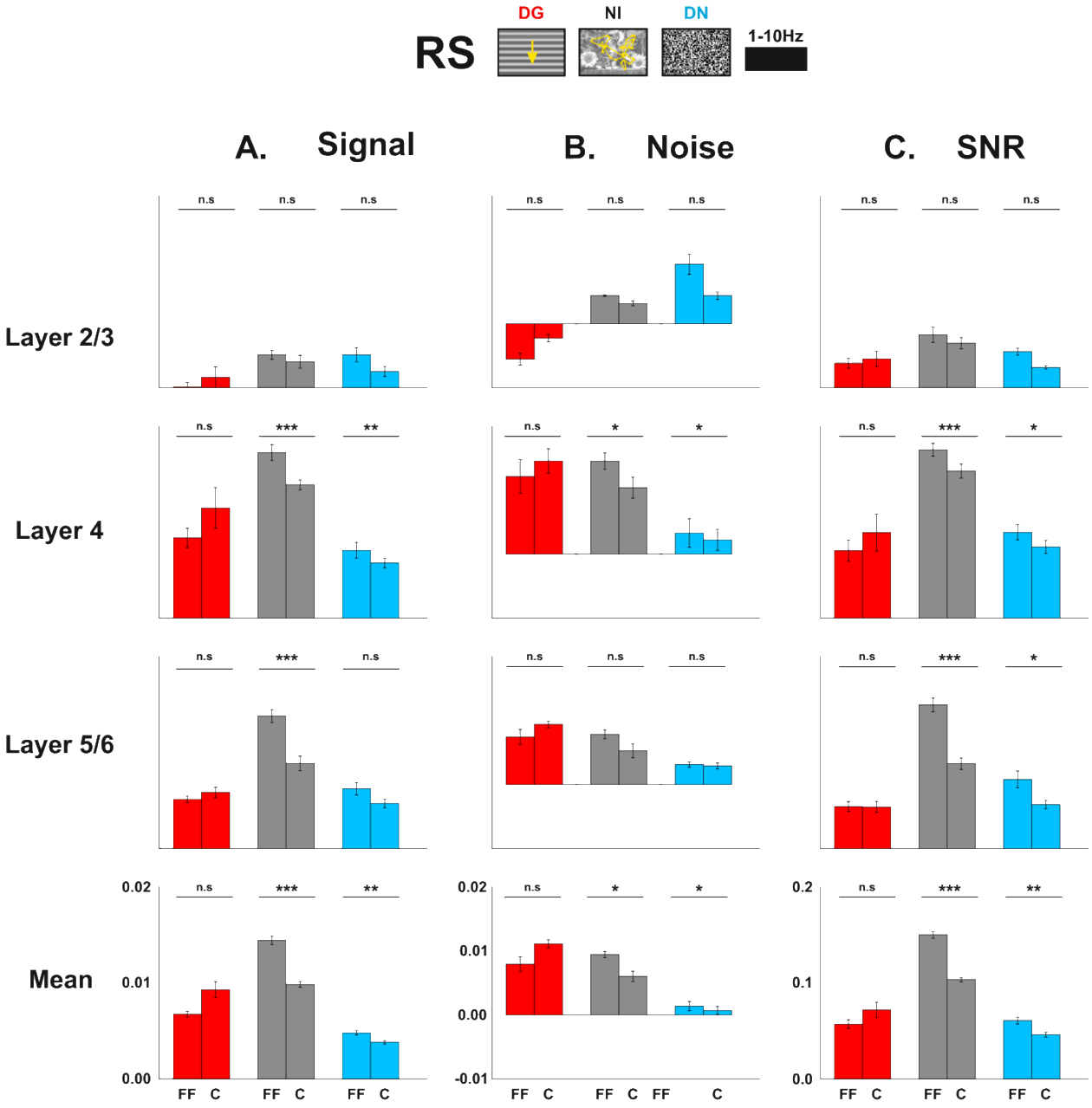

Figure 3.4.53: Bar plots of the low frequency SNR of RS cells in response to our stimulus set. A. Mean low frequency Signal across layers and for the complete population. **B.** Mean low frequency Noise across layers and for the complete population. **C.** Mean low frequency SNR across layers and for the complete population.(Total neurons = 138; L2/3 = 7; L4 = 50; L5/6 = 81 neurons) *: all conditions are significantly different from each other; * : $p < 0.05$; ** : $p < 0.01$; *** : $p < 0.001$; Error bars : SEM.

Our previous results showed that the alteration of the natural statistics had no impact on the center surround interactions observed for natural images. We wondered if these observations were also true when computing a time frequency analysis and in which frequency range their impact is the higher. At all levels of spiking activity (single and multi-unit activities), the center condition evoked the same response pattern as the full field one (table 3.4.16).
We then investigated the impact of the center surround condition in the low frequency responses. At the single unit level (and its subclasses) the full field condition always evoked a higher mean signal, noise and SNR than the center condition. However, these differences were not significant. On the other hand, the same response pattern was observed at the multi-unit scale, but all the values were significantly different (Because of this, we only plotted the MUA results in figure 3.4.54, but all values are reported in table 3.4.16). These observations were also true at the high frequency range. This suggest that the number of well isolated units used to perform the time frequency analysis is not sufficient to reach a significant difference. However, by increasing the number of isolated neurons we should reach significantly different values. In summary, our results show that at the spiking level, the altered and unaltered natural statistics participate in the same way to the center surround modulations.

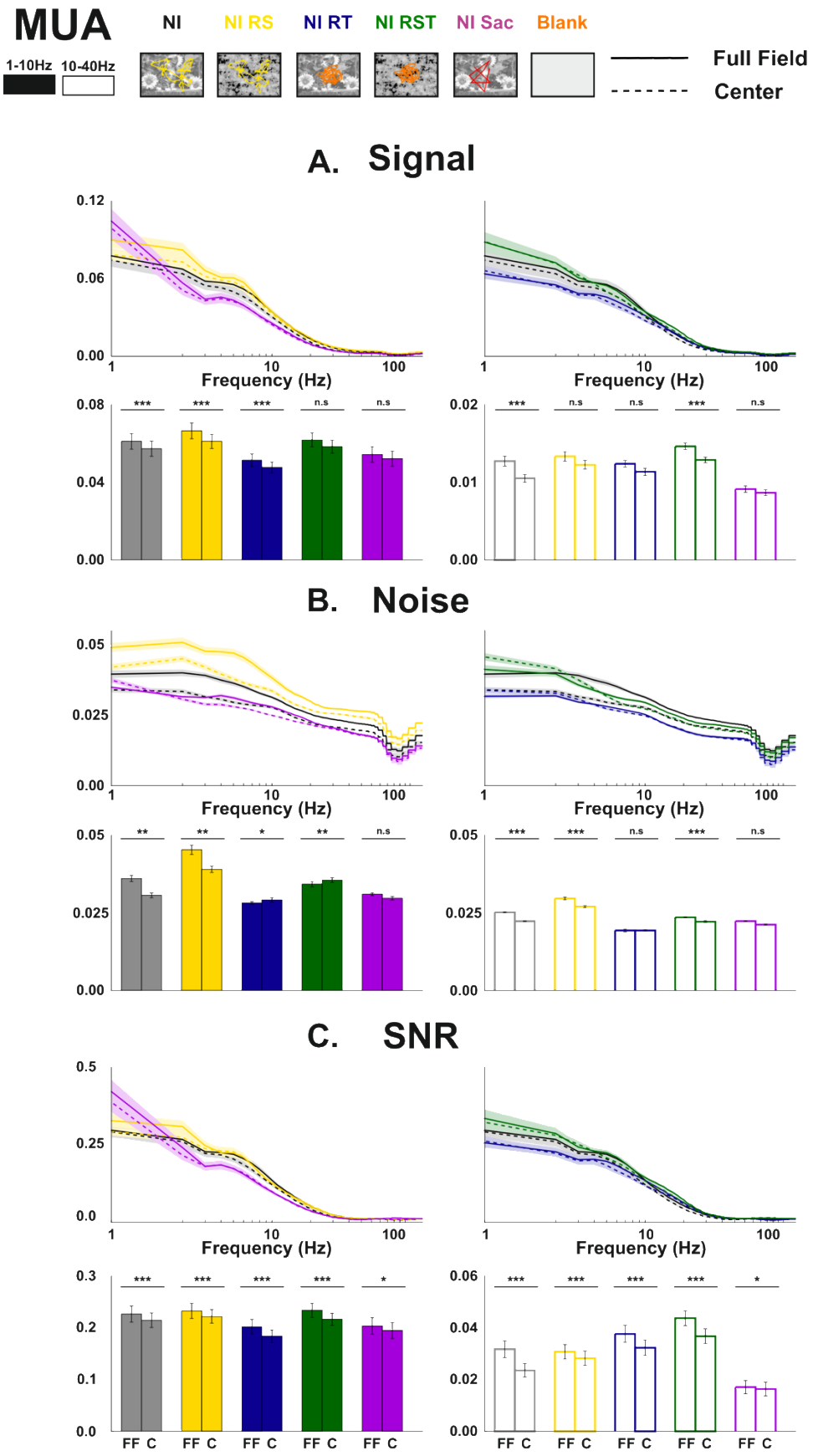

Figure 3.4.54: Time Frequency analysis of the MUA (n =150 sites) in response to natural and artificial stimuli presented on the full field (full line) and center (big dashed lines) conditions (top row) and the mean low and high frequencies responses (bottow row).

FULL FIELD	LOW FREQUENCY SIGNAL (SUA)		
	DG	NI	DN
L2/3	0.000 ± 0.000	0.010 ± 0.002	0.007 ± 0.001
L4	0.012 ± 0.001	0.026 ± 0.002	0.012 ± 0.001
L5/6	0.012 ± 0.004	0.022 ± 0.005	0.014 ± 0.003
Mean	0.012 ± 0.001	0.024 ± 0.001	0.011 ± 0.001

CENTER		
DG	NI	DN
0.001 ± 0.001	0.009 ± 0.002	0.005 ± 0.001
0.014 ± 0.002	0.021 ± 0.002	0.010 ± 0.001
0.015 ± 0.005	0.020 ± 0.005	0.014 ± 0.004
0.015 ± 0.002	0.019 ± 0.001	0.010 ± 0.001

FULL FIELD	LOW FREQUENCY NOISE (SUA)		
	DG	NI	DN
L2/3	-0.005 ± 0.002	0.014 ± 0.000	0.017 ± 0.001
L4	0.018 ± 0.002	0.018 ± 0.001	0.007 ± 0.001
L5/6	0.011 ± 0.003	0.011 ± 0.002	0.006 ± 0.001
Mean	0.015 ± 0.001	0.015 ± 0.001	0.006 ± 0.001

CENTER		
DG	NI	DN
0.002 ± 0.001	0.013 ± 0.000	0.012 ± 0.000
0.020 ± 0.002	0.015 ± 0.001	0.006 ± 0.002
0.015 ± 0.003	0.010 ± 0.003	0.006 ± 0.002
0.018 ± 0.001	0.012 ± 0.001	0.005 ± 0.001

FULL FIELD	LOW FREQUENCY SNR (SUA)		
	DG	NI	DN
L2/3	0.014 ± 0.001	0.102 ± 0.025	0.063 ± 0.015
L4	0.091 ± 0.011	0.231 ± 0.011	0.124 ± 0.009
L5/6	0.068 ± 0.020	0.182 ± 0.034	0.109 ± 0.023
Mean	0.085 ± 0.007	0.211 ± 0.009	0.106 ± 0.006

CENTER		
DG	NI	DN
0.023 ± 0.005	0.088 ± 0.018	0.051 ± 0.012
0.102 ± 0.017	0.198 ± 0.010	0.107 ± 0.009
0.083 ± 0.025	0.148 ± 0.032	0.103 ± 0.025
0.099 ± 0.011	0.167 ± 0.007	0.096 ± 0.006

FULL FIELD	HIGH FREQUENCY SIGNAL (SUA)		
	DG	NI	DN
L2/3	-0.001 ± 0.000	0.002 ± 0.000	0.004 ± 0.001
L4	0.006 ± 0.001	0.006 ± 0.001	0.007 ± 0.001
L5/6	0.004 ± 0.001	0.005 ± 0.002	0.008 ± 0.003
Mean	0.005 ± 0.000	0.006 ± 0.000	0.007 ± 0.001

CENTER		
DG	NI	DN
0.000 ± 0.000	0.002 ± 0.000	0.003 ± 0.000
0.006 ± 0.001	0.005 ± 0.000	0.005 ± 0.001
0.005 ± 0.001	0.004 ± 0.001	0.009 ± 0.003
0.005 ± 0.000	0.004 ± 0.000	0.006 ± 0.001

FULL FIELD	HIGH FREQUENCY NOISE (SUA)		
	DG	NI	DN
L2/3	-0.007 ± 0.000	0.008 ± 0.001	0.014 ± 0.002
L4	0.021 ± 0.003	0.016 ± 0.001	0.008 ± 0.002
L5/6	0.012 ± 0.003	0.009 ± 0.002	0.007 ± 0.002
Mean	0.017 ± 0.001	0.013 ± 0.001	0.007 ± 0.001

CENTER		
DG	NI	DN
-0.000 ± 0.000	0.007 ± 0.000	0.010 ± 0.001
0.020 ± 0.002	0.013 ± 0.001	0.007 ± 0.001
0.015 ± 0.003	0.008 ± 0.003	0.006 ± 0.002
0.018 ± 0.001	0.010 ± 0.001	0.006 ± 0.001

FULL FIELD	HIGH FREQUENCY SNR (SUA)		
	DG	NI	DN
L2/3	0.005 ± -0.000	0.012 ± 0.000	0.021 ± 0.004
L4	0.031 ± 0.005	0.032 ± 0.002	0.048 ± 0.004
L5/6	0.012 ± 0.005	0.022 ± 0.006	0.051 ± 0.018
Mean	0.023 ± 0.003	0.027 ± 0.001	0.047 ± 0.004

CENTER		
DG	NI	DN
0.005 ± -0.000	0.012 ± 0.000	0.021 ± 0.004
0.031 ± 0.005	0.032 ± 0.002	0.048 ± 0.004
0.012 ± 0.005	0.022 ± 0.006	0.051 ± 0.018
0.023 ± 0.003	0.027 ± 0.001	0.047 ± 0.004

Table 3.4.12: Mean high and low frequency signal, noise and SNR of the single unit activity in response to our stimulus set presented full field or on the center (mean ± SEM)

FULL FIELD	LOW FREQUENCY SIGNAL (MUA)		
	DG	NI	DN
L2/3	0.001 ± 0.000	0.059 ± 0.007	0.025 ± 0.003
L4	0.038 ± 0.002	0.101 ± 0.003	0.054 ± 0.002
L5/6	0.032 ± 0.001	0.090 ± 0.004	0.036 ± 0.001
Mean	0.031 ± 0.001	0.089 ± 0.001	0.043 ± 0.001

CENTER		
DG	NI	DN
0.002 ± 0.000	0.006 ± 0.001	0.011 ± 0.002
0.013 ± 0.000	0.016 ± 0.001	0.030 ± 0.002
0.009 ± 0.000	0.012 ± 0.000	0.018 ± 0.001
0.010 ± 0.000	0.014 ± 0.000	0.022 ± 0.001

FULL FIELD	LOW FREQUENCY NOISE (MUA)		
	DG	NI	DN
L2/3	-0.015 ± -0.003	0.024 ± 0.000	0.015 ± 0.001
L4	0.036 ± 0.002	0.038 ± 0.001	0.017 ± 0.001
L5/6	0.030 ± 0.002	0.022 ± 0.002	0.010 ± 0.001
Mean	0.029 ± 0.001	0.030 ± 0.001	0.015 ± 0.001

CENTER		
DG	NI	DN
-0.003 ± -0.002	0.015 ± 0.000	0.012 ± 0.000
0.045 ± 0.002	0.032 ± 0.001	0.017 ± 0.001
0.030 ± 0.002	0.021 ± 0.002	0.010 ± 0.001
0.035 ± 0.001	0.026 ± 0.001	0.015 ± 0.001

FULL FIELD	LOW FREQUENCY SNR (MUA)		
	DG	NI	DN
L2/3	0.013 ± -0.000	0.232 ± 0.015	0.089 ± 0.004
L4	0.123 ± 0.006	0.382 ± 0.010	0.229 ± 0.008
L5/6	0.103 ± 0.004	0.342 ± 0.016	0.152 ± 0.003
Mean	0.101 ± 0.002	0.344 ± 0.005	0.184 ± 0.003

CENTER		
DG	NI	DN
0.021 ± -0.000	0.179 ± 0.011	0.083 ± 0.004
0.139 ± 0.007	0.331 ± 0.008	0.209 ± 0.008
0.099 ± 0.006	0.275 ± 0.011	0.135 ± 0.004
0.107 ± 0.003	0.286 ± 0.004	0.165 ± 0.003

FULL FIELD	HIGH FREQUENCY SIGNAL (MUA)		
	DG	NI	DN
L2/3	0.000 ± 0.000	0.009 ± 0.001	0.013 ± 0.002
L4	0.013 ± 0.001	0.021 ± 0.001	0.033 ± 0.002
L5/6	0.010 ± 0.000	0.016 ± 0.001	0.021 ± 0.001
Mean	0.011 ± 0.000	0.018 ± 0.000	0.025 ± 0.001

CENTER		
DG	NI	DN
0.002 ± 0.000	0.006 ± 0.001	0.011 ± 0.002
0.013 ± 0.000	0.016 ± 0.001	0.030 ± 0.002
0.009 ± 0.000	0.012 ± 0.000	0.018 ± 0.001
0.010 ± 0.000	0.014 ± 0.000	0.022 ± 0.001

FULL FIELD	HIGH FREQUENCY NOISE (MUA)		
	DG	NI	DN
L2/3	-0.002 ± -0.001	0.017 ± -0.000	0.016 ± 0.001
L4	0.048 ± 0.002	0.031 ± 0.001	0.022 ± 0.000
L5/6	0.037 ± 0.002	0.026 ± 0.002	0.017 ± 0.001
Mean	0.039 ± 0.001	0.027 ± 0.000	0.019 ± 0.000

CENTER		
DG	NI	DN
0.006 ± -0.000	0.012 ± 0.000	0.012 ± 0.000
0.046 ± 0.002	0.025 ± 0.001	0.019 ± 0.000
0.031 ± 0.001	0.022 ± 0.001	0.014 ± 0.001
0.037 ± 0.001	0.023 ± 0.000	0.016 ± 0.000

FULL FIELD	HIGH FREQUENCY SNR (MUA)		
	DG	NI	DN
L2/3	-0.001 ± -0.001	0.023 ± -0.000	0.044 ± 0.002
L4	0.017 ± 0.001	0.060 ± 0.002	0.133 ± 0.008
L5/6	0.011 ± 0.001	0.047 ± 0.002	0.085 ± 0.003
Mean	0.013 ± 0.001	0.051 ± 0.001	0.101 ± 0.003

CENTER		
DG	NI	DN
-0.001 ± -0.001	0.015 ± -0.001	0.041 ± 0.001
0.017 ± 0.001	0.047 ± 0.002	0.123 ± 0.007
0.010 ± 0.001	0.032 ± 0.001	0.078 ± 0.003
0.013 ± 0.001	0.038 ± 0.001	0.093 ± 0.003

Table 3.4.13: Mean high and low frequency signal, noise and SNR of the multi-unit activity in response to our stimulus set presented full field or on the center (mean ± SEM)

FULL FIELD	LOW FREQUENCY SIGNAL (FS)		
	DG	NI	DN
L2/3	-0.001 ± 0.001	0.017 ± 0.004	0.011 ± 0.002
L4	0.016 ± 0.001	0.035 ± 0.003	0.016 ± 0.001
L5/6	0.018 ± 0.007	0.031 ± 0.011	0.022 ± 0.007
Mean	0.018 ± 0.001	0.034 ± 0.003	0.017 ± 0.001

CENTER		
DG	NI	DN
0.002 ± 0.000	0.015 ± 0.003	0.009 ± 0.001
0.017 ± 0.002	0.027 ± 0.003	0.015 ± 0.001
0.025 ± 0.009	0.031 ± 0.010	0.024 ± 0.008
0.020 ± 0.002	0.028 ± 0.002	0.017 ± 0.002

FULL FIELD	LOW FREQUENCY NOISE (FS)		
	DG	NI	DN
L2/3	-0.006 ± 0.004	0.024 ± 0.001	0.024 ± 0.001
L4	0.024 ± 0.002	0.022 ± 0.001	0.010 ± 0.001
L5/6	0.015 ± 0.005	0.015 ± 0.003	0.008 ± 0.002
Mean	0.021 ± 0.001	0.020 ± 0.001	0.010 ± 0.001

CENTER		
DG	NI	DN
0.006 ± 0.002	0.022 ± 0.000	0.020 ± -0.001
0.025 ± 0.002	0.019 ± 0.001	0.009 ± 0.001
0.022 ± 0.005	0.015 ± 0.004	0.009 ± 0.003
0.024 ± 0.001	0.018 ± 0.001	0.010 ± 0.001

FULL FIELD	LOW FREQUENCY SNR (FS)		
	DG	NI	DN
L2/3	0.002 ± -0.001	0.150 ± 0.043	0.090 ± 0.026
L4	0.112 ± 0.012	0.287 ± 0.017	0.160 ± 0.011
L5/6	0.093 ± 0.036	0.214 ± 0.062	0.146 ± 0.038
Mean	0.114 ± 0.010	0.272 ± 0.015	0.151 ± 0.008

CENTER		
DG	NI	DN
0.015 ± 0.002	0.129 ± 0.031	0.080 ± 0.022
0.114 ± 0.015	0.242 ± 0.013	0.141 ± 0.011
0.123 ± 0.044	0.208 ± 0.059	0.161 ± 0.045
0.126 ± 0.014	0.231 ± 0.012	0.146 ± 0.010

FULL FIELD	HIGH FREQUENCY SIGNAL (FS)		
	DG	NI	DN
L2/3	-0.001 ± 0.000	0.004 ± 0.001	0.007 ± 0.001
L4	0.009 ± 0.001	0.009 ± 0.001	0.010 ± 0.001
L5/6	0.006 ± 0.002	0.008 ± 0.003	0.015 ± 0.006
Mean	0.008 ± 0.000	0.009 ± 0.001	0.012 ± 0.00

CENTER		
DG	NI	DN
0.001 ± 0.000	0.004 ± 0.000	0.005 ± 0.001
0.008 ± 0.001	0.007 ± 0.001	0.009 ± 0.001
0.008 ± 0.002	0.007 ± 0.003	0.016 ± 0.007
0.008 ± 0.001	0.007 ± 0.001	0.011 ± 0.001

FULL FIELD	HIGH FREQUENCY NOISE (FS)		
	DG	NI	DN
L2/3	-0.007 ± 0.002	0.015 ± 0.002	0.021 ± 0.003
L4	0.030 ± 0.003	0.019 ± 0.001	0.012 ± 0.001
L5/6	0.015 ± 0.005	0.012 ± 0.004	0.010 ± 0.003
Mean	0.026 ± 0.002	0.018 ± 0.001	0.012 ± 0.001

CENTER		
DG	NI	DN
0.004 ± 0.001	0.014 ± 0.000	0.016 ± 0.001
0.028 ± 0.002	0.016 ± 0.001	0.011 ± 0.001
0.021 ± 0.005	0.012 ± 0.004	0.010 ± 0.004
0.026 ± 0.001	0.016 ± 0.001	0.011 ± 0.001

FULL FIELD	HIGH FREQUENCY SNR (FS)		
	DG	NI	DN
L2/3	0.004 ± 0.000	0.019 ± 0.005	0.042 ± 0.013
L4	0.040 ± 0.006	0.059 ± 0.003	0.082 ± 0.005
L5/6	0.020 ± 0.009	0.044 ± 0.012	0.083 ± 0.031
Mean	0.031 ± 0.003	0.057 ± 0.003	0.083 ± 0.005

CENTER		
DG	NI	DN
0.003 ± 0.001	0.015 ± 0.002	0.033 ± 0.010
0.044 ± 0.006	0.049 ± 0.003	0.071 ± 0.005
0.021 ± 0.008	0.037 ± 0.010	0.093 ± 0.035
0.035 ± 0.004	0.046 ± 0.002	0.080 ± 0.006

Table 3.4.14: Mean high and low frequency signal, noise and SNR of the fast spiking neurons in response to our stimulus set presented full field or on the center (mean ± SEM)

FULL FIELD	LOW FREQUENCY SIGNAL (RS)		
	DG	NI	DN
L2/3	0.000 ± 0.000	0.003 ± 0.000	0.003 ± 0.001
L4	0.008 ± 0.001	0.017 ± 0.001	0.007 ± 0.001
L5/6	0.005 ± 0.000	0.013 ± 0.001	0.006 ± 0.001
Mean	0.006 ± 0.000	0.014 ± 0.000	0.004 ± 0.000

CENTER		
DG	NI	DN
0.001 ± 0.001	0.003 ± 0.001	0.002 ± 0.001
0.011 ± 0.002	0.014 ± 0.001	0.006 ± 0.001
0.006 ± 0.001	0.009 ± 0.001	0.005 ± 0.000
0.009 ± 0.001	0.010 ± 0.000	0.004 ± 0.000

FULL FIELD	LOW FREQUENCY NOISE (RS)		
	DG	NI	DN
L2/3	-0.005 ± -0.001	0.004 ± 0.000	0.009 ± 0.001
L4	0.012 ± 0.002	0.014 ± 0.001	0.003 ± 0.002
L5/6	0.007 ± 0.001	0.007 ± 0.001	0.003 ± 0.000
Mean	0.007 ± 0.001	0.009 ± 0.001	0.001 ± 0.001

CENTER		
DG	NI	DN
-0.002 ± 0.001	0.003 ± 0.000	0.004 ± 0.001
0.015 ± 0.002	0.010 ± 0.002	0.002 ± 0.002
0.009 ± 0.001	0.005 ± 0.001	0.003 ± 0.000
0.011 ± 0.001	0.006 ± 0.001	0.001 ± 0.001

FULL FIELD	LOW FREQUENCY SNR (RS)		
	DG	NI	DN
L2/3	0.025 ± 0.005	0.055 ± 0.007	0.037 ± 0.003
L4	0.070 ± 0.011	0.175 ± 0.006	0.089 ± 0.008
L5/6	0.043 ± 0.005	0.149 ± 0.007	0.072 ± 0.008
Mean	0.057 ± 0.004	0.150 ± 0.003	0.060 ± 0.003

CENTER		
DG	NI	DN
0.030 ± 0.008	0.046 ± 0.006	0.021 ± 0.002
0.089 ± 0.019	0.153 ± 0.007	0.074 ± 0.007
0.043 ± 0.006	0.088 ± 0.006	0.046 ± 0.004
0.072 ± 0.008	0.104 ± 0.002	0.046 ± 0.002

FULL FIELD	HIGH FREQUENCY SIGNAL (RS)		
	DG	NI	DN
L2/3	-0.001 ± -0.000	0.001 ± -0.000	0.002 ± 0.000
L4	0.003 ± 0.001	0.004 ± 0.000	0.003 ± 0.000
L5/6	0.002 ± 0.000	0.003 ± 0.000	0.002 ± 0.000
Mean	0.002 ± 0.000	0.003 ± 0.000	0.002 ± 0.000

CENTER		
DG	NI	DN
-0.001 ± -0.000	0.000 ± 0.000	0.001 ± 0.000
0.004 ± 0.001	0.003 ± 0.000	0.002 ± 0.000
0.002 ± 0.000	0.002 ± 0.000	0.002 ± 0.000
0.003 ± 0.000	0.002 ± 0.000	0.001 ± 0.000

FULL FIELD	HIGH FREQUENCY NOISE (RS)		
	DG	NI	DN
L2/3	-0.007 ± -0.002	0.002 ± -0.000	0.007 ± 0.001
L4	0.012 ± 0.003	0.012 ± 0.001	0.004 ± 0.002
L5/6	0.009 ± 0.001	0.007 ± 0.001	0.003 ± 0.000
Mean	0.008 ± 0.001	0.008 ± 0.000	0.002 ± 0.001

CENTER		
DG	NI	DN
-0.004 ± -0.000	0.000 ± -0.000	0.003 ± 0.000
0.013 ± 0.002	0.009 ± 0.001	0.002 ± 0.001
0.009 ± 0.000	0.004 ± 0.001	0.003 ± 0.000
0.010 ± 0.001	0.005 ± 0.001	0.001 ± 0.001

FULL FIELD	HIGH FREQUENCY SNR (RS)		
	DG	NI	DN
L2/3	0.008 ± -0.001	0.012 ± -0.001	0.013 ± -0.000
L4	0.015 ± 0.003	0.021 ± 0.002	0.028 ± 0.003
L5/6	0.002 ± 0.001	0.015 ± 0.001	0.018 ± 0.002
Mean	0.004 ± 0.001	0.015 ± 0.001	0.017 ± 0.001

CENTER		
DG	NI	DN
0.007 ± -0.001	0.008 ± -0.001	0.008 ± -0.001
0.019 ± 0.005	0.016 ± 0.002	0.025 ± 0.003
0.004 ± 0.001	0.006 ± 0.001	0.009 ± 0.001
0.010 ± 0.002	0.007 ± 0.001	0.014 ± 0.001

Table 3.4.15: Mean high and low frequency signal, noise and SNR of the regular spiking neurons in response to our stimulus set presented full field or on the center (mean ± SEM)

FULL FIELD	SIGNAL				
	NI	NI-RS	NI-RT	NI-RST	NI-SAC
FS	0.027 ± 0.007	0.030 ± 0.008	0.021 ± 0.006	0.028 ± 0.009	0.023 ± 0.007
RS	0.017 ± 0.001	0.018 ± 0.001	0.015 ± 0.001	0.017 ± 0.001	0.013 ± 0.001
SUA	0.022 ± 0.004	0.024 ± 0.004	0.018 ± 0.003	0.022 ± 0.005	0.018 ± 0.004
MUA	0.061 ± 0.004	0.066 ± 0.004	0.051 ± 0.003	0.061 ± 0.003	0.054 ± 0.004

FULL FIELD	NOISE				
	NI	NI-RS	NI-RT	NI-RST	NI-SAC
FS	0.016 ± 0.002	0.019 ± 0.003	0.012 ± 0.001	0.015 ± 0.002	0.014 ± 0.003
RS	0.012 ± 0.001	0.015 ± 0.001	0.011 ± 0.001	0.011 ± 0.001	0.009 ± 0.001
SUA	0.014 ± 0.001	0.017 ± 0.002	0.011 ± 0.001	0.013 ± 0.001	0.012 ± 0.002
MUA	0.036 ± 0.001	0.045 ± 0.001	0.028 ± 0.001	0.034 ± 0.001	0.031 ± 0.001

FULL FIELD	SNR				
	NI	NI-RS	NI-RT	NI-RST	NI-SAC
FS	0.199 ± 0.038	0.215 ± 0.039	0.169 ± 0.034	0.220 ± 0.045	0.172 ± 0.036
RS	0.183 ± 0.006	0.189 ± 0.008	0.160 ± 0.009	0.185 ± 0.010	0.139 ± 0.008
SUA	0.191 ± 0.022	0.202 ± 0.024	0.164 ± 0.022	0.202 ± 0.027	0.156 ± 0.022
MUA	0.226 ± 0.015	0.232 ± 0.014	0.202 ± 0.014	0.233 ± 0.013	0.203 ± 0.016

CENTER	SIGNAL				
	NI	NI-RS	NI-RT	NI-RST	NI-SAC
FS	0.026 ± 0.007	0.029 ± 0.007	0.022 ± 0.006	0.028 ± 0.007	0.022 ± 0.007
RS	0.012 ± 0.000	0.015 ± 0.001	0.011 ± 0.001	0.013 ± 0.001	0.010 ± 0.001
SUA	0.019 ± 0.004	0.022 ± 0.004	0.017 ± 0.003	0.020 ± 0.004	0.016 ± 0.004
MUA	0.057 ± 0.004	0.061 ± 0.003	0.047 ± 0.002	0.058 ± 0.003	0.052 ± 0.003

CENTER	NOISE				
	NI	NI-RS	NI-RT	NI-RST	NI-SAC
FS	0.017 ± 0.003	0.018 ± 0.003	0.015 ± 0.002	0.019 ± 0.004	0.0149± 0.003
RS	0.009 ± 0.002	0.012 ± 0.002	0.007 ± 0.002	0.008 ± 0.002	0.005 ± 0.002
SUA	0.013 ± 0.002	0.015 ± 0.002	0.011 ± 0.002	0.013 ± 0.003	0.010 ± 0.002
MUA	0.030 ± 0.001	0.039 ± 0.001	0.029 ± 0.001	0.035 ± 0.001	0.029 ± 0.001

CENTER	SNR				
	NI	NI-RS	NI-RT	NI-RST	NI-SAC
FS	0.199 ± 0.038	0.224 ± 0.039	0.180 ± 0.033	0.213 ± 0.041	0.180 ± 0.036
RS	0.138 ± 0.008	0.156 ± 0.009	0.123 ± 0.009	0.147 ± 0.010	0.115 ± 0.010
SUA	0.169 ± 0.023	0.190 ± 0.024	0.151 ± 0.021	0.180 ± 0.026	0.148 ± 0.023
MUA	0.214 ± 0.014	0.222 ± 0.013	0.183 ± 0.012	0.216 ± 0.011	0.194 ± 0.015

Table 3.4.16: Mean low frequency signal, noise and SNR of the spiking activity in response to our control stimulus set presented full field or on the center (mean ± SEM)

4.2.2 Time Frequency Analysis of the Local Field Potential

Our previous measurements showed that at the in response to natural images the reliability of the spiking activity is modulated by center surround interactions. This modulation mainly occurs in the low frequency range (1-10Hz). We also showed that the reliability of the local field potential is strongly modulated by center surround interactions and that the surround takes a major role in the generation of a reliable response. However, we did not investigate yet the frequency dependency of the LFP reliability. Will we observe an increase in reliability mainly in the low frequency range? Moreover, will the frequency content of the reliability be similar across layers? As performed in section 4.1 we computed the subtracted the spontaneous activity from the signal, noise and signal to noise ratio, yet we will refer to them as signal, noise and signal to noise ratio.

- **Impact of the center surround interactions on the SNR**

We computed the time frequency analysis for all stimuli presented in the center or surround conditions (Figure 3.4.55 to 3.4.58; tables 3.4.17 and 3.4.18). The mean responses of the center and the surround followed the same pattern as the ones evoked by the full field.
Natural images evoked the highest low frequency reliability for the full field condition across the population ($p < 0.001$; Friedman test). This higher reliability is the result of a higher low frequency signal evoked by the full field condition but also a higher low frequency noise ($p < 0.001$). Despite this increase in noise, the SNR was still higher than the one evoked by the center and the surround. Interestingly, the surround stimulation evoked a higher level of low frequency reliability than the center ($p < 0.001$). This increase originates from a higher noise and a higher signal ($p < 0.001$). Both full field and center conditions displayed a higher noise than the center. This suggests that the surround participates in the noise increase but also on the signal increase that we observe. All artificial stimuli evoked the highest low frequency reliability for the full field condition and the lowest for the surround (Figures 3.4.56 and 3.3.57). All stimuli elicited the highest signal and noise when presented full field.
We also investigated the impact of our stimulations on the high frequency reliability (Figures 3.4.55, 3.4.56 and 3.4.58; table 3.4.18). When presented in the full field condition, DN evoked the highest signals while the surround evoked the lowest ones. We also observed an increase of noise at the center condition. This led to the highest high frequency reliability being elicited by a full field stimulation and the lowest one by the surround.

- **Laminar impact of the center surround interactions**

As observed for the full field condition, natural images evoked, for both center and surround conditions, the most reliable response in the low frequency range, within all layers ($p < 0.001$; Friedman test). However, the different conditions of stimulation had different impact across layers. Within all layers, the full field presentation of the natural images evoked the most reliable low frequency response. Again, this is linked to higher low frequency signal and noise ($p < 0.001$). In layers 2/3 and 5/6, *i.e.* the layers containing horizontal connections, the surround evoked a more reliable low frequency response than the center. On the other hand, in layer 4 no difference in reliability was observed between the center and surround conditions ($p > 0.05$). This absence of difference is caused by a high signal and a high noise evoked by the surround condition, while the center condition induced a lower noise and a lower signal than the surround condition. This led to

similar ratios. This suggest that the surround play an important part in the generation of a highly reliable response and that the latter is mediated by horizontal connections.
The full field presentation of the animated gratings evoked the most reliable low frequency response within all layers ($p < 0.001$). In layer 4, the center condition evoked a higher low frequency response than the surround (table 3.4.17). However, in layers 2/3 and 5/6, no difference between the center and surround conditions was observed. This is linked the fact that, for the two conditions, almost no difference in signal and noise were observed in these layers, leading to an absence of difference in the reliability. This result highlights the impact of the horizontal connections in the generation of a reliable response. In addition, it shows that the surround is sensitive to natural temporal statistics but that natural spatial statistics are also important in the generation of a reliable response.
Finally, dense noise and drifting gratings evoked, within layers, the same response pattern as the one observed for the complete population.
Regarding the high frequency reliability, the full field condition generally evoked the highest reliability levels and the surround the lowest ones. This was not observed in layers 2/3 and 5/6 when NI and GEM where presented in the surround.

In summary, we showed that natural images low frequency reliability is strongly modulated by center surround interactions. This originates from an interplay between an increase in signal and an increase in noise, higher for NI than the other stimuli, thus leading to a higher reliability. In addition, we showed that the sole stimulation of the surround with natural images evokes a more reliable response than the center stimulation.

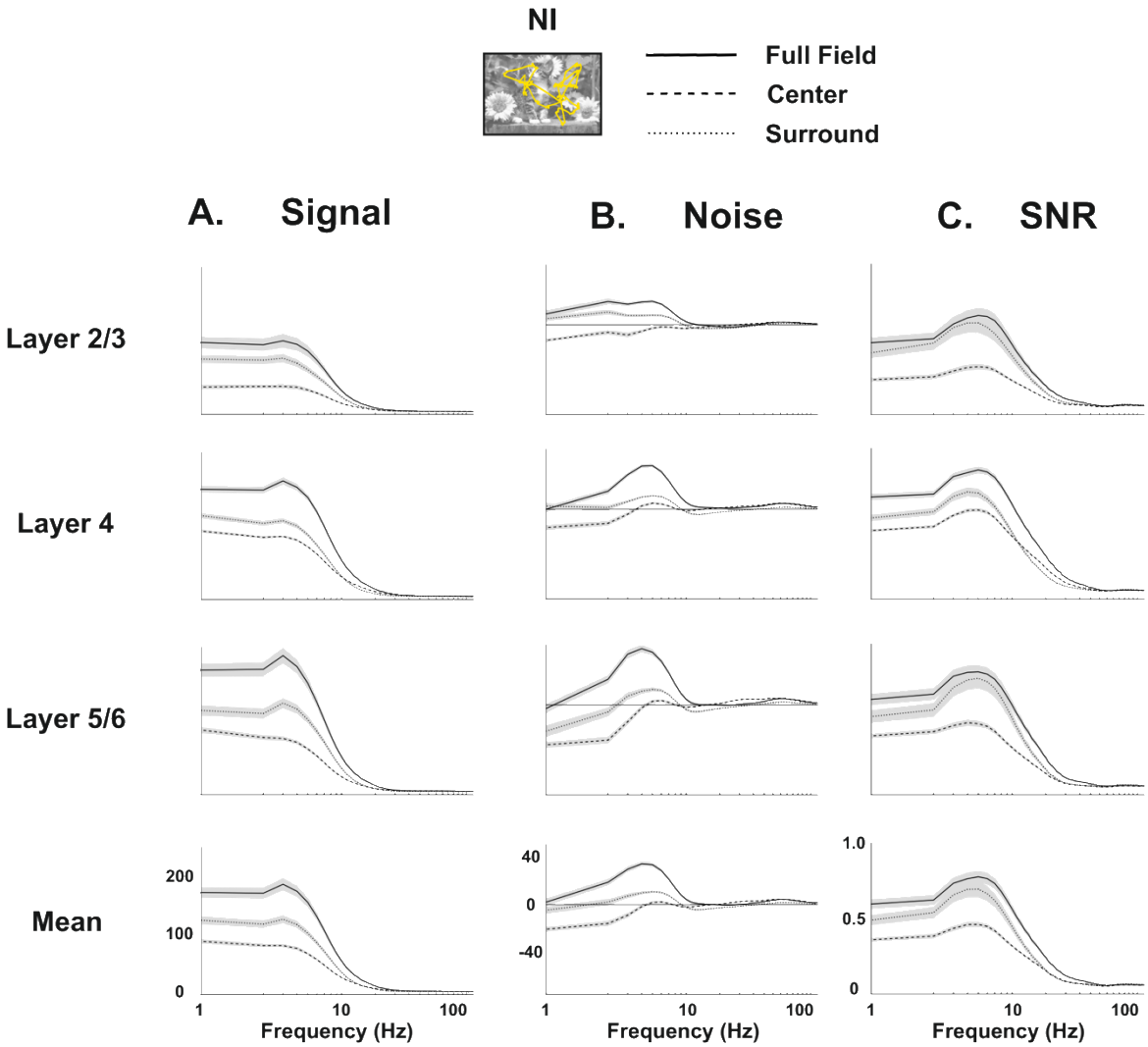

Figure 3.4.55: Time Frequency analysis of the local field potential in response to natural images presented on the full field (full line), center (big dashed lines) and surround (small dashed lines) conditions. The center surround interactions increase the reliability evoked by Natural Images. Surround stimulation with NI evoked a higher low frequency reliability than the center condition in layers 2/3 and 5/6.

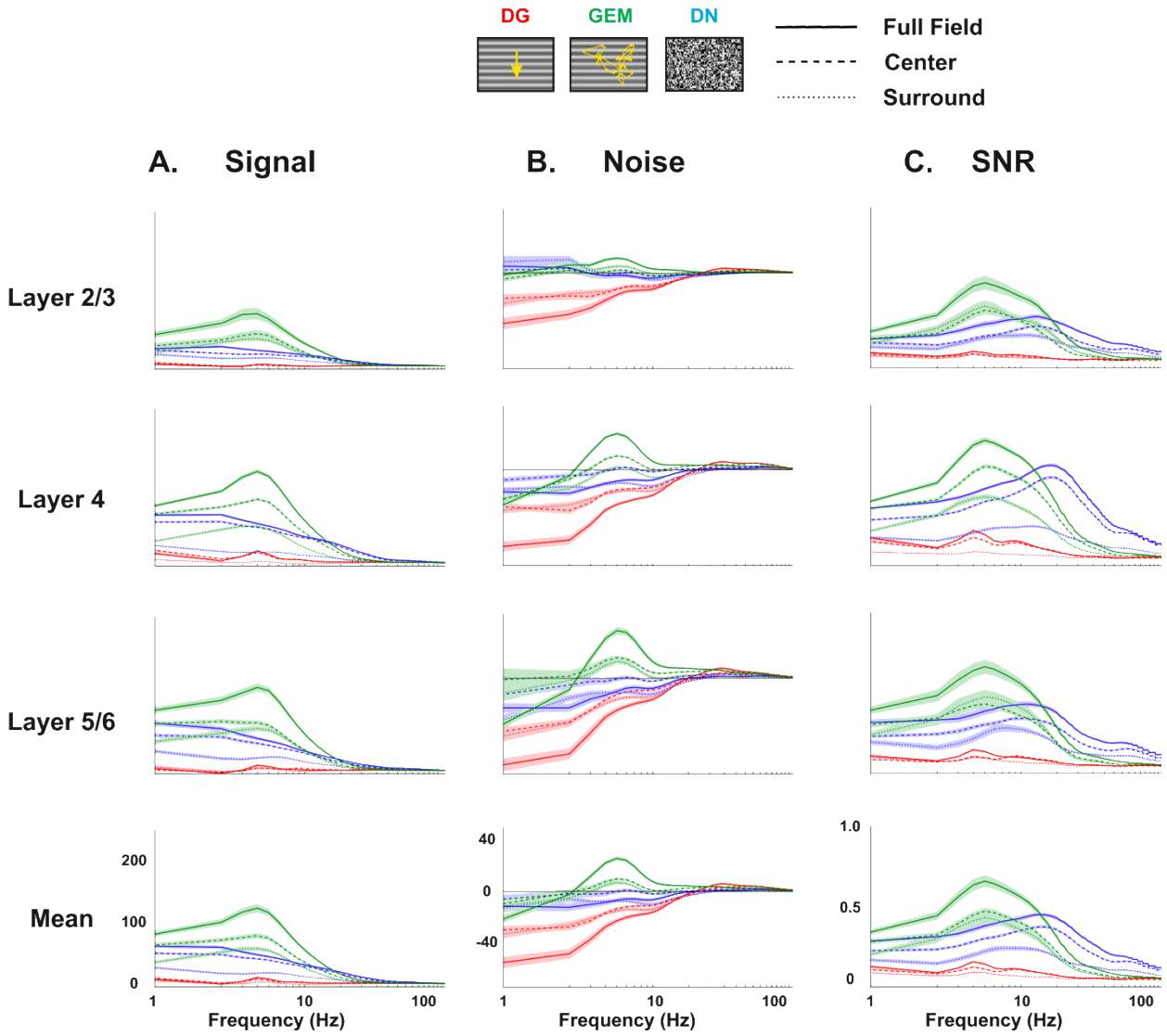

Figure 3.4.56: Time Frequency analysis of the local field potential in response to artificial stimuli presented on the full field (full line), center (big dashed lines) and surround (small dashed lines) conditions. Artificial stimuli' reliability is not strongly modulated by the surround alone.

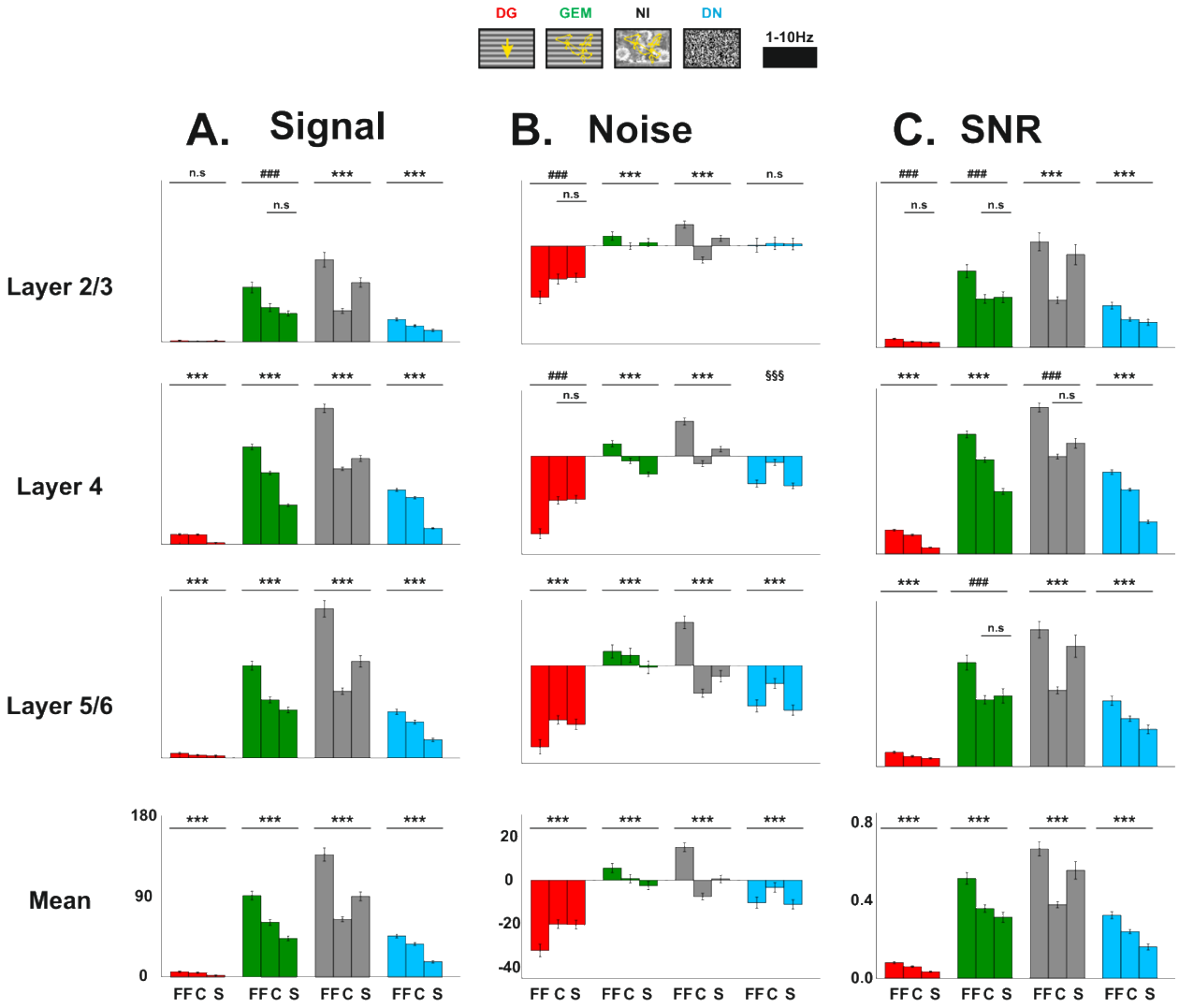

Figure 3.4.57: Bar plots of the low frequency SNR of LFP in response to our stimulus set. A. Mean low frequency Signal across layers and for the complete population. **B.** Mean low frequency Noise across layers and for the complete population. **C.** Mean low frequency SNR across layers and for the complete population. *: all conditions are significantly different from each other; # Full field is significantly different from the other conditions; § center is significantly different from the other conditions. * : $p < 0.05$; ** : $p < 0.01$; *** : $p < 0.001$; Error bars : SEM.

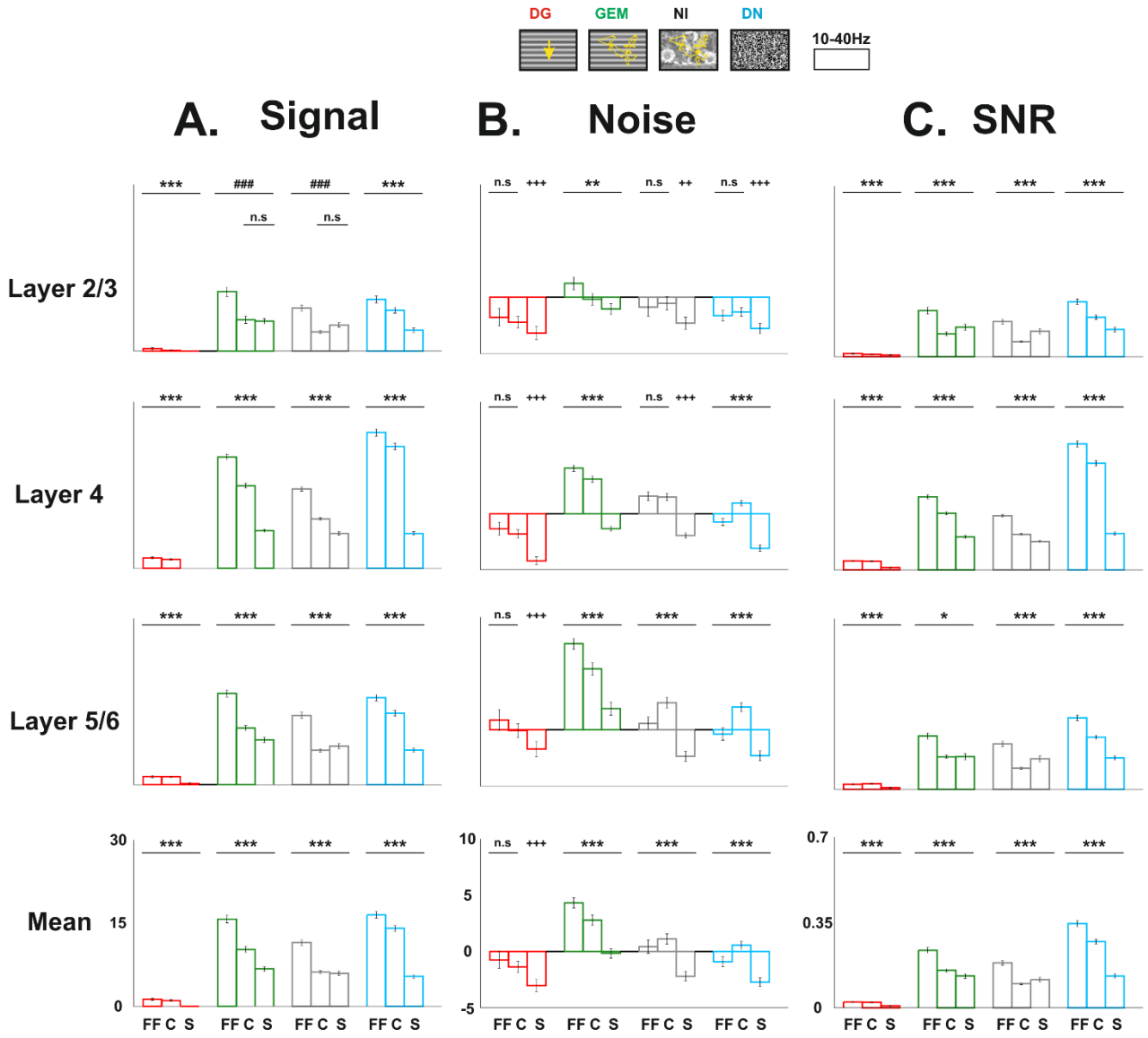

Figure 3.4.58: Bar plots of the high frequency SNR of LFP in response to our stimulus set. A. Mean high frequency Signal across layers and for the complete population. **B.** Mean high frequency Noise across layers and for the complete population. **C.** Mean high frequency SNR across layers and for the complete population. *: all conditions are significantly different from each other; # Full Field is significantly different from the other conditions; + Surround is significantly different from the other conditions; * : $p < 0.05$; ** : $p < 0.01$; *** : $p < 0.001$; Error bars : SEM.

- **Impact of the natural statistics on the center surround interactions**

Our results showed that natural images and grating animated with eye movements do not elicit the same reliability levels, in particular for the surround only stimulations. Is this difference linked to the spatial statistics of the natural images? Will we observe different responses if the temporal or spatial statistics are altered? We first compared the low frequency signal evoked by all stimuli for the center and surround conditions (Figure 3.4.59; Table 3.4.19). When presented in the center, the unaltered natural images evoked a higher SNR than all altered stimuli, except NI-SAC that displayed a higher reliability ($p < 0.001$). For the surround condition, we observed the same reliability pattern, except for NI-SAC that evoked the same reliability as NI. Natural images evoked the highest reliability for the full field condition and the lowest one for the center ($p < 0.001$) while NI-RS and NI-SAC displayed the highest levels of reliability for the full field condition, but no difference was observed between the center and surround conditions (figure 3.4.59). On the other hand, NI-RT and NI-RST displayed no difference between the full field and center conditions that evoked a higher level of reliability than the surround ($p < 0.001$). All the reliability levels that we observed originate from a similar response patter in the signal and noise values. These results confirm the strong impact of the surround on the generation of a reliable response. This reliable response is the result of interactions between natural spatial and temporal statistics.

At the high frequency range, all stimuli evoked the most reliable response for the FF condition and the lowest for the surround. Interestingly, the center condition evoked a higher noise level than the other conditions.

In summary our results show that, at the LFP level, in order to elicit reliable responses both center and surround need to be stimulated with unaltered spatio-temporal natural statistics. The center is more suited to the processing of spatial and temporal statistics while the surround is more suited to process temporal statistics.

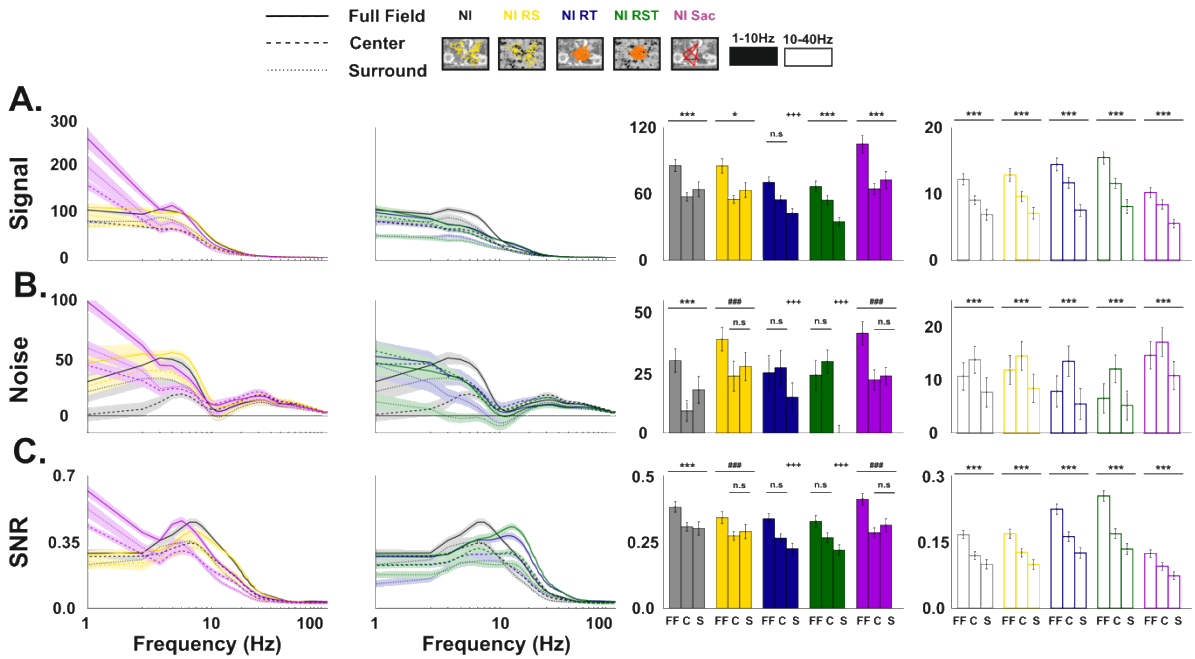

Figure 3.4.59: Time Frequency analysis of the local field potential in response to our set of control stimuli presented on the full field (full line), center (big dashed lines) and surround (small dashed lines) conditions. A. Mean Signal. B. Mean Noise. C. Mean SNR. *: all conditions are significantly different from each other; # Full field is significantly different from the other conditions; + Surround is significantly different from the other conditions. * : $p < 0.05$; ** : $p < 0.01$; *** : $p < 0.001$; Error bars : SEM.

In these sections, we computed the time frequency analysis of both LFP and spiking activity. For both signals, our results showed that natural images evoked the highest levels of reliability in the low frequency range. LFP evoked the higher levels of reliability while SUA the lowest ones, confirming the observations previously made with the trial-to-trial cross correlation. For both spiking activities and LFP, this increase in reliability comes from a high noise that is compensated by a high signal. At the spiking level, we also observed a high level of reliability evoked by DG at the grating frequency. This peak was present but reduced for the local field potential since the LFP averages anti-correlated signals. At the LFP level, DG evoked a strong reduction in the low frequency noise that was absent for the spiking activity. We also observed a high reliability evoked by DN in the high frequency range, for both signals. However, this increase was more visible for the LFP than the spiking activity.
We also showed that in response to NI, layers 4 and 5/6 evoked similar reliability levels. However, these two layers did not display the same noise and signals. Indeed layer 5/6 displayed a higher noise and signal than layer 4 but resulting in the same ratio. This highlights the different intrinsic properties of each layer. We also showed that natural images are strongly modulated by center surround interactions at the spiking and LFP levels. However, as observed for the trial-to-trial cross correlations the LFP display a stronger modulation than the spiking activity. Moreover, when natural images are presented on the surround, a strong low frequency reliability is elicited at the LFP level.
Finally, our results showed that the alteration of the spatial statistics reduced the low frequency reliability and that the temporal statistics seem to be optimally integrated by the surround.

FULL FIELD	LOW FREQUENCY SIGNAL			
	DG	GEM	NI	DN
Layer 2/3	1.3 ± 0.7	60.9 ± 6.2	91.7 ± 8.3	25.1 ± 1.7
Layer 4	11.0 ± 0.9	108.7 ± 3.0	151.8 ± 4.7	60.8 ± 1.6
Layer 5/6	5.1 ± 1.1	103.2 ± 5.1	166.6 ± 9.2	51.5 ± 2.9
Mean	5.8 ± 0.9	90.9 ± 4.8	136.7 ± 7.4	45.8 ± 2.1

CENTER	LOW FREQUENCY SIGNAL			
	DG	GEM	NI	DN
Layer 2/3	0.6 ± 0.6	38.3 ± 4.4	34.6 ± 3.0	17.9 ± 1.2
Layer 4	10.8 ± 0.8	80.0 ± 2.2	84.4 ± 1.9	52.3 ± 1.4
Layer 5/6	3.0 ± 0.8	64.8 ± 3.4	74.5 ± 3.6	40.2 ± 2.1
Mean	4.8 ± 0.7	61.0 ± 3.3	64.5 ± 2.8	36.8 ± 1.6

SURROUND	LOW FREQUENCY SIGNAL			
	DG	GEM	NI	DN
Layer 2/3	1.1 ± 0.5	31.6 ± 2.8	66.2 ± 5.2	12.8 ± 1.3
Layer 4	1.8 ± 0.3	43.9 ± 1.7	96.0 ± 3.4	17.9 ± 0.7
Layer 5/6	2.3 ± 0.8	53.6 ± 3.3	107.8 ± 6.4	20.3 ± 2.0
Mean	1.7 ± 0.5	43.0 ± 2.6	90.0 ± 5.0	17.0 ± 1.4

FULL FIELD	LOW FREQUENCY NOISE			
	DG	GEM	NI	DN
Layer 2/3	-23.5 ± 2.9	4.6 ± 1.9	9.9 ± 1.6	0.3 ± 3.2
Layer 4	-35.7 ± 2.4	5.7 ± 1.4	15.9 ± 1.6	-12.7 ± 1.7
Layer 5/6	-37.4 ± 3.4	6.4 ± 3.0	19.8 ± 2.9	-18.6 ± 2.7
Mean	-32.2 ± 2.9	5.6 ± 2.1	15.2 ± 2.0	-10.3 ± 2.5

CENTER	LOW FREQUENCY NOISE			
	DG	GEM	NI	DN
Layer 2/3	-15.1 ± 2.3	0.0 ± 1.5	-6.4 ± 1.4	1.3 ± 2.9
Layer 4	-20.3 ± 1.7	-2.3 ± 1.2	-3.5 ± 1.4	-2.9 ± 1.4
Layer 5/6	-25.0 ± 1.9	4.6 ± 3.2	-12.8 ± 1.8	-8.4 ± 2.3
Mean	-20.2 ± 2.0	0.8 ± 2.0	-7.6 ± 1.5	-3.3 ± 2.2

SURROUND	LOW FREQUENCY NOISE			
	DG	GEM	NI	DN
Layer 2/3	-14.5 ± 2.0	1.7 ± 1.8	3.6 ± 1.4	1.0 ± 2.7
Layer 4	-19.8 ± 1.7	-8.4 ± 1.0	3.2 ± 1.2	-13.7 ± 1.2
Layer 5/6	-27.1 ± 2.4	-0.8 ± 3.0	-5.0 ± 2.7	-20.6 ± 2.3
Mean	-20.4 ± 2.0	-2.5 ± 1.9	0.6 ± 1.8	-11.1 ± 2.1

FULL FIELD	LOW FREQUENCY SNR			
	DG	GEM	NI	DN
Layer 2/3	0.04 ± 0.00	0.39 ± 0.03	0.54 ± 0.05	0.21 ± 0.02
Layer 4	0.12 ± 0.01	0.62 ± 0.02	0.75 ± 0.02	0.42 ± 0.01
Layer 5/6	0.07 ± 0.01	0.54 ± 0.04	0.70 ± 0.04	0.34 ± 0.02
Mean	0.08 ± 0.00	0.51 ± 0.03	0.67 ± 0.0	0.32 ± 0.02

CENTER	LOW FREQUENCY SNR			
	DG	GEM	NI	DN
Layer 2/3	0.03 ± 0.00	0.25 ± 0.02	0.24 ± 0.02	0.14 ± 0.01
Layer 4	0.10 ± 0.00	0.48 ± 0.01	0.50 ± 0.01	0.33 ± 0.01
Layer 5/6	0.05 ± 0.00	0.34 ± 0.02	0.39 ± 0.02	0.25 ± 0.01
Mean	0.06 ± 0.00	0.36 ± 0.02	0.38 ± 0.02	0.24 ± 0.01

SURROUND	LOW FREQUENCY SNR			
	DG	GEM	NI	DN
Layer 2/3	0.03 ± 0.00	0.26 ± 0.03	0.48 ± 0.05	0.13 ± 0.02
Layer 4	0.03 ± 0.00	0.32 ± 0.01	0.57 ± 0.03	0.16 ± 0.01
Layer 5/6	0.04 ± 0.00	0.36 ± 0.04	0.62 ± 0.06	0.19 ± 0.02
Mean	0.03 ± 0.00	0.31 ± 0.03	0.56 ± 0.04	0.16 ± 0.02

Table 3.4.17: Mean low frequency signal, noise and SNR of the LFP in response to our stimulus set presented full field, on the center or on the surround (mean ± SEM)

FULL FIELD	HIGH FREQUENCY SIGNAL			
	DG	GEM	NI	DN
Layer 2/3	0.4 ± 0.2	10.7 ± 0.9	7.7 ± 0.6	9.3 ± 0.6
Layer 4	1.9 ± 0.2	20.1 ± 0.5	14.3 ± 0.4	24.5 ± 0.6
Layer 5/6	1.5 ± 0.2	16.5 ± 0.6	12.5 ± 0.6	15.7 ± 0.6
Mean	1.3 ± 0.2	15.7 ± 0.7	11.5 ± 0.5	16.5 ± 0.6

CENTER	HIGH FREQUENCY SIGNAL			
	DG	GEM	NI	DN
Layer 2/3	0.1 ± 0.1	5.6 ± 0.6	3.4 ± 0.2	7.4 ± 0.5
Layer 4	1.6 ± 0.1	14.9 ± 0.4	8.9 ± 0.2	22.0 ± 0.6
Layer 5/6	1.4 ± 0.1	10.2 ± 0.5	6.2 ± 0.3	12.9 ± 0.5
Mean	1.0 ± 0.1	10.3 ± 0.5	6.2 ± 0.3	14.1 ± 0.5

SURROUND	HIGH FREQUENCY SIGNAL			
	DG	GEM	NI	DN
Layer 2/3	-0.1 ± 0.1	5.4 ± 0.5	4.7 ± 0.4	3.8 ± 0.4
Layer 4	-0.3 ± 0.1	6.8 ± 0.3	6.3 ± 0.3	6.3 ± 0.3
Layer 5/6	0.2 ± 0.2	8.1 ± 0.5	6.9 ± 0.5	6.3 ± 0.4
Mean	-0.1 ± 0.1	6.7 ± 0.4	6.0 ± 0.4	5.4 ± 0.4

FULL FIELD	HIGH FREQUENCY NOISE			
	DG	GEM	NI	DN
Layer 2/3	-1.8 ± 0.8	1.2 ± 0.6	-0.9 ± 0.8	-1.6 ± 0.5
Layer 4	-1.3 ± 0.6	4.1 ± 0.3	1.6 ± 0.4	-0.7 ± 0.3
Layer 5/6	0.9 ± 0.9	7.7 ± 0.5	0.6 ± 0.6	-0.4 ± 0.5
Mean	-0.7 ± 0.8	4.3 ± 0.5	0.4 ± 0.6	-0.9 ± 0.5

CENTER	HIGH FREQUENCY NOISE			
	DG	GEM	NI	DN
Layer 2/3	-2.2 ± 0.5	-0.2 ± 0.5	-0.5 ± 0.6	-1.3 ± 0.4
Layer 4	-1.8 ± 0.4	3.1 ± 0.3	1.5 ± 0.3	1.0 ± 0.2
Layer 5/6	-0.1 ± 0.6	5.4 ± 0.6	2.4 ± 0.5	2.0 ± 0.4
Mean	-1.4 ± 0.5	2.8 ± 0.5	1.1 ± 0.5	0.6 ± 0.4

SURROUND	HIGH FREQUENCY NOISE			
	DG	GEM	NI	DN
Layer 2/3	-3.2 ± 0.6	-1.0 ± 0.5	-2.3 ± 0.5	-2.8 ± 0.5
Layer 4	-4.2 ± 0.4	-1.3 ± 0.2	-2.0 ± 0.2	-3.1 ± 0.3
Layer 5/6	-1.7 ± 0.7	1.9 ± 0.6	-2.3 ± 0.4	-2.3 ± 0.5
Mean	-3.0 ± 0.5	-0.2 ± 0.4	-2.2 ± 0.4	-2.7 ± 0.4

FULL FIELD	HIGH FREQUENCY SNR			
	DG	GEM	NI	DN
Layer 2/3	0.01 ± 0.00	0.19 ± 0.01	0.14 ± 0.01	0.23 ± 0.01
Layer 4	0.04 ± 0.00	0.30 ± 0.01	0.22 ± 0.01	0.52 ± 0.01
Layer 5/6	0.02 ± 0.00	0.22 ± 0.01	0.19 ± 0.01	0.29 ± 0.01
Mean	0.02 ± 0.00	0.24 ± 0.01	0.18 ± 0.01	0.35 ± 0.01

CENTER	HIGH FREQUENCY SNR			
	DG	GEM	NI	DN
Layer 2/3	0.01 ± 0.00	0.09 ± 0.01	0.06 ± 0.00	0.16 ± 0.01
Layer 4	0.04 ± 0.00	0.23 ± 0.01	0.15 ± 0.00	0.44 ± 0.01
Layer 5/6	0.02 ± 0.00	0.13 ± 0.01	0.09 ± 0.00	0.21 ± 0.01
Mean	0.02 ± 0.00	0.15 ± 0.01	0.10 ± 0.00	0.27 ± 0.01

SURROUND	HIGH FREQUENCY SNR			
	DG	GEM	NI	DN
Layer 2/3	0.01 ± 0.00	0.12 ± 0.01	0.10 ± 0.01	0.11 ± 0.01
Layer 4	0.01 ± 0.00	0.14 ± 0.01	0.12 ± 0.01	0.15 ± 0.01
Layer 5/6	0.01 ± 0.00	0.13 ± 0.01	0.12 ± 0.01	0.13 ± 0.01
Mean	0.01 ± 0.00	0.13 ± 0.01	0.12 ± 0.01	0.13 ± 0.01

Table 3.4.18: Mean high frequency signal, noise and SNR of the LFP in response to our stimulus set presented full field, on the center or on the surround (mean ± SEM)

FULL FIELD	LFP				
	NI	NI-RS	NI-RT	NI-RST	NI-SAC
SIGNAL	85.7 ± 5.4	85.4 ± 6.5	70.7 ± 4.8	66.8 ± 4.8	105.3 ± 8.0
NOISE	30.0 ± 4.8	38.9 ± 4.8	25.0 ± 7.0	24.1 ± 6.2	41.4 ± 4.8
SNR	0.38 ± 0.02	0.34 ± 0.02	0.33 ± 0.02	0.32 ± 0.02	0.41 ± 0.02

CENTER	LFP				
	NI	NI-RS	NI-RT	NI-RST	NI-SAC
SIGNAL	57.4 ± 3.8	55.2 ± 3.7	54.8 ± 3.8	54.4 ± 3.9	64.6 ± 4.9
NOISE	9.2 ± 4.3	23.6 ± 6.2	27.1 ± 7.2	29.6 ± 4.8	22.0 ± 4.1
SNR	0.25 ± 0.02	0.19 ± 0.02	0.18 ± 0.02	0.19 ± 0.02	0.21 ± 0.03

SURROUND	LFP				
	NI	NI-RS	NI-RT	NI-RST	NI-SAC
SIGNAL	64.2 ± 6.6	63.5 ± 6.6	42.6 ± 4.1	34.9 ± 3.9	72.7 ± 7.6
NOISE	17.9 ± 5.5	27.71 ± 5.9	14.8 ± 5.9	-1.5 ± 4.7	23.6 ± 3.6
SNR	0.29 ± 0.03	0.26 ± 0.03	0.18 ± 0.02	0.17 ± 0.02	0.32 ± 0.03

Table 3.4.19: Mean low frequency signal, noise and SNR of the LFP in response to our control stimulus set presented full field, on the center or on the surround (mean ± SEM)

4.2.3 Power Spectral Density and Reliability of the Local Field Potential

As shown in the previous section, our different stimuli modulate the LFP in different ways and that in different frequency bands. Moreover, we showed that the center surround interactions strongly modulate the stimulus locked response and its reliability, in particular when natural images were presented. Therefore, we wondered which frequency bands the center surround interactions would affect the most. In addition, will we observe the same modulation across layers? In order to answer these questions, we first computed the power spectrum density and the relative power spectrum density of the stimulus locked response (figures 3.4.60 and 3.4.61; tables 3.4.20 and 3.4.21).

- **Mean evoked PSD**

We first investigated the response in the low frequency range. As observed for the full field condition, for both center and surround conditions, natural images always evoked the highest PSD ($p < 0.001$; Friedman test). We then investigated the impact of the center surround interactions on the power spectrum density. At the global population level, natural images evoked their highest PSD (and R-PSD) when they were presented full field ($p < 0.001$; Friedman test). As observed previously, the sole stimulation of the surround with natural images evoked a higher PSD (and R-PSD) than the stimulation of the center ($p < 0.001$; Friedman test). The difference between the spectral density evoked by the center and the surround is increased for the R-PSD, compared to the PSD. Indeed, the R-PSD evoked by natural images presented on the center is very low (Table 3.4.21). This suggest that a great part of the center response emerges from an intrinsic variability present within each layer. We then compared the impact of the center surround modulations evoked by artificial stimuli. The full field presentation of GEM and DN always evoked a higher PSD (and R-SPD) than the other conditions ($p < 0.001$; Friedman test). Unlike what was observed for NI, for these stimuli, the center condition always evoked a higher PSD (and R-PSD) than the surround, except in some cases where they were similar (figures 3.4.60 and 3.4.61; tables 3.4.20 and 3.4.21). On the other hand, drifting gratings evoked their highest PSD (and R-PSD) when presented on the center. This is not surprising since it is known that the stimulation of both center and surround with DG tend to suppress the response. As observed for the full field condition, DG only displayed a positive R-PSD at the grating frequency and its harmonics.
We then investigated the high frequency power spectrum density. As observed for the full field condition, GEM evoked the highest and DG the lowest PSD and R PSD ($p < 0.001$). For all stimuli, the full field condition evoked a higher PSD and R-PSD than the center and surround conditions ($p < 0.001$). Unlike what was observed for the low frequencies, the center condition always evoked a higher spectral density than the surround, even for NI. This suggest that this frequency range is not modulated in the same way by the center surround interactions present in natural scenes. We will not describe the very high frequencies power spectrum since at the full field and center conditions and within each layer, all stimuli evoked the same mean PSD and R-PSD ($p > 0.05$). For the surround condition, all stimuli evoked the same very high frequency PSD, lower than the one observed for the FF and C conditions.

- **Laminar impact of the center surround interactions**

As observed for the complete population, within all layers natural images evoked their highest PSD (and R-PSD) when they were presented full field ($p < 0.001$; Friedman test).However, unlike what was observed when the stimulation was performed on the whole screen, some stimuli, when presented on the center, evoked a similar spectrum density as NI.
At the PSD level, in layer 2/3, dense noise evoked the same PSD as natural images ($p = 0.33$; Friedman test). In addition, in both layers 4 and 5/6, animated gratings evoked the same spectral density as natural images ($p > 0.23$). However, when we looked at the R-PSD, all these equivalent responses were different. This implies that the similarity that we observe comes from a strong PSD of the spontaneous activity and the stimulus dependent response do not modulate sufficiently this PSD in order to reach a significantly different response. The highest PSD was observed, for both center and surround conditions and for each stimulus respectively, in layer 5/6 while the lowest in layer 2/3 ($p < 0.001$; Kruskal-Wallis test). This is linked to the spectral density of the spontaneous activity in layer 5/6 that is higher than the one recorded in other layers. Indeed, when we compare the relative spectral density between layers we end up with different results. For the center condition, all stimuli elicited the highest R-PSD in layer 4 and the lowest in layer 2/3 ($p < 0.001$; Kruskal-Wallis test). On the other hand, for the surround condition, both NI and GEM evoked their highest R-PSD in layer 5/6 and the lowest in layer 2/3 ($p < 0.001$). This is probably linked to horizontal connections present in this layer that are sensitive to the surround and to temporal frequencies of eye movements. Regarding the difference in the spectral density evoked by our different conditions of stimulation, within each layer we observed the same response pattern as in the mean response (figures 3.4.60 and 3.4.61; tables 3.4.20 and 3.4.21).

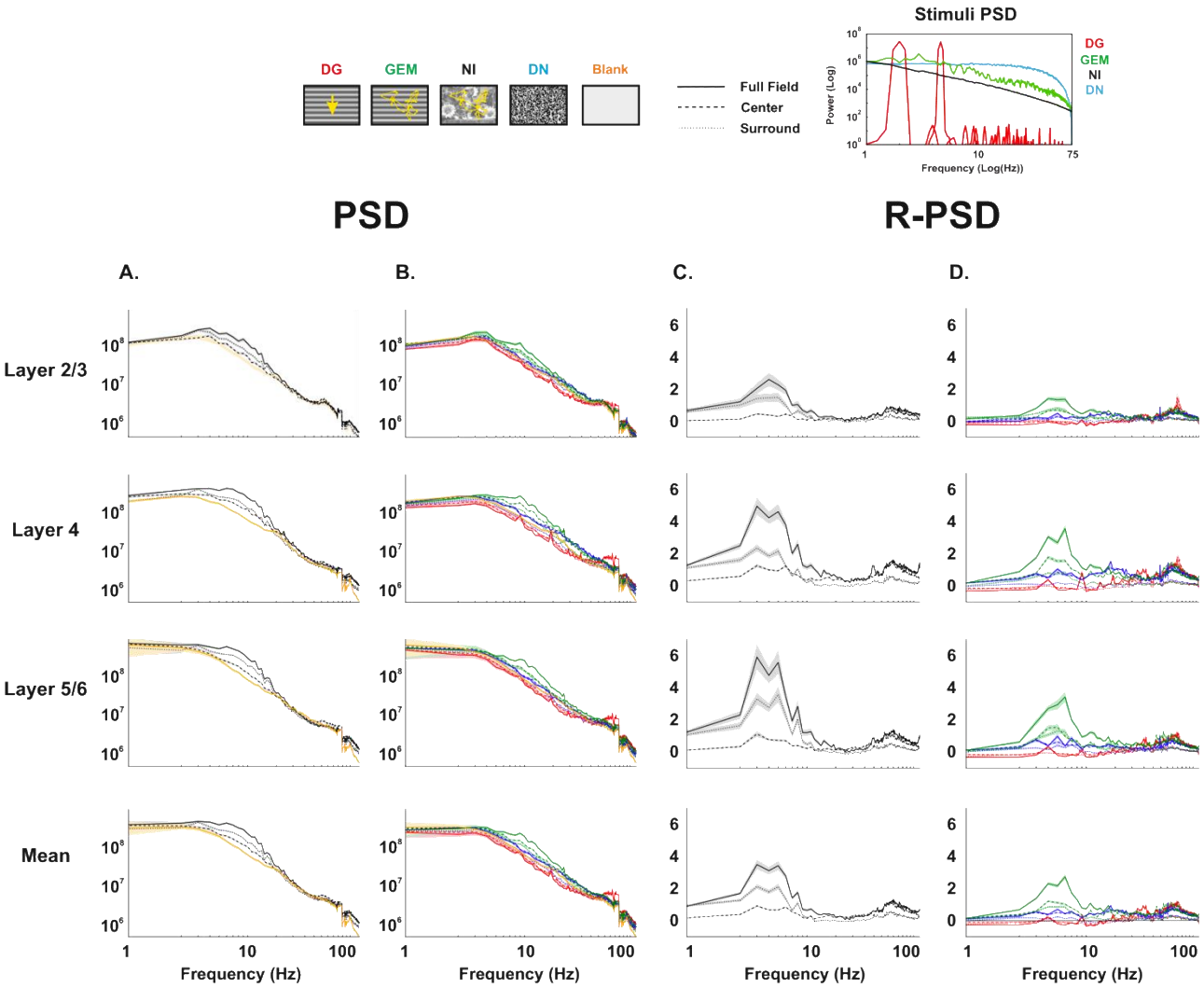

Figure 3.4.60: Power Spectrum density and relative power spectrum density of the LFP in response to our set of stimuli presented full field, on the center and surround conditions. The center surround interactions increase the PSD evoked by Natural Images. Surround stimulation with NI evoked a higher low frequency PSD than the center condition in layers 2/3 and 5/6. The power spectrum of the stimuli is shown above. (Shaded Area : SEM)

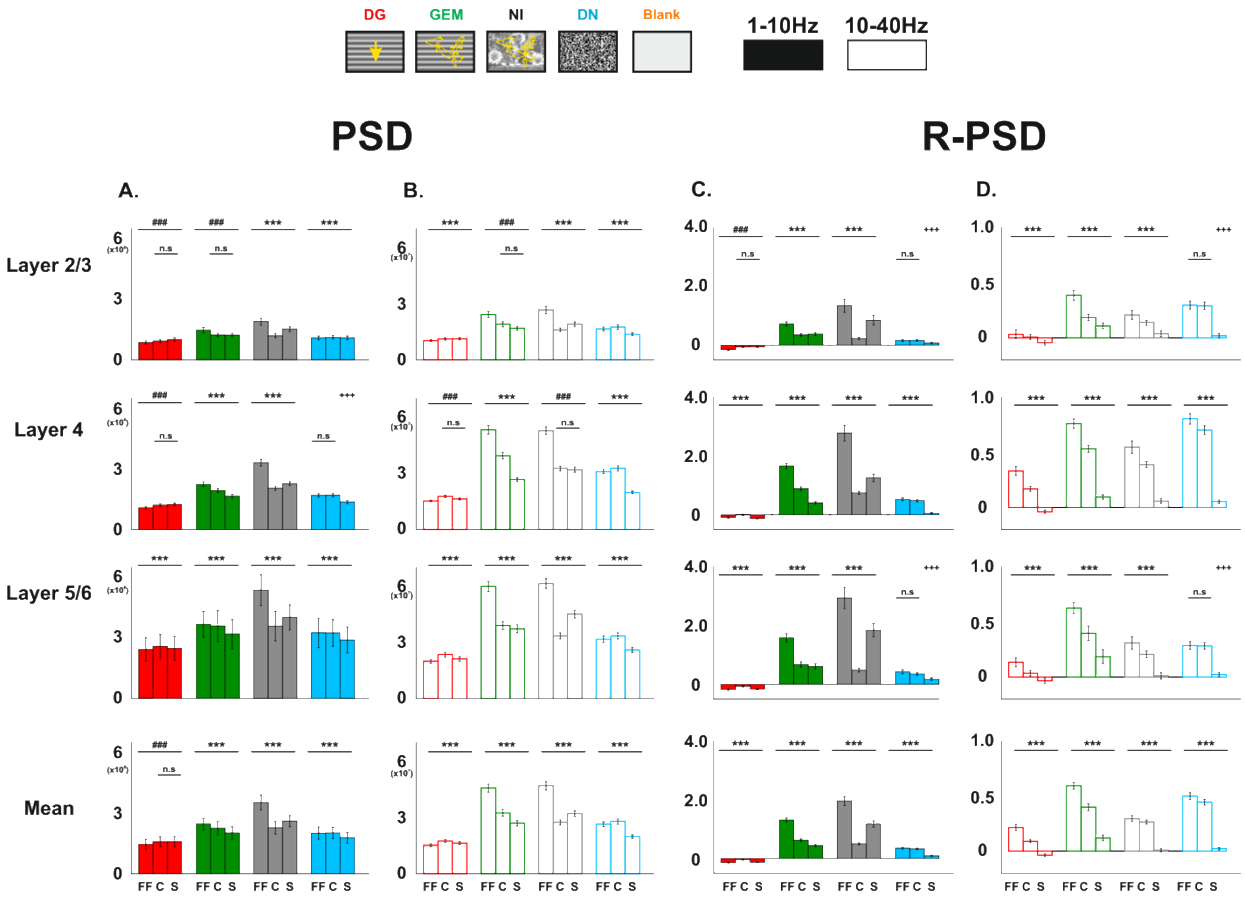

Figure 3.4.61: Barplots of the power Spectrum density and relative power spectrum density of the LFP in response to our set of stimuli presented full field, on the center and surround conditions. *: all conditions are significantly different from each other; # Full field is significantly different from the other conditions. * : p < 0.05; ** : p < 0.01; *** : p < 0.001; Error bars : SEM.

- **Impact of the center surround interactions on the frequency-based reliability**

We then wondered if, as observed for the full field condition, the increase in PSD observed for the low frequency range was accompanied by an increase in reliability. Moreover, will we also observe a strong center surround modulation in the low frequency range? In order to answer these questions, we computed the trial-to-trial coherence and the same time frequency analysis as in section 4.1, in order to obtain the SNR. As described in before, we computed the relative SNR. The differences between the coherence and SNR analysis will be commented, if no difference is observed the results will be described as a whole. These two analyses will indicate the level of reliability of the stimulus locked LFP for all frequencies. The results are reported in figures 3.4.61 and 3.4.62 (and tables 3.4.22 and 3.4.23). We will first describe the results obtained for low frequencies.

Our results showed that natural images evoked within all layers and at the level of the mean population, the highest levels of reliability for both center and surround conditions ($p < 0.001$; Friedman test). However, one exception can be noted. In layer 2/3, for both SNR and Coherence, the presentation of NI and GEM on the center evoked the same low frequency reliability ($p > 0.05$).

We also compared the reliability evoked by the full field, center and surround conditions. When presented full field natural images evoked, within all layers and at the mean population level, a most reliable response than the center and surround conditions ($p < 0.001$; Friedman test). In layers 2/3, 5/6 and at population level, natural images, when presented on the surround condition evoked a more reliable response than the center condition ($p < 0.001$). However, in layer 4, for the coherence the center evoked a more reliable response than the surround, while for SNR, despite a higher mean evoked by the center, no significant difference was observed between the two responses ($p > 0.05$). This suggest that the horizontal connections present in layers 2/3 and 5/6 are activated by the surround stimulation and elicit a reliable response. On the other hand, layer 4 is more sensitive to center stimulations, which explains this increase for the center stimulation. We wondered if the artificial stimuli would be impacted the same way by the center surround interactions. For all artificial stimuli, the full field condition always evoked the most reliable response ($p < 0.001$). However, we observed a pattern different from NI when we compared the impact of the center and surround conditions. Indeed, for DG and DN, the center condition always evoked a more reliable response than the surround ($p < 0.001$). On the other hand, when animated gratings were presented, we observed the same reliability for the center and surround conditions in layers 2/3 and 5/6 ($p > 0.05$). This suggest that the eye movements activate in a reliable manner the horizontal connections. However, since NI is more reliable than GEM, this implies that the simple spatial statistics of the animated gratings are not sufficient to elicit a response as reliable as NI. This suggest that the spatial statistics also play a role in the generation of a reliable response and that surround plays a key role in the processing of natural scenes, in particular in the low frequency range.

As observed for the full field condition, dense noise evoked for the center, the highest high frequency reliability ($p < 0.001$; Friedman test). On the other hand, when only the surround was stimulated, the levels of reliability evoked by GEM were the highest ($p < 0.001$). The highest levels of reliability were observed in layer 4. For all stimuli, the highest levels of reliability were observed for the full field condition ($p < 0.001$). When NI was presented on the surround condition, it evoked a higher high frequency reliability than the center ($p < 0.001$). The opposite was observed for the artificial stimuli.

It is important to note that for all stimuli, except dense noise, the reliability was higher in the low frequency than in the high frequency band ($p < 0.001$; Kruskal-Wallis test).

Taken together, our results highlight the fact that one of the most commonly used stimuli in the field of visual neurosciences, *i.e.* drifting gratings induce responses that are very different from what we

observe with other stimuli. Therefore, in some cases, before drawing new conclusions, studies need to investigate V1 responses with more than one simple stimulus such as DG.

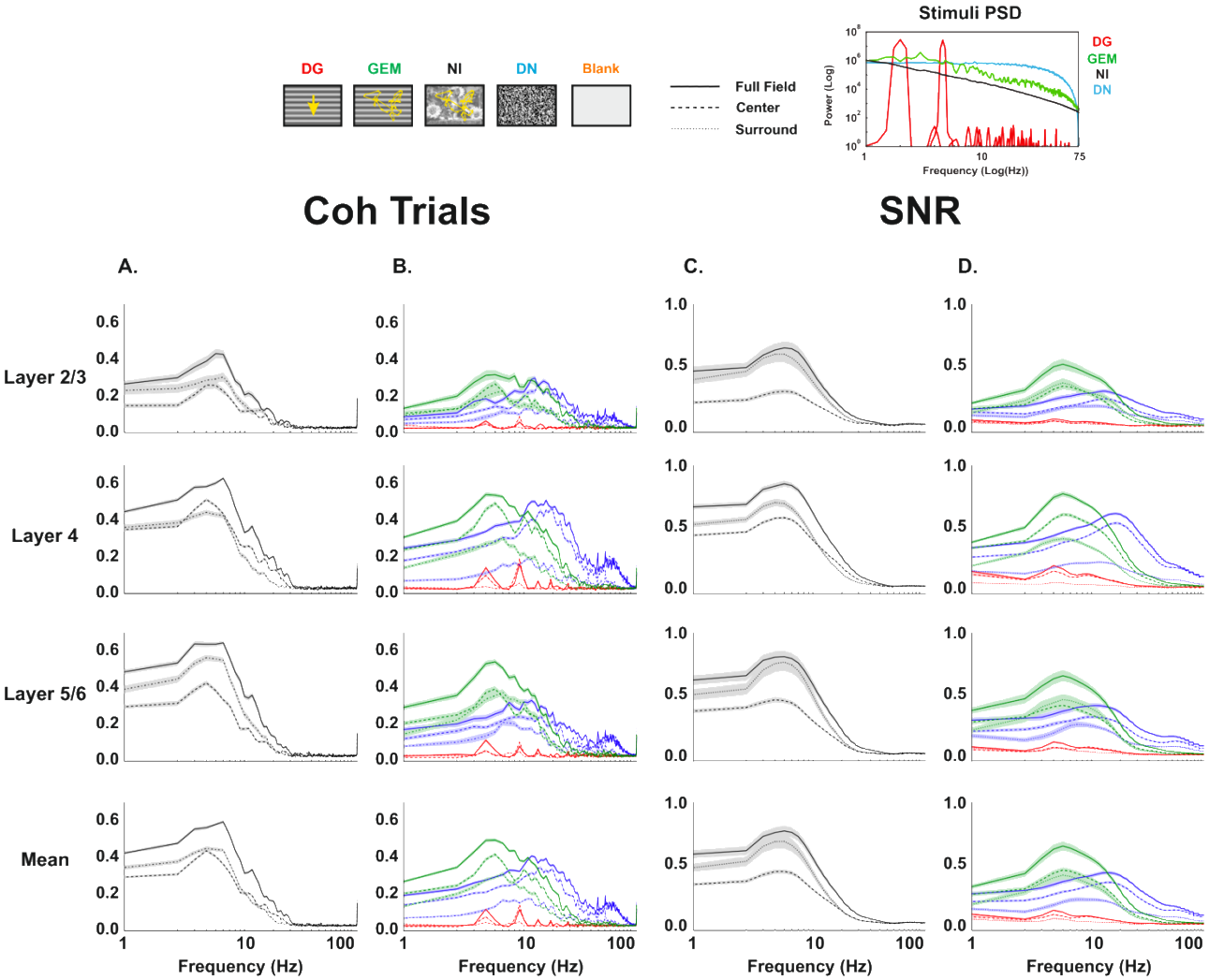

Figure 3.4.61: Coherence and SNR of the LFP in response to our set of stimuli presented full field, on the center and surround conditions. The center surround interactions increase the reliability evoked by Natural Images. Surround stimulation with NI evoked a higher low frequency reliability than the center condition in layers 2/3 and 5/6. The power spectrum of the stimuli is shown at the top of the figure (Shaded area : SEM)

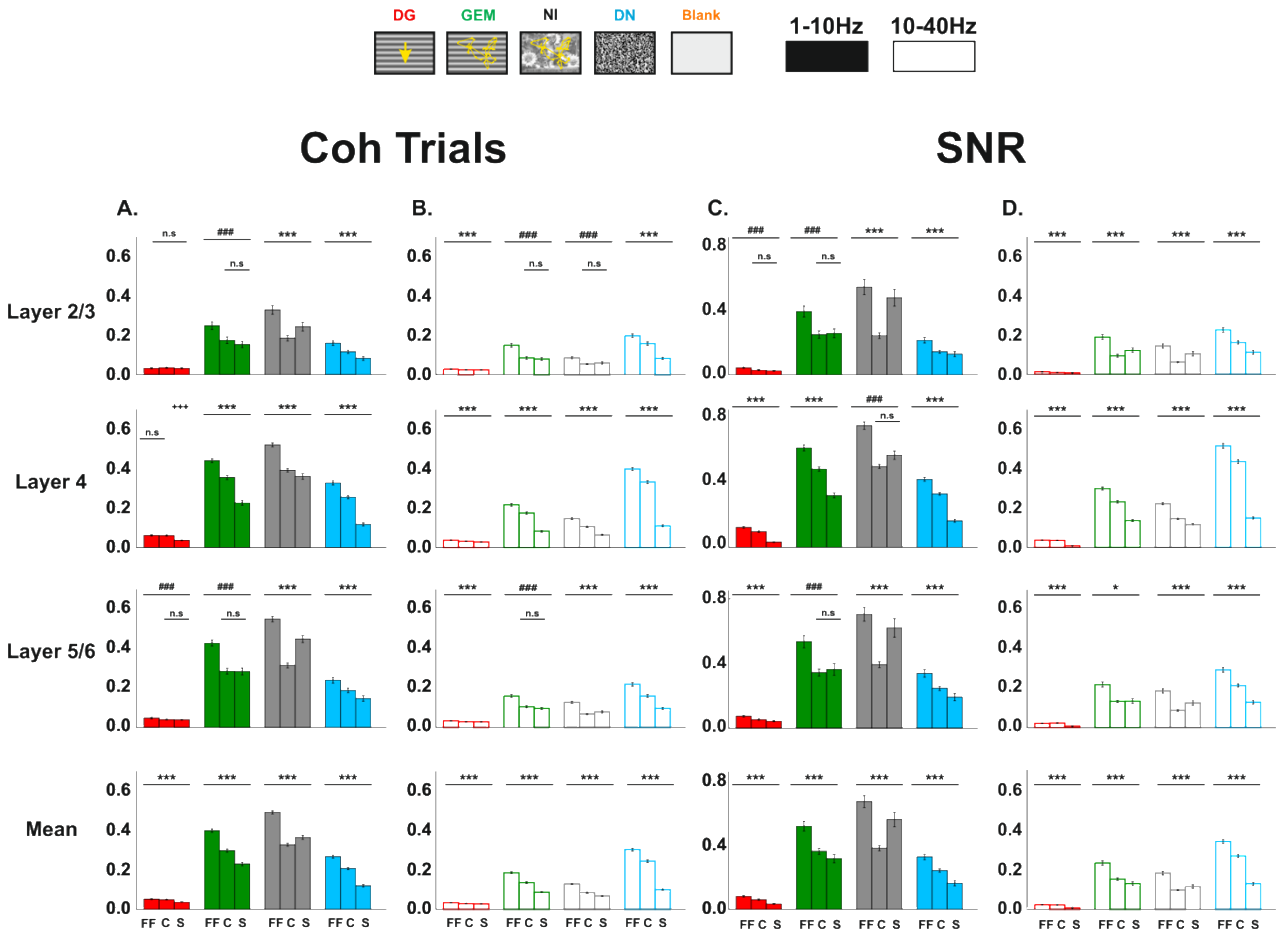

Figure 3.4.62: Barplots of the Coherence and SNR of the LFP in response to our set of stimuli presented full field, on the center and surround conditions. *: all conditions are significantly different from each other; # Full field is significantly different from the other conditions. * : $p < 0.05$; ** : $p < 0.01$; *** : $p < 0.001$; Error bars : SEM.

- **Impact of the natural statistics on the time frequency response**

Our results showed that animated gratings evoked strong responses and levels of reliability when the surround only was stimulated. However, these levels of reliability were lower than the ones observed for natural images, suggesting that spatial statistics play a role in the generation of a reliable response. We wondered if by altering the spatial and/or temporal statistics we would still the same center surround modulations. In order to answer this question, we computed the PSD, R-PSD, Coherence and SNR of the LFP response evoked by our set of control stimuli (Figure 3.4.63; table 3.4.24).

Our results showed that for both PSD and R-PSD (figure 3.4.63-A-B), when presented in the center, the unaltered natural image evoked the same spectral density as the natural image where both spatial and temporal statistics were altered ($p > 0.55$) while all the other altered natural image displayed a higher spectral density than NI ($p < 0.001$). Regarding the surround condition, NI and NI-RST displayed the same PSD and R-PSD, higher than the one evoked by the other stimuli ($p < 0.001$). For the surround condition, the natural images with altered spatial frequencies displayed the lowers PSDs. This suggest that unaltered temporal statistics are necessary in the generation of the strong response and that the surround processes them. In addition, the fact that NI-SAC displays a lower spectral density than the unaltered NI suggest that all eye movements, not only saccades, are important in the generation of strong PSD. The importance of the surround in the processing of eye movements in confirmed by the fact that all stimuli containing eye movements displayed a higher PSD for the surround than the center condition while those containing altered eye movements displayed the opposite behavior ($p < 0.001$; Friedman test). However, since for all stimuli the full field condition evoked a higher PSD than the other conditions, center surround modulations are still present even when the statistics are altered.

We then investigated the levels of reliability evoked by the altered stimuli (Figure 3.4.63-C-D; table 3.4.24). The coherence and the SNR analysis resulted in the same response patterns. When presented on the center condition, the unaltered natural image evoked a higher low frequency reliability than the other stimuli ($p < 0.001$; Friedman test). On the other hand, when presented on the surround, NI and NI-SAC evoked equivalent levels of reliability, higher than the other stimuli ($p < 0.001$). We then wondered if the three conditions of stimulation evoked the same levels of reliability. Our results showed that, for both the coherence and the SNR, the full field condition evoked, for all stimuli respectively, the most reliable response ($p < 0.001$; Friedman test). With the coherence analysis, we observed that the presentation of unaltered NI on the surround evoked a higher reliability than the center, while the opposite was observed for natural images. However, the difference between the two conditions, for both analyses is very small. This absence of difference comes from an oversampling of layer 4. NI-RS and NI-SAC displayed the same results with both analyses, *i.e.* the presentation of these stimuli on the center or the surround evoked the same levels of reliability ($p > 0.05$). Finally, when we computed the coherence and the SNR, NI-RT and NI-RST evoked a higher correlation for the center condition than the surround. Despite the differences between the coherence and SNR analysis, we obtained the same patterns of responses with both analyses. These results confirm the fact that the surround plays a key role in the processing of temporal frequencies.

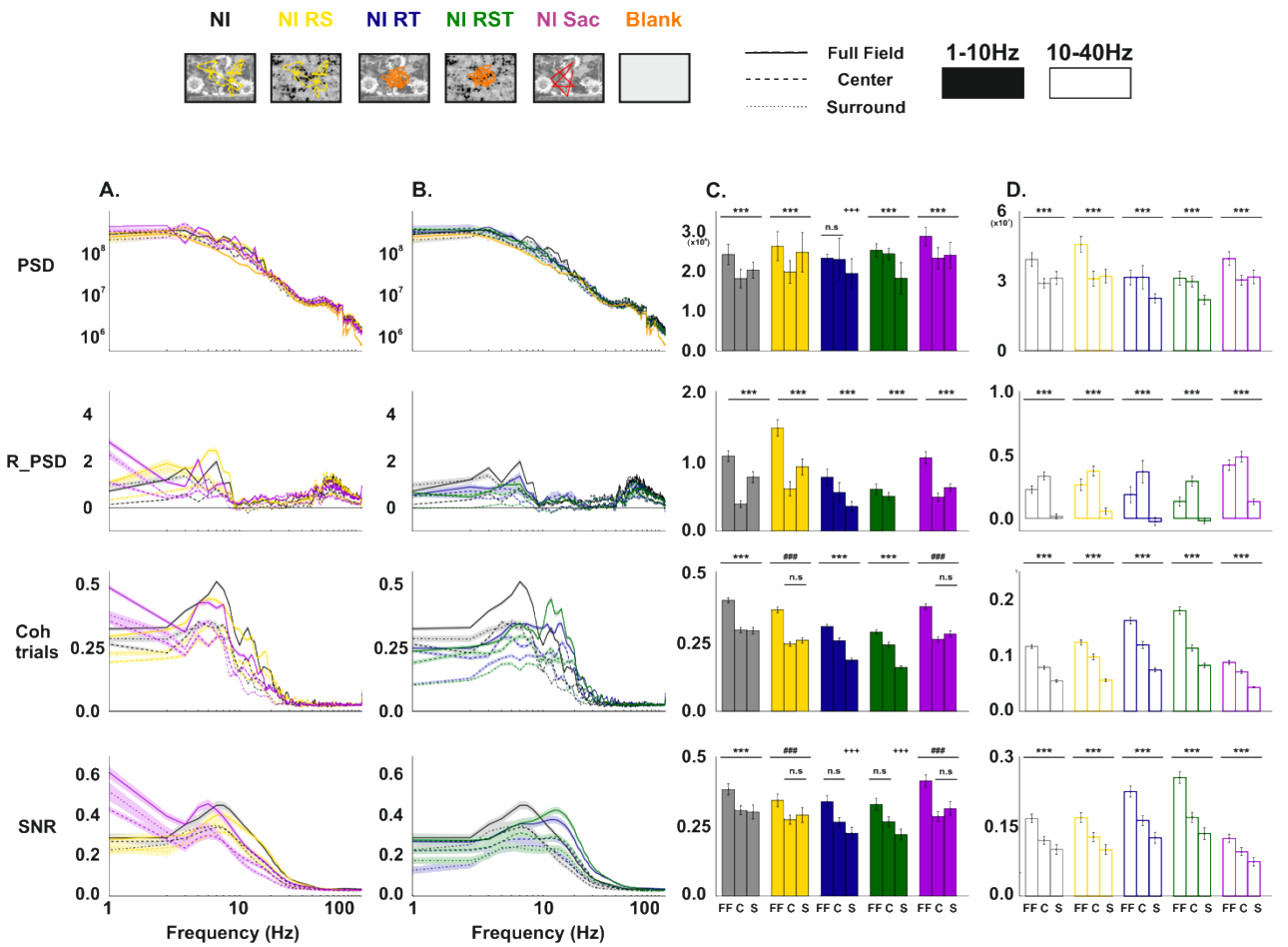

Figure 3.4.63: Frequency based analysis of the local field potential in response to our set of control stimuli presented on the full field (full line), center (big dashed lines) and surround (small dashed lines) conditions. A. PSD. B. R-PSD C. Mean Coherence. D. SNR. *: all conditions are significantly different from each other; # Full field is significantly different from the other conditions. * : $p < 0.05$; ** : $p < 0.01$; *** : $p < 0.001$; Error bars : SEM.

FULL FIELD	LOW FREQUENCY PSD				
	DG	GEM	NI	DN	BLK
Layer 2/3	8.6e+07 ± 8.3e+06	1.5e+08 ± 1.4e+07	1.9e+08 ± 1.8e+07	1.1e+08 ± 9.2e+06	1.1e+08 ± 1.2e+07
Layer 4	1.1e+08 ± 7.3e+06	2.2e+08 ± 1.1e+07	3.3e+08 ± 1.6e+07	1.7e+08 ± 8.1e+06	1.5e+08 ± 1.2e+07
Layer 5/6	2.4e+08 ± 5.7e+07	3.7e+08 ± 6.4e+07	5.4e+08 ± 7.6e+07	3.3e+08 ± 7.3e+07	3.1e+08 ± 8.4e+07
Mean	1.5e+08 ± 2.4e+07	2.5e+08 ± 3.0e+07	3.5e+08 ± 3.7e+07	2.0e+08 ± 3.0e+07	1.9e+08 ± 3.6e+07

CENTER	LOW FREQUENCY PSD				
	DG	GEM	NI	DN	BLK
Layer 2/3	9.4e+07 ± 8.2e+06	1.2e+08 ± 1.0e+07	1.2e+08 ± 1.0e+07	1.1e+08 ± 9.2e+06	1.1e+08 ± 1.2e+07
Layer 4	1.2e+08 ± 6.6e+06	1.9e+08 ± 9.9e+06	2.1e+08 ± 1.0e+07	1.7e+08 ± 8.3e+06	1.5e+08 ± 1.2e+07
Layer 5/6	2.6e+08 ± 5.9e+07	3.6e+08 ± 7.7e+07	3.6e+08 ± 7.3e+07	3.3e+08 ± 6.6e+07	3.1e+08 ± 8.4e+07
Mean	1.6e+08 ± 2.5e+07	2.3e+08 ± 3.2e+07	2.3e+08 ± 3.1e+07	2.0e+08 ± 2.8e+07	1.9e+08 ± 3.6e+07

SURROUND	LOW FREQUENCY PSD				
	DG	GEM	NI	DN	BLK
Layer 2/3	1.0e+08 ± 8.8e+06	1.2e+08 ± 1.0e+07	1.5e+08 ± 1.2e+07	1.1e+08 ± 9.5e+06	1.1e+08 ± 1.2e+07
Layer 4	1.3e+08 ± 6.0e+06	1.7e+08 ± 9.2e+06	2.3e+08 ± 9.6e+06	1.4e+08 ± 7.3e+06	1.5e+08 ± 1.2e+07
Layer 5/6	2.5e+08 ± 6.0e+07	3.2e+08 ± 7.2e+07	4.0e+08 ± 6.2e+07	2.9e+08 ± 6.4e+07	3.1e+08 ± 8.4e+07
Mean	1.6e+08 ± 2.5e+07	2.0e+08 ± 3.0e+07	2.6e+08 ± 2.8e+07	1.8e+08 ± 2.7e+07	1.9e+08 ± 3.6e+07

FULL FIELD	LOW FREQUENCY R-PSD			
	DG	GEM	NI	DN
Layer 2/3	-0.16 ± 0.03	0.72 ± 0.07	1.34 ± 0.22	0.16 ± 0.04
Layer 4	-0.09 ± 0.03	1.66 ± 0.09	2.78 ± 0.26	0.53 ± 0.06
Layer 5/6	-0.17 ± 0.03	1.58 ± 0.14	2.94 ± 0.36	0.43 ± 0.07
Mean	-0.14 ± 0.02	1.31 ± 0.07	1.95 ± 0.15	0.36 ± 0.03

CENTER	LOW FREQUENCY R-PSD			
	DG	GEM	NI	DN
Layer 2/3	-0.06 ± 0.03	0.35 ± 0.04	0.23 ± 0.04	0.16 ± 0.03
Layer 4	0.00 ± 0.03	0.89 ± 0.06	0.75 ± 0.06	0.48 ± 0.04
Layer 5/6	-0.06 ± 0.02	0.68 ± 0.09	0.48 ± 0.06	0.36 ± 0.05
Mean	-0.03 ± 0.02	0.63 ± 0.04	0.50 ± 0.03	0.33 ± 0.02

SURROUND	LOW FREQUENCY R-PSD			
	DG	GEM	NI	DN
Layer 2/3	-0.05 ± 0.03	0.38 ± 0.06	0.85 ± 0.16	0.07 ± 0.03
Layer 4	-0.13 ± 0.01	0.41 ± 0.04	1.25 ± 0.13	0.06 ± 0.03
Layer 5/6	-0.16 ± 0.02	0.61 ± 0.09	1.85 ± 0.23	0.18 ± 0.05
Mean	-0.13 ± 0.01	0.44 ± 0.04	1.17 ± 0.10	0.09 ± 0.02

Table 3.4.20: Mean low frequency PSD and R-PSD in response to our stimulus set presented full field, on the center or on the surround (mean ± SEM)

FULL FIELD	HIGH FREQUENCY PSD				
	DG	GEM	NI	DN	BLK
Layer 2/3	1.0e+07 ± 6.0e+05	2.4e+07 ± 1.7e+06	2.7e+07 ± 2.1e+06	1.6e+07 ± 1.1e+06	1.4e+07 ± 1.4e+06
Layer 4	1.5e+07 ± 5.5e+05	5.3e+07 ± 2.3e+06	5.3e+07 ± 2.0e+06	3.1e+07 ± 1.2e+06	2.4e+07 ± 1.7e+06
Layer 5/6	2.0e+07 ± 1.1e+06	6.0e+07 ± 2.8e+06	6.1e+07 ± 2.7e+06	3.2e+07 ± 1.6e+06	2.9e+07 ± 2.3e+06
Mean	1.5e+07 ± 7.6e+05	4.6e+07 ± 2.2e+06	4.7e+07 ± 2.3e+06	2.6e+07 ± 1.3e+06	2.2e+07 ± 1.8e+06

CENTER	HIGH FREQUENCY PSD				
	DG	GEM	NI	DN	BLK
Layer 2/3	1.1e+07 ± 6.3e+05	1.9e+07 ± 1.3e+06	1.6e+07 ± 9.8e+05	1.7e+07 ± 1.2e+06	1.4e+07 ± 1.4e+06
Layer 4	1.8e+07 ± 6.6e+05	3.9e+07 ± 1.7e+06	3.3e+07 ± 1.3e+06	3.3e+07 ± 1.4e+06	2.4e+07 ± 1.7e+06
Layer 5/6	2.4e+07 ± 1.4e+06	3.9e+07 ± 2.2e+06	3.4e+07 ± 1.6e+06	3.3e+07 ± 1.6e+06	2.9e+07 ± 2.3e+06
Mean	1.7e+07 ± 8.8e+05	3.2e+07 ± 1.7e+06	2.7e+07 ± 1.3e+06	2.8e+07 ± 1.4e+06	2.2e+07 ± 1.8e+06

SURROUND	HIGH FREQUENCY PSD				
	DG	GEM	NI	DN	BLK
Layer 2/3	1.1e+07 ± 6.3e+05	1.7e+07 ± 1.0e+06	1.9e+07 ± 1.2e+06	1.4e+07 ± 7.8e+05	1.4e+07 ± 1.4e+06
Layer 4	1.6e+07 ± 5.7e+05	2.7e+07 ± 1.2e+06	3.2e+07 ± 1.4e+06	2.0e+07 ± 7.6e+05	2.4e+07 ± 1.7e+06
Layer 5/6	2.1e+07 ± 1.2e+06	3.7e+07 ± 2.2e+06	4.5e+07 ± 2.1e+06	2.6e+07 ± 1.4e+06	2.9e+07 ± 2.3e+06
Mean	1.6e+07 ± 8.1e+05	2.7e+07 ± 1.5e+06	3.2e+07 ± 1.5e+06	2.0e+07 ± 9.7e+05	2.2e+07 ± 1.8e+06

FULL FIELD	HIGH FREQUENCY R-PSD			
	DG	GEM	NI	DN
Layer 2/3	0.03 ± 0.04	0.38 ± 0.05	0.21 ± 0.04	0.30 ± 0.04
Layer 4	0.33 ± 0.04	0.76 ± 0.04	0.55 ± 0.06	0.80 ± 0.05
Layer 5/6	0.13 ± 0.04	0.63 ± 0.05	0.31 ± 0.06	0.29 ± 0.04
Mean	0.21 ± 0.03	0.59 ± 0.03	0.30 ± 0.03	0.50 ± 0.03

CENTER	HIGH FREQUENCY R-PSD			
	DG	GEM	NI	DN
Layer 2/3	0.01 ± 0.02	0.18 ± 0.03	0.14 ± 0.02	0.29 ± 0.03
Layer 4	0.17 ± 0.02	0.53 ± 0.03	0.39 ± 0.03	0.70 ± 0.04
Layer 5/6	0.04 ± 0.02	0.40 ± 0.07	0.21 ± 0.03	0.28 ± 0.03
Mean	0.09 ± 0.02	0.40 ± 0.03	0.27 ± 0.02	0.44 ± 0.03

SURROUND	HIGH FREQUENCY R-PSD			
	DG	GEM	NI	DN
Layer 2/3	-0.05 ± 0.02	0.11 ± 0.03	0.04 ± 0.03	0.02 ± 0.02
Layer 4	-0.04 ± 0.01	0.09 ± 0.02	0.06 ± 0.02	0.05 ± 0.02
Layer 5/6	-0.03 ± 0.02	0.19 ± 0.06	0.01 ± 0.03	0.02 ± 0.02
Mean	-0.04 ± 0.01	0.12 ± 0.03	0.01 ± 0.01	0.02 ± 0.01

Table 3.4.21: Mean high frequency PSD and R-PSD in response to our stimulus set presented full field, on the center or on the surround (mean ± SEM)

FULL FIELD	LOW FREQUENCY Coherence			
	DG	GEM	NI	DN
Layer 2/3	0.03 ± 0.00	0.25 ± 0.02	0.33 ± 0.02	0.16 ± 0.01
Layer 4	0.06 ± 0.00	0.44 ± 0.01	0.52 ± 0.01	0.33 ± 0.01
Layer 5/6	0.05 ± 0.00	0.43 ± 0.01	0.55 ± 0.01	0.24 ± 0.02
Mean	0.05 ± 0.00	0.40 ± 0.01	0.49 ± 0.01	0.27 ± 0.01

CENTER	LOW FREQUENCY Coherence			
	DG	GEM	NI	DN
Layer 2/3	0.04 ± 0.00	0.18 ± 0.02	0.19 ± 0.01	0.12 ± 0.01
Layer 4	0.06 ± 0.00	0.36 ± 0.01	0.39 ± 0.01	0.26 ± 0.01
Layer 5/6	0.04 ± 0.00	0.29 ± 0.01	0.31 ± 0.01	0.19 ± 0.01
Mean	0.05 ± 0.00	0.30 ± 0.01	0.33 ± 0.01	0.21 ± 0.01

SURROUND	LOW FREQUENCY Coherence			
	DG	GEM	NI	DN
Layer 2/3	0.03 ± 0.00	0.15 ± 0.02	0.24 ± 0.02	0.08 ± 0.01
Layer 4	0.04 ± 0.00	0.23 ± 0.01	0.36 ± 0.01	0.12 ± 0.01
Layer 5/6	0.04 ± 0.00	0.28 ± 0.02	0.45 ± 0.02	0.15 ± 0.01
Mean	0.04 ± 0.00	0.23 ± 0.01	0.37 ± 0.01	0.12 ± 0.01

FULL FIELD	LOW FREQUENCY SNR			
	DG	GEM	NI	DN
Layer 2/3	0.04 ± 0.00	0.39 ± 0.03	0.54 ± 0.05	0.21 ± 0.02
Layer 4	0.12 ± 0.01	0.62 ± 0.02	0.75 ± 0.02	0.42 ± 0.01
Layer 5/6	0.07 ± 0.01	0.54 ± 0.04	0.70 ± 0.04	0.34 ± 0.02
Mean	0.08 ± 0.00	0.51 ± 0.03	0.67 ± 0.0	0.32 ± 0.02

CENTER	LOW FREQUENCY SNR			
	DG	GEM	NI	DN
Layer 2/3	0.03 ± 0.00	0.25 ± 0.02	0.24 ± 0.02	0.14 ± 0.01
Layer 4	0.10 ± 0.00	0.48 ± 0.01	0.50 ± 0.01	0.33 ± 0.01
Layer 5/6	0.05 ± 0.00	0.34 ± 0.02	0.39 ± 0.02	0.25 ± 0.01
Mean	0.06 ± 0.00	0.36 ± 0.02	0.38 ± 0.02	0.24 ± 0.01

SURROUND	LOW FREQUENCY SNR			
	DG	GEM	NI	DN
Layer 2/3	0.03 ± 0.00	0.26 ± 0.03	0.48 ± 0.05	0.13 ± 0.02
Layer 4	0.03 ± 0.00	0.32 ± 0.01	0.57 ± 0.03	0.16 ± 0.01
Layer 5/6	0.04 ± 0.00	0.36 ± 0.04	0.62 ± 0.06	0.19 ± 0.02
Mean	0.03 ± 0.00	0.31 ± 0.03	0.56 ± 0.04	0.16 ± 0.02

Table 3.4.22: Mean low frequency Coherence and SNR in response to our stimulus set presented full field, on the center or on the surround (mean ± SEM)

FULL FIELD	HIGH FREQUENCY Coherence			
	DG	GEM	NI	DN
Layer 2/3	0.03 ± 0.00	0.15 ± 0.01	0.09 ± 0.01	0.20 ± 0.01
Layer 4	0.04 ± 0.00	0.22 ± 0.01	0.15 ± 0.00	0.40 ± 0.01
Layer 5/6	0.03 ± 0.00	0.16 ± 0.01	0.13 ± 0.01	0.22 ± 0.01
Mean	0.03 ± 0.00	0.19 ± 0.01	0.13 ± 0.00	0.30 ± 0.01

CENTER	HIGH FREQUENCY Coherence			
	DG	GEM	NI	DN
Layer 2/3	0.02 ± 0.00	0.09 ± 0.01	0.05 ± 0.00	0.16 ± 0.01
Layer 4	0.03 ± 0.00	0.18 ± 0.01	0.11 ± 0.00	0.33 ± 0.01
Layer 5/6	0.03 ± 0.00	0.11 ± 0.01	0.07 ± 0.00	0.16 ± 0.01
Mean	0.03 ± 0.00	0.14 ± 0.00	0.08 ± 0.00	0.24 ± 0.01

SURROUND	HIGH FREQUENCY Coherence			
	DG	GEM	NI	DN
Layer 2/3	0.02 ± 0.00	0.08 ± 0.01	0.06 ± 0.01	0.08 ± 0.01
Layer 4	0.03 ± 0.00	0.08 ± 0.00	0.06 ± 0.00	0.11 ± 0.01
Layer 5/6	0.03 ± 0.00	0.10 ± 0.01	0.08 ± 0.01	0.10 ± 0.01
Mean	0.03 ± 0.00	0.09 ± 0.00	0.07 ± 0.00	0.10 ± 0.00

FULL FIELD	HIGH FREQUENCY SNR			
	DG	GEM	NI	DN
Layer 2/3	0.01 ± 0.00	0.19 ± 0.01	0.14 ± 0.01	0.23 ± 0.01
Layer 4	0.04 ± 0.00	0.30 ± 0.01	0.22 ± 0.01	0.52 ± 0.01
Layer 5/6	0.02 ± 0.00	0.22 ± 0.01	0.19 ± 0.01	0.29 ± 0.01
Mean	0.02 ± 0.00	0.24 ± 0.01	0.18 ± 0.01	0.35 ± 0.01

CENTER	HIGH FREQUENCY SNR			
	DG	GEM	NI	DN
Layer 2/3	0.01 ± 0.00	0.09 ± 0.01	0.06 ± 0.00	0.16 ± 0.01
Layer 4	0.04 ± 0.00	0.23 ± 0.01	0.15 ± 0.00	0.44 ± 0.01
Layer 5/6	0.02 ± 0.00	0.13 ± 0.01	0.09 ± 0.00	0.21 ± 0.01
Mean	0.02 ± 0.00	0.15 ± 0.01	0.10 ± 0.00	0.27 ± 0.01

SURROUND	HIGH FREQUENCY SNR			
	DG	GEM	NI	DN
Layer 2/3	0.01 ± 0.00	0.12 ± 0.01	0.10 ± 0.01	0.11 ± 0.01
Layer 4	0.01 ± 0.00	0.14 ± 0.01	0.12 ± 0.01	0.15 ± 0.01
Layer 5/6	0.01 ± 0.00	0.13 ± 0.01	0.12 ± 0.01	0.13 ± 0.01
Mean	0.01 ± 0.00	0.13 ± 0.01	0.12 ± 0.01	0.13 ± 0.01

Table 3.4.23: Mean low frequency Coherence and SNR in response to our stimulus set presented full field, on the center or on the surround (mean ± SEM)

FULL FIELD						
	NI	NI-RS	NI-RT	NI-RST	NI-SAC	BLK
PSD	2.4e+08 ± 2.5e+07	2.6e+08 ± 3.6e+07	2.3e+08 ± 9.2e+06	2.5e+08 ± 1.6e+07	2.8e+08 ± 2.3e+07	1.5e+08 ± 2.2e+07
R-PSD	1.07 ± 0.07	1.47 ± 0.11	0.77 ± 0.12	0.59 ± 0.07	1.05 ± 0.08	X
Coherence	0.37 ± 0.01	0.34 ± 0.01	0.28 ± 0.01	0.26 ± 0.01	0.35 ± 0.01	X
SNR	0.38 ± 0.02	0.34 ± 0.02	0.34 ± 0.02	0.33 ± 0.02	0.41 ± 0.02	X

CENTER						
	NI	NI-RS	NI-RT	NI-RST	NI-SAC	BLK
PSD	1.8e+08 ± 2.3e+07	1.9e+08 ± 2.8e+07	2.2e+08 ± 5.3e+07	2.4e+08 ± 1.4e+07	2.3e+08 ± 2.6e+07	1.5e+08 ± 2.2e+07
R-PSD	0.38 ± 0.04	0.60 ± 0.10	0.55 ± 0.13	0.49 ± 0.05	0.48 ± 0.05	X
Coherence	0.25 ± 0.01	0.21 ± 0.01	0.22 ± 0.01	0.21 ± 0.01	0.22 ± 0.01	X
SNR	0.31 ± 0.02	0.27 ± 0.02	0.26 ± 0.02	0.27 ± 0.02	0.29 ± 0.02	X

SURROUND						
	NI	NI-RS	NI-RT	NI-RST	NI-SAC	BLK
PSD	2.0e+08 ± 2.0e+07	2.4e+08 ± 4.9e+07	1.9e+08 ± 3.7e+07	1.8e+08 ± 3.9e+07	2.4e+08 ± 3.3e+07	1.5e+08 ± 2.2e+07
R-PSD	0.77 ± 0.08	0.92 ± 0.11	0.35 ± 0.06	0.02 ± 0.03	0.62 ± 0.05	X
Coherence	0.28 ± 0.02	0.25 ± 0.02	0.18 ± 0.01	0.16 ± 0.01	0.27 ± 0.02	X
SNR	0.30 ± 0.03	0.29 ± 0.03	0.23 ± 0.02	0.22 ± 0.02	0.31 ± 0.03	X

Table 3.4.24: Mean low frequency PSD, R-PSD, Coherence and SNR in response to our control stimulus set presented full field, on the center or on the surround (mean ± SEM)

4.2.4 Spectral Analysis of the Unlocked LFP

In the previous section, we investigated the impact of unlocked LFP, we showed that the eye movements induced a strong increase in the alpha band and that this increase might be a prediction error message conveyed by the feedback. It is known that the surround stimulation strongly activates the surround (Angelucci et al., 2002). On the other hand, the center stimulation strongly activates the feedforward pathway. Thus, we wondered if the sole stimulation of the center or the surround would affect the frequency bands linked to the bottom up and top down pathways.

- **Impact of the center surround interactions**

As observed for the full field condition, the presentation of all stimuli in center and the surround conditions respectively, evoked the same PSD and R-PSD between 1-4Hz. In addition, our results show that the main responses are between 4-20 Hz (alpha band) and 40-150 Hz (gamma band). We will first focus on the alpha band (4-20Hz; Figures 3.4.64 and 3.4.65; tables 3.4.25 and 3.4.26). When the results are similar, we will comment both PSD and R-PSD together and the differences will be commented.

When stimuli were presented in the center, the highest spectral density was evoked by animated gratings and the lowest one by drifting gratings ($p < 0.001$; Friedman test). This was observed both for the PSD and R-PSD. However, it is important to note than in layer 2/3, with the PSD analysis NI, GEM and DN evoked the same mean spectral density ($p > 0.6$). This was not the case for the R-PSD were all stimuli evoked different values, suggesting that the PSD of the spontaneous activity has a strong influence in layer 2/3. When presented in the surround only, natural images evoked, in all layers and at the mean population level, the highest spectral density and DG the lowest ones ($p < 0.001$).

We then compared the impact of the different conditions of stimulation on the response. The full field presentation of NI and GEM evoked the highest spectral density ($p < 0.001$). Regarding NI, the surround condition evoked a higher PSD than the center. The presentation of natural images on the center evoked lower PSD than the one of the spontaneous activities. On the other hand, for animated gratings, the center stimulation evoked a higher spectral density than the surround, except in layer 2/3 were the opposite was observed. This suggest that the statistics of the two stimuli are not treated in the same way. Indeed, since the unlocked LFP evoked by NI is high on the surround and negative for the center, it suggests that the surround processes the temporal and spatial statistics in another way than the center. Moreover, this is linked to the spatial statistics of the natural scenes since we do not observe this for GEM. It is known that the surround activates feedback connections. This increase in alpha observed for the surround and not the center stimulation might be the signature of the feedback that is only present for highly informative stimuli that allow the generation of a prediction error message.

We then investigated the PSD and R-PSD for the gamma band. For the center condition, NI, GEM and DG evoked the same high frequency PSD, higher than the one observed for dense noise ($p < 0.001$). For the surround condition, all stimuli evoked the same spectral density in layer 2/3, while in the other layers and at the population level, DG evoked the highest values of PSD and DN the lowest one. All stimuli, except DG, displayed their highest spectral density for the center condition and the lowest one for the surround. Again, the center is linked to feedforward message that is conveyed by gamma bands. This increase in gamma might be the signature of the feedforward message.

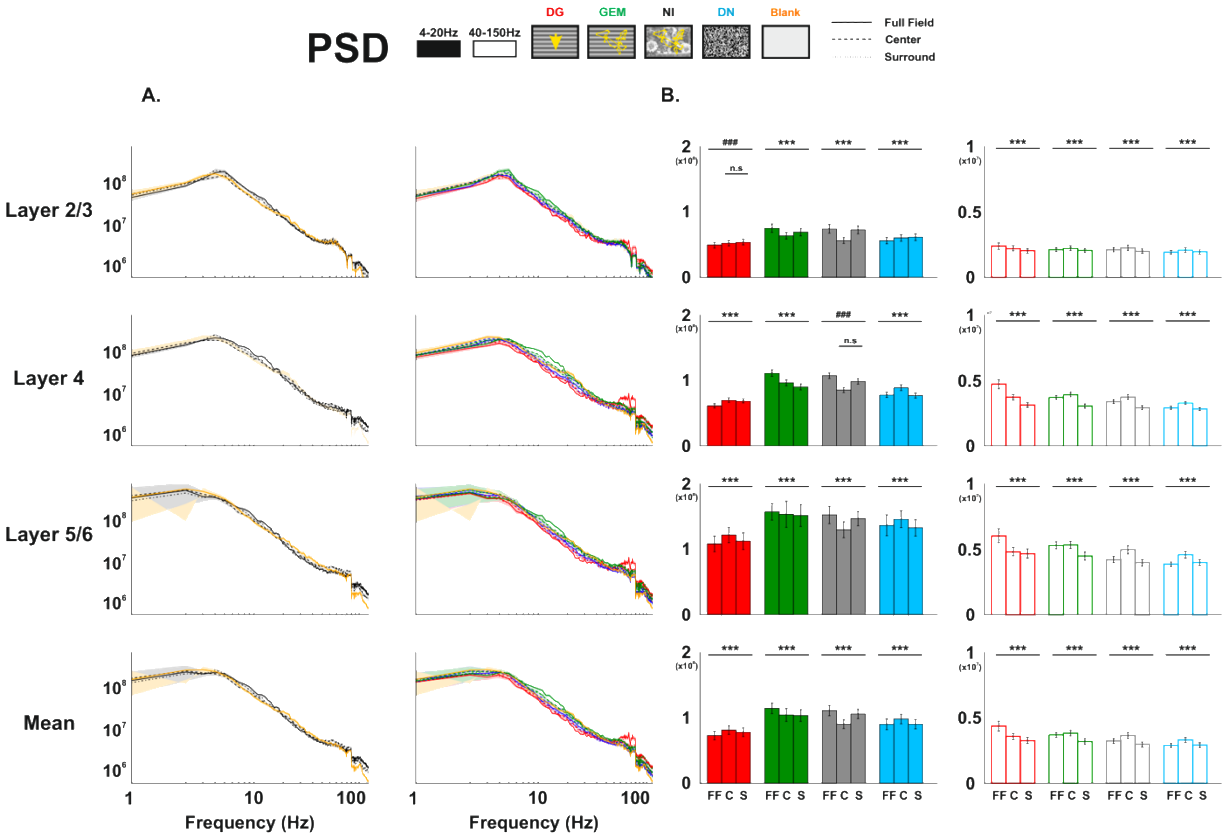

Figure 3.4.64: Power Spectrum of the unlocked local field potential in response to our set of stimuli presented on the full field (full line), center (big dashed lines) and surround (small dashed lines) conditions. The feedback frequencies are strongly modulated by the surround condition. *: all conditions are significantly different from each other. * : $p < 0.05$; ** : $p < 0.01$; *** : $p < 0.001$; Error bars : SEM.

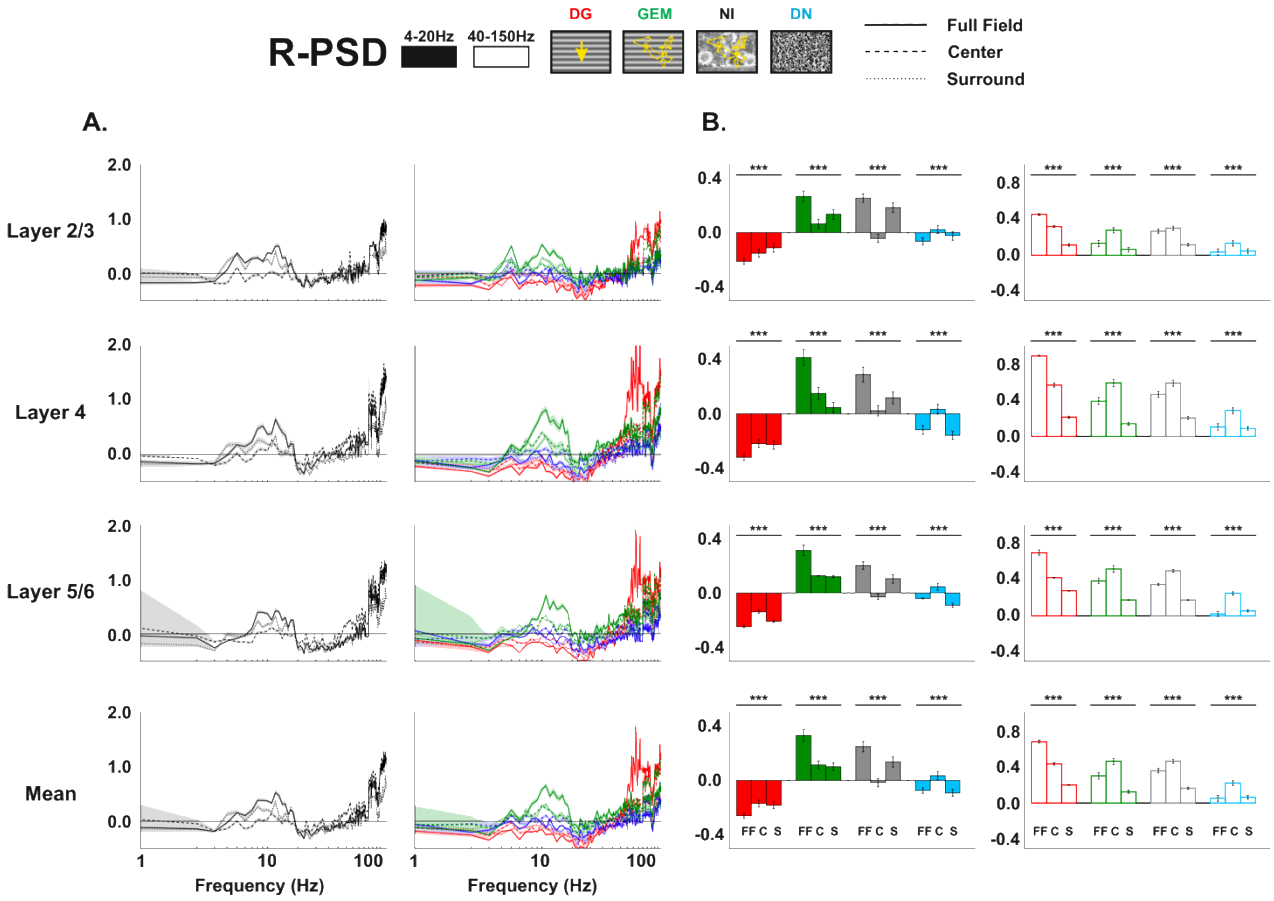

Figure 3.4.65: Relative Power Spectrum of the unlocked local field potential in response to our set of stimuli presented on the full field (full line), center (big dashed lines) and surround (small dashed lines) conditions. The feedback frequencies are strongly modulated by the surround condition. *: all conditions are significantly different from each other. * : $p < 0.05$; ** : $p < 0.01$; *** : $p < 0.001$; Error bars : SEM.

- **Impact of the natural statistics on the unlocked LFP response**

We then wondered how the spatial and temporal statistics present on natural images impact the unlocked LFP (figure 3.4.66 and table 3.4.27). We first focused on the spectral density of the alpha band.

Our results showed that when presented on the center natural images evoked a lower PSD than NI-RS and NI-RT but a similar PSD as NI-RST and NI-RT. On the other hand, with the R-PSD analysis, natural images evoked the lowest R-PSD ($p < 0.001$). When presented on the surround, NI and NI-RS evoked the same spectral density ($p = 0.9$), higher than the one evoked by the other stimuli ($p < 0.001$). The stimuli containing unaltered eye movements displayed the highest PSD when presented full field. In addition, the surround condition evoked a higher spectral density than the center ($p < 0.001$), except for NI-RS where no significant difference was observed despite a higher mean for the surround condition. However, NI-RT and NI-RST displayed the highest spectral density when presented on the center only ($p < 0.001$) and the lowest for the surround only stimulation ($p < 0.001$). This confirms the importance of the surround in the processing of unaltered temporal statistics and that high order temporal statistics might strongly activate the feedback and the error message conveyed by the alpha band. In addition, this error message seems present only when saccades animate the image. This suggest that small eye movements do not generate a prediction error. However, this need to be confirmed on awake animals.

Finally, we investigated the PSD in the gamma band (figure 3.4.66-B; table 3.4.27). For the center condition, natural images evoked a lower PSD than NI-RS ($p < 0.001$), the same as NI-SAC ($p = 0.9$) and a higher than NI-RT and NI-RST ($p < 0.001$).,When the stimuli were presented on the surround NI and NI-RS evoked the same PSD, higher than the one evoked by the other stimuli ($p < 0.001$). For all stimuli the center condition evoked the highest PSD and the surround the lowest one, except for NI-RST, implying that the feedforward message in mainly conveyed by the center stimulation.

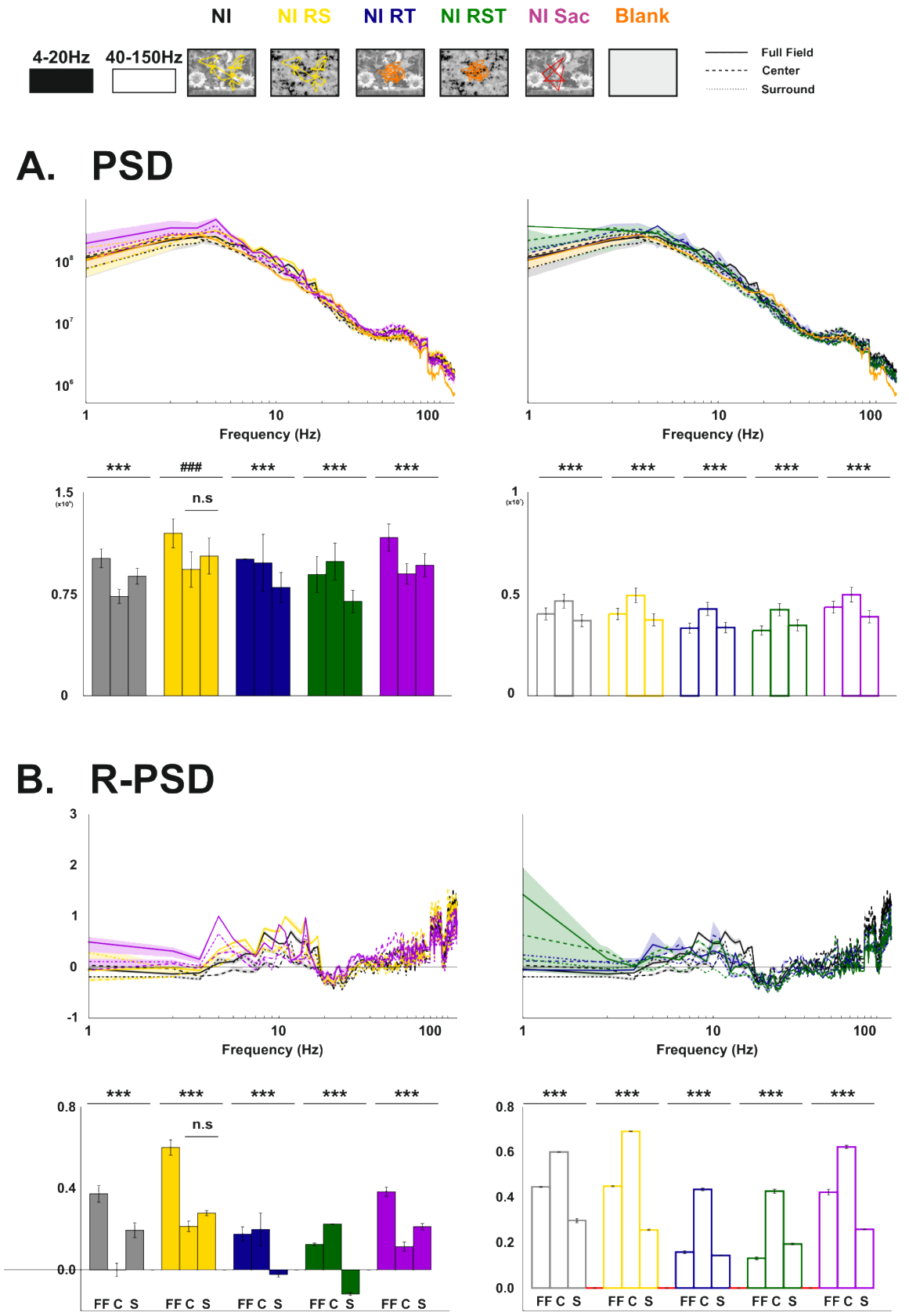

Figure 3.4.66: Spectral analysis of the unlocked the local field potential evoked by our set of control stimuli. **A.** Power spectrum density. Top row: mean plots. Bottom row: bar plots of the mean intermediate and high frequencies PSD. **B.** Relative power spectrum density. Top row: mean plots. Bottom row: bar plots of the mean intermediate and high frequencies R-PSD. *: all conditions are significantly different from each other; # Full Field is significantly different from the other conditions; * : $p < 0.05$; ** : $p < 0.01$; *** : $p < 0.001$; Error bars and shaded area : SEM.

FULL FIELD	ALPHA BAND PSD				
	DG	GEM	NI	DN	BLK
Layer 2/3	4.9e+07 ± 4.6e+06	7.5e+07 ± 6.4e+06	7.4e+07 ± 6.6e+06	5.6e+07 ± 5.0e+06	6.0e+07 ± 6.8e+06
Layer 4	6.1e+07 ± 3.3e+06	1.1e+08 ± 4.9e+06	1.1e+08 ± 4.2e+06	7.8e+07 ± 3.9e+06	8.7e+07 ± 7.4e+06
Layer 5/6	1.1e+08 ± 1.2e+07	1.6e+08 ± 1.3e+07	1.5e+08 ± 1.3e+07	1.4e+08 ± 1.6e+07	1.4e+08 ± 1.6e+07
Mean	7.3e+07 ± 6.5e+06	1.1e+08 ± 8.0e+06	1.1e+08 ± 8.0e+06	9.0e+07 ± 8.2e+06	9.5e+07 ± 1.0e+07

CENTER	ALPHA BAND PSD				
	DG	GEM	NI	DN	BLK
Layer 2/3	5.2e+07 ± 4.3e+06	6.4e+07 ± 5.0e+06	5.6e+07 ± 4.5e+06	6.0e+07 ± 5.0e+06	6.0e+07 ± 6.8e+06
Layer 4	7.0e+07 ± 3.4e+06	9.7e+07 ± 4.6e+06	8.6e+07 ± 3.8e+06	8.9e+07 ± 4.3e+06	8.7e+07 ± 7.4e+06
Layer 5/6	1.2e+08 ± 1.2e+07	1.5e+08 ± 2.0e+07	1.3e+08 ± 1.2e+07	1.5e+08 ± 1.3e+07	1.4e+08 ± 1.6e+07
Mean	8.1e+07 ± 6.5e+06	1.0e+08 ± 9.8e+06	9.1e+07 ± 6.8e+06	9.8e+07 ± 7.4e+06	9.5e+07 ± 1.0e+07

SURROUND	ALPHA BAND PSD				
	DG	GEM	NI	DN	BLK
Layer 2/3	5.4e+07 ± 4.2e+06	6.9e+07 ± 5.7e+06	7.3e+07 ± 6.0e+06	6.1e+07 ± 5.1e+06	6.0e+07 ± 6.8e+06
Layer 4	6.9e+07 ± 2.9e+06	9.0e+07 ± 4.5e+06	9.9e+07 ± 4.2e+06	7.7e+07 ± 3.8e+06	8.7e+07 ± 7.4e+06
Layer 5/6	1.1e+08 ± 1.3e+07	1.5e+08 ± 1.7e+07	1.5e+08 ± 1.1e+07	1.3e+08 ± 1.3e+07	1.4e+08 ± 1.6e+07
Mean	7.8e+07 ± 6.7e+06	1.0e+08 ± 9.0e+06	1.1e+08 ± 7.1e+06	9.0e+07 ± 7.2e+06	9.5e+07 ± 1.0e+07

FULL FIELD	ALPHA BAND R-PSD			
	DG	GEM	NI	DN
Layer 2/3	-0.21 ± -0.02	0.27 ± -0.04	0.25 ± -0.03	-0.06 ± -0.03
Layer 4	-0.32 ± -0.02	0.42 ± -0.06	0.29 ± -0.05	-0.12 ± -0.03
Layer 5/6	-0.25 ± -0.01	0.31 ± -0.04	0.20 ± -0.03	-0.04 ± -0.00
Mean	-0.26 ± -0.02	0.33 ± -0.04	0.25 ± -0.04	-0.07 ± -0.02

CENTER	ALPHA BAND R-PSD			
	DG	GEM	NI	DN
Layer 2/3	-0.15 ± -0.03	0.06 ± -0.03	-0.04 ± -0.03	0.02 ± -0.03
Layer 4	-0.22 ± -0.03	0.15 ± -0.04	0.02 ± -0.04	0.03 ± -0.04
Layer 5/6	-0.14 ± -0.01	0.13 ± -0.00	-0.03 ± -0.02	0.05 ± -0.02
Mean	-0.17 ± -0.02	0.11 ± -0.03	-0.02 ± -0.03	0.03 ± -0.03

SURROUND	ALPHA BAND R-PSD			
	DG	GEM	NI	DN
Layer 2/3	-0.11 ± -0.03	0.14 ± -0.04	0.18 ± -0.04	-0.02 ± -0.03
Layer 4	-0.23 ± -0.03	0.05 ± -0.04	0.12 ± -0.04	-0.16 ± -0.03
Layer 5/6	-0.21 ± -0.01	0.12 ± -0.01	0.11 ± -0.03	-0.09 ± -0.02
Mean	-0.18 ± -0.02	0.10 ± -0.03	0.14 ± -0.04	-0.09 ± -0.03

Table 3.4.25: Mean low frequency PSD, R-PSD of the unlocked LFP in response to our stimulus set presented full field, on the center or on the surround (mean ± SEM)

FULL FIELD	GAMMA BAND PSD				
	DG	GEM	NI	DN	BLK
Layer 2/3	2.4e+06 ± 2.5e+05	2.1e+06 ± 1.6e+05	2.1e+06 ± 1.8e+05	1.9e+06 ± 1.5e+05	2.0e+06 ± 2.4e+05
Layer 4	4.7e+06 ± 3.5e+05	3.7e+06 ± 1.7e+05	3.4e+06 ± 1.6e+05	2.9e+06 ± 1.2e+05	2.8e+06 ± 2.0e+05
Layer 5/6	6.0e+06 ± 5.4e+05	5.3e+06 ± 2.8e+05	4.2e+06 ± 2.4e+05	3.9e+06 ± 1.8e+05	4.1e+06 ± 3.2e+05
Mean	4.4e+06 ± 3.8e+05	3.7e+06 ± 2.0e+05	3.2e+06 ± 1.9e+05	2.9e+06 ± 1.5e+05	3.0e+06 ± 2.6e+05

CENTER	GAMMA BAND PSD				
	DG	GEM	NI	DN	BLK
Layer 2/3	2.2e+06 ± 2.0e+05	2.2e+06 ± 1.8e+05	2.2e+06 ± 2.0e+05	2.1e+06 ± 1.7e+05	2.0e+06 ± 2.4e+05
Layer 4	3.7e+06 ± 2.1e+05	3.9e+06 ± 1.9e+05	3.7e+06 ± 1.9e+05	3.3e+06 ± 1.5e+05	2.8e+06 ± 2.0e+05
Layer 5/6	4.8e+06 ± 3.3e+05	5.3e+06 ± 2.8e+05	5.0e+06 ± 3.1e+05	4.6e+06 ± 2.6e+05	4.1e+06 ± 3.2e+05
Mean	3.6e+06 ± 2.5e+05	3.8e+06 ± 2.2e+05	3.7e+06 ± 2.3e+05	3.3e+06 ± 1.9e+05	3.0e+06 ± 2.6e+05

SURROUND	GAMMA BAND PSD				
	DG	GEM	NI	DN	BLK
Layer 2/3	2.0e+06 ± 1.8e+05	2.1e+06 ± 1.7e+05	2.0e+06 ± 1.8e+05	1.9e+06 ± 1.7e+05	2.0e+06 ± 2.4e+05
Layer 4	3.1e+06 ± 1.8e+05	3.1e+06 ± 1.6e+05	2.9e+06 ± 1.6e+05	2.8e+06 ± 1.4e+05	2.8e+06 ± 2.0e+05
Layer 5/6	4.7e+06 ± 3.5e+05	4.5e+06 ± 3.1e+05	4.0e+06 ± 2.5e+05	4.0e+06 ± 2.3e+05	4.1e+06 ± 3.2e+05
Mean	3.3e+06 ± 2.4e+05	3.2e+06 ± 2.1e+05	3.0e+06 ± 1.9e+05	2.9e+06 ± 1.8e+05	3.0e+06 ± 2.6e+05

FULL FIELD	GAMMA BAND R-PSD			
	DG	GEM	NI	DN
Layer 2/3	0.45 ± 0.01	0.13 ± -0.03	0.27 ± -0.02	0.04 ± -0.03
Layer 4	0.89 ± 0.01	0.39 ± -0.04	0.47 ± -0.03	0.10 ± -0.04
Layer 5/6	0.70 ± 0.03	0.38 ± -0.03	0.34 ± -0.02	0.02 ± -0.03
Mean	0.68 ± 0.02	0.30 ± -0.03	0.36 ± -0.02	0.05 ± -0.03

CENTER	GAMMA BAND R-PSD			
	DG	GEM	NI	DN
Layer 2/3	0.32 ± -0.01	0.28 ± -0.03	0.30 ± -0.02	0.13 ± -0.03
Layer 4	0.57 ± -0.02	0.59 ± -0.04	0.59 ± -0.03	0.28 ± -0.03
Layer 5/6	0.42 ± -0.01	0.52 ± -0.04	0.50 ± -0.02	0.25 ± -0.02
Mean	0.43 ± -0.01	0.46 ± -0.04	0.46 ± -0.02	0.22 ± -0.03

SURROUND	GAMMA BAND R-PSD			
	DG	GEM	NI	DN
Layer 2/3	0.11 ± -0.01	0.06 ± -0.03	0.12 ± -0.02	0.05 ± -0.02
Layer 4	0.21 ± -0.01	0.14 ± -0.02	0.20 ± -0.02	0.09 ± -0.02
Layer 5/6	0.28 ± 0.01	0.17 ± -0.00	0.17 ± -0.00	0.05 ± -0.01
Mean	0.20 ± -0.01	0.13 ± -0.02	0.16 ± -0.01	0.06 ± -0.02

Table 3.4.26: Mean high frequency PSD, R-PSD of the unlocked LFP in response to our stimulus set presented full field, on the center or on the surround (mean ± SEM)

FULL FIELD (ALPHA BAND)						
	NI	NI-RS	NI-RT	NI-RST	NI-SAC	BLK
PSD	1.01e+08 ± 6.83e+06	1.20e+08 ± 1.08e+07	1.01e+08 ± -2.99e+05	8.95e+07 ± 1.34e+07	1.17e+08 ± 1.00e+07	7.42e+07 ± 7.71e+06
R-PSD	0.374 ± -0.042	0.601 ± -0.038	0.176 ± 0.035	0.126 ± 0.007	0.384 ± -0.023	X

CENTER (ALPHA BAND)						
	NI	NI-RS	NI-RT	NI-RST	NI-SAC	BLK
PSD	7.34e+07 ± 5.31e+06	9.32e+07 ± 1.31e+07	9.80e+07 ± 2.11e+07	9.90e+07 ± 1.36e+07	9.00e+07 ± 7.65e+06	7.42e+07 ± 7.71e+06
R-PSD	0.000 ± -0.033	0.214 ± 0.026	0.199 ± 0.081	0.225 ± 0.002	0.114 ± -0.023	X

SURROUND (ALPHA BAND)						
	NI	NI-RS	NI-RT	NI-RST	NI-SAC	BLK
PSD	8.83e+07 ± 5.88e+06	1.03e+08 ± 1.32e+07	7.99e+07 ± 1.11e+07	6.97e+07 ± 8.27e+06	9.63e+07 ± 8.47e+06	7.42e+07 ± 7.71e+06
R-PSD	0.194 ± -0.036	0.279 ± -0.013	-0.023 ± -0.013	-0.119 ± -0.007	0.212 ± -0.016	X

FULL FIELD (GAMMA BAND)						
	NI	NI-RS	NI-RT	NI-RST	NI-SAC	BLK
PSD	4.03e+06 ± 2.94e+05	4.02e+06 ± 2.83e+05	3.33e+06 ± 2.49e+05	3.21e+06 ± 2.34e+05	4.36e+06 ± 2.97e+05	3.29e+06 ± 2.74e+05
R-PSD	0.447 ± 0.003	0.451 ± -0.003	0.158 ± -0.007	0.131 ± -0.007	0.424 ± -0.013	X

CENTER (GAMMA BAND)						
	NI	NI-RS	NI-RT	NI-RST	NI-SAC	BLK
PSD	4.66e+06 ± 3.48e+05	4.93e+06 ± 3.67e+05	4.27e+06 ± 3.25e+05	4.24e+06 ± 3.03e+05	4.97e+06 ± 3.59e+05	3.29e+06 ± 2.74e+05
R-PSD	0.601 ± 0.001	0.693 ± 0.001	0.436 ± -0.006	0.428 ± -0.009	0.624 ± -0.008	X

SURROUND (GAMMA BAND)						
	NI	NI-RS	NI-RT	NI-RST	NI-SAC	BLK
PSD	3.70e+06 ± 2.99e+05	3.73e+06 ± 2.93e+05	3.36e+06 ± 2.65e+05	3.46e+06 ± 2.77e+05	3.89e+06 ± 3.03e+05	3.29e+06 ± 2.74e+05
R-PSD	0.298 ± 0.010	0.257 ± 0.003	0.143 ± 0.000	0.194 ± 0.004	0.259 ± 0.001	X

Table 3.4.27: Mean low and high frequency PSD, R-PSD of the unlocked LFP in response to our control stimulus set presented full field, on the center or on the surround (mean ± SEM)

5. CORRELATION OF THE NEURONAL ACTIVITY

In the previous sections, we investigated different indexes and showed that natural images elicit a more reliable and sparser response than the other stimuli. These results are in agreement with Barlow's efficient coding theory stating that exposure to natural-like statistics should decrease the stimulus-locked response variability at the single neuron level, increase the sparseness of the global population activity and reduce the redundancy present in the spike trains of populations of individual neuron. The last step that need to be investigated is if natural images reduce the redundancy in the neuronal activity. The seminal work of Vinje and Gallant (2000) showed that natural images decorrelate the neuronal response in macaque primary visual cortex. A few years later, Yen and colleagues (2006), computed the correlation of neurons recorded in the same tetrode. They obtained a heterogeneous distribution of correlations with cell pairs displaying correlation values ranging from -0.2 to 0.9. They also observed different levels of correlation for neurons recorded in the same or in different tetrodes. Recent studies performed on mice showed that different levels of correlation are found across the cortex. Indeed, mouse V1 contains neuronal clusters of low and high correlation (Kampa et al., 2011; Rikhye and Sur, 2015). These papers found that the neurons belonging to the highly correlated clusters display a higher reliability that those found in poorly correlated clusters. In addition, they also observed that neurons spatially closed were more correlated than neurons spatially distant. Moreover, it has been found on primates and mice that the levels of correlation are linked to the stimulus statistics (Bányai et al., 2019; Rikhye and Sur, 2015). Thus, we should expect a higher correlation in response to natural images that are highly correlated stimuli.
Our recordings allowed a laminar exploration of the correlations while recording hundreds of neuronal pairs and LFP sites. Will we observe a decorrelation between neurons for an increase in the stimulation size, as observed by Vinje and Gallant (2000)? Moreover, what is the impact of the natural spatio-temporal statistics on the neuronal correlation?

In order to answer these questions, we computed the two main types of correlations: signal correlation (SC) and noise correlation (NC).

5.3. Impact of the Full Field Stimulation

5.3.1 Correlation of the Spiking Activity

- **Signal Correlation**

We first computed the signal correlation of the spiking activity, which is the correlation between the mean responses of two different signals (SUA or MUA) in response to the same stimulus. Signal correlation is used to quantify the degree to which different neurons have similar functional properties.
Based on the results of Tanaka et al (20104) and Yen et al (2006) we decided to separate our signal correlations into two groups.
A first one that regroups the signal correlation of neurons belonging to the same layer *i.e.* **the signal correlation within layers**.
A second one that regroups the signal correlation of neurons belonging to different layers *i.e.* **the signal correlation between layers**.
Based the results of the studies cited above, the signal correlation between layers should be lower than the one within layers.

Figures 3.5.1 and 3.5.2 show an example of signal correlation computed for 2 recordings sites for both SUA and MUA. The signal correlation corresponds to the value at 0. The reference-recording site (red square) has a SC of 1 while the other channels have lower ones. We can observe that for the SUA, when DG are presented some neurons will be anti-correlated because a difference in phase preference. The signal correlation is higher for the MUA than the SUA. In addition, at the multi-unit level all channels displayed a very similar signal correlation, which is not the case for the SUA.

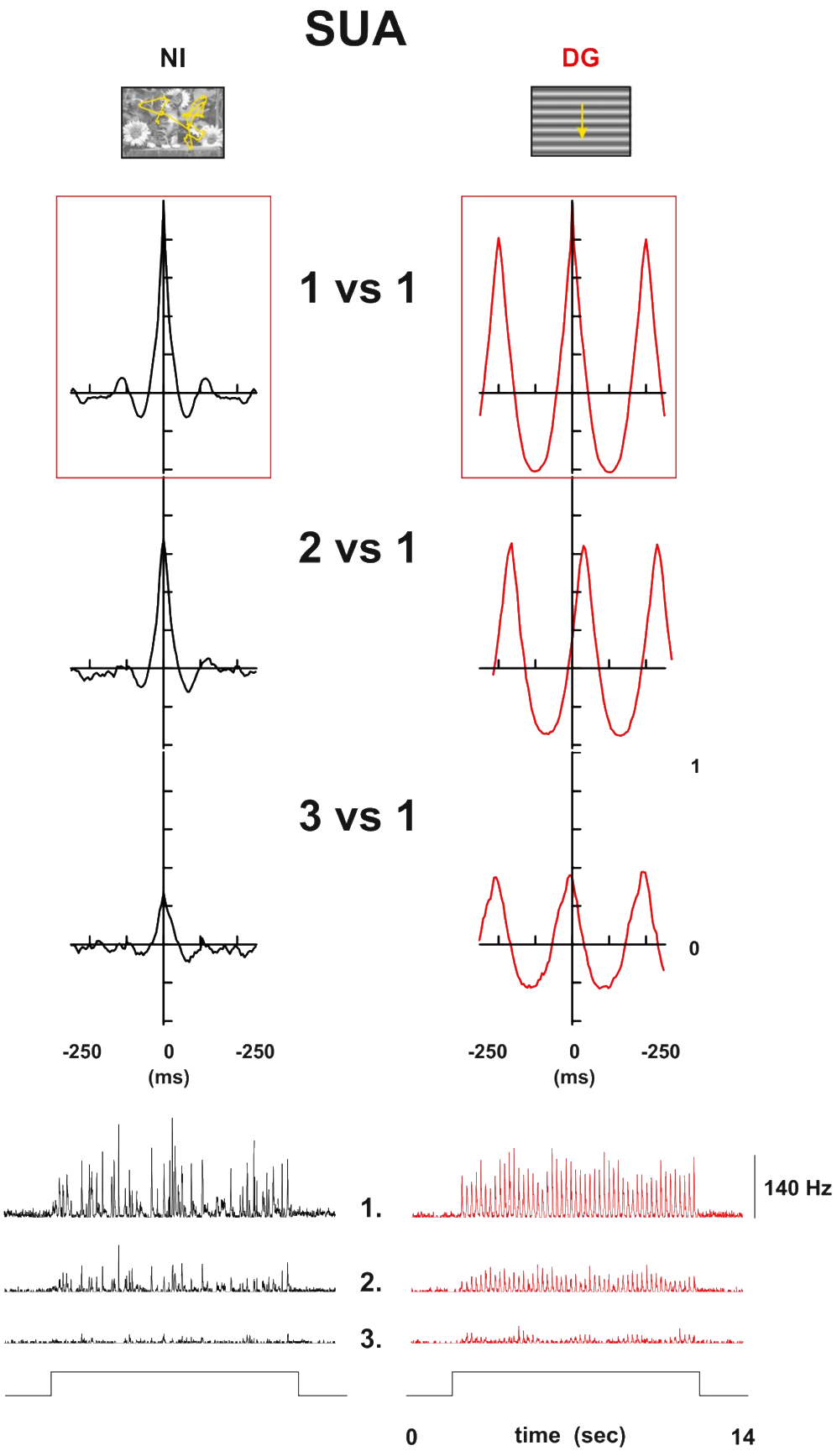

Figure 3.5.1. Example of signal correlation of the single unit activity across 3 different channels. The PSTHs of each channel are displayed below. The signal correlation corresponds to the value at 0. Red square: reference neuron

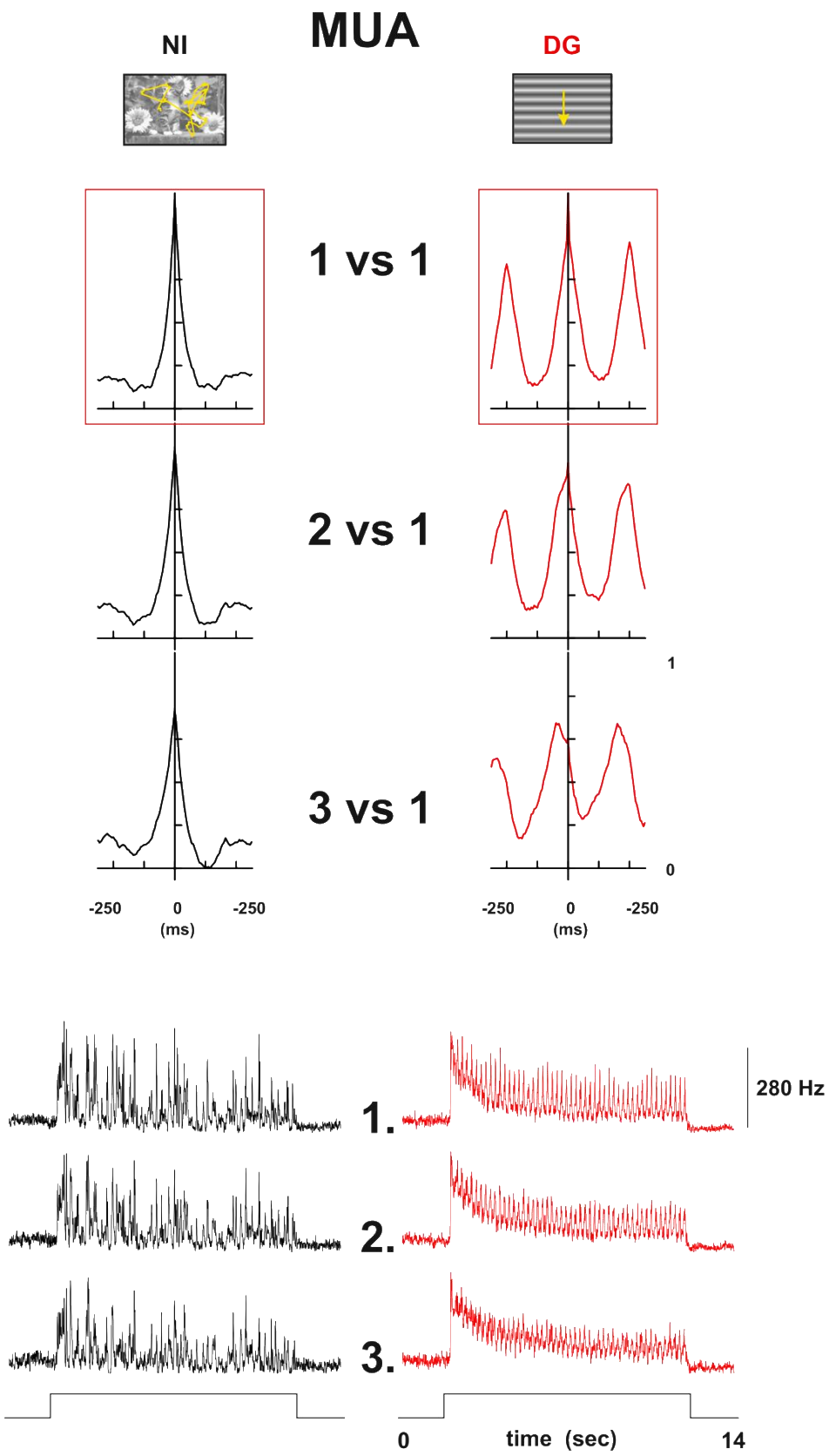

Figure 3.5.2. Example of signal correlation of the multi-unit activity across 3 different channels. The PSTHs of each channel are displayed below. The signal correlation corresponds to the value at 0. Red square: reference site

We computed the SC for both single and multi-unit populations. We obtained 776 pairs of neurons within layers and 694 between layers. Regarding the multi-unit, we computed our analysis on 3710 pairs of sites within layers and 5132 between layers. The signal correlation of the single unit activity is the correlation of all recorded neurons, without any subclass specification.

The mean signal correlation was plotted with bar plots, in order to be able to determine the stimulus eliciting the highest correlations and we also plotted the scatter plots with the distribution in order identify the different clusters of correlation, if they are present. Our results are reported in in figures 3.5.3 to 3.5.5 and table 3.5.1. When we computed the signal correlation within layers, natural images evoked the highest values both SUA and MUA ($p < 0.001$; Friedman test). For both spiking activities, the artificial stimuli evoked an equivalent signal correlation ($p > 0.05$; Friedman test). The multi-unit activity was about 5 times more correlated than the single unit was. In our knowledge, no study investigated, experimentally, the signal correlation of the MUA. However, a theoretical study performed by Cohen and Kohn (2011) showed that by increasing the number of neurons that contribute to the multi-unit one will obtain an increase in the correlation levels. Thus, when computed on the multi-unit, an increase in the signal correlation is also expected. The fact that natural images evoke a higher correlation than the other stimuli is not surprising since the natural image by itself is a very correlated stimulus. We confirmed previous results observed in the literature, stating that natural images evoke a more correlated mean response than the other stimuli (Yen et al., 2006; Martin and Schröder, 2013). Two-photons studies performed on mice observed that neurons organize themselves in poorly and highly correlated groups (Kampa et al, 2011; Rikhye and Sur, 2015). However, do we observe in cats, these highly and poorly correlated clusters? The scatters plots and the distribution of the single unit activity in figure 3.5.4 reveal that we do not observe a clustering as they did. However, we do observe a great heterogeneity in the obtained values. Martin and Schröder (2013) already observed this heterogeneity. However, they obtained higher signal correlations than us. This could be linked to three factors. The first one is that they only computed the correlation on neurons recorded from the same channel. When we restricted our neuronal population with the same criteria, we observed an increase in the signal correlation (SC around 0.2 for NI). Yet, our values are lower than theirs are. This could either be linked to the chosen PSTH bin or the number of pairs that they recorded. In their study, they show that the bin size can increase the signal correlation. We chose a bin lower than theirs (5ms vs 10ms), explaining this difference. Finally, their small number of pairs (46) might give a biased vision of correlations in V1. In a study performed in cat V1, Spacek and Swindale (2016) obtained signal correlation values, in response to NI, similar to ours.

Then, we computed the signal correlation between layers. The correlation between layers is computed for neurons that are spatially distant. Thus, it is not surprising that the values of signal correlation that we obtained are lower than the ones observed within layers ($p < 0.001$; Mann Whitney U test). For the SUA, the SC between layers is two times lower than the within layers while for the MUA the difference is less important (less than two times). Despite this decrease in signal correlation, we obtained the same pattern of response both within and between layers. At the single unit level, the scatter plot and distribution show no clusters of correlation. This is not surprising since distant neurons are poorly correlated. Regarding the MUA the correlation is higher since the multi-unit activity captures responses shared by many other neurons. Both single unit and multi-unit populations sometimes showed, for the same neuron, higher values of signal correlation for DG when we compared the response to DG and NI (figure 3.5.4 and 3.5.5). This is caused by the fact that two neurons preferentially tuned to the grating will display very high levels of correlation.

In summary, we showed that natural images evoke a more correlated signal than the other stimuli. Unsurprisingly, the multi-unit activity is more correlated than the single unit activity. In addition, we

showed that the correlation within layers, *i.e.* between neurons that are spatially close is higher than the correlation between layers *i.e.* neurons that are spatially apart. This confirms the findings of Yen et al (2006) and Tanaka et al., (2014)

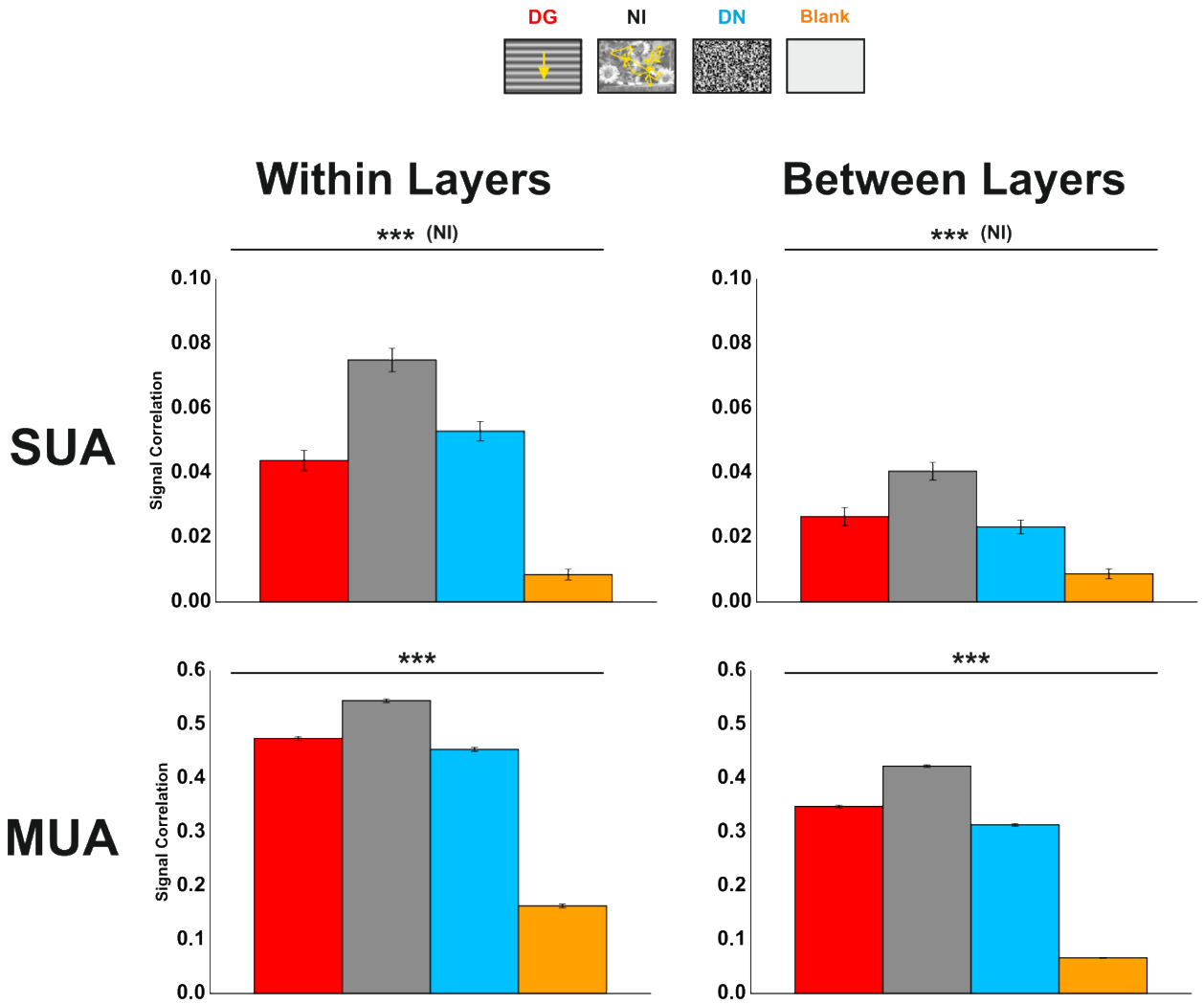

Figure 3.5.3. Signal correlation of the spiking activity within and between layers. Natural images evoke the most correlated response. The correlations are higher within layers than between them. Top row: single unit activity. Bottom row: Multi-unit activity. Stars indicate a significant statistical difference with the NI condition. n.s: non-significant; *: $p < 0.05$; **: $p < 0.01$; ***: $p < 0.001$

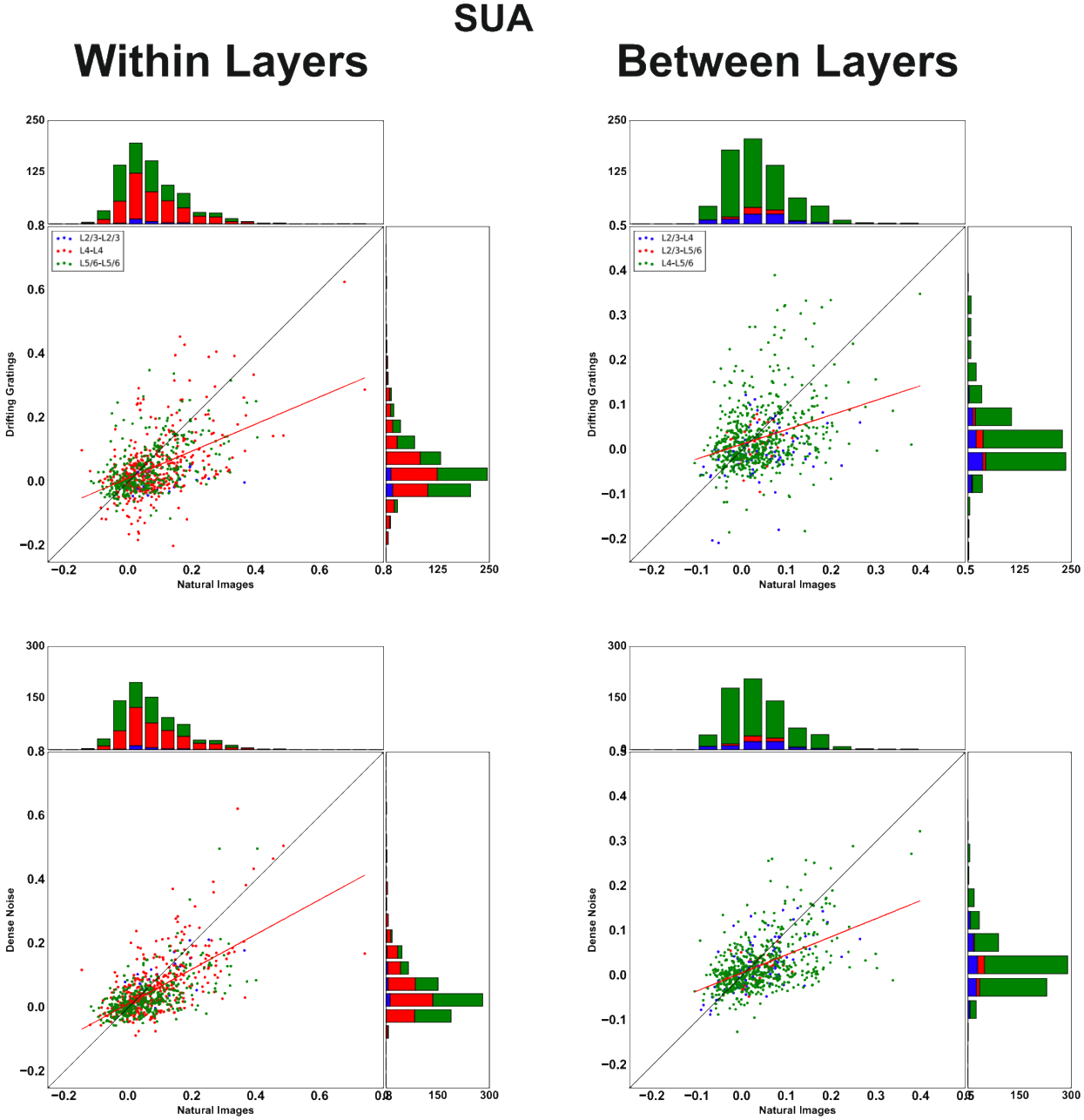

Figure 3.5.4. Scatter plots and distribution of the signal correlation of the single unit activity within and between layers. Blue: correlation computed within L2/3 or between L2/3 and L4; Red: correlation computed within L4 or between L2/3 and L5/6; Green: correlation computed within L4 or between L4 and L5/6.

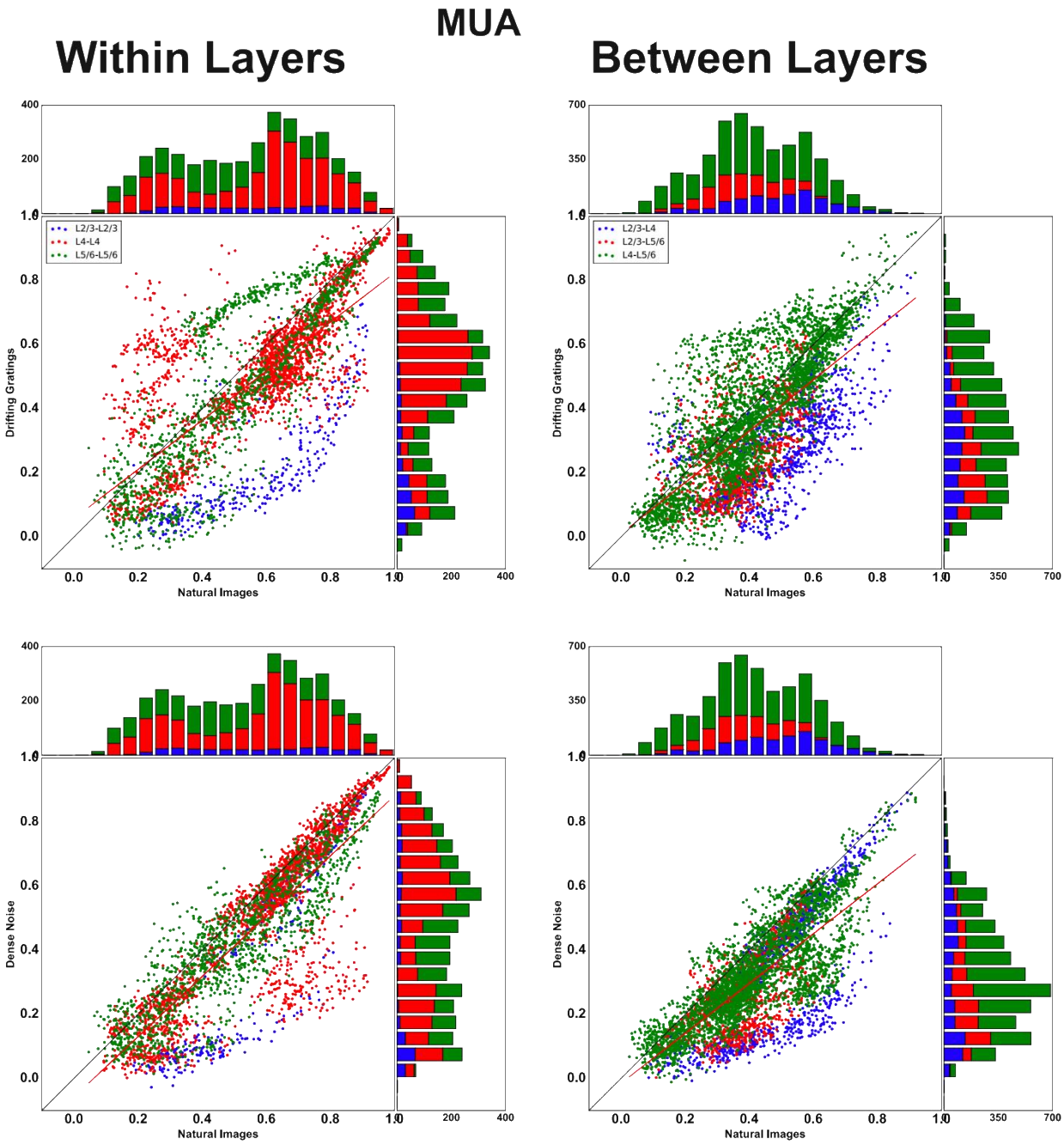

Figure 3.4.5. Scatter plots and distribution of the signal correlation of the multi-unit activity within and between layers. Blue: correlation computed within L2/3 or between L2/3 and L4; Red: correlation computed within L4 or between L2/3 and L5/6; Green: correlation computed within L4 or between L4 and L5/6.

We also subdivided our neuronal population into regular and fast spiking neurons (Figures 3.5.6 to 3.5.8; table 3.5.2). We correlated FS neurons between, them and RS neurons between them. We observed that for all stimuli, fast spiking neurons were more correlated than regular spiking neurons both between and within layers ($p < 0.001$; Mann Whitney U test).
Regular spiking cells displayed the same pattern of response as the one observed for the SUA. However, among FS cells no difference in SC was observed for all stimuli, despite a NI evoking a higher mean SC ($p > 0.05$). Since we only have about a hundred pairs of neurons for FS cells, an increase in the number in this number will be needed in the future.

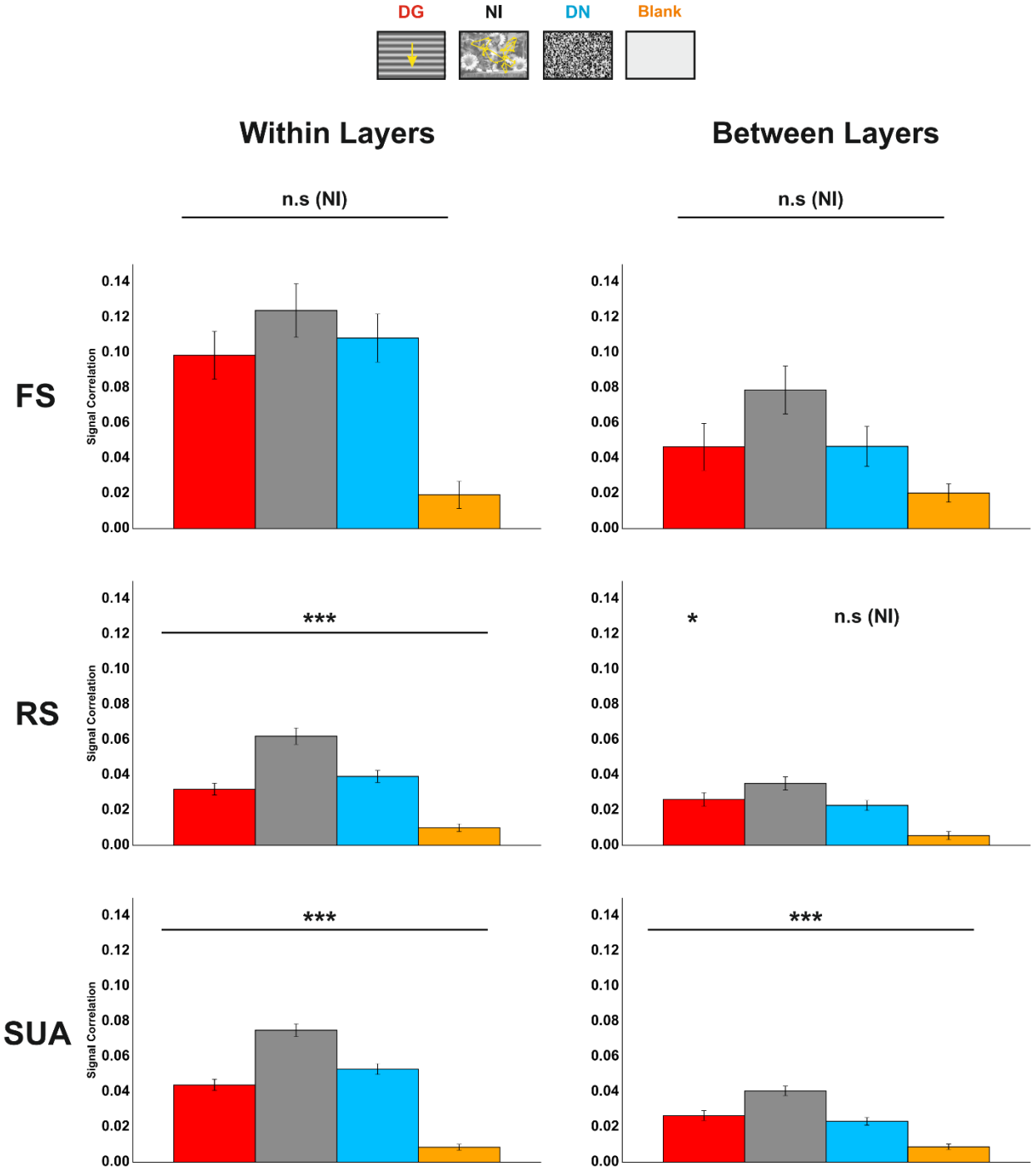

Figure 3.5.6. Signal correlation of the spiking activity within and between layers. FS neurons evoke the most correlated activity. Top row : Fast spiking neurons. Middle row: regular spiking neurons Bottom row: single unit activity. Stars indicate a significant statistical difference with the NI condition. n.s: non-significant; *: $p < 0.05$; **: $p < 0.01$; ***: $p < 0.001$

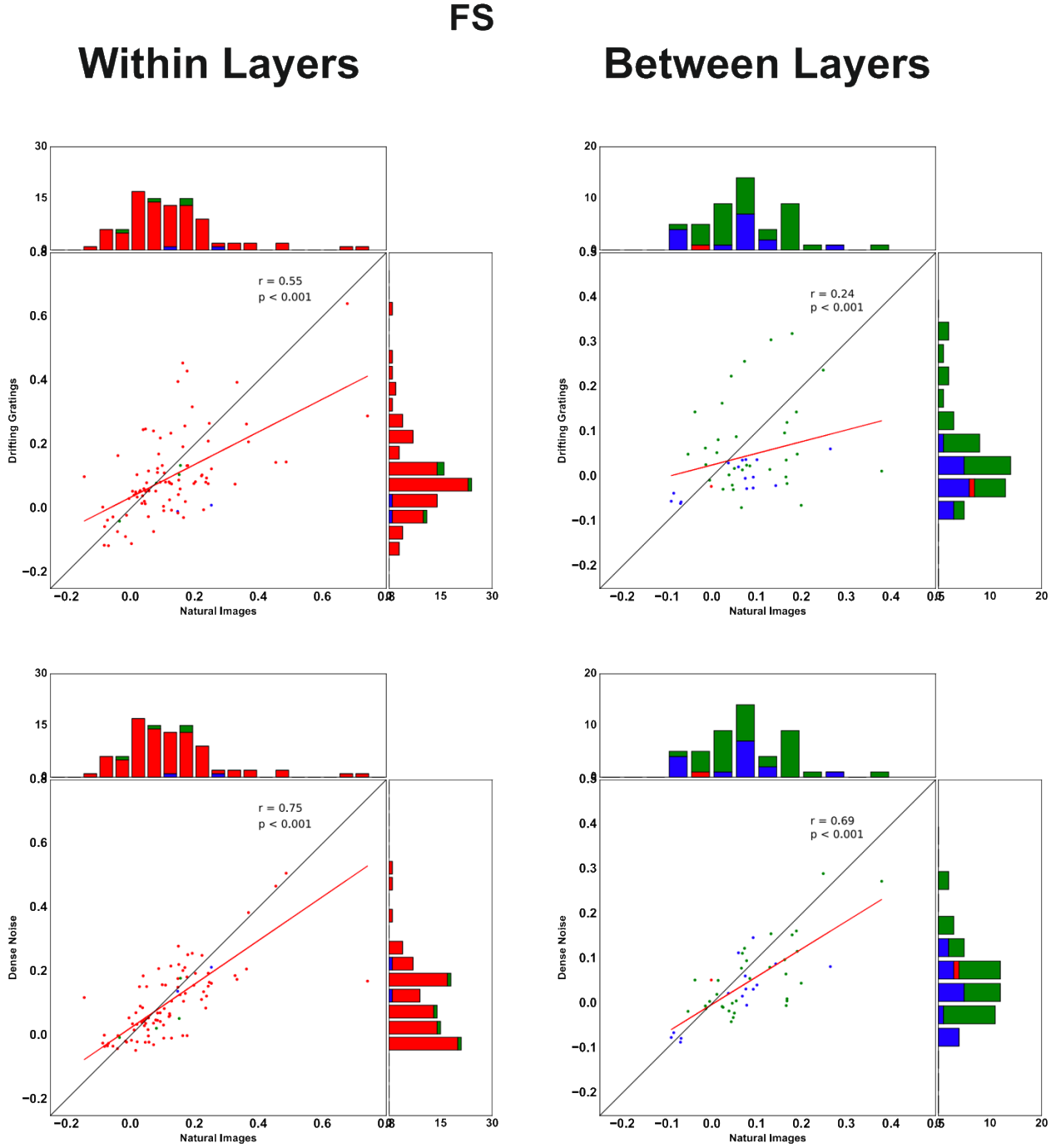

Figure 3.5.7. Scatter plots and distribution of the signal correlation of the fast spiking neurons within and between layers. Blue: correlation computed within L2/3 or between L2/3 and L4; Red: correlation computed within L4 or between L2/3 and L5/6; Green: correlation computed within L4 or between L4 and L5/6.

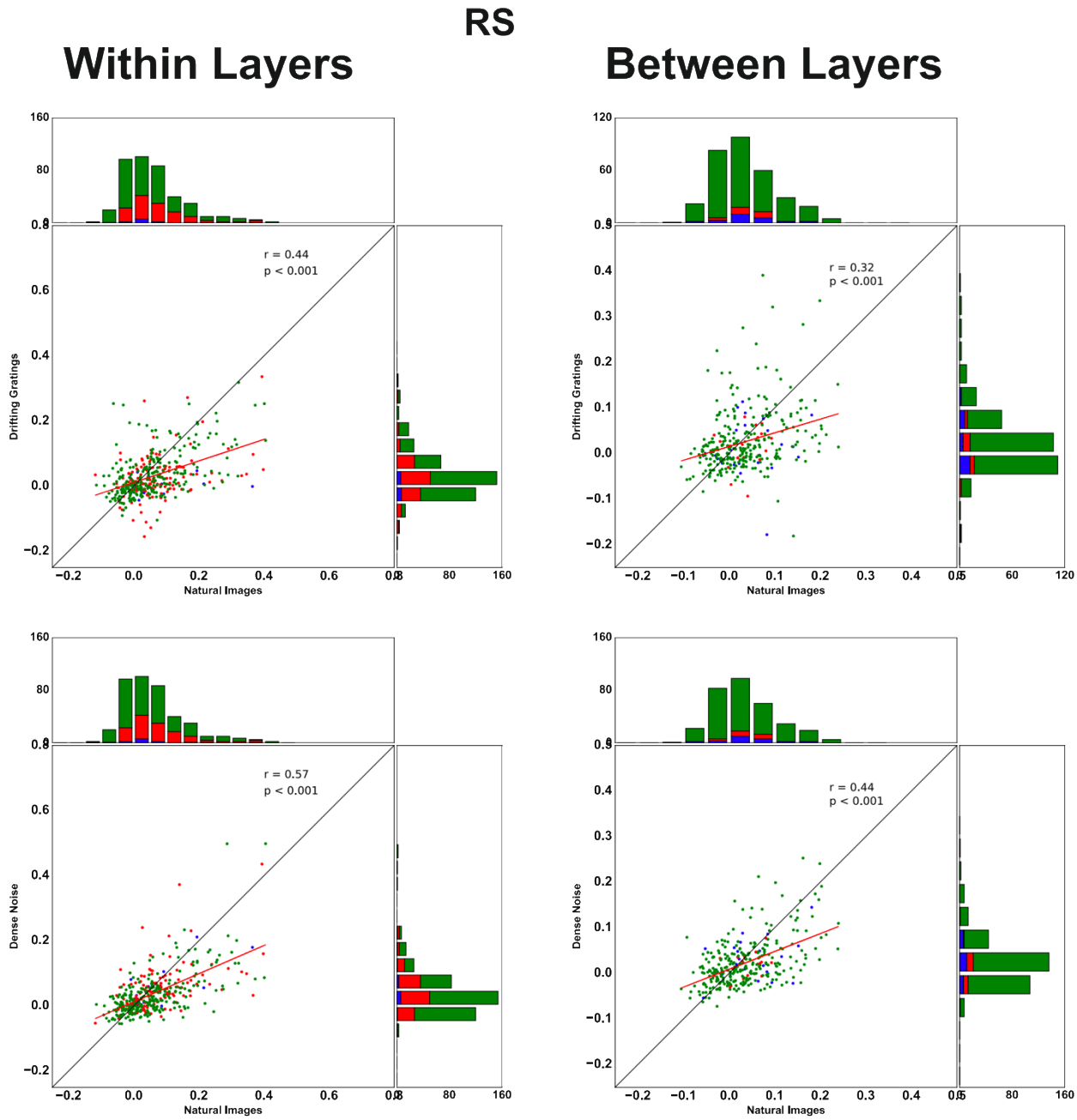

Figure 3.5.8. Scatter plots and distribution of the signal correlation of the regular spiking neurons within and between layers. Blue: correlation computed within L2/3 or between L2/3 and L4; Red: correlation computed within L4 or between L2/3 and L5/6; Green: correlation computed within L4 or between L4 and L5/6.

It has been shown, on mice, that a natural stimulus containing strong low frequency spatial correlations will evoke a more correlated (Rikhye and Sur (2015)). We wondered if our control stimuli, were we randomized the phase at the spatial level and the eye movements at the temporal one, would evoke different levels of correlation (Figure 3.5.9; table 3.5.3). Both within and between layers, at the single unit level, all the altered natural images, except NI-RST, evoked a similar correlation level that the unaltered natural image ($p > 0.05$; Friedman test). At a more global level (*i.e.* the MUA), all the altered natural images evoked different correlations that the unaltered natural image ($p < 0.001$; Friedman test). At this scale, the differences between the SC evoked by the different stimuli are very low (table 3.5.3). The only main difference observed was for the correlations evoked by NI-RT. No significant difference between the evoked correlations was observed within our RS and FS populations (Figure 3.5.10; table 3.5.3; $p > 0.05$; Friedman test).

In summary, the signal correlation does not seem strongly impacted by the alterations of the spatio-temporal statistics of natural images. In their study performed in primate, Freeman et al., (2013), did not observe any difference in V1 response for natural and altered natural stimuli. However, they observed a difference in V2. Since mice are not visual animals (see table 1.1.1), the different response that takes place in V2 in higher mammals might already be present in V1.

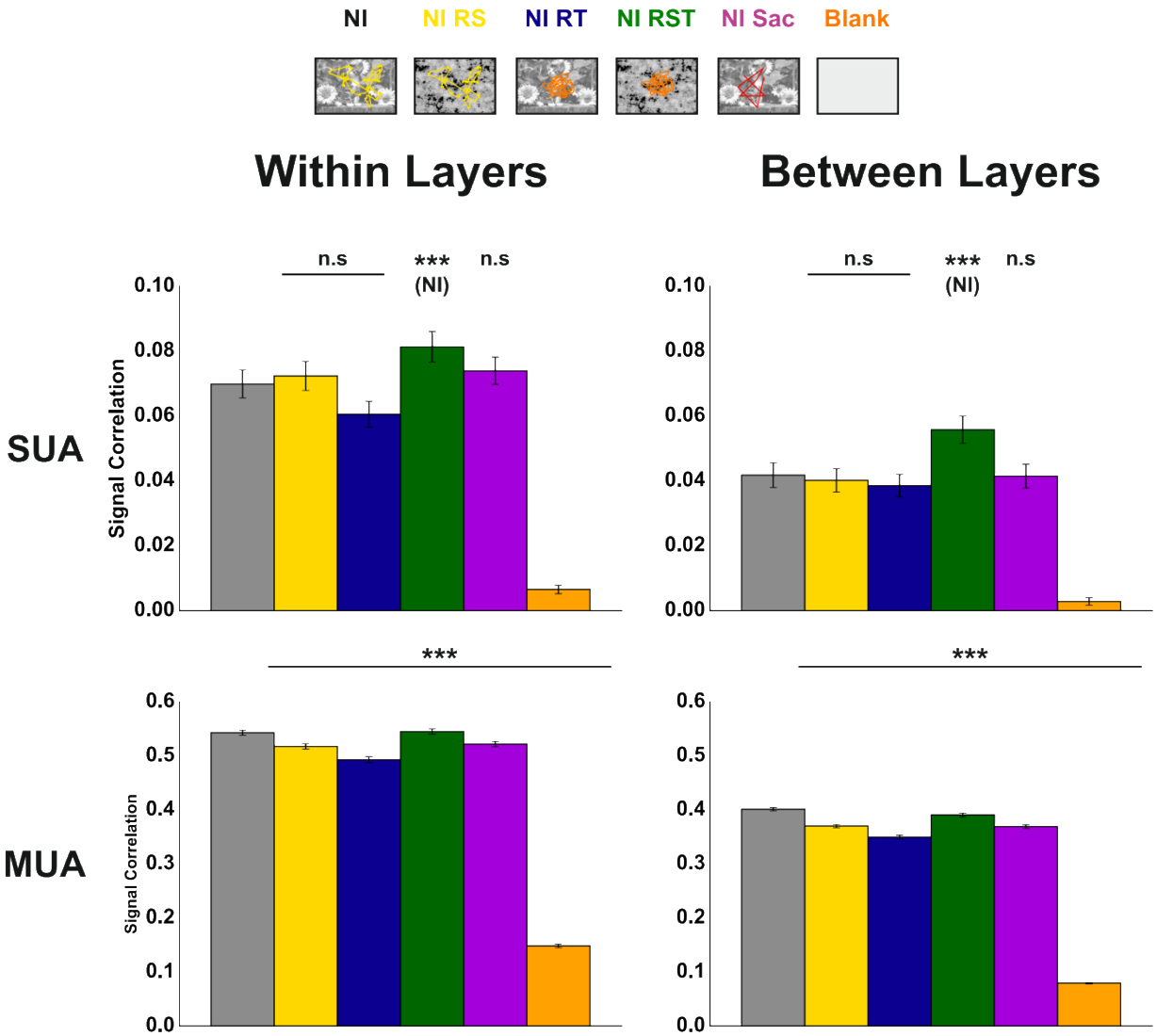

Figure 3.5.9. Signal correlation of the spiking activity, in response to our control stimuli, within and between layers. Top row: single unit activity. Bottom row: Multi-unit activity. Stars indicate a significant statistical difference with the NI condition. n.s: non-significant; *: $p < 0.05$; **: $p < 0.01$; ***: $p < 0.001$

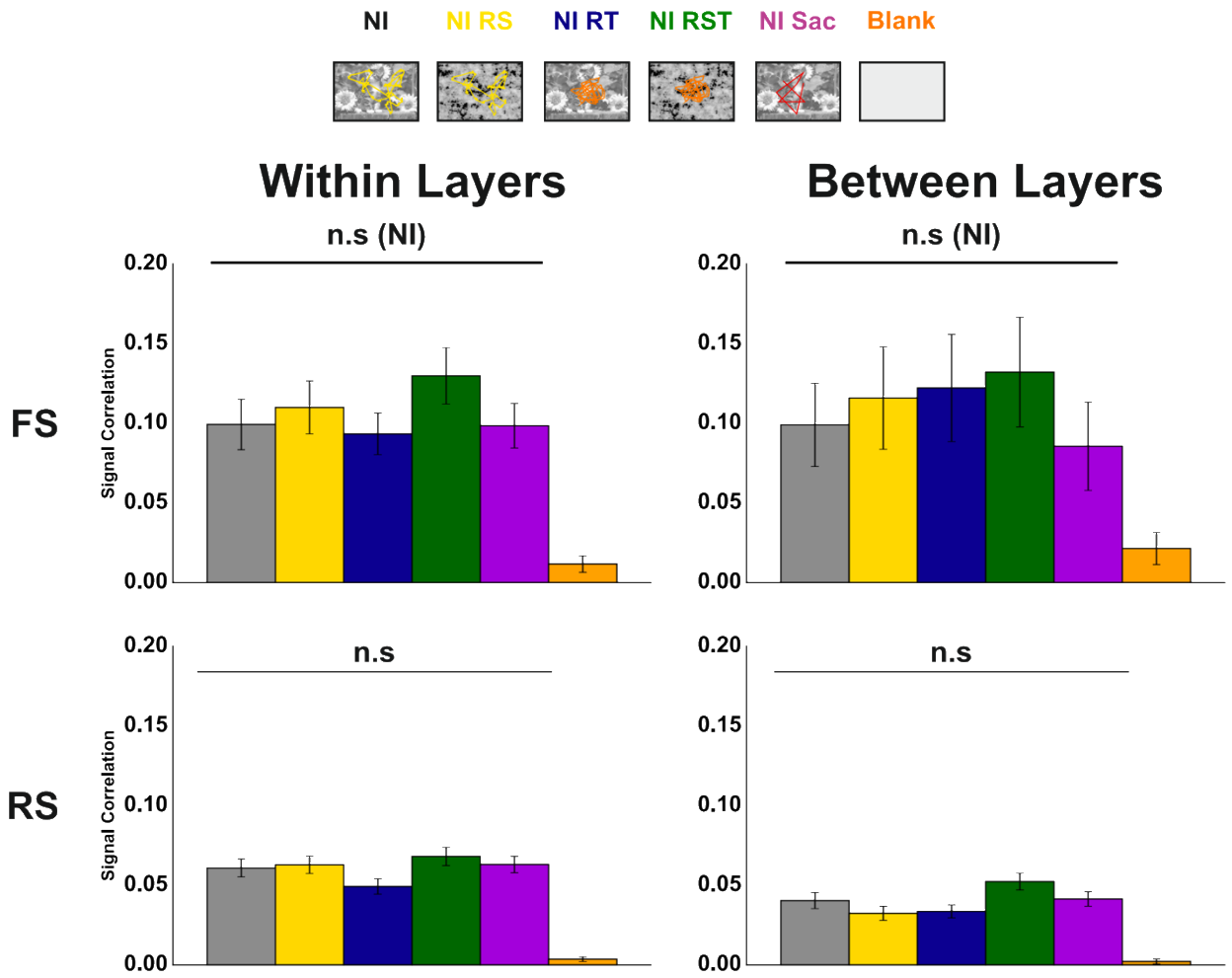

Figure 3.5.10. Signal correlation of the spiking activity within and between layers. Top row: Fast spiking neurons. Bottom row: regular spiking. Stars indicate a significant statistical difference with the NI condition. n.s: non-significant; *: $p < 0.05$; **: $p < 0.01$; ***: $p < 0.001$

FULL FIELD	Signal Correlation (SUA)			
	DG	NI	DN	BLK
Within Layers	0.044 ± 0.003	0.075 ± 0.004	0.053 ± 0.003	0.008 ± 0.002
Between Layers	0.026 ± 0.003	0.04 ± 0.003	0.023 ± 0.002	0.009 ± 0.002

FULL FIELD	Signal Correlation (MUA)			
	DG	NI	DN	BLK
Within Layers	0.474 ± 0.004	0.544 ± 0.004	0.454 ± 0.004	0.163 ± 0.004
Between Layers	0.348 ± 0.003	0.423 ± 0.002	0.314 ± 0.002	0.066 ± 0.001

Table 3.5.1: Signal correlation of the single and multi-unit activities computed within and between layers in response to our stimulus set (Mean ± SEM)

FULL FIELD	Signal Correlation (FS)			
	DG	NI	DN	BLK
Within Layers	0.098 ± 0.014	0.124 ± 0.015	0.108 ± 0.014	0.019 ± 0.008
Between Layers	0.046 ± 0.013	0.079 ± 0.014	0.047 ± 0.011	0.02 ± 0.005

FULL FIELD	Signal Correlation (RS)			
	DG	NI	DN	BLK
Within Layers	0.032 ± 0.003	0.062 ± 0.005	0.039 ± 0.003	0.01 ± 0.002
Between Layers	0.026 ± 0.004	0.035 ± 0.004	0.023 ± 0.003	0.006 ± 0.002

Table 3.5.2: Signal correlation of the fast and regular spiking neurons computed within and between layers in response to our stimulus set (Mean ± SEM)

FULL FIELD	WITHIN LAYERS					
	NI	NI-RS	NI-RT	NI-RST	NI-SAC	BLK
FS	0.099 ± 0.016	0.11 ± 0.017	0.093 ± 0.013	0.13 ± 0.018	0.098 ± 0.014	0.012 ± 0.005
RS	0.061 ± 0.006	0.063 ± 0.005	0.049 ± 0.005	0.068 ± 0.006	0.063 ± 0.005	0.004 ± 0.001
SUA	0.07 ± 0.004	0.072 ± 0.004	0.061 ± 0.004	0.081 ± 0.005	0.074 ± 0.004	0.007 ± 0.001
MUA	0.543 ± 0.005	0.518 ± 0.005	0.493 ± 0.006	0.545 ± 0.005	0.522 ± 0.005	0.149 ± 0.003

FULL FIELD	BETWEEN LAYERS					
	NI	NI-RS	NI-RT	NI-RST	NI-SAC	BLK
FS	0.099 ± 0.026	0.116 ± 0.032	0.122 ± 0.034	0.132 ± 0.034	0.086 ± 0.028	0.021 ± 0.01
RS	0.04 ± 0.005	0.032 ± 0.004	0.034 ± 0.004	0.052 ± 0.005	0.041 ± 0.005	0.002 ± 0.002
SUA	0.042 ± 0.004	0.04 ± 0.004	0.039 ± 0.003	0.056 ± 0.004	0.042 ± 0.004	0.003 ± 0.001
MUA	0.401 ± 0.003	0.37 ± 0.003	0.35 ± 0.004	0.391 ± 0.003	0.369 ± 0.004	0.08 ± 0.002

Table 3.5.3: Signal correlation of the spiking activity computed within and between layers in response to our control stimulus set (Mean ± SEM)

- **Noise Correlation**

The noise correlation is the measure of the shared fluctuations between two neurons (Martin and Schröder, 2013). The latter is the correlation of each trial response (after mean subtraction) between two different neurons (SUA or MUA) in response to the same stimulus. An example of two trial responses that will be correlated is shown in figure 3.5.11.
It has been shown that noise correlation is stimulus dependent (Kohn and Smith, 2005; Rikhye and Sur, 2015) and that spatially distant pairs of evoke a lower correlation than spatially close pairs of neurons (Smith and Kohn, 2008; Rikhye and Sur, 2015). However, these studies were performed on primates or mice. On cats, Martin and Schroder (2013), showed artificial and natural stimuli evoked the same values of noise correlation. Based on the findings of the literature, we decided to investigate in our data if a stimulus and a spatial dependency of the noise correlations were observed. As performed for the signal correlation, we divided our analysis into two groups.
A first one that regroups the noise correlation of neurons belonging to the same layer *i.e.* **the noise correlation within layers**.
A second one that regroups the noise correlation of neurons belonging to different layers *i.e.* **the signal noise between layers**.

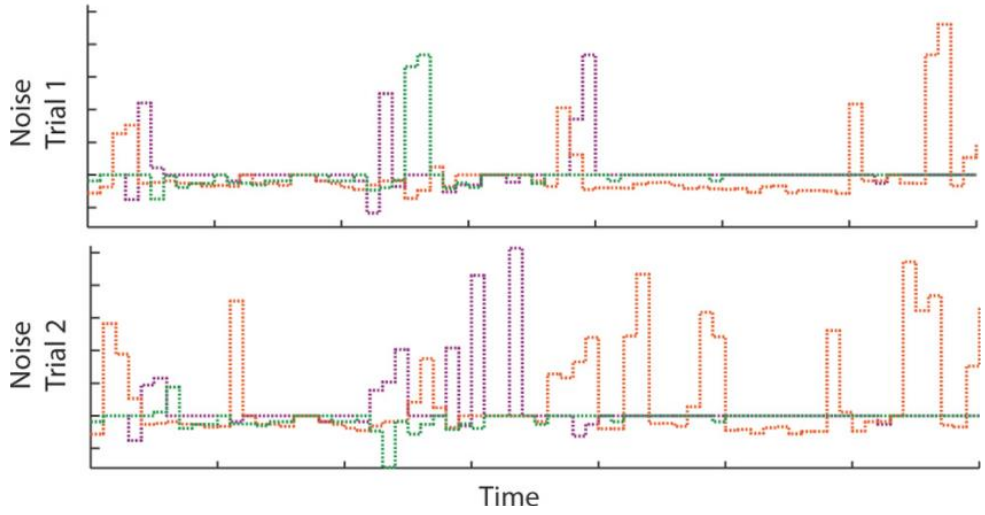

Figure 3.5.11. Trial response of three different neurons (in purple, green and orange). These trial responses are correlated in order to obtain the noise correlation (reprinted from Martin and Schröder, 2013)

We obtained 776 pairs of neurons within layers and 694 between layers. Regarding the multi-unit we computed our analysis on 3710 pairs of sites within layers and 5132 between layers. The noise correlation of the single unit activity is the correlation of all recorded neurons, without any subclass specification. Our results are reported in in figures 3.5.12 to 3.5.15 and table 3.5.4.
We first computed the noise correlation within layers. Our results show that, at the single unit level, all stimuli evoked a similar noise correlation ($p > 0.55$; Friedman test; table 3.5.4). The noise correlation values that we obtained for the single unit activity are in the range of those obtained in the literature (see chapter I section 1. and Cohen and Kohn, 2011). One could argue that our values are different from the ones obtained by Ecker et al. (2006), however they used an improved noise correlation computation method on the awake primate. They claim that their difference is linked to a more efficient spike sorting while the main reason might come from their new method and the animal state (they showed later (Ecker et al, 2013) that anesthesia increases the noise correlations). In addition, our results match the ones of the literature. Indeed as observed by Martin and Schroder

(2013) on cats but also Ecker et al, (2013) on primates, we obtained very heterogeneous values of noise correlation.

On the other hand, we obtained different NC values at multi-unit level: DG evoked the highest noise correlation and DN the lowest ($p < 0.001$). Again, we obtained very heterogeneous noise correlation values. The MUA noise correlation is higher than the SUA ($p < 0.001$; Mann Whitney U test). This is not surprising, since the MUA is a signal that regroups the activity of many neurons it averages out variability that is independent of each neuron, so the correlation between two clusters of multiunit activity will be larger than between pairings of the constituent neurons (Cohen and Kohn, 2011). Ecker and colleagues (2014) showed that anesthesia has a strong impact on the variability of the response. In addition, Spacek and Swindale (2016) observed that during an experiment, anesthetized cats will display different levels of synchronization in V1. These different levels of synchronization resulted in different values of NC. Thus, the heterogeneous values that we observed could also be linked to the state of the animal across the experiment.

When computed between layers, at the single unit level, DG and NI evoked a similar noise correlation ($p = 0.052$), higher than the one evoked by DN ($p < 0.01$). Again, we obtained very heterogeneous noise correlation values. We then computed the noise correlation of the MUA, between layers and obtained the same response pattern as the one obtained between layers

For both single unit and multi-unit activities respectively, the correlation within layers evoked a higher value than the correlation between layers. These results are in agreement with the ones observed by Smith and Kohn (2008) and Rikhye and Sur (2015), showing that distance decreased the noise correlation.

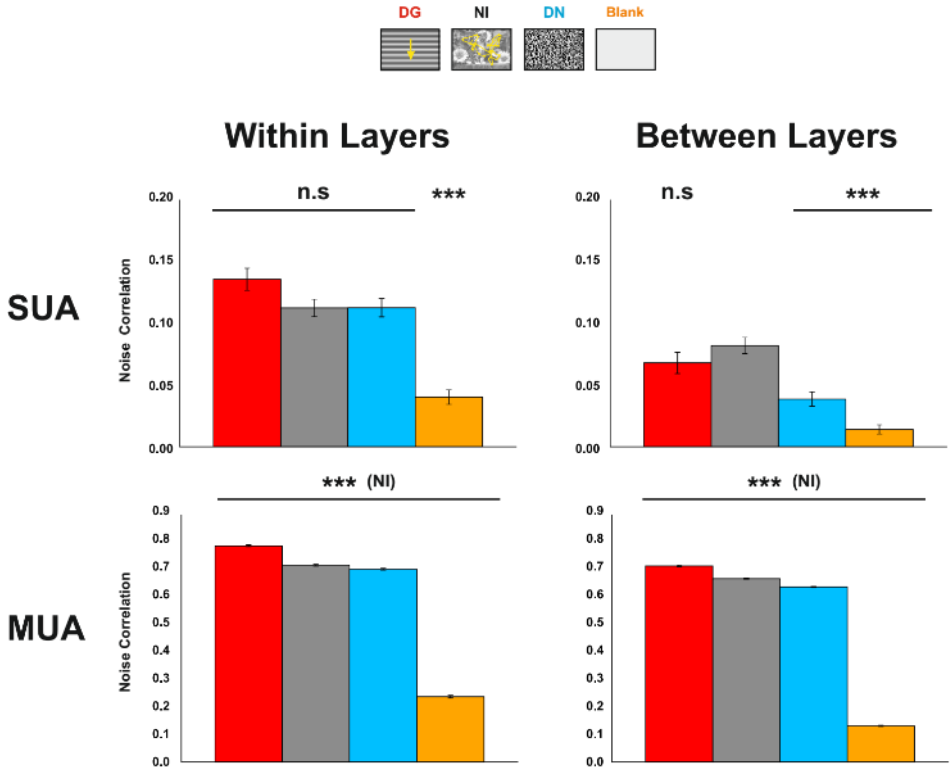

Figure 3.5.12. Noise correlation of the spiking activity within and between layers. Small differences are observed between the evoked correlations. The correlations are higher within layers than between them. Top row: single unit activity. Bottom row: Multi-unit activity. Stars indicate a significant statistical difference with the NI condition. n.s: non-significant; *: $p < 0.05$; **: $p < 0.01$; ***: $p < 0.001$

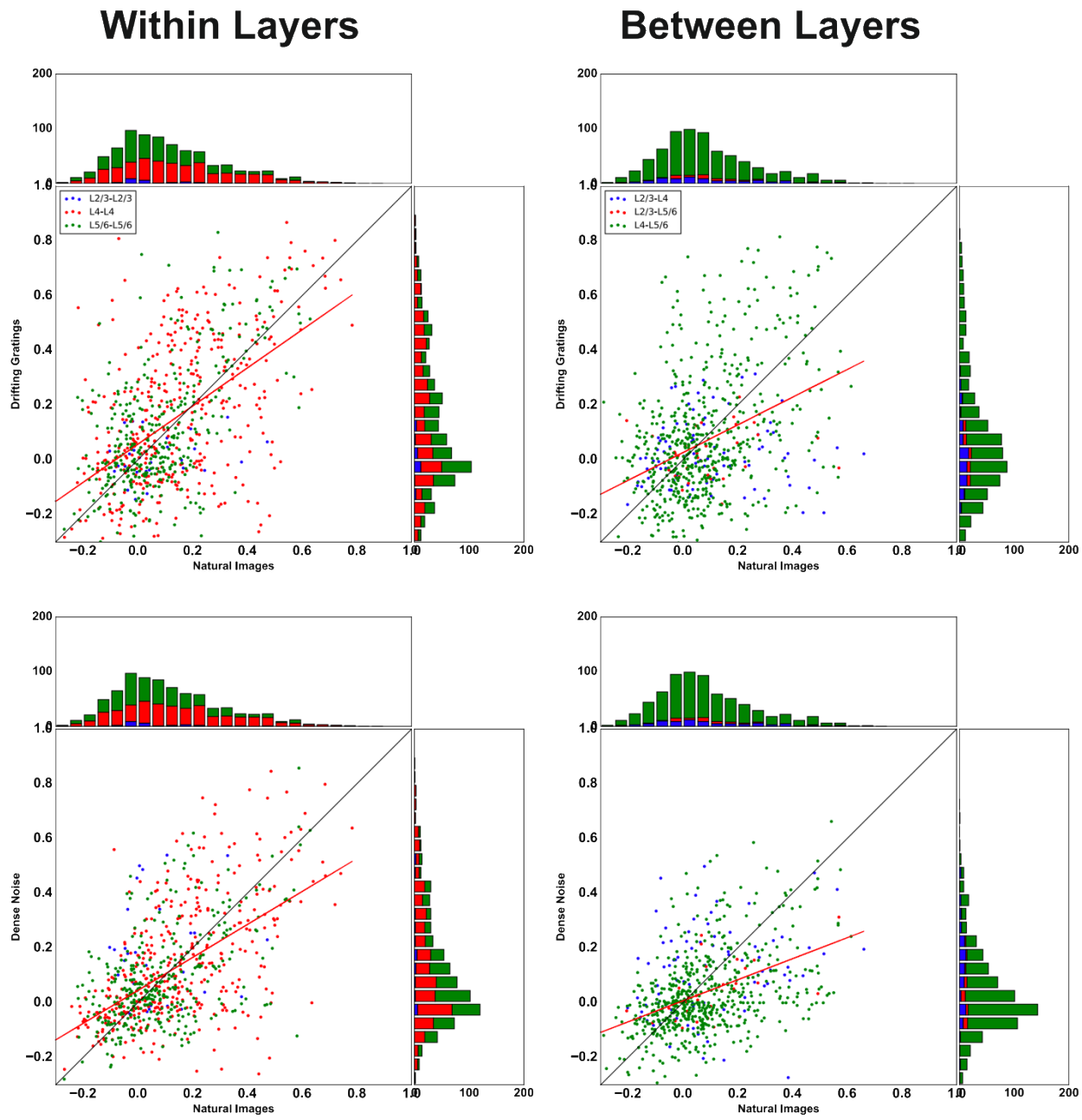

Figure 3.5.13. Scatter plots and distribution of the noise correlation of the single unit activity within and between layers. Blue: correlation computed within L2/3 or between L2/3 and L4; Red: correlation computed within L4 or between L2/3 and L5/6; Green: correlation computed within L4 or between L4 and L5/6.

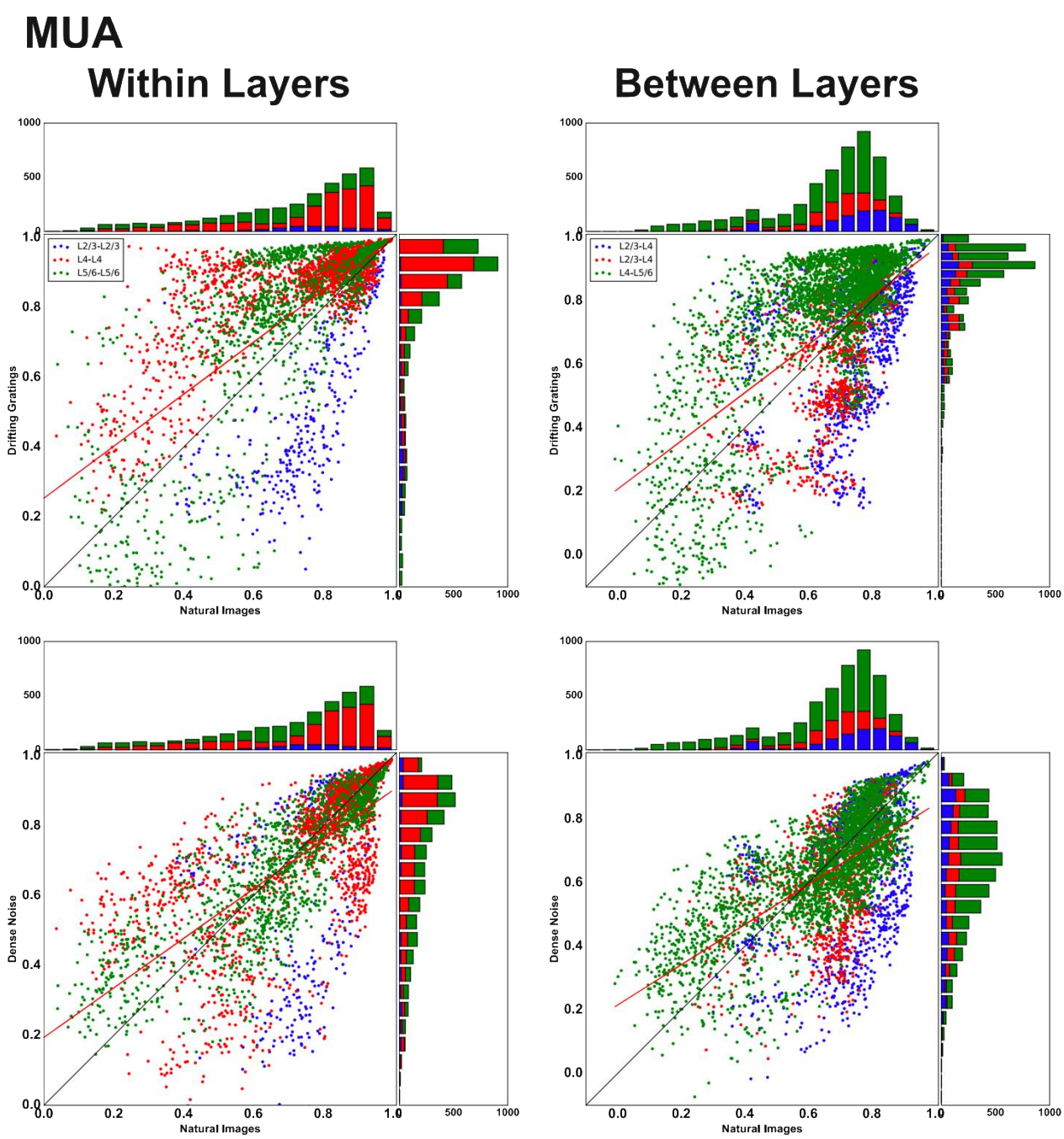

Figure 3.5.14. Scatter plots and distribution of the noise correlation of the multi-unit activity within and between layers. Blue: correlation computed within L2/3 or between L2/3 and L4; Red: correlation computed within L4 or between L2/3 and L5/6; Green: correlation computed within L4 or between L4 and L5/6.

We also subdivided our neuronal population into regular and fast spiking neurons. We showed that these two neuronal subclasses displayed different signal levels. Will we observe the same behavior for the noise correlation? We first computed the correlation within layers (Figures 3.5.15 to .5.17; table 3.5.5). When DG was presented fast spiking, cells displayed a higher noise correlation than when the other stimuli were ($p < 0.01$). At the level of the regular spiking population, all stimuli evoked a similar noise correlation ($p > 0.6$). However, for FS cells, when computed between layers, all stimuli evoked the same levels of noise correlation ($p > 0.5$). On the other hand, among RS cells, level, DG and NI evoked a similar noise correlation ($p = 0.57$), higher than the one evoked by DN ($p < 0.01$). For both correlations, fast spiking cells evoked the highest noise while RS the lowest one ($p < 0.001$; Kruskal Wallis test). This was also observed at the level of the time frequency analysis, where FS cells evoked the noisiest response but also the strongest signal. The higher levels of noise correlation observed for FS neurons are probably linked to their high firing rate. Indeed, the noise correlation levels are directly linked to the cells firing rates (Cohen and Kohn, 2011). Interestingly, the noise correlations values obtained with the RS neurons is close to the ones obtained by Ecker et al (2013) in the anesthetized monkey. Therefore, the low values that they obtained could be linked with an oversampling of regular spiking neurons.
Finally, both subclasses displayed very heterogeneous levels of correlations. Again, this heterogeneity could be linked to different dynamic brain states as observed by Spacek and Swindale (2016).

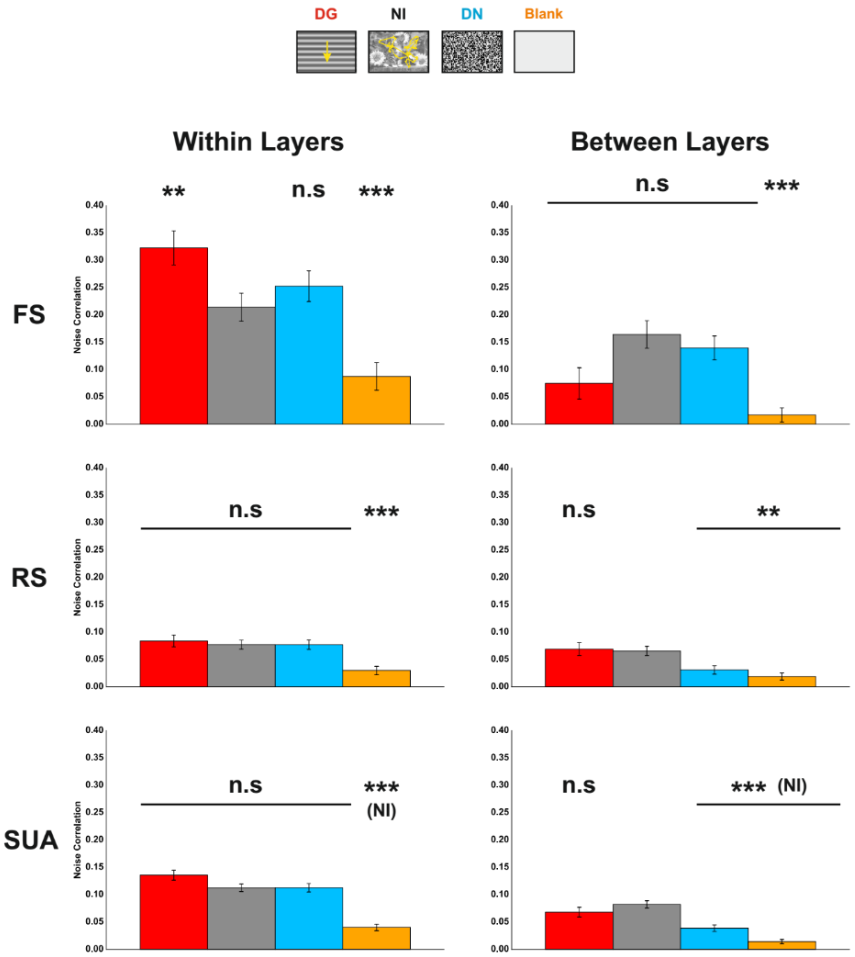

Figure 3.5.15. Noise correlation of the spiking activity within and between layers. Top row : Fast spiking neurons. Middle row: regular spiking neurons Bottom row: single unit activity. Stars indicate a significant statistical difference with the NI condition. n.s: non-significant; *: $p < 0.05$; **: $p < 0.01$; ***: $p < 0.001$

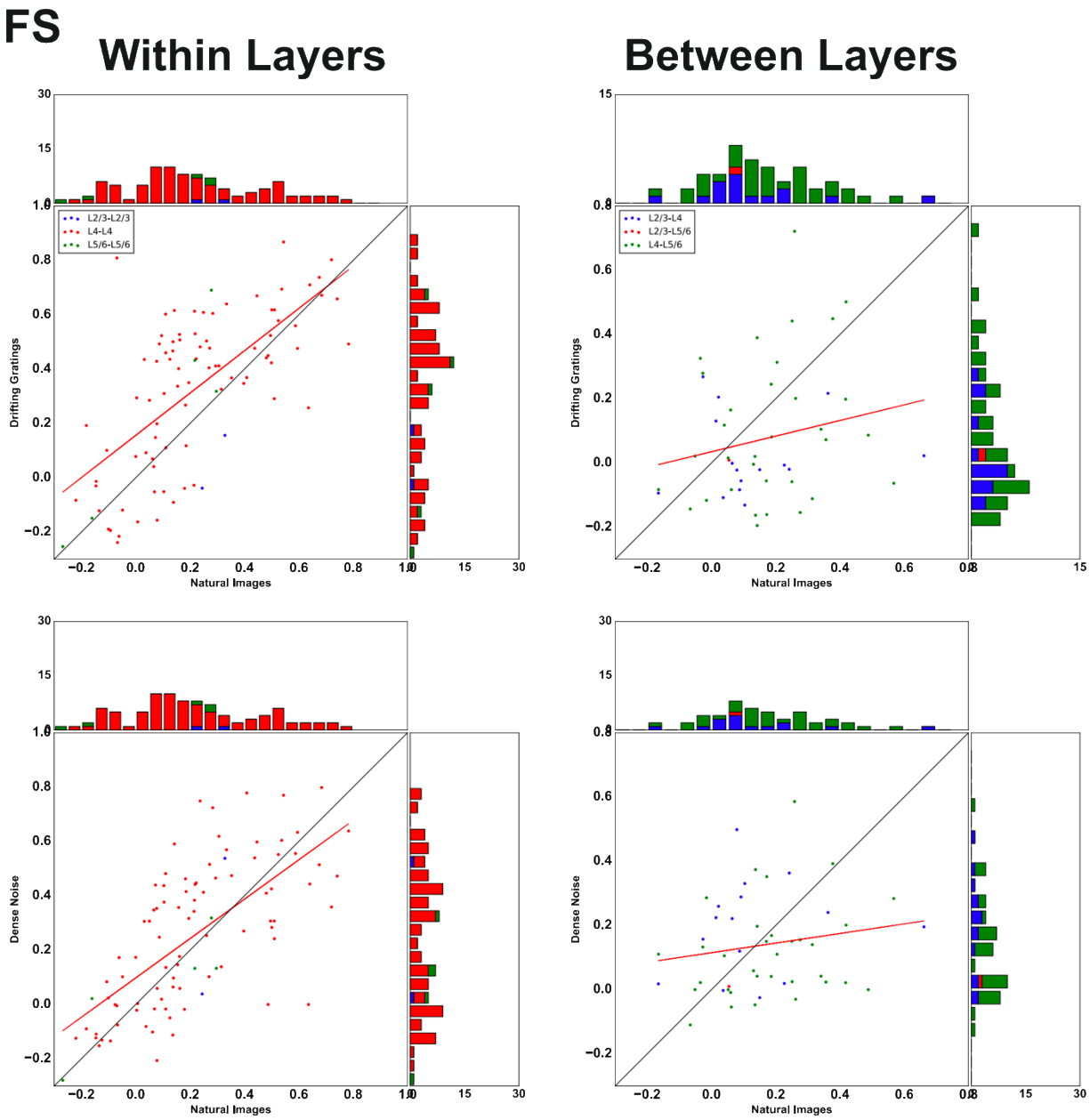

Figure 3.5.16. Scatter plots and distribution of the noise correlation of the fast spiking neurons within and between layers. Blue: correlation computed within L2/3 or between L2/3 and L4; Red: correlation computed within L4 or between L2/3 and L5/6; Green: correlation computed within L4 or between L4 and L5/6.

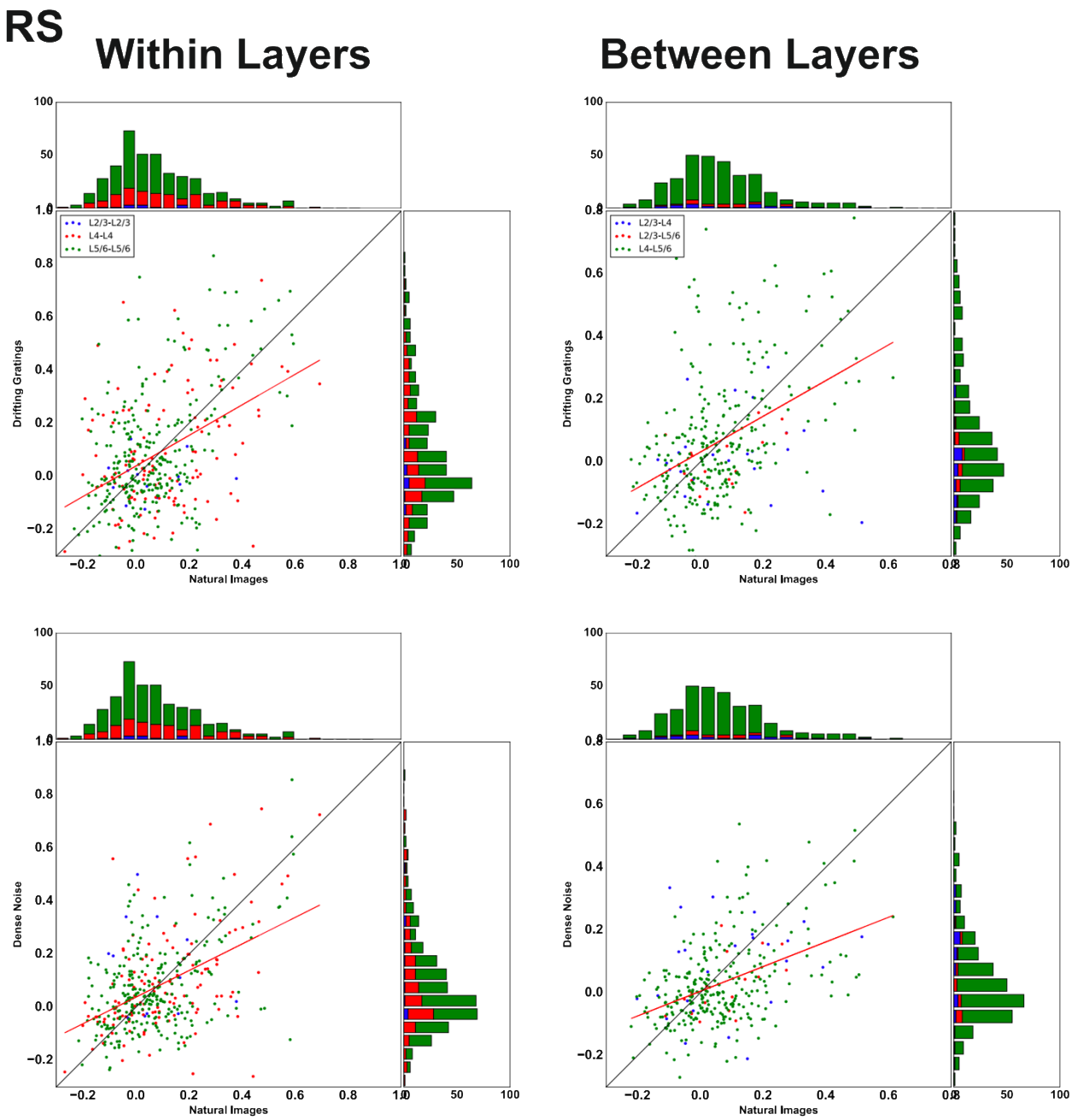

Figure 3.5.17. Scatter plots and distribution of the noise correlation of the regular spiking neurons within and between layers. Blue: correlation computed within L2/3 or between L2/3 and L4; Red: correlation computed within L4 or between L2/3 and L5/6; Green: correlation computed within L4 or between L4 and L5/6.

In their paper De Vries et al. (2019) showed that neurons showing a high level of synchrony exhibited positively correlated trial-by-trial fluctuations. In practice this correspond to signal and noise correlation being positively correlated. They and others (Cohen and Kohn, 2011), suggested that this correlation is a common feature of cortical representations. These two studies were either performed on mice or on primates. We wondered if this would be also observed on cat primary visual cortex. We compared the signal and noise correlation values for both single and multi-unit activities (Figures 3.4.18 and 3.4.19). Within layers, the SUA the noise and signal correlations exhibited a positive correlation, about the same level as the one observed by de Vries et al ($p < 0.001$; Spearman test) On the other hand, the MUA displayed a very high correlation level ($p < 0.001$). Between layers, a higher correlation was observed for the single unit activity while the same correlation levels were observed for the MUA ($p < 0.001$). The FS and RS neurons displayed similar correlation levels as the single unit population, thus we will not plot them. These results show that on cat primary visual cortex we also observed a correlation between the signal and noise correlations and this latter is a feature of cortical representation.

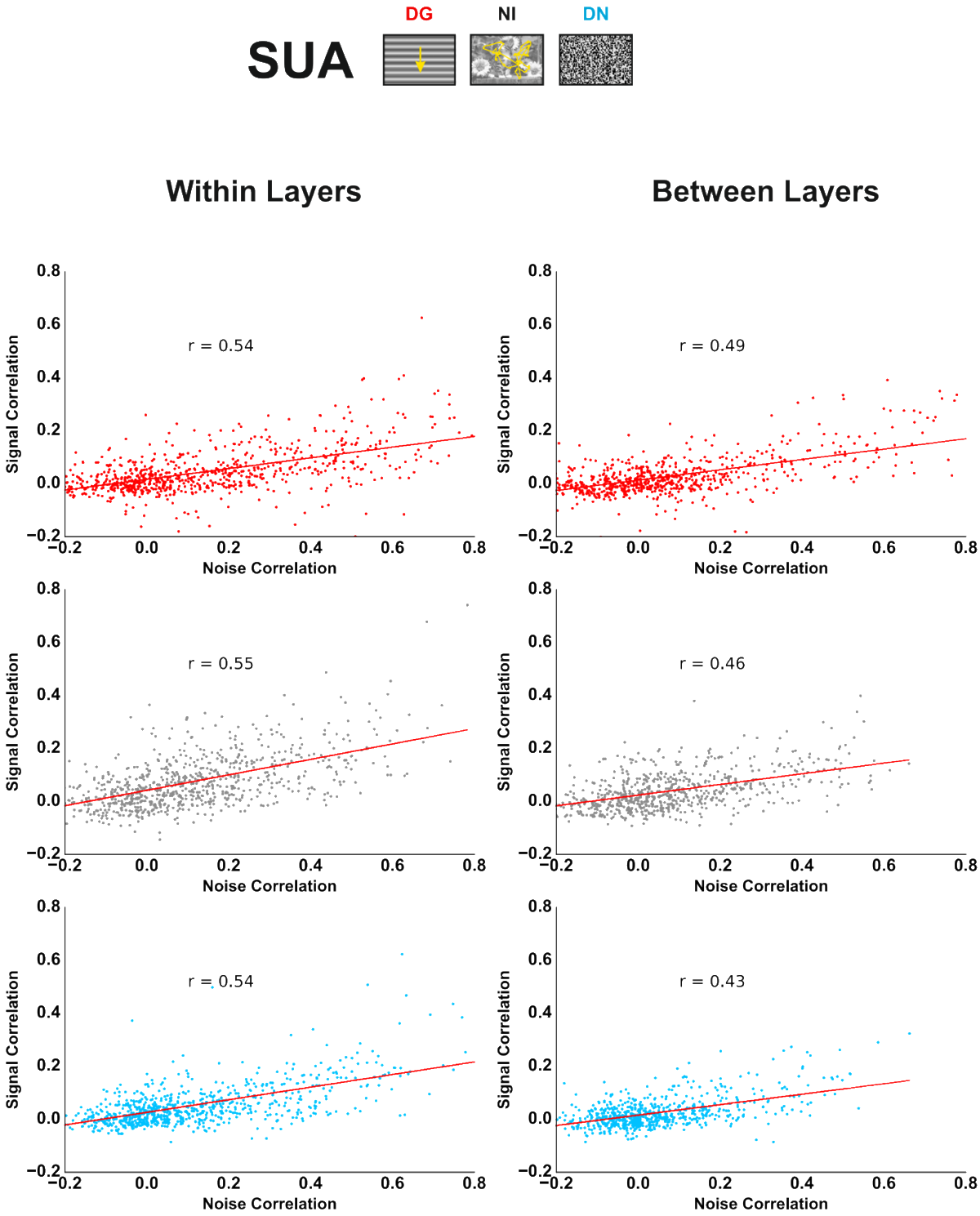

Figure 3.4.18. Correlation between noise and signal correlations of the single unit activity within and between layers (r = spearman's correlation).

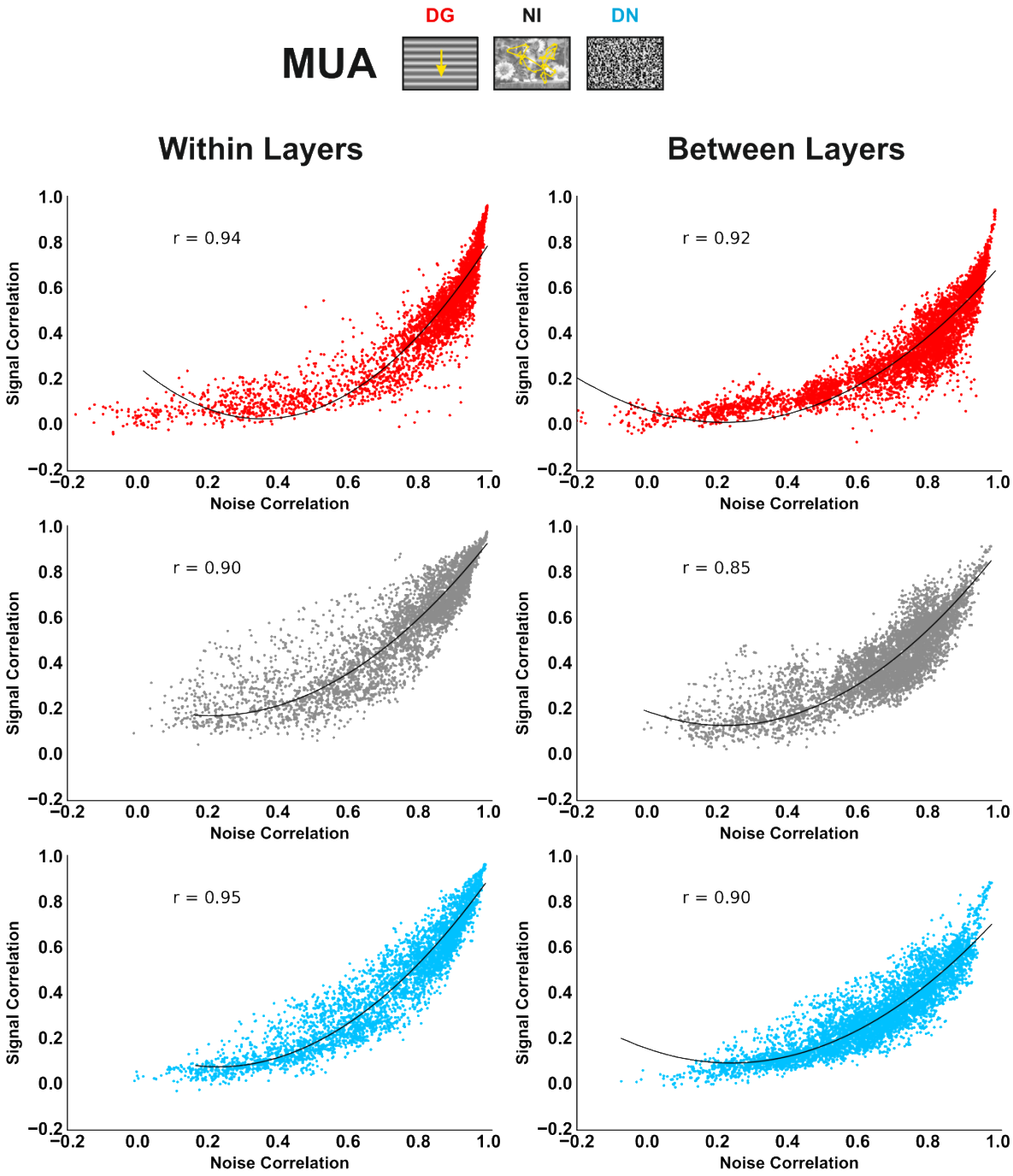

Figure 3.4.19. Correlation between noise and signal correlations of the single unit activity within and between layers (r = spearman's correlation). Black curve: exponential fit.

In this section, we showed that the noise correlation does not display a stimulus dependency at the single unit level. However, we compared the noise correlation evoked by a natural and two artificial stimuli. In their study performed on mice, Rikhye and Sur (2015) showed that natural images containing highly, or poorly correlated spatial statistics displayed different levels of correlation. We wondered if our set of altered natural stimulus would impact the noise correlation of cat V1 neurons in the same way as in mouse V1. Within layers, for the single unit activity, we observed that the natural image where the spatial phase is randomized displayed a higher noise correlation than the other stimuli, that evoked the same NC ($p > 0.1$; Friedman test: Figure 3.4.20; table 3.5.6). Regarding the MUA, all altered stimuli evoked a lower NC than the unaltered natural image ($p < 0.001$). The lowest mean noise correlation was evoked by the natural image where spatial were randomized. The other stimuli evoked close, but significantly different noise correlation ($p < 0.001$). When computed between layers, all the stimuli evoked the same noise correlation for the single unit population ($p > 0.18$). However, a pattern of response was visible, with NI inducing the highest mean correlation and NI-RT the lowest one. Interestingly, the noise correlations of FS cells displayed the same patter as the MUA, while the RS cells showed a similar response pattern as the SUA (Figure 3.5.21).

The results that we obtain for the SUA are probably biased by the RS cells response since we recorded more RS than FS cells. We observed that the phase of the statistics of the natural scene have an impact on the noise correlation. In addition, we showed that temporal statistics, and their alteration, also impact the noise correlation. However, the alterations of spatial statistics seem to have a stronger impact on the noise correlation than the temporal ones.

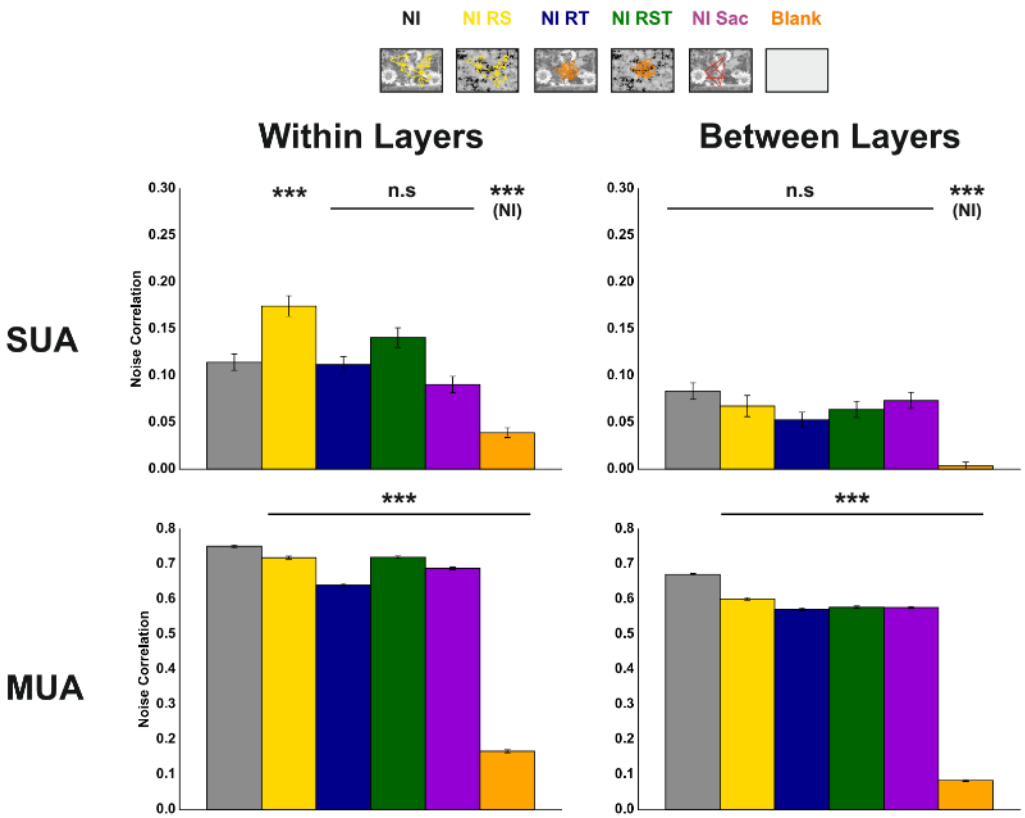

Figure 3.5.20. Noise correlation of the spiking activity, in response to our control stimuli, within and between layers. Top row: single unit activity. Bottom row: Multi-unit activity. Stars indicate a significant statistical difference with the NI condition. n.s: non-significant; *: $p < 0.05$; **: $p < 0.01$; ***: $p < 0.001$

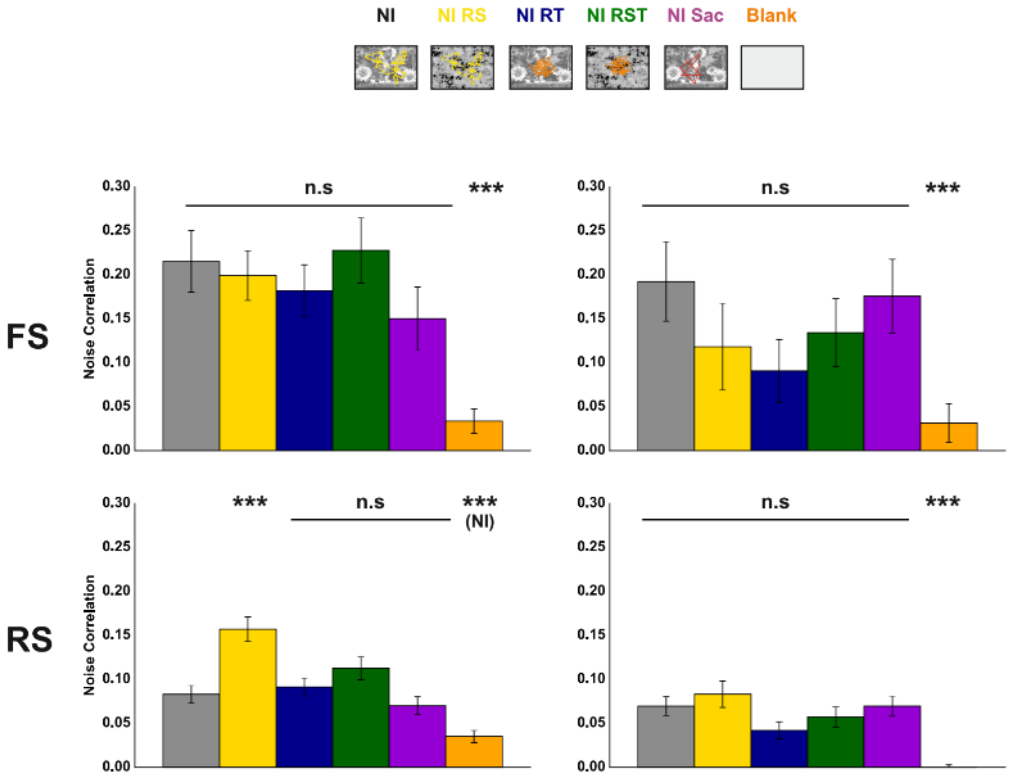

Figure 3.5.21. Signal correlation of the spiking activity within and between layers. Top row: Fast spiking neurons. Bottom row: regular spiking. Stars indicate a significant statistical difference with the NI condition. n.s: non-significant; *: $p < 0.05$; **: $p < 0.01$; ***: $p < 0.001$

FULL FIELD	Noise Correlation (SUA)			
	DG	NI	DN	BLK
Within Layers	0.136 ± 0.009	0.113 ± 0.007	0.113 ± 0.008	0.04 ± 0.006
Between Layers	0.068 ± 0.009	0.082 ± 0.007	0.039 ± 0.006	0.014 ± 0.004

FULL FIELD	Noise Correlation (MUA)			
	DG	NI	DN	BLK
Within Layers	0.788 ± 0.004	0.718 ± 0.004	0.703 ± 0.004	0.238 ± 0.005
Between Layers	0.714 ± 0.003	0.669 ± 0.003	0.638 ± 0.003	0.131 ± 0.002

Table 3.5.4: Noise correlation of the fast and regular spiking neurons computed within and between layers in response to our stimulus set (Mean ± SEM)

FULL FIELD	Noise Correlation (FS)			
	DG	NI	DN	BLK
Within Layers	0.322 ± 0.031	0.214 ± 0.026	0.253 ± 0.028	0.087 ± 0.025
Between Layers	0.075 ± 0.029	0.164 ± 0.025	0.14 ± 0.022	0.017 ± 0.013

FULL FIELD	Noise Correlation (RS)			
	DG	NI	DN	BLK
Within Layers	0.084 ± 0.011	0.077 ± 0.008	0.077 ± 0.009	0.03 ± 0.008
Between Layers	0.069 ± 0.012	0.066 ± 0.008	0.031 ± 0.007	0.019 ± 0.006

Table 3.5.5: Noise correlation of the fast and regular spiking neurons computed within and between layers in response to our stimulus set (Mean ± SEM)

FULL FIELD	WITHIN LAYERS					
	NI	NI-RS	NI-RT	NI-RST	NI-SAC	BLK
FS	0.215 ± 0.035	0.199 ± 0.028	0.182 ± 0.029	0.228 ± 0.037	0.15 ± 0.036	0.034 ± 0.014
RS	0.083 ± 0.01	0.157 ± 0.014	0.091 ± 0.01	0.112 ± 0.013	0.07 ± 0.01	0.035 ± 0.007
SUA	0.114 ± 0.009	0.174 ± 0.011	0.112 ± 0.009	0.141 ± 0.01	0.091 ± 0.009	0.039 ± 0.005
MUA	0.751 ± 0.004	0.718 ± 0.004	0.64 ± 0.005	0.719 ± 0.004	0.688 ± 0.004	0.166 ± 0.004

FULL FIELD	BETWEEN LAYERS					
	NI	NI-RS	NI-RT	NI-RST	NI-SAC	BLK
FS	0.192 ± 0.045	0.118 ± 0.049	0.091 ± 0.035	0.134 ± 0.039	0.176 ± 0.042	0.031 ± 0.022
RS	0.069 ± 0.011	0.083 ± 0.015	0.042 ± 0.01	0.057 ± 0.011	0.07 ± 0.011	-0.003 ± 0.005
SUA	0.084 ± 0.009	0.068 ± 0.011	0.053 ± 0.008	0.064 ± 0.009	0.073 ± 0.009	0.004 ± 0.004
MUA	0.671 ± 0.003	0.601 ± 0.004	0.571 ± 0.004	0.577 ± 0.004	0.576 ± 0.003	0.083 ± 0.002

Table 3.5.6: Noise correlation of the spiking activity computed within and between layers in response to our control stimulus set (Mean ± SEM)

5.4. Impact of the Center Surround Interactions

In their extracellular study performed in the awake monkey, Vinje and Gallant (2000) that in V1 the full field stimulation with natural images decorrelate the activity compared to a center stimulation. This has also been shown in the primate, where the stimulation of the surround with drifting gratings decreased the correlation levels (Snyder et al., 2014). The stimulation of the surround activates the feedback pathway (Angelucci et al, 2002). Our study (and others: Huang et al., 2007) showed that feedback might be still present in an anesthetized animal. However, the strength of the feedback is reduced by anesthesia. The two studies mentioned above were performed on the awake monkey. Therefore, we wondered of these effects would still be observed in our preparation.

5.4.1 Correlation of the Spiking Activity

- **Signal Correlation**

As performed in the previous section we computed the signal correlation within and between layers for the single and multi-unit activities.
Figure 3.5.22 shows an example of signal correlations computed for full field, center and surround. In this example, the center surround interactions seem to have no impact on the response. As stated before the surround stimulation elicits almost no activity, thus we will not focus on this condition.

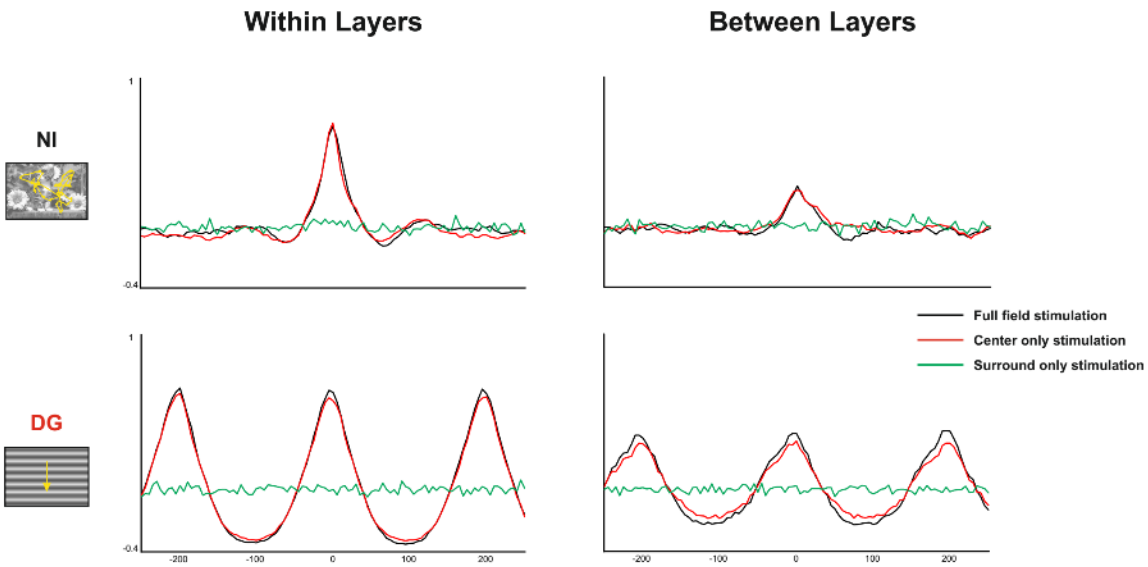

Figure 3.5.22. Example of signal correlation of the single unit activity computed within and between layers in response to full field, center and surround stimulations.

The signal correlations evoked by the center condition are reported in figures 3.5.23 to 3.5.25 and table 3.5.7. At the single and multi-unit levels, as observed for the full field condition, both within and between layers, the presentation of natural images only on the center evoked a more correlated activity than the presentation of the other stimuli ($p < 0.001$; Friedman test). At the single unit level, no surround modulation was observed in response to natural images or dense noise ($p > 0.25$; Wilcoxon test). A small decorrelation was observed when drifting gratings were presented on both center and surround ($p < 0.05$; Wilcoxon test). We then compared the correlations between layers. As observed within layers, natural images evoked the same level of correlation for both full field and center conditions ($p = 0.31$; Wilcoxon test). However, both drifting gratings and dense noise evoked higher levels of correlation for the center condition ($p < 0.01$). It is important to note that despite an absence of significant difference, natural images display a higher mean when both center and surround are stimulated. This absence of significant difference could originate from the size of our center stimulation that might reduce the effect of the increase, as observed for sparseness.

We then compared the correlations among the multi-unit population. Both within and between layers, drifting gratings and dense noise evoked higher levels of correlation for the center condition ($p < 0.001$), while natural images evoked a higher correlation for the full field condition ($p < 0.001$). This confirms the results that we observed at the single unit level and the tendency that we observed for natural images. The results obtained in response to natural images are in contradiction to the ones observed by Vinje and Gallant (2000). This difference could be linked to the difference in state between the two preparations.

It is important to note, as reported in figures 3.4.24 and 3.2.25 that the correlation between the center and full field stimulations is very high. This suggest that the two stimulations evoke small differences.

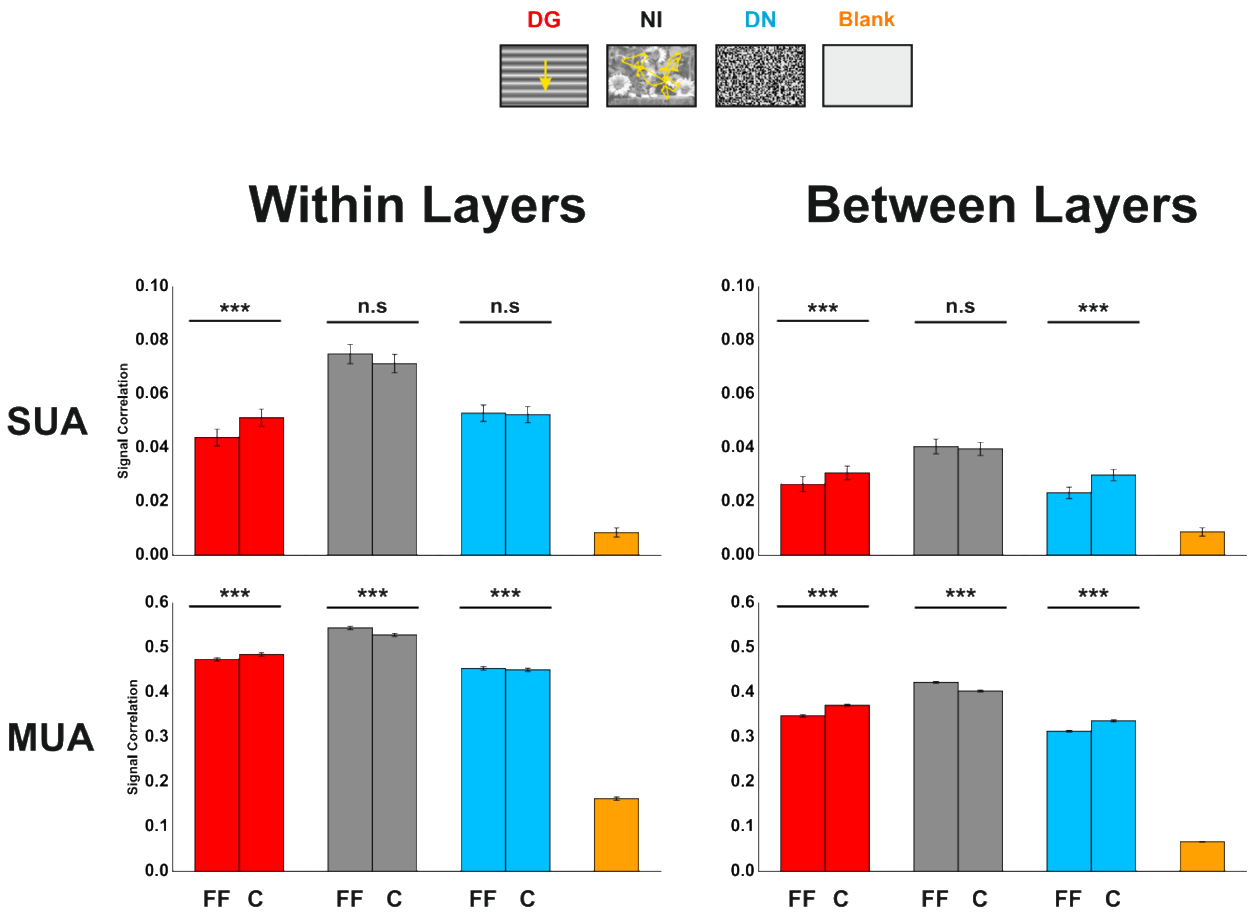

Figure 3.5.23. Signal correlation of the spiking activity within and between layers in response to a center stimulation. Top row: single unit activity. Bottom row: Multi-unit activity. FF: full field stimulation. C: center stimulation. n.s: non-significant; *: $p < 0.05$; **: $p < 0.01$; ***: $p < 0.001$

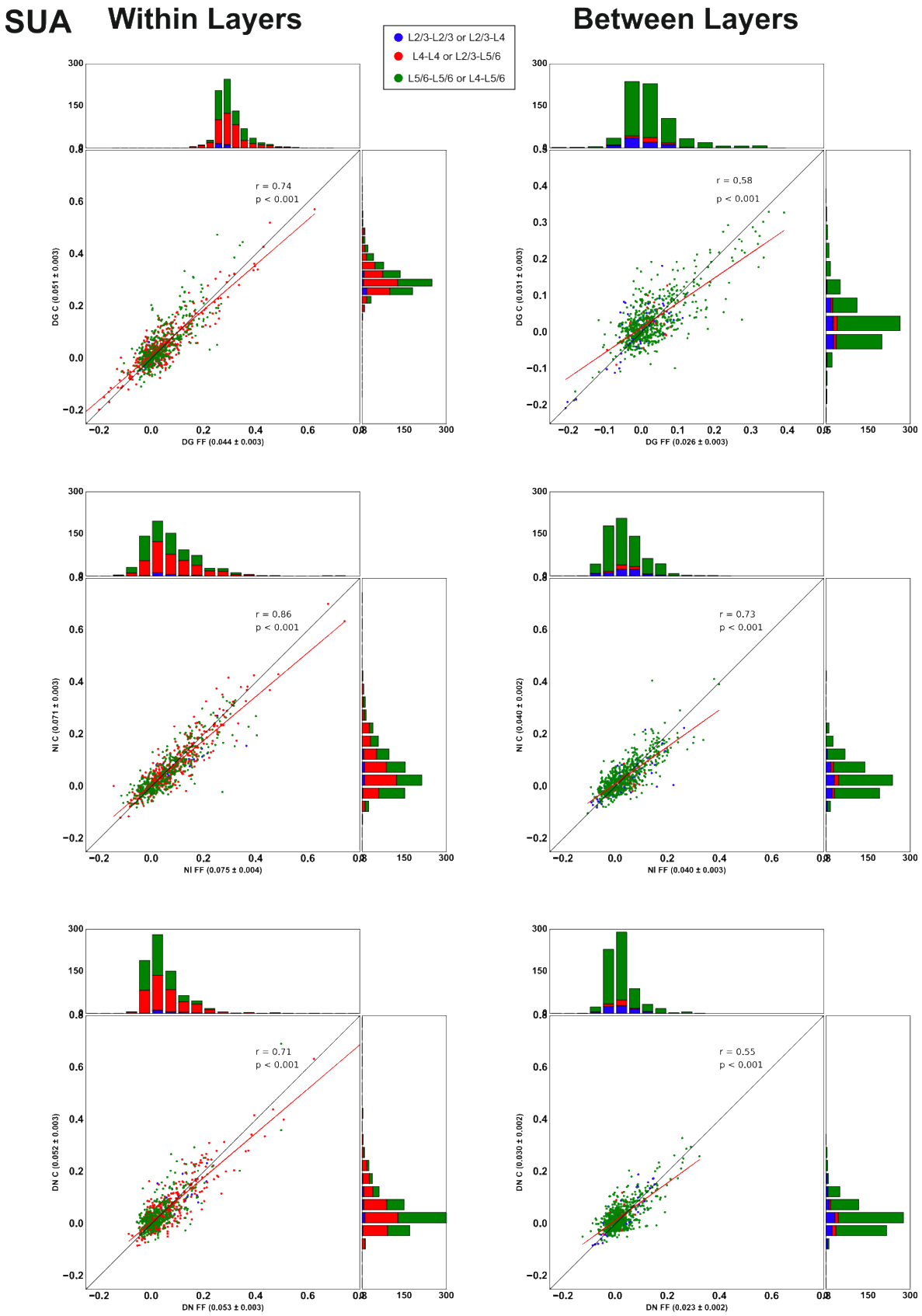

Figure 3.5.24. Scatter plots and distribution of the signal correlation of the single unit activity within and between layers in response to full field and center stimulations. Blue: correlation computed within L2/3 or between L2/3 and L4; Red: correlation computed within L4 or between L2/3 and L5/6; Green: correlation computed within L4 or between L4 and L5/6.

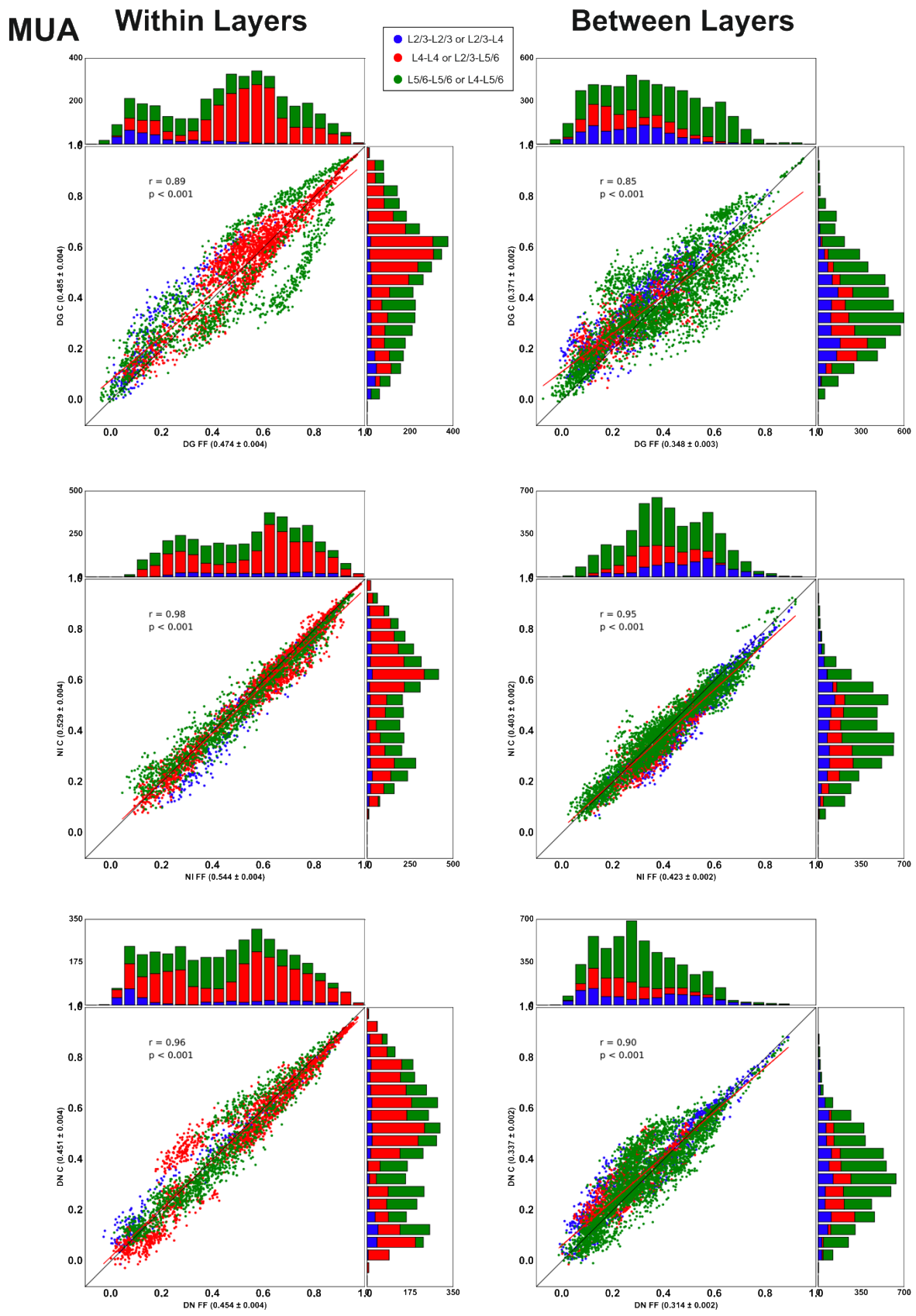

Figure 3.5.25. Scatter plots and distribution of the signal correlation of the multi-unit activity within and between layers in response to full field and center stimulations. Blue: correlation computed within L2/3 or between L2/3 and L4; Red: correlation computed within L4 or between L2/3 and L5/6; Green: correlation computed within L4 or between L4 and L5/6.

Our previous results showed that both FS and RS cells were modulated by the center surround interactions. Will we also observe a modulation in the signal correlation of these neuron subclasses? When presented on the center, all stimuli evoked the same correlation pattern as in the full field condition. We observed an absence of difference in the correlations evoked by the full field and center conditions ($p > 0.05$; Wilcoxon test; Figure 3.5.26 and table 3.5.8). Despite this absence of significant differences between the two conditions, the tendency was the same as the one observed across the complete population. Because of this absence of difference, we did not plot the associated the raster plots. By increasing the number of pairs, we should observe the same pattern of correlations as in the complete SUA population.

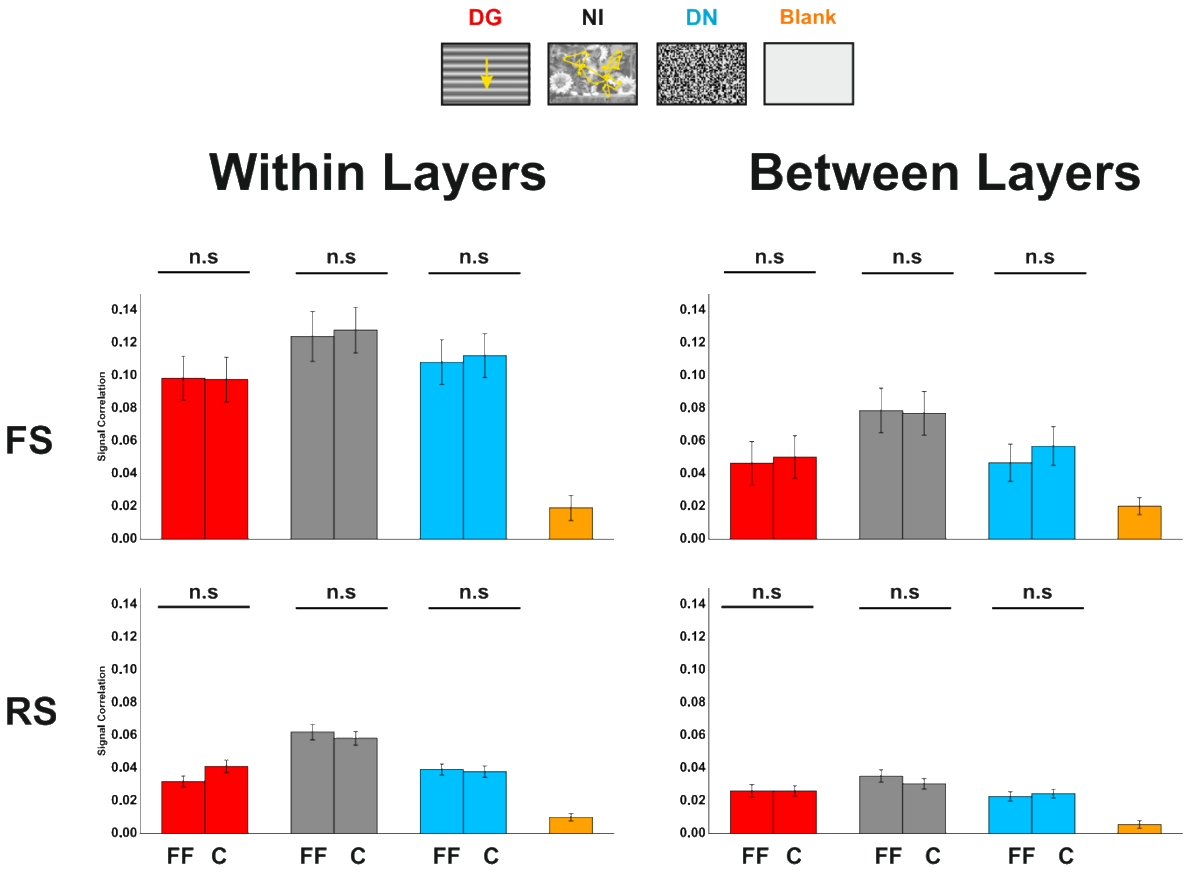

Figure 3.5.26. Signal correlation of the spiking activity within and between layers evoked by a center stimulation. Top row : Fast spiking neurons. Middle row: regular spiking neurons Bottom row: single unit activity. Stars indicate a significant statistical difference with the NI condition. n.s: non-significant; *: $p < 0.05$; **: $p < 0.01$; ***: $p < 0.001$

We then investigated the impact of the center surround interactions on the signal correlation evoked by the altered natural stimuli. We observed the same response pattern for the full field and center conditions, both for the single unit and multi-unit activities (Figures 3.5.27 to 3.5.29; Table 3.5.9).
At the single unit level, when computed within layers, only NI-RST displayed a higher correlation for the full field condition ($p < 0.05$; Wilcoxon Test). On other hand, NI-RT evoked higher levels of correlation for the center condition ($p < 0.001$). The other stimuli evoked the same levels of correlations for both conditions of stimulation. When computed between layers all stimuli except NI-RST, evoked the same correlation for the full field and center conditions, respectively ($p > 0.25$).
At the multi-unit level, when computed within layers, each stimulus evoked a different level of correlation in function of the stimulation condition ($p < 0.001$; Wilcoxon test). All control stimuli evoked the highest signal correlation for the center condition while the unaltered natural image evoked the highest correlation for the full field condition (Figure 3.5.27). This suggest that in order to increase the level of correlation both spatial and temporal statistics need to be unaltered. As observed for all stimuli, the correlation levels between the two conditions are very high for all stimuli (Figures 3.5.28 and 3.5.29).
Regular spiking and Fast spiking cells evoked the same response, respectively, for the center and full field condition, thus we decided to not display this result ($p > 0.05$; Wilcoxon test).

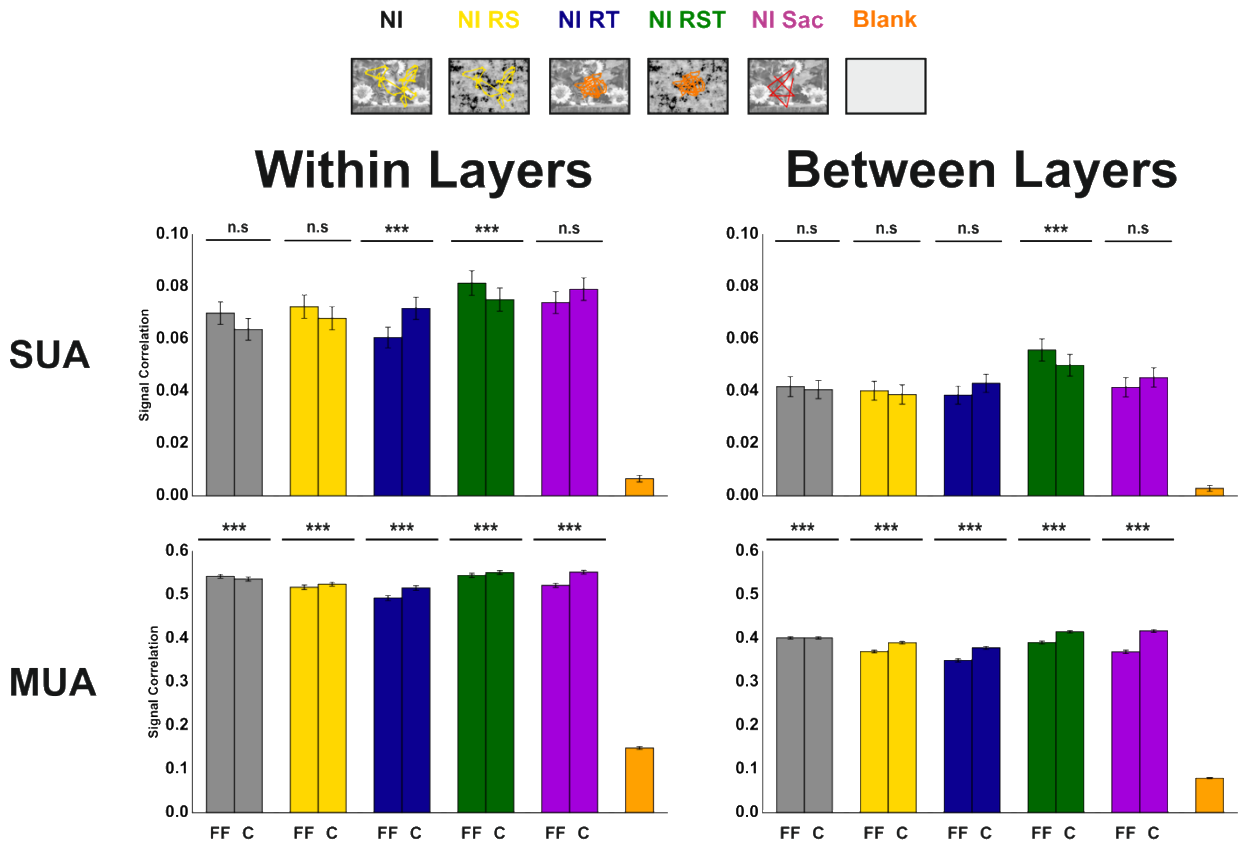

Figure 3.5.27. Signal correlation of the spiking activity, in response to our control stimuli presented on the center condition, within and between layers. Top row: single unit activity. Bottom row: Multi-unit activity. FF: full field condition. C: center condition. n.s: non-significant; *: $p < 0.05$; **: $p < 0.01$; ***: $p < 0.001$

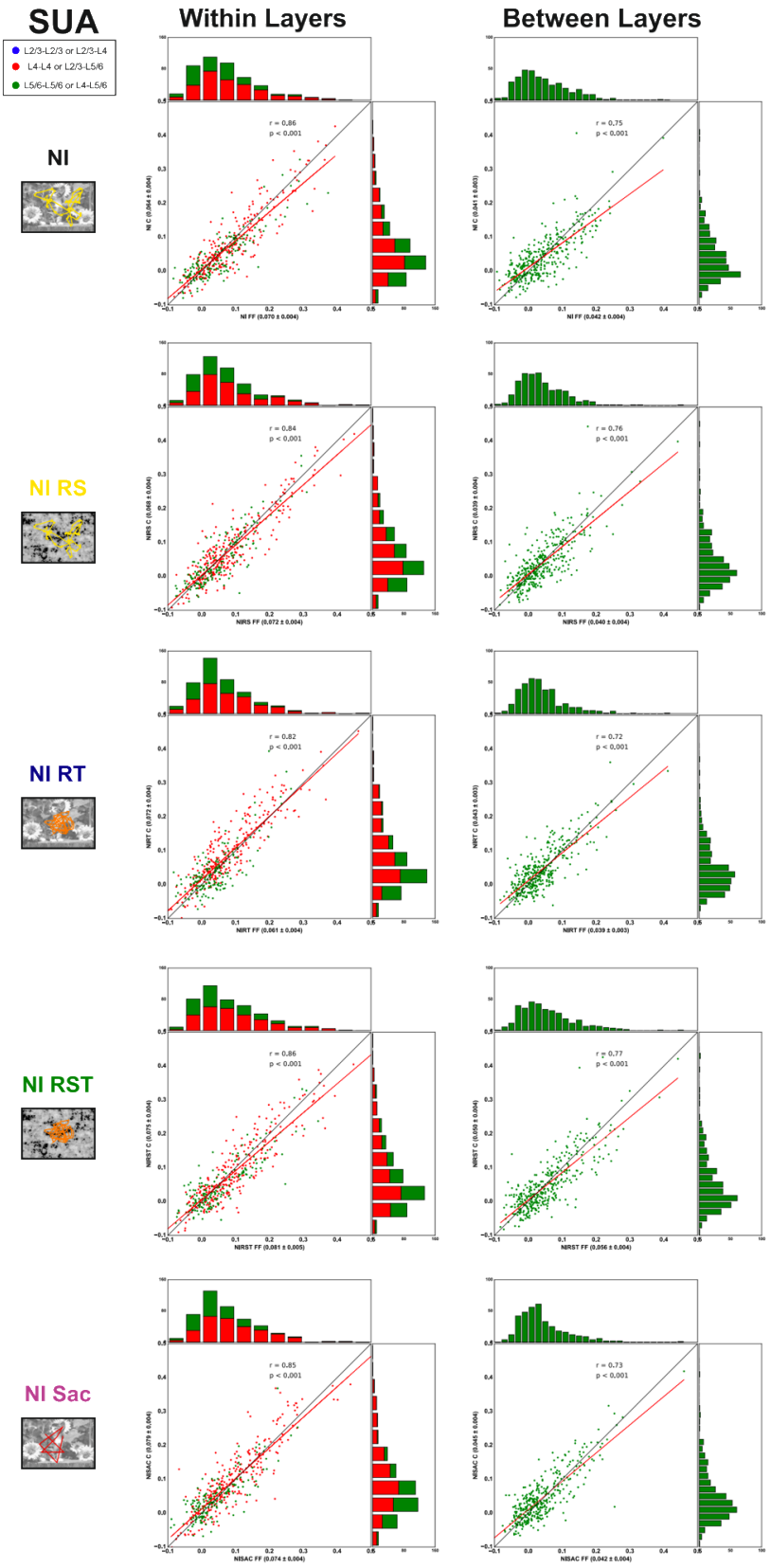

Figure 3.5.28. Scatter plots of the signal correlation of single unit activity within and between layers in response to our set of control stimuli presented on the full field and center conditions. Blue: correlation computed within L2/3 or between L2/3 and L4; Red: correlation computed within L4 or between L2/3 and L5/6; Green: correlation computed within L4 or between L4 and L5/6.

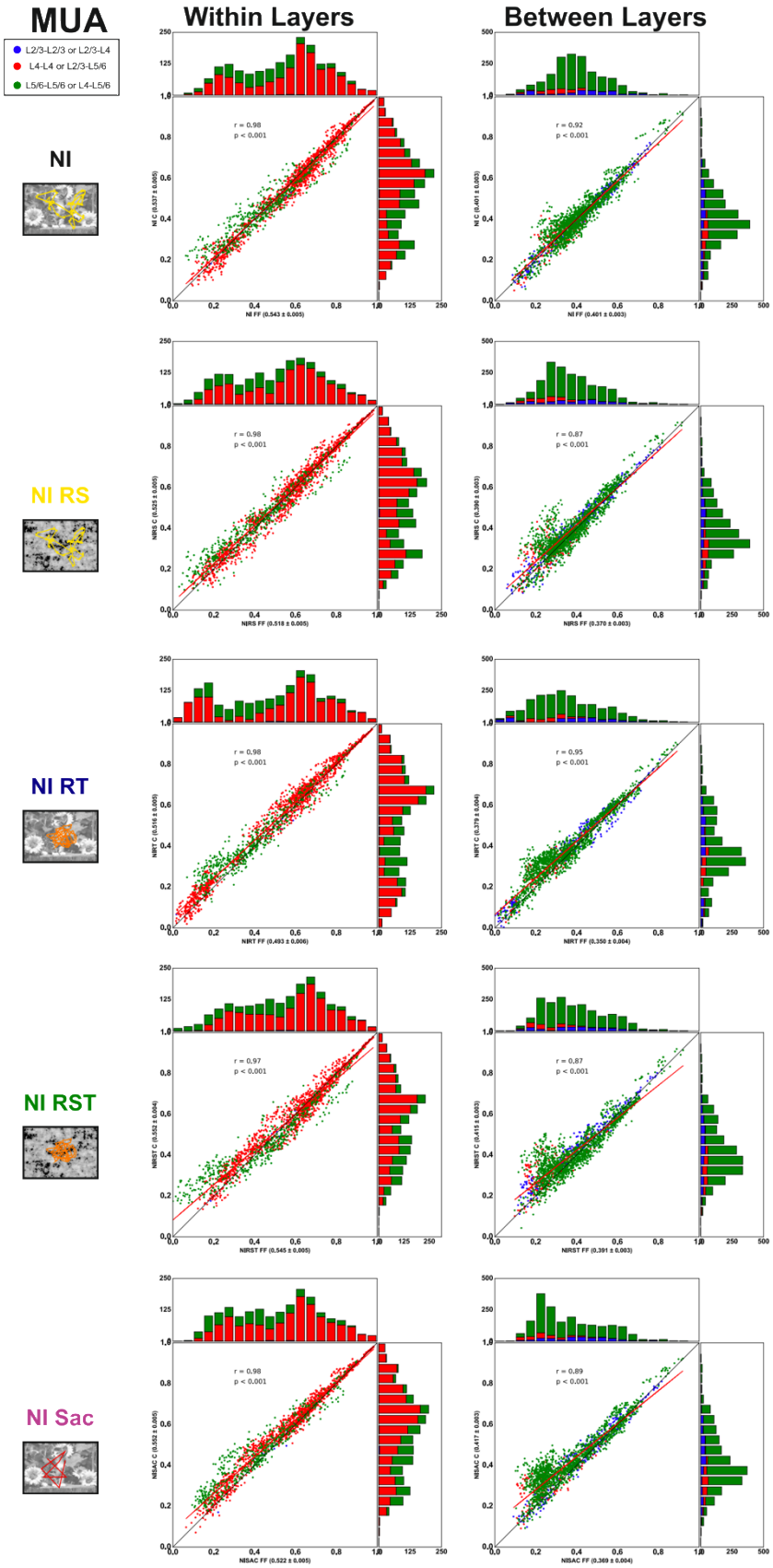

Figure 3.5.29. Scatter plots of the signal correlation of multi-unit activity within and between layers in response to our set of control stimuli presented on the full field and center conditions. Blue: correlation computed within L2/3 or between L2/3 and L4; Red: correlation computed within L4 or between L2/3 and L5/6; Green: correlation computed within L4 or between L4 and L5/6.

FULL FIELD	Signal Correlation (SUA)			
	DG	NI	DN	BLK
Within Layers	0.026 ± 0.003	0.04 ± 0.003	0.023 ± 0.002	0.009 ± 0.002
Between Layers	0.044 ± 0.003	0.075 ± 0.004	0.053 ± 0.003	0.008 ± 0.002

CENTER	Signal Correlation (SUA)			
	DG	NI	DN	BLK
Within Layers	0.051 ± 0.003	0.071 ± 0.003	0.052 ± 0.003	0.009 ± 0.002
Between Layers	0.031 ± 0.003	0.04 ± 0.002	0.03 ± 0.002	0.008 ± 0.002

FULL FIELD	Signal Correlation (MUA)			
	DG	NI	DN	BLK
Within Layers	0.474 ± 0.004	0.544 ± 0.004	0.454 ± 0.004	0.163 ± 0.004
Between Layers	0.348 ± 0.003	0.423 ± 0.002	0.314 ± 0.002	0.066 ± 0.001

CENTER	Signal Correlation (MUA)			
	DG	NI	DN	BLK
Within Layers	0.485 ± 0.004	0.529 ± 0.004	0.451 ± 0.004	0.163 ± 0.004
Between Layers	0.371 ± 0.002	0.403 ± 0.002	0.337 ± 0.002	0.066 ± 0.001

Table 3.5.7: Signal correlation of the single and multi-unit activities computed within and between layers in response to our stimulus set presented full field or on the center (Mean ± SEM)

FULL FIELD	Signal Correlation (FS)			
	DG	NI	DN	BLK
Within Layers	0.098 ± 0.014	0.124 ± 0.015	0.108 ± 0.014	0.019 ± 0.008
Between Layers	0.046 ± 0.013	0.079 ± 0.014	0.047 ± 0.011	0.02 ± 0.005

CENTER	Signal Correlation (FS)			
	DG	NI	DN	BLK
Within Layers	0.098 ± 0.014	0.128 ± 0.014	0.112 ± 0.013	0.019 ± 0.008
Between Layers	0.05 ± 0.013	0.077 ± 0.013	0.057 ± 0.012	0.02 ± 0.005

FULL FIELD	Signal Correlation (RS)			
	DG	NI	DN	BLK
Within Layers	0.032 ± 0.003	0.062 ± 0.005	0.039 ± 0.003	0.01 ± 0.002
Between Layers	0.026 ± 0.004	0.035 ± 0.004	0.023 ± 0.003	0.006 ± 0.002

CENTER	Signal Correlation (RS)			
	DG	NI	DN	BLK
Within Layers	0.026 ± 0.003	0.03 ± 0.003	0.024 ± 0.003	0.01 ± 0.002
Between Layers	0.041 ± 0.004	0.058 ± 0.004	0.038 ± 0.003	0.006 ± 0.002

Table 3.5.8: Signal correlation of the regular and fast spiking neurons computed within and between layers in response to our stimulus set presented full field or on the center (Mean ± SEM)

FULL FIELD	WITHIN LAYERS					
	NI	NI-RS	NI-RT	NI-RST	NI-SAC	BLK
FS	0.099 ± 0.016	0.11 ± 0.017	0.093 ± 0.013	0.13 ± 0.018	0.098 ± 0.014	0.012 ± 0.005
RS	0.061 ± 0.006	0.063 ± 0.005	0.049 ± 0.005	0.068 ± 0.006	0.063 ± 0.005	0.004 ± 0.001
SUA	0.07 ± 0.004	0.072 ± 0.004	0.061 ± 0.004	0.081 ± 0.005	0.074 ± 0.004	0.007 ± 0.001
MUA	0.543 ± 0.005	0.518 ± 0.005	0.493 ± 0.006	0.545 ± 0.005	0.522 ± 0.005	0.149 ± 0.003

CENTER	BETWEEN LAYERS					
	NI	NI-RS	NI-RT	NI-RST	NI-SAC	BLK
FS	0.098 ± 0.025	0.12 ± 0.029	0.118 ± 0.03	0.123 ± 0.027	0.093 ± 0.03	0.021 ± 0.01
RS	0.033 ± 0.004	0.032 ± 0.004	0.036 ± 0.004	0.046 ± 0.005	0.045 ± 0.005	0.002 ± 0.002
SUA	0.064 ± 0.004	0.068 ± 0.004	0.072 ± 0.004	0.075 ± 0.004	0.079 ± 0.004	0.003 ± 0.001
MUA	0.401 ± 0.003	0.39 ± 0.003	0.379 ± 0.004	0.415 ± 0.003	0.417 ± 0.003	0.08 ± 0.002

FULL FIELD	BETWEEN LAYERS					
	NI	NI-RS	NI-RT	NI-RST	NI-SAC	BLK
FS	0.099 ± 0.026	0.116 ± 0.032	0.122 ± 0.034	0.132 ± 0.034	0.086 ± 0.028	0.021 ± 0.01
RS	0.04 ± 0.005	0.032 ± 0.004	0.034 ± 0.004	0.052 ± 0.005	0.041 ± 0.005	0.002 ± 0.002
SUA	0.042 ± 0.004	0.04 ± 0.004	0.039 ± 0.003	0.056 ± 0.004	0.042 ± 0.004	0.003 ± 0.001
MUA	0.401 ± 0.003	0.37 ± 0.003	0.35 ± 0.004	0.391 ± 0.003	0.369 ± 0.004	0.08 ± 0.002

CENTER	WITHIN LAYERS					
	NI	NI-RS	NI-RT	NI-RST	NI-SAC	BLK
FS	0.107 ± 0.014	0.109 ± 0.016	0.125 ± 0.014	0.119 ± 0.016	0.12 ± 0.015	0.012 ± 0.005
RS	0.054 ± 0.005	0.059 ± 0.005	0.057 ± 0.005	0.065 ± 0.005	0.07 ± 0.005	0.004 ± 0.001
SUA	0.041 ± 0.003	0.039 ± 0.004	0.043 ± 0.003	0.05 ± 0.004	0.045 ± 0.004	0.007 ± 0.001
MUA	0.537 ± 0.005	0.525 ± 0.005	0.516 ± 0.005	0.552 ± 0.004	0.552 ± 0.005	0.149 ± 0.003

Table 3.5.9: Signal correlation of the spiking activity computed within and between layers in response to our control stimulus set presented full field or on the center (Mean ± SEM)

- **Noise Correlation**

We also computed the other main correlation analysis, *i.e.* the noise correlation. Our previous results showed that when stimuli were presented full field, they all evoked very similar noise correlation values, in particular at the single unit level. A recent study performed on primate (Snyder et al, 2014) showed that the surround stimulation tends to decrease, the correlation values. However, their study only focused on the response to drifting gratings. We wondered if the noise correlation of the SUA and MUA would be impacted the same way by the presentation of a different artificial stimulus (*i.e.* dense noise) and more importantly by the presentation of natural images.

The noise correlation evoked by the center condition are reported in figures 3.5.30 to 3.5.32 and table 3.5.10. The center stimulation evoked the same pattern of correlation as the full field stimulation, thus we will only focus on the differences between these two stimulations.
We first investigated the impact of the center surround interactions on the single unit activity. When computed within layers, only NI displayed a significantly higher noise correlation for the center condition than the surround ($p < 0.05$; Wilcoxon test). Both artificial stimuli showed no significant difference between the two conditions, despite a higher mean evoked by the full field presentation of the drifting gratings (Figure 3.5.30; table 3.5.10). This absence of difference might be linked to the heterogeneity of the population. Indeed, some neurons are decorrelated by the surround stimulation while others are correlated by the later. In addition, the small decorrelation that we observed might be linked to the size of our center stimulation. Snyder and colleagues (2014), who recorded in V1 with a multielectrode array, and observed a decorrelation evoked by the surround, did not separate the recorded neurons into close and distant neurons. By combining the noise correlation values obtained within and between layers, we observed similar results and similar noise correlation values, as the ones observed by Snyder and colleagues. This highlights the importance of dividing the neuronal population into close and distant neurons and confirms that our results are consistent with theirs. We observed a similar pattern of response when the correlations were computed between layers. In this situation, artificial stimuli evoked a different response between the full field and center conditions ($p < 0.001$; Wilcoxon test) while no difference was observed for natural images ($p = 0.49$). However, we observed again the same behavior for the center surround interactions, *i.e.* a reduction of the noise correlation for the full field condition for low noise correlations value and an increase for the full field condition for high correlation values.
Multi and single unit activities were not affected in the same way by the center surround interactions. While DG always displayed a more decorrelated response when it stimulated the surround, this was not the case for NI and DN. However, the difference observed for the presentation of these two stimuli on the center and full field is so small (table 3.5.10) and their correlation so high that we can argue that no real difference is observed.

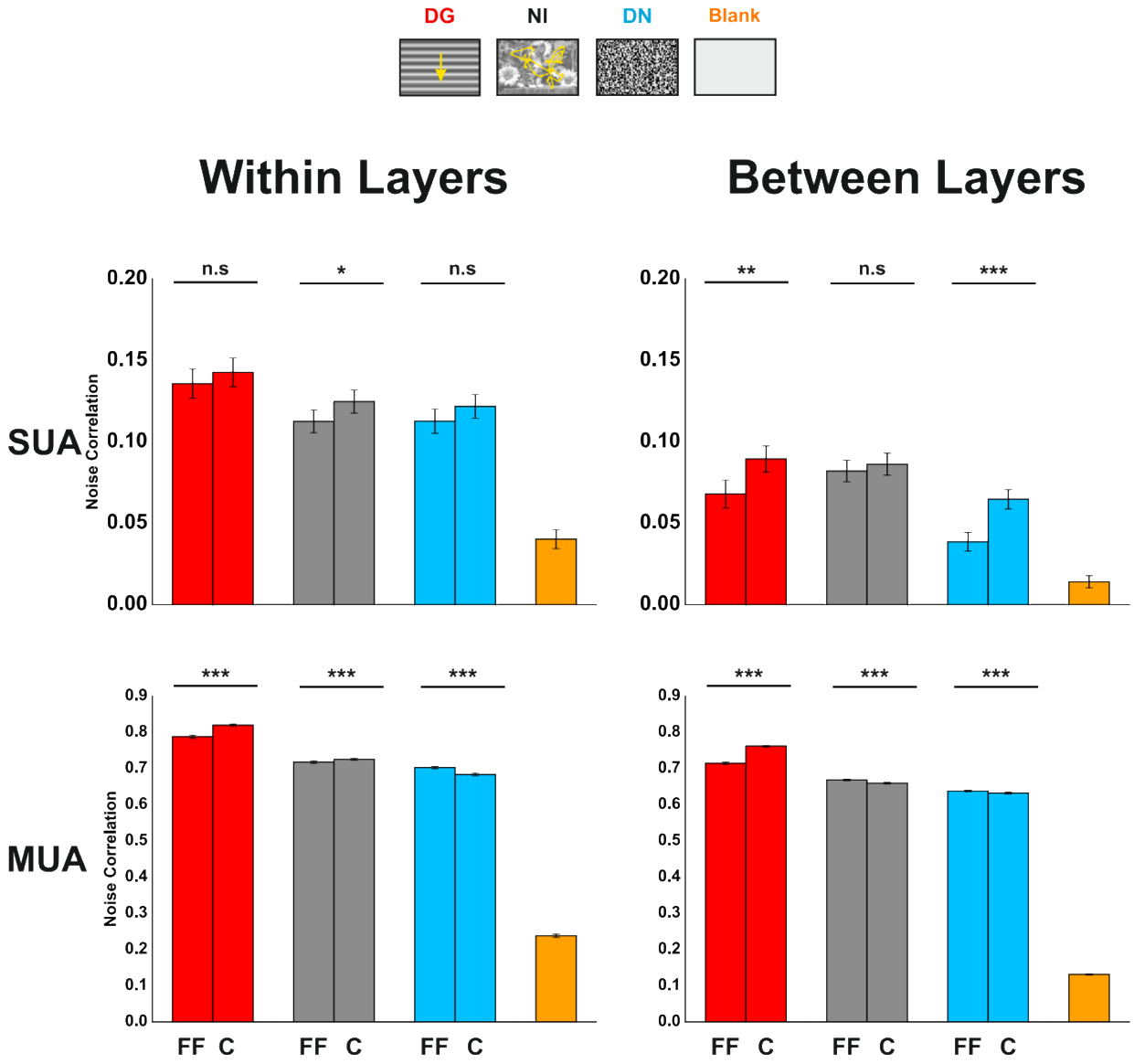

Figure 3.5.30. Noise correlation of the spiking activity within and between layers in response to a center stimulation. Top row: single unit activity. Bottom row: Multi-unit activity. Stars indicate a significant statistical difference with the NI condition. n.s: non-significant; *: $p < 0.05$; **: $p < 0.01$; ***: $p < 0.001$

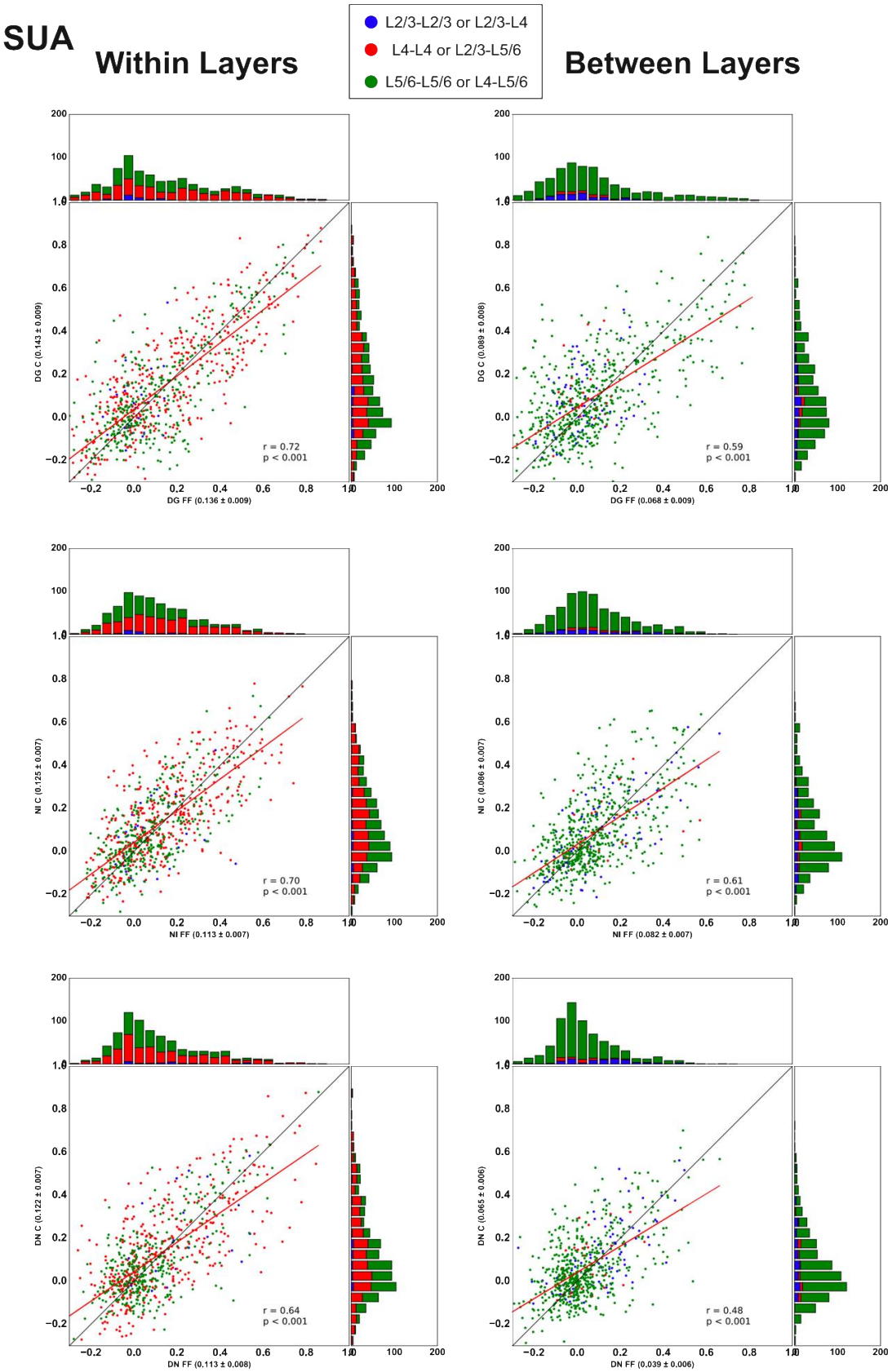

Figure 3.5.31. Scatter plots of the noise correlation of the single unit activity within and between layers in response to full field and center stimulations. Blue: correlation computed within L2/3 or between L2/3 and L4; Red: correlation computed within L4 or between L2/3 and L5/6; Green: correlation computed within L4 or between L4 and L5/6. r : sperman's correlation

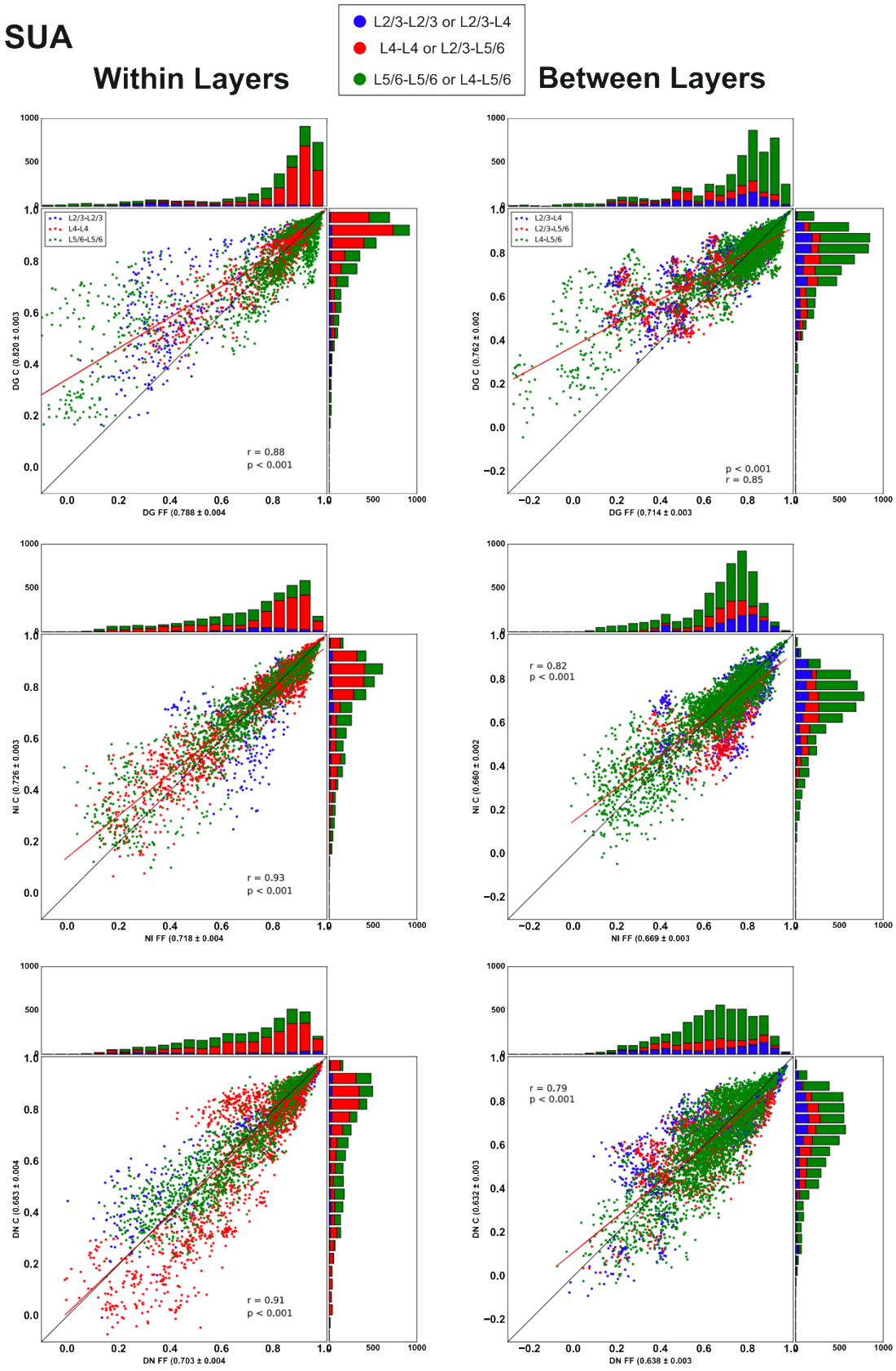

Figure 3.5.32. Scatter plots of the noise correlation of the multi-unit activity within and between layers in response to full field and center stimulations. Blue: correlation computed within L2/3 or between L2/3 and L4; Red: correlation computed within L4 or between L2/3 and L5/6; Green: correlation computed within L4 or between L4 and L5/6. r : sperman's correlation

In previous sections we showed that both RS and FS neurons responses were modulated by center surround interactions. Thus, we wondered if the noise correlation of these subtypes was impacted in the same way.

Within each subclass, within and between layers respectively, all stimuli evoked an equal noise correlation ($p > 0.2$). We then compared the noise correlation evoked by the center and full field conditions (Figure 3.5.33 and 3.5.11). Among fast spiking neurons, within layers, natural images and dense noise evoked a higher noise correlation for the full field condition than the center, while drifting gratings evoked the opposite behavior. However, these differences were not significant, despite a visible trend. An increase in the number of recorded fast spiking cells will be necessary in order to confirm these observations. Between layers, the presentation of the artificial stimuli on the center condition evoked a higher noise correlation than the full field ($p < 0.001$; Wilcoxon test). On the other hand, NI displayed a higher NC for the full field condition. Among the regular spiking population, all stimuli evoked a higher noise correlation for the center condition than the full field. Thus, the absence of significant difference observed for the complete single unit population probably could come from the difference in these two populations. However, in order to confirm this observation, it would be necessary to isolate the noise correlations between pairs of RS and FS neurons.

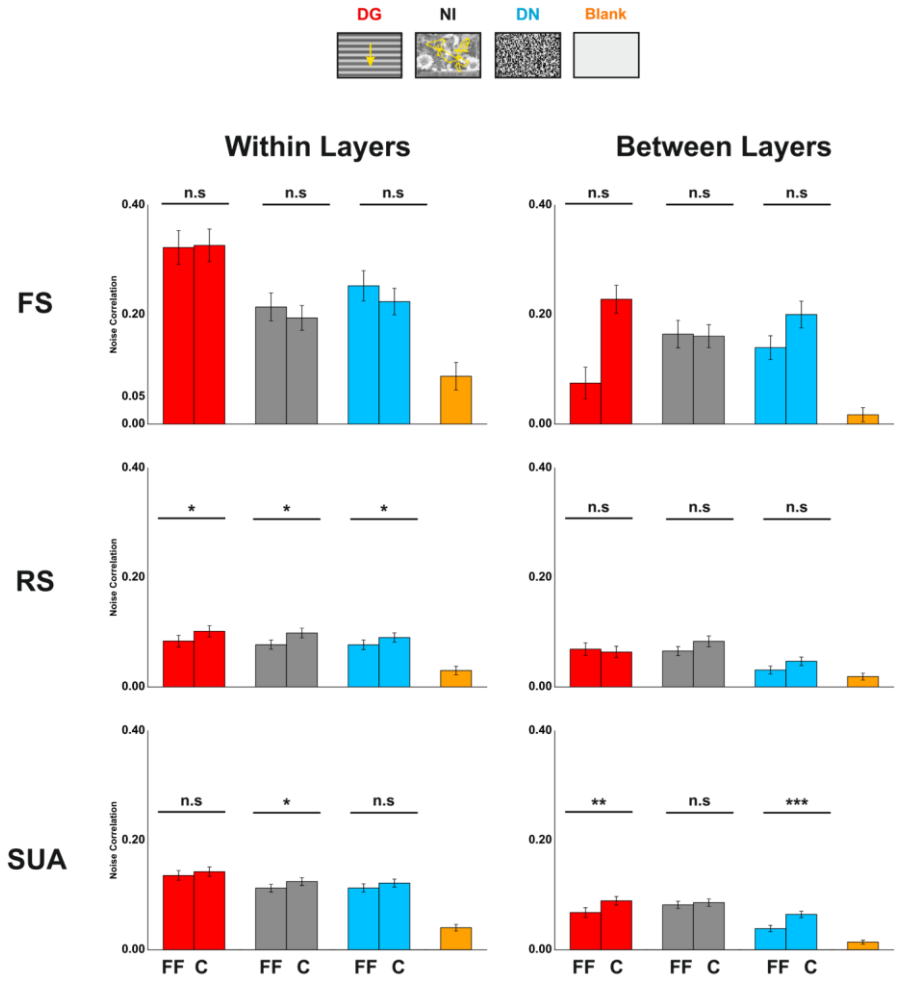

Figure 3.5.33. Noise correlation of the spiking activity within and between layers evoked by a center stimulation. Top row : Fast spiking neurons. Middle row: regular spiking neurons Bottom row: single unit activity. Stars indicate a significant statistical difference with the NI condition. n.s: non-significant; *: $p < 0.05$; **: $p < 0.01$; ***: $p < 0.001$

The alteration of the natural statistics led to different values of noise correlation both at the spiking level. In addition, we showed that their alteration impacted the reliability and the signal correlation among others. Thus, we wondered if the alteration of the natural statistics would have an impact on the center surround modulations of the noise correlation (Figures 3.5.34 to 3.5.36; table 3.5.12). At both single unit and multi-unit level, the center stimulation evoked an almost similar noise correlation pattern as the full field one. However, two differences happened at the single unit level. The first one, within layers, NI-RS evoked the same levels of correlation as all the other stimuli ($p > 0.05$). The second one, between layers, NI-SAC evoked a higher noise correlation than the other stimuli ($p < 0.001$)

At the single unit level, within layers, NI and NI-SAC evoked a higher noise correlation for the center condition than the full field, while NI-RS displayed the opposite behavior ($p < 0.01$; Wilcoxon test). On the other hand, NI-RST and NI-RT respectively, evoked the same correlations for the center and full field conditions ($p > 0.56$). The absence of center surround modulation when the temporal statistics were randomized was already observed for other measurements. Between layers, all stimuli displayed a higher mean noise correlation for the center condition than the full field one. In addition, as observed for the other stimuli, the center condition evoked a higher noise correlation for low correlation values while the full field condition evoked a higher noise correlation for high correlation values.

At the multi-unit level, both within and between layers, all stimuli displayed a decorrelation for the full field condition compared to the center one ($p < 0.001$; Wilcoxon test). However, for NI-RT and NI-RST, the difference between these two conditions was very small. Confirming the small impact of the altered temporal statistics on the center surround modulation.

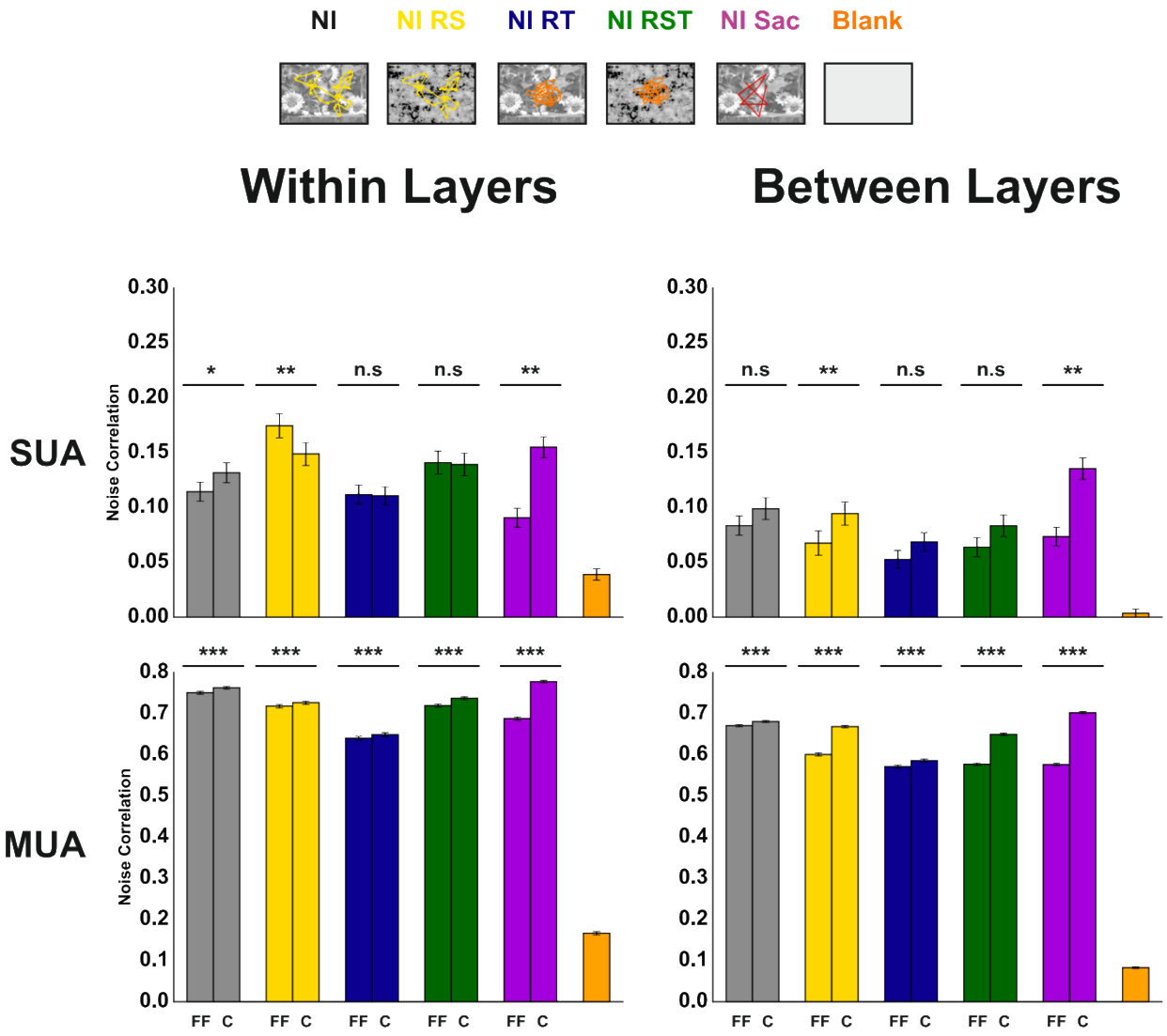

Figure 3.5.34. Noise correlation of the spiking activity, in response to our control stimuli presented on the center condition, within and between layers. Top row: single unit activity. Bottom row: Multi-unit activity. Stars indicate a significant statistical difference with the NI condition. n.s: non-significant; *: $p < 0.05$; **: $p < 0.01$; ***: $p < 0.001$

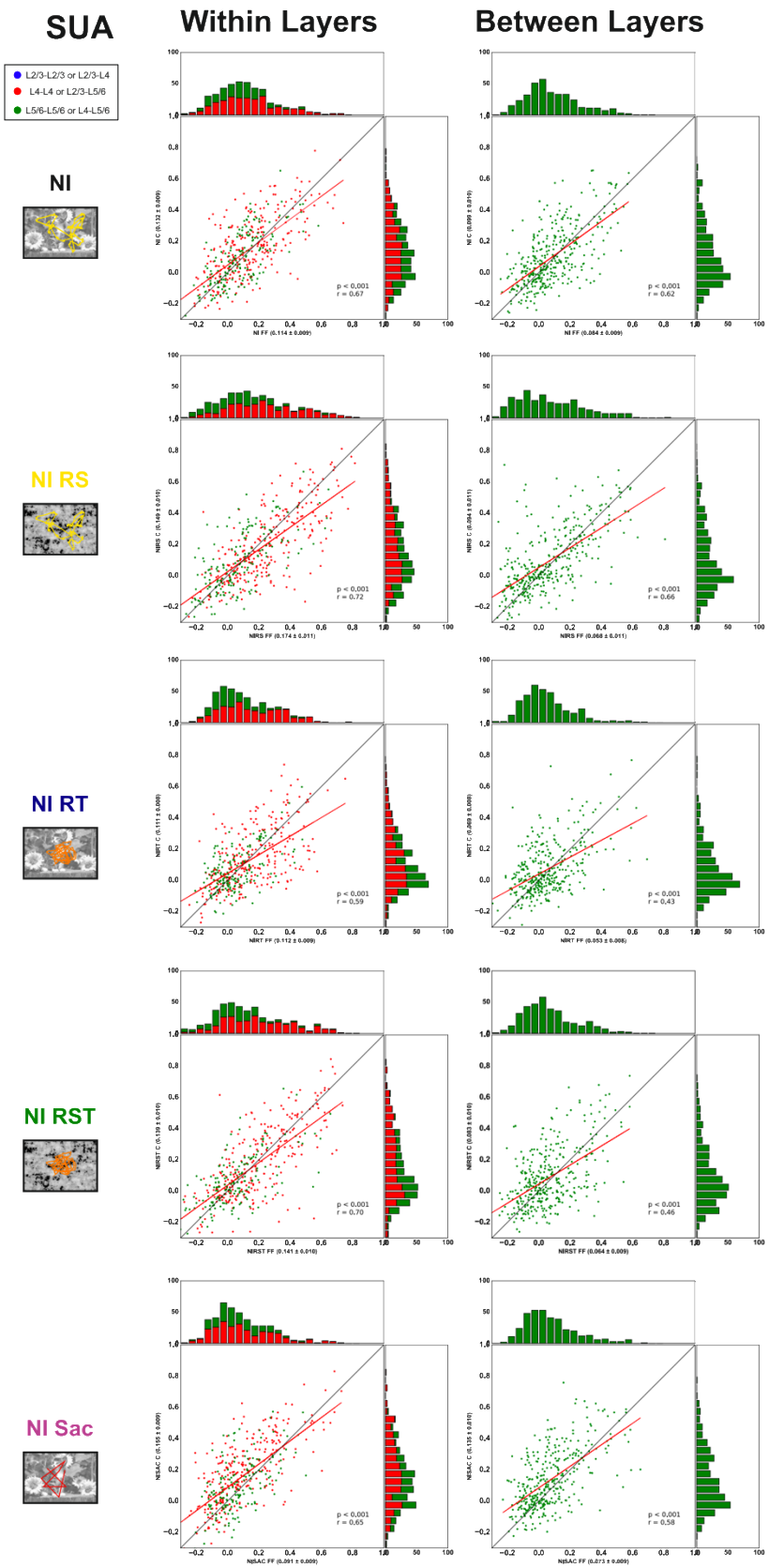

Figure 3.5.35. Scatter plots of the noise correlation of single unit activity within and between layers in response to our set of control stimuli presented on the full field and center conditions. Blue: correlation computed within L2/3 or between L2/3 and L4; Red: correlation computed within L4 or between L2/3 and L5/6; Green: correlation computed within L5/6 or between L4 and L5/6.

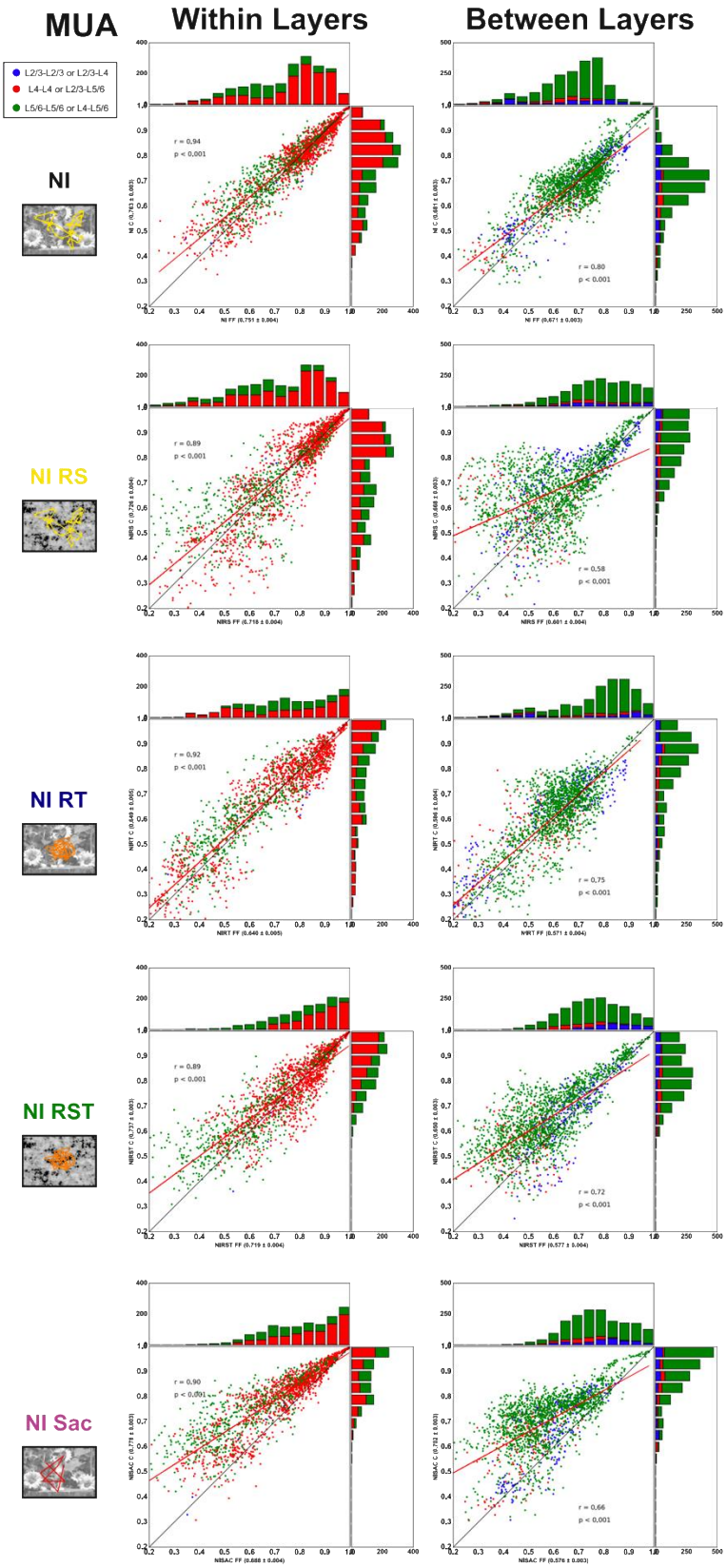

Figure 3.5.36. Scatter plots of the noise correlation of multi-unit activity within and between layers in response to our set of control stimuli presented on the full field and center conditions. Blue: correlation computed within L2/3 or between L2/3 and L4; Red: correlation computed within L4 or between L2/3 and L5/6; Green: correlation computed within L5/6 or between L4 and L5/6.

FULL FIELD	Noise Correlation (SUA)			
	DG	NI	DN	BLK
Within Layers	0.136 ± 0.009	0.113 ± 0.007	0.113 ± 0.008	0.04 ± 0.006
Between Layers	0.068 ± 0.009	0.082 ± 0.007	0.039 ± 0.006	0.014 ± 0.004

CENTER	Noise Correlation (SUA)			
	DG	NI	DN	BLK
Within Layers	0.143 ± 0.009	0.125 ± 0.007	0.122 ± 0.007	0.04 ± 0.006
Between Layers	0.089 ± 0.008	0.086 ± 0.007	0.065 ± 0.006	0.014 ± 0.004

FULL FIELD	Noise Correlation (MUA)			
	DG	NI	DN	BLK
Within Layers	0.788 ± 0.004	0.718 ± 0.004	0.703 ± 0.004	0.238 ± 0.005
Between Layers	0.714 ± 0.003	0.669 ± 0.003	0.638 ± 0.003	0.131 ± 0.002

CENTER	Noise Correlation (MUA)			
	DG	NI	DN	BLK
Within Layers	0.82 ± 0.003	0.726 ± 0.003	0.683 ± 0.004	0.238 ± 0.005
Between Layers	0.762 ± 0.002	0.66 ± 0.002	0.632 ± 0.003	0.131 ± 0.002

Table 3.5.10: Noise correlation of the single and multi-unit activities computed within and between layers in response to our stimulus set presented full field or on the center (Mean ± SEM)

FULL FIELD	Noise Correlation (FS)			
	DG	NI	DN	BLK
Within Layers	0.322 ± 0.031	0.214 ± 0.026	0.253 ± 0.028	0.087 ± 0.025
Between Layers	0.075 ± 0.029	0.164 ± 0.025	0.14 ± 0.022	0.017 ± 0.013

CENTER	Noise Correlation (FS)			
	DG	NI	DN	BLK
Within Layers	0.326 ± 0.03	0.194 ± 0.023	0.224 ± 0.024	0.087 ± 0.025
Between Layers	0.228 ± 0.026	0.16 ± 0.021	0.2 ± 0.024	0.017 ± 0.013

FULL FIELD	Noise Correlation (RS)			
	DG	NI	DN	BLK
Within Layers	0.084 ± 0.011	0.077 ± 0.008	0.077 ± 0.009	0.03 ± 0.008
Between Layers	0.069 ± 0.012	0.066 ± 0.008	0.031 ± 0.007	0.019 ± 0.006

CENTER	Noise Correlation (RS)			
	DG	NI	DN	BLK
Within Layers	0.102 ± 0.01	0.099 ± 0.009	0.09 ± 0.009	0.03 ± 0.008
Between Layers	0.064 ± 0.01	0.083 ± 0.01	0.047 ± 0.008	0.019 ± 0.006

Table 3.5.11: Noise correlation of the fast and regular spiking neurons computed within and between layers in response to our stimulus set presented full field or on the center (Mean ± SEM)

FULL FIELD	WITHIN LAYERS					
	NI	NI-RS	NI-RT	NI-RST	NI-SAC	BLK
FS	0.215 ± 0.035	0.199 ± 0.028	0.182 ± 0.029	0.228 ± 0.037	0.15 ± 0.036	0.034 ± 0.014
RS	0.083 ± 0.01	0.157 ± 0.014	0.091 ± 0.01	0.112 ± 0.013	0.07 ± 0.01	0.035 ± 0.007
SUA	0.114 ± 0.009	0.174 ± 0.011	0.112 ± 0.009	0.141 ± 0.01	0.091 ± 0.009	0.039 ± 0.005
MUA	0.751 ± 0.004	0.718 ± 0.004	0.64 ± 0.005	0.719 ± 0.004	0.688 ± 0.004	0.166 ± 0.004

CENTER	WITHIN LAYERS					
	NI	NI-RS	NI-RT	NI-RST	NI-SAC	BLK
FS	0.196 ± 0.033	0.203 ± 0.035	0.148 ± 0.031	0.214 ± 0.034	0.237 ± 0.029	0.034 ± 0.014
RS	0.11 ± 0.011	0.14 ± 0.013	0.099 ± 0.01	0.124 ± 0.012	0.13 ± 0.012	0.035 ± 0.007
SUA	0.132 ± 0.009	0.149 ± 0.01	0.111 ± 0.008	0.139 ± 0.01	0.155 ± 0.009	0.039 ± 0.005
MUA	0.763 ± 0.003	0.726 ± 0.004	0.649 ± 0.005	0.737 ± 0.003	0.778 ± 0.003	0.166 ± 0.004

FULL FIELD	BETWEEN LAYERS					
	NI	NI-RS	NI-RT	NI-RST	NI-SAC	BLK
FS	0.192 ± 0.045	0.118 ± 0.049	0.091 ± 0.035	0.134 ± 0.039	0.176 ± 0.042	0.031 ± 0.022
RS	0.069 ± 0.011	0.083 ± 0.015	0.042 ± 0.01	0.057 ± 0.011	0.07 ± 0.011	-0.003 ± 0.005
SUA	0.084 ± 0.009	0.068 ± 0.011	0.053 ± 0.008	0.064 ± 0.009	0.073 ± 0.009	0.004 ± 0.004
MUA	0.671 ± 0.003	0.601 ± 0.004	0.571 ± 0.004	0.577 ± 0.004	0.576 ± 0.003	0.083 ± 0.002

CENTER	BETWEEN LAYERS					
	NI	NI-RS	NI-RT	NI-RST	NI-SAC	BLK
FS	0.177 ± 0.033	0.137 ± 0.046	0.184 ± 0.047	0.145 ± 0.055	0.236 ± 0.048	0.031 ± 0.022
RS	0.107 ± 0.013	0.088 ± 0.014	0.047 ± 0.01	0.073 ± 0.013	0.13 ± 0.013	-0.003 ± 0.005
SUA	0.099 ± 0.01	0.094 ± 0.011	0.069 ± 0.008	0.083 ± 0.01	0.135 ± 0.01	0.004 ± 0.004
MUA	0.681 ± 0.003	0.668 ± 0.003	0.586 ± 0.004	0.65 ± 0.003	0.702 ± 0.003	0.083 ± 0.002

Table 3.5.12: Noise correlation of the spiking activity computed within and between layers in response to our control stimulus set presented full field or on the center (Mean ± SEM)

IV. DISCUSSION

In this study, we performed multiscale recordings where we recorded the response of microscopic (SUA) and mesoscopic signals (MUA and LFP) to natural and artificial stimuli.
These recordings allowed us to address different questions. The first one was to determine if the variability of the multiscale response to natural and artificial stimuli was different across the cortical microcircuit.
Another important aspect of our study was to specify the role of signal and noise correlations of the microscopic and mesoscopic signals in the process of redundancy reduction. Indeed, in their study, Rikhye and Sur (2015) (but also Bányai et al., 2019) showed that the correlation levels are linked to the correlations present in the stimulus. Thus, natural images that contain highly correlated features evoke a correlated response. It is important to note that Rikhye and Sur only focused on the spatial correlations, while we investigated the impact of spatial and temporal statistics on the response. The increase in the response correlations result in a larger normalization pool, which allows the generation of a reliable response (Figure 4.1). The activation of the normalization pool is mediated by an increase of the neuronal ensemble synchronization levels and are not necessarily linked to their global activity levels. In their study, Baudot and colleagues (2013) showed that the frequency content of the stimuli constrain the response at different frequencies. Therefore, we decided to investigate how the spatio-temporal statistics of the stimulus affects the processes described in figure 4.1 and their laminar dependency.
We also investigated the impact of the activation of the center surround interactions on the reliability and the correlations. It has been shown that the concomitant stimulation of both the center and the surround of the receptive field with natural images increases the reliability and affects the response correlations in V1 (Vinje & Gallant, 2000; Haider et al., 2010).
In this section, we will describe and discuss in detail the main results obtained during this thesis and then draw a global picture about natural images and their processing in primary visual cortex.

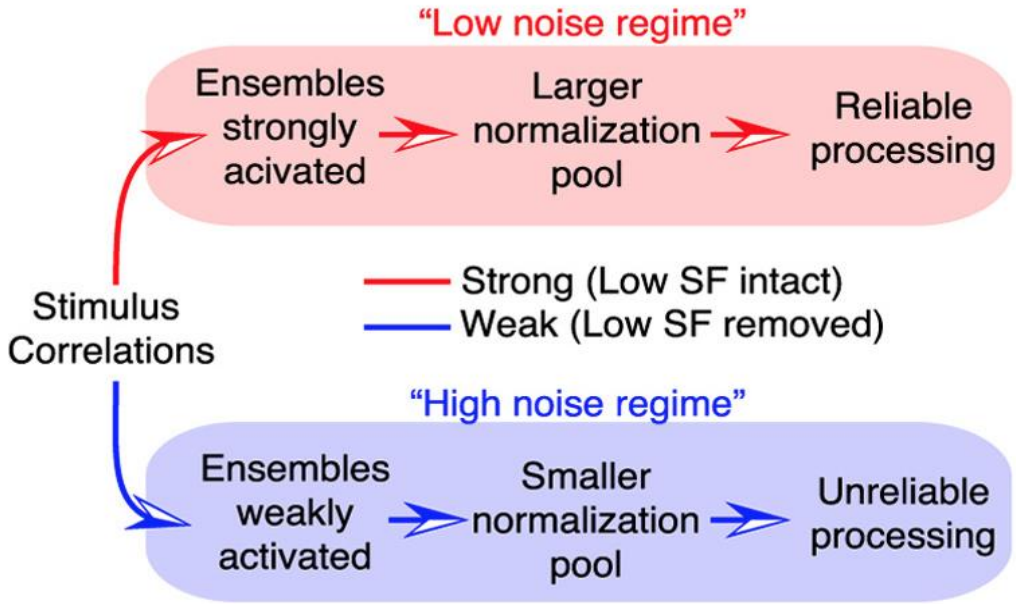

Figure 4.1. Schematic summarizing the main findings of this study. In the low noise regime, strong spatial correlations in the stimulus dynamically alter interneuronal correlations to change the normalization pool, ensuring reliable processing. In the high noise regime, weak stimulus correlations fail to activate ensembles, resulting in unreliable processing

- **Main Results**

In this manuscript, we generated a high number of results in order to propose a complete and thorough overview of the impact of natural scenes on the reliability and correlations in cat primary visual cortex. Because of the different conclusions issued in the previous chapter, we decided to summarize our main results in four different figures: One for the SUA (figure 4.2), one for the MUA (figure 4.3) and two for the LFP (figures 4.4 and 4.5). These results will first be described in this subsection and then discussed throughout this chapter.
At the spiking level (SUA and MUA), we focused on four main results: the firing rate, the sparseness, the reliability and the correlations. It is important to note that MUA exhibits a higher firing rate, reliability and correlations than SUA and a lower sparseness.
At both spiking levels, drifting gratings evoked the highest mean firing rates (Figure 4.2 and 4.3). Firing was the highest in layer 4 and the lowest in layer 2/3. We then focused on the sparseness since natural images are known to be sparsely coded (Vinje and Gallant, 2000; Haider et al., 2010; Baudot et al., 2013). Our results did show that natural images evoked a sparser response than the artificial stimuli and that this sparseness was increase when both center and surround were stimulated together. While the SUA displayed the highest sparseness in layer 5/6, at the multi-unit level the sparsest response was observed in layer 4. Natural images also evoked the highest levels of reliability. When presented full field the lowest reliability was observed in layer 2/3 while layers 4 and 5/6 showed similar levels of reliability. The center stimulation reduced the reliability evoked by NI. This decrease was higher in layer 5/6, where horizontal connections are present. In addition, this decrease led to a difference in reliability between layer 4 and 5/6 (layer 4 displaying a more reliable response than layer 5/6).
Finally we investigated both signal and noise correlations. Natural images evoked the highest signal correlations both within and between layers. Yet, the correlations within layers were higher than the ones obtained between. Regarding the noise correlations, all stimuli evoked similar values. However, as observed for signal correlations, the correlations within layers were higher than the ones obtained between. Both correlations showed a decorrelation when both center and surround were stimulated, compared to a center only stimulation.

We also investigated the amplitude of the LFP response, its reliability and its power spectral density (Figure 4.4). Our results show that natural images evoke the most synchronized response. The amplitude was the highest in layers 4 and 5/6 when NI were presented full field. Surprisingly, the stimulation of the surround with NI also evoked a highly synchronized response, in particular in the layers containing horizontal connections. Animated gratings also evoked high levels of synchronization for the full field stimulation, yet their presentation on the surround had less of an impact than NI. The pattern of amplitude exhibited by the LFP was also observed at the power spectral density and reliability levels. Indeed, full field natural images evoked the most reliable responses (and PSD) in layers 4 and 5/6 and a lower one in layer 2/3. This response was highly modulated by the surround. Indeed, when NI were presented on the surround only, the reliability of layers 2/3 and 5/6 was higher than in the center condition (no difference was observed in layer 4). These results highlight the importance of the surround in the processing of natural scenes.
In addition, we investigated the time-frequency dependent reliability of the LFP and the spectral density of the unlocked LFP response (Figure 4.5). The low frequency reliability displayed a similar pattern as the reliability analysis displayed in figure 4.4. On the other hand, dense noise displayed the highest reliability between 40 and 120Hz. These differences in reliability as a function of the frequency band are directly related to the frequency content of the stimuli. These results highlight

the fact that the neuronal ensembles described in figure 4.1 will be more or less synchronized as a function of the stimulus frequency content.
Another striking result is the increase of the alpha and gamma bands of the unlocked PSD. Indeed, it has been shown that the alpha and gamma bands are linked to feedback and feedforward processing, respectively (Kerkoerle et al., 2014). Our results indicate that only the stimuli containing eye movements induce a strong alpha power spectral density. This increase was almost absent for the center stimulation, arguing for a strong contribution of the surround, which is known to incorporate feedback pathways (Angelucci et al., 2002). In addition, this alpha band increase could be linked to an error message created by the eye movements (VanRullen et al., 2011). On the other hand, all stimuli evoked an increase in the gamma band. This is strongest for the center stimulation, which is associated with feedforward processing (Angelucci et al., 2002).

We will now discuss in detail the results obtained during this PhD. The main results described above will be discussed and put in perspective with our other findings.

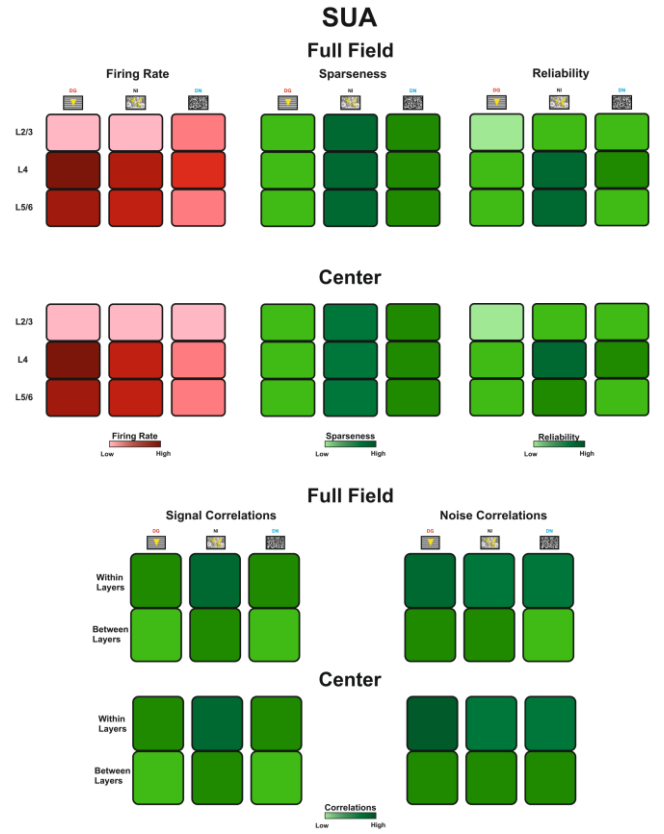

Figure 4.2: Summary of the main results obtained at the single unit level

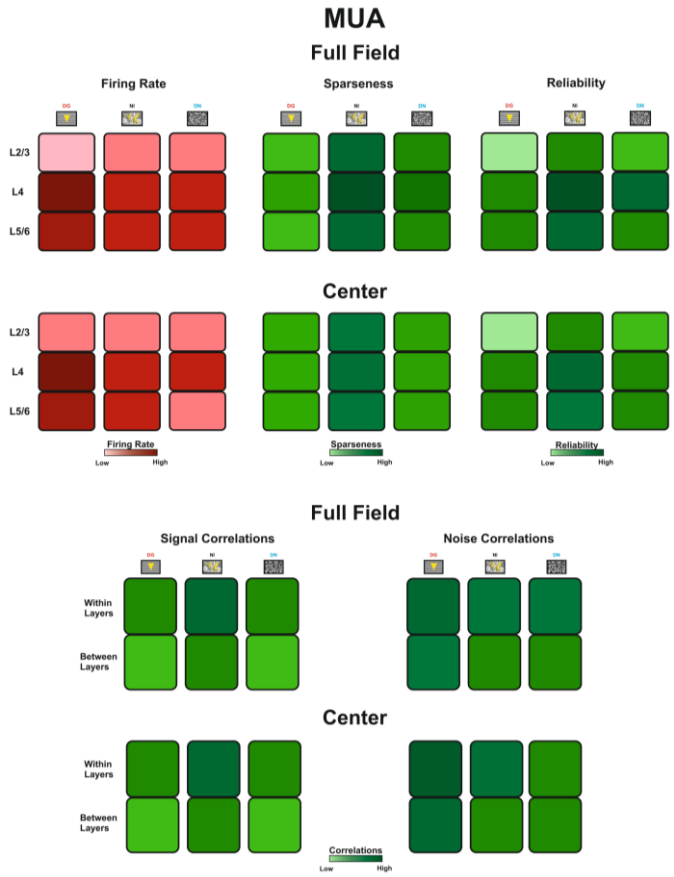

Figure 4.3: Summary of the main results obtained at the multi-unit level

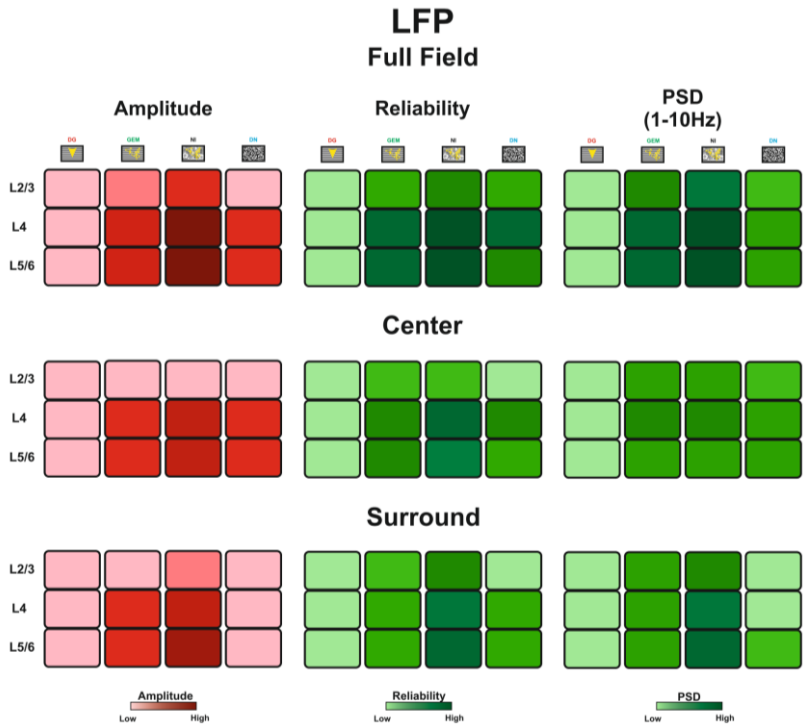

Figure 4.4: Summary of the main results obtained at the local field potential level

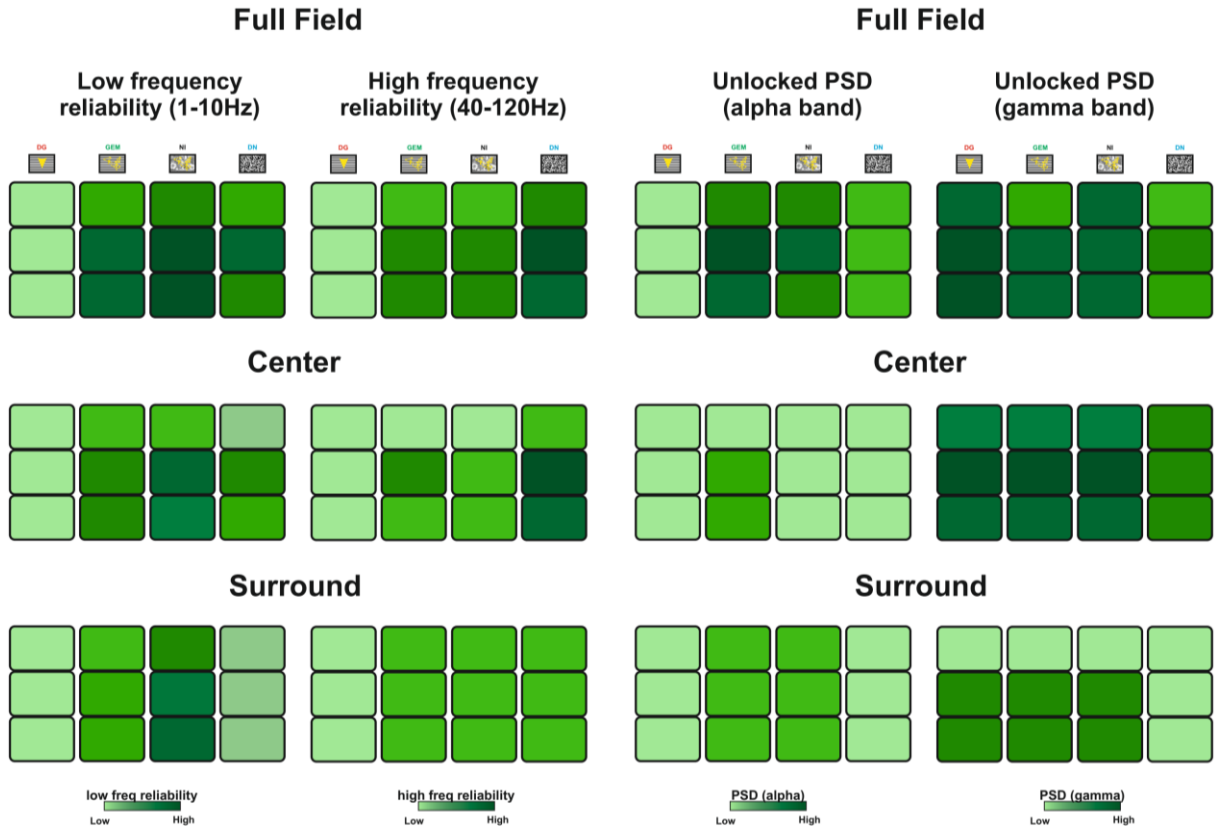

Figure 4.5: Summary of the main results obtained at the unlocked local field potential level

- **Cell classification**

The first main result obtained in this PhD manuscript is the separation of the single unit population into regular spiking and fast spiking cells. Indeed, an intracellular experiment performed by Haider et al., (2010) in cat primary visual cortex showed that RS and FS neurons do not respond the same way when natural scenes are presented. Yet, they performed an intracellular classification, which differs from the extracellular classification (see chapter I-section 2.3 of this manuscript for the intracellular classification criteria). Since we recorded the extracellular activity, performing a precise classification like Haider and colleagues (2008) would be impossible. Further complicating classification, bursting activity of the cells can vary depending on what anesthetic, on the depth of anesthesia and on the type of stimulation that is performed. On the other hand, intracellular recordings allow the modulation of the spiking activity by current injection. Therefore, extracellularly, it is impossible to rely on the bursting activity to reliably classify neurons, hence reducing the number of neuronal classes (Bartho et al., 2004). In addition, CH cells are very rare in primary visual cortex (Nowak et al., 2003). Moreover, extracellular recordings cause a derivation of the electrical signal and change the length of an action potential (Houk et al., 1995). Therefore, it becomes impossible to classify chattering and intrinsic bursting cells and more importantly, interneurons that are classified as FS cells with the intracellular method can be categorized as RS neurons. Despite this lack of precise characterization, many extracellular studies observed functional differences between RS and FS cells classified extracellularly (Bartho et al., 2004; Cardin et al., 2009; Isett et al., 2018 in rodents; Peyrache et al., 2012 in humans; but see Bachatene et al., 2011 and Chen et al., 2015 for a classification in cat primary visual cortex). Because of the existence of functional differences observed in the cited studies, we assumed that it was pertinent to perform this RS/FS classification of our single unit recordings. However, we decided to develop a new method of classification (see the methods section of this manuscript). Indeed, by performing a PCA on many classically used criteria (peak-to-peak; half-width; but not the firing rate) we were able to perform a precise characterization of the single unit waveforms.
Thus, we developed a novel and more accurate sorting method than the ones classically used. This new technique should be used in other extracellular studies that want to investigate the functional impact of FS and RS neurons. These results justify the fact that we computed our analysis for the complete single unit population but also for the regular and fast spiking neuronal population.
However, one complementary analysis needed to be performed in order to refine our cell classification. The extracellular classification does not allow the labelling of interneurons or excitatory neurons. Yet, by computing the cross correlation between the RS and FS neurons, as performed by Peyrache and colleagues (2012), we could determine which FS neurons are inhibitory and which RS neurons are excitatory. However, this method does not allow a labelling as precise as the intracellular one.

- **Functional differences between fast and regular spiking neurons**

Our study relies on two strong statements that need to be discussed: The separation between regular and fast spiking neurons and the laminar identification. Regarding the separation of the two subpopulations, if the method commented above is efficient, we should also observe functional differences between the two classes. Therefore, in this subsection, we will discuss the differences between regular and fast spiking neurons.
The first observed difference is the firing rate between the neuronal classes. We observed, as described in the literature (Nowak et al., 2003; Bachatene et al., 2012), a higher firing rate for the

fast spiking neurons than regular spiking ones. It is important to keep in mind that the PCA of our sorting method did not take in account the firing rate. Therefore, obtaining this functional result is a strong argument for a good separation between FS and RS cells. In their intracellular paper, Haider and colleagues (2019) showed that fast and regular spiking neuron sparseness was modulated in different ways by the center surround interactions of natural images. Fast spiking neurons showed a decrease in sparseness when the surround was stimulated while regular spiking neurons displayed an increase. Our results show that FS neurons are not impacted by center surround interactions when natural images were presented. On the other hand, these interactions elicited a sparseness increase among RS neurons. Despite this significant absence of center surround modulation observed among FS cells, the full field condition evoked a higher mean sparseness than the center. The same small difference, caused by the size of our center stimulation, was observed for RS cells, the main difference between the two populations is the number of recorded cells. Thus, by increasing the number of FS neurons we should obtain a significant difference. Fast spiking neurons displayed either an increase or decrease in sparseness when the surround was stimulated. A decrease would be in agreement with the Haider et al. (2010) results. However, they only recorded 9 FS cells and might have missed cells displaying a sparseness increase. Another explanation is that we included RS neurons in our FS population. As stated above a classification of inhibitory and excitatory neurons among the fast spiking neurons is needed.

We also observed that fast spiking neurons evoked a more reliable response than regular spiking. This was also observed by Haider and colleagues (2010) in their intracellular study. One could argue that this higher level of reliability is linked to the difference in firing rate between the two cell types. However, we showed that the firing rate and the reliability are not totally correlated. In order to get rid of the bin size dependency of the reliability, we carried out a time frequency analysis of the reliability. This analysis allowed us to extract the signal, the noise and the SNR of the response. Fast spiking neurons evoked a higher signal, a higher noise but also a higher signal to noise ratio, in the low frequency range than the regular spiking cells. The increased reliability observed for FS cells originates from this high increase in signal that compensates the noise increase and result in a high SNR.

Finally, we investigated both signal and noise correlations among our two neuronal subtypes. Fast spiking neurons evoked higher signal and noise correlations than regular spiking neurons. In addition, the noise and signal correlations of the two subtypes were positively correlated. Thus, when FS cells displayed an increase in noise correlation this was also the case for the noise correlation. This can be related to our time frequency analysis results where a high noise is linked to a high signal.

Overall, our different analyses confirm the accuracy of our classification. However, a refinement of the separation of inhibitory and excitatory neurons among our cell classes could give additional precious insights to our observations.

- **Laminar processing of the visual information**

The second key point of this manuscript is the identification of the laminar compartments. We based the characterization on both physiological (CSD) and anatomical (histology) data. Functional differences between layers have been identified in V1 (Hansen et al., 2012; Kim and Freeman, 2016; Maier et al., 2010). We also observed a laminar specificity of the neuronal response across layers. The main differences that we observed were between layers 2/3 and layers 4/5/6. We will focus on these differences both at microscopic and mesoscopic levels. Since layer 4 and 5/6 generally evoke

a similar response, they will be discussed together. When they display a different behavior, this will be discussed.

The spiking activity displayed the lowest firing rate in layer 2/3 and the highest in layer 4. One could think that the low firing rates observed in the supragranular layer is linked to the small amount of isolated single units, however the same pattern is observed with the multi-unit activity. This pattern of firing rates was also observed in higher mammals and rodents (Sakata and Harris, 2009; Schmidt et al., 2018). The characterization of the LFP resulted in a different pattern. Indeed, in response to natural images and drifting gratings, the highest levels of energy were observed in layer 5/6. On the other hand, dense noise and animated gratings evoked the highest levels of energy in layer 4. These differences are linked to the intrinsic properties of each layer and will be discussed below.

The analysis of the sparseness revealed that, at the single unit level, the sparsest response was found in layer 5/6 while no difference was observed in the other layers. On the other hand, the multi-unit activity displayed the sparsest response in layer 4 and the least sparse response in layer 2/3. Interestingly, when natural images were presented, the difference in sparseness between the center and full field conditions was the highest in layers 2/3 and 5/6. The neurons in these layers are connected by horizontal connections, which are activated by the stimulation of the surround (Bringuier et al., 1999; Gerard-Mercier et al., 2016). This suggests that horizontal connections are recruited by natural statistics when presented in the surround and that they play a role in the generation of a sparse response.

The analysis of the reliability revealed pronounced laminar dependency. On one hand, as observed for the firing rate, artificial stimuli evoked the least reliable response in layer 2/3 and the most reliable one in layer 4. On the other hand, no difference was observed for NI between layers 4 and 5/6, which evoked a more reliable response than layer 2/3. When natural images are presented, layer 4 displays a lower signal and noise than layer 5/6 but a similar ratio, leading to similar levels of reliability. This is not the case for artificial stimuli that evoked the highest signal and noise in layer 4 but also a higher SNR. This difference likely originates from V1 functional and anatomical properties. Indeed, both layers 4 and 6 receive precise and reliable thalamic inputs (Kumbhani et al., 2007). Therefore, a more reliable response is expected in these layers. In our study, we did not separate the neurons located in layers 5 and 6, instead we considered both as a whole. This could explain why the reliability evoked by artificial stimuli in layer 5/6 is lower than in layer 4. However, no difference is observed between these two layers when natural images are presented. Thus, this increase in reliability could be linked to the fact that natural images optimally activate the thalamic neurons that will send a more precise and reliable signal to V1 (Butts et al., 2007; Sedigh-Sarvestani et al., 2019).

The LFP displayed the same response patterns as the spiking activity. Our signal to noise ratio analysis allowed us to remove the variability linked to the intrinsic properties of each layer. It confirmed the observations previously made with the energy analysis *i.e.* a higher signal was observed in layer 5/6. A striking result only obtained with the LFP is the strong laminar modulation of the response when our stimuli where only presented in the surround. Indeed, the sole stimulation of the surround with NI, evokes in layers 2/3 and 5/6 a more reliable response than the center only stimulation, while in layer 4 the center and surround induced similar reliability levels. This increase in the LFP reliability for the surround only condition suggests horizontal connections play a strong role in the processing of the statistics present in the surround.

We will now discuss all the obtained results and put them in perspective with the previous observations.

- **Characterization of the multiscale response**

Since we recorded the single unit activity, multi-unit activity and local field potential, the first step of this study was to simply characterize these response types to our set of stimuli.
We first computed the firing rate of the single unit activity and the multi-unit activity. As Olshausen said in his 2013 review, we need an exploratory based approach to determine the different firing rates across layers when a natural image is presented. We did compute the mean firing rate and the firing rate for each layer for the SUA and its two subpopulations and the MUA. We used the same set of stimuli as Baudot and colleagues (2013) did in their intracellular study performed on the anesthetized and paralyzed cat. Therefore, it is natural to directly compare our results with theirs. However, it is important to keep in mind that they recorded a low number of cells, without any laminar labelling (less than 30) and that we did not used the same anesthesia (Althesin for them, Isoflurane for us). Thus, we will limit our comparison to the global population. Both single unit and multi-unit activity exhibited a similar firing pattern to the one observed intracellularly, *i.e.* both gratings evoked the higher firing rates. However, the multi-unit activity showed a higher firing rate than the single unit activity. This is linked to the fact that the multi-unit activity corresponds to the activity of many neurons, thus increasing the mean firing rate (Einevoll et al., 2007; Pettersen et al., 2008). Only multi-unit activity displayed center surround modulations; the full field condition evoked a higher firing rate than the center condition. This is probably linked to the size of our center stimulation. Indeed, in their work, Haider and colleagues (2003) showed that natural images also evoke a plateau of maximum suppression. This plateau is reached for stimulations 3 times bigger than the size of the receptive field. However, they stopped their analysis at a stimulation 4 times higher than the size of the RF. Thus, with a 5° stimulation, we are above this 3-times limit. A visual stimulation with different mask sizes would allow us to determine the limit of maximum suppression. However, it is important to note that both signals displayed, for all stimuli, either a suppression or a facilitation when the surround was stimulated. Guo et al. (2005), showed in monkeys that V1 cells can either be facilitated or suppressed when natural images are presented. This phenomena was also observed for gratings (Blakemore and Tobin, 1972; Maffei and Fiorentini, 1976). The observed facilitations and suppressions could be linked to the size tuning properties of the cells. A quantification of the size tuning of each cell and its facilitation or suppression could be performed in order to address this question.
At the laminar level, for both SUA and MUA, the highest firing rates were observed in layer 4 and the lowest in layer 2/3. One could argue that the low firing levels could be linked to the reduced number of neurons recorded in this layer, yet the multi-unit also displays a strong reduction in the firing rate. As observed for the mean response, no mean center surround modulation was observed for the SUA. On the other hand, the MUA displayed a modulation in all layers. Again, for both signals facilitation and suppression were observed across all layers.
We observed different results among the regular and fast spiking neurons. Fast spiking neurons displayed a higher mean firing rate than the single unit population while regular spiking neurons displayed a lower firing rate than the single unit population. This is not surprising, since fast spiking neurons are known to display high firing rates (Bachatene et al., 2012; Chen et al., 2015; Nowak et al., 2003). As observed for the single unit activity, both subpopulations were not affected by the center surround interactions. Yet, among the two cell types, we observed cells displaying facilitation and suppression behaviors. This differs from Haider and colleagues' results (2010). Indeed, they observed that all cell types displayed either a facilitation or a suppression in response to natural images. This difference could be linked to the fact that they recorded of very small subset of cells (less than 20) and mainly recorded cells displaying one of the two mechanisms. The observed

difference could also be linked to the cell classification that we performed. Indeed, while intracellular recordings allow a precise characterization of the FS and RS cells this is not possible extracellularly. The characterization of the inhibitory and excitatory cells among our populations (Peyrache et al., 2012) could clarify this aspect.
The single unit activity and its subpopulations displayed similar firing patterns in response to our control stimuli while the multi-unit activity displayed a higher firing rate in response to the stimuli containing an altered eye movement pattern. This suggests that temporal statistics have a small impact on the firing and a great number of neurons is needed in order to observe a difference.

The characterization of the LFP response was performed by computing the energy of the signal. Unlike what was observed for the spiking activity, the highest energy was evoked by natural images and not drifting gratings. The latter evoked the lowest levels of energy. A high energy implies a very synchronized signal while a low energy implies a very desynchronized one. The LFP is a mean field signal that records the activity of many neurons, yet neurons responding to DG are regrouped in phase columns and display a phase preference (Wang et al., 2015). Thus, the LFP corresponds to a mixture of neurons displaying different phase preferences, which leads to a desynchronized signal. Moreover, the neurons strongly adapt their response to DG, as shown in chapter II, which is not the case for the other stimuli. This results in a total desynchronization of the LFP despite spiking activity and a membrane potential locked to the stimulus (as shown in Baudot et al., 2013; Figure 2). This suggests that the mesoscopic information carried by LFPs and the local integration of synaptic input realized by a single cell are dissociated unlike what was claimed by Kamondi and colleagues (1998).
Unlike what was observed for the single and multi-unit activity, natural images evoked the highest energy in layer 5/6, while the lowest one was found in layer 2/3. This difference in energy observed between layers can be linked to the pattern of currents observed in each layer (Jin et al., 2011; Mitzdorf, 1985). Indeed, the connectivity present within each layer results in unique sink and source currents across the layers. These currents might have an impact on the energy of the LFP. In order to test this, a CSD of the response can be performed, and linked to the amplitude of the local field potential. In addition, it would be interesting to divide the LFP into different frequency bands and investigate the frequency based CSD of the response but also the link between the frequency-based energy and the MUA, as performed by Sellers et al. (2015) in the ferret. They showed that changes in delta and alpha power are negatively correlated with the MUA responses, whereas increases in gamma power are positively correlated with MUA responses.
A striking result obtained with the LFP, but absent in the spiking activity, is the strong synchronization of the response when our animated stimuli where only presented in the surround. Indeed, stimulation of the surround with NI and GEM evoked higher levels of energy than stimulation of the center. The work performed in the laboratory showed that stimulation of the “silent surround” evokes a response at the membrane potential level (Bringuier et al., 1999; Chavane et al., 2011; Gerard-Mercier et al., 2016). In addition, the stimulation of the silent surround at high speed also evoked an increase in V_m (Le Bec et al, in preparation). Thus, the eye movement pattern present in GEM and NI might have a strong impact on the neuronal activity and strongly affect the LFP response. This increase in the LFP energy for the surround only condition is higher in layers 2/3 and 5/6 where horizontal connections are present. This suggests that they play a strong role in the processing of the statistics present in the surround.

Finally, at the LFP level, the control stimuli evoked different energy levels. When presented full field, the natural images lacking structured eye movements evoked a lower energy than the other stimuli. On the other hand, the natural images only animated with saccades evoked a higher energy than all

the other stimuli. This implies that saccades evoke a synchronized neuronal response. The unaltered eye movements are mainly processed by the surround. Indeed, when presented in the center, all stimuli evoked the same energy while the surround stimulation evoked the same response pattern as the full field condition. This suggests that the surround is suited to process eye movements and shows that temporal statistics have a strong impact on the response and need to be taken in account in natural scene studies.

- **Sparseness**

An influential hypothesis in the visual field is that visual processing is adapted to the natural statistics of our environment. This hypothesis, proposed by Barlow (1961) and called the "efficient coding hypothesis", suggests that efficient coding should increase the sparseness of individual neurons.
Many studies have investigated the sparseness of the single unit activity in response to natural images. These studies uncovered important functional properties in V1. Two studies reported the impact of the center surround interactions on the sparseness of V1 neurons (Vinje & Gallant, 2000, in primates; Haider et al., 2010 in cats). They both found that the center surround interactions increase the sparseness of V1 neurons (it is important to note that Vinje & Gallant first thought that this sparseness increase was linked to attentional effects, but other studies showed that this hypothesis was false). In addition, Haider and colleagues (2010) showed that only excitatory cells have their sparseness impacted by center surround interactions. In addition to these studies, an intracellular study performed in cat primary visual cortex showed that natural images evoke a higher sparseness than classic artificial stimuli (Baudot et al., 2013). Finally, two studies performed in mice (Froudarakis et al., 2014) and in primates (Tang et al., 2018) showed that sparseness facilitates the encoding of natural scenes, as hypothesized by Barlow (1961). In our knowledge, no study compared the impact of the center surround interactions on the laminar sparseness, nor compared the stimulus dependency of the sparseness across layers.
When our set of stimuli were presented full field, our results show that at the single unit level, its two subpopulations (regular spiking and fast spiking cells) and the multi-unit activity, natural images animated with eye movements evoked the sparsest response.
We first compared our results to those obtained intracellularly by Baudot and colleagues. Despite a similar pattern (*i.e.* natural images evoked the sparsest response), we obtained lower values than they did. This can be explained in two ways. First, our results show that different values of sparseness are obtained for the SUA, ranging from 0.2 to 0.9. Since we computed the sparseness on 99 neurons while they only did it on 26, we might have recorded more low sparseness cells than they did. The second source of difference might rely on the different anesthetic used in their study. Indeed, Althesin, the anesthetic used by Baudot and colleagues (2013), evokes a higher post synaptic depression than isoflurane (El-Beheiry and Puil, 1989).Therefore, a higher inhibition leads to sparser spiking activity.
We also computed the sparseness of the multi-unit activity. As observed by Haider and colleagues (2010; supplementary data), the MUA exhibited a lower sparseness than the SUA. We obtained the same response pattern for these two signals, *i.e.* Natural images evoked the sparsest response. Yet, unlike the observations made by Haider et al (2010), we did not observe any difference in sparseness between regular spiking cells, fast spiking cells and the complete single unit population. The differences between our study and their study can be explained by four main arguments. First, we recorded more than 200 cells while in their intracellular study less than 40 cells were recorded. Our study captures better the diversity of responses present in primary visual cortex. Another strong argument is that the natural stimuli used in their study and ours are different. We used animated eye

movements while they presented a movie. The difference in the temporal frequencies might impact the sparseness. Their recording technique allowed the precise classification of RS and FS cells as excitatory and inhibitory neurons. A better determination of the type of neurons among our RS and FS cells is necessary. Finally, the brain state of the animal is linked to different sparseness levels (Froudarakis et al., 2014; Spacek and Swindale, 2016), thus the difference between our two studies might come from different brain states.
We then compared the sparseness evoked by the stimulation of the center alone and the stimulation of both center and surround. When natural images were presented, both single unit and multi-unit activity showed a sparsification of the response for the full field condition compared to the center. This result, and similar ones obtained in higher mammals (cats and primates) and rodents (Baudot et al., 2013; Froudarakis et al., 2014; Haider et al., 2010; Tang et al., 2018; Vinje and Gallant, 2000; Yao et al., 2007) argue that sparse encoding of natural scenes could be a hallmark of V1 intracortical organization. This general principle of sparsification is thought to be linked to a better readout of natural scenes by the cortex (Froudarakis et al., 2014). However, the full field stimulation evoked a smaller sparsification of the response than in other studies (Haider et al., 2010; Vinje and Gallant, 2000). This is linked to the difference in the size of the center stimulation between our study and theirs. Indeed, our center stimulation is performed on a mask of 5x5° while these two studies, the performed the center stimulation on 2x2°. Therefore, the small difference that we observe, between the center surround and center condition sparseness might come from the fact that a 5° center stimulation also stimulates the surround. We are probably close to the limit where the sparseness will not be strongly modulated anymore by an increase of the stimulation size. Our preliminary results, where we compared the sparseness evoked by different center sizes tend to confirm this hypothesis.
Regarding the laminar sparseness, at the single unit level, only layer 5/6 displayed a sparser response for the full field stimulation while no difference was observed in the other layers. On the other hand, at the MUA level, the full field stimulation with NI evoked the sparsestresponse in all layers. The layers where the difference in sparseness between the center and full field conditions was the highest are layers 2/3 and 5/6. The neurons in these layers are connected by horizontal connections coming from other neurons. These neurons are activated by the stimulation of the surround (Bringuier et al., 1999; Gerard-Mercier et al., 2016). Our results suggest that horizontal connections are recruited by natural statistics presented in the surround and play a role in the generation of a sparse response. While the regular spiking cells displayed the same behavior as the complete single unit population, fast spiking cells were not affected by the center surround interactions. This result is different from the one obtained by Haider and colleagues (2010) and can be explained by the same 4 arguments stated above.
Finally, we showed that the altered natural stimuli also evoked a higher sparseness when presented full field. This suggests that only the higher order correlations present in the natural spatial and temporal statistics are necessary for the sparsening of the response. These results are in agreement with the findings of Freeman and colleagues (2013) that observed, in the primate, that V1 responds the same way to natural stimuli and naturalistic stimuli only containing higher order correlations.

- **Reliability of the evoked visual response**

The second aspect of Barlow's efficient coding theory is the fact that the variability of the response should decrease when primary visual cortex is stimulated with natural images.
This reduction of response variability (i.e. an increase in the reliability) has been largely studied in sensory cortices. The modulation of reliability of the response by natural scenes has been largely

studied in the past 20 years in different species (Yao et al., (2007); Haider et al., (2010); Baudot et al., (2013): in cats. Goard & Dan (2009); Froudarakis et al., (2014) Rikhye & Sur (2015), De Vries et al., (2018): in mice; Montermurro et al., (2008) in primate). All these studies showed in different ways that natural images induce a reliable response in primary visual cortex. In this section, we will describe and discuss the modulation of variability that we obtained in cat primary visual cortex.

In this manuscript, we measured the variability in two different ways: by computing the reliability of the response, without any frequency aspect, and by computing the frequency dependency of the reliability. We will discuss these two measures of variability together since they are complementary. Since the Fano Factor and the trial-to-trial reliability of the spiking activity resulted in similar results, we will refer to both as the "reliability of the spiking activity". We will also consider the SNR and the trial-to-trial coherence together, since they give similar results.

Yao et al. (2007) showed, in their extracellular study performed in cat V1, that natural movies evoke a higher level of reliability than artificial stimuli. Baudot and colleagues (2013) confirmed this result intracellularly. They showed that natural images animated with eye movements induced a more reliable response than artificial stimuli. We obtained the same pattern of reliability as they did. However, the reliability levels obtained at the single unit level were lower than theirs. This difference could be because of the fact that we recorded hundreds of cells, with a low selection bias, while they recorded about 30 cells that were selected based on their responses. Among our hundreds of cells, we observed very heterogeneous levels of variability. They might have decided not to proceed with these cells displaying low levels of variability because intracellular recordings are time consuming and it might not be worthwhile to study a cell with only marginal visual responses. The multi-unit activity evoked a higher mean reliability than the single unit activity. Yet, we also observed low and high levels of reliability among our MUA sites. A cell displaying a high reliability in response to a stimulus also displayed a high reliability in response to the other stimuli. This heterogeneity was also observed in cat (Yen et al., 2007) and mice primary visual cortex (Kampa et al., 2011). Kampa and colleagues showed that in response to both artificial and natural stimuli, a great proportion of cells displayed low reliability levels and a small proportion of cells displayed high reliability levels. The prediction performance of the complete variable cell population was equivalent to the prediction of the performance of the reliable cell population. This result was also observed in cat primary visual cortex where we observed similar prediction performances for these two populations in response to artificial and natural stimuli (Jonathan Vacher Thesis, 2017). This implies that this reliability distribution is a hallmark of primary visual cortex and that the processes occurring in V1 need to be considered at the population level and not at the single cell level.

By computing a time-frequency based analysis, Baudot and colleagues (2013) were able to identify the most reliable frequencies and the impact of the signal and the noise on this reliability. In their study, the reliability of the spiking activity evoked by drifting gratings was almost equal to 0. The frequency-based analysis revealed that DG actually evoke a reliable response but only at the grating frequency. They also showed that the levels of reliability observed for GEM and NI originated from a decrease in variability in the low frequency range, while dense noise reliability comes from high frequencies.

Our extracellular recordings resulted in similar results. However, one striking difference is that, extracellularly, the high reliability observed for NI originates from a high signal and a high noise in the low frequency band. Intracellularly, this high reliability is linked to a high signal but mainly to a low noise level. We also computed the reliability of the fast and regular spiking cells. The fast spiking cells exhibited a higher mean reliability than the single unit population while the regular spiking cells exhibited lower levels of reliability than the single unit population. The two cellular subtypes displayed the same response frequency dependent pattern as the single unit population. This higher reliability

observed for fast spiking neurons, that are supposedly mainly inhibitory neurons, could play a role in the generation of sparse and reliable activity among the excitatory neurons (Lee et al., 2012; Zhu et al., 2015). A thorough classification of the cell type among our FS and RS populations would allow to affirm (or not) this hypothesis.

The higher low frequency reliability evoked by natural images, at all scales, is reminiscent of the demonstration already made in vitro that a broadband somatic current signal is required, covering both low and high frequencies, in order to produce reliable spiking activity (Mainen and Sejnowski, 1995b; Nowak et al., 1997).

A novelty of our study is the investigation of the reliability across layers. Our results show that across all layers natural images evoked the most reliable response and that this reliability is linked to an increase of the SNR in the low frequency range. The reliability evoked by NI was similar in layers 4 and 5/6 (for both SUA and MUA). On the other hand, artificial stimuli evoked the highest levels of reliability in layer 4. The highly reliable response observed in layer 4 probably originates from the reliable and precise thalamic inputs coming to layer 4 (Desbordes et al., 2008; Kumbhani et al., 2007; Nawrot et al., 2009). Layer 5/6, which also receives thalamic inputs, displayed different reliability levels than layer 4 when stimulated with artificial stimuli, and similar levels when natural images were presented. Despite similar levels of reliability, in response to NI layer 5/6 displayed a higher signal and noise than layer 4, but resulted in a similar ratio. On the other hand, for artificial stimuli the highest noise and signals were observed in layer 4. The differences between these two layers could be linked to the fact that natural images activate more densely the thalamic inputs, leading to a more reliable response in layers 4 and 5/6 (Desbordes et al., 2008). This increased response might also be combined with the impact of the eye movements present in natural scenes, which might strongly activate Y-thalamic axons.

A striking result is the reduction in reliability observed between layers 4-5/6 and 2/3. A strong reduction in the reliability levels is also observed between the thalamus and layers 4 and 5/6. This reduction has been linked to a computational function and ethological functions (Evans et al., 2018; Sedigh-Sarvestani et al., 2019). Thus the reliability reduction observed in layer 2/3 might serve an important function such as the one described above or others like the filtering of irrelevant information (Luczak et al., 2013; Vidyasagar, 1998).

The analysis of the LFP led to similar conclusions as the ones drawn with the MUA and SUA, *i.e.* natural images evoke a more reliable response than the artificial stimuli and we observed a laminar difference in the reliability levels. However, the LFP exhibits higher levels of reliability than the spiking activity. These levels are close to the ones obtained by Baudot and colleagues (2013) with the membrane potential. Yet, these two signals are different. Indeed, the reliability evoked by drifting gratings is very low for the LFP and not for the V_m. As explained in the results section, this is linked to the fact that the LFP integrates the activity of cells having different phase preferences, thus leading to a “flattening” of the signal. This result confirms the fact the mesoscopic information carried by LFPs and the local integration of synaptic inputs realized by a single cell are clearly dissociated, unlike what has been previously stated (Kamondi et al., 1998). Another important difference between the LFP and the spiking activity is that the increased low frequency reliability evoked by NI in layers 4 and 5/6 originates from equal levels of signal and noise in these two layers. It is important that the low frequencies that are more represented in the natural stimulation happen to be the most informative frequencies of the LFP (Belitski et al., 2008). Thus, we can suppose that this increase is also associated with an increase in the efficiency of the message transmission. An analysis of the information contained in each frequency band should confirm this hypothesis.

The generation of a reliable response in cat primary visual cortex has been modeled in order to unveil the mechanisms underlying this (Antolík et al., 2019; Kremkow et al., 2016). These two papers

showed that the reliable response evoked by natural images originates from an interplay between inhibitory and excitatory cells (push-pull organization) and a thalamo-cortical feedforward depression. Other fundamental mechanisms of V1 such as the spontaneous activity levels, contrast and orientation tuning also modulate the reliability.

Our results also showed that the reliability is strongly modulated by center surround interactions. As reported in the literature (Haider et al., 2010; Vinje and Gallant, 2000), natural images evoke higher reliability levels when both center and surround are stimulated. This was observed at all scales (SUA, MUA and LFP). This increase in reliability is linked to an interplay between excitatory and inhibitory neurons as described by Haider and colleagues (2010). However, one cannot exclude the impact of the horizontal connections, which are known to boost the response when the surround is stimulated (Bringuier et al., 1999; Gerard-Mercier et al., 2016). This increase in reliability evoked by the surround of natural scenes could also be linked to the statistical properties of the image. It has been shown that the non-redundancy between center and surround has an impact on the surround modulation that could also affect the reliability (Coen-Cagli et al., 2015). A detailed statistical analysis of our natural image could answer this question. By linking the statistics of the image with the reliability of the response we could have a more precise insight into the visual features inducing highly reliable responses.
Unlike the spiking activity, the local field potential evoked a highly reliable response when natural images were only presented in the surround. The reliability evoked by the surround was higher than the one elicited by the center stimulation. This was not observed for the artificial stimuli and suggests that surround has a strong impact in the processing of natural scenes.
We observed, for all signals, a similar response pattern across layers. However, for all signals the difference between the full field and center stimulations was higher in layers containing horizontal connections. The laminar reliability obtained with the LFP confirms the importance of horizontal connections in the generation of a reliable response. Indeed, in layers 2/3 and 5/6 when GEM was presented in the center or the surround, the same reliability levels were obtained. On the other hand, in layer 4, the center stimulation evoked a more reliable response than the surround. These effects were exacerbated when natural images were presented. Indeed, in layers 2/3 and 5/6 the surround stimulation evoked a more reliable response than the center, while in layer 4 the center and surround induced similar reliability levels. These results were absent for the other stimuli. This suggests that eye movements have a strong impact on the surround and that this impact is amplified when the stimulus contains natural spatial statistics.
In order to confirm the impact of the spatio-temporal statistics on the reliability, we investigated it by stimulating V1 with altered natural stimuli. At the spiking level, no difference was observed between the different control stimuli. This confirms the previous observations made for the sparseness. Different results might be obtained with different controls, indeed Rikhye and Sur (2015) showed that the level of spatial correlations affected the reliability of the response. In our study, we randomized the phase of the natural scenes. However, by modifying their spatial correlations we might influence the reliability of the spiking activity in V1. At the LFP level, we observed lower levels of reliability for natural stimuli containing altered eye movements. This suggests that the reliability is strongly dependent on temporal statistics but that its modulation is only visible at a subthreshold level and/or that the difference in reliability is so small that a great number of neurons is needed to unveil it. All signals displayed higher levels of reliability for the full field condition compared to the center. However, at the LFP level, when eye movements were unaltered, the reliability levels evoked by the surround were higher than the ones evoked by the center and the opposite was observed for stimuli containing altered eye movements. This suggests that the surround is better suited to process

unaltered eye movements than altered ones. A thorough decomposition across time of the altered and unaltered artificial eye scan path would allow us to identify the movements eliciting high reliable responses and compare it to the observations of Le Bec and colleagues.

- **Power Spectral Density of the Stimulus-locked LFP**

The power spectral density of the local field potential and the signal obtained with the time frequency wavelet analysis globally resulted in very similar results. However, some notable differences were present. The main difference between these two analyses is the strong PSD increase observed in the gamma range (60-150 Hz). This increase is not stimulus dependent but linked to the visual processing and has been described in cats (Gray and Singer, 1989; Kayser et al., 2003; Martin and Schröder, 2016) and primates (Brunet et al., 2015, 2014; Fries et al., 2007; Maier et al., 2010). This increase in the gamma band may generate temporal “windows of opportunity” for neurons to spike (Buzsaki, 2006). In order to “use” this window of opportunity, spikes need be locked to different LFP phases in order to transmit different stimulus information. Martin and Schröder (2016) showed that this locking was absent in cat V1. However, investigating this hypothesis with our set of stimuli (different from theirs) could lead to different results. As observed by Maier et al (2010), we observed the strongest gamma band PSD in layer 4. This criterion, among others, can be used to determine the position of the electrode across layers.
The other main difference was the PSD evoked by DN in the beta band (10-40Hz). The signal evoked by dense noise, in this frequency band, was higher than the one evoked by the other stimuli, while the PSD is at the same level as the one computed by the spontaneous activity. This suggests that the simple power spectral analysis performed with a Fourier transfer masks some important features that are observed with complex analysis.

- **Power Spectral Analysis of the Unlocked LFP**

By subtracting the mean evoked LFP over trials from each trial, we separated the component of the LFP that is stimulus-locked from the component evoked by the presence of the stimuli but unlocked to its presentation. The analysis of the unlocked LFP recently showed that the alpha/beta band is linked to feedback processes while the gamma is linked to feedforward ones (Bastos et al., 2014, 2015; Kerkoerle et al., 2014). These observations have been made on awake primates and humans. One could argue that feedback is absent in anesthetized animals. However, recent studies from the Angelucci group showed that feedback is also present on anesthetized animals (Bijanzadeh et al., 2018; Nurminen et al., 2018). Thus, the analysis of these signals seems pertinent in the anesthetized cat. Feedback projections are present in layers 2/3 and 5/6 yet we did not observe a strong laminar impact of the feedback message. This could be linked to the fact that we computed the unlocked PSD across the complete presentation of the stimulus (10s). In their work, Kerkoerle and colleagues (2014) showed that the feedback message (through an increase in the alpha band) propagates to all layers. Thus, by computing the PSD across the 10s of stimulation we might lose the laminar impact of the response because of this processing. A more precise analysis of the temporal increase of the alpha band could unveil the laminar impact of the feedback message.
Interestingly, only animated gratings and natural images showed an increase in the frequencies linked to feedback processes. The increase observed in this frequency band has also been linked to prediction error messages (Bastos et al., 2012; VanRullen et al., 2011). Eye movements generate unpredictable responses. The fact that only stimuli containing eye movements showed an increase

in the alpha/beta band argues for a prediction error message conveyed by the feedback. The center condition evoked almost no increase in the alpha/beta band while the surround did. The surround is known to activate feedback pathways (Angelucci et al., 2002, 2017). Therefore, we can hypothesize that the stimulation of the surround activated more strongly the feedback pathways than the center. We also observed that, when presented full field, all stimuli evoked a strong gamma PSD. This was particularly strong in layer 4, the main recipient of the feedforward inputs coming from the thalamus. This increase in the gamma band was absent for the surround stimulation, which do not stimulate the feedforward pathway.
It is important to note that these hypotheses need to be confirmed in the anesthetized cat. The easiest way to perform it in cats would be to do simultaneous paired recordings in V1 and in the LGN and evaluate the frequency contentof the communication between the two areas, as performed by Bastos and colleagues (2014) or by using the stimuli and CSD analyses contained in Van Kerkoerle and colleagues (2014) work.

- **Impact of the correlations in the visual processing**

Our study also focused on both signal and noise correlations of the microscopic and mesoscopic neuronal activity. Signal correlations unveil the level of synchrony between two different responses. While noise correlations were intensively studied in primary visual cortex, only a few studies focused on signal correlation. In addition, because of technical limitations most studies focused on neuronal pairs recorded from the same electrode tip. Our dense laminar recordings allowed us to compute the signal correlations of hundreds of pairs located in the same layer or in different layers.
Our results showed that the single units displayed the lowest correlation levels and the MUA the highest. This is not surprising because as the scale of the signal is increased, the signal becomes more global and shared across recording sites, increasing the correlations levels. In addition, for all signals, natural images always evoked the most synchronized response.
In their extracellular study, Martin and Schröder (2013) obtained a similar correlation pattern in a reduced single unit population (n = 15). However, our correlation values are about 10 times lower than theirs are. This is linked to the fact that, unlike them, we also computed the correlation of neuronal pairs that were not recorded from the same recording site. In our data, the signal correlations of neurons recorded from the same recording site resulted in values close to the ones observed by Martin and Schröder (but also Yen et al. (2007)). This increase in correlation is thought to have a functional purpose. Indeed, correlated neurons are more connected than uncorrelated ones (Ko et al., 2011), this results in clusters of functionally coupled neurons that are recruited to represent visual features (Miller et al., 2014; Rikhye and Sur, 2015). These neuronal ensembles are not set and can be modified by the type of visual stimulus that is presented (Ko et al., 2011; Miller et al., 2014) or by the adaptation of V1 neurons to the presented stimulus (Bharmauria et al., 2016). It would be interesting to track the same selected neuronal pairs across our stimulus presentations and evaluate how the different stimuli modify the correlation strength between these pairs. In their study, Rikhye and Sur (2015) showed that these clusters tend to regroup into both highly and poorly correlated clusters of neurons. This was not observed in our data. However, they performed 2-photon calcium imaging within the same layer in mouse V1. The differences between our studies might come from the difference in animal model and/or the measurement spanning one layer for them (versus a vertical one of different layers for us). This could be tested by recording the responses within the same layer with 8-shank silicon probes.
Our results also showed that the correlation within layers is higher than the correlation between layers for all stimuli. This has already been observed in cat primary visual cortex by Tanaka et al.

(2014). They showed that the signal correlations decrease with the distance for pairs of neurons vertically separated. Indeed, pairs located in different layers tend to be less functionally coupled, thus a decrease in correlation is expected.
Finally, we investigated the impact of the center surround interactions on the signal correlations. At the spiking level, the stimulation of both center and surround decreased the correlation when artificial stimuli were presented. The opposite effect was observed with natural images. An increased signal correlation is linked to better signal processing (Miller et al., 2014). Therefore, these results tend to confirm the importance of the surround in the efficient processing of natural images.
One could argue that our results are not in agreement with Barlow's efficient coding theory. Indeed, his theory claims that neuronal pairs should be decorrelated when natural stimuli are presented. Yet, the theory fits perfectly with the fact that neighboring neurons sharing functional properties are strongly correlated but separated neurons are decorrelated.

We then computed the noise correlations. Again, the SUA exhibited the lowest levels of correlation while the MUA showed the highest ones. However, unlike what was observed for the signal correlations, the noise correlations evoked by our different stimuli were very close. This absence of a marked difference was also observed in the cat by Martin and Schröder (2013). All stimuli evoked very heterogeneous values of noise correlation. This great heterogeneity has also been observed in other studies performed in anesthetized cats (Martin and Schröder, 2013) and anesthetized primates (Ecker et al., 2014). One could argue that this heterogeneity is linked to the up and down states present in the anesthetized animals. However, such a distribution was also observed during these two states (Spacek and Swindale, 2016) and in awake primates (Ecker et al., 2014). The noise correlation levels that we obtained are different from those obtained by Martin and Schröder (2013) in cats but also Ecker et al. (2010) in monkeys. As explained for the signal correlations, this is probably linked to the fact that we also computed the noise correlations of cells that were not recorded from the same site. The noise correlations were higher within layers than between layers, indeed neurons spatially close share more inputs and thus more variability (Miller et al., 2014). This result was already observed in primate V1 by Smith and Kohn (2008). Our results differ from those obtained by Ecker and colleagues (2013) in anesthetized monkeys. Indeed, we obtained higher noise correlation values than they did. Different hypotheses can explain this difference. The first one is that they used an "improved" noise correlation computation, leading to different values. The second one is that during their spike sorting, they oversampled the regular spiking neuron population that displays a lower noise correlation than the fast spiking.. Finally, a recent paper by Banyai and colleagues (2019) showed that noise correlations are strongly stimulus dependent. The noise correlation of the same pair of neurons can be highly increased in function of the stimulus statistics.
Finally, we showed that the stimulation of the surround decreased the noise correlations. This result was already observed by Snyder et al. (2014). A reduction in noise correlations is associated with better visual processing. Therefore, our results suggest that the surround stimulation enhances the processing of visual stimuli in primary visual cortex.

- **Conclusion**

In this PhD work, we performed a multiscale study of the laminar reliability and the neuronal correlations in response to natural and artificial stimuli. By presenting our stimuli on the center surround, center or surround of the receptive fields, we also studied the impact of center surround interactions on the neuronal response.

We showed that all signals evoked very heterogeneous levels of reliability but despite this heterogeneity, natural images induced the most reliable response in primary visual cortex. In addition, we are the first ones to show that reliability is layer dependent, at all scales. We also demonstrated that responses to natural images are strongly modulated by the surround at all scales and that the “silent surround” evokes reliable responses at the mesoscopic level.
Finally, we showed that natural scenes evoke more correlated responses than artificial stimuli and that this increase in correlation facilitates improved visual processing.

V. ANNEX

Electrophysiology started in 1791 with Luigi Galvani. He observed that when the leg nerve and the muscle of a frog were connected through a metal conductor a contraction happened (Galviani, 1791). After succeeding at recreating this contraction with artificial electricity, he concluded that intrinsic electricity was present in the animal and the contraction was induced by the flow of electricity going through the conductor. Galvani's discovery paved the way for the emergence of many electrophysiological techniques and tools to record neuronal activity. Among these techniques, two of them allow the recording of activity from cortical cells, Intracellular and extracellular recordings.

1. INTRACELLULAR RECORDINGS

Intracellular recordings are a technique allowing the precise measurement of electrical currents passing through a neuron and its membrane potential by inserting a probe in it. In order to perform these types of recording a thin glass pipette with a very sharp tip has to be made. The pipette is filled with an electrolyte solution, the tip of the electrode is in continuity with the inside of the cell while the other end contains a silver metal wire. This wire is connected to an amplifier that also connects a reference electrode placed in an extracellular medium. The amplifier will measure the potential of the microelectrode relative to the reference electrode. Spiking activity and membrane potential variations can be recorded (Purves, 1981). Two types of pipettes are used for cortical intracellular recordings: sharp electrodes and patch clamp electrodes: Sharp electrodes, which are named this way because of their very sharp tip (around 0.2 microns), that can penetrate the neuron membrane without causing damage. Most recordings are generally done in the soma although intradendritic recordings are possible. Patch clamp electrodes reflect the name of the technique developed by Neher and Sakmann in 1976, and can be achieved in various parts of the neuropil (soma, dendrite). These electrodes have a relatively wide tip lumen (around 2 microns) that is placed on the surface of the membrane. Once in position, a suction is applied through the electrode, resulting in a seal between the glass tip and the neuron membrane. This recording technique, called "whole-cell" allows more stable and less noisy recordings compared to those performed with sharp electrodes (Hamill et al., 1981).

Two recording techniques were developed along the use of intracellular electrodes: the voltage clamp and the current clamp (Purves, 1981). The voltage clamp technique permits to maintain, through the glass pipette, the neuron membrane potential at a fixed value determined by the experimenter and allowing him to measure the ionic currents crossing the membrane at any given voltage (for an implementation in vivo, see Borg-Graham et al., 1998; Monier et al., 2003). On the other hand, the current clamp technique allows the recording of the membrane potential by injecting, through the electrode, a chosen amount of current into the neuron.

A very important aspect of the intracellular recordings is the fact that they allow the staining of the recorded cell, its dendrites and axons. Indeed, by filling the glass pipette with biocytin, for example, the neurons its dendrites and axons are stained. Thus, allowing the complete histological reconstruction of the recorded cell (see Fournier et al., 2014 for an example of cell reconstruction).

2. EXTRACELLULAR RECORDINGS

Before the development of intracellular recordings, another method was (and is) still widely used: extracellular recordings. This technique consists in recording, with a metal electrode or a glass pipette, the currents produced by a neuron and flowing out of this latter. In order to record it, the electrode is placed close to a neuron in the extracellular medium. The experimenter will measure potential difference between the extracellular currents and a reference (Humphrey & Schmidt, 1990). Three types of signals can be recorded extracellularly but unlike intracellular recordings, this technique does not give information about membrane potential and ionic currents. The three extracellular signals are the local field potential (LFP), the multi-unit activity (MUA) and the single unit activity (SUA).

The particularity about these three signals is that they originate from the same raw signal. Indeed, an extracellular electrode allows the recording of a signal between 0.3 Hz and 7.5 kHz. The three extracellular signals result from different filtering of these signals. The LFP can be extracted from the raw extracellular signal by applying a low pass filter at 250 Hz. SUA and MUA are extracted from the high frequency band (> 500 Hz) of the raw extracellular signal. Multi-unit activity corresponds to a more global activity coming from close and distant neurons. The MUA can be obtained by using a less restrictive detection threshold or by integrating the high frequency signal.

Low impedance probes allow far recordings thus give better local field potentials and multi-unit recordings. On the other hand, the recording of the single units requires medium range impedance probes, indeed high impedance rejects better the signal from the multitude of neurons located around the electrode. However, the impedance of extracellular electrodes is lower than the one required for intracellular recordings.

2.1. Single Unit Activity

The first type of signal is the recording of individual spike activity, also called single unit activity. Two types of probes can be used for extracellular recordings glass micropipettes or wire electrodes. By placing the electrode tip close enough to a cell (few tens of um), one is able to record action potentials produced by one single neuron. The action potentials recorded by an extracellular probe are close to those obtained intracellularly but they are about ten times smaller (a few millivolts for an extracellular signal vs 80 millivolts for an intracellular one (Heinricher, 2012)).

However, if the tip of the electrode is close to many neurons, many action potentials coming from different neurons will be recorded at the same time. If some of these neurons have waveforms having the same shape, it will be impossible to separate their activity. Then, two options exist in order to isolate the different neurons. The first one is to get the tip of the electrode closer to one of the neurons (a few µm, this recording technique is called juxtacellular recording and record only this neuron. Interestingly, the polarity in the vicinity of the membrane potential changes during the action potential may be the same as for intracellular recordings, but without de d.c. component (“quasi-intracellular” recordings in Creutzfeldt and Ito, 1968).

The second technique consists in adding another electrode. Using more recording sites allows identifying individual neurons because recorded spike amplitude depends on the distance between

the neuron and electrode (Buzsaki, 2004). The first major advance in recording technology was made with of stereotrodes and tetrodes. By twisting pairs or tetrads of sharp wires together, 2 or 4 recording sites very close to each other (the tips are 25µm apart) were obtained (O'Keefe and Recce, 1993; Wilson and McNaughton, 1993). Increasing the number of closely spaced recording sites improves single unit isolation. Two neurons that have the same spike size on one recording site will have a different spike size on another recording site, which means that their distance from the second recording tip is different. This principle allows a precise triangulation of the recorded neurons and their reliable separation (Buzsaki, 2004). Since the beginning of the 2000's a new type of probe started to replace the tetrodes. These new probes, called multi electrode arrays (MEA), have electrophysiological recording capabilities way beyond tetrodes. Because of the impedance of their recording sites, they record the three types of extracellular signals: LFP, MUA and SUA.

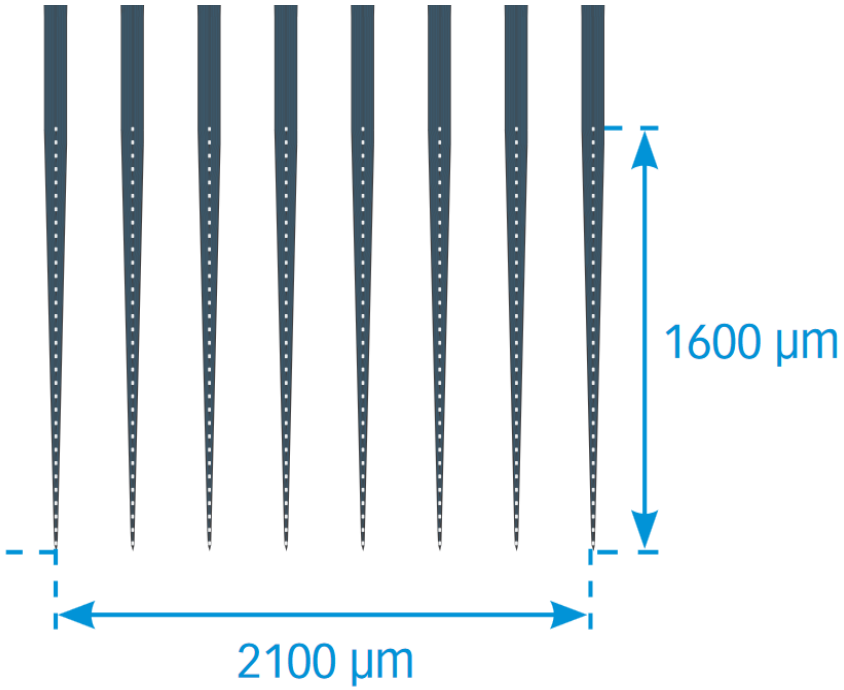

Figure 5.1: example of a silicon probe composed of 8 shanks, each having 32 recording sites (reprinted from the Neuronexus 2016 catalog)

MEAs, in particular one specific type called silicon probes, can have dozens of recording sites on the same electrode, hence record dozens of neurons at the same time (Blanche et al., 2005). These silicon probes can be made of many shanks and span a vast cortical region both horizontally and vertically (Figure 2.1). Since we are able to record vertically across an entire cortical layer, CSD became a standard procedure to determine experimentally in which layers the recordings sites across the probe are located.

Silicon probes can record dozens of neurons across the recording sites and many neurons on the same recording site. It has become crucial to perfectly isolate each single unit. A technique called spike sorting became an essential step in the processing of electrophysiological data. New techniques have emerged in order to be able to perform this task in the best possible way (Rossant et al., 2016; Yger et al., 2018). These techniques are described in the methods section of this thesis.

2.2. Multi-Unit Activity

Multi-Unit activity is seen as a measure of the firing rate of the neuronal population, about 250 µm, around the recording tip (Einevoll et al, 2007; Pettersen et al., 2012). Since MUA is a reflect of the neuronal population activity, it gives a better Signal-to noise-ratio than SUA for information shared among neurons. It has been largely studied on many species (Gray and Singer, 1989; Berens et al., 2008 Xing et al., 2009) and its use in highly stratified laminar structures regrouping cells of rather uniform morphology such as hippocampus and cerebellum has allowed to extract mesoscopic measures of spike potential synchrony (Andersen et al, (1991)).

2.3. Local Field Potential

The last type of signal that can be recorded extracellularly is the Local Field Potential (LFP). Local field potential is the combined activity of small neuronal populations located hundreds of microns around the electrode tip (Xing et al., 2009; Einevoll et al., 2013). A close correspondence between LFP and synaptic potentials has been found, indeed the cross correlation between the membrane potential and the LFP results in a high correlation value (Kamondi et al., 1998). As a result, LFP is considered as a synchronized activity of synaptic currents coming from cortical neurons hundreds of microns around the recording site. Nonetheless, even if synaptic currents are the major LFP contributors, action potentials (fast sodium spikes, slow calcium spikes and spike afterhyperpolarization) still participate to the signal formation (Einevoll et al., 2013).

A study performed on rats compared the LFP and the membrane potential (Okun et al., 2010). They showed that the spike-triggered local field potential average (STA-LFP) reflects the synchrony between the mean synaptic activity of the population and the membrane potential of the single neuron.

In addition, since the LFP is the measure of the electrical activity happening on the extracellular medium it is possible to determine the density of current entering or leaving this medium through cell membranes. This method, called current source density (CSD), measures CSD as the inverted sign value of the double spatial derivative of the LFP signal (Mitzdorf, 1985). The current sink, which is when the current leaves the extracellular domain and enter cells and the current source that describe when the current leaves the cell to enter the extracellular domain. It has been showed that each cortical layer has its own particular signature of sinks and sources. Based on this pattern of currents it is possible to experimentally identify the layer position of the recording probe by searching the depth at which the CSD sign reverts (layer 4 for cortex, where main thalamic afferents terminate (these patterns will be discussed in detail later on this thesis). Since the electrode can be positioned within a cortical column spanning in depth all layers, CSD became a standard procedure in cortex (but also subcortical structures such as the hippocampus, Buzsáki et al., 1986) to determine experimentally in which layers the recordings sites across the probe are located (Jin et al., 2011; Dragoi et al., 2012).

Local field potential is commonly divided into several frequency bands, each of them is thought to be linked to a physiological property of the brain. Delta band is composed of frequencies between 0 and 4 Hz, theta band is composed of frequencies between 4 and 7 Hz, alpha band is composed of frequencies between 8 and 12 Hz, beta band is composed of the frequencies between 12 and 30 Hz

and finally gamma band is composed of all frequencies above 30 Hz. Low frequencies reflect a very synchronous neuronal activity whereas high frequencies reflect a desynchronous neuronal activity. For the local field potential, the position of the reference has a massive impact on the signal and has to be determined carefully in order to avoid a biased recording as described in the work Parabucki & Lampl (2017).

VI. BIBLIOGRAPHY

Adams, D.L., and Horton, J.C. (2003). A precise retinotopic map of primate striate cortex generated from the representation of angioscotomas. J. Neurosci. *23*, 3771–3789.

Agmon, A., and Connors, B.W. (1989). Repetitive burst-firing neurons in the deep layers of mouse somatosensory cortex. Neurosci. Lett. *99*, 137–141.

Anderson, P.A., Olavarria, J., and Van Sluyters, R.C. (1988). The overall pattern of ocular dominance bands in cat visual cortex. J. Neurosci. *8*, 2183–2200.

Angelucci, A., Levitt, J.B., Walton, E.J.S., Hupe, J.-M., Bullier, J., and Lund, J.S. (2002). Circuits for local and global signal integration in primary visual cortex. J. Neurosci. *22*, 8633–8646.

Angelucci, A., Bijanzadeh, M., Nurminen, L., Federer, F., Merlin, S., and Bressloff, P.C. (2017). Circuits and Mechanisms for Surround Modulation in Visual Cortex. Annu. Rev. Neurosci. *40*, 425–451.

Antolík, J., Hofer, S.B., Bednar, J.A., and Mrsic-Flogel, T.D. (2016). Model Constrained by Visual Hierarchy Improves Prediction of Neural Responses to Natural Scenes. PLoS Comput. Biol. *12*, e1004927.

Antolík, J., Monier, C., Frégnac, Y., and Davison, A.P. (2019). A comprehensive data-driven model of cat primary visual cortex. BioRxiv 416156.

Azzopardi, P., and Cowey, A. (1996). The overrepresentation of the fovea and adjacent retina in the striate cortex and dorsal lateral geniculate nucleus of the macaque monkey. Neuroscience *72*, 627–639.

Bachatene, L., Bharmauria, V., Rouat, J., and Molotchnikoff, S. (2012). Adaptation-induced plasticity and spike waveforms in cat visual cortex. Neuroreport *23*, 88–92.

Baker, C.L. (1988). Spatial and temporal determinants of directionally selective velocity preference in cat striate cortex neurons. J. Neurophysiol. *59*, 1557–1574.

Baker, C.L. (1990). Spatial- and temporal-frequency selectivity as a basis for velocity preference in cat striate cortex neurons. Vis. Neurosci. *4*, 101–113.

Bányai, M., Lazar, A., Klein, L., Klon-Lipok, J., Stippinger, M., Singer, W., and Orbán, G. (2019). Stimulus complexity shapes response correlations in primary visual cortex. PNAS *116*, 2723–2732.

Barlow, H. (1961). Possible Principles Underlying the Transformations of Sensory Messages. Sensory Communication *1*.

Barlow, H.B. (1953). Action potentials from the frog's retina. J. Physiol. (Lond.) *119*, 58–68.

Barthó, P., Hirase, H., Monconduit, L., Zugaro, M., Harris, K.D., and Buzsáki, G. (2004). Characterization of neocortical principal cells and interneurons by network interactions and extracellular features. J. Neurophysiol. *92*, 600–608.

Bastos, A.M., Usrey, W.M., Adams, R.A., Mangun, G.R., Fries, P., and Friston, K.J. (2012). Canonical microcircuits for predictive coding. Neuron *76*, 695–711.

Bastos, A.M., Briggs, F., Alitto, H.J., Mangun, G.R., and Usrey, W.M. (2014). Simultaneous Recordings from the Primary Visual Cortex and Lateral Geniculate Nucleus Reveal Rhythmic Interactions and a Cortical Source for Gamma-Band Oscillations. J. Neurosci. *34*, 7639–7644.

Bastos, A.M., Vezoli, J., Bosman, C.A., Schoffelen, J.-M., Oostenveld, R., Dowdall, J.R., De Weerd, P., Kennedy, H., and Fries, P. (2015). Visual Areas Exert Feedforward and Feedback Influences through Distinct Frequency Channels. Neuron *85*, 390–401.

Baudot, P., Levy, M., Marre, O., Monier, C., Pananceau, M., and Frégnac, Y. (2013). Animation of natural scene by virtual eye-movements evokes high precision and low noise in V1 neurons. Front. Neural Circuits *7*.

Belitski, A., Gretton, A., Magri, C., Murayama, Y., Montemurro, M.A., Logothetis, N.K., and Panzeri, S. (2008). Low-Frequency Local Field Potentials and Spikes in Primary Visual Cortex Convey Independent Visual Information. J. Neurosci. *28*, 5696–5709.

Beltramo, R., and Scanziani, M. (2019). A collicular visual cortex: Neocortical space for an ancient midbrain visual structure. Science *363*, 64–69.

Benucci, A., Frazor, R.A., and Carandini, M. (2007). Standing Waves and Traveling Waves Distinguish Two Circuits in Visual Cortex. Neuron *55*, 103–117.

Berens, P., Keliris, G.A., Ecker, A.S., Logothetis, N.K., and Tolias, A.S. (2008). Feature selectivity of the gamma-band of the local field potential in primate primary visual cortex. Front Neurosci *2*, 199–207.

Beul, S.F., Grant, S., and Hilgetag, C.C. (2015). A predictive model of the cat cortical connectome based on cytoarchitecture and distance. Brain Struct Funct *220*, 3167–3184.

Bharmauria, V., Bachatene, L., Cattan, S., Brodeur, S., Chanauria, N., Rouat, J., and Molotchnikoff, S. (2016). Network-selectivity and stimulus-discrimination in the primary visual cortex: cell-assembly dynamics. European Journal of Neuroscience *43*, 204–219.

Bijanzadeh, M., Nurminen, L., Merlin, S., Clark, A.M., and Angelucci, A. (2018). Distinct Laminar Processing of Local and Global Context in Primate Primary Visual Cortex. Neuron *100*, 259-274.e4.

Binzegger, T., Douglas, R.J., and Martin, K.A.C. (2004). A quantitative map of the circuit of cat primary visual cortex. J. Neurosci. *24*, 8441–8453.

Blakemore, C., and Tobin, E.A. (1972). Lateral inhibition between orientation detectors in the cat's visual cortex. Exp Brain Res *15*, 439–440.

Bonhoeffer, T., and Grinvald, A. (1991). Iso-orientation domains in cat visual cortex are arranged in pinwheel-like patterns. Nature *353*, 429–431.

Bonhoeffer, T., and Grinvald, A. (1993). The layout of iso-orientation domains in area 18 of cat visual cortex: optical imaging reveals a pinwheel-like organization. J. Neurosci. *13*, 4157–4180.

Bonhoeffer, T., Kim, D.S., Malonek, D., Shoham, D., and Grinvald, A. (1995). Optical imaging of the layout of functional domains in area 17 and across the area 17/18 border in cat visual cortex. Eur. J. Neurosci. *7*, 1973–1988.

Brady, N., and Field, D.J. (2000). Local contrast in natural images: normalisation and coding efficiency. Perception *29*, 1041–1055.

Bringuier, V., Chavane, F., Glaeser, L., and Frégnac, Y. (1999). Horizontal Propagation of Visual Activity in the Synaptic Integration Field of Area 17 Neurons. Science *283*, 695–699.

Brumberg, J.C., Nowak, L.G., and McCormick, D.A. (2000). Ionic mechanisms underlying repetitive high-frequency burst firing in supragranular cortical neurons. J. Neurosci. *20*, 4829–4843.

Brunet, N., Bosman, C.A., Roberts, M., Oostenveld, R., Womelsdorf, T., De Weerd, P., and Fries, P. (2015). Visual cortical gamma-band activity during free viewing of natural images. Cereb. Cortex *25*, 918–926.

Brunet, N.M., Bosman, C.A., Vinck, M., Roberts, M., Oostenveld, R., Desimone, R., Weerd, P.D., and Fries, P. (2014). Stimulus repetition modulates gamma-band synchronization in primate visual cortex. PNAS *111*, 3626–3631.

Brunswik, E. (1943). Organismic achievement and environmental probability. Psychological Review *50*, 255–272.

Bullier, J., and Henry, G.H. (1979). Laminar distribution of first-order neurons and afferent terminals in cat striate cortex. J. Neurophysiol. *42*, 1271–1281.

Bullier, J., Kennedy, H., and Salinger, W. (1984). Bifurcation of subcortical afferents to visual areas 17, 18, and 19 in the cat cortex. Journal of Comparative Neurology *228*, 309–328.

Butts, D.A., Weng, C., Jin, J., Yeh, C.-I., Lesica, N.A., Alonso, J.-M., and Stanley, G.B. (2007). Temporal precision in the neural code and the timescales of natural vision. Nature *449*, 92–95.

Buzsaki, G. (2006). Rhythms of the Brain (Oxford University Press).

Carandini, M., Heeger, D.J., and Anthony Movshon, J. (1999). Linearity and Gain Control in V1 Simple Cells. In Models of Cortical Circuits, P.S. Ulinski, E.G. Jones, and A. Peters, eds. (Boston, MA: Springer US), pp. 401–443.

Carandini, M., Demb, J.B., Mante, V., Tolhurst, D.J., Dan, Y., Olshausen, B.A., Gallant, J.L., and Rust, N.C. (2005). Do we know what the early visual system does? J. Neurosci. *25*, 10577–10597.

Cardin, J.A., Carlén, M., Meletis, K., Knoblich, U., Zhang, F., Deisseroth, K., Tsai, L.-H., and Moore, C.I. (2009). Driving fast-spiking cells induces gamma rhythm and controls sensory responses. Nature *459*, 663–667.

Casanova, C., Nordmann, J.P., Ohzawa, I., and Freeman, R.D. (1992). Direction selectivity of cells in the cat's striate cortex: differences between bar and grating stimuli. Vis. Neurosci. *9*, 505–513.

Cavanaugh, J.R., Bair, W., and Movshon, J.A. (2002). Nature and interaction of signals from the receptive field center and surround in macaque V1 neurons. J. Neurophysiol. *88*, 2530–2546.

Chao-Yi, L., and Wu, L. (1994). Extensive integration field beyond the classical receptive field of cat's striate cortical neurons—Classification and tuning properties. Vision Research *34*, 2337–2355.

Chavane, F., Sharon, D., Jancke, D., Marre, O., Frégnac, Y., and Grinvald, A. (2011). Lateral Spread of Orientation Selectivity in V1 is Controlled by Intracortical Cooperativity. Front Syst Neurosci *5*, 4.

Chen, K., Ding, A.-M., Liang, X.-H., Zhang, L.-P., Wang, L., and Song, X.-M. (2015). Effect of Contrast on Visual Spatial Summation in Different Cell Categories in Cat Primary Visual Cortex. PLoS ONE *10*, e0144403.

Chen, W., Zhang, J.J., Hu, G.Y., and Wu, C.P. (1996). Different mechanisms underlying the repolarization of narrow and wide action potentials in pyramidal cells and interneurons of cat motor cortex. Neuroscience *73*, 57–68.

Chichilnisky, E.J., and Kalmar, R.S. (2002). Functional asymmetries in ON and OFF ganglion cells of primate retina. J. Neurosci. *22*, 2737–2747.

Churchland, M.M., Yu, B.M., Cunningham, J.P., Sugrue, L.P., Cohen, M.R., Corrado, G.S., Newsome, W.T., Clark, A.M., Hosseini, P., Scott, B.B., et al. (2010). Stimulus onset quenches neural variability: a widespread cortical phenomenon. Nat Neurosci *13*, 369–378.

Clancy, K.B., Schnepel, P., Rao, A.T., and Feldman, D.E. (2015). Structure of a Single Whisker Representation in Layer 2 of Mouse Somatosensory Cortex. J. Neurosci. *35*, 3946–3958.

Coen-Cagli, R., Kohn, A., and Schwartz, O. (2015). Flexible gating of contextual influences in natural vision. Nat. Neurosci. *18*, 1648–1655.

Cohen, M.R., and Kohn, A. (2011). Measuring and interpreting neuronal correlations. Nature Neuroscience *14*, 811–819.

Crair, M.C., Gillespie, D.C., and Stryker, M.P. (1998). The role of visual experience in the development of columns in cat visual cortex. Science *279*, 566–570.

Cui, Y., Liu, L.D., McFarland, J.M., Pack, C.C., and Butts, D.A. (2016). Inferring Cortical Variability from Local Field Potentials. J. Neurosci. *36*, 4121–4135.

Cunningham, M.O., Whittington, M.A., Bibbig, A., Roopun, A., LeBeau, F.E.N., Vogt, A., Monyer, H., Buhl, E.H., and Traub, R.D. (2004). A role for fast rhythmic bursting neurons in cortical gamma oscillations in vitro. Proc. Natl. Acad. Sci. U.S.A. *101*, 7152–7157.

David, S.V., Vinje, W.E., and Gallant, J.L. (2004). Natural stimulus statistics alter the receptive field structure of v1 neurons. J. Neurosci. *24*, 6991–7006.

De Valois, R.L., Cottaris, N.P., Mahon, L.E., Elfar, S.D., and Wilson, J.A. (2000). Spatial and temporal receptive fields of geniculate and cortical cells and directional selectivity. Vision Res. *40*, 3685–3702.

De Valois, R.L., Albrecht, D.G., and Thorell, L.G. (1982). Spatial frequency selectivity of cells in macaque visual cortex. Vision Res. *22*, 545–559.

Dean, A.F., and Tolhurst, D.J. (1983). On the distinctness of simple and complex cells in the visual cortex of the cat. J. Physiol. (Lond.) *344*, 305–325.

DeAngelis, G.C., Ohzawa, I., and Freeman, R.D. (1993). Spatiotemporal organization of simple-cell receptive fields in the cat's striate cortex. II. Linearity of temporal and spatial summation. J. Neurophysiol. *69*, 1118–1135.

DeAngelis, G.C., Freeman, R.D., and Ohzawa, I. (1994a). Length and width tuning of neurons in the cat's primary visual cortex. J. Neurophysiol. *71*, 347–374.

DeAngelis, G.C., Ohzawa, I., and Freeman, R.D. (1995). Receptive-field dynamics in the central visual pathways. Trends Neurosci. *18*, 451–458.

DeAngelis, G.C., Ghose, G.M., Ohzawa, I., and Freeman, R.D. (1999). Functional micro-organization of primary visual cortex: receptive field analysis of nearby neurons. J. Neurosci. *19*, 4046–4064.

Deneve, S., and Chalk, M. (2016). Efficiency turns the table on neural encoding, decoding and noise. Current Opinion in Neurobiology *37*, 141–148.

Desbordes, G., Jin, J., Weng, C., Lesica, N.A., Stanley, G.B., and Alonso, J.-M. (2008). Timing Precision in Population Coding of Natural Scenes in the Early Visual System. PLOS Biology *6*, e324.

Desimone, R. (1996). Neural mechanisms for visual memory and their role in attention. Proc. Natl. Acad. Sci. U.S.A. *93*, 13494–13499.

Ditchburn, R. W. (1973). Eye-Movements and Visual Perception. Oxford: Clarendon Press

Ditchburn, R.W., and Ginsborg, B.L. (1952). Vision with a stabilized retinal image. Nature *170*, 36–37.

Dong, D.W., and Atick, J.J. (1995). Statistics of natural time-varying images. Network Computation in Neural Systems *6*, 345–358.

Douglas, R.J., and Martin, K.A. (1991). A functional microcircuit for cat visual cortex. J. Physiol. (Lond.) *440*, 735–769.

Douglas, R.J., and Martin, K.A.C. Canonical Cortical Circuits (Oxford University Press).

Durand, S., Freeman, T.C.B., and Carandini, M. (2007). Temporal properties of surround suppression in cat primary visual cortex. Vis. Neurosci. *24*, 679–690.

Ecker, A.S., Berens, P., Keliris, G.A., Bethge, M., Logothetis, N.K., and Tolias, A.S. (2010). Decorrelated Neuronal Firing in Cortical Microcircuits. Science *327*, 584–587.

Ecker, A.S., Berens, P., Cotton, R.J., Subramaniyan, M., Denfield, G.H., Cadwell, C.R., Smirnakis, S.M., Bethge, M., and Tolias, A.S. (2014). State dependence of noise correlations in macaque primary visual cortex. Neuron *82*, 235–248.

Eckert, M.P., and Zeil, J. (2001). Towards an Ecology of Motion Vision. In Motion Vision: Computational, Neural, and Ecological Constraints, J.M. Zanker, and J. Zeil, eds. (Berlin, Heidelberg: Springer Berlin Heidelberg), pp. 333–369.

Einevoll, G.T., Pettersen, K.H., Devor, A., Ulbert, I., Halgren, E., and Dale, A.M. (2007). Laminar population analysis: estimating firing rates and evoked synaptic activity from multielectrode recordings in rat barrel cortex. J. Neurophysiol. *97*, 2174–2190.

Einevoll, G.T., Kayser, C., Logothetis, N.K., and Panzeri, S. (2013). Modelling and analysis of local field potentials for studying the function of cortical circuits. Nat. Rev. Neurosci. *14*, 770–785.

Einstein, G., and Fitzpatrick, D. (1991). Distribution and morphology of area 17 neurons that project to the cat's extrastriate cortex. J. Comp. Neurol. *303*, 132–149.

Eizenman, M., Hallett, P.E., and Frecker, R.C. (1985). Power spectra for ocular drift and tremor. Vision Res. *25*, 1635–1640.

El-Beheiry, H., and Puil, E. (1989). Postsynaptic depression induced by isoflurane and Althesin in neocortical neurons. Exp Brain Res *75*, 361–368.

Emerson, R.C., Citron, M.C., Vaughn, W.J., and Klein, S.A. (1987). Nonlinear directionally selective subunits in complex cells of cat striate cortex. J. Neurophysiol. *58*, 33–65.

Enroth-Cugell, C., and Robson, J.G. (1966). The contrast sensitivity of retinal ganglion cells of the cat. J. Physiol. (Lond.) *187*, 517–552.

Evans, D.A., Stempel, A.V., Vale, R., Ruehle, S., Lefler, Y., and Branco, T. (2018). A synaptic threshold mechanism for computing escape decisions. Nature *558*, 590–594.

Everson, R.M., Prashanth, A.K., Gabbay, M., Knight, B.W., Sirovich, L., and Kaplan, E. (1998). Representation of spatial frequency and orientation in the visual cortex. Proc. Natl. Acad. Sci. U.S.A. *95*, 8334–8338.

Felleman, D.J., and Van Essen, D.C. (1991). Distributed hierarchical processing in the primate cerebral cortex. Cereb. Cortex *1*, 1–47.

Felsen, G., and Dan, Y. (2005). A natural approach to studying vision. Nat. Neurosci. *8*, 1643–1646.

Felsen, G., Touryan, J., Han, F., and Dan, Y. (2005). Cortical sensitivity to visual features in natural scenes. PLoS Biol. *3*, e342.

Field, D.J. (1987). Relations between the statistics of natural images and the response properties of cortical cells. J Opt Soc Am A *4*, 2379–2394.

Fino, E., and Yuste, R. (2011). Dense inhibitory connectivity in neocortex. Neuron *69*, 1188–1203.

Foster, K.H., Gaska, J.P., Nagler, M., and Pollen, D.A. (1985). Spatial and temporal frequency selectivity of neurones in visual cortical areas V1 and V2 of the macaque monkey. J. Physiol. (Lond.) *365*, 331–363.

Fournier, J., Monier, C., Pananceau, M., and Frégnac, Y. (2011). Adaptation of the simple or complex nature of V1 receptive fields to visual statistics. Nat. Neurosci. *14*, 1053–1060.

Fournier, J., Monier, C., Levy, M., Marre, O., Sári, K., Kisvárday, Z.F., and Frégnac, Y. (2014). Hidden complexity of synaptic receptive fields in cat V1. J. Neurosci. *34*, 5515–5528.

Fournier, J., Müller, C.M., Schneider, I., and Laurent, G. (2018). Spatial Information in a Non-retinotopic Visual Cortex. Neuron *97*, 164-180.e7.

Freeman, J., Ziemba, C.M., Heeger, D.J., Simoncelli, E.P., and Movshon, J.A. (2013). A functional and perceptual signature of the second visual area in primates. Nature Neuroscience *16*, 974–981.

Frégnac, Y. (2012). Reading Out the Synaptic Echoes of Low-Level Perception in V1. In Computer Vision – ECCV 2012. Workshops and Demonstrations, A. Fusiello, V. Murino, and R. Cucchiara, eds. (Springer Berlin Heidelberg), pp. 486–495.

Frégnac, Y., and Bathellier, B. (2015). Cortical Correlates of Low-Level Perception: From Neural Circuits to Percepts. Neuron *88*, 110–126.

Frégnac, Y., and Bringuier, V. (1996). - Spatio-temporal dynamics of synaptic integration in cat visual cortical receptive fields. In Brain Theory, A. Aertsen, and V. Braitenberg, eds. (Amsterdam: Elsevier Science B.V.), pp. 143–199.

Friedman-Hill, S., Maldonado, P.E., and Gray, C.M. (2000). Dynamics of striate cortical activity in the alert macaque: I. Incidence and stimulus-dependence of gamma-band neuronal oscillations. Cereb. Cortex *10*, 1105–1116.

Friedrich, R.W. (2013). Neuronal computations in the olfactory system of zebrafish. Annu. Rev. Neurosci. *36*, 383–402.

Friend, S.M., and Baker, C.L. (1993). Spatio-temporal frequency separability in area 18 neurons of the cat. Vision Res. *33*, 1765–1771.

Fries, P., Nikolić, D., and Singer, W. (2007). The gamma cycle. Trends Neurosci. *30*, 309–316.

Froudarakis, E., Berens, P., Ecker, A.S., Cotton, R.J., Sinz, F.H., Yatsenko, D., Saggau, P., Bethge, M., and Tolias, A.S. (2014). Population code in mouse V1 facilitates readout of natural scenes through increased sparseness. Nature Neuroscience *17*, 851–857.

Gabbott, P.L., and Somogyi, P. (1986). Quantitative distribution of GABA-immunoreactive neurons in the visual cortex (area 17) of the cat. Exp Brain Res *61*, 323–331.

Galambos, R. (1992). A Comparison of Certain Gamma Band (40-HZ) Brain Rhythms in Cat and Man. In Induced Rhythms in the Brain, E. Başar, and T.H. Bullock, eds. (Boston, MA: Birkhäuser Boston), pp. 201–216.

Galerne, B., Gousseau, Y., and Morel, J.-M. (2011). Random Phase Textures: Theory and Synthesis. IEEE Transactions on Image Processing *20*, 257–267.

Gardner, J.L., Anzai, A., Ohzawa, I., and Freeman, R.D. (1999). Linear and nonlinear contributions to orientation tuning of simple cells in the cat's striate cortex. Vis. Neurosci. *16*, 1115–1121.

Gaska, J.P., Jacobson, L.D., Chen, H.W., and Pollen, D.A. (1994). Space-time spectra of complex cell filters in the macaque monkey: a comparison of results obtained with pseudowhite noise and grating stimuli. Vis. Neurosci. *11*, 805–821.

Gatys, L.A., Ecker, A.S., and Bethge, M. (2015). A Neural Algorithm of Artistic Style. ArXiv:1508.06576 [Cs, q-Bio].

Geisler, W.S. (2008). Visual perception and the statistical properties of natural scenes. Annu Rev Psychol *59*, 167–192.

Geisler, W.S., Perry, J.S., Super, B.J., and Gallogly, D.P. (2001). Edge co-occurrence in natural images predicts contour grouping performance. Vision Res. *41*, 711–724.

Gerard-Mercier, F., Carelli, P.V., Pananceau, M., Troncoso, X.G., and Frégnac, Y. (2016). Synaptic Correlates of Low-Level Perception in V1. J. Neurosci. *36*, 3925–3942.

Gibaldi, A., and Banks, M.S. (2019). Binocular Eye Movements are Adapted to the Natural Environment. J. Neurosci. 2591–18.

Gilbert, C.D., and Wiesel, T.N. (1983). Clustered intrinsic connections in cat visual cortex. J. Neurosci. *3*, 1116–1133.

Gilbert, C.D., and Wiesel, T.N. (1989). Columnar specificity of intrinsic horizontal and corticocortical connections in cat visual cortex. J. Neurosci. *9*, 2432–2442.

Goldin, M.A., and Mindlin, G.B. (2017). Temperature manipulation of neuronal dynamics in a forebrain motor control nucleus. PLOS Computational Biology *13*, e1005699.

Goldin, M.A., Harrell, E.R., Estebanez, L., and Shulz, D.E. (2018). Rich spatio-temporal stimulus dynamics unveil sensory specialization in cortical area S2. Nat Commun *9*, 1–11.

Gollisch, T., and Meister, M. (2010). Eye smarter than scientists believed: neural computations in circuits of the retina. Neuron *65*, 150–164.

Goris, R.L.T., Movshon, J.A., and Simoncelli, E.P. (2014). Partitioning neuronal variability. Nature Neuroscience *17*, 858–865.

Goris, R.L.T., Simoncelli, E.P., and Movshon, J.A. (2015). Origin and Function of Tuning Diversity in Macaque Visual Cortex. Neuron *88*, 819–831.

Gray, C.M., and McCormick, D.A. (1996). Chattering cells: superficial pyramidal neurons contributing to the generation of synchronous oscillations in the visual cortex. Science *274*, 109–113.

Gray, C.M., and Singer, W. (1989). Stimulus-specific neuronal oscillations in orientation columns of cat visual cortex. Proc. Natl. Acad. Sci. U.S.A. *86*, 1698–1702.

Guitton, D., Douglas, R.M., and Volle, M. (1984). Eye-head coordination in cats. Journal of Neurophysiology *52*, 1030–1050.

Guo, K., Robertson, R.G., Mahmoodi, S., and Young, M.P. (2005). Centre-surround interactions in response to natural scene stimulation in the primary visual cortex. Eur. J. Neurosci. *21*, 536–548.

Guo, Z.V., Li, N., Huber, D., Ophir, E., Gutnisky, D., Ting, J.T., Feng, G., and Svoboda, K. (2014). Flow of cortical activity underlying a tactile decision in mice. Neuron *81*, 179–194.

Haider, B., Krause, M.R., Duque, A., Yu, Y., Touryan, J., Mazer, J.A., and McCormick, D.A. (2010). Synaptic and Network Mechanisms of Sparse and Reliable Visual Cortical Activity during Nonclassical Receptive Field Stimulation. Neuron *65*, 107–121.

Hall, A.J., and Lomber, S.G. (2008). Auditory cortex projections target the peripheral field representation of primary visual cortex. Exp Brain Res *190*, 413–430.

Hall, J.A., Foster, R.E., Ebner, F.F., and Hall, W.C. (1977). Visual cortex in a reptile, the turtle (Pseudem ys scripta and Chrysem ys picta). Brain Research *130*, 197–216.

Hamilton, D.B., Albrecht, D.G., and Geisler, W.S. (1989). Visual cortical receptive fields in monkey and cat: spatial and temporal phase transfer function. Vision Res. *29*, 1285–1308.

Hansen, B.J., Chelaru, M.I., and Dragoi, V. (2012). Correlated Variability in Laminar Cortical Circuits. Neuron *76*, 590–602.

Harris, K.D., and Mrsic-Flogel, T.D. (2013). Cortical connectivity and sensory coding. Nature *503*, 51–58.

Hartline, H.K. (1938). The response of single optic nerve fibers of the vertebrate eye to illumination of the retina. American Journal of Physiology *121*, 400–415.

Hirsch, J.A., Gallagher, C.A., Alonso, J.M., and Martinez, L.M. (1998). Ascending projections of simple and complex cells in layer 6 of the cat striate cortex. J. Neurosci. *18*, 8086–8094.

Hirsch, J.A., Martinez, L.M., Alonso, J.-M., Desai, K., Pillai, C., and Pierre, C. (2002). Synaptic physiology of the flow of information in the cat's visual cortex in vivo. J. Physiol. (Lond.) *540*, 335–350.

Hofer, S.B., Ko, H., Pichler, B., Vogelstein, J., Ros, H., Zeng, H., Lein, E., Lesica, N.A., and Mrsic-Flogel, T.D. (2011). Differential connectivity and response dynamics of excitatory and inhibitory neurons in visual cortex. Nat. Neurosci. *14*, 1045–1052.

Houk, J.C., Adams, J.L., and Barto, A.G. (1995). A model of how the basal ganglia generate and use neural signals that predict reinforcement. In Models of Information Processing in the Basal Ganglia, (Cambridge, MA, US: The MIT Press), pp. 249–270.

Houzel, J.C., Milleret, C., and Innocenti, G. (1994). Morphology of callosal axons interconnecting areas 17 and 18 of the cat. Eur. J. Neurosci. *6*, 898–917.

Hubel, D.H., and Wiesel, T.N. (1959). Receptive fields of single neurones in the cat's striate cortex. J. Physiol. (Lond.) *148*, 574–591.

Hubel, D.H., and Wiesel, T.N. (1962). Receptive fields, binocular interaction and functional architecture in the cat's visual cortex. J. Physiol. (Lond.) *160*, 106–154.

Hubel, D.H., and Wiesel, T.N. (1969). Anatomical demonstration of columns in the monkey striate cortex. Nature *221*, 747–750.

Hübener, M., Schwarz, C., and Bolz, J. (1990). Morphological types of projection neurons in layer 5 of cat visual cortex. J. Comp. Neurol. *301*, 655–674.

Humphrey, A.L., Sur, M., Uhlrich, D.J., and Sherman, S.M. (1985). Termination patterns of individual X- and Y-cell axons in the visual cortex of the cat: projections to area 18, to the 17/18 border region, and to both areas 17 and 18. J. Comp. Neurol. *233*, 190–212.

Ichida, J.M., Schwabe, L., Bressloff, P.C., and Angelucci, A. (2007). Response Facilitation From the "Suppressive" Receptive Field Surround of Macaque V1 Neurons. Journal of Neurophysiology *98*, 2168–2181.

Ikeda, H., and Wright, M.J. (1974). Sensitivity of neurones in visual cortex (area 17) under different levels of anaesthesia. Exp Brain Res *20*, 471–484.

Ikeda, H., and Wright, M.J. (1975). The relationship between the "sustained-transient" and the "simple-complex" classifications of neurones in area 17 of the cat. J. Physiol. (Lond.) *244*, 58P-59P.

Isett, B.R., Feasel, S.H., Lane, M.A., and Feldman, D.E. (2018). Slip-Based Coding of Local Shape and Texture in Mouse S1. Neuron *97*, 418-433.e5.

Issa, N.P., Trepel, C., and Stryker, M.P. (2000). Spatial frequency maps in cat visual cortex. J. Neurosci. *20*, 8504–8514.

Istvan, P.J., and Zarzecki, P. (1994). Intrinsic discharge patterns and somatosensory inputs for neurons in raccoon primary somatosensory cortex. J. Neurophysiol. *72*, 2827–2839.

Jin, J., Wang, Y., Swadlow, H.A., and Alonso, J.M. (2011). Population receptive fields of ON and OFF thalamic inputs to an orientation column in visual cortex. Nat. Neurosci. *14*, 232–238.

Jin, J.Z., Weng, C., Yeh, C.-I., Gordon, J.A., Ruthazer, E.S., Stryker, M.P., Swadlow, H.A., and Alonso, J.-M. (2008). On and off domains of geniculate afferents in cat primary visual cortex. Nat. Neurosci. *11*, 88–94.

Jones, J.P., and Palmer, L.A. (1987a). An evaluation of the two-dimensional Gabor filter model of simple receptive fields in cat striate cortex. J. Neurophysiol. *58*, 1233–1258.

Jones, J.P., and Palmer, L.A. (1987b). The two-dimensional spatial structure of simple receptive fields in cat striate cortex. J. Neurophysiol. *58*, 1187–1211.

Kamondi, A., Acsády, L., Wang, X.J., and Buzsáki, G. (1998). Theta oscillations in somata and dendrites of hippocampal pyramidal cells in vivo: activity-dependent phase-precession of action potentials. Hippocampus *8*, 244–261.

Kampa, B.M., Roth, M.M., Göbel, W., and Helmchen, F. (2011). Representation of visual scenes by local neuronal populations in layer 2/3 of mouse visual cortex. Front Neural Circuits *5*.

Kara, P., Reinagel, P., and Reid, R.C. (2000). Low Response Variability in Simultaneously Recorded Retinal, Thalamic, and Cortical Neurons. Neuron *27*, 635–646.

Katz, L.C. (1987). Local circuitry of identified projection neurons in cat visual cortex brain slices. J. Neurosci. *7*, 1223–1249.

Kayser, A., Priebe, N.J., and Miller, K.D. (2001). Contrast-dependent nonlinearities arise locally in a model of contrast-invariant orientation tuning. J. Neurophysiol. *85*, 2130–2149.

Kayser, C., Salazar, R.F., and König, P. (2003). Responses to Natural Scenes in Cat V1. Journal of Neurophysiology *90*, 1910–1920.

Kelly, J.P., and Van Essen, D.C. (1974). Cell structure and function in the visual cortex of the cat. J. Physiol. (Lond.) *238*, 515–547.

Kelly, S.T., Kremkow, J., Jin, J., Wang, Y., Wang, Q., Alonso, J.-M., and Stanley, G.B. (2014). The Role of Thalamic Population Synchrony in the Emergence of Cortical Feature Selectivity. PLOS Computational Biology *10*, e1003418.

Kerkoerle, T. van, Self, M.W., Dagnino, B., Gariel-Mathis, M.-A., Poort, J., Togt, C. van der, and Roelfsema, P.R. (2014). Alpha and gamma oscillations characterize feedback and feedforward processing in monkey visual cortex. PNAS *111*, 14332–14341.

Kim, T., and Freeman, R.D. (2016). Direction selectivity of neurons in the visual cortex is non-linear and lamina-dependent. Eur. J. Neurosci. *43*, 1389–1399.

Kisvárday, Z.F., Martin, K.A., Freund, T.F., Maglóczky, Z., Whitteridge, D., and Somogyi, P. (1986). Synaptic targets of HRP-filled layer III pyramidal cells in the cat striate cortex. Exp Brain Res *64*, 541–552.

Kisvárday, Z.F., Beaulieu, C., and Eysel, U.T. (1993). Network of GABAergic large basket cells in cat visual cortex (area 18): implication for lateral disinhibition. J. Comp. Neurol. *327*, 398–415.

Kisvárday, Z.F., Buzás, P., and Eysel, U.T. (2001). Calculating direction maps from intrinsic signals revealed by optical imaging. Cereb. Cortex *11*, 636–647.

Ko, H., Hofer, S.B., Pichler, B., Buchanan, K.A., Sjöström, P.J., and Mrsic-Flogel, T.D. (2011). Functional specificity of local synaptic connections in neocortical networks. Nature *473*, 87–91.

Kohn, A., and Smith, M.A. (2005). Stimulus Dependence of Neuronal Correlation in Primary Visual Cortex of the Macaque. J. Neurosci. *25*, 3661–3673.

Kohn, A., Coen-Cagli, R., Kanitscheider, I., and Pouget, A. (2016). Correlations and Neuronal Population Information. Annu. Rev. Neurosci. *39*, 237–256.

Körding, K.P., Kayser, C., Betsch, B.Y., and König, P. (2001). Non-contact eye-tracking on cats. J. Neurosci. Methods *110*, 103–111.

Kremkow, J., and Alonso, J.-M. (2018). Thalamocortical Circuits and Functional Architecture. Annu Rev Vis Sci.

Kremkow, J., Jin, J., Komban, S.J., Wang, Y., Lashgari, R., Li, X., Jansen, M., Zaidi, Q., and Alonso, J.-M. (2014). Neuronal nonlinearity explains greater visual spatial resolution for darks than lights. Proc. Natl. Acad. Sci. U.S.A. *111*, 3170–3175.

Kremkow, J., Jin, J., Wang, Y., and Alonso, J.M. (2016). Principles underlying sensory map topography in primary visual cortex. Nature *533*, 52–57.

Kremkow, J., Perrinet, L.U., Monier, C., Alonso, J.-M., Aertsen, A., Frégnac, Y., and Masson, G.S. (2016b). Push-Pull Receptive Field Organization and Synaptic Depression: Mechanisms for Reliably Encoding Naturalistic Stimuli in V1. Front. Neural Circuits *10*.

Kuffler, S.W. (1953). Discharge patterns and functional organization of mammalian retina. J. Neurophysiol. *16*, 37–68.

Kulikowski, J.J., and Bishop, P.O. (1981). Linear analysis of the responses of simple cells in the cat visual cortex. Exp Brain Res *44*, 386–400.

Kumbhani, R.D., Nolt, M.J., and Palmer, L.A. (2007). Precision, Reliability, and Information-Theoretic Analysis of Visual Thalamocortical Neurons. Journal of Neurophysiology *98*, 2647–2663.

Land, R., Engler, G., Kral, A., and Engel, A.K. (2013). Response properties of local field potentials and multiunit activity in the mouse visual cortex. Neuroscience *254*, 141–151.

Lashgari, R., Li, X., Chen, Y., Kremkow, J., Bereshpolova, Y., Swadlow, H.A., and Alonso, J.-M. (2012). Response properties of local field potentials and neighboring single neurons in awake primary visual cortex. J. Neurosci. *32*, 11396–11413.

Le Bec B., Troncoso X.G., Desbois C., Fregnac Y. and Pananceau M. (2018) Propagation of "network belief" in the primary visual cortex : synaptic contribution of the horizontal intrinsic connectivity. Annual meeting of the Society for Neuroscience, San Diego.

Lee, S.-H., Kwan, A.C., Zhang, S., Phoumthipphavong, V., Flannery, J.G., Masmanidis, S.C., Taniguchi, H., Huang, Z.J., Zhang, F., Boyden, E.S., et al. (2012). Activation of specific interneurons improves V1 feature selectivity and visual perception. Nature *488*, 379–383.

Leon, P.S., Vanzetta, I., Masson, G.S., and Perrinet, L.U. (2012). Motion clouds: model-based stimulus synthesis of natural-like random textures for the study of motion perception. Journal of Neurophysiology *107*, 3217–3226.

LeVay, S., and Gilbert, C.D. (1976). Laminar patterns of geniculocortical projection in the cat. Brain Res. *113*, 1–19.

Levitt, J.B., and Lund, J.S. (1997). Contrast dependence of contextual effects in primate visual cortex. Nature *387*, 73–76.

Lewicki, M.S. (1998). A review of methods for spike sorting: the detection and classification of neural action potentials. 26.

Lin, I.-C., Okun, M., Carandini, M., and Harris, K.D. (2015). The Nature of Shared Cortical Variability. Neuron *87*, 644–656.

Luczak, A., Bartho, P., and Harris, K.D. (2013). Gating of Sensory Input by Spontaneous Cortical Activity. J. Neurosci. *33*, 1684–1695.

Lund, J.S., Henry, G.H., MacQueen, C.L., and Harvey, A.R. (1979). Anatomical organization of the primary visual cortex (area 17) of the cat. A comparison with area 17 of the macaque monkey. J. Comp. Neurol. *184*, 599–618.

Maffei, L., and Fiorentini, A. (1976). The unresponsive regions of visual cortical receptive fields. Vision Research *16*, 1131-IN5.

Maier, A., Adams, G.K., Aura, C., and Leopold, D.A. (2010). Distinct superficial and deep laminar domains of activity in the visual cortex during rest and stimulation. Front Syst Neurosci *4*.

Mainen, Z.F., and Sejnowski, T.J. (1995). Reliability of spike timing in neocortical neurons. Science *268*, 1503–1506.

Mante, V., Frazor, R.A., Bonin, V., Geisler, W.S., and Carandini, M. (2005). Independence of luminance and contrast in natural scenes and in the early visual system. Nat. Neurosci. *8*, 1690–1697.

Mariño, J., Schummers, J., Lyon, D.C., Schwabe, L., Beck, O., Wiesing, P., Obermayer, K., and Sur, M. (2005). Invariant computations in local cortical networks with balanced excitation and inhibition. Nature Neuroscience *8*, 194–201.

Markov, N.T., Vezoli, J., Chameau, P., Falchier, A., Quilodran, R., Huissoud, C., Lamy, C., Misery, P., Giroud, P., Ullman, S., et al. (2013). Anatomy of hierarchy: Feedforward and feedback pathways in macaque visual cortex. J Comp Neurol *522*, 225–259.

Markram, H., Toledo-Rodriguez, M., Wang, Y., Gupta, A., Silberberg, G., and Wu, C. (2004). Interneurons of the neocortical inhibitory system. Nat. Rev. Neurosci. *5*, 793–807.

Martin, K.A., and Whitteridge, D. (1984). Form, function and intracortical projections of spiny neurones in the striate visual cortex of the cat. J. Physiol. (Lond.) *353*, 463–504.

Martin, K.A.C., and Schröder, S. (2013). Functional Heterogeneity in Neighboring Neurons of Cat Primary Visual Cortex in Response to Both Artificial and Natural Stimuli. J. Neurosci. *33*, 7325–7344.

Martin, K.A.C., and Schröder, S. (2016). Phase Locking of Multiple Single Neurons to the Local Field Potential in Cat V1. J. Neurosci. *36*, 2494–2502.

Martinez, L.M., and Alonso, J.-M. (2003). Complex receptive fields in primary visual cortex. Neuroscientist *9*, 317–331.

Martinez, L.M., Alonso, J.-M., Reid, R.C., and Hirsch, J.A. (2002). Laminar processing of stimulus orientation in cat visual cortex. J. Physiol. (Lond.) *540*, 321–333.

Martinez, L.M., Wang, Q., Reid, R.C., Pillai, C., Alonso, J.-M., Sommer, F.T., and Hirsch, J.A. (2005). Receptive field structure varies with layer in the primary visual cortex. Nat. Neurosci. *8*, 372–379.

McCormick, D.A., Connors, B.W., Lighthall, J.W., and Prince, D.A. (1985). Comparative electrophysiology of pyramidal and sparsely spiny stellate neurons of the neocortex. J. Neurophysiol. *54*, 782–806.

Meir, I., Katz, Y., and Lampl, I. (2018). Membrane Potential Correlates of Network Decorrelation and Improved SNR by Cholinergic Activation in the Somatosensory Cortex. J. Neurosci. *38*, 10692–10708.

Meyer, G., and Albus, K. (1981). Spiny stellates as cells of origin of association fibres from area 17 to area 18 in the cat's neocortex. Brain Res. *210*, 335–341.

Miller, J.K., Ayzenshtat, I., Carrillo-Reid, L., and Yuste, R. (2014). Visual stimuli recruit intrinsically generated cortical ensembles. PNAS *111*, E4053–E4061.

Mitchell, J.F., Reynolds, J.H., and Miller, C.T. (2014). Active vision in marmosets: a model system for visual neuroscience. J. Neurosci. *34*, 1183–1194.

Mitzdorf, U. (1985). Current source-density method and application in cat cerebral cortex: investigation of evoked potentials and EEG phenomena. Physiol. Rev. *65*, 37–100.

Mochizuki, Y., Onaga, T., Shimazaki, H., Shimokawa, T., Tsubo, Y., Kimura, R., Saiki, A., Sakai, Y., Isomura, Y., Fujisawa, S., et al. (2016). Similarity in Neuronal Firing Regimes across Mammalian Species. J. Neurosci. *36*, 5736–5747.

Molotchnikoff, S., Gillet, P.-C., Shumikhina, S., and Bouchard, M. (2007). Spatial frequency characteristics of nearby neurons in cats' visual cortex. Neurosci. Lett. *418*, 242–247.

Monier, C., Fournier, J., and Frégnac, Y. (2008). In vitro and in vivo measures of evoked excitatory and inhibitory conductance dynamics in sensory cortices. J. Neurosci. Methods *169*, 323–365.

Morasso, P., Bizzi, E., and Dichgans, J. (1973). Adjustment of saccade characteristics during head movements. Exp Brain Res *16*, 492–500.

Mountcastle, V.B. (1957). Modality and topographic properties of single neurons of cat's somatic sensory cortex. J. Neurophysiol. *20*, 408–434.

Movshon, J.A., Thompson, I.D., and Tolhurst, D.J. (1978). Spatial and temporal contrast sensitivity of neurones in areas 17 and 18 of the cat's visual cortex. J. Physiol. (Lond.) *283*, 101–120.

Mulligan, K.A., and Ulinski, P.S. (1990). Organization of geniculocortical projections in turtles: isoazimuth lamellae in the visual cortex. J. Comp. Neurol. *296*, 531–547.

Nauhaus, I., Benucci, A., Carandini, M., and Ringach, D.L. (2008). Neuronal selectivity and local map structure in visual cortex. Neuron *57*, 673–679.

Nawrot, M.P., Schnepel, P., Aertsen, A., and Boucsein, C. (2009). Precisely timed signal transmission in neocortical networks with reliable intermediate-range projections. Front. Neural Circuits *3*.

Nishimura, Y., Asahi, M., Saitoh, K., Kitagawa, H., Kumazawa, Y., Itoh, K., Lin, M., Akamine, T., Shibuya, H., Asahara, T., et al. (2001). Ionic mechanisms underlying burst firing of layer III sensorimotor cortical neurons of the cat: an in vitro slice study. J. Neurophysiol. *86*, 771–781.

Nishiyama, M., Matsui, T., Murakami, T., Hagihara, K.M., and Ohki, K. (2019). Cell-Type-Specific Thalamocortical Inputs Constrain Direction Map Formation in Visual Cortex. Cell Reports *26*, 1082-1088.e3.

Nowak, L.G., and Bullier, J. (1997). The Timing of Information Transfer in the Visual System. In Extrastriate Cortex in Primates, K.S. Rockland, J.H. Kaas, and A. Peters, eds. (Boston, MA: Springer US), pp. 205–241.

Nowak, L.G., Sanchez-Vives, M.V., and McCormick, D.A. (1997). Influence of low and high frequency inputs on spike timing in visual cortical neurons. Cereb. Cortex *7*, 487–501.

Nowak, L.G., Azouz, R., Sanchez-Vives, M.V., Gray, C.M., and McCormick, D.A. (2003). Electrophysiological classes of cat primary visual cortical neurons in vivo as revealed by quantitative analyses. J. Neurophysiol. *89*, 1541–1566.

Nurminen, L., Merlin, S., Bijanzadeh, M., Federer, F., and Angelucci, A. (2018). Top-down feedback controls spatial summation and response amplitude in primate visual cortex. Nat Commun *9*, 1–13.

Ohki, K., Chung, S., Ch'ng, Y.H., Kara, P., and Reid, R.C. (2005). Functional imaging with cellular resolution reveals precise micro-architecture in visual cortex. Nature *433*, 597–603.

Okun, M., Naim, A., and Lampl, I. (2010). The Subthreshold Relation between Cortical Local Field Potential and Neuronal Firing Unveiled by Intracellular Recordings in Awake Rats. J. Neurosci. *30*, 4440–4448.

O'Leary, J.L. (1941). Structure of the area striata of the cat. Journal of Comparative Neurology *75*, 131–164.

Olivier, E., Grantyn, A., Chat, M., and Berthoz, A. (1993). The control of slow orienting eye movements by tectoreticulospinal neurons in the cat: behavior, discharge patterns and underlying connections. Exp Brain Res *93*, 435–449.

Olshausen, B.A. (2013). Perception as an Inference Problem.

Orban, G.A., Kennedy, H., and Maes, H. (1981a). Response to movement of neurons in areas 17 and 18 of the cat: direction selectivity. J. Neurophysiol. *45*, 1059–1073.

Orban, G.A., Kennedy, H., and Maes, H. (1981b). Response to movement of neurons in areas 17 and 18 of the cat: velocity sensitivity. J. Neurophysiol. *45*, 1043–1058.

Orban, G.A., Hoffmann, K.P., and Duysens, J. (1985). Velocity selectivity in the cat visual system. I. Responses of LGN cells to moving bar stimuli: a comparison with cortical areas 17 and 18. J. Neurophysiol. *54*, 1026–1049.

Ouelhazi, A., Bharmauria, V., Chanauria, N., Bachatene, L., Lussiez, R., and Molotchnikoff, S. (2019). Effects of ketamine on orientation selectivity and variability of neuronal responses in primary visual cortex. Brain Research *1725*, 146462.

Ozeki, H., Sadakane, O., Akasaki, T., Naito, T., Shimegi, S., and Sato, H. (2004). Relationship between Excitation and Inhibition Underlying Size Tuning and Contextual Response Modulation in the Cat Primary Visual Cortex. J. Neurosci. *24*, 1428–1438.

Ozeki, H., Finn, I.M., Schaffer, E.S., Miller, K.D., and Ferster, D. (2009). Inhibitory stabilization of the cortical network underlies visual surround suppression. Neuron *62*, 578–592.

Parabucki, A., and Lampl, I. (2017). Volume Conduction Coupling of Whisker-Evoked Cortical LFP in the Mouse Olfactory Bulb. Cell Rep *21*, 919–925.

Paulk, A., Millard, S.S., and van Swinderen, B. (2013). Vision in Drosophila: seeing the world through a model's eyes. Annu. Rev. Entomol. *58*, 313–332.

Pecka, M., Han, Y., Sader, E., and Mrsic-Flogel, T.D. (2014). Experience-dependent specialization of receptive field surround for selective coding of natural scenes. Neuron *84*, 457–469.

Peters, A., and Payne, B.R. (1993). Numerical relationships between geniculocortical afferents and pyramidal cell modules in cat primary visual cortex. Cereb. Cortex *3*, 69–78.

Peters, A., and Regidor, J. (1981). A reassessment of the forms of nonpyramidal neurons in area 17 of cat visual cortex. J. Comp. Neurol. *203*, 685–716.

Peterson, M.R., Li, B., and Freeman, R.D. (2004). The derivation of direction selectivity in the striate cortex. J. Neurosci. *24*, 3583–3591.

Petilla Interneuron Nomenclature Group, Ascoli, G.A., Alonso-Nanclares, L., Anderson, S.A., Barrionuevo, G., Benavides-Piccione, R., Burkhalter, A., Buzsáki, G., Cauli, B., Defelipe, J., et al. (2008). Petilla terminology: nomenclature of features of GABAergic interneurons of the cerebral cortex. Nat. Rev. Neurosci. *9*, 557–568.

Pettersen, K.H., Hagen, E., and Einevoll, G.T. (2008). Estimation of population firing rates and current source densities from laminar electrode recordings. J Comput Neurosci *24*, 291–313.

Peyrache, A., Dehghani, N., Eskandar, E.N., Madsen, J.R., Anderson, W.S., Donoghue, J.A., Hochberg, L.R., Halgren, E., Cash, S.S., and Destexhe, A. (2012). Spatiotemporal dynamics of neocortical excitation and inhibition during human sleep. Proc. Natl. Acad. Sci. U.S.A. *109*, 1731–1736.

Portilla, J., and Simoncelli, E.P. A Parametric Texture Model Based on Joint Statistics of Complex Wavelet Coefficients. 23.

Pritchard, R.M., and Heron, W. (1960). Small eye movements of the cat. Can J Psychol *14*, 131–137.

Rasch, M.J., Schuch, K., Logothetis, N.K., and Maass, W. (2011). Statistical comparison of spike responses to natural stimuli in monkey area V1 with simulated responses of a detailed laminar network model for a patch of V1. J. Neurophysiol. *105*, 757–778.

Ratliff, F., and Riggs, L.A. (1950). Involuntary motions of the eye during monocular fixation. J Exp Psychol *40*, 687–701.

Rauske, P.L., Shea, S.D., and Margoliash, D. (2003). State and neuronal class-dependent reconfiguration in the avian song system. J. Neurophysiol. *89*, 1688–1701.

Reinagel, P., and Reid, R.C. (2000). Temporal coding of visual information in the thalamus. J. Neurosci. *20*, 5392–5400.

Ribot, J., Aushana, Y., Bui-Quoc, E., and Milleret, C. (2013). Organization and origin of spatial frequency maps in cat visual cortex. J. Neurosci. *33*, 13326–13343.

Rikhye, R.V., and Sur, M. (2015). Spatial Correlations in Natural Scenes Modulate Response Reliability in Mouse Visual Cortex. J. Neurosci. *35*, 14661–14680.

Rodieck, R.W. (1965). Quantitative analysis of cat retinal ganglion cell response to visual stimuli. Vision Research *5*, 583–601.

Rossant, C., Kadir, S.N., Goodman, D.F.M., Schulman, J., Hunter, M.L.D., Saleem, A.B., Grosmark, A., Belluscio, M., Denfield, G.H., Ecker, A.S., et al. (2016). Spike sorting for large, dense electrode arrays. Nat. Neurosci. *19*, 634–641.

Rougeul-Buser, A., and Buser, P. (1997). Rhythms in the alpha band in cats and their behavioural correlates. Int J Psychophysiol *26*, 191–203.

Rowe, M.H., and Palmer, L.A. (1995). Spatio-temporal receptive-field structure of phasic W cells in the cat retina. Vis. Neurosci. *12*, 117–139.

Rucci, M., and Desbordes, G. (2003). Contributions of fixational eye movements to the discrimination of briefly presented stimuli. J Vis *3*, 852–864.

Ruderman, and Bialek, (1994). Statistics of natural images: Scaling in the woods. Phys. Rev. Lett. *73*, 814–817.

Rust, N.C., Schwartz, O., Movshon, J.A., and Simoncelli, E.P. (2005). Spatiotemporal Elements of Macaque V1 Receptive Fields. Neuron *46*, 945–956.

Rust, N.C., and Movshon, J.A. (2005). In praise of artifice. Nat. Neurosci. *8*, 1647–1650.

Sakata, S., and Harris, K.D. (2009). Laminar structure of spontaneous and sensory-evoked population activity in auditory cortex. Neuron *64*, 404–418.

Samonds, J.M., Geisler, W.S., and Priebe, N.J. (2018). Natural image and receptive field statistics predict saccade sizes. Nat. Neurosci. *21*, 1591–1599.

Scannell, J.W., Blakemore, C., and Young, M.P. (1995). Analysis of connectivity in the cat cerebral cortex. J. Neurosci. *15*, 1463–1483.

Sceniak, M.P., Hawken, M.J., and Shapley, R. (2001). Visual spatial characterization of macaque V1 neurons. J. Neurophysiol. *85*, 1873–1887.

Schmidt, M., Bakker, R., Shen, K., Bezgin, G., Diesmann, M., and Albada, S.J. van (2018). A multi-scale layer-resolved spiking network model of resting-state dynamics in macaque visual cortical areas. PLOS Computational Biology *14*, e1006359.

Schwartz, O., and Simoncelli, E.P. (2001). Natural signal statistics and sensory gain control. Nature Neuroscience *4*, 819–825.

Schwartz, O., Hsu, A., and Dayan, P. (2007). Space and time in visual context. Nat. Rev. Neurosci. *8*, 522–535.

Sedigh-Sarvestani, M., Palmer, L.A., and Contreras, D. (2019). Thalamocortical synapses in the cat visual system in vivo are weak and unreliable. Elife *8*.

Sellers, K. K., Bennett, D. V, & Frölich, F. (2015). Frequency-band signatures of visual responses to naturalistic input in ferret primary visual cortex during free viewing, Brain Research 1598, 31–45.

Seriès, P., Lorenceau, J., and Frégnac, Y. (2003). The “silent” surround of V1 receptive fields: theory and experiments. J. Physiol. Paris *97*, 453–474.

Shadlen, M.N., and Newsome, W.T. (1998). The variable discharge of cortical neurons: implications for connectivity, computation, and information coding. J. Neurosci. *18*, 3870–3896.

Shannon, C.E. (1948). A Mathematical Theory of Communication. Bell System Technical Journal *27*, 379–423.

Shapley, R., and Victor, J. (1986). Hyperacuity in cat retinal ganglion cells. Science *231*, 999–1002.

Sherman, S.M., and Spear, P.D. (1982). Organization of visual pathways in normal and visually deprived cats. Physiol. Rev. *62*, 738–855.

Shmuel, A., and Grinvald, A. (1996). Functional Organization for Direction of Motion and Its Relationship to Orientation Maps in Cat Area 18. J. Neurosci. *16*, 6945–6964.

Shoham, D., Hübener, M., Schulze, S., Grinvald, A., and Bonhoeffer, T. (1997). Spatio-temporal frequency domains and their relation to cytochrome oxidase staining in cat visual cortex. Nature *385*, 529–533.

Shushruth, S., Ichida, J.M., Levitt, J.B., and Angelucci, A. (2009). Comparison of spatial summation properties of neurons in macaque V1 and V2. J. Neurophysiol. *102*, 2069–2083.

Shushruth, S., Nurminen, L., Bijanzadeh, M., Ichida, J.M., Vanni, S., and Angelucci, A. (2013). Different orientation tuning of near- and far-surround suppression in macaque primary visual cortex mirrors their tuning in human perception. J. Neurosci. *33*, 106–119.

Sillito, A.M. (1975). The contribution of inhibitory mechanisms to the receptive field properties of neurones in the striate cortex of the cat. J. Physiol. (Lond.) *250*, 305–329.

Simoncelli, E.P., and Olshausen, B.A. (2001). Natural image statistics and neural representation. Annu. Rev. Neurosci. *24*, 1193–1216.

Sirovich, L., and Uglesich, R. (2004). The organization of orientation and spatial frequency in primary visual cortex. Proc. Natl. Acad. Sci. U.S.A. *101*, 16941–16946.

Skottun, B.C., De Valois, R.L., Grosof, D.H., Movshon, J.A., Albrecht, D.G., and Bonds, A.B. (1991). Classifying simple and complex cells on the basis of response modulation. Vision Res. *31*, 1079–1086.

Smith, M.A., and Kohn, A. (2008). Spatial and Temporal Scales of Neuronal Correlation in Primary Visual Cortex. J. Neurosci. *28*, 12591–12603.

Snyder, A.C., Morais, M.J., Kohn, A., and Smith, M.A. (2014). Correlations in V1 Are Reduced by Stimulation Outside the Receptive Field. J Neurosci *34*, 11222–11227.

Somers, D.C., Nelson, S.B., and Sur, M. (1995). An emergent model of orientation selectivity in cat visual cortical simple cells. J. Neurosci. *15*, 5448–5465.

Somogyi, P., Freund, T.F., Hodgson, A.J., Somogyi, J., Beroukas, D., and Chubb, I.W. (1985). Identified axo-axonic cells are immunoreactive for GABA in the hippocampus and visual cortex of the cat. Brain Res. *332*, 143–149.

Somogyi, P., Tamás, G., Lujan, R., and Buhl, E.H. (1998). Salient features of synaptic organisation in the cerebral cortex. Brain Res. Brain Res. Rev. *26*, 113–135.

Soto-Sánchez, C., Wang, X., Vaingankar, V., Sommer, F.T., and Hirsch, J.A. (2017). Spatial scale of receptive fields in the visual sector of the cat thalamic reticular nucleus. Nat Commun *8*, 800.

Spacek, M.A., and Swindale, N.V. (2016). Cortical state and natural movie responses in cat visual cortex. BioRxiv 031765.

Steriade, M., McCormick, D.A., and Sejnowski, T.J. (1993). Thalamocortical oscillations in the sleeping and aroused brain. Science *262*, 679–685.

Steriade, M., Timofeev, I., Dürmüller, N., and Grenier, F. (1998). Dynamic properties of corticothalamic neurons and local cortical interneurons generating fast rhythmic (30-40 Hz) spike bursts. J. Neurophysiol. *79*, 483–490.

Sterling, P. (1983). Microcircuitry of the cat retina. Annu. Rev. Neurosci. *6*, 149–185.

Stone, J. (1965). A quantitative analysis of the distribution of ganglion cells in the cat's retina. Journal of Comparative Neurology *124*, 337–352.

Swindale, N.V., Matsubara, J.A., and Cynader, M.S. (1987). Surface organization of orientation and direction selectivity in cat area 18. J. Neurosci. *7*, 1414–1427.

Swindale, N.V., Grinvald, A., and Shmuel, A. (2003). The spatial pattern of response magnitude and selectivity for orientation and direction in cat visual cortex. Cereb. Cortex *13*, 225–238.

Szulborski, R.G., and Palmer, L.A. (1990). The two-dimensional spatial structure of nonlinear subunits in the receptive fields of complex cells. Vision Res. *30*, 249–254.

Tamás, G., Buhl, E.H., and Somogyi, P. (1997). Massive autaptic self-innervation of GABAergic neurons in cat visual cortex. J. Neurosci. *17*, 6352–6364.

Tan, A.Y.Y., Chen, Y., Scholl, B., Seidemann, E., and Priebe, N.J. (2014). Sensory stimulation shifts visual cortex from synchronous to asynchronous states. Nature *509*, 226–229.

Tanaka, K. (1983). Distinct X- and Y-streams in the cat visual cortex revealed by bicuculline application. Brain Res. *265*, 143–147.

Tanaka, H., Tamura, H., and Ohzawa, I. (2014). Spatial range and laminar structures of neuronal correlations in the cat primary visual cortex. J. Neurophysiol. *112*, 705–718.

Tang, S., Zhang, Y., Li, Z., Li, M., Liu, F., Jiang, H., and Lee, T.S. (2018). Large-scale two-photon imaging revealed super-sparse population codes in the V1 superficial layer of awake monkeys. ELife Sciences *7*, e33370.

Tarczy-Hornoch, K., Martin, K.A., Jack, J.J., and Stratford, K.J. (1998). Synaptic interactions between smooth and spiny neurones in layer 4 of cat visual cortex in vitro. J. Physiol. (Lond.) *508 (Pt 2)*, 351–363.

Thomson, A.M., and Lamy, C. (2007). Functional maps of neocortical local circuitry. Front Neurosci *1*, 19–42.

Tolhurst, D.J., and Movshon, J.A. (1975). Spatial and temporal contrast sensitivity of striate cortical neurones. Nature *257*, 674–675.

Tolhurst, D.J., Tadmor, Y., and Chao, T. (1992). Amplitude spectra of natural images. Ophthalmic Physiol Opt *12*, 229–232.

Touryan, J., Lau, B., and Dan, Y. (2002). Isolation of relevant visual features from random stimuli for cortical complex cells. J. Neurosci. *22*, 10811–10818.

Touryan, J., Felsen, G., and Dan, Y. (2005). Spatial structure of complex cell receptive fields measured with natural images. Neuron *45*, 781–791.

Troy, J.B. (1987). Do Y geniculate neurons have greater contrast sensitivity than X geniculate neurons at all visual field locations? Vision Res. *27*, 1733–1735.

Tusa, R.J., Palmer, L.A., and Rosenquist, A.C. (1978). The retinotopic organization of area 17 (striate cortex) in the cat. J. Comp. Neurol. *177*, 213–235.

Usrey, W.M., and Alitto, H.J. (2015). Visual Functions of the Thalamus. Annu Rev Vis Sci *1*, 351–371.

Vacher, J., Meso, A.I., Perrinet, L.U., and Peyré, G. (2018). Bayesian Modeling of Motion Perception Using Dynamical Stochastic Textures. Neural Computation *30*, 3355–3392.

Van Hooser, S.D. (2007). Similarity and Diversity in Visual Cortex: Is There a Unifying Theory of Cortical Computation? Neuroscientist *13*, 639–656.

VanRullen, R., Busch, N.A., Drewes, J., and Dubois, J. (2011a). Ongoing EEG Phase as a Trial-by-Trial Predictor of Perceptual and Attentional Variability. Front Psychol *2*.

VanRullen, R., Busch, N., Drewes, J., and Dubois, J. (2011b). Ongoing EEG Phase as a Trial-by-Trial Predictor of Perceptual and Attentional Variability. Front. Psychol. *2*.

Vidyasagar, T.R. (1998). Gating of neuronal responses in macaque primary visual cortex by an attentional spotlight. NeuroReport *9*, 1947.

Vidyasagar, T.R., and Urbas, J.V. (1982). Orientation sensitivity of cat LGN neurones with and without inputs from visual cortical areas 17 and 18. Exp Brain Res *46*, 157–169.

Vinje, W.E., and Gallant, J.L. (2000). Sparse Coding and Decorrelation in Primary Visual Cortex During Natural Vision. Science *287*, 1273–1276.

van Vreeswijk, C., and Sompolinsky, H. (1996). Chaos in neuronal networks with balanced excitatory and inhibitory activity. Science *274*, 1724–1726.

Vries, S.E.J. de, Lecoq, J., Buice, M.A., Groblewski, P.A., Ocker, G.K., Oliver, M., Feng, D., Cain, N., Ledochowitsch, P., Millman, D., et al. (2018). A large-scale, standardized physiological survey reveals higher order coding throughout the mouse visual cortex. BioRxiv 359513.

Wallace, D.J., Greenberg, D.S., Sawinski, J., Rulla, S., Notaro, G., and Kerr, J.N.D. (2013). Rats maintain an overhead binocular field at the expense of constant fusion. Nature *498*, 65–69.

Wang, Y., Jin, J., Kremkow, J., Lashgari, R., Komban, S.J., and Alonso, J.M. (2015). Columnar organization of spatial phase in visual cortex. Nat. Neurosci. *18*, 97–103.

Webb, B.S., Dhruv, N.T., Solomon, S.G., Tailby, C., and Lennie, P. (2005). Early and late mechanisms of surround suppression in striate cortex of macaque. J. Neurosci. *25*, 11666–11675.

Weliky, M., Fiser, J., Hunt, R.H., and Wagner, D.N. (2003). Coding of Natural Scenes in Primary Visual Cortex. Neuron *37*, 703–718.

Willmore, B., and Tolhurst, D.J. (2001). Characterizing the sparseness of neural codes. Network: Computation in Neural Systems *12*, 255–270.

Wilson, M.E., and Cragg, B.G. (1967). Projections from the lateral geniculate nucleus in the cat and monkey. J. Anat. *101*, 677–692.

Xing, D., Yeh, C.-I., and Shapley, R.M. (2009). Spatial spread of the local field potential and its laminar variation in visual cortex. J. Neurosci. *29*, 11540–11549.

Yao, H., Shi, L., Han, F., Gao, H., and Dan, Y. (2007). Rapid learning in cortical coding of visual scenes. Nat. Neurosci. *10*, 772–778.

Yarbus, A.L. (1967). Eye Movements During Perception of Complex Objects. In Eye Movements and Vision, A.L. Yarbus, ed. (Boston, MA: Springer US), pp. 171–211.

Yeh, C.-I., Xing, D., Williams, P.E., and Shapley, R.M. (2009). Stimulus ensemble and cortical layer determine V1 spatial receptive fields. Proc. Natl. Acad. Sci. U.S.A. *106*, 14652–14657.

Yen, S.-C., Baker, J., and Gray, C.M. (2007). Heterogeneity in the Responses of Adjacent Neurons to Natural Stimuli in Cat Striate Cortex. Journal of Neurophysiology *97*, 1326–1341.

Yuste, R. (2015). From the neuron doctrine to neural networks. Nature Reviews Neuroscience *16*, 487–497.

Zhang, L., and Li, B. (2013). Surround modulation characteristics of local field potential and spiking activity in primary visual cortex of cat. PLoS ONE *8*, e64492.

Zhu, Y., Qiao, W., Liu, K., Zhong, H., and Yao, H. (2015). Control of response reliability by parvalbumin-expressing interneurons in visual cortex. Nature Communications *6*, 6802.

Ziemba, C.M., Freeman, J., Movshon, J.A., and Simoncelli, E.P. (2016). Selectivity and tolerance for visual texture in macaque V2. Proc. Natl. Acad. Sci. U.S.A. *113*, E3140-3149.

Ziemba, C.M., Freeman, J., Simoncelli, E.P., and Movshon, J.A. (2018). Contextual modulation of sensitivity to naturalistic image structure in macaque V2. J. Neurophysiol. *120*, 409–420.

(2002). The Cat Primary Visual Cortex (Elsevier).